



AMERICAN METEOROLOGICAL SOCIETY

Monthly Weather Review

EARLY ONLINE RELEASE

This is a preliminary PDF of the author-produced manuscript that has been peer-reviewed and accepted for publication. Since it is being posted so soon after acceptance, it has not yet been copyedited, formatted, or processed by AMS Publications. This preliminary version of the manuscript may be downloaded, distributed, and cited, but please be aware that there will be visual differences and possibly some content differences between this version and the final published version.

The DOI for this manuscript is doi: 10.1175/MWR-D-16-0417.1

The final published version of this manuscript will replace the preliminary version at the above DOI once it is available.

If you would like to cite this EOR in a separate work, please use the following full citation:

Bengtsson, L., U. Andrae, T. Aspelien, Y. Batrak, J. Calvo, W. de Rooy, E. Gleeson, B. Hansen-Sass, M. Homleid, M. Hortal, K. Ivarsson, G. Lenderink, S. Niemelä, K. Pagh Nielsen, J. Onvlee, L. Rontu, P. Samuelsson, D. Santos Muñoz, A. Subias, S. Tijm, V. Toll, X. Yang, and M. Ødegaard Køltzow, 2017: The HARMONIE-AROME model configuration in the ALADIN-HIRLAM NWP system. Mon. Wea. Rev. doi:10.1175/MWR-D-16-0417.1, in press.



1 The HARMONIE-AROME model configuration in the ALADIN-HIRLAM 2 NWP system

3 Lisa Bengtsson*

4 Swedish Meteorological and Hydrological Institute, SMHI, Norrköping, Sweden.

5 Ulf Andrae

6 Swedish Meteorological and Hydrological Institute, SMHI, Norrköping, Sweden.

7 Trygve Aspelien

8 Norwegian Meteorological Institute, MET, Oslo, Norway

9 Yurii Batrak

10 Norwegian Meteorological Institute, MET, Oslo, Norway

11 Javier Calvo

12 Agencia Estadal de Meteorologia, AEMET, Madrid, Spain

13 Wim de Rooy

14 The Royal Netherlands Meteorological Institute, KNMI, De Bilt, Netherlands

15 Emily Gleeson

16 Met Éireann, Dublin, Ireland

17

Bent Hansen-Sass

18

Danish Meteorological Institute, DMI, Copenhagen, Denmark

19

Mariken Homleid

20

Norwegian Meteorological Institute, MET, Oslo, Norway

21

Mariano Hortal

22

Agencia Estadal de Meteorología AEMET, Madrid, Spain

23

Karl-Ivar Ivarsson

24

Swedish Meteorological and Hydrological Institute, SMHI, Norrköping, Sweden

25

Geert Lenderink

26

The Royal Netherlands Meteorological Institute, KNMI, De Bilt, Netherlands

27

Sami Niemelä

28

Finnish Meteorological Institute, FMI, Helsinki, Finland

29

Kristian Pagh Nielsen

30

Danish Meteorological Institute, DMI, Copenhagen, Denmark

31

Jeanette Onvlee

32

The Royal Netherlands Meteorological Institute, KNMI, De Bilt, Netherlands

33

Laura Rontu

34

Finnish Meteorological Institute, FMI, Helsinki, Finland

35

Patrick Samuelsson

³⁶ *Swedish Meteorological and Hydrological Institute, SMHI, Norrköping, Sweden*

³⁷ **Daniel Santos Muñoz**

³⁸ *Agencia Estatal de Meteorología AEMET, Madrid, Spain*

³⁹ **Alvaro Subias**

⁴⁰ *Agencia Estatal de Meteorología AEMET, Madrid, Spain*

⁴¹ **Sander Tijm**

⁴² *The Royal Netherlands Meteorological Institute, KNMI, De Bilt, Netherlands*

⁴³ **Velle Toll**

⁴⁴ *University of Tartu, Tartu, Estonia*

⁴⁵ **Xiaohua Yang**

⁴⁶ *Danish Meteorological Institute, DMI, Copenhagen, Denmark*

⁴⁷ **Morten Ødegaard Køltzow**

⁴⁸ *Norwegian Meteorological Institute, MET, Oslo, Norway*

⁴⁹ *Corresponding author address: Research Department., SMHI, Folkborgsvagen 17, Norrkoping,
⁵⁰ Sweden.

⁵¹ E-mail: lisa.bengtsson@smhi.se

ABSTRACT

52 The aim of this article is to describe the reference configuration of
53 the convection permitting Numerical Weather Prediction (NWP) model
54 HARMONIE-AROME which is used for operational short range weather
55 forecasts in Denmark, Estonia, Finland, Iceland, Ireland, Lithuania, Nether-
56 lands, Norway, Spain and Sweden. It is developed, maintained and vali-
57 dated as part of the shared ALADIN-HIRLAM system by a collaboration
58 of 26 countries in Europe and Northern Africa on short range meso-scale
59 NWP. HARMONIE-AROME is based on the model AROME-France devel-
60 oped within the ALADIN consortium. Along with the joint modelling frame-
61 work, AROME was implemented and utilised in both northern and southern
62 European conditions by the above listed countries, and this activity has led
63 to extensive updates to the model's physical parameterizations. In this pa-
64 per we present the differences in model dynamics and physical parameteri-
65 zations compared with AROME-France, as well as important configuration
66 choices of the reference, such as lateral boundary conditions, model levels,
67 horizontal resolution, model time-step, as well as topography, physiography
68 and aerosol data-bases used. Separate documentation will be provided for the
69 atmospheric and surface data-assimilation algorithms and observation types
70 used, as well as a separate description of the Ensemble Prediction System
71 based on HARMONIE-AROME, which is called HarmonEPS.

⁷² **1. Introduction**

⁷³ There is a strong history of active collaboration between European meteorological institutes on
⁷⁴ Numerical Weather Prediction (NWP), in order to develop and maintain numerical short-range
⁷⁵ weather forecasting systems for operational use.

⁷⁶ The international research program HIRLAM (HIgh Resolution Limited Area Model) was ini-
⁷⁷ tiated in 1985, and consists today of the National Meteorological Services (NMSs) from 10 coun-
⁷⁸ tries: Denmark, Estonia, Finland, Iceland, Ireland, Lithuania, Netherlands, Norway, Spain and
⁷⁹ Sweden, with France as an associate member. Similarly, the collaboration among the NMSs of
⁸⁰ central Europe, ALADIN (Aire Limitée Adaptation dynamique Développement InterNational)
⁸¹ started in 1991, and consists today of 16 member countries: Algeria, Austria, Belgium, Bulgaria,
⁸² Croatia, the Czech Republic, France, Hungary, Morocco, Poland, Portugal, Romania, Slovakia,
⁸³ Slovenia, Tunisia and Turkey.

⁸⁴ The ALADIN NWP system is being developed within the frameworks of ARPEGE (Action
⁸⁵ de Recherche Petite Echelle Grande Echelle) and IFS (Integrated Forecasting System) software,
⁸⁶ developed jointly by the European Centre for Medium-range Weather Forecasts (ECMWF) and
⁸⁷ Météo-France. A more detailed explanation of the ALADIN code architecture and its canon-
⁸⁸ ical model configurations; AROME (Application of Research to Operations at Mesoscale) and
⁸⁹ ALARO can be found in Termonia et al. (2017).

⁹⁰ On December 5, 2005, a cooperation agreement between the ALADIN and HIRLAM consortia
⁹¹ was signed with the prime objective “to provide the ALADIN and the HIRLAM Members with a
⁹² state-of-the-art NWP-model for short and very short range forecasting including nowcasting, for
⁹³ both research and development activities and operational usage” (Malcorps and Ågren 2005). In
⁹⁴ 2014, the ALADIN and HIRLAM consortia further agreed on the formation of a single, united

95 consortium by 2020 and are currently working on this objective. Since 2005, the focus of the
96 HIRLAM research collaboration has been on the convection-permitting scale, and on adapting the
97 AROME model (Seity et al. 2011) for use in the common ALADIN-HIRLAM NWP system, in
98 order to make it accessible for all 26 countries.

99 The scripting system, which facilitates data-assimilation and observation handling, climate gen-
100 eration, lateral boundary coupling and post-processing required to run AROME operationally
101 within the HIRLAM countries, is referred to as the “HARMONIE (HIRLAM ALADIN Research
102 on Meso-scale Operational NWP in Europe) script system”. However, the implementation and
103 optimization of AROME for both northern and southern European conditions, has led to extensive
104 adaptations and improvements to the model’s physical parameterizations. This was done in order
105 to reduce existing biases and improve the physical description of clouds (mixed phase) and the
106 land surfaces, especially in northern latitude conditions. The model configuration which uses the
107 updates in the physical parameterizations has also been referred to as “HARMONIE”, in order
108 to distinguish it from the AROME-France setup. Thus, there is an increased need to clarify and
109 document what is meant by “HARMONIE”.

110 The aim of this paper is to describe the reference model configuration of AROME as defined
111 by the HIRLAM consortia; HARMONIE-AROME. It summarizes the changes to the physical
112 parameterizations and dynamics used in HARMONIE-AROME with respect to the description of
113 AROME-France given by Seity et al. (2011) and Brousseau et al. (2016). This paper is limited to
114 the forecast model description of version cycle 40h1.1¹. Separate documentation will be provided
115 for the atmospheric and surface data-assimilation algorithms and observation types used, as well as

¹The ALADIN-HIRLAM limited area system is part of the code base of the IFS/ARPEGE system of ECMWF and Météo-France. The cycle number refers to the main model version as released by ECMWF. The subsequent letter (r,t or h) refers to new model updates released by ECMWF, ALADIN or HIRLAM consortia, respectively.

₁₁₆ a separate description of the Ensemble Prediction System based on HARMONIE-AROME, which
₁₁₇ is called HarmonEPS.

₁₁₈ **2. Model Dynamics**

₁₁₉ HARMONIE-AROME uses the same non-hydrostatic (NH) dynamical core as AROME-France,
₁₂₀ which has been developed by ALADIN (Bubnova et al. 1995; Bénard et al. 2010). It is based on
₁₂₁ the fully compressible Euler equations (Simmons and Burridge 1981; Laprise 1992). The evo-
₁₂₂ lution of the equations is discretized in time and space using a semi-Lagrangian (SL) advection
₁₂₃ scheme on an A-grid and a semi-Implicit (SI) two-time level scheme, with spectral representation
₁₂₄ of most prognostic variables based on a double Fourier decomposition. The spectral SI SL scheme
₁₂₅ originates from the global IFS used operationally at ECMWF (ECMWF 2015a). Horizontal diffu-
₁₂₆ sion is applied both by linear spectral diffusion and nonlinear flow dependent diffusion which acts
₁₂₇ through semi-Lagrangian (SL) advection, and thus was given the name semi-Lagrangian horizon-
₁₂₈ tal diffusion (SLHD) (Váňa et al. 2008; Bengtsson et al. 2012). Quasi-monotonic operators in the
₁₂₉ interpolation process are used in order to remove the appearance of negative values for positive
₁₃₀ definite fields, as well as an unrealistic increase of eddy kinetic energy during the forecast (Seity
₁₃₁ et al. 2011).

₁₃₂ The so called Stable Extrapolation Two-Time-Level Scheme or SETTLS, specific to the
₁₃₃ HARMONIE-AROME configuration, is used as the second order two-time-level scheme in or-
₁₃₄ der to avoid extrapolation in time of the velocities used for the computation of the trajectories,
₁₃₅ and for the nonlinear terms, of the evolution equations (Hortal 2002). Furthermore, in order to
₁₃₆ assure stability of the integrations, a new method for treating the upper boundary conditions was
₁₃₇ implemented, using the same Davies-Kallberg relaxation scheme as for the horizontal (Davies
₁₃₈ 1976). This method makes it possible to use SETTLS also for horizontal resolutions below 1 km,

139 so there is no need to use the so called “Predictor-Corrector” method which was previously used
140 for very high resolution simulations. Another method introduced in order to ensure stability for
141 cases where data assimilation is not used, is to limit the 3-dimensional divergence for the first few
142 time-steps until equilibrium is reached. This was done in order to avoid occasional crashes when
143 the model starts from model data which is interpolated from a lower-resolution hydrostatic model.

144 There is also a possibility to run the IFS/ARPEGE software with alternative spectral grids, such
145 as cubic and quadratic grids and for such grids, a further spectral truncation is performed. Test
146 simulations in HARMONIE-AROME with a cubic grid shows a reduction of the computational
147 time with more than 20%. However, noticeable smoothing and degradation for wind speed in
148 areas of steep orography can be seen compared with the linear grid. Two reasons to consider
149 it nonetheless are 1) to permit running meso-scale ensembles at a reasonable cost, though with
150 somewhat reduced performance with respect to the linear grid, or 2) to reduce model costs of a
151 model upgrade to higher grid-point resolution. In case of the linear grid, the use of a filter to the
152 vorticity part of the pressure-gradient term is applied, in order to eliminate some noise. The method
153 has been applied in the ECMWF model (Nils Weidi, personal comm. 2016), and is introduced in
154 HARMONIE-AROME with the addition of filtering the pressure departure. In case of quadratic
155 and the cubic grids, the filter is not necessary since the waves modified by the procedure are cut
156 out in those cases.

157 The Euler equations in AROME-France (and HARMONIE-AROME) are formulated in a
158 terrain-following pressure-based sigma-coordinate system (Simmons and Burridge 1981; Laprise
159 1992; Bubnova et al. 1995). For the model dynamics, the mean orography may be truncated and
160 smoothed, depending on the transformation between spectral and grid-point representations. For
161 the linear grid of HARMONIE-AROME, a reduction by a factor of five of the shortest wavelength
162 spectrum of the surface elevation is obtained by means of a 16th order diffusion operator. After

163 smoothing, the atmospheric and surface physical parametrizations refer to the smoothed grid-scale
164 surface elevation. The smoothed or truncated grid-scale surface elevation represents scales some-
165 what greater than the model's nominal horizontal resolution.

166 In the reference cycle of HARMONIE-AROME cycle 40h1.1 lateral boundary conditions are
167 routinely used from the ECMWF model, as opposed to the AROME-France configuration in which
168 the global ARPEGE model is used to provide the lateral boundary conditions (the HARMONIE
169 script system however allows to couple the model to a number of global forecast models). Sixty-
170 five levels are used in the vertical, with model top at ca 10 hpa and lowest level at 12 m. The
171 horizontal resolution is 2.5 km, and the model time-step is 75 seconds.

172 3. Model Physics

173 a. Radiation

174 The default shortwave (SW) radiation parametrization in AROME-France and HARMONIE-
175 AROME is the Morcrette radiation scheme from ECMWF, IFS cycle 25R1, and contains six spec-
176 tral intervals ($0.185 - 0.25 - 0.44 - 0.69 - 1.1 - 2.38 - 4.00 \mu\text{m}$). The default longwave (LW) radi-
177 ation scheme contains 16 spectral bands between 3.33 and $1000 \mu\text{m}$. This uses the Rapid Radiative
178 Transfer Model (RRTM) of Mlawer et al. (1997). Both the SW and LW schemes are described in
179 the IFS (ECMWF 2015b) and the meso-scale research model Meso-NH (Mascart and Bougeault
180 2011) documentation. Due to computational constraints the full radiation calculations are currently
181 performed every 15 minutes. The more affordable single-band radiation schemes from ALARO
182 physics (ACRANE2, Mašek et al. 2016; Geleyn et al. 2017) and HIRLAM (HLRADIA, Savijärvi
183 1990; Wyser et al. 1999), which can be run at each time-step, have also been implemented in
184 HARMONIE-AROME for experimentation purposes. Hereafter, unless stated otherwise, when

185 we refer to the SW and LW radiation schemes the default parametrizations are implied. The fol-
186 lowing description focuses on SW parametrizations because the LW RRTM scheme is applied
187 with minimal modifications.

188 The clear-sky SW radiative transfer is calculated using the Fouquart and Bonnel (1980) two-
189 stream equations. The reflectance, absorption and transmittance of the clear-sky fraction of the
190 atmospheric layers are calculated in a similar manner to that outlined in Coakley Jr. and Chylek
191 (1975). The cloudy sky SW computations are done using the delta-Eddington approximation
192 of Joseph et al. (1976). The radiative transfer calculations use the inherent optical properties
193 (IOPs: optical thickness, single scattering albedo (SSA), asymmetry factor (g)) of cloud particles
194 (prognostic specific cloud liquid and cloud ice content), aerosols (monthly climatologies) and
195 atmospheric gases (prognostic H₂O, a fixed composition mixture of CO₂, N₂O, CH₄ and O₂,
196 monthly climatologies of O₃).

197 A variety of options for the parametrization of cloud particle size and shape, and for the conse-
198 quent derivation of cloud optical properties, are available within the IFS radiation scheme. Table
199 1 shows the choices recommended for the HARMONIE-AROME reference cycle 40h1.1. These
200 choices differ from the defaults used in the AROME-France cycle 40t1 set-up (Seity et al. 2011).
201 In particular, we have introduced an improved cloud liquid optical property scheme (Nielsen et al.
202 2014; Gleeson et al. 2015), which is based on detailed Mie theory computations. In comparison
203 with the accurate one-dimensional radiative transfer model, DISORT (Stamnes et al., 1988, 2000)
204 the new cloud liquid optical property scheme is shown superior than the previous scheme. Fur-
205 thermore, in the previous version of the model, the cloud inhomogeneity factor was assumed to
206 be 0.7 in order to account for a variability of cloud in a grid-box. This assumption is no longer
207 valid with increased model grid resolution (pers. comm. Hogan 2014; unpublished Townsend
208 dissertation 2015), thus we have assumed that the clouds are homogeneous where present in a

grid cell. As a first approximation, the radiative effect of precipitating graupel and snow particles is included by assuming these to have the same inherent optical properties as cloud ice; this was done in conjunction with the inclusion of the cloud microphysics updates described in Section b in “Model physics”. Both the Nielsen scheme and the reduced cloud inhomogeneity lead to a decrease in the downwelling SW radiation flux (Gleeson et al. 2015). However, an over-estimation of low level clouds have been reduced in the new cycle by introducing stronger mixing in the boundary layer, using a new turbulence scheme (described further down), thus the overall impact of the radiation updates in the new cycle are rather neutral, albeit more correct. In each column, a maximum-random cloud overlap is assumed in the vertical.

The direct SW radiative effect of aerosols is calculated using vertically integrated aerosol optical depth (AOD) at a wavelength of 550 nm (AOD550) and the following aerosol IOPs: AOD spectral scaling coefficients and spectral SSA and g. The indirect radiative effect of aerosols due to cloud particle formation is not included in the current version of HARMONIE-AROME. Monthly climatologies of AOD550 of land, sea, desert and urban tropospheric aerosols from the Tegen et al. (1997) climatology are used along with background stratospheric aerosols in a similar manner to the IFS model (ECMWF 2015b). These are distributed among the model levels using the Tanré et al. (1984) climatological vertical profiles for each aerosol type (see Gleeson et al. 2016; Toll et al. 2016). The spectral dependence of AOD, SSA and g for each aerosol type is parameterized following Hess et al. (1998). Toll et al. (2016) showed that in the Tegen et al. (1997) climatology the AODs are underestimated over Europe compared to more recent datasets, especially near the Atlantic Ocean coasts. This leads to some overestimation of the clear-sky SW irradiance at the surface.

Grid-scale surface SW albedo and LW emissivity, required as a boundary condition by the radiation parametrizations, are based on surface characteristics given by the 1 km resolution

233 ECOCLIMAP database (Faroux et al. 2013) and processed by the SURFEX externalised surface
234 scheme (Masson et al. 2013, described in more detail in Section e in “Model physics”). Ultravio-
235 let, visible and near-infrared values of the surface albedo are mapped to the six SW spectral bands
236 for the ECMWF IFS scheme (IFS cycle 25R1; ECMWF 2015b) though the UV albedo is unused
237 in practice. The single-band ACRANE2 scheme is interfaced to SURFEX using one SW spec-
238 tral interval on both sides. By default, SURFEX assumes the same value for the direct and diffuse
239 albedo for each band. We improved this by applying an empirical correction, which depends on
240 the solar zenith angle (*SZA*), to the diffuse albedo(α_{dif}) in order to derive the direct beam albedo
241 (α_{dir}): $\alpha_{dir} = \alpha_{dif} + 0.2/(1 + \cos(SZA)) - 0.12$. This correction was imported from the HIRLAM
242 model (Unden 2002).

243 Diagnostic output from the radiation parametrizations includes accumulated spectrally averaged
244 downwelling SW global, direct and direct normal irradiances at the surface and net SW and LW
245 radiative fluxes at the top of the atmosphere, at the surface and on each model level. The down-
246 welling diffuse SW radiation can be obtained from the difference between the global and direct ra-
247 diation at the surface. Diffuse radiation includes both cloudy and clear sky contributions, whereas
248 a small part of the direct radiation is assumed to come from the cloudy sky. In the original IFS
249 cycle 25R1 scheme, direct and clear-sky radiation were assumed to be identical as were diffuse
250 and cloudy-sky radiation fluxes, which are incorrect assumptions.

251 *b. Clouds and Cloud Microphysics*

252 The microphysics scheme used in AROME-France and HARMONIE-AROME is a one-moment
253 bulk scheme, which uses a three-class ice parametrization, referred to as ICE3, originally devel-
254 oped for meso-NH (Pinty and Jabouille 1998; Lascaux et al. 2006). It contains the following
255 solid hydrometeors as prognostic variables; cloud ice, snow and a combination of graupel and

256 hail. Graupel and hail may be separated by using an own prognostic variable for hail, but this is
257 still in research mode at present. The other prognostic variables used in the cloud microphysics
258 scheme are water vapour, cloud liquid water and rain. All hydrometeors are advected horizon-
259 tally by a semi-Lagrangian scheme and vertically by a sedimentation scheme described in detail
260 in Bouteloup et al. (2011). 3D cloud fraction is not a prognostic variable but instead is determined
261 using a statistical cloud and condensation scheme (Bougeault 1982; Bechtold et al. 1995).

262 Some weaknesses in the original scheme have been detected, particularly in the stable boundary
263 layer during winter over Northern Europe. In these situations the model generates ice too quickly
264 when temperatures in the clouds are between -5°C and -10°C , where some supercooled liquid
265 would be expected. Furthermore, at temperatures lower than -20°C , spurious clouds are often
266 present at the lowest model level and may be treated as “fog” by users of the model output, while
267 observations show clear skies. The reason for this is that the original scheme, by construction, re-
268 moves most supersaturation with respect to ice in regions where the temperature is below -20°C ,
269 and forms ice-clouds, while in reality supersaturation in such conditions is common, since ice
270 clouds are formed at a much slower rate than the typical time step used in the model.

271 In order to address these weaknesses, substantial updates have been made to the cloud micro-
272 physics scheme under the option “OCND2”, which were introduced in order to improve clouds in
273 cold conditions, described in more detail in Müller et al. (2016). The main difference compared
274 to the original scheme is that in OCND2, the fraction of the grid box with cloud ice (and with
275 supersaturation with respect to ice) is no longer handled by the large-scale condensation and ther-
276 modynamic adjustment scheme; instead, it is parameterized using a cloud-scheme based on the
277 critical relative humidity with respect to ice. In the original scheme, even though cloud ice is a
278 prognostic variable, it is treated similarly to a diagnostic quantity as it is a function of temperature
279 only. In OCND2, only cloud water is handled by the large scale condensation and thermodynamic

adjustment scheme, cloud ice is treated by the rest of the ICE3 microphysics, which includes
sublimation, evaporation and interactions with other water species.

Besides this improved separation between the fast liquid processes and the slower ice water processes, some other updates are included in the OCND2 scheme; a reduction of the deposition rate of the ice-phase water species, a correction of the total cloud cover to address the lower optical thickness of ice clouds compared with water clouds, and a reduction of the ice nucleolus concentration in temperatures between 0 °C and –25 °C. Furthermore, the process of rain drop activation from cloud droplets (auto-conversion) is parameterized using the “Kogan auto-conversion” parameterization (Khairoutdinov and Kogan 2000) as opposed to the Kessler (1969) scheme used in AROME-France.

An example of the impact of OCND2 on modelled cloud liquid and ice phases can be seen in Figure 1. The cloud liquid and cloud ice phases from model runs with and without OCND2 are compared with observations from the Hyytiälä station located close to Helsinki, Finland for the month of February, 2014. Hyytiälä is an “ARM mobile facility”, and data from the site are used within the CLOUDNET project (Illingsworth et al. 2007) to evaluate the representation of clouds in climate and weather forecast models. The observed cloud liquid water content is calculated within CLOUDNET using both cloud radar and lidar as well as dual-wavelength microwave radiometers. More information about the CLOUDNET method can be found in Illingworth et al. (2007) and references therein. The OCND2 scheme improves the representation of mixed-phase and pure ice-clouds in the model in the wintertime by increasing the amount of liquid water in low level clouds in cold conditions, and decreasing the amount of ice water content (ice+graupel+snow) in low level clouds, such that they are closer to the observed (by CLOUDNET) values of liquid and ice water content (Figure 1). In the summertime the impact is not as large; however, more super-

303 cooled liquid can be seen in higher altitude clouds with the OCND2 scheme in the summer time
304 which is closer to the observations (not shown).

305 The new representation of mixed-phase clouds has led to an improvement in many of the mete-
306 orological fields. In particular it has led to a reduction of a cold bias in the 2 meter temperature
307 during wintertime (over Scandinavia) and reduction of an existing dry bias in relative humidity
308 throughout the lower atmosphere in winter (see Figure 2).

309 *c. Turbulence*

310 In earlier versions of HARMONIE-AROME a number of persistent deficiencies in the represen-
311 tation of the boundary layer could be observed: too low boundary layer heights and clouds base,
312 too much cloud cover, and too much fog, in particular over sea (de Rooy 2014). 1D versions of
313 AROME-France and HARMONIE-AROME participated in the Atlantic Stratocumulus to Cumu-
314 lus Transition Experiment (ASTEX) inter-comparison study. Results of HARMONIE-AROME
315 with the CBR turbulence scheme used in AROME-France (Cuxart et al. 2000; Seity et al. 2011)
316 revealed a substantial underestimation of the cloud top entrainment by the turbulence scheme for
317 this case (de Rooy 2014).

318 Therefore, a new turbulence scheme, HARATU (HARMONIE with RACMO Turbulence),
319 which has a larger cloud top entrainment, has been implemented in HARMONIE-AROME cy-
320 cle 40h1.1. HARATU is based on a scheme that was originally developed for use in the regional
321 climate model RACMO (Van Meijgaard et al. 2012; Lenderink and Holtslag 2004). Similar to
322 the CBR scheme it uses a framework with a prognostic equation for the turbulent kinetic energy
323 (TKE) combined with a diagnostic length scale. The TKE equation includes source (+) and sink
324 (-) terms due to wind shear (+), buoyancy (+ for unstable and - for stable conditions), transport
325 (locally + or -, but no net effect) and dissipation of TKE (-).

326 Compared to the CBR scheme there are considerable changes in the length scale formulation
327 and the constants used. In the CBR scheme there is one “master” length scale, which is multiplied
328 by a number of stability dependent functions. In HARATU the stability corrections are part of the
329 length scale formulation. As such, there are different length scales for heat and momentum. Also,
330 the numerical implementation of the TKE equation has been changed from “full” levels (where
331 the temperature, moisture and wind are computed) to “half” levels (where the fluxes are com-
332 puted). This choice avoids unnecessary vertical interpolations in the computation of the turbulent
333 fluxes, and the source and sink terms of the TKE equation. In particular in the case of strong
334 gradient this gives more reliable estimates of the turbulent fluxes, and vastly improves the cloud
335 top entrainment.

336 The length scale formulation in HARATU essentially consists of two parts, one for stable con-
337 dition and one for near neutral to convective conditions (see Lenderink and Holtslag (2004) for
338 an extensive description). The stable length scale formulation is the commonly used buoyancy
339 based length scale given by the square root of TKE divided by the vertical stability (Deardorff
340 1980; Baas et al. 2008). The neutral/unstable length scale consist of vertical integrals of stability
341 dependent functions. This is done in an upward and a downward computation, and the resulting
342 upward and downward length scale are averaged to obtain the neutral/unstable length scale. The
343 stability functions use the Richardson number (Ri), which allows us to match with surface layer
344 similarity for near neutral conditions (Lenderink and Holtslag 2004).

345 Stability coefficients take into account moist processes; i.e the effect of latent heat on stability
346 due to condensation or evaporation of cloud droplets. In general, these moist processes introduce a
347 strong coupling between the turbulence scheme and the cloud and condensation scheme, and this
348 makes moist turbulence schemes very susceptible to numerical instability and noise (Lenderink
349 et al. 2004; Lenderink and Van Meijgaard 2001). The length scale formulation here is rather

350 insensitive to those numerical instabilities mainly because of its formulation where the integral
351 over stability is used. Having this formulation generally produces smooth and continuous results,
352 in particular in the presence of clouds (Lenderink and Holtslag 2004; Lenderink et al. 2004).

353 With respect to the original turbulence scheme described in Lenderink and Holtslag (2004), a
354 few important modifications have been made when implementing the scheme in HARMONIE-
355 AROME. In order to combine the scheme with the dual mass flux scheme described below, the
356 stability functions for the near neutral/unstable length scale formulation had to be modified for the
357 following reason. The mixing of heat due to the mass flux scheme in a convective boundary layer
358 leads to a slightly stable temperature profile in the upper part of the mixed layer, which is consistent
359 with Large Eddy Simulation (LES) of a convective boundary layer (de Roode et al. 2004). With
360 the original formulation this leads to a strong and unrealistic reduction of the mixing length in
361 the upper part of the convective boundary layer. To avoid this, we adjusted the stability functions
362 using a first order approximation of the change in the profile due to the mass flux contribution.
363 Also, a small modification was made to avoid the discontinuity in the Richardson number in the
364 case of vanishing wind shear.

365 The maximum wind speeds over land in strong wind conditions ($> 10 \text{ m/s}$) with the original
366 formulation described in Lenderink and Holtslag (2004) turned out to be approximately 10% lower
367 than with the CBR scheme, and appeared to be too low compared to measurements. For this
368 reason, we performed a small retuning of the scheme by enhancing the mixing length near the
369 surface (effectively by 20% for neutral conditions) and adjusting the “downward” length scale
370 formulation, leading to a more effective downward mixing of momentum in the case of strong
371 winds over land. This modification has almost no influence over sea, and for weak to moderate
372 (below 10 ms^{-1}) wind speeds over land.

373 The implementation of HARATU has considerably reduced the cloud cover, and resulted in an
374 increase in clouds base height compared to the CBR scheme (de Rooy and de Vries 2017). Fur-
375 thermore, the HARATU scheme also considerably improves the wind climatology of the model.
376 As an example, over the Netherlands domain, the bias in the diurnal cycle of the mean wind speed
377 is almost zero during the whole day, whereas the previous turbulence scheme as well as the scheme
378 used in the operational ECMWF model (cy41, T1279) shows a clear diurnal signal in the bias over
379 the same domain (see Figure 3a). This reduction of 10m wind speed bias has also been seen in all
380 of the other domains running HARMONIE-AROME operationally (not shown). The scheme also
381 improves the standard error and absolute error of the wind forecast (Figure 3b). In addition, the
382 wind shear in the lower boundary layer is better captured compared to tower observations from the
383 Cabauw measurement site (see Figure 3c-d). Further evaluation of the wind speed over sea using
384 scatterometer data shows clear improvement to the CBR scheme (de Rooy and de Vries 2017).

385 *d. Convection*

386 At 2.5 km resolution deep convection is expected to be roughly resolved, and explicitly repre-
387 sented by the model's non-hydrostatic dynamics, thus in HARMONIE-AROME there is no param-
388 eterization of deep convection. However, shallow convection still needs to be parameterized. For
389 this, usually a mass flux framework is applied consisting of one or more updrafts, which transport
390 heat, moisture and momentum. The convective transport is proportional to the difference between
391 the updraft properties and the environment, times the amount of mass transported by the updraft.
392 The upward mass flux M is described by a simple budget equation:

$$\frac{\partial M}{\partial z} = (\varepsilon - \delta)M \quad (1)$$

393 where ε is the fractional entrainment, describing the inflow of environmental air into the up-
394 draft (herewith diluting the updraft) and δ is the fractional detrainment describing the outflow of
395 updraft air into the environment. These coefficients can be considered as the key elements in a
396 convection scheme. HARMONIE-AROME uses a different scheme for shallow convection than
397 AROME-France (Seity et al. 2011), called EDMFm. According to the original ideas of Siebesma
398 and Teixeira (2000), Soares et al. (2004), Siebesma et al. (2007) and Rio and Hourdin (2008),
399 the mass flux concept can be applied in a so-called EDMF (Eddy Diffusivity Mass Flux) frame-
400 work. The eddy diffusivity, or turbulence part is given by the turbulence scheme “HARATU”
401 explained above. Here we discuss the mass flux component, which describes the transport by
402 cloudy as well as dry (unsaturated) updrafts. The focus will be on what distinguishes EDMFm in
403 HARMONIE-AROME from the mass-flux scheme used in AROME-France, which is referred to
404 as EDKF (Pergaud et al. 2009).

405 1) DUAL MASS-FLUX

406 Contrary to EDKF, EDMFm uses a dual mass flux approach in which two updrafts are distin-
407 guished; a dry updraft that never reaches the lifting condensation level and a moist updraft that
408 condenses and becomes a cloud. As schematically illustrated in Figure 4, three different con-
409 vective boundary layer regimes are considered. In contrast to Neggers et al. (2009) where the
410 subdivision between dry and moist updraft fractions is flexible, EDMFm uses fixed values only
411 depending on the regime.

412 The scheme starts with the initialization of the excess of the updrafts (Neggers et al. 2009).
413 Subsequently, a vertical velocity equation is used to determine updraft vertical velocity and the
414 corresponding height to which the updraft can penetrate. This provides the inversion, or cloud
415 base height, z_i and cloud top height, z_t . The applied formulation of the vertical velocity equation

⁴¹⁶ (based on Siebesma et al. (2007), Simpson and Wiggert (1969), de Rooy and Siebesma (2010)) is
⁴¹⁷ recently also supported by de Roode et al. (2012).

⁴¹⁸ With the inversion height known, the profiles of entrainment rate are defined because they are
⁴¹⁹ functions of just z and z_i (see Figure 4). For the dry updraft we adopt the ε formulation of Siebesma
⁴²⁰ et al. (2007), based on LES results for the dry convective boundary layer. The ε profile for the
⁴²¹ moist updraft in the sub-cloud layer extrapolates the work of Siebesma et al. (2007) for dry up-
⁴²² drafts that stop at z_i , to the larger sub-cloud thermals that do not stop at z_i . These larger, faster
⁴²³ rising thermals are associated with smaller entrainment rates in comparison with the dry updraft
⁴²⁴ (see Figure 4b). For the moist updraft, the value of entrainment at cloud base scales with z_i^{-1}
⁴²⁵ as suggested by LES, reflecting that deeper mixed layers can be associated with higher vertical
⁴²⁶ velocities and larger thermals (de Rooy and Siebesma 2010).

⁴²⁷ Finally, the entrainment formulation in the cloud layer decreases with height as z^{-1} (Siebesma
⁴²⁸ et al. 2003; de Rooy and Siebesma 2008). A small refinement in EDMFm concerns the value of
⁴²⁹ ε at cloud base which is connected to the value of ε at the top of the subcloud layer, and thus
⁴³⁰ depends on the mixed layer height.

⁴³¹ 2) PARAMETERIZATION OF DЕТRAINMENT

⁴³² The essential difference between EDMFm and EDKF concerns the parameterization of the de-
⁴³³ trainment in the cloud layer. As first pointed out by de Rooy and Siebesma (2008), variations in
⁴³⁴ the mass flux profile from case to case and hour to hour can be almost exclusively related to the
⁴³⁵ fractional detrainment (δ). This is supported by numerous LES studies, revealing orders of mag-
⁴³⁶ nitude larger variations in δ than in ε (e.g. Jonker et al. (2006), Derbyshire et al. (2011) ,Böing
⁴³⁷ et al. (2012), de Rooy et al. (2013)). Apart from this empirical evidence, the much larger varia-
⁴³⁸ tion in δ and its strong link to the mass flux is explained by theoretical considerations in de Rooy

and Siebesma (2010). For the first time, the implications of the aforementioned considerations are used in an operational scheme. As a result EDMFm behaves fundamentally different than other operational schemes. For example a Kain-Fritsch type scheme (Kain and Fritsch 1990; Kain 2004), like the EDKF option used in AROME, (Pergaud et al. 2009), in which ε and δ vary in an opposite but similar manner to environmental conditions, is not able to capture the order of magnitude variations in δ due to cloud layer depth (de Rooy et al. 2013). In EDMFm this cloud layer depth dependence is included by considering the mass flux profile in a non-dimensionalised way (de Rooy and Siebesma 2008). Apart from the cloud layer depth, the detrainment value is influenced by environmental conditions. For this dependency we use a parameter called χ_c (Kain and Fritsch 1990). As shown by de Rooy and Siebesma (2008), χ_c increases with the relative humidity and buoyancy excess of the updraft. Therefore, the LES based functional dependence of δ (or mass flux profile) on χ_c is physically plausible: high values of χ_c can be associated with large clouds, with high updraft velocities that have large buoyancy excess and/or clouds rising in a humid environment. Accordingly, high χ_c values correspond to small detrainment values and slowly decreasing mass flux with height. Further details on the detrainment formulation can be found in de Rooy and Siebesma (2008).

Describing lateral mixing in the cloud layer in this way is supported by observational (see e.g. Lamer et al. (2015)) and LES studies. The most convincing support from LES can be found in Böing et al. (2012), who used 90 LES runs to explore the sensitivity of ε , δ and the mass flux profile in deep convection to a broad spectrum of relative humidities and stability of the environment. This study confirms the much larger variation of δ and its strong link with the mass flux profile. Figure 5 from Böing et al. (2012) shows the results of parameterizing the mass flux profile according to de Rooy and Siebesma (2008). Another difference between HARMONIE-AROME cycle 40h1.1 and AROME-France is the method by which convection influences the total cloud

463 cover and subgrid liquid and ice water content. In HARMONIE-AROME the method proposed by
464 Soares et al. (2004) is applied, in which the mixing from turbulence and convection is used to pro-
465 duce the variance of the distance to saturation in the statistical cloud scheme. In AROME-France
466 only turbulence contributes in this way to the variance, whereas the impact of convection on the
467 cloud cover and subgrid liquid and ice water content is assumed to be proportional to the updraft
468 area fraction of the mass flux of the previous time step.

469 *e. Surface*

470 The surface physics in AROME-France and HARMONIE-AROME is simulated by the surface
471 scheme named “SURFEX”. SURFEX (Surface Externalisée, Masson et al. (2013)) is a surface
472 modelling platform developed mainly by Météo-France in cooperation with the scientific commu-
473 nity. SURFEX is composed of various physical models for natural land surface, urbanized areas,
474 lakes and oceans. It also simulates chemistry and aerosols surface processes and can be used for
475 assimilation of surface and near surface variables. SURFEX has its own initialisation procedures
476 and can be used in stand alone mode and coupled to an atmospheric model (Masson et al. 2013).
477 In SURFEX, each model grid box is represented by four surface tiles: sea or ocean, lakes, urban
478 areas and nature (soil and vegetation). The nature tile can further be divided into several so-called
479 patches depending on vegetation type. Each surface tile is modelled with a specific surface model
480 and the total flux of the grid box results from the addition of the individual fluxes weighted by
481 their respective fraction.

482 HARMONIE-AROME cycle 40h1.1 uses SURFEX version 7.3. The exchange of energy and
483 water between the land surface and the atmosphere above is simulated by the Interaction Soil-
484 Biosphere-Atmosphere (ISBA) scheme with a force-restore approach (Boone et al. 1999) in com-
485 bination with the Douville snow scheme Douville et al. (1995). Currently, the surface characteris-

tics are aggregated, and only one patch is used in the flux calculations on the nature tile. For the sea tile the ECUME scheme by Belamari (2005) is used over water and the “Simple Ice Model” for sea ice, as described below, has been added in the latest version of HARMONIE-AROME. For the inland water tile (lakes and rivers) the Charnock (1955) formula is used over water. The lake surface temperature is initialised by deep soil temperature (extrapolated if necessary) and is kept constant during the forecast. For water temperature below the freezing point, surface properties for snow is applied, e.g. surface momentum roughness is set to 0.001 m and albedo to 0.85. Finally, the urban tile is simulated by the Town-Energy Balance (TEB) model (Masson 2000).

Over the water and sea tiles, diagnostic quantities at 2 m and 10 m are calculated by interpolating between atmospheric forcing variables and surface temperature and humidity variables. Over land the Surface Boundary Layer (SBL) scheme by Masson and Seity (2009) is used. The 1-D prognostic turbulence scheme calculates TKE, wind, temperature and humidity on 6 vertical levels 0.5, 2, 4, 6.5, 9 and 12 m above ground. The motivation for using the SBL scheme is to improve the performance in stable situations. However, experiences show that whilst the scheme might give realistic and low temperatures in some situations, it can also yield much too low temperatures in some situations, often in combination with too weak winds. The physiography databases related to land use, topography and clay/sand are currently all revisited for domains used within the HIRLAM consortia. The default surface land-cover physiography in cycle 40h1.1 is based on ECOCLIMAPv2.2 (Faroux et al. 2013). Modifications have been included in places where the ECOCLIMAP description was found to be sub-optimal, e.g. over the permanent snow areas over Norway. Also, over Greenland and Iceland, local modifications of these data bases, e.g. permanent snow areas and leaf-area index, have shown significantly improved results in near-surface wind and temperature scores, demonstrating the importance of carefully looking into the physiography used. The default surface topography is based on GMTED2010 (Danielson and Gesch

510 2011). The default clay and sand proportions are still based on FAO (FAO 2006) since the newer
511 HWSD data base (Nachtergaele et al. 2012) shows dubious values over Scandinavia. Monthly cli-
512 matologies of vertically integrated optical depth of four aerosol species (Tegen et al. 1997) dataset
513 are introduced to the forecast model along with the physiography and topography data.

514 Previous versions of HARMONIE-AROME treated areas covered by sea ice in a quite simplified
515 manner, using a constant value for sea ice surface temperature during the whole forecast. However,
516 it was found that such a configuration led to a noticeable bias of 2 meter temperature over ice
517 covered areas which grew with increasing forecast lead time. In order to solve this problem the
518 “Simple ICE” model – SICE was introduced in HARMONIE-AROME cycle 40h1.1 (not activated
519 by default, but switched on and used by some services where sea ice is a big part of the domain).
520 SICE is built on top of SURFEX’s soil heat-diffusion solver, and represents a layer of sea ice
521 with fixed thickness and prognostic temperature within the ice slab. The ice pack is divided into a
522 number of layers in order to solve the heat diffusion. Here the uppermost layer is defined by the ice
523 surface temperature, which is derived from the thermal balance equation, and the lowermost layer
524 holds the freezing point temperature. Ice covered areas are determined by the ice concentration
525 field provided by an external source. The flux from a sea tile grid cell is calculated as the weighted
526 contribution from the ice and open water schemes. HARMONIE-AROME cycle 40h1.1 uses SICE
527 configuration with 0.75 m thick ice slab divided into four layers.

528 Figure 6 shows the impact of the SICE scheme over seven stations in the Gulf of Bothnia for
529 the time period 01 March 2013 to 31 March 2013, forecasts initialized at 00 UTC. Black curves
530 represents the HARMONIE-AROME model without the SICE scheme, and red curves are with the
531 SICE scheme. Here it can be seen that the SICE scheme improves the forecast of surface pressure,
532 temperature and wind speed. Temperature is particularly improved, with a better daily cycle and a
533 smaller model bias.

534 **4. Future developments in HARMONIE-AROME**

535 *a. Dynamics*

536 In the dynamics, a development for the near future is the introduction of vertical finite elements,
537 which has been done in close collaboration with the ALADIN consortia. An advantage of this
538 vertical discretization is the exclusive use of full levels, skipping a computational mode created
539 from the interpolation from full levels to half levels. The vertical finite elements were successfully
540 introduced by Untch and Hortal (2004) in the hydrostatic ECMWF IFS model. The implementa-
541 tion of vertical finite elements has also been extended to work for the non-hydrostatic dynamics.
542 However, the non-hydrostatic model needs to solve a constraint called C1 involving the SI vertical
543 operators, which is not present in the hydrostatic version. If this constraint is fulfilled then one
544 can write the SI set of linear equations only in terms of the vertical divergence. This has been
545 done in the finite difference discretization, but unfortunately, the C1-constraint is not guaranteed
546 in the construction of the finite element operators. An iterative method was developed by (Vivoda
547 and Smolíková 2013) in order to relax the C1-constraint. Based on this approach a theoretical
548 development to solve the C1-constraint was proposed by Subias (2015) which has been tested in
549 HARMONIE-AROME in cycle 40h1.1. The implementation of the vertical integral operators in-
550 volved in the C1-constraint shows no impact in 3D tests when they replace the default operators
551 in a purely finite difference configuration. Thus, these operators are good candidates for use in a
552 non-hydrostatic finite element configuration because they satisfy the C1-constraint. However, the
553 tests are very sensitive to the choice of the vertical levels, so future work is needed to adapt the
554 scheme to work for any given set of levels.

555 We will also continue to seek adaptations of the Semi-Lagrangian method which conserve mass
556 better but do not involve a large increase in computational cost. In this context we will explore

further the use of the “COntinuous Mapping about Departure points” COMAD scheme (Malardel and Ricard 2015) which introduces a correction applied to the standard interpolation weights in the SL scheme, and takes into account the deformation of the air parcels along each direction of interpolation. The scheme is already used in AROME-France, and recent tests in HARMONIE-AROME shows that the scheme helps to reduce excessive build up of cloud hydrometeors in isolated grid-points. As a next step, it may be considered to enhance mass conservation for individual atmospheric components in the SL treatment of the mixing ratio equations.

On a longer time scale, the semi-implicit time stepping scheme will be reconsidered at very high (sub-km) resolutions; here we will look at steep slope behaviour and computational performance, and assess the potential of the alternative HEVI (horizontal explicit vertical implicit) scheme (Lock et al. 2014).

b. Radiation

The ACRANEB2 radiation scheme from the ALARO model (Mašek et al. 2016; Geleyn et al. 2017) and the HLRADIA radiation scheme from the HIRLAM model (Savijärvi 1990, see also Nielsen et al. 2014) are now available for testing in HARMONIE-AROME, we will investigate whether the ability to have fast interactions between clouds and radiation and the surface and radiation are of greater importance for model performance than accounting for the spectral details of clear-sky radiation. Also, it will be investigated whether these radiation schemes can be used in individual ensemble members for HARMONIE-AROME ensemble simulations.

For direct and indirect aerosol parametrizations, input information on the atmospheric aerosol distribution and its optical and chemical properties is required. To improve the present aerosol climatology (Tegen et al. 1997), an update of the aerosol climatology to the Monitoring Atmospheric Composition and Climate (MACC) reanalysis (Inness et al. 2013) dataset which includes

assimilated AOD measurements is considered, as well as the use of real-time aerosol data from Copernicus Atmosphere Monitoring Service (CAMS). Updated aerosol data will be utilized both by the radiation and cloud-precipitation microphysics parametrizations.

c. Clouds and microphysics

Improvements in the parameterizations of cloud microphysics and hydrometeor interactions within the clouds are sought with the aim to enhance forecast accuracy for extreme precipitation events and the prediction of fog and low clouds. In future model versions we will explore the two-moment cloud microphysics scheme “Liquid Ice Multiple Aerosols” (LIMA) developed by the meso-NH community and at Météo-France (Vié et al. 2016), which has been derived from the ICE3 microphysics scheme. The scheme introduces prognostic variables for droplet number concentration for cloud, rain and ice, and allows for a more realistic description of cloud-aerosol interactions. We will work in close collaboration with the ALADIN consortia on testing the scheme with various sources of aerosol, MACC reanalysis and real-time aerosol analysis from Copernicus.

d. Turbulence and convection

Work to prepare the model for operational use at increased resolution (100 layers, $0.5 - 1.3\text{km}$) will be a priority the coming years, as well as exploring the model behaviour in the grey zone of shallow convection and turbulence. Experiences of using the model at these resolutions can be drawn from e.g. Brousseau et al. (2016) and Honnert et al. (2011). There are also plans to understand better the behaviour of the HARATU scheme in the stable boundary layer, and if the model can be improved further in this regime.

600 e. *Surface*

601 A number of deficiencies in the performance of the HARMONIE-AROME configuration can
602 be attributed to surface processes and physiography issues. These concern for instance a cold
603 and humid spring bias over northern Europe, a humid and cold early spring in western Europe,
604 followed by a warm and dry late spring and summer period and a shift in temperature climate
605 nearby deep and large lakes.

606 One promising step towards an improved surface description is to increase the number of patches
607 over the nature part from one to two, i.e. sub-divide the nature tile into a forest and an open land
608 patch, respectively. With one patch all surface properties are averaged to land-averaged values
609 while with two patches each patch is given its unique surface properties. Preliminary results look
610 promising and show an increase in Bowen ratio and a reduced problem with respect to the too
611 humid spring conditions over northern Europe, but also show a reduced winter temperature bias
612 over south-western Europe.

613 However, achievement of a more complete solution requires utilisation of more advanced sur-
614 face modules which have become available in SURFEXv8 in cycle 43 of the ALADIN-HIRLAM
615 NWP system. These processes concern multi-layer soil and snow schemes and an explicit canopy
616 treatment where the canopy vegetation, energy-budget wise, is separated from the soil and snow
617 beneath. Assessing the potential of these schemes should be done in close connection to the cor-
618 responding data assimilation methods. For their initialization, the surface data assimilation needs
619 to be based on more sophisticated algorithms than the present Optimum Interpolation, such as the
620 Extended Kalman Filter (EKF). This will also make it possible to utilize a wide range of remote
621 sensing products for surface data assimilation.

622 The temperature problem connected to lakes will be addressed by activating the lake model
623 FLake (Mironov et al. 2010) for all inland water (lakes and rivers). FLake is already used oper-
624 ationally in NWP by e.g. COSMO (Mironov et al. 2010) and ECMWF (ECMWF 2015b), and in
625 climate applications of the ALADIN-HIRLAM system using the HARMONIE Climate configura-
626 tion (Lind et al. 2016). The most important physiography information for lakes is the lake depth.
627 For this we use the Global Lake Depth Database (GLDB) by Choulga et al. (2014). The large ther-
628 mal inertia of lakes does also require a careful initialisation. For this the global lake climatology
629 by Kourzeneva et al. (2012) is used. In the coming years, an EKF lake data assimilation scheme
630 will be developed in which satellite and in-situ observations of lake surface temperature and ice
631 cover can be assimilated.

632 Furthermore, parametrizations of the orography impact on surface-level radiation fluxes based
633 on Senkova et al. (2007) (see also Rontu et al. 2016), have been prepared within SURFEX. Cou-
634 pling of these parametrizations to the full HARMONIE-AROME model will be tested within the
635 next cycle of the system.

636 *f. Coupling with sea surface and ocean*

637 The use of the HARMONIE-AROME model is gradually extending beyond NWP to include
638 more earth system components, and to longer time frames. Preliminary experiments in Norway
639 have indicated that coupling HARMONIE-AROME with the wave model WAM is beneficial in
640 the sense that it reduces the systematic increase in near-surface wind bias for strong winds, which
641 has been observed in verification against scatterometer data and buoys (Süld et al. 2015). For
642 this reason, and considering the relevance of this benefit for accurately predicting polar lows, a
643 two-way coupling with WAM has been incorporated in model simulations over an Arctic domain
644 used in operations by Met-Norway. Having a two way coupled ocean-atmosphere model is a

possible step for the future, in particularly for the regional climate modelling community. In this regard, ALADIN partners, in particular Météo-France and Croatia have made progress; at Météo-France by coupling AROME-France to the ocean model NEMO (Madec et al. 2015), using the OASIS coupler (Valcke 2013), which exists within SURFEX (Masson et al. 2013), this work is described in the PhD thesis of Rainaud (2015). In Croatia by testing a two-way coupling between the ALADIN model on the atmosphere side, and an Adriatic setup of Princeton ocean mode, POM (Blumberg and Mellor 1987), on the ocean side as described by Ličer et al. (2016). Based on these experiences we aim to make progress on atmosphere-ocean coupling in the coming years in the ALADIN-HIRLAM NWP system.

5. Acknowledgement

We would like to thank our colleagues within the HIRLAM and ALADIN consortia for active and stimulating collaboration leading up to the completion of this manuscript.

References

- Baas, P., S. R. de Roode, and G. Lenderink, 2008: The scaling behaviour of a turbulent kinetic energy closure model for stably stratified conditions. *Boundary-layer meteorology*, **127** (1), 17–36.
- Bechtold, P., J. Cuipers, P. Marscart, and P. Trouillet, 1995: Modeling of trade wind cumuli with a low-order turbulence model: Toward a unified description of Cu and Sc clouds in meteorological models. *Journal of the Atmospheric Sciences*, **127**, 869–886.
- Belamari, S., 2005: Report on uncertainty estimates of an optimal bulk formulation for surface turbulent fluxes. Tech. Rep. Deliverable D4.1.2, Marine Environment and Security for the European Area–Integrated Project (MERSEA IP).

- 667 Bénard, P., J. Vivoda, J. Mašek, P. Smolíková, K. Yessad, C. Smith, R. Brožková, and J.-F. Geleyn,
668 2010: Dynamical kernel of the Aladin-NH spectral limited-area model: revised formulation and
669 sensitivity experiments. *Q.J.R. Meteorol. Soc.*, **136**, 155–169.
- 670 Bengtsson, L., S. Tijm, F. Váňa, and G. Svensson, 2012: Impact of flow-dependent horizontal
671 diffusion on resolved convection in AROME. *J. of Applied Met. and Clim.*, **51**, 54–67.
- 672 Blumberg, A. F., and G. L. Mellor, 1987: A description of a three-dimensional coastal ocean
673 circulation model. *Three-dimensional coastal ocean models*, 1–16.
- 674 Böing, S. J., A. Siebesma, J. Korpershoek, and H. Jonker, 2012: Detrainment in deep convection.
675 *Geophys. Res. Letters*, **39**.
- 676 Boone, A., J.-C. Calvet, and J. Noilhan, 1999: Inclusion of a third soil layer in a land surface
677 scheme using the force-restore method. *Journal of Applied Meteorology*, **38** (11), 1611–1630.
- 678 Bougeault, P., 1982: Cloud-ensemble relations based on the gamma probability distributions for
679 the higher-order moments of the planetary boundary layer. *Mon. Wea. Rev.*, **117**, 1870–1888.
- 680 Bouteloup, Y., S. Y, and B. E, 2011: Description of the sedimentation scheme used operationally
681 in all Météo-France NWP models. *Tellus A*, **63**, 300–311.
- 682 Brousseau, P., Y. Seity, D. Ricard, and J. Lger, 2016: Improvement of the forecast of convective
683 activity from the AROME-France system. *Q. J. R. Meteorol. Soc.*, **142**, 2231–2243.
- 684 Bubnova, R., G. Hello, P. Bénard, and J.-F. Geleyn, 1995: Integration of the fully elastic equa-
685 tions cast in the hydrostatic pressure terrain-following coordinate in the framework of the
686 ARPEGE/ALADIN NWP system. *Mon. Wea. Rev.*, **123**, 515–535.
- 687 Charnock, H., 1955: Wind stress on a water surface. *Quarterly Journal of the Royal Meteorologi-*
688 *cal Society*, **81** (350), 639–640.

- 689 Choulga, M., E. Kourzeneva, E. Zakharova, and A. Doganovsky, 2014: Estimation of the mean
690 depth of boreal lakes for use in numerical weather prediction and climate modelling. *Tellus A*,
691 **66**.
- 692 Coakley Jr., J. A., and P. Chylek, 1975: The two-stream approximation in radiative transfer: In-
693 cluding the angle of the incident radiation. *J.Atmos. Sci.*, **32**, 409–418.
- 694 Cuxart, J., P. Bougeault, and J.-L. Redelsperger, 2000: A turbulence scheme allowing for
695 mesoscale and large-eddy simulations. *Quarterly Journal of the Royal Meteorological Society*,
696 **126 (562)**, 1–30.
- 697 Danielson, J., and D. Gesch, 2011: Global multi-resolution terrain elevation data 2010
698 (GMTED2010). Tech. Rep. Open-File Report 20111073, U.S. Geological Survey. 26 p.
- 699 Davies, H., 1976: A lateral boundary formulation for multi-level prediction models. *Quarterly*
700 *Journal of the Royal Meteorological Society*, **102 (432)**, 405–418.
- 701 de Roode, S., A. Siebesma, H. Jonker, and Y. de Voogd, 2012: Parameterization of the Vertical
702 Velocity Equation for Shallow Cumulus Clouds. *Mon. Wea. Rev.*, **140**, 2424–2436.
- 703 de Roode, S. R., H. J. Jonker, P. G. Duynkerke, and B. Stevens, 2004: Countergradient fluxes of
704 conserved variables in the clear convective and stratocumulus-topped boundary layer: the role
705 of the entrainment flux. *Boundary-layer meteorology*, **112 (1)**, 179–196.
- 706 de Rooy, W. C., 2014: The fog above sea problem: Part 1 Analysis. Tech. rep., Aladin Hirlam,
707 9–15 pp.
- 708 de Rooy, W. C., and H. de Vries, 2017: Harmonie verification and evaluation. Tech. rep., HIRLAM
709 technical report.

- 710 de Rooy, W. C., and A. Siebesma, 2010: Analytical expressions for entrainment and detrainment in
711 cumulus convection. *Quarterly Journal of the Royal Meteorological Society*, **136 (650)**, 1216–
712 1227.
- 713 de Rooy, W. C., and A. P. Siebesma, 2008: A simple parameterization for detrainment in shallow
714 cumulus. *Monthly Weather Review*, **136 (2)**, 560–576.
- 715 de Rooy, W. C., and Coauthors, 2013: Entrainment and detrainment in cumulus convection: an
716 overview. *Quarterly Journal of the Royal Meteorological Society*, **139 (670)**, 1–19.
- 717 Deardorff, J. W., 1980: Stratocumulus-capped mixed layers derived from a three-dimensional
718 model. *Boundary-Layer Meteorology*, **18 (4)**, 495–527.
- 719 Derbyshire, S., A. Maidens, S. Milton, R. Stratton, and M. Willett, 2011: Adaptive detrainment in
720 a convective parameterization. *Quart. J. Roy. Met. Soc.*, **137**, 1856–1871.
- 721 Douville, H., J. F. Royer, and J. F. Mahfouf, 1995: A new snow parameterization for the Météo-
722 France climate model. Part I: validation in stand-alone experiments. *Climate Dyn.*, **12**, 21–35.
- 723 ECMWF, 2015a: Part III: Dynamics and numerical procedures. IFS documentation Cy41r1. Op-
724 erational implementation 12 May 2015. European Centre for Medium-Range Weather Fore-
725 casts. Available at: <http://www.ecmwf.int/en/elibrary/9210-part-iii-dynamics-and-numerical-procedures>.
- 726
- 727 ECMWF, 2015b: Part IV: Physical processes. IFS documentation Cy41r1. Operational imple-
728 mentation 12 May 2015. European Centre for Medium-Range Weather Forecasts. Available at:
729 <http://www.ecmwf.int/en/elibrary/16648-part-iv-physical-processes>.

- 730 FAO, 2006: World reference base for soil resources 2006, A framework for international classifi-
731 cation, correlation and communication. Tech. Rep. World soil resources report No. 103, Food
732 and Agriculture Organization of the United Nations.
- 733 Faroux, S., A. T. Kaptu   Tchuent  , J.-L. Roujean, V. Masson, E. Martin, and P. Le Moigne, 2013:
734 ECOCLIMAP-II/Europe: a twofold database of ecosystems and surface parameters at 1 km
735 resolution based on satellite information for use in land surface, meteorological and climate
736 models. *Geoscientific Model Development*, **6** (2), 563–582, doi:10.5194/gmd-6-563-2013, URL
737 <http://www.geosci-model-dev.net/6/563/2013/>.
- 738 Fouquart, Y., and B. Bonnel, 1980: Computations of solar heating of the earth's atmosphere – A
739 new parameterization. *Beitr. Phys. Atmos.*, **53**, 35–62.
- 740 Fu, Q., 1996: An Accurate Parameterization of the Solar Radiative Properties of Cirrus Clouds
741 for Climate Models. *Journal of Climate*, **9** (9), 2058–2082, doi:10.1175/1520-0442(1996)
742 009<2058:AAPOTS>2.0.CO;2.
- 743 Fu, Q., P. Yang, and W. B. Sun, 1998: An Accurate Parameterization of the Infrared Radiative
744 Properties of Cirrus Clouds for Climate Models. *Journal of Climate*, **11** (9), 2223–2237, doi:
745 10.1175/1520-0442(1998)011<2223:AAPOTI>2.0.CO;2.
- 746 Geleyn, J., J. J. Ma  ek, R. Bro  kov  , P. Kuma, D. Degrauwe, G. Hello, and N. Pristov, 2017:
747 Single interval longwave radiation scheme based on the net exchanged rate decomposition with
748 bracketing. *submitted to Q. J. R. Meteorol. Soc.*
- 749 Gleeson, E., K. Nielsen, V. Toll, and L. Rontu, 2015: Shortwave Radiation Experiments in HAR-
750 MONIE. Tests of the cloud inhomogeneity factor and a new cloud liquid optical property scheme
751 compared to observations. *ALADIN-HIRLAM Newsletter*, **5**, 92–106.

- 752 Gleeson, E., V. Toll, K. P. Nielsen, L. Rontu, and J. Mašek, 2016: Effects of aerosols on clear-sky
753 solar radiation in the ALADIN-HIRLAM NWP system. *Atmospheric Chemistry and Physics*,
754 **16** (9), 5933–5948, doi:10.5194/acp-16-5933-2016, URL <http://www.atmos-chem-phys.net/16/5933/2016/>.
- 755
- 756 Grant, A., 2001: Cloud-base fluxes in the cumulus-capped boundary layer. *Quart. J. Roy. Met.*
757 *Soc.*, **127**, 407–422.
- 758
- 759 Hess, M., P. Köpke, and I. Schult, 1998: Optical properties of aerosols and clouds. the software
package OPAC. *Bull. Am. Meteorol. Soc.*, **79** (5), 831–844.
- 760 Honnert, R., V. Masson, and F. Couvreux, 2011: A new diagnostique for evaluating the represen-
761 tation of turbulence in atmospheric models at the kilometric scale. *J. Atmos. Sci.*, **68**, 31123131.
- 762 Hortal, M., 2002: The development and testing of a new twotimelevel semiLagrangian scheme
763 (SETTLS) in the ECMWF forecast model. *Quarterly Journal of the Royal Meteorological So-*
764 *ciet*, **128**(583), 1671–1687.
- 765 Illingworth, A. J., and Coauthors, 2007: Cloudnet - continuous evaluation of cloud profiles in
766 seven operational models using ground-based observations. *Bull. Am. Meteorol. Soc.*, **88**, 883–
767 898.
- 768
- 769 Inness, A., and Coauthors, 2013: The MACC reanalysis: an 8 yr data set of atmospheric composi-
770 tion. *Atmospheric Chemistry and Physics*, **13** (8), 4073–4109, doi:10.5194/acp-13-4073-2013,
771 URL <http://www.atmos-chem-phys.net/13/4073/2013/>.
- 772
- 773 Jonker, H., R. Verzijlbergh, T. Heus, and A. Siebesma, 2006: The influence of the sub-cloud mois-
774 ture field on cloud size distributions and the consequences for entrainment. *Extended abstract*

773 from the 17th Symposium on Boundary Layers and Turbulence, San Diego, USA, Americal Me-
774 teorological Society.

775 Joseph, J. H., W. J. Wiscombe, and J. A. Weinman, 1976: The Delta-Eddington Approximation
776 for Radiative Flux Transfer. *J. Atmos. Sci.*, **33**, 2452–2459.

777 Kain, J. S., 2004: The KainFritsch Convective Parameterization: An Update . *Journal of Applied*
778 *Meteorology and Climatology*, **43**, 170–180.

779 Kain, J. S., and J. M. Fritsch, 1990: A One-Dimensional entraining/detraining Plume Model and
780 its applications in convective parametrization. *J. Atmos. Sci.*, **47**, 2784–2801.

781 Kessler, E., 1969: On the distribution and continuity of water substance in atmospheric circulation.
782 *Meteor. Monogr.*, **32**, 84.

783 Khairoutdinov, M., and Y. Kogan, 2000: A New Cloud Physics Parameterization in a Large-Eddy
784 Simulation Model of Marine Stratocumulus. *Mon. Wea. Rev.*, **128**, 229–243.

785 Kourzeneva, E., E. Martin, Y. Batrak, and P. Le Moigne, 2012: Climate data for parameterisation
786 of lakes in numerical weather prediction models. *Tellus A*, **64**.

787 Lamer, K., P. Kollias, and L. Nuijens, 2015: Observations of the variability of shallow trade wind
788 cumulus cloudiness and mass flux. *Journal of Geophysical Research: Atmospheres*, **120**, 6161–
789 6178.

790 Laprise, R., 1992: The Euler Equations of Motion with Hydrostatic Pressure as an Independent
791 Variable . *Mon. Wea. Rev.*, **120(1)**, 197207.

792 Lascaux, F., E. Richard, and J.-P. Pinty, 2006: Numerical simulations of three different MAP IOPs
793 and the associated microphysical processes. *Quarterly Journal of the Royal Meteorological So-*
794 *ciety*, **132 (619)**, 1907–1926.

- 795 Lenderink, G., and A. A. Holtslag, 2004: An updated length-scale formulation for turbulent mix-
796 ing in clear and cloudy boundary layers. *Quarterly Journal of the Royal Meteorological Society*,
797 **130 (604)**, 3405–3427.
- 798 Lenderink, G., and E. Van Meijgaard, 2001: Impacts of cloud and turbulence schemes on inte-
799 grated water vapor: Comparison between model predictions and GPS measurements. *Meteorol-*
800 *ogy and Atmospheric Physics*, **77 (1-4)**, 131–144.
- 801 Lenderink, G., and Coauthors, 2004: The diurnal cycle of shallow cumulus clouds over land:
802 A single-column model intercomparison study. *Quarterly Journal of the Royal Meteorological*
803 *Society*, **130 (604)**, 3339–3364.
- 804 Ličer, M., and Coauthors, 2016: Modeling the ocean and atmosphere during an extreme bora event
805 in northern Adriatic using one-way and two-way atmosphere–ocean coupling. *Ocean Science*,
806 **12 (1)**, 71–86.
- 807 Lind, P., D. Lindstedt, E. Kjellström, and C. Jones, 2016: Spatial and temporal characteristics of
808 summer precipitation over central Europe in a suite of high-resolution climate models. *Journal*
809 *of Climate*, **29 (10)**, 3501–3518.
- 810 Lock, S.-J., N. Wood, and H. Weller, 2014: Numerical analyses of Runge–Kutta implicit–explicit
811 schemes for horizontally explicit, vertically implicit solutions of atmospheric models. *Quarterly*
812 *Journal of the Royal Meteorological Society*, **140 (682)**, 1654–1669.
- 813 Madec, G., and Coauthors, 2015: NEMO ocean engine.
- 814 Malardel, S., and D. Ricard, 2015: An alternative cellaveraged departure point reconstruction for
815 pointwise semiLagrangian transport schemes. *Quarterly Journal of the Royal Meteorological*
816 *Society*, **691**, 2114–2126.

- 817 Malcorps, H., and M. Ågren, 2005: HIRLAM-ALADIN Agreement. URL http://www.hirlam.org/index.php/component/docman/doc_view/24-aladin-hirlam-a-cooperation-agreement?Itemid=70.
- 818
- 819
- 820 Martin, G. M., D. W. Johnson, and A. Spice, 1994: The measurement and parameterization of
821 effective radius of droplets in warm stratocumulus clouds. *Journal of the Atmospheric Sciences*,
822 **51** (13), 1823–1842, doi:10.1175/1520-0469(1994)051<1823:TMAPOE>2.0.CO;2.
- 823
- 824 Mascart, P. J., and P. Bougeault, 2011: The Meso-NH atmospheric simulation system: Scientific
825 documentation. Tech. rep., Meteo France, Toulouse, France.
- 826
- 827 Masson, V., 2000: A physically-based scheme for the urban energy budget in atmospheric models.
828 *Boundary-layer meteorology*, **94** (3), 357–397.
- 829
- 830 Masson, V., and Y. Seity, 2009: Including atmospheric layers in vegetation and urban offline
831 surface schemes. *Journal of Applied Meteorology and Climatology*, **48** (7), 1377–1397.
- 832
- 833 Masson, V., and Coauthors, 2013: The SURFEXv7.2 land and ocean surface platform for coupled
834 or offline simulation of earth surface variables and fluxes. *Geoscientific Model Development*,
835 **6** (4), 929–960, doi:10.5194/gmd-6-929-2013, URL <http://www.geosci-model-dev.net/6/929/2013/>.
- 836
- 837 Mašek, J., J.-F. Geleyn, R. Brožková, O. Giot, H. O. Achom, and P. Kuma, 2016: Single interval
838 shortwave radiation scheme with parameterized optical saturation and spectral overlaps. *Quarterly
839 Journal of the Royal Meteorological Society*, **142** (694), 304–326, doi:10.1002/qj.2653,
840 URL <http://dx.doi.org/10.1002/qj.2653>.

- 837 Mironov, D., E. Heise, E. Kourzeneva, B. Ritter, N. Schneider, and A. Terzhevik, 2010: Implementation
838 of the lake parameterisation scheme FLake into the numerical weather prediction model
839 COSMO. *Boreal environment research*, **15** (2).
- 840 Mlawer, E. J., S. J. Taubman, P. D. Brown, M. J. Iacono, and S. A. Clough, 1997: Radiative transfer for inhomogeneous atmospheres: RRTM, a validated correlated-k model for the
841 longwave. *Journal of Geophysical Research: Atmospheres*, **102** (D14), 16 663–16 682, doi:
842 10.1029/97JD00237, URL <http://dx.doi.org/10.1029/97JD00237>.
- 843 Müller, M., and Coauthors, 2016: AROME - MetCoOp : A Nordic convective scale operational
844 weather prediction model. *Weather and Forecasting*.
- 845 Nachtergael, F., H. van Velthuizen, L. Verelst, and D. Wiberg, 2012: Harmonized
846 World Soil Database, version 1.2. [http://www.iiasa.ac.at/Research/LUC/External-World-soil-
847 database/HTML/](http://www.iiasa.ac.at/Research/LUC/External-World-soil-database/HTML/) (last access: 23 August 2016).
- 848 Neggers, R. A., M. Köhler, and A. C. Beljaars, 2009: A dual mass flux framework for boundary
849 layer convection. part I: Transport. *Journal of the Atmospheric Sciences*, **66** (6), 1465–1487.
- 850 Nielsen, K. P., E. Gleeson, and L. Rontu, 2014: Radiation sensitivity tests of the HARMONIE
851 37h1 NWP model. *Geosci. Model Dev.*, **7**, 1433–1449.
- 852 Pergaud, J., V. Masson, S. Malardel, and F. Couvreux, 2009: A parameterization of dry thermals
853 and shallow cumuli for mesoscale numerical weather prediction. *Boundary-layer meteorology*,
854 **132** (1), 83–106.
- 855 Pinty, J.-P., and P. Jabouille, 1998: A mixed-phase cloud parameterization for use in a mesoscale
856 non-hydrostatic model: Simulations of a squall line and of orographic precipitation. *Conf. on
857 Cloud Physics*, Everett, WA Amer. Meteor. Soc., 217–220.

- 859 Rainaud, R., 2015: Modélisation couplée océan–atmosphère pour l'étude des événements
860 météorologiques intenses en Méditerranée'. Ph.D. thesis, PhD thesis. University Paul Sabatier-
861 Toulouse III: Toulouse, France.
- 862 Rio, C., and F. Houdin, 2008: A thermal plume model for the convective boundary layer: Repre-
863 sentation of cumulus clouds. *J. Atmos. Sci.*, **65**, 407–424.
- 864 Rontu, L., C. Wastl, and S. Niemelä, 2016: Influence of the Details of Topography on Weather
865 Forecast Evaluation of HARMONIE Experiments in the Sochi Olympics Domain over the
866 Caucasian Mountains. *Frontiers in Earth Science*, **4**, 13.
- 867 Savijärvi, H., 1990: Fast Radiation Parameterization Schemes for Mesoscale and Short-Range
868 Forecast Models. *J. Appl. Meteorol.*, **29**, 437–447.
- 869 Seity, Y., P. Brousseau, S. Malardel, G. Hello, P. Benard, F. Bouttier, C. Lac, and V. Masson, 2011:
870 The AROME-France convective-scale operational model. *Mon. Wea. Rev.*, **139**, 976–991.
- 871 Senkova, A., L.Rontu, and H. Savijärvi, 2007: Parametrization of orographic effects on surface
872 radiation in HIRLAM. *Tellus*, **59A**, 279–291.
- 873 Siebesma, A., and J. Teixeira, 2000: An advection-diffusion scheme for the convective boundary
874 layer, description and 1D-results. *Proceedings of 14th Symposium on Boundary Layers and*
875 *Turbulence, Aspen, USA*, Americal Meteorological Society, 133–136.
- 876 Siebesma, A. P., P. M. Soares, and J. Teixeira, 2007: A combined eddy-diffusivity mass-flux
877 approach for the convective boundary layer. *Journal of the atmospheric sciences*, **64 (4)**, 1230–
878 1248.
- 879 Siebesma, A. P., and Coauthors, 2003: A large eddy simulation intercomparison study of shallow
880 cumulus convection. *Journal of the Atmospheric Sciences*, **60 (10)**, 1201–1219.

- 881 Simmons, A., and D. M. Burridge, 1981: An Energy and Angular-Momentum Conserving Vertical
882 Finite-Difference Scheme and Hybrid Vertical Coordinates. *Mon. Wea. Rev.*, **109**(4), 758766.
- 883 Simpson, J., and V. Wiggert, 1969: Models of precipitating cumulus towers. *Mon. Wea. Rev.*,
884 **97** (7), 471–489.
- 885 Smith, E. A., and L. Shi, 1992: Surface Forcing of the Infrared Cooling Profile over the Tibetan
886 Plateau. Part I: Influence of Relative Longwave Radiative Heating at High Altitude. *Journal of*
887 *the Atmospheric Sciences*, **49** (10), 805–822, doi:10.1175/1520-0469(1992)049<0805:SFOTIC>
888 2.0.CO;2.
- 889 Soares, P., P. Miranda, A. Siebesma, and J. Teixeira, 2004: An eddy-diffusivity/mass-flux
890 parametrization for dry and shallow cumulus convection. *Quarterly Journal of the Royal Mete-*
891 *orological Society*, **130** (604), 3365–3383.
- 892 Subias, A., 2015: B-splines as a Tool to Solve Constraints in Non-Hydrostatic Forecast Model.
893 *arXiv:1601.03446v2*.
- 894 Süld, J. K., A. Rasheed, J. Kristiansen, Ø. Sætra, A. Carrasco, and T. Kvamsdal, 2015: Mesoscale
895 Numerical Modelling of Met-ocean Interactions. *Energy Procedia*, **80**, 433–441.
- 896 Sun, Z., 2001: Reply to comments by Greg M. McFarquhar on ‘Parametrization of effective sizes
897 of cirrus-cloud particles and its verification against observations’. *Q. J. R. Meteorol. Soc.*, **127**,
898 267–271.
- 899 Sun, Z., and L. Rikus, 1999: Parametrization of effective sizes of cirrus-cloud particles and its
900 verification against observations. *Q. J. R. Meteorol. Soc.*, **125**, 3037–3055.
- 901 Tanré, D., J.-F. Geleyn, and J. Slingo, 1984: First results of the introduction of an advanced
902 aerosol-radiation interaction in the ECMWF low resolution global model. *Aerosols and their*

- 903 *climatic effects*, H. E. Gerber, and A. Deepak, Eds., A. Deepak Publ., Hampton, VA, USA,
904 133–177.
- 905 Tegen, I., P. Hollrig, M. Chin, I. Fung, D. Jacob, and J. Penner, 1997: Contribution of different
906 aerosol species to the global aerosol extinction optical thickness: Estimates from model results.
907 *Journal of Geophysical Research: Atmospheres*, **102 (D20)**, 23 895–23 915.
- 908 Termonia, P., and Coauthors, 2017: The ALADIN System and its Canonical Model Configurations
909 of cycles CY40T1 and CY41T1. *In preparation for Geosci. Model Dev.*
- 910 Toll, V., E. Gleeson, K. Nielsen, A. Mnnik, J. Mašek, L. Rontu, and P. Post, 2016: Importance of
911 the direct radiative effect of aerosols in numerical weather prediction for the European region.
912 *Atmospheric Research*, **172-172**, 163–173.
- 913 Unden, P., 2002: Hirlam-5 scientific documentation HIRLAM-5 Project Report SMHI. Tech. rep.,
914 HIRLAM.
- 915 Untch, A., and M. Hortal, 2004: A finiteelement scheme for the vertical discretization of the
916 semiLagrangian version of the ECMWF forecast model. *Quarterly Journal of the Royal Mete-*
917 *orological Society*, **130 (599)**, 1505–1530.
- 918 Valcke, S., 2013: The OASIS3 coupler: a European climate modelling community software. *Geo-*
919 *scientific Model Development*, **6 (2)**, 373–388.
- 920 Van Meijgaard, E., L. Van Ulft, G. Lenderink, S. De Roode, E. L. Wipfler, R. Boers, and R. van
921 Timmermans, 2012: *Refinement and application of a regional atmospheric model for climate*
922 *scenario calculations of Western Europe*. KVR 054/12, KVR.

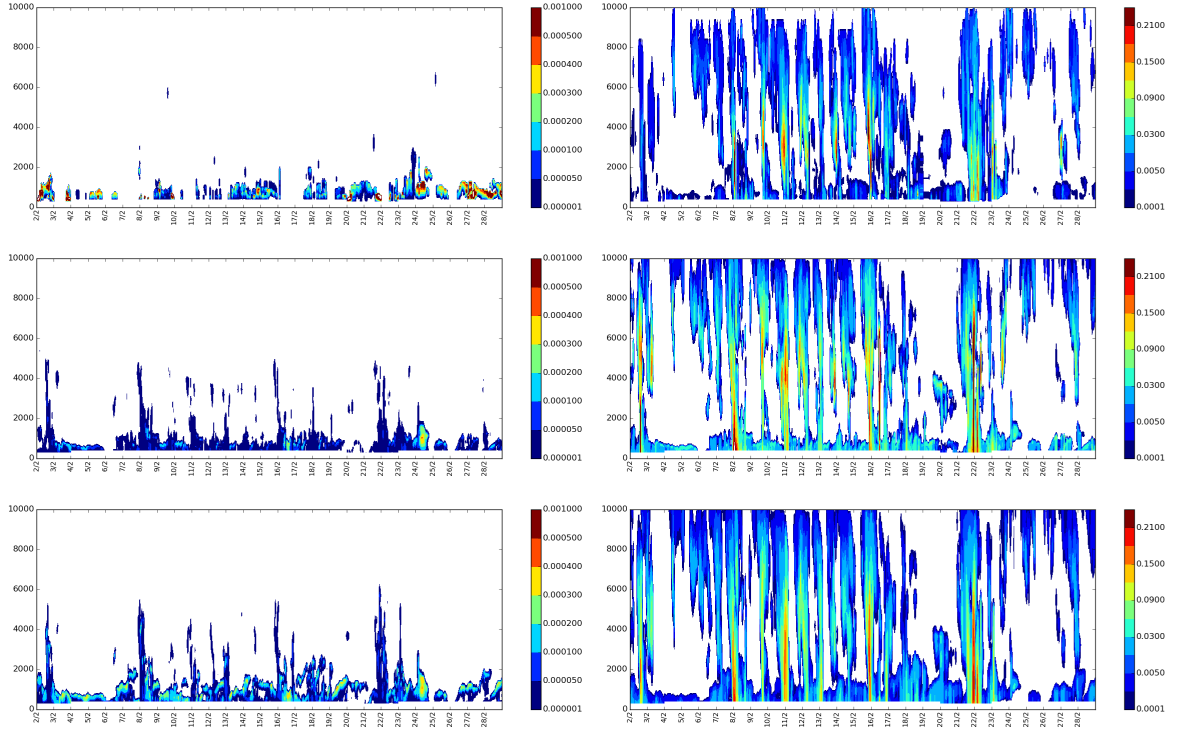
- 923 Váňa, F., P. Bénard, J. F. Geleyn, A. Simon, and Y. Seity, 2008: Semi-Lagrangian advection
924 scheme with controlled damping: An alternative to nonlinear horizontal diffusion in a numerical
925 weather prediction model. *Q.J.R Meteorol. Soc.*, **134**, 523–537.
- 926 Vié, B., J.-P. Pinty, S. Berthet, and M. Leriche, 2016: LIMA (v1. 0): A quasi two-moment mi-
927 crophysical scheme driven by a multimodal population of cloud condensation and ice freezing
928 nuclei. *Geoscientific Model Development*, **9** (2), 567–586.
- 929 Vivoda, J., and P. Smolíková, 2013: Finite elements used in the vertical discretization of the fully
930 compressible forecast model ALADIN-NH. *ALADIN-HIRLAM Newsletter*, **1**, 31–46.
- 931 Wyser, K., L. Rontu, and H. Savijärvi, 1999: Introducing the Effective Radius into a Fast Radiation
932 Scheme of a Mesoscale Model. *Contr. Atmos. Phys.*, **72** (3), 205–218.

933 **LIST OF TABLES**

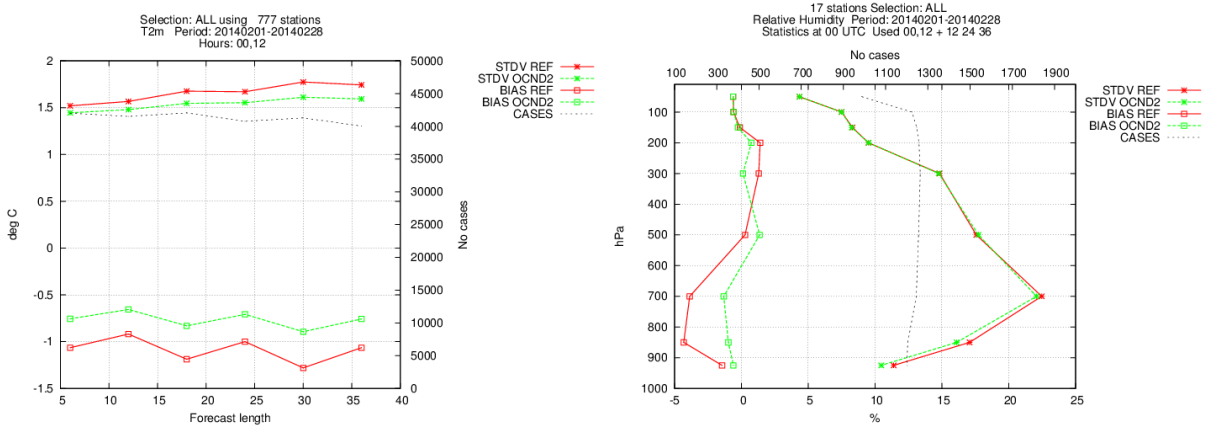
934 **Table 1.** Default parametrizations of cloud microphysical and optical properties for ra-
935 diative transfer used in HARMONIE-AROME 43

936 TABLE 1. Default parametrizations of cloud microphysical and optical properties for radiative transfer used
937 in HARMONIE-AROME

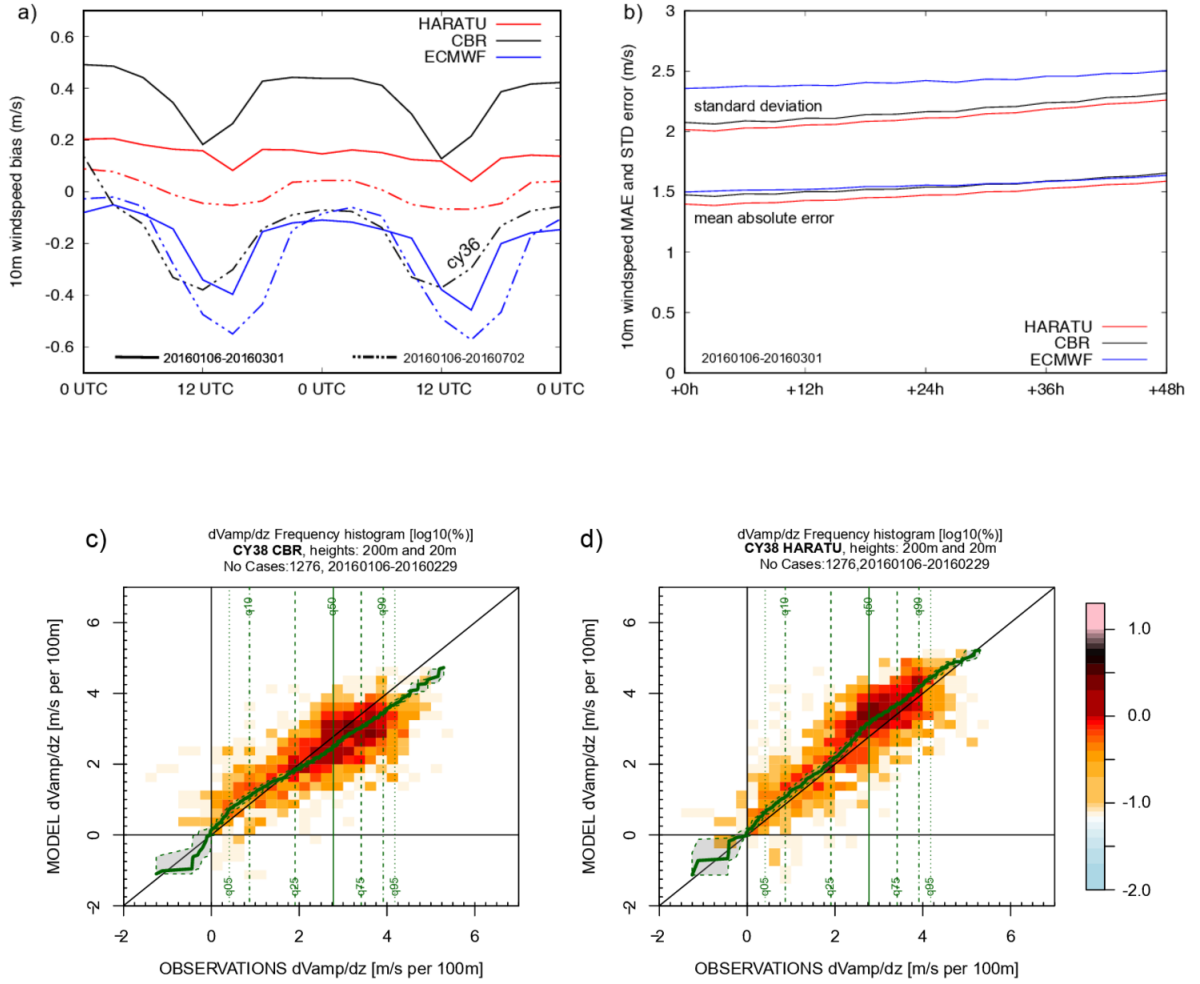
Parametrization	Reference
SW cloud liquid droplets	Nielsen et al. (2014)
SW ice crystals	Fu (1996)
LW cloud liquid droplets	Smith and Shi (1992)
LW cloud ice crystals	Fu et al. (1998)
Cloud liquid droplet effective radius	Martin et al. (1994)
Cloud ice crystal equivalent radius	Sun and Rikus (1999); Sun (2001)



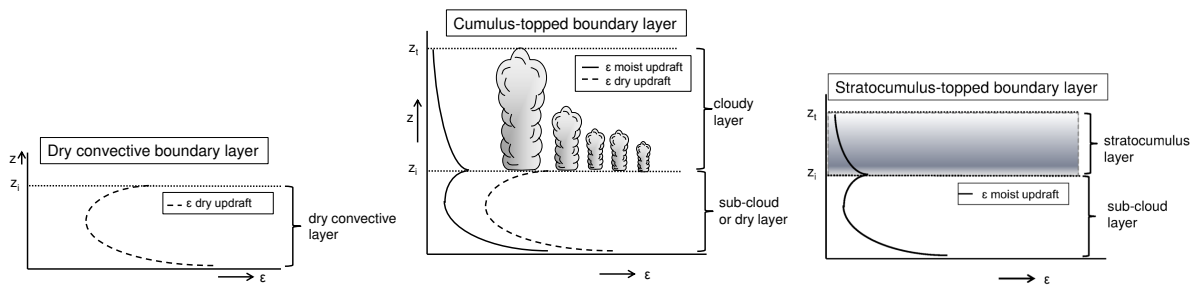
971 FIG. 1. Observed cloud liquid water content (kg/kg) (top-left) and cloud ice water content (g/kg) (top-right)
972 from Hytiälä, February, 2014. Modelled liquid water content (kg/kg) without OCND2 (middle-left) and ice
973 water content (ice+graupel+snow) (g/kg) (middle-right), and modelled liquid water (kg/kg) content with OCND2
974 (bottom-left) and ice water content (ice+graupel+snow) (g/kg) (bottom-right).



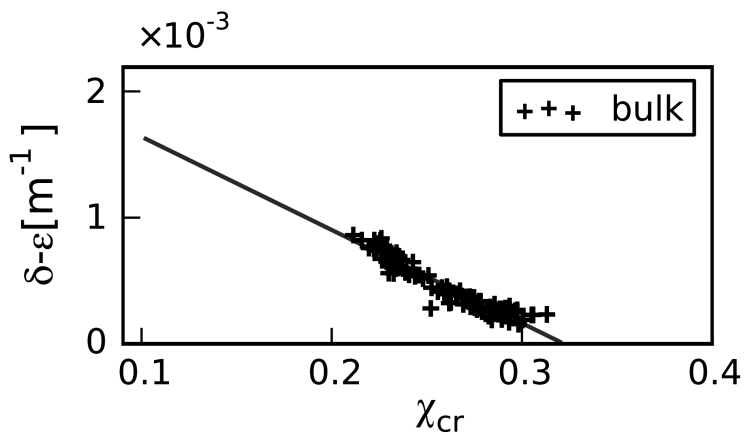
975 FIG. 2. Left: bias and standard deviation of 2 meter temperature for REF (red) and OCND2 (green) simu-
 976 lations with HARMONIE-AROME cycle 40h1.1, as a function of forecast lead time. Right: bias and standard
 977 deviation of relative humidity as a function of height.



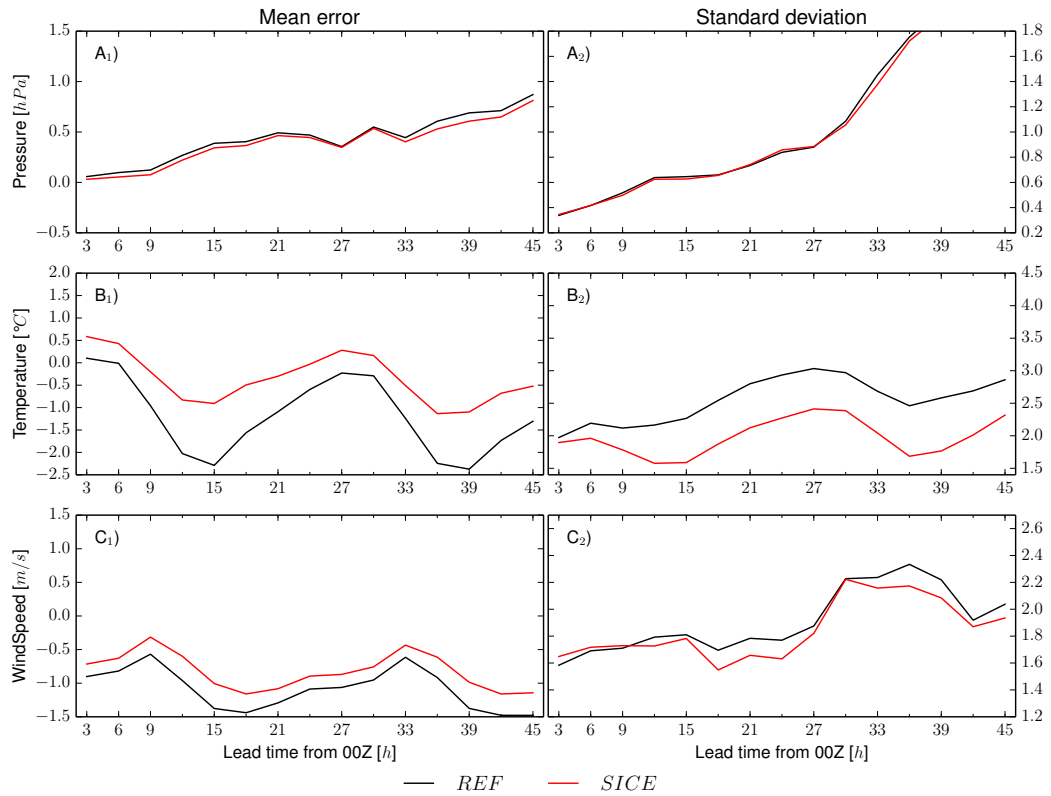
978 FIG. 3. a) Wind speed bias over all station in the domain used by The Netherlands for operational forecasting.
979 Shown are results from the run starting midnight using the CBR turbulence scheme and HARATU turbulence
980 scheme, for two verification periods in comparison with the operational ECMWF forecast (cy41, T1279). The
981 HARMONIE-AROME runs are based on cy38 with the HARATU scheme included, except the CBR run for the
982 later period which uses cy36 as indicated in the plot. b) mean absolute error and standard deviation of the error
983 for HARATU, CBR (in cy38) in comparison with ECMWF as a function of forecast length (based on 4 model
984 cycles a day). c) Wind speed stratification verification against Cabauw tower measurements for CBR and b) using
985 the HARATU scheme. Both for the period 06/01/2016 to 29/02/2016. The color of each bin denotes the density
986 of points in that bin. The green line denotes a quantile-quantile plot, with quantiles indicated by the vertical
987 lines.



988 FIG. 4. Schematic diagrams of the convective boundary layer regimes and their corresponding entrainment
 989 formulations. The inversion height and cloud top height are respectively denoted as z_i and z_t . The shape of the
 990 entrainment profiles reflects the inverse dependency on the vertical velocity of the updraft. For the moist updraft,
 991 the mass flux at cloud base is described using Grant (2001)



992 FIG. 5. Dependence of $\delta - \varepsilon$, i.e. the fractional decrease of the mass flux with height, on χ_c (see text). The
 993 values are averaged over the lowest half of the cloud layer. (a) American Geophysical Union 2012, from Fig. 3
 994 of Böing et al. (2012)



995 FIG. 6. SICE scheme over seven stations in Gulf of Bothnia for time period from 01 March 2013 to 31 March
 996 2013, forecasts initialized at 00 UTC. Black curves represents the HARMONIE-AROME cycle 401.1 without
 997 the SICE scheme, and red curves are with the SICE scheme.

Characterization of the impact of geostationary clear-sky radiances on wind analyses in a 4D-Var context

C. Peubey* and A.P. McNally

European Centre for Medium-Range Forecasts, Reading, UK

ABSTRACT: The impact of geostationary clear-sky radiances (CSRs) on 4D-Var wind analyses has been investigated by running a set of observing system experiments. Analysis scores have been calculated to measure the ability of individual satellite datasets to improve the wind analysis, starting from a no-satellite baseline. In this context, the assimilation of CSRs from the two water-vapour channels on Meteosat-9 has been found to improve the wind analysis throughout the troposphere, with the strongest signal at 300 and 500 hPa. Indeed, for the Northern Hemisphere and the Tropics, the CSR impact at these levels exceeds that of the Meteosat-9 atmospheric motion vectors (AMVs), the sampling of the latter in the assimilation being rather limited. Conversely, the impact of AMVs exceeds that of CSRs in the lower troposphere, where the latter provide very little direct information. This demonstrates the complementarity of the two datasets in the operational 4D-Var wind analysis. The mechanisms through which the assimilation of CSRs can impact wind analyses have been isolated. The dominant effect is that of humidity-tracer advection, by which the wind field is adjusted in order to fit observed humidity features via the minimization of the 4D-Var cost function. Other mechanisms, such as balance constraints and the cycling of the forecast model that links the humidity and wind variables, have been found to play a minor role. The benefit of having frequent CSR images within the assimilation window has also been demonstrated.

Copyright © 2009 Royal Meteorological Society

Received 16 February 2009; Revised 17 June 2009; Accepted 21 July 2009

1. Introduction

The importance of infrared radiances as a source of humidity information in the middle and upper troposphere has been demonstrated in a number of studies (Soden and Bretherton, 1996; Andersson *et al.*, 2007). These data can also influence the wind field via a number of different mechanisms (McNally and Vesperini, 1996). In 3D-Var and 4D-Var multivariate data assimilation schemes, explicit background-error correlations and balance relationships mean that changes to one variable cannot happen in isolation. Thus a humidity increment due to the assimilation of humidity-sensitive infrared radiances will, in general, be accompanied by an increment in temperature and wind.

In 4D-Var assimilation schemes, where a time-series or trajectory of model states is fitted to the available observations, different analysis variables are linked through the model governing equations and physical parametrizations. Thus changes made to fit humidity-sensitive observations will result in the adjustment of the trajectory of other model variables; for example, the wind field can be changed to advect humidity to and from other areas. This process is sometimes referred to as the ‘tracer advection effect’. It is similar to the way in which information about

the flow is inferred from the assimilation of tracer constituents using a Kalman filter or 4D-Var schemes (Daley, 1995; Riishøjgaard, 1996; Holm *et al.*, 1999; Peuch *et al.*, 2000).

Finally, any changes to the humidity field that occur in one analysis time window result in adjustments to other variables (such as wind) when the assimilation system is cycled over many time windows. Information is passed from one analysis window to the next by a short-range forecast where the time evolution of different variables is again linked by the thermodynamic model equations. Indeed, radiances have been shown to affect winds in assimilation schemes such as 3D-Var and optimal interpolation systems (McNally and Vesperini, 1996).

In this particular study, we investigate the impact of humidity-sensitive geostationary clear-sky radiances (CSRs) on the European Centre for Medium-Range Forecasts (ECMWF) 4D-Var wind field. Previous studies have noted wind changes due to the assimilation of CSR data (Munro *et al.*, 2004; Köpken *et al.*, 2004). However, the changes have resulted from a combination of the mechanisms described above in systems that simultaneously assimilate a variety of other observations of wind and humidity. Here we quantify the magnitude of the CSR wind impact in isolation and compare results with the wind impact of other satellite data – namely geostationary atmospheric motion vectors (AMVs) and polar orbiting radiances (PORs, see section 2.2.3 for the list of instruments). We then attempt to identify

*Correspondence to: Carole Peubey, European Centre for Medium-Range Weather Forecasts, Shinfield Park, Reading RG2 9AX, UK.
E-mail: carole.peubey@ecmwf.int

the dominant mechanism by which CSRs achieve this wind impact ('balance constraints', 'tracer advection' or 'model cycling'). Finally, we examine to what extent the unique time resolution offered by geostationary radiance observations is important. These three different issues have been addressed by running three sets of observing system experiments (OSEs).

The OSEs are performed from a baseline that contains no other satellite data. There are a number of advantages to this: firstly, the addition of satellite data from a single source to a poor-quality baseline produces much larger and clearer signals compared with the situation when the data are added to a densely observed system (Kelly and Thépaut, 2007). Secondly, we can attribute any changes directly to the newly added observations (eliminating potentially complex interactions with other observations). Finally, in this particular study, it allows us to deliberately suppress individual wind-impact mechanisms for CSRs, allowing us to assess the relative importance of each. This approach has been used before by Kelly and Thépaut (2007) and differs from OSE studies based on denial experiments (Zapotocny *et al.*, 2008), where particular types of data are removed individually from a densely observed system.

In section 2 we describe the details of the data, the assimilation experiments and the metrics used to measure the impact on wind analyses. Sections 3–5 respectively present the results of the three sets of OSEs. Finally a summary and discussion from the study are given in section 6.

2. Methodology

2.1. General set-up

All the experiments run in this study use version 32r2 of the ECMWF assimilation system (see

<http://www.ecmwf.int/research/ifsdocs/> for documentation on earlier model versions, as no later documentation is yet available), composed of a 4D-Var assimilation scheme (Mahfouf and Rabier, 2000; Rabier *et al.*, 2000) and a forecast model run at a resolution of $T511$ (approximately 40 km). The impact of assimilating the different satellite datasets (CSRs, AMVs and PORs) is measured in comparison with the same baseline experiment (*base*), which does not assimilate any satellite data. The performance of all the experiments is verified against the ECMWF operational analysis as explained in section 2.3. The *base* runs from 23 May–26 June 2007 and is initialized with the ECMWF operational analysis. The conventional humidity data removed, the only assimilated observations are conventional *in situ* data from radiosondes, aircraft and surface observations.

CSR, AMV or POR observations are then individually assimilated in experiments initialized with the *base* on 3 June 2007, the base system having thus degraded from the operational analysis over a period of 10 days. As mentioned in the Introduction, the use of an artificially degraded baseline makes increments due to a given assimilated dataset much more identifiable than in the case of the full data system. Removing all satellite data in the baseline experiment also leads to fast-growing errors in regions that are poor in conventional data. In similar OSE studies, Kelly and Thépaut (2007) have assimilated AMSU-A data in the baseline experiment in order to keep a realistic model state in the Southern Hemisphere (SH). This has not been done here. Indeed the fact that the atmospheric state in the SH is far from the truth is considered a good opportunity to test the accuracy of the tangent-linear hypothesis implicit in the 4D-Var assimilation technique. The configurations of the OSEs from Sets 1 and 2 are given in Table I.

Table I. Summary of experiments from Sets 1 and 2. The *Operations*, *base* and *base+CSRs* experiments are used in the two sets.

		Observations				4D-Var configuration		
		Conventional data	CSRs	AMVs	PORs	Full 4D-Var	No humidity-tracer effect	No increments in T from CSRs
	<i>Operations</i>	X	X	X	X	X		
	<i>Base</i>	X				X		
	<i>Base+CSRs</i>	X	X			X		
Set 1	<i>Base+AMVs</i>	X		X		X		
	<i>Base+CSRs+AMVs</i>	X		X	X	X		
	<i>Base+PORs</i>	X			X	X		
Set 2	<i>No-qtracing</i>	X	X				X	
	<i>No-δT</i>	X	X					X
	<i>No-δT-no-qtracing</i>	X	X				X	X

2.2. Satellite data

2.2.1. Clear-sky radiances

The CSR data used in this study are produced by EUMETSAT from radiances measured by SEVIRI (Schmetz *et al.*, 2000) on board Meteosat-9 in full-disc scan mode. The satellite disc is centred at 0° longitude and covers around $\pm 60^{\circ}$ in both latitude and longitude directions. This instrument has eight infrared channels, two of them being primarily sensitive to water vapour (WV) (6.2 and 7.3 μm) with weighting functions peaking respectively around 300 and 500 hPa. CSRs are calculated by averaging radiances from cloud-free pixels over a segment of 16×16 pixels, which approximately corresponds to a $50 \text{ km} \times 50 \text{ km}$ square at the sub-satellite point. The full-disc CSR data (non-rapid scan) from SEVIRI are disseminated hourly by EUMETSAT. Daily comparisons of Meteosat-9 CSRs against the ECMWF model first-guess show that WV CSRs have a level of noise close to that of equivalent channels on HIRS and IASI. Similar results were found for SEVIRI on board Meteosat-8 and HIRS WV channels (Szyndel *et al.*, 2004).

The procedure to assimilate CSRs in this article is the same as in the current operational ECMWF system, which uses a 12 hour assimilation window. For the CSRs, this means that 12 images are used for each analysis. Prior to the assimilation, CSRs are thinned down to a spatial resolution of around 120 km and undertake a series of quality control tests. Firstly, an initial bias correction generated during the previous analysis is applied to the data. CSR observations are then compared with CSRs calculated with the RTTOV-8 radiance forward model (Matricardi and Saunders, 1999) from the previous short-range forecast, which has been interpolated to the observation locations. When the absolute departure of the observation from the calculated values exceeds a certain threshold (typically around 6 K), the observation is discarded (Köpken *et al.*, 2004). Observations with scanning angle greater than 60° , or above high orography, are also rejected. Finally, in order to exclude cloud-contaminated data, only CSRs calculated from segments having more than 70% clear pixels are kept. Over sea, this test is reinforced by rejecting data having a model departure in the window channel (10.8 μm) outside the ± 3 K range, which approximately corresponds to three standard deviations (this test cannot be used over land because the uncertainty in the model skin-temperature is too large). The remaining data are then assimilated in the 4D-Var system with an observation error of 2 K (also accounting for error in the forward modelling of the CSRs). The CSR departures – together with all other observations and constraints – then drive increments (adjustments) of the analysis variables (temperature, humidity, ozone concentration and wind). More details on the way CSRs are assimilated in the ECMWF 4D-Var system can be found in Munro *et al.* (2004) and Köpken *et al.* (2004).

2.2.2. Atmospheric motion vectors

AMVs have been part of numerical weather prediction (NWP) systems since the early 1990s (Velden *et al.*,

1997; Rohn *et al.*, 2001) and are considered as an important source of information about the atmospheric flow (Kelly *et al.*, 1998; Zapotocny *et al.*, 2008) throughout the troposphere. The AMV data used in this study are the Meteosat-9 AMVs assimilated in the ECMWF operational suite (Delsol *et al.*, 2005). No other sources of AMVs (from other geostationary or polar platforms) have been assimilated in the OSEs presented in this article. Meteosat-9 AMVs are produced by EUMETSAT by tracking clouds in successive images in window, WV and visible channels (Schmetz *et al.*, 1993). A clear-sky AMV product (Holmlund, 1995), where wind vectors are inferred from humidity structures in WV images, is also available at EUMETSAT but it is not assimilated in the ECMWF operational suite. It has not been used in this study, mainly because of unresolved difficulties in assimilating this type of data, which are representative of much deeper layers of atmosphere than are cloudy AMVs.

The number of AMV observations assimilated in the ECMWF system depends on the availability of targets to be tracked (e.g. the low number of clouds at heights above 200 hPa in midlatitudes) as well as on the strict quality control applied to these data, especially in the tropical middle troposphere, where they are affected by large biases (Delsol *et al.*, 2005). More details on the AMV quality control at ECMWF can be found in http://www.metoffice.gov.uk/research/interproj/nwpsaf/satwind_report/. AMV data are also horizontally thinned by selecting the AMV with the highest forecast-independent quality indicator (Holmlund, 1998) provided by EUMETSAT in boxes of $200 \times 200 \text{ km}^2$. AMVs are then assimilated hourly with observation errors of $2\text{--}6 \text{ m s}^{-1}$.

2.2.3. Polar orbiter radiances

PORs are radiances from polar orbiters, measured by both infrared (AIRS and HIRS) and microwave (AMSU-A, AMSU-B, MHS and SSMI) sensors. The use is the same as in the ECMWF operational system but over a restricted area (latitudes between 50°E and 50°W and longitude between 50°N and 50°S), which roughly corresponds to the Meteosat-9 scanning disc. Like CSRs, infrared and microwave data are thinned down to a horizontal resolution of around 120 km and are attributed an observation error of 2 K. Further details on the assimilation of these data are described in Bauer *et al.* (2002) and McNally *et al.* (2006). PORs have been shown to have a major impact on the ECMWF system (Kelly and Thépaut, 2007).

2.2.4. Bias correction of the satellite data

Since September 2006, the ECMWF system has had an adaptive variational bias correction scheme (VarBC; see Auligné *et al.*, 2007) for satellite radiances which allows the readjustments of the correction coefficients at every 4D-Var minimization. In principle, removing all satellite data from the system as in *base* could have an impact on the VarBC coefficients, as these depend on all the observation departures from the model state. However,

the radiosonde data, which are assimilated in the present study, are not corrected adaptively and have been shown to act as a strong constraint upon the satellite data bias correction (Auligné *et al.*, 2007), so that VarBC should still be suitable in the present study. To check that this is the case, two prior experiments have been run, both assimilating CSRs as the only satellite data, but one uses VarBC while the other uses a constant bias correction. Both give similar wind-analysis scores, which justifies the use of VarBC for this work.

2.3. Analysis scores

For each experiment the analysis error is compared with that of *base* to provide an ‘analysis score’, which is a measure of how much *base* is improved by the assimilation of each set of satellite data. Errors are defined as departures from the ECMWF operational analysis, considered here as the best available estimate of the true wind field. The operational suite runs at *T799* resolution and assimilates conventional observations, AMVs, PORs, CSRs as well as scatterometer and GPSRO data.

Analysed fields have been interpolated on to pressure levels and on to a regular $2.5^\circ \times 2.5^\circ$ latitude – longitude grid. For every cycle j , the root-mean-square analysis error $RMSE_j$ is

$$RMSE_j = \sqrt{\frac{1}{n} \sum_{i=1}^n (u_i - u_i^r)^2 + (v_i - v_i^r)^2}, \quad (1)$$

where u_i and v_i are the analysis values of the zonal and meridional wind components at a grid point i and n is the number of grid points inside an area that roughly corresponds to the Meteosat-9 disc (longitude within 35° W– 35° E, latitude within 20° N– 50° N for the NH, 20° S– 20° N for the Tropics and 50° S– 20° S for the SH). An area-weighted factor is included in the summation over latitude. u_i^r and v_i^r are the corresponding wind analyses from ECMWF operations. The same quantity is calculated for the *base*, having u_i^b and v_i^b as wind components:

$$RMSE_j^b = \sqrt{\frac{1}{n} \sum_{i=1}^n (u_i^b - u_i^r)^2 + (v_i^b - v_i^r)^2}. \quad (2)$$

The wind-analysis error of the experiment under consideration is then compared with that of *base* by subtracting $RMSE_j$ from $RMSE_j^b$. The analysis score $\Delta RMSE$ is found by averaging over all m assimilation cycles and normalizing by the mean wind error of *base* as follows:

$$\Delta \overline{RMSE} = \frac{\sum_{j=1}^m (RMSE_j^b - RMSE_j)}{\sum_{i=j}^m RMSE_j^b}. \quad (3)$$

Hence a value of the analysis score equal to zero means no improvement over *base*, while a value of 1 (or 100% as percentages are used in this article) corresponds to an analysis that has no error with respect to the high-resolution (*T799*) operational analysis.

Averages have been calculated over all assimilation windows starting at 0900 UTC and 2100 UTC. Hence, the day-night dependence of some of the datasets is ignored, as for the AMVs from the visible channels (lower troposphere). Averages over 2100 UTC assimilation windows only have also been carried out and show very similar results to those presented in this study, although slightly less favourable to AMVs in the lowermost troposphere due to the limited number of visible AMVs in the 2100 UTC assimilation window. 95% confidence intervals for the $\sum_{j=1}^m (RMSE_j - RMSE_j^b)$ quantity were calculated with the *T*-test. In order to remove autocorrelations between successive cycles, the degree of freedom of the sample used in the *T*-test formula was calculated using equation (6.13) of Bretherton *et al.* (1999). To obtain error bars on $\Delta \overline{RMSE}$, the confidence intervals were normalized by the denominator of (3).

3. Set 1: The impact of CSRs on wind analyses

The impact of CSRs on the wind analysis via all possible mechanisms (4D-Var, model cycling and balance constraints) is investigated. For each experiment, one or two types of observations are added on top of the *base*: CSRs (*base+CSRs*), AMVs (*base+AMVs*), both CSRs and AMVs (*base+CSRs+AMVs*) and PORs (*base+PORs*).

Figure 1 shows the wind-analysis scores as a percentage for each of the four experiments. Note that the analysis scores are here limited by the use of the *T511* resolution; the best possible scores obtained by running the operational suite at *T511* resolution are around 60% in the NH and Tropics and 80% in the SH. The results of *base+CSRs* (dark grey bars) are all positive at the four considered levels, clearly demonstrating improvement of the wind analysis via CSR assimilation. Scores in the SH are affected by a high degree of spread, which makes the improvement at 850 hPa not statistically significant. This is due to the fast-growing errors affecting this region, which is poor in conventional data.

The best scores for CSRs are found at 300 and 500 hPa, which correspond to the maxima of the two WV channel-weighting functions. In the Tropics and NH, the impact of CSRs exceeds that of AMVs (white bars), especially at 500 hPa. However, the number of assimilated AMV observations varies with height and latitude. In the Tropics, all AMVs are actually rejected at 500 hPa, which explains the zero score. Nevertheless, at 300 hPa in the NH, where a reasonable number of AMVs are assimilated, the *base+CSRs* score is similar to that of *base+AMVs*.

At 850 and 200 hPa, levels to which the CSRs have little direct sensitivity, the *base+CSRs* scores are still noticeably positive. In the lower troposphere, very rich in AMV observations, the scores are half those of *base+AMVs*. The same is true at 200 hPa in the Tropics, but not at higher latitudes, as the cloud occurrence at this pressure level is much lower.

Hence, AMVs and CSRs appear to have their maximum impacts on wind analysis at different levels

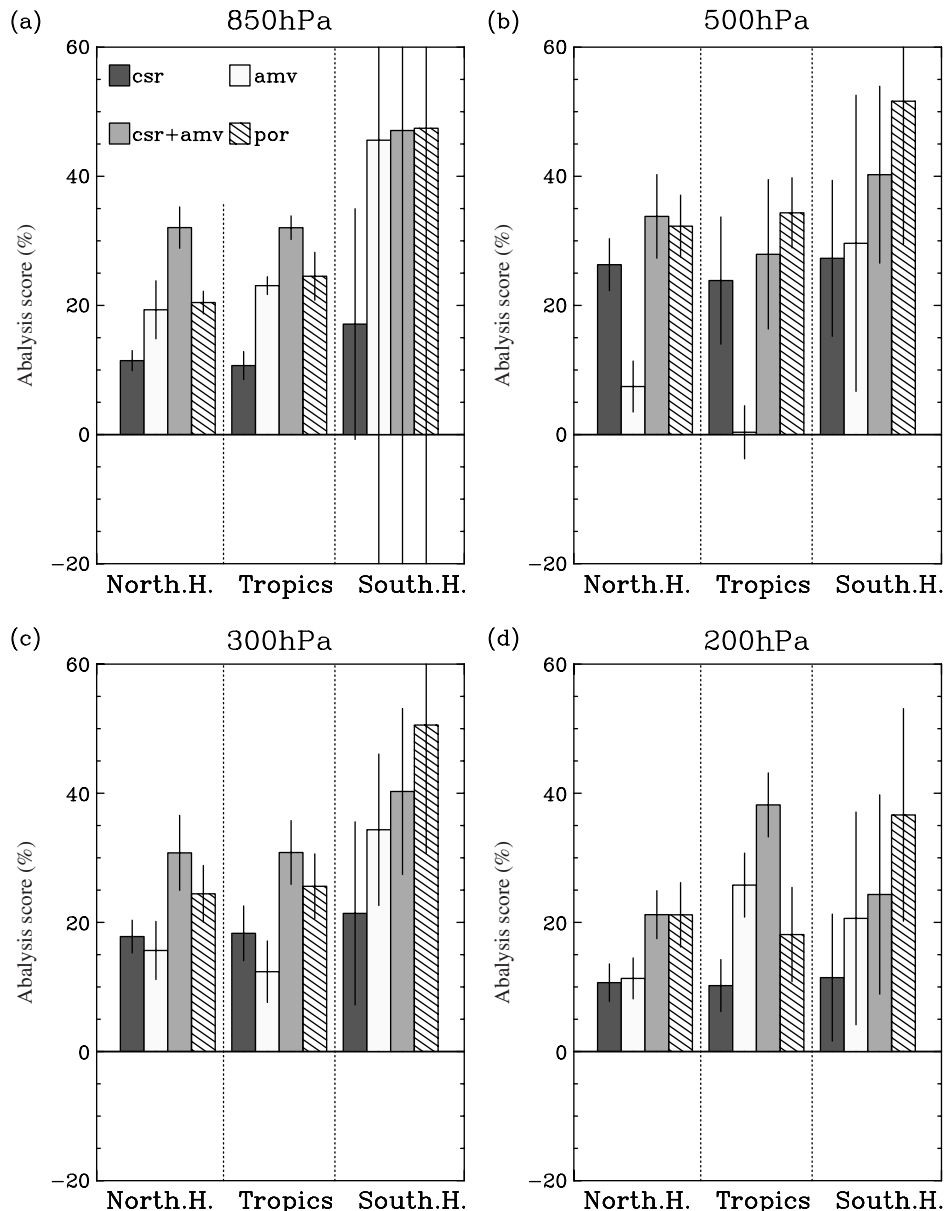


Figure 1. Wind analysis scores for the experiment of Set 1: *base+CSRs* (dark grey), *base+AMVs* (white), *base+CSRs+AMVs* (light grey) and *base+PORs* (hatched).

and latitudes, which shows the complementarity of the two datasets. Moreover, comparing the individual results of *base+CSRs* and *base+AMVs* with those of *base+CSRs+AMVs* (light grey bars in Figure 1) suggests that the benefit of each dataset is roughly additive in the NH and Tropics, which stresses the advantage of having both datasets in an assimilation system.

In the SH, the error growth means that the tangent linear hypothesis implicit in 4D-Var is likely to be violated, which should limit the positive impact of assimilated observations. Conversely, in this same region, the lack of conventional data, which strongly constrain the *base*, should emphasize the impact of satellite data. Compared with the rest of the globe, the AMV and POR impacts in Figure 1 are much larger in the SH (except at 200 hPa in the midlatitudes, where AMVs have a poor coverage). However, this is not the same for CSRs, which could

imply that the wind information extracted from WV CSRs is more sensitive to the accuracy of the model state than is direct wind information such as AMVs. In the case of PORs, wind information is also extracted from thermal channels. As these are primarily used over oceans (dominant in the southern part of the Meteosat-9 disc), their impact is particularly important in the SH. Hence, the POR thermal channels contribute to limit analysis errors in the SH, which could also lead to improvement of the wind impact of the WV channels.

In the Tropics, the absence of geostrophic balance means that wind information extracted from WV channels should be particularly important, as shown in Anderson *et al.* (2007). In particular, AIRS, HIRS and AMSU-B have channels sensitive to the middle- and high-troposphere WV, and the combination of the three instruments assures nearly complete coverage of the Meteosat-9 disc

within a six-hour period. Although this frequency of data is less than that of CSRs, the PORs benefit from a much better vertical coverage. For instance, AIRS has around 50 assimilated WV channels peaking throughout the troposphere (McNally *et al.*, 2006). Nevertheless, the CSR scores in the tropical middle troposphere are roughly two thirds those of the PORs, which makes CSRs an important source of wind information in this region, also poor in high-quality AMVs.

Wind forecast scores have also been calculated by replacing analysis by forecast for the experiment under consideration in (1) and for the *base* in (2). Table II summarizes the forecast scores of *base+CSRs* with respect to *base* for the 300 and 500 hPa levels. Values of the forecast scores are all positive, with significant signal at the 95% level up to day 3 in the NH and up to at least day 5 in the SH. The impact of CSRs on forecast scores compared with that of AMVs (Table III) and PORs (Table IV) is very consistent with the analysis score results. The forecast scores of *base+PORs* are in general higher than those of *base+CSRs* and more persistent at 500 hPa in the Tropics.

4. Set 2: Identifying the mechanisms of the CSR impact on winds

Having demonstrated that there is a strong impact of CSRs on wind analyses, we now attempt to identify the mechanism responsible for it. The following CSR assimilation experiments have thus been run with modified settings of the 4D-Var scheme (see Appendix for more details).

Table II. Normalized root-mean-square percentage differences between *base* and *base+CSRs* for 300 and 500 hPa vector winds verified versus the operational analysis over the 4–26 June 2007 period. Positive values indicate a positive impact from the assimilation of CSRs. Figures in bold indicate signals significant at the 95% level or better.

		Day 1	Day 3	Day 5
NH	300 hPa	+2.2	+1.5	+0.1
	500 hPa	+3.1	+1.2	0.0
Tropics (20° S–20° N)	300 hPa	+1.8	+2	+1.7
	500 hPa	+6.0	+4.5	+3.0
SH	300 hPa	+13.5	+9.5	+6.8
	500 hPa	+13.2	+10.1	+7.5

Table III. Same as Table II but for *base+AMVs*.

		Day 1	Day 3	Day 5
NH	300 hPa	+1.8	+0.1	-0.8
	500 hPa	+2.1	-0.2	-0.8
Tropics (20° S–20° N)	300 hPa	+0.2	+0.6	+2.4
	500 hPa	+2.2	+2.1	+3.0
SH	300 hPa	+16.1	+12.1	+7.2
	500 hPa	+13.5	+10.2	+7.3

Table IV. Same as Table II but for *base+PORs*.

		Day 1	Day 3	Day 5
NH	300 hPa	+3.2	+1.7	+0.6
	500 hPa	+3.1	+1.4	+1.0
Tropics (20° S–20° N)	300 hPa	+0.4	+1.5	+2.5
	500 hPa	+5.8	+4.8	+4.1
SH	300 hPa	+19.2	+13.4	+8.8
	500 hPa	+19.0	+11.8	+8.3

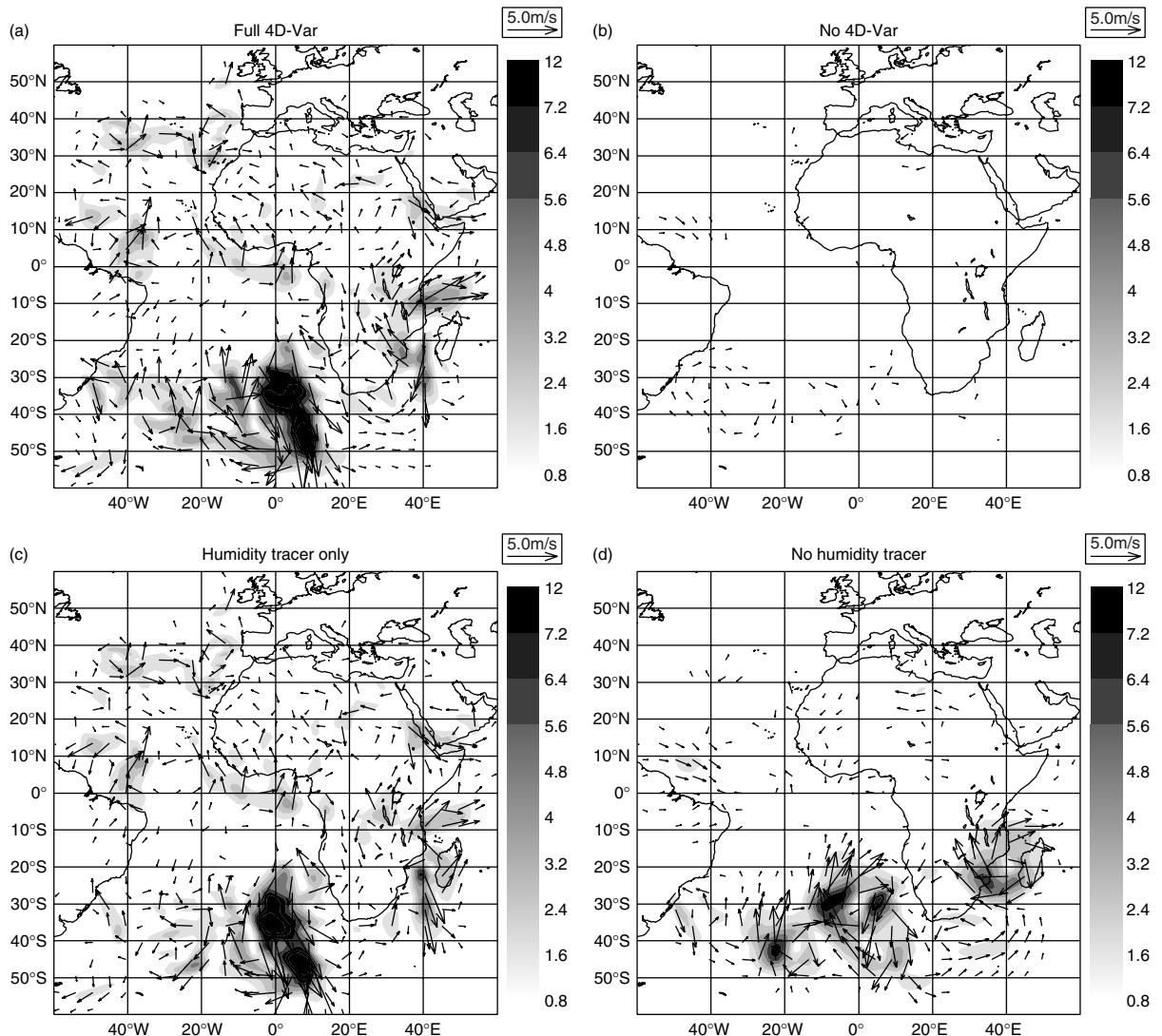


Figure 2. First-cycle 300 hPa wind increment on 3 June 2007 at 2100 UT produced by the assimilation of CSRs for the Set 2 experiments: (a) the full 4D-Var experiment (*base+CSRs*), (b) the ‘no 4D-Var’ experiment (*no- δT -no-qtracing*), (c) the experiment with the humidity-tracer effect only (*no- δT*) and (d) the experiment with no humidity-tracer effect (*no-qtracing*). The contours indicate the wind speed in m s^{-1} .

humidity and temperature fields, which in turn provide positive feedback on winds through the cycling of the model. To remove this effect, experiments *base+CSRs*, *no- δT -no-qtracing* and *no- δT* are repeated, but with no transfer of CSR information between successive assimilation windows. This is achieved by initializing every

analysis using the first-guess of *base*, preventing any dynamical adjustment due to any increments generated by CSRs.

Increments generated by CSRs at 300 hPa in the beginning at the first 12 hour assimilation window are shown in Figure 2 for experiments *base+CSRs*,

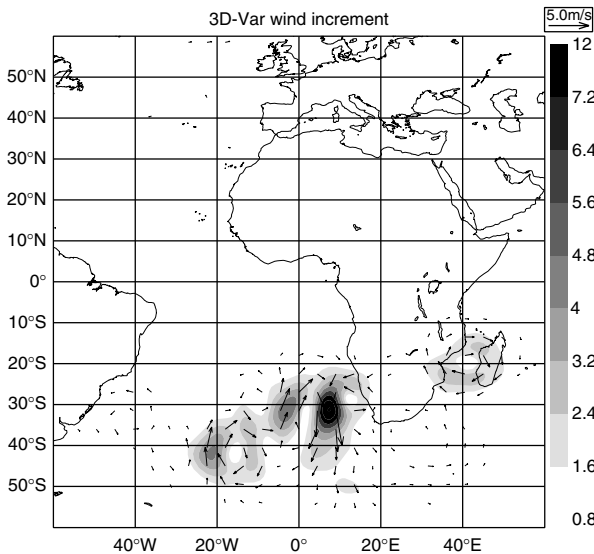


Figure 3. First-cycle 300 hPa wind increment from CSRs on 4 June 2007 at 0000 UT produced by the 3D-Var assimilation of CSRs in m s^{-1} .

no- δT -no-qtracing, *no- δT* and *no-qtracing*. These have been estimated by subtracting the increments of *base* from the increments of the considered experiments. Panel (a) shows the *base+CSRs* increment, produced by the full 4D-Var system. This has maximum values over the Atlantic, southeast of South Africa. In the NH, the impact of CSRs can be clearly seen up to 40° . Similar results have been found for the 500 hPa increments (not shown).

Comparing panels (a) and (c) of Figure 2, the *base+CSRs* and *no- δT* increments are very similar in structure and magnitude, which shows that the temperature changes retrieved from CSR observations have only a weak impact on the wind analysis. Conversely, the comparison between *base+CSRs* and *no-qtracing* increments indicates that removing tracer advection completely changes the structure of the wind increment. This clearly suggests that the effect of humidity-tracer advection is the dominant process involved in the production of wind increments from CSR WV channels.

The *no-qtracing* increment (Figure 2(d)) is actually very similar in structure to the equivalent 3D-Var increment obtained by running the ECMWF 3D-Var assimilation system (Rabier *et al.*, 1998) using a six-hour assimilation window (Figure 3). This implies that the 3D-Var and *no-qtracing* increments have been mainly produced by the same process of balance constraints imposed on the analysis (as this is the only possible way radiance observations can generate 3D-Var wind increments). One example of this balance relationship in the extratropics is the cyclonic pattern centred between Africa and Madagascar in Figures 2(d) and 3, which has been found to be associated with a localized negative pattern in temperature increments (not shown). Processes other than balance involved in the *no-qtracing* wind increments appear to play only minor roles. A small contribution of these can be noticed in the Tropics, where the geostrophic balance is very weak.

The addition of the increments from *no- δT* and *no-qtracing* does not correspond to the full 4D-Var increment, as adding the processes of geostrophic balance constraints and humidity advection individually is different from applying the full 4D-Var process, where temperature, humidity and wind variables are allowed to readjust simultaneously. In *no- δT -no-qtracing* (Figure 2(b)), the effect of tracer advection is disabled and the impact through the balance constraints in error correlations is limited, as radiance observations are prevented from producing direct changes in temperature. The other way to create wind increments in this case is through the wind-humidity links in the physical parametrization. However, the very small size of the *no- δT -no-qtracing* wind increments indicates that this process is of minor importance.

The dominant role played by the effect of humidity-tracer advection in producing 4D-Var wind increments from radiance observations is confirmed by the analysis scores evaluated over a three-week period (Figure 4). The *no-qtracing* scores (hatched bars) are much lower than those of the full 4D-Var experiment (dark grey bars). Hence, without tracer advection effects, wind analyses obtain little benefit from the assimilation of CSRs. The similarity of *base+CSRs* and *no- δT* scores confirms the weak impact of temperature changes on wind increments. Finally, the scores of *no- δT -no-qtracing* are insignificant or considerably smaller than those of *base+CSRs*.

In the Tropics, the *no-qtracing* scores are slightly positive to neutral. This low impact can mostly be explained by the weakness of the temperature information extracted from the 6.2 and 7.3 μm channels. In the SH, however, the first wind increment (Figure 2(d)) is comparable in amplitude to that of *base+CSRs* (Figure 2(a)), but the *no-qtracing* scores are negative in the upper troposphere (Figure 4). This suggests that the extraction of wind via the balance from WV CSRs does not work when the model state is affected by very large errors.

Finally, the effect of removing the CSR impact on wind completely through the cycling of the model is shown in Figure 5. Because CSRs are assimilated using the first guess of the *base* at every assimilation cycle, the analysis remains close to the *base* throughout the experiment, which explains the lower values of the analysis scores compared to those in Figure 4. These scores can thus be regarded as averages over single-cycle assimilation experiments starting at different times. Figure 5 shows that the positive impact of CSRs assimilated with the full 4D-Var system (dark grey bars) is limited to the 300 and 500 hPa levels and is neutral to negative at the other levels. This means that the positive scores found at 850 and 200 hPa in Figure 4 are due to the model cycling effect, which propagates the benefit of the wind increment at 300 and 500 hPa to levels above and below. In *base+CSRs*, the scores at 200 and 850 hPa are neutral to negative and generally lower than those of *no- δT* , which suggestss that the full 4D-Var system misinterprets very weak and indirect temperature information from the

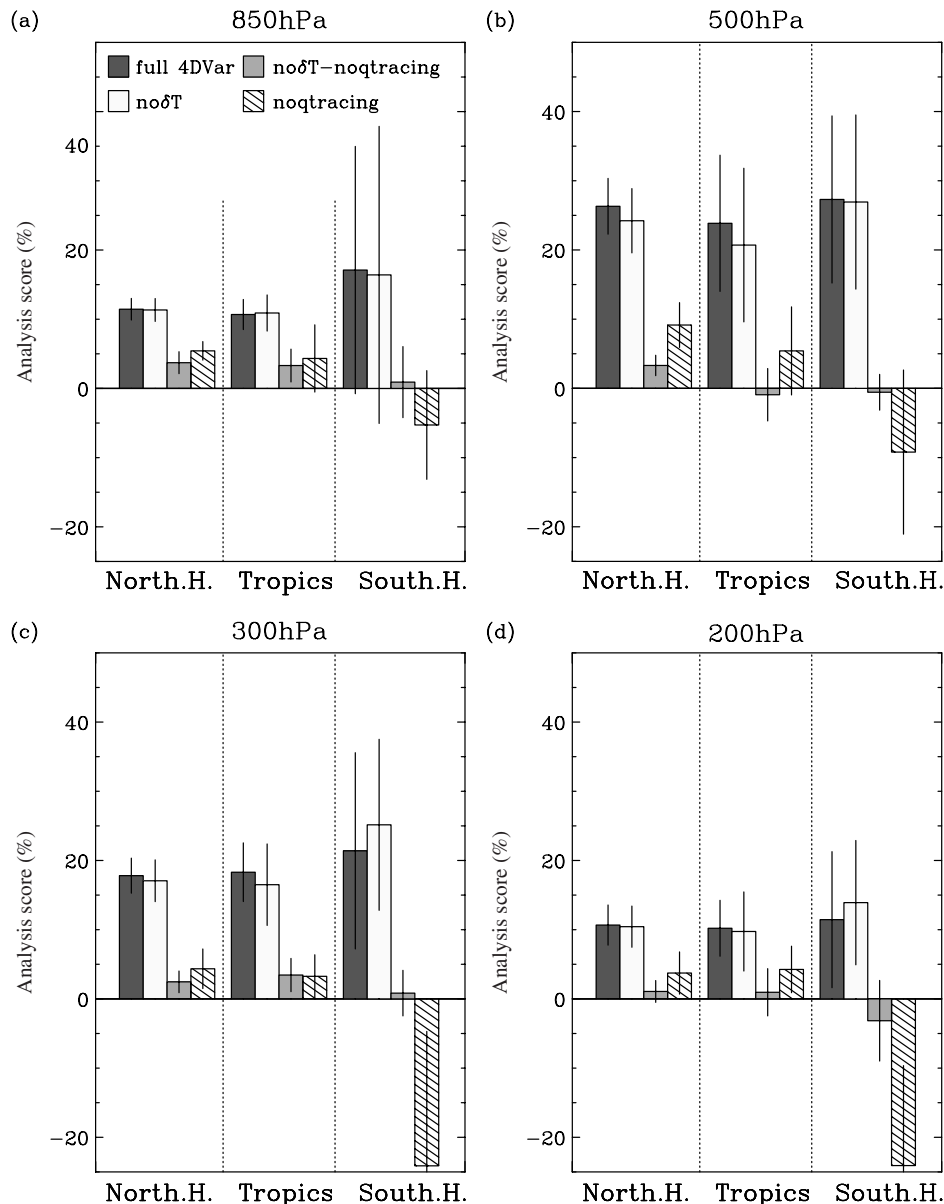


Figure 4. Wind analysis scores for the experiments of Set 2: the full 4D-Var experiment *base+CSRs* (dark grey), *no- δT* (white), *no- δT -no-qtracing* (light grey) and *no-qtracing* (hatched bars).

WV channels at these levels. As expected, the scores for *no- δT -no-qtracing* with no model cycling (light grey bars) are neutral at all levels.

5. Set 3: Sensitivity to the frequency of assimilated images

In *base+CSRs*, one CSR image is assimilated every hour, as in operations. The effect of the CSR image frequency has been examined by running four experiments, all similar to *base+CSRs*, but with different numbers of CSR data per twelve-hour assimilation window: 6 images, 3 images, a single image at the beginning of the window and a single image at the end of the window.

Figure 6 shows that the frequency of images within the window does impact the quality of the wind analysis at

all levels. It is worth noting that the impact of the image frequency does not seem to saturate at 12 images per assimilation window, which suggests that better scores may be obtained from assimilating CSRs with even higher frequency (e.g. 30 minutes), noting that higher time resolution may also require finer spatial resolution. Having the image at the end of the window (light grey bars) also gives much better scores than having it at the beginning of the window (cross-hatched bars). This result clearly demonstrates the ability of CSRs to improve the wind analysis through 4D-Var: while a single image at the beginning of the window does not carry much information about winds, the image at the end of the window enables the assimilation process to use humidity as an advected tracer from which information about the flow can be extracted.

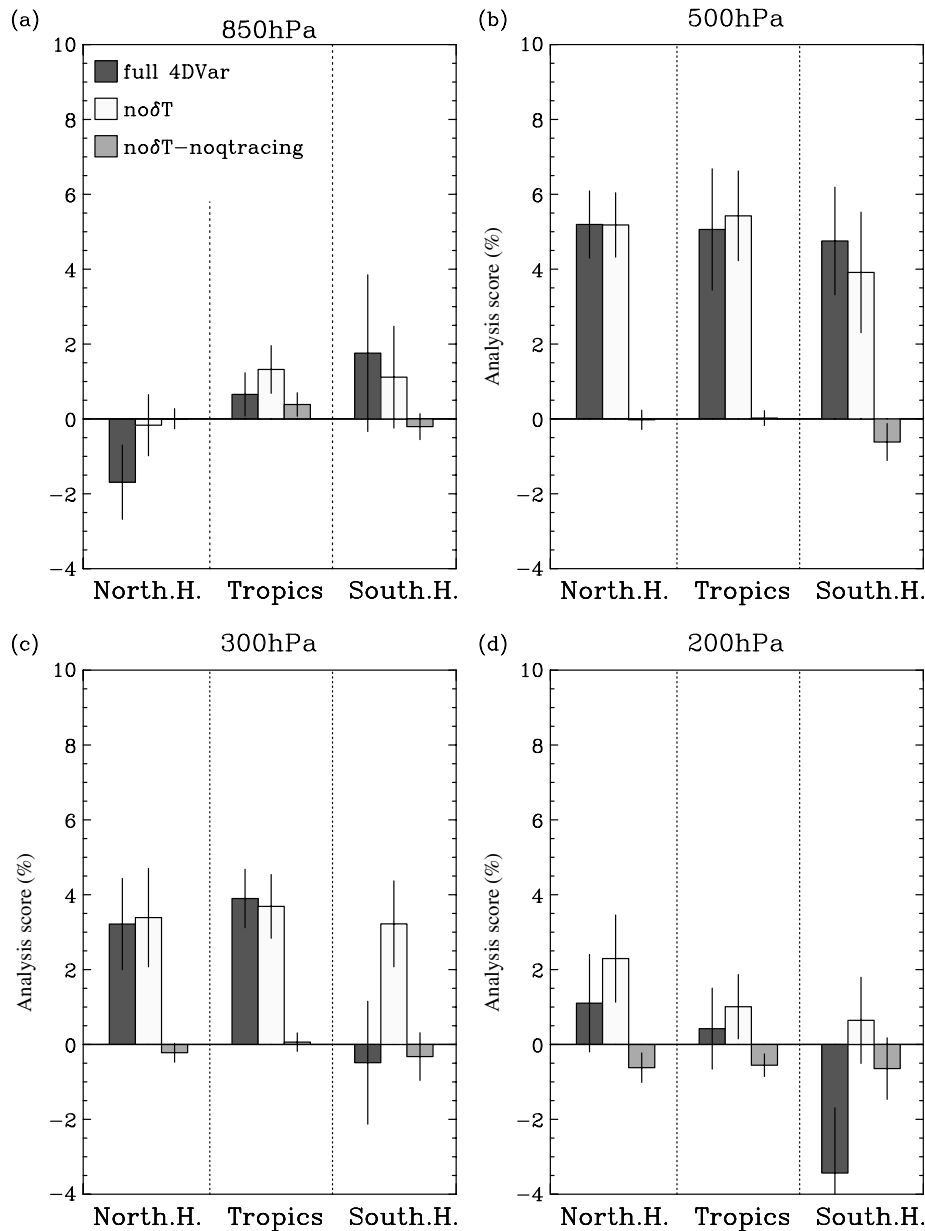


Figure 5. Wind analysis scores for experiments with the ‘no cycling’ setup: the full 4D-Var experiment *base+CSRs* (dark grey), *no- δ T* (white) and *no- δ T-no-qtracing* (light grey).

6. Summary and discussion

This study has shown that, in the context of a no-satellite baseline experiment, CSRs have a positive impact on wind analyses throughout the troposphere. The best results are found at 300 and 500 hPa, which correspond to the peaks of the weighting functions of the two assimilated WV channels. The main mechanism involved in the CSR impact on winds has been found to be the humidity-tracer advection induced by the 4D-Var process. This clearly dominates over the effects of balance constraints imposed on the analysis and model cycling. The process of model cycling is nevertheless important to propagate the benefit of the tracer advection effect throughout the troposphere. Results suggest that CSRs under-performed in the SH, where fast-growing errors violate the tangent-linear hypothesis implicit to 4D-Var.

However, the wind analysis in the SH is still better with the full 4D-Var assimilation of CSRs than when the effect of humidity-tracer advection is switched off.

The benefit of having frequent CSR images within the assimilation window has been demonstrated, and this result does not appear to saturate with one CSR image per hour. Moreover, more benefit comes from CSR images at the end of the assimilation window, which provide the most tracer information. This result thus confirms the essential role of 4D-Var in producing wind increments from CSRs.

The performance of CSRs has been found similar to that of AMVs at 300 hPa and better than AMVs at 500 hPa (partly because fewer AMVs are assimilated at this level). Conversely, the impact of AMVs is significantly larger at 850 and 200 hPa. This underlines

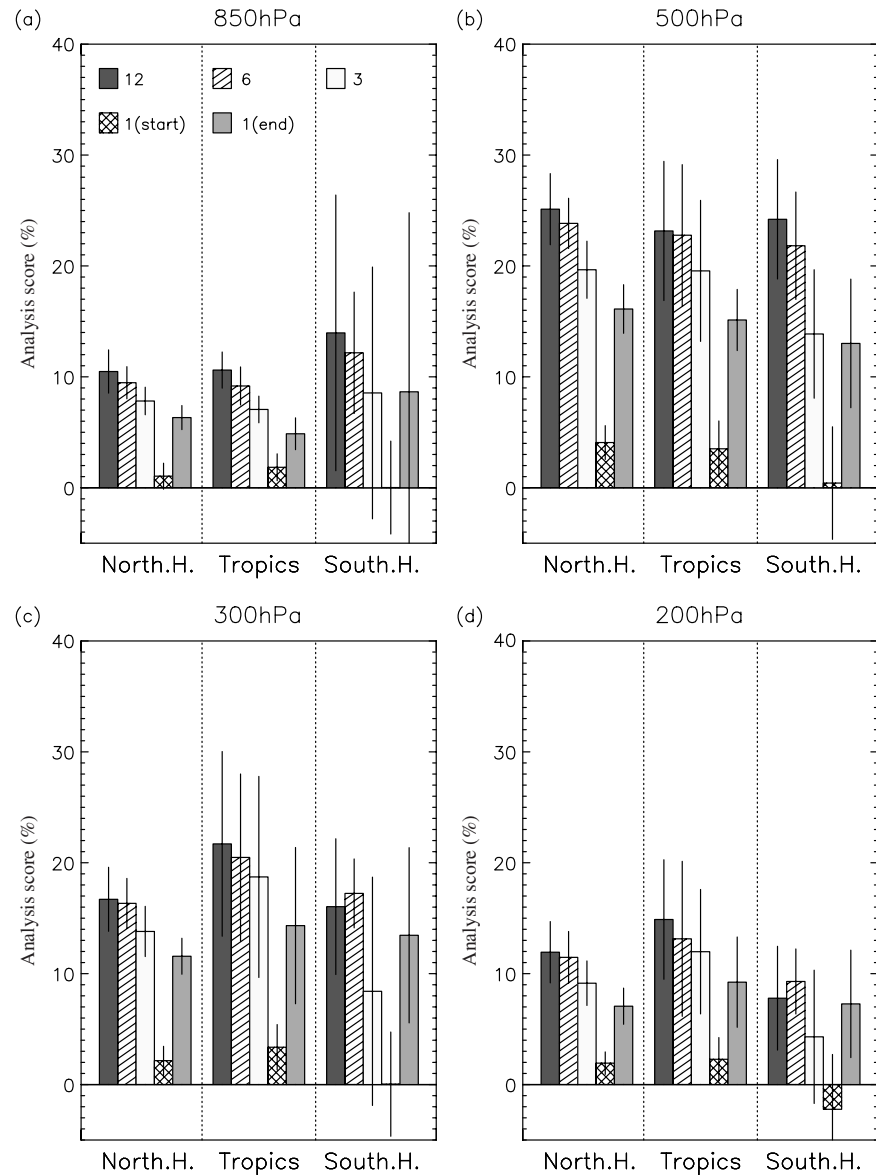


Figure 6. Wind analysis scores for the Set 3 experiments, which have different numbers of CSR images per 12 hour assimilation window: 12 (dark grey), 6 (hatched), 3 (white), a single image at the beginning (cross-hatched) and the end (light grey) of the assimilation window.

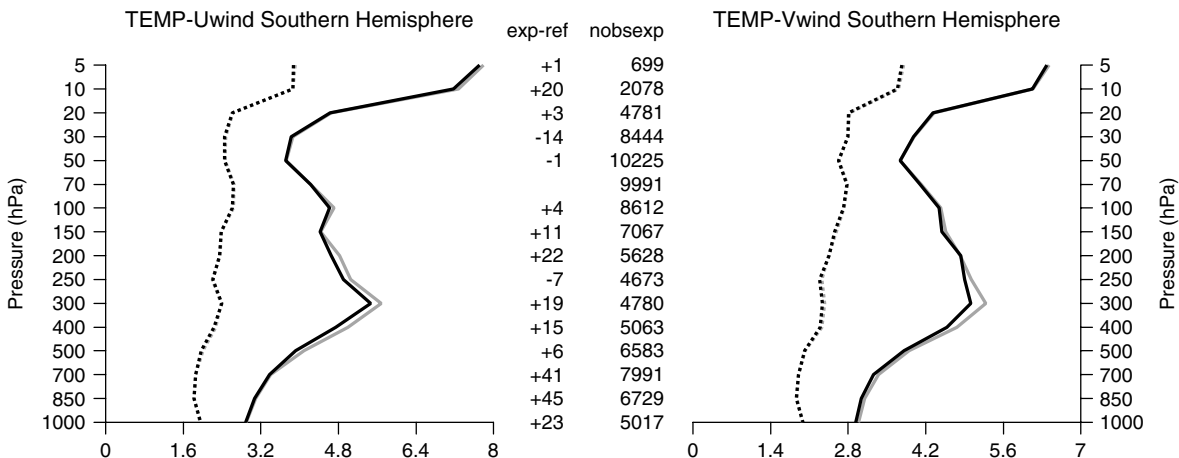


Figure 7. Standard deviation of the first-guess (solid line) and analysis (dotted line) departures from radiosonde observations for the u (left panel) and v (right panel) components of the vector winds and for the *base+CSRs* (black) and *base* (grey) experiments, calculated over 3–26 June 2007 in the SH. The numbers in the ‘nobsexp’ column correspond to the number of observations assimilated in the *base+CSRs* experiment and the numbers in the ‘exp-ref’ column correspond to the difference in number of observations between the *base+CSRs* and *base* experiments.

the complementarity of CSR and AMV data and the benefit to have both of these data in an operational assimilation system: in regions where it is more difficult to retrieve good-quality AMVs, information about the flow contained in sequences of geostationary satellite images can still be inferred via the assimilation of CSRs. Moreover, the improvements brought by each of the datasets have been shown to be fairly additive in the NH and Tropics. This is consistent with the fact that the wind information extracted from CSR and AMV datasets has different origins: in the case of AMVs, it is derived from cloud motions about a given height, while in the case of CSRs it is partly inferred from the displacement of clear-sky air masses having a significant vertical depth (typically 200 hPa).

In the Tropics, most AMVs in the lower and middle troposphere are not used due to their poor quality, and a lack of geostrophic balance constraints limits the impact of thermal channels on board polar orbiters. Hence, the 4D-Var assimilation of CSRs at these latitudes is a significant source of wind information, its positive impact being about two-thirds that of all polar orbiters together (with data only used inside the Meteosat-9 disc).

The positive impact of CSRs on wind analyses could in principle be verified against non-satellite wind observations. The assimilation of CSRs has actually been found to improve the model fit to wind measurements from radiosondes, which are assimilated in the system. The most obvious impact of CSRs is seen for TEMP radiosondes in the SH (Figure 7). However, this improvement remains in general small because the model winds at the sonde locations are closely tied to the radiosonde values themselves, as these have low observation errors. Since little could be inferred from this result, analysis scores have thus been preferred to demonstrate the effect of CSRs on wind analysis.

One may question the role of the verifying analysis in these scores. The operational analysis is arguably the best estimate of ‘truth’ available, but a dominant role of either AMVs or CSRs in the operational analysis itself may prejudice the scores in favour of one or the other. To test this, cross-verifications have been performed using operations-minus-CSRs and operations-minus-AMVs as verifying experiments (not shown). While the magnitude of some signals changes, the results are broadly the same for CSRs and we may conclude that the signals are robust with respect to the choice of verification. This is less the case for AMVs, for which using operations-minus-AMVs as the verifying experiment leads to significantly lower scores compared with verification against the operational analysis. This suggests that the verifying analysis may be favouring the AMVs.

The other satellite radiances used in the ECMWF operational system have been shown to have, together, an important impact on winds. This raises the question of the role of CSRs in the full operational system, when all other satellite radiances are also assimilated. Analysis scores have been calculated for two experiments starting from operations, each with operational settings, but one does not assimilate CSRs while the other one does

not assimilate AMVs. Results (not shown) demonstrate a positive impact of CSRs on winds, although in comparison with AMV results this impact is smaller than in the no-satellite context. This can be explained by the high level of redundancy in the information brought by all the different sources of radiance observations (particularly WV channels from HIRS, AIRS and AMSU-B). Results using a no-satellite baseline have nevertheless revealed the potential of CSR images for improving the wind analysis in a 4D-Var context and enable us to identify the mechanisms involved. The effect of some of the assimilation parameters on the present results could be further investigated, such as the observation errors or the horizontal thinning of the CSRs, which has been shown to affect the relative importance of PORs and CSRs in NWP assimilation systems (Montmerle *et al.*, 2007).

One of the future challenges of radiance assimilation is the use of cloudy data (Pavelin *et al.*, 2008; McNally, 2009). A major difficulty regarding cloudy infrared radiances is the non-linearity of the observation operator with respect to cloud variables (e.g. cloud fraction and cloud height). These data can provide important information about temperature, humidity (hence horizontal wind via humidity tracing) and vertical winds (via interaction with the model physics). When these data are assimilated in the system, it will be interesting to compare their impact on wind with that of the currently assimilated cloudy-sky AMV data. Moreover, the future launch of Meteosat third-generation satellites (Stuhlmann *et al.*, 2005), with high spectral sounders on board providing enhanced vertical resolution of the humidity, should greatly improve the capabilities of extracting wind information from the assimilation of geostationary data images.

A. Appendix: 4D-Var wind increments from radiance observations

This appendix explains how the 4D-Var system is modified to perform the experiments described in section 4. The 4D-Var technique combines the knowledge of the first-guess state \mathbf{x}^b at t_0 , the beginning of the assimilation time window and the observations \mathbf{y} at time $t > t_0$. The analysis is found at t_0 and it corresponds to the minimum of the cost function J , which is obtained by finding the solution of $\nabla J(\mathbf{x}(t_0)) = 0$. This is done by iteratively evaluating ∇J . A simplified expression (ignoring the incremental method) of $\nabla J(\mathbf{x})$ in the present 4D-Var assimilation system is

$$\begin{aligned}\nabla J(\mathbf{x}(t_0)) = \mathbf{B}^{-1}[\mathbf{x}(t_0) - \mathbf{x}^b(t_0)] \\ + \mathbf{M}^T \mathbf{H}^T \mathbf{R}^{-1} [\mathcal{H}\mathcal{M}(\mathbf{x}(t_0)) - \mathbf{y}].\end{aligned}\quad (\text{A1})$$

Here, \mathcal{H} is the observation operator that projects observations in the model space, \mathbf{H} is its corresponding tangent linear operator, \mathbf{R} and \mathbf{B} are the error covariance

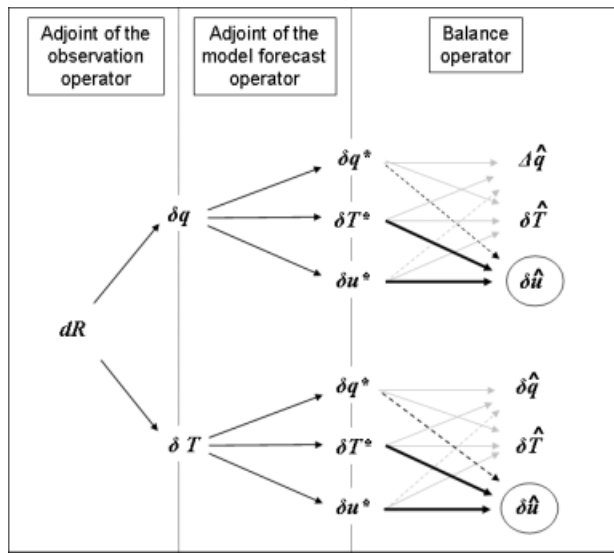


Figure A1. Schematic of the action of the adjoints of the observation and model forecast operators and the balance operator on the radiance observation departures to produce increments in humidity, temperature and wind.

matrices of the observations and the first-guess, respectively. \mathcal{M} is the forecast model evolving the model state from t_0 to the observation time t_{obs} and \mathbf{M} is its corresponding tangent linear operator. At each step, ∇J is evaluated with an updated value of $\mathbf{x}(t_0)$. During this process the transposed operators of \mathbf{M} and \mathbf{H} and the inverse of \mathbf{R} are applied to the departure from observations. When the correct value of ∇J is reached, the analysis at t_0 is found by multiplying Equation (A1) by \mathbf{B} . Thus, the minimization process can be regarded as a series of transformations of the observation departure $[\mathbf{y} - \mathcal{H}\mathcal{M}\{\mathbf{x}(t_0)\}]$, applying successively the operators \mathbf{R}^{-1} , \mathbf{H}^T , \mathbf{M}^T and \mathbf{B} .

For a model state composed of humidity, wind and temperature variables, the whole process can be summarized as in Figure A1. This shows that, through the action of \mathbf{H}^T , a radiance observation generates changes in humidity (δq) and temperature (δT). Then, through the action of \mathbf{M}^T , δq and δT generate the changes δq^* , δT^* and δu^* at the beginning of the time window. Finally, these are converted into increments ($\delta \hat{q}$, $\delta \hat{T}$ and $\delta \hat{u}$) by taking into account the error correlation between model variables in \mathbf{B} .

δu^* is produced by the action of the adjoint model on δq through both dynamical and physical equations. The effect of humidity-tracer advection, which is generated by the dynamical equations alone, has been removed in the experiment *no-qtracing* by setting the contribution to δu^* from the adjoint of the model dynamics to zero. The tracer advection effect is then removed for any humidity observations. In order to isolate the specific effect of CSRs, the other sources of humidity observations (humidity conventional data) have not been assimilated in this study.

In experiment *no- δT* , the effect of temperature changes δT on $\delta \hat{u}$ is removed. Because of the more complex

relationship between temperature and wind, and because we want to keep the conventional temperature observations in the assimilation, it is not possible to break the link between δT and δu^* . To circumvent this obstacle, the temperature changes generated by CSRs via the observation operator have been ignored, setting δT to zero in the output of the radiative transfer code.

Acknowledgements

We thank Elias Holm for sharing his insights into the humidity-tracer effect and providing very useful assistance in setting up some of the experiments. This work also benefited from discussions with Alan Geer, Niels Bormann, Claire Delsol, Iliana Genkova and Peter Bauer. The first author was founded by a EUMETSAT Fellowship.

References

- Anderson E, Paillex J, Thépaut J-N, Eyre J, McNally AP, Kelly GA, Courtier P. 1994. Use of cloud-cleared radiances in three-four-dimensional variational data assimilation. *Q. J. R. Meteorol. Soc.* **120**: 627–654.
- Anderson E, Hólm E, Bauer P, Beljaars A, Kelly GA, McNally AP, Simmons AJ, Thépaut J-N, Tompkins AM. 2007. Analysis and forecast impact of the main humidity observing systems. *Q. J. R. Meteorol. Soc.* **133**: 1473–1485.
- Auligné T, McNally AP, Dee DP. 2007. Adaptive bias correction for satellite data in a numerical weather prediction system. *Q. J. R. Meteorol. Soc.* **133**: 631–642.
- Bauer P, Kelly G, Andersson E. 2002. ‘SSM/I radiance assimilation at ECMWF’. In *Proceedings of ECMWF/GEWEX Workshop on Humidity Analysis*, 8–11 July 2002. ECMWF: Reading, UK; pp 167–175.
- Bretherton CS, Widmann M, Dymnikov VP, Wallace JM, Bladé I. 1999. The effective number of spatial degree of freedom of a time-varying field. *J. Climatol.* **12**: 1990–2009.
- Daley R. 1995. Estimating the wind field from chemical constituent observations: Experiments with a one-dimensional extended Kalman filter. *Mon. Weather Rev.* **123**: 185–198.
- Dee DP. 2004. ‘Variational bias correction of radiance data in the ECMWF system’. In *Proceedings of ECMWF Workshop on Assimilation of High Spectral Resolution Sounders in NWP*, 28 June–1 July 2004. ECMWF: Reading, UK.
- Delsol C, Von Bremen L, Thépaut J-N. 2005. ‘Impact of Atmospheric Motion Vectors from Meteosat 8 on ECMWF analyses and forecast’, *ECMWF Research Internal Memo Number 0562*. ECMWF: Reading, UK.
- Hólm EV, Untch A, Simmons A, Saunders R, Bouttier F, Andersson E. 1999. ‘Multivariate ozone assimilation in four-dimensional data assimilation’. In *Proceedings of the SODA Workshop on Chemical Data Assimilation*, 9–10 December 1998. KNMI: De Bilt, Netherlands; pp 89–94.
- Holmlund K. 1995. Half-hourly wind data from satellite derived water vapour measurements. *Adv. Space Res.* **16**: 59–68.
- Holmlund K. 1998. The utilisation of statistical properties of satellite-derived atmospheric motion vectors to derive quality indicators. *Weather Forecasting* **13**: 1093–1104.
- Kelly G, Munro R, Rohn M, Holmlund K. 1998. Impact of atmospheric motion vectors (AMVs) on the ECMWF system and the development of a water vapour AMV observation operator. In *Proceeding of the Third International Winds Workshop*, 10–12 June 1996, EUMETSAT Publ. 18. EUMETSAT: Ascona, Switzerland; pp. 77–84.
- Kelly G, Thépaut J-N. 2007. Evaluation of the impact of the space component of the global observing system through observing system experiments. *ECMWF Newsletter* **113**: 16–28.
- Köpken C, Kelly G, Thépaut J-N. 2004. Assimilation of Meteosat radiance data within the 4D-Var system at ECMWF: Data quality monitoring, bias correction and single-cycle experiments. *Q. J. R. Meteorol. Soc.* **130**: 2293–2313.

- Mahfouf J-F, Rabier F. 2000. The ECMWF operational implementation of four-dimensional variational assimilation. II: Experimental results with improved physics. *Q. J. R. Meteorol. Soc.* **126**: 1171–1190.
- Matricardi M, Saunders R. 1999. Fast radiative transfer model for simulations of Infrared Atmospheric Sounding Interferometer radiances. *Appl. Optics* **38**: 5679–5691.
- McNally AP. 2009. The direct assimilation of cloud-affected satellite infrared radiances in the ECMWF 4D-Var. *Q. J. R. Meteorol. Soc.* Submitted.
- McNally AP, Vesperini M. 1996. Variational analysis of humidity information from TOVS radiances. *Q. J. R. Meteorol. Soc.* **122**: 1521–1544.
- McNally AP, Watts PD, Smith JA, Engelen R, Kelly GA, Thépaut JN, Matricardi M. 2006. The assimilation of AIRS radiance data at ECMWF. *Q. J. R. Meteorol. Soc.* **132**: 935–958.
- Montmerle T, Rabier F, Fischer C. 2007. Relative impact of polar-orbiting and geostationary satellite radiances in the Aladin/France numerical weather prediction system. *Q. J. R. Meteorol. Soc.* **133**: 655–671.
- Munro R, Köpken C, Kelly G, Thépaut J-N, Saunders R. 2004. Assimilation of Meteosat radiance data within the 4D-Var system at ECMWF: Assimilation experiments and forecast impact. *Q. J. R. Meteorol. Soc.* **130**: 2277–2292.
- Pavelin EG, English SJ, Eyre JR. 2008. The assimilation of cloud-affected infrared satellite radiances for numerical weather prediction. *Q. J. R. Meteorol. Soc.* **134**: 737–749.
- Peuch A, Thépaut J-N, Pailleux J. 2000. Dynamical impact of total ozone observations in a four-dimensional variational assimilation. *Q. J. R. Meteorol. Soc.* **126**: 1641–1659.
- Rabier F, McNally AP, Andersson E, Courtier P, Undén P, Eyre J, Hollingsworth A, Bouttier F. 1998. The ECMWF implementation of three-dimensional variational assimilation (3D-Var). II: Structure function. *Q. J. R. Meteorol. Soc.* **124**: 1809–1829.
- Rabier F, Järvinen H, Klinker E, Mahfouf J-F, Simon A. 2000. The ECMWF operational implementation of four-dimensional variational assimilation. I: Structure function. *Q. J. R. Meteorol. Soc.* **126**: 1143–1170.
- Riishøjgaard LP. 1996. On four-dimensional variational assimilation of ozone data in weather-prediction models. *Q. J. R. Meteorol. Soc.* **122**: 1545–1571.
- Rohn M, Kelly G, Saunders R. 2001. Impact of a new cloud motion product from Meteosat on NWP analyses and forecasts. *Mon. Weather Rev.* **129**: 2392–2403.
- Schmetz J, Holmlund K, Hoffman J, Strauss B, Mason B, Gaetner V, Koch A, van de Berg L. 1993. Operational cloud motion winds from Meteosat infrared images. *J. Appl. Meteorol.* **32**: 1206–1225.
- Schmetz J, Pili P, Tjemkes S. 2000. Meteosat Second Generation (MSG). In *Proceedings of Seminars in Exploitation of the New Generation of Satellite Instruments for Numerical Weather Prediction, 4–8 September 2000*. ECMWF: Reading, UK; pp 111–121.
- Soden BJ, Bretherton FP. 1996. Interpretation of TOVS water vapor radiances in terms of layer-average relative humidities: Method and climatology for the upper, middle, and lower troposphere. *J. Geophys. Res.* **101**: 9333–9343.
- Stuhlmann R, Rodríguez A, Tjemkes S, Grandell J, Arriaga A, Bézy J-L, Aminou D, Bensi P. 2005. Plans for EUMETSAT Third Generation Meteosat (MTG) Geostationary Satellite Program. *Adv. Space Res.* **36**: 975–981.
- Szyndel M, Kelly GA, Thépaut JN. 2004. ‘Evaluation of calibration and potential for assimilation of SEVIRI radiance data from Meteosat-8’. EUMETSAT/ECMWF Research Report No. 15.
- Velden CS, Niemann SJ, Menzel WP, Wanrong ST. 1997. Upper tropospheric winds derived from geostationary satellite water vapour observations. *Bull. Am. Meteorol. Soc.* **78**: 173–195.
- Zapotocny TH, Jung JA, Le Marshall JF, Treadon RE. 2008. A two-season impact study of four satellite data types and Rawinsonde data in the NCEP Global Data Assimilation System. *Weather Forecasting* **23**: 80–100.

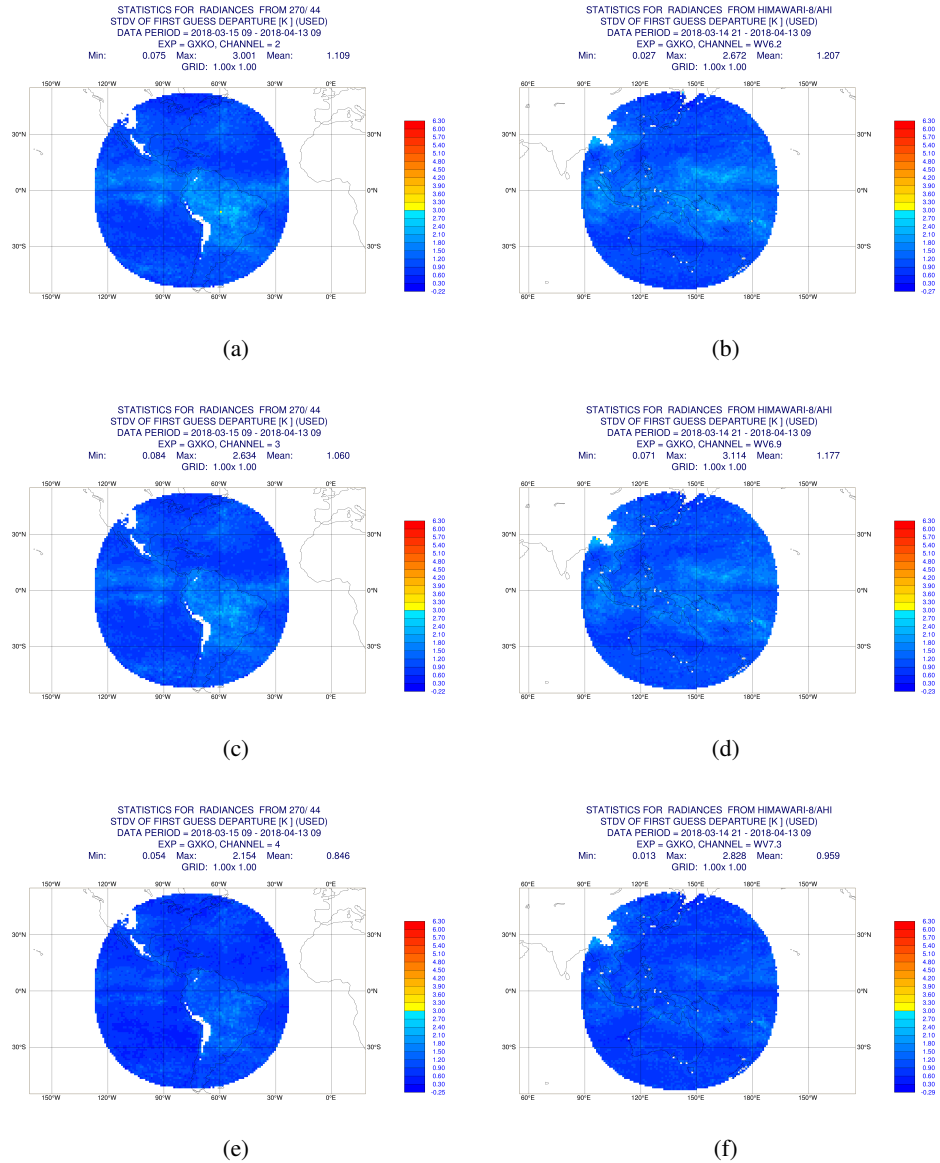


Figure 21: CSR standard deviation of first guess departures for the $6.15\mu\text{m}$ (top), $7.00\mu\text{m}$ (middle) and $7.40\mu\text{m}$ (bottom) WV channels from GOES-16 (left) and Himawari-8 (right). Statistics are based on observations that were assimilated (i.e. after observation screening, quality control etc.).

The bias characteristics of the three water vapour channels after the bias corrections have been applied are very similar between GOES-16 and Himawari-8, indicating that VarBC is working well at removing biases in both, and that the residual biases in the GOES-16 CSRs are not likely to be prohibitive. The most significant region of residual bias is over the northernmost part of the Andes, and it is more significant for higher-peaking channels. A similar signal is seen in the region of the Tibetan Plateau that is at the edge of the Himawari-8 disc. If this were simply related to the influence of the surface on the observations, it might be expected that the lower peaking channels would show the largest effect in the statistics. It could, however, be related to the model, if a moist bias exists in the upper tropospheric humidity field above high orography, though the exact reason for this is yet to be understood.

The standard deviations of the first guess departures are similar to Himawari-8 but slightly smaller, which may be expected as the “used” Himawari-8 data includes data from averaging boxes that contain fewer cloud-free pixels, which are intrinsically noisier.

2 Research to maximise the impact of geostationary radiance data when assimilated

2.1 Effect of spacecraft position and orbit on SEVIRI CSRs

When assessing Meteosat-11 during the transition from Meteosat-10, it was discovered that during the drift, there existed a clear east-west bias structure in geographical plots of the mean of the first guess departure statistics. As noted in the previous section, there was no period during which the two satellites were at the same nominal longitude, so an exact like-for-like comparison is difficult. Figure 22 shows geographic plots of the mean first guess departures of the $6.2\mu m$ WV on both Meteosat-10 and Meteosat-11. The observations that contributed to the statistics were from 31/1/18 to 14/2/18, including periods when both satellites were drifting. Meteosat-10 was drifting from 0° toward the east, and Meteosat-11 was drifting to 0° from the west.

In Section 1.2 it was noted that there was a net bias difference between the first guess departures of the equivalent WV channels on Meteosat-10 and Meteosat-11, and this can be seen in Figure 22, hence demonstrating that the observations from Meteosat-11 $6.2\mu m$ channel are systematically warmer than those from Meteosat-10. As well as this difference, there is a superposed east-west bias present in each plot, but it can be seen that the sign of the bias is opposite between Meteosat-10 and Meteosat-11. This east-west bias would appear to be correlated with the longitude of the sub-satellite point; if the satellite is east of 0° (i.e. Meteosat-10), the observations east of 0° have a positive bias and those to the west have a negative bias (and vice versa for Meteosat-11 which is west of 0°). Physically, there is no reason for such an east-west bias to be present in the measured radiances, nor in the first guess fields, if the radiative transfer is computed correctly. Importantly, each brightness temperature observation is provided with the satellite zenith angle in the BUFR file, thus allowing the radiative transfer calculations to be modified to account for the oblique path through the atmosphere (for geostationary radiances this is currently done by scaling the layer thicknesses of a single interpolated model column, but Section 2.2 discusses progress towards accounting for the slant path radiative transfer more correctly). So, it is possible that this bias characteristic may be related to some aspect of the low-level observation processing.

The ASR products are based on Level-1.5 images, which are derived from the Level-1 data, and have undergone radiometric and geometric corrections ([EUMETSAT \[2015, 2017\]](#)). Notably, this processing step involves the transformation of the raw images to appear as if the satellite was above 0° for the 0° Full Disc Service and at $41.5^\circ E$ for the Indian Ocean Data Coverage (IODC) service. To attempt to ascertain whether the source of the bias is due to the Level-1.5 data, simultaneous images from Meteosat-10 and Meteosat-11 were obtained for comparison (thanks to Crispian Batstone, Met Office). These images are from the $6.2\mu m$ WV channel and are valid for 12Z on 9/2/18 (Figure 23). This was a unique date because Meteosat-10 was at $1.5^\circ E$ and Meteosat-11 was at $1.5^\circ W$, thus equidistant from the rectification centre (i.e. 0°).

STATISTICS FOR RADIANCES FROM METEOSAT-10/SEVIRI

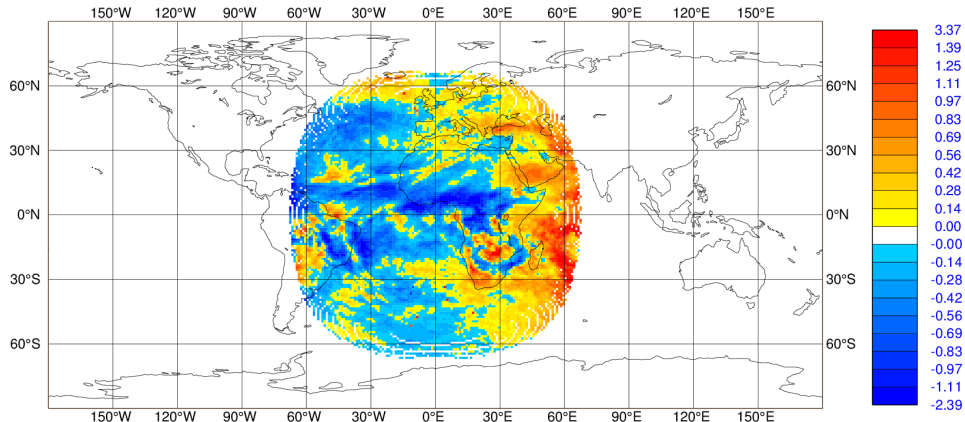
MEAN FIRST GUESS DEPARTURE (OBS-FG) (ALL)

DATA PERIOD = 2018-01-31 21 - 2018-02-14 21

EXP = GVYX, CHANNEL = WV6.2

Min: -2.248 Max: 3.227 Mean: -0.077

GRID: 1.00x 1.00

(a) Meteosat-10: Sub-satellite longitude: $0.9^{\circ}E - 4.0^{\circ}E$

STATISTICS FOR RADIANCES FROM METEOSAT-11/SEVIRI

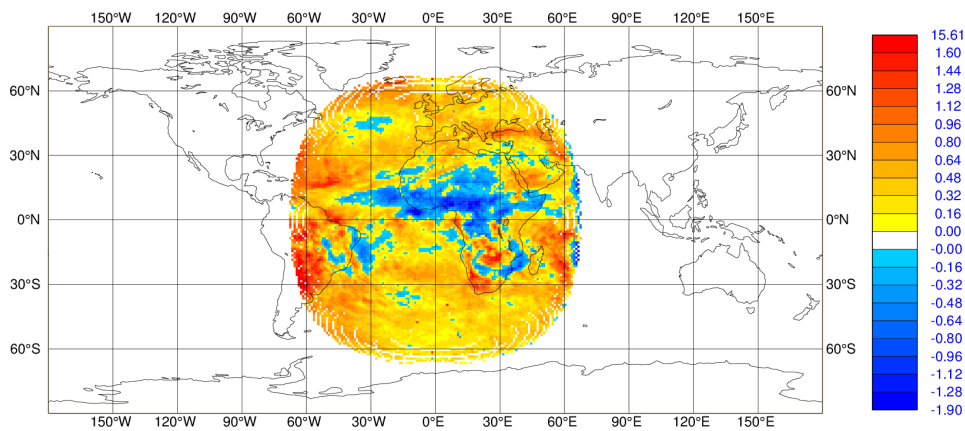
MEAN FIRST GUESS DEPARTURE (OBS-FG) (ALL)

DATA PERIOD = 2018-01-31 21 - 2018-02-14 21

EXP = GVYX, CHANNEL = 2

Min: -1.740 Max: 15.455 Mean: 0.267

GRID: 1.00x 1.00

(b) Meteosat-11: Sub-satellite longitude: $3.5^{\circ}W - 0.0^{\circ}W$ Figure 22: Mean of the first guess departures of the $6.2\mu m$ WV channel on Meteosat-10 (a) and Meteosat-11 (b) during the period when the two satellites were drifting.

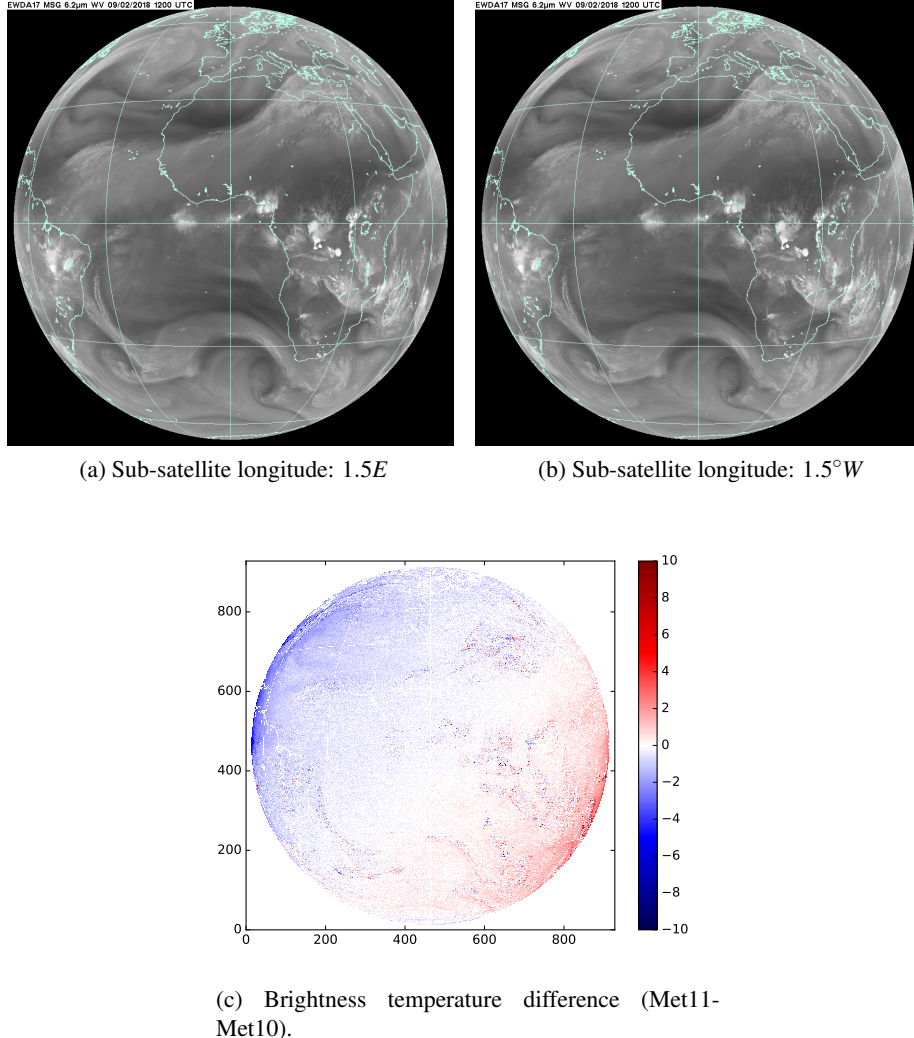


Figure 23: Reduced-resolution level-1.5 images from the $6.2\mu\text{m}$ WV channel on Meteosat-10 (a) and Meteosat-11 (b) during the period when the two satellites were drifting (12Z on 9/2/18). The images have been rectified to appear as if the sub-satellite point is at $0^\circ\text{N}, 0^\circ\text{E}$. The absolute difference of the brightness temperature between the two satellites is also shown (c).

It is difficult to see differences between the images from Meteosat-10 and Meteosat-11 by eye, but discernible differences are present. When the brightness temperature difference is plotted (Figure 23c), it is clear that there is a bias pattern very roughly in the east-west direction. This would appear to be consistent with the bias characteristics in Figure 22, though the axis of negative mirror symmetry in Figure 23c is rotated somewhat from the north-south direction. Pursuing the line that the bias pattern is related to the rectification step from the true sub-satellite point to $0^\circ\text{N}, 0^\circ\text{E}$, we can look at the latitude of the sub-satellite points to determine more accurately the axis along which the rectification has been applied. On 9/2/18, when the images were obtained, the orbital inclinations of Meteosat-10 and Meteosat-11 were 0.87° and 1.43° respectively. From this, and other information available from EUMETSAT (<https://www.eumetsat.int/website/home/Data/ServiceStatus/MeteosatOrbitalParameters/index.html>), the sub-satellite point at a given time can be calculated (Arthur de Smet, private communication). This al-

lows us to determine the directions in which the observations have been transformed — this is shown graphically in Figure 24.

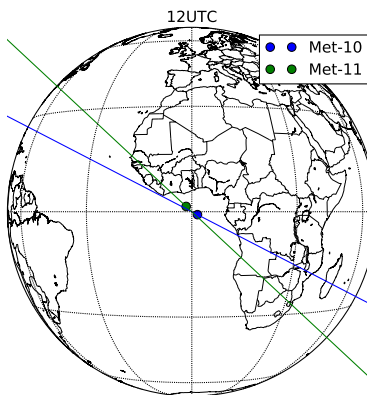


Figure 24: The sub-satellite positions of Meteosat-10 and Meteosat-11 at 12Z on 9/2/18. Also shown are the directions in which the rectification of the data from each satellite has been performed in the Level-1.5 processing.

The rectification directions are approximately consistent with the brightness temperature differences shown in Figure 23c. This comparison is only valid for one moment, and the north-south diurnal variation of the sub-satellite point would result in a cancellation of any north-south biases when statistics are accumulated over 24 hours, which is consistent with Figure 22.

If this bias is due to the rectification, it would be expected that the error should scale with the magnitude of the distance from the true sub-satellite point to the centre of rectification. Currently, Meteosat-8 has a particularly large orbital inclination since the north-south station-keeping manoeuvres ceased in 2010. Since then, the inclination has grown larger monotonically, and it is currently over 5° (see Figure 25a). This means that diurnally, the sub-satellite point oscillates in the north-south direction with an amplitude of $\sim 5^\circ$ in geocentric latitude. Figure 25 also shows the subset of *used* (i.e. assimilated) data for Meteosat-8 at 00Z and 12Z on a particular day in February 2017. The disc is seen to move significantly in the north-south direction. The reason for this is that observations with satellite zenith angles greater than 60° are not currently assimilated, and the zenith angles provided in the BUFR files are those of the true satellite positions, hence the sub-disc of assimilated data is centred on the true sub-satellite position. Note also that there are fewer assimilated observations in the western part of the disc; this is due to the thinning procedure, where Meteosat-8 and Meteosat-10 (at this time) were being thinned together where they overlap.

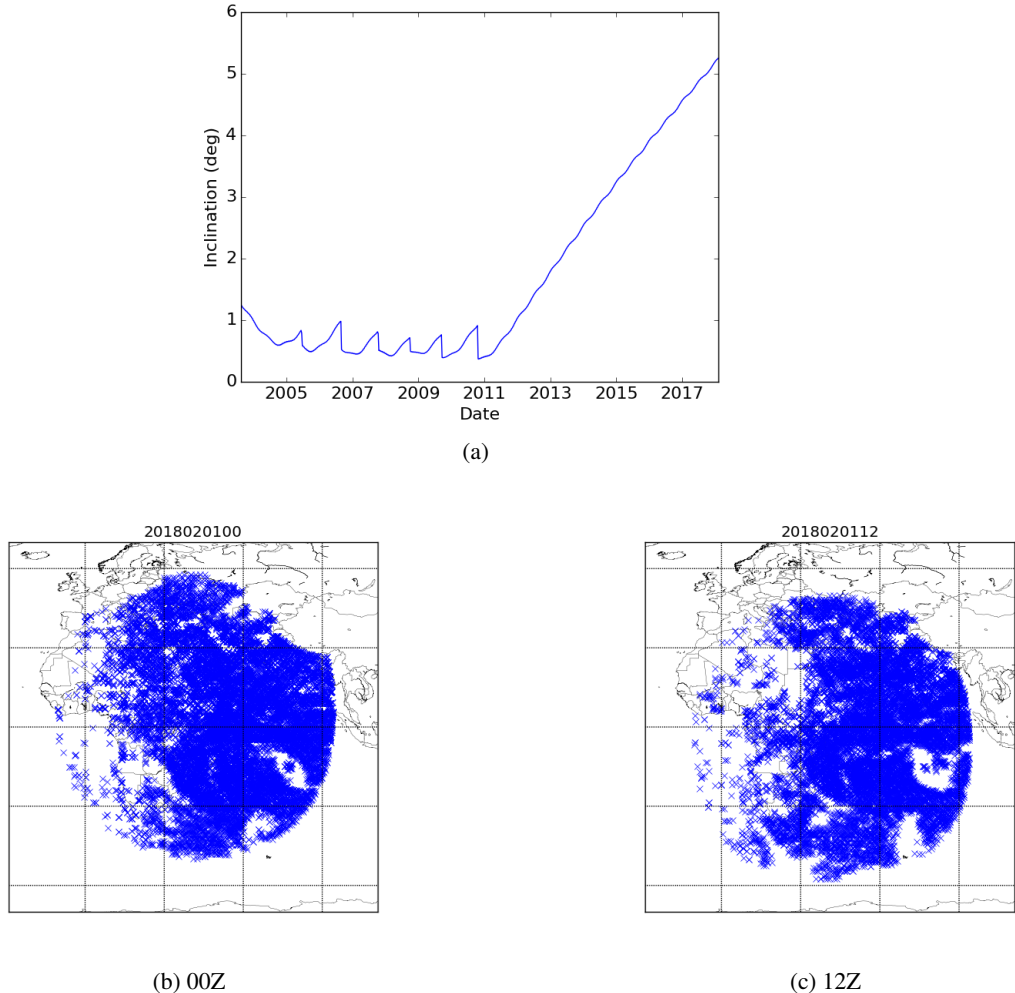


Figure 25: Time series of the orbital inclination of Meteosat-8 (a), and the subset of assimilated data at 00Z (b) and 12Z (c) on 1/2/18, showing the truncated disc centred on the true sub-satellite point.

Although the true sub-satellite position is used in the computation of the satellite zenith angles, the experience from the Meteosat-10/11 transition has shown that systematic differences appear to exist along the rectification direction, so it may be expected that similar differences are present in the diurnal variation of Meteosat-8, but in the north-south direction.

The equator crossing time of Meteosat-8 varies continually. In fact, the UTC time at which the satellite reaches its most northerly position regresses by approximately two hours per month, see Figure 26.

In order to assess any potential bias between the north and south parts of the Meteosat-8 orbit, geographic plots need to be produced for the northernmost and southernmost extremes of the orbit. Based on Figure 26, for the period of 1 February 2018 to 1 April 2018, statistics were accumulated from 19Z to 21Z to sample the northernmost part of the orbit, and 07Z to 09Z to sample the southernmost part. The means of the first guess departures for these two windows are shown in Figure 27 for the $6.25\mu\text{m}$ WV channel and Figure 28 for the $7.35\mu\text{m}$ WV channel, for both raw and bias-corrected observations.

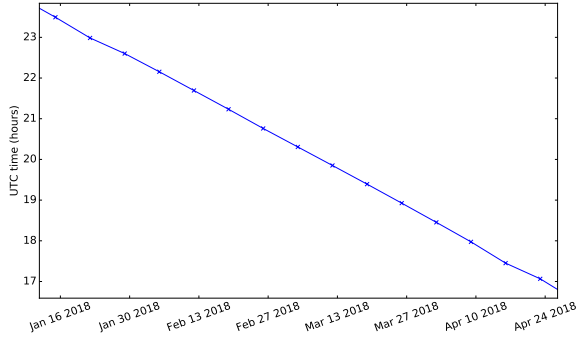


Figure 26: The UTC time at which Meteosat-8 reached its most northerly position in early 2018.

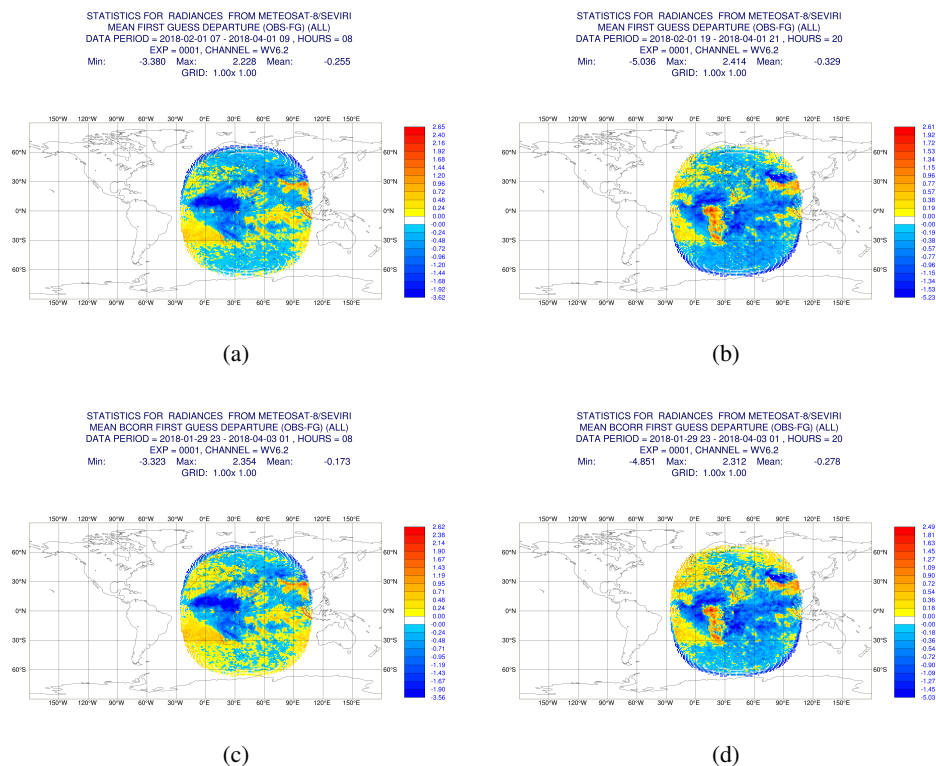


Figure 27: Mean first guess departures for the $6.25\mu\text{m}$ WV channel from Meteosat-8 before (top) and after (bottom) bias correction. The left-hand plots include statistics from 07Z to 09Z (when the satellite was at the most southerly part of its orbit for this period) and the right-hand plots include statistics from 19Z to 21Z when the satellite was at its most northerly extent.

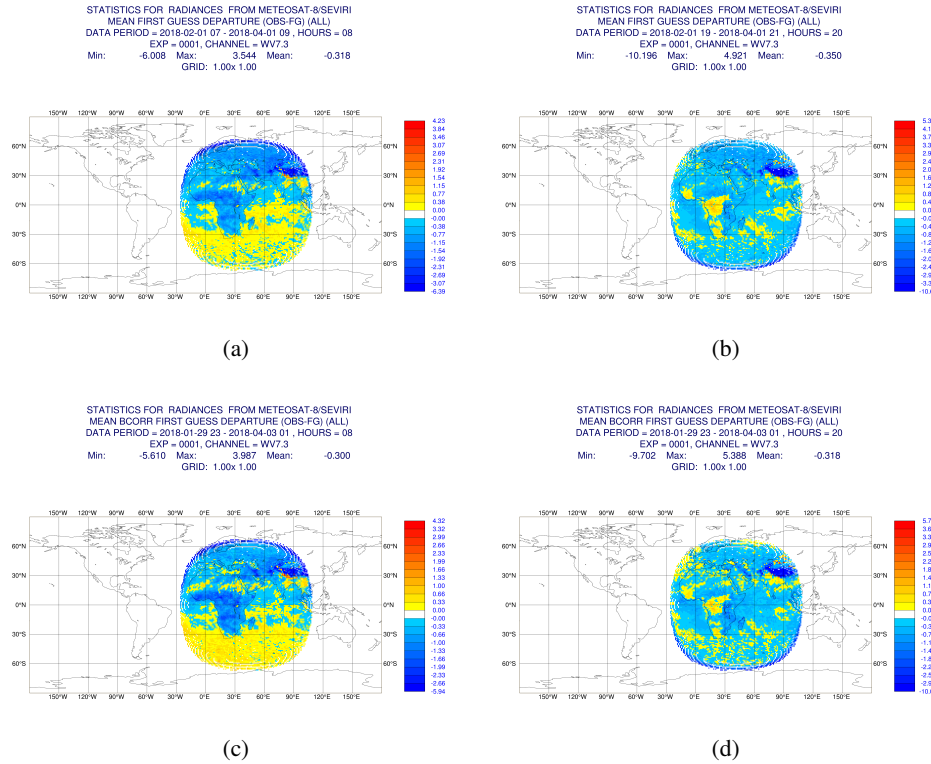


Figure 28: Mean first guess departures for the $7.35\mu\text{m}$ WV channel from Meteosat-8 before (top) and after (bottom) bias correction. The left-hand plots include statistics from 07Z to 09Z (when the satellite was at the most southerly part of its orbit for this period) and the right-hand plots include statistics from 19Z to 21Z when the satellite was at its most northerly extent.

The $6.25\mu\text{m}$ channel of Meteosat-8 (Figure 27) shows a clear north-south bias pattern whose sign depends on whether the satellite is at the northern or southern part of its orbit, and this seems to be consistent with the relation between the bias and the spacecraft position highlighted in Figure 22. The pattern is even more pronounced when the bias correction has been applied. The $7.35\mu\text{m}$ channel (Figure 28) shows a similar pattern that is particularly striking when the satellite is at its most southerly extent, but at its most northerly point, the pattern is much less pronounced, except for a large negative bias at the southern edge of the disc. A comparison with Meteosat-11 (results not presented) has shown that the north-south pattern does not exist, thus indicating that the Meteosat-8 bias is due to the satellite's position relative to the rectification centre and not a different diurnal factor specific to the measurements or the first guess fields.

This topic of investigation has not been pursued further, but clearly, in order to maximise the impact of the radiances, the removal of systematic biases is desirable, whether this is done by updating processing algorithms or by introducing appropriate bias predictors to account for these biases at the assimilation stage.

2.2 Assimilation of geostationary radiance data at high zenith angles with slant path radiative transfer

If a geostationary radiance observation is measured with a satellite zenith angle of more than 60° , it is rejected from the assimilation. This restriction was originally implemented due to limitations within RTTOV (Munro et al. [2004]). Currently, warnings are produced by RTTOV if the zenith angle is larger than 75° , so the purpose of this section is to assess whether we can make use of data with larger zenith angles. Figure 29 shows concentric rings of constant zenith angle for the example of a Meteosat satellite over the prime 0° longitude position. The shaded area indicates the data we currently reject, but could possibly make use of.

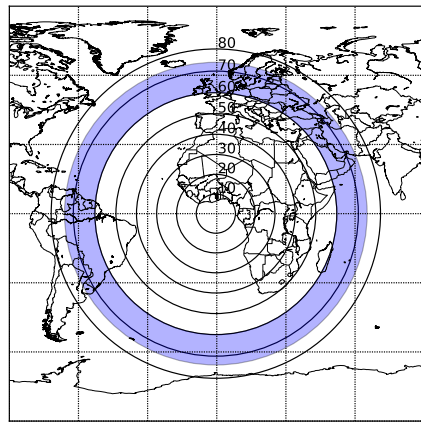


Figure 29: Lines of constant zenith angle for a geostationary satellite at $\text{lat}=0^\circ$, $\text{lon}=0^\circ$. The blue shaded region indicates the data that would currently be discarded but which RTTOV could process in principle.

The maximum additional geographic coverage provided by relaxing this threshold can be calculated for a single satellite:

$$\begin{aligned} A_{\text{before}} &= \int_{0^\circ}^{360^\circ} \int_{0^\circ}^{60^\circ} r^2 \sin \theta d\theta d\phi = 1.27 \times 10^{14} m^2 \\ A_{\text{after}} &= \int_{0^\circ}^{360^\circ} \int_{0^\circ}^{74^\circ} r^2 \sin \theta d\theta d\phi = 1.85 \times 10^{14} m^2 \end{aligned}$$

This is an increase in surface area of a factor of approximately 1.4. Of course, some of this additional coverage would overlap with the discs of other satellites, and some satellites do not provide data to 74° , but additional overall coverage would be obtained at the northern and southernmost parts of the geostationary coverage. An indication of this can be inferred from Figure 2.

The observations are provided with latitude and longitude values that describe a point on the Earth's surface, and during the assimilation process, an interpolated vertical model profile centred at this position

is used to perform the radiative transfer calculations. For observations close to nadir, this is perfectly representative, but for observations with large zenith angles, the true line-of-sight to the satellite is poorly described by this vertical approximation, particularly if the observations are sensitive to features high in the atmosphere. In order to minimise this source of error, the “slant-path” can be accounted for in the radiative transfer calculation, by tracing a straight line path from the point on the surface of the Earth to the satellite and interpolating model columns to this path in order to best represent the true path of radiation received by the instrument. This was implemented in the IFS system for polar-orbiting satellites ([Bormann et al. \[2007\]](#), [Bormann \[2016\]](#)) so, in order to extend this to work for geostationary radiances, only minimal additions were required. The main addition required was that the BUFR files for the geostationary radiances do not include the satellite azimuth angle, which is required in order to know which direction the satellite is in for a given observation location. Unfortunately, the files do not contain sufficient metadata to compute this accurately, but by assuming a fixed sub-satellite point, the azimuth can be calculated to a good approximation. Figure 30 shows an example of computed azimuth angles for a geostationary satellite at 0° latitude, 0° longitude. Also shown is the error introduced by assuming that the satellite is at 0° lat, 0° lon when it is really at 5° lat, 0° lon. The magnitude of this error would be the consistent with the maximum extent of the north-south diurnal variation in the position of Meteosat-8 (see Section 2.1).

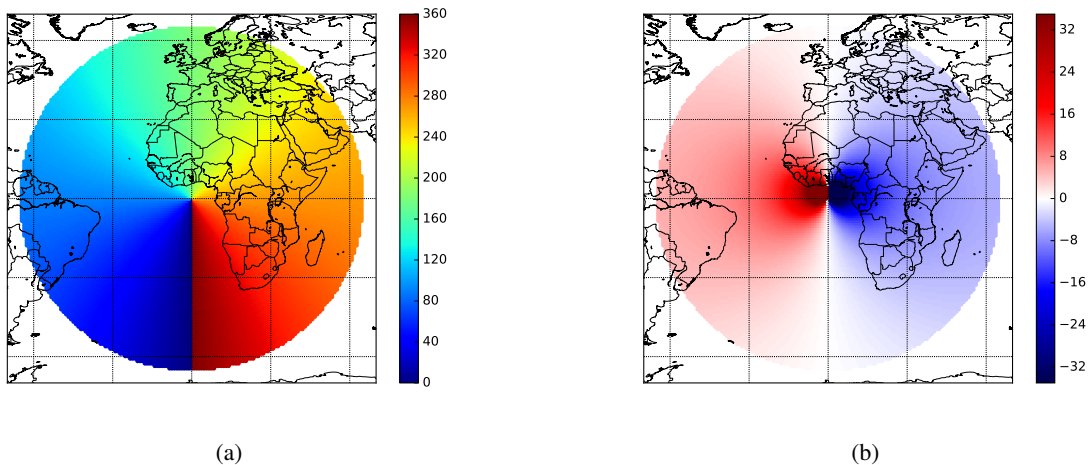


Figure 30: Computed satellite azimuth angles (degrees) for a satellite at 0° latitude, 0° longitude (a) and the error in computed azimuth angle if the true sub-satellite point is displaced to 5° latitude (b).

The error introduced by misplacing the nominal satellite position is largest between the true and nominal positions, where the error is 180° . This seems very large, but fortunately for our purposes, these locations are close enough to nadir that the zenith angle will be so small that the error in the computed azimuth is irrelevant. To the east and west of the nominal sub-satellite point there is a significant error in computed azimuth angle which decreases rapidly with distance from the nominal position. For this example, along the line $\text{lat}=0^\circ$, for zenith angles greater than 20° , the absolute azimuth error is less than 19° and for zenith angles greater than 40° the absolute azimuth error is less than 9° . Although a 5° displacement is the maximum we would currently expect from the operational satellites, these are clearly deficiencies in the calculation, but compared to neglecting the slant path altogether, this is still likely to be an improvement. In particular, the fact that the errors are largest where the zenith angle is smallest indicates that the

Name	Latitude	Longitude
Meteosat-7	0.0°	57.3°
Meteosat-8	0.0°	41.5°
Meteosat-10	0.0°	0.0°
Meteosat-11	0.0°	0.0°
GOES-13	0.0°	-75.0°
GOES-15	0.0°	-135°
GOES-16	0.0°	-75.2°
Himawari-8	0.0°	140.7°

Table 1: Nominal sub-satellite positions used for azimuth calculations.

slant-path calculation should still be relatively robust given fixed nominal sub-satellite positions.

The nominal sub-satellite positions are given in Table 1.

An assessment of the geolocation error introduced by the neglect of the slant path calculation has been performed. Note that this neglects any error in the azimuth. Consider a geostationary satellite over a point on the equator. For a measurement at the sub-satellite position (i.e. nadir), there is no need to account for the slant path, but as we consider observations at higher zenith angles, it becomes increasingly important. To keep the geometry simple, we focus here on the plane shown in Figure 31, whereby the satellite is over the equator and it measures radiation coming from the direction of a point on the north-south meridian that intersects the sub-satellite point. When assimilating radiances from WV channels, these observations are sensitive to water vapour in the troposphere, and from the geometry in the diagram it can be seen that if these features are at a height h above the surface, the satellite will, for an off-nadir observation, measure radiation which is sensitive to the atmospheric state at the point p_2 . Although, unless slant-path considerations are made, the model information that would be used to compute the simulated radiance would actually come from point p_1 . The distance between these points, dx , is a proxy for the spatial error of representation, and this increases with zenith angle.

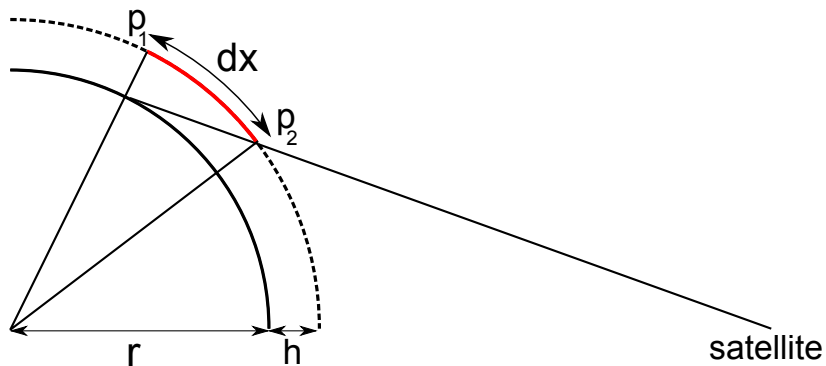


Figure 31: Diagram illustrating the spatial error of representation, dx , introduced when observing a feature at height h when slant-path processing is not performed.

Remaining with the geometry in Figure 31, we can calculate the spatial error dx produced by neglecting slant path processing as a function of the latitude north of the equator. These absolute errors have been plotted in Figure 32 for a range of heights of features. For example, for a feature at 8km¹, if the

¹ 8km was chosen to be approximately consistent with the weighting function peaks of typical GEO WV channels.

observation is at a latitude of 50° on the meridian, the spatial error from neglecting the slant-path is approximately 11km, but at a latitude of 65° this error increases to 27km, thus indicating the importance for accounting for the slant path if the maximum zenith angle limit is increased for geostationary radiances. At the time of writing, the operational horizontal resolution of nonlinear integrations of the IFS model is approximately 10km, so, for zenith angles greater than about 50° , the error is greater than the model grid spacing (cf. Figure 29).

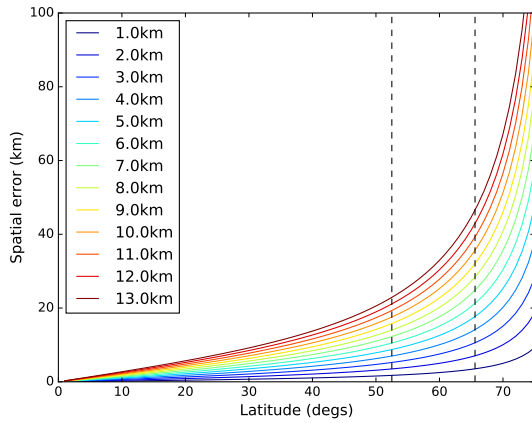


Figure 32: Absolute spatial error of representation of observations along the north-south meridian defined by the sub-satellite point that is due to the neglect of slant-path radiative transfer. These errors are plotted for features at a range of heights. The current 60° zenith angle limit is marked (equivalent to a latitude of 52.5°), as is the proposed limit of 74° (equivalent to a latitude of 65.6°).

Although the azimuth angle must always be calculated, the zenith angle is provided in all CSR and ASR BUFR files, though this was only a relatively recent addition for the SEVIRI ASR data, and during the period for which the slant-path processing was tested (December 2016), zenith angles were not available from Meteosat-10 (they were being provided, but not yet being extracted from the BUFR files), and so these too were calculated using the nominal sub-satellite positions in Table 1. During this period, the orbital inclination of Meteosat-10 was approximately 0.6° . As well as the error due to the neglect of slant-path processing, for this inclination we can also calculate the error that originates from assigning the wrong latitude of the sub-satellite point. These absolute errors are shown in Figure 33 for a feature at a height of 8km (roughly where the water vapour sensitivity is greatest for $\sim 6.25\mu\text{m}$ channels). Note that this plot is for the northern hemisphere only. When the satellite is at the most northerly extent of its orbit, the errors are slightly reduced because the observations are closer to nadir. Conversely, when the satellite is at its most southerly position, the errors are increased slightly, as the true zenith angle is larger. Despite this, the magnitude of the spatial error caused by neglecting the slant-path radiative transfer is much larger than the small perturbation seen as a result of assuming the satellite is always above the equator.

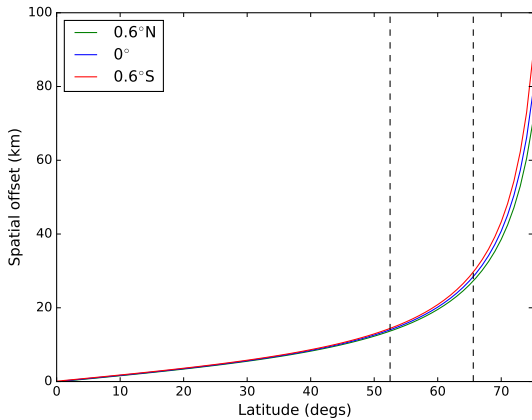


Figure 33: Absolute spatial error of representation of observations along the north-south meridian defined by the sub-satellite point that is due to the neglect of slant-path radiative transfer. This graph is valid for features at a height of 8km. Also shown are the maximum perturbations that would occur if the true zenith angle was neglected, i.e. if the sub-satellite latitude of Meteosat-10 was assumed to be 0° , but it was really orbiting with an inclination of 0.6° .

Of all the available satellites during the period of testing, Meteosat-10 provided observations up to the largest zenith angles, and so provided the best source of data for assessing the utility of data at high zenith angles, and the impact of slant-path processing. From Figure 33 we can see that for an orbital inclination as small as 0.6° , the calculated zenith angle for a fixed satellite position is adequately representative, so we will proceed with this process.

The first question in assessing whether to consider using observations at large zenith angles operationally is to examine the first guess departures of the water vapour channels, binned by zenith angle. These are shown in Figure 34.

Observing-system experiments in the ECMWF 4D-Var data assimilation system

By F. BOUTTIER* and G. KELLY

European Centre for Medium-Range Weather Forecasts, UK

(Received 4 September 2000; revised 10 January 2001)

SUMMARY

A set of global observing-system experiments is run by excluding classes of observations from the European Centre for Medium-Range Weather Forecasts (ECMWF) four-dimensional variational (4D-Var) data assimilation and forecast system. This indicates how efficiently the observations are used in this particular system. The observing systems tested were mainly TIROS (Television Infra-Red Observation Satellite) Operational Vertical Sounder (TOVS) radiances, SATellite OBservation (SATOB) atmospheric-motion winds, radiosondes, aircraft, drifting buoys and Australian pseudo observations (PAOBs). The impact is assessed in both summer and winter 1999, over a total period of six weeks, in terms of the average objective quality of the deterministic forecast of tropospheric wind and geopotential height at medium (5–7 day) and short (1–3 day) ranges. It is shown that the choice of verification method matters in data-poor areas such as the tropics and the southern hemisphere.

Some interesting conclusions can be drawn about the ECMWF 4D-Var system. Each observing system tested has a notable positive impact on the medium-range forecast performance. This is not always true at shorter ranges. The TOVS radiances have a large impact on all areas and ranges. Drifting buoys and PAOBs both have some impact in the southern hemisphere. In the northern hemisphere, the relative impact of TOVS, aircraft and radiosondes depends on the area considered. For Europe, the statistical significance of the results is limited, but the most important observing system among those tested appears to be the radiosondes.

KEYWORDS: Forecast verification Observing-system experiment Variational data assimilation

1. INTRODUCTION

Observing-system experiments (OSEs) are regularly conducted at the European Centre for Medium-Range Weather Forecasts (ECMWF) in order to review the efficiency of the data assimilation system. This data assimilation system has been developed as an accumulation of incremental modifications to the data assimilation algorithm, to the forecast model, and to the data selection. Each modification is known to improve the forecast skill, but there are interactions between them, and the observing systems have themselves evolved a lot over the past few years, with an increasing coverage and quality of satellite-based observing systems, and a reducing coverage of many conventional networks.

Reports from OSEs in other numerical-weather-prediction centres can be found in relevant publications of the World Meteorological Organization, for instance see Pailleux *et al.* (1997).

Previous OSEs have been carried out at ECMWF using the Optimal Interpolation system with emphasis on TIROS (Television Infra-Red Observation Satellite) Operational Vertical Sounder (TOVS) radiances and SATellite OBservation (SATOB) winds (Uppala *et al.* 1985; Andersson *et al.* 1991; Kelly *et al.* 1993), and a few years later using a three-dimensional variational assimilation system (Undén *et al.* 1997), with emphasis on the scatterometer winds. The set of OSEs presented here was run using the four-dimensional variational (4D-Var) data assimilation system described in Rabier *et al.* (2000), Mahfouf and Rabier (2000), Derber and Bouttier (1999), Järvinen and Undén (1997) and Klinker *et al.* (2000), which contains a few OSE results as well. The data selection is summarized in the following section. Apart from the assimilation system itself, the most original feature of this set of OSEs is the relatively large sample of

* Corresponding author; present address: CNRM Météo-France, 42 Av. Coriolis, 31057 Toulouse cedex, France.
e-mail: bouttier@meteo.fr

almost six weeks spread over winter and summer. Its making represented over 328 days of 4D-Var data assimilation and 321 10-day forecasts.

2. EXPERIMENTAL FRAMEWORK

The data assimilation system, forecast model and data used are nearly the same as the ones used in operations at ECMWF in the first half of 2000. The assimilating and forecast model is a global spectral primitive-equations model with T319 linear truncation and 60 hybrid levels in the vertical, the lowest at 10 m above ground, the highest at 10 hPa. A comprehensive physics package is used, including prognostic treatment of cloud variables, ozone, and ocean surface waves to couple surface wind and sea roughness. The atmospheric data assimilation algorithm is an incremental 4D-Var assimilation run in 6-hour cycles, at a reduced resolution of T63 to compute the corrections to the previous forecast (Courtier *et al.* 1994). Asynoptic observations are processed at the correct time, frequently reporting platforms can be used at a frequency of up to one per hour. The observation operators are nonlinear and, for most observations, use the calibrated measured physical quantity from each observing instrument.

The reference atmospheric data assimilation system processes about 200 000 pieces of information per 6-hour period, comprising: SYNOP land reports (station pressure and screen-level relative humidity), SYNOP ship reports (surface pressure and anemometer wind), drifting and moored buoys (surface pressure and anemometer wind), TEMP and PILOT profiles (wind, temperature and humidity where available, potentially at all reported levels), US profilers (wind), dropsondes (wind and temperature), aircraft at cruise level and in ascents/descents (wind and temperature), Australian pseudo observations (PAOBs) (surface pressure), SATOB retrievals of atmospheric-motion winds (wind), ambiguous wind retrievals from the European Remote Sensing Satellite (ERS) scatterometer backscatter (SCAT) (10 m winds over sea), Special Sensor Microwave/Imager (SSMI) retrievals (total water vapour and surface wind speed, over sea), TOVS level 1-C Microwave Sounding Unit (MSU)/Advanced Microwave Sounding Unit (AMSU)-A radiances (mainly sensitive to stratospheric and upper-tropospheric temperature, some channels are sensitive to lower-tropospheric temperatures as well). All data are subjected to a complex quality control (Järvinen and Undén 1997; Andersson and Järvinen 1999), and spatially dense datasets are thinned down to a resolution similar to that of 4D-Var in order to minimize correlated representativeness errors. Note that a few North Atlantic dropsondes were used in the summer cases, and that the winter cases did not use US profilers. Except for the data that are explicitly denied to the experiments, all data are used in each experiment as they would have been in operations, with the same cut-off time and real-time decisions for data selection.

In order to sample a variety of atmospheric situations most OSEs were broken down into two periods, a 3-week summer period with assimilation from 00 UTC 20 Sept 1999 to 12 UTC 10 October 1999, and a winter period from 00 UTC 16 December 1998 to 12 UTC 6 January 1999. Ten-day forecasts were run from each 12 UTC analysis, totalling, respectively, 22 and 21 forecasts from the summer and winter periods, with a 12-hour warm-up period before the first forecast in each period. A very similar set-up was used in Cardinali (2000) in order to assess the impact of European radiosondes and regional aircraft data, so the results of these two studies can be compared directly. As in any OSE, the forecasts drawn from consecutive days are not statistically independent, and not all the weather situations were sampled. Consequently, one needs to interpret

the results with caution, since they might not be consistent with the effect of excluding data for much longer periods.

3. VERIFICATION METHOD

This section explains the methodology used in interpreting the forecast differences between the OSEs.

Experience gathered at ECMWF with this assimilation and forecast system shows that two 3-week periods represent the minimum sample necessary to obtain a reliable indication of whether a typical change to the system is beneficial or detrimental to the average medium-range forecast quality. This may not be enough for changes that have a very small impact. For significant changes, the sign of the impact is reliably estimated up to about a 6-day forecast range over large areas such as the northern and southern hemispheres. Even then, one needs to be careful not to choose spells for which the atmospheric circulation exhibits unusual and persistent anomalies, or emphasizes weaknesses in the assimilation and forecasting system. In order to obtain a fully reliable estimate, with useful indications on smaller areas, several months would have been necessary, but it was unfortunately not affordable for this work.

A meaningful measure of the impact of a given modification on the forecast quality is normally obtained by averaging over time and areas, the forecast scores verified against the ECMWF operational analysis. In the medium range, six weeks of experimentation provide a reliable estimate of the impact over the extratropical hemispheres (north of 20°N and south of 20°S) at about a 5-day range and to a lesser extent on smaller, data-rich areas such as Europe, North America, eastern Asia or Australia/New Zealand. A result is convincing only if the impact on the scores is consistent across several ranges, vertical levels (1000, 500, 200 hPa were checked here) and parameters (wind-vector root mean square (r.m.s.) error and geopotential-anomaly correlation). The comparison of one experiment against another over a three-week period will usually contain a mixture of positive and negative impacts, so it is hazardous to look at individual cases: the assimilation system is only designed to minimize the analysis error on average. No single feature of the system ever provides a systematic improvement to the forecasts, which always have some random, chaotic character. A *t*-test for statistical significance can be applied in order to increase confidence in the forecast score differences, but even this will not guarantee a fully reliable interpretation of the results, because forecast errors can be correlated in time.

It is interesting to assess the forecast impact on shorter ranges as well. In general, the spread of forecast score differences is smaller at the 1–3-day range, yielding more stable averages; unfortunately, the forecast verification is more difficult at these ranges, because the forecast errors are smaller than at medium range. In data-poor areas, and particularly over the tropics, the very nature of OSEs makes this a noteworthy problem, even in the medium range: the atmosphere being chaotic and only partially observed, large errors can develop over time in the data assimilation. It means that the analysis itself may differ notably between one assimilation and the other. This is compounded by the fact that the spectral 4D-Var analysis system performs a global analysis which allows differences to propagate instantaneously over large distances (this has been observed on large-scale diurnal and semi-diurnal atmospheric waves). As a result, very short-range forecasts from any given experiment may differ a lot from the operational ECMWF analysis, simply because they started from different analyses, without one analysis being really better than the other. A solution is to verify each short-range forecast from the analyses of the assimilation it started from, which gives by construction a zero forecast

TABLE 1. DEFINITION OF THE AREAS NAMED IN THE TEXT

Northern hemisphere	North of 20°N
Southern hemisphere	South of 20°S
Tropics	Between 20°N and 20°S
Europe	75°N–35°N, 12.5°W–42.5°E
North America	60°N–25°N, 120°W–75°W
Asia	80°N–25°N, 45°E–170°E
East Asia	60°N–25°N, 102.5°E–150°E
Australia/New Zealand	12.5°S–45°S, 120°E–175°E
North Atlantic	65°N–25°N, 70°W–10°W
North Pacific	60°N–25°N, 130°E–145°W

error at zero range. Each assimilation experiment considered here compared well with a large number of observations, yielded forecasts of reasonable quality and is thus believed to provide realistic verifying analyses.

The verification of each experiment against its own set of analyses is satisfactory for most purposes, but not necessarily in OSEs, because the difference between two such experiments arises from many scattered observations. These observations perturb the assimilated state, making each forecast more different to the previous one; this is noticeable over data-poor areas such as the tropics and the southern hemisphere. As a result, using more data sometimes results in forecasts looking poorer against their own analyses over data-poor areas. The answer is to use observations as a completely independent verification system. Obviously, this only works in areas where good-quality observations are regularly available; following WMO recommendations, quality-controlled radiosonde observations of wind and geopotential height were used here. This is useful over Australia/New Zealand and on average over the whole tropical area. Unfortunately, there is no fully satisfactory verification method available over smaller areas in the tropics or elsewhere in the southern hemisphere. Perhaps high-quality aircraft, buoy or satellite data will provide a better reference for forecast verification in the future.

There is insufficient space available in this publication to display all the score plots that justify the statements made in the following sections. For the sake of clarity, only a few representative areas, variables and levels are presented, and the forecast range has been limited to 7 days (3 days for scores against observations). The area names follow WMO recommendations for verification; they are defined in Table 1.

The statements expressed in the following sections have all been based on a comparison of all three verification methods (operational analysis, own analysis, observations), on each available period, for several levels and parameters; only the genuinely convincing features have been cited. Even then, one should remember that the periods considered are rather short and thus not representative of all weather conditions.

4. NOMENCLATURE

In the plots, each experiment is identified by a name according to the following nomenclature:

ECMWF the reference summer and winter assimilation/forecast experiments, using exactly the same software and data as the other experiments on the corresponding dates, as mentioned. This is very close to, but not completely identical to ECMWF operations at the same times, mainly because the 'ECMWF' experiments contain some recent software improvements, that were only implemented in ECMWF operations in either October 1999 or April 2000.

noTOVS the reference minus the TOVS level 1C radiances: MSU channels 2, 3, 4 from National Oceanic and Atmospheric Administration (NOAA)-14, AMSU-A channels 5 to 13 from NOAA-15.

noSATOB the reference minus the SATOB atmospheric-motion winds: infrared and water vapour from Global Operational Environmental Satellites (GOES) 8 and 10, infrared, water-vapour and visible images from Meteosat-5 and 7, and infrared from Geostationary Meteorological Satellite (GMS)-5.

noUPPERSAT the reference minus all upper-level satellite data, i.e. TOVS, SATOB, and SSM/I total water-vapour retrievals from Defense Meteorological Satellite Program (SCAT winds and SSM/I low-level wind speed are still used).

noAIRCRAFT the reference minus all aircraft data (wind and temperature), including Aircraft weather reports (AIREPs), Aircraft Communication Addressing and Reporting System (ACARS) and Aircraft Meteorological Data Acquisition and Relay (AMDAR) observations.

noSONDE the reference minus all in-situ upper-level sounding data, including TEMP, PILOT, US profilers and dropsondes (the reference used no profilers and dropsondes over the winter period).

noDRIBU the reference minus all buoy wind and pressure data received as such over the Global Telecommunications System.

noPAOB the reference minus all PAOB pressure pseudo observations. The reference only used them south of 20°S.

noDRIBUnoPAOB the combination of noDRIBU and noPAOB impacts.

All experiments used ambiguous scatterometer winds over sea and surface pressure data from ships and land stations. These observing systems, along with the ones mentioned in section 2, guarantee that each experiment used a minimum amount of data to keep the data assimilation system in a realistic state in all areas.

The summer experiments can be compared directly with the first three weeks of the EUMetnet Composite Observing System (EUCOS)/Global Aircraft Data Set (GADS) impact experiments presented by Cardinali (2000). All these experiments used the 'ECMWF' experiment as a reference, extended over a two-month period. Only a tiny average impact was observed on the regional forecast scores, which suggests that, in the medium range, on large areas and over a few weeks, OSEs can only be used to assess the impact of large-scale changes to the observing network. No definite result can be obtained in this context for limited, regional changes.

5. THE IMPACT OF THE OBSERVING SYSTEMS

(a) Comparison between satellite observing systems

The impact of upper-level satellite data can be assessed by comparing the ECMWF, noTOVS, noSATOB, and noUPPERSAT experiments (Figs. 1 and 2). The noUPPERSAT experiment includes the denial of SSM/I total-water retrievals, whose separate impact has been studied by Gérard and Saunders (1999): in terms of scores, it is usually weak, but not always so. Most notably, SSM/I data affect the model climate, so one has to assume that they play a non-negligible part in the noUPPERSAT impact.

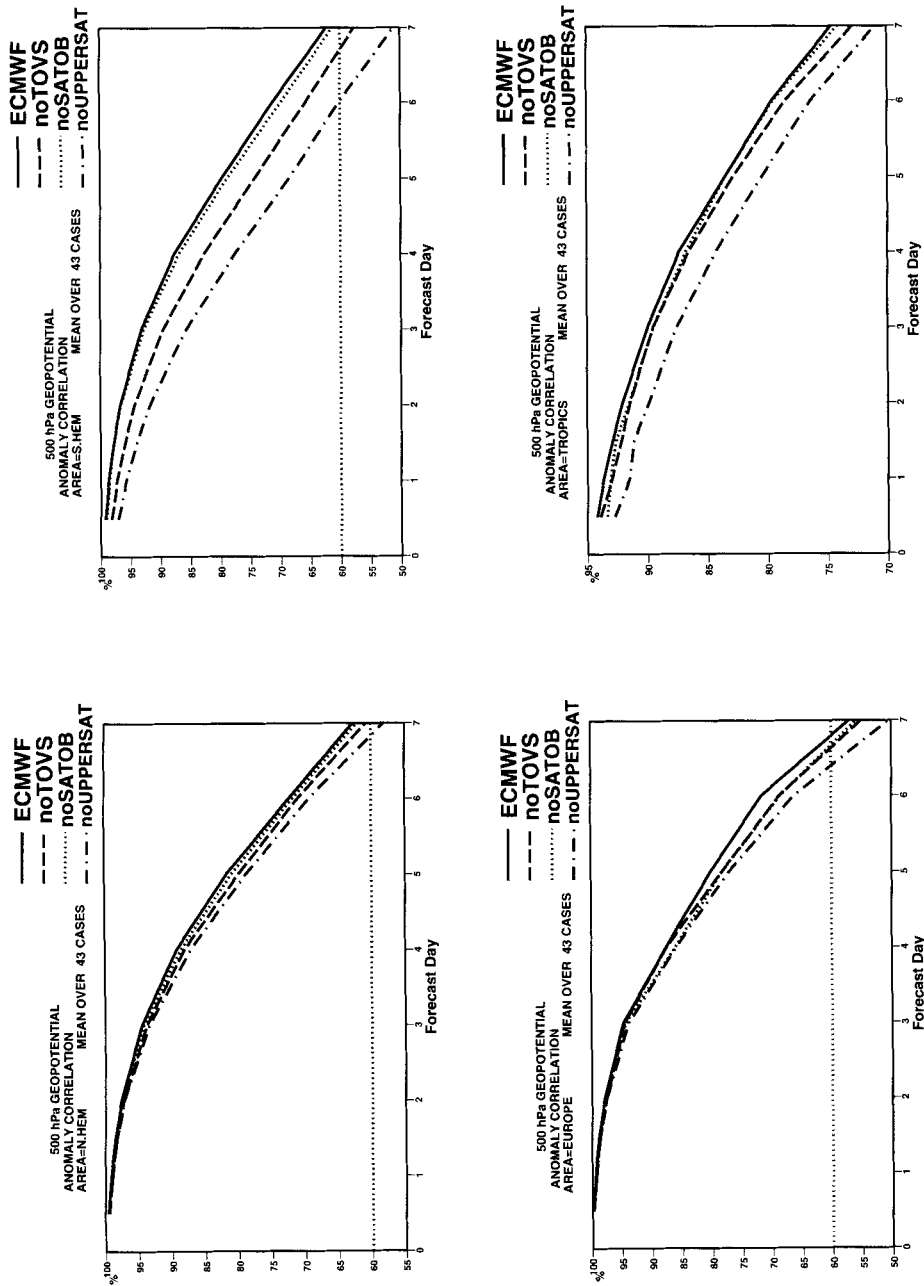


Figure 1. Average impact on the forecast of the 500 hPa geopotential-height anomaly correlation, over four areas, of denying TIROS (Television Infra-Red Observation Satellite) Operational Vertical Sounder (TOVS) data, SATEllite OBservation (SATOB) and all upper-level satellite data in the ECMWF four-dimensional variational assimilation system (verification against the ECMWF operational analysis).

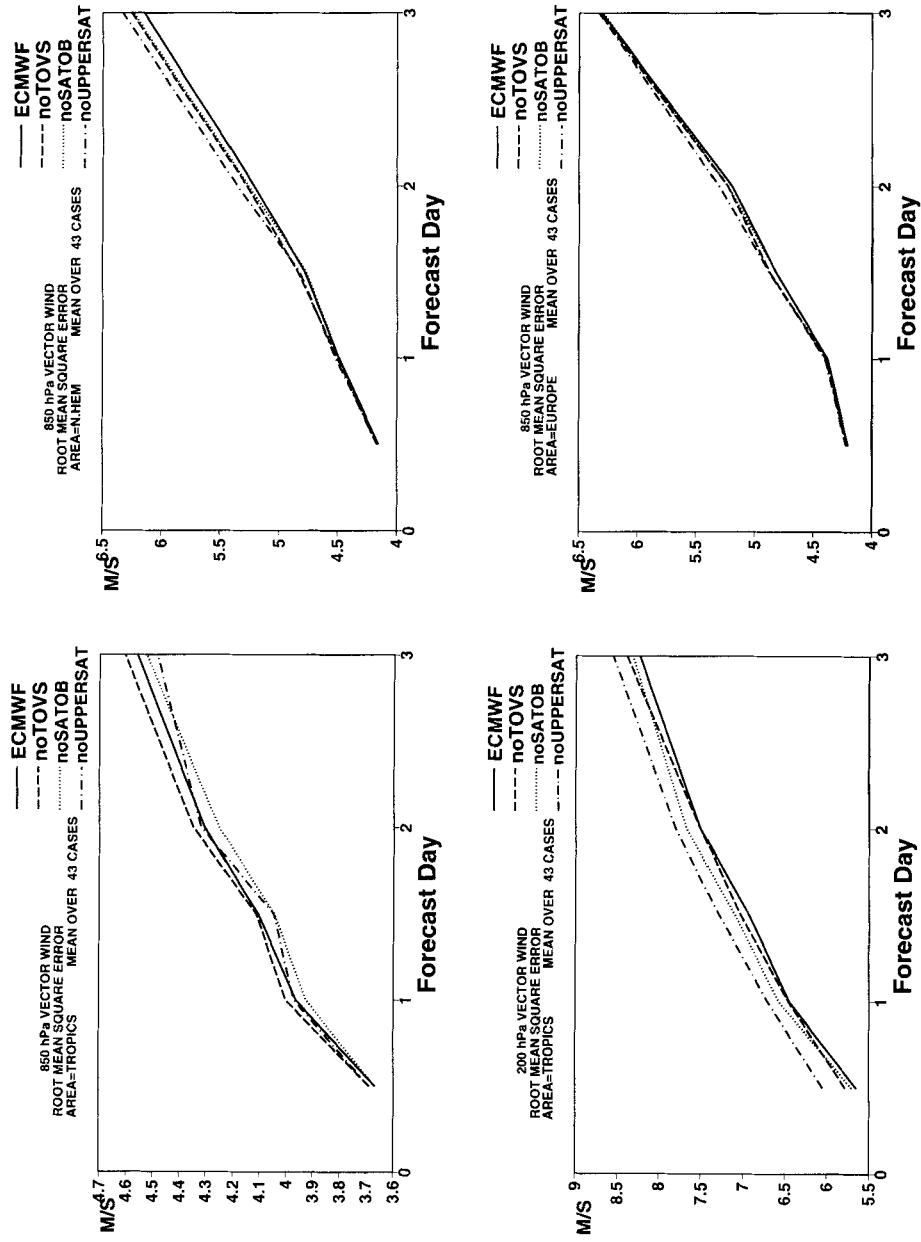


Figure 2. Average impact on the root-mean-square forecast error of the 850 hPa wind over three areas (plus 200 hPa wind over the tropics), of denying TIROS (Television Infra-Red Observation Satellite) Operational Vertical Sounder (TOVS) data, SAtellite OBservation (SATOB) and all upper-level satellite data in the ECMWF four-dimensional variational assimilation system (verification against radiosonde observations).

A common feature of TOVS, SATOB and SSM/I water retrievals is that they all affect the very large scales of the assimilation system, mainly over the tropical and southern oceans. They are also remotely sensed data with difficult representativeness problems, which means that the measurement quality can be low. Remotely sensed data can easily be misused in a way that will create local analysis errors. Such errors will limit the overall short-range forecast quality. On the other hand, it is generally accepted that medium-range forecasts are mainly sensitive to the analysis of the large scales of the atmospheric circulation. Hence, one expects TOVS, SATOB and SSM/I water retrievals to have a significant impact in the medium range. The main results shown in Figs. 1 and 2 are:

- In the northern hemisphere, the average medium-range impact of TOVS is larger than SATOBs. The combined impact of upper-level satellite data is large and significantly beneficial, they contribute to about 12 hours of forecast skill at the 7-day range.
- In the southern hemisphere and the tropics, the medium-range impact of all satellite data is even larger than in the northern hemisphere, bringing a combined benefit of about 30 hours at the 6-day range, i.e. about 25% of the total forecast skill.
- Over Europe, the relative benefits of using TOVS data and SATOBs are similar, and are mainly apparent in the medium range, beyond the 4-day range.
- In the short range, TOVS data are very beneficial but the impact of SATOBs is unclear until the 48-hour range. This could be caused by specific SATOB retrieval problems, such as speed biases (Tomassini *et al.* 1999), or an improper wind height assignment technique. A SATOB speed bias with respect to radiosondes would cause SATOBs to look particularly detrimental on scores verified against observations (Fig. 2).
- The impacts are not additive in the short range over the northern hemisphere and Europe, because the noUPPERSAT impact is clearly different from the sum of noTOVS and noSATOB. This could be related to problems using the SSM/I data, and to interactions between TOVS data and SATOBs.
- In the tropics, the choice of verification method is crucial, notably in the short range: SATOBs do improve the upper-tropospheric forecasts (around 200 hPa, Fig. 2), but there are problems at low levels and in the short range (probably because of speed biases, as suggested above). Imbalances between the assimilation and the model's physics (such as the depiction of convective systems) are suspected in this area.

(b) Comparison between satellite and conventional observing systems

The impact of conventional versus satellite data can be seen from the comparison between ECMWF, noUPPERSAT, noSONDE, and noAIRCRAFT experiments (Figs. 3 and 4). This is far from assessing the total weights of the whole conventional and satellite observing systems, because all experiments used a common dataset (SYNOP and SHIP pressure data, and SCAT winds), which is known to have a large impact on the assimilation system. Note that the noSONDE experiment measures the impact of conventional radiosondes, US wind profilers, and dropsondes. The latter two are known to have some limited impact over North America, the North Atlantic and Europe. A comparison between TOVS/SATOBs, radiosondes and aircraft data in OSEs has already been already carried out in previous years (Undén *et al.* 1997). The present work can thus be used to gauge the improvement in the use of satellite data at ECMWF. Unfortunately, the comparison with earlier OSEs is affected by the decline in radiosonde data coverage, which has been rather dramatic over the Siberian area. On the other hand, the ECMWF use of radiosondes has been improved since the early 1990s by switching from using geopotential standard-level data to temperature data (they are

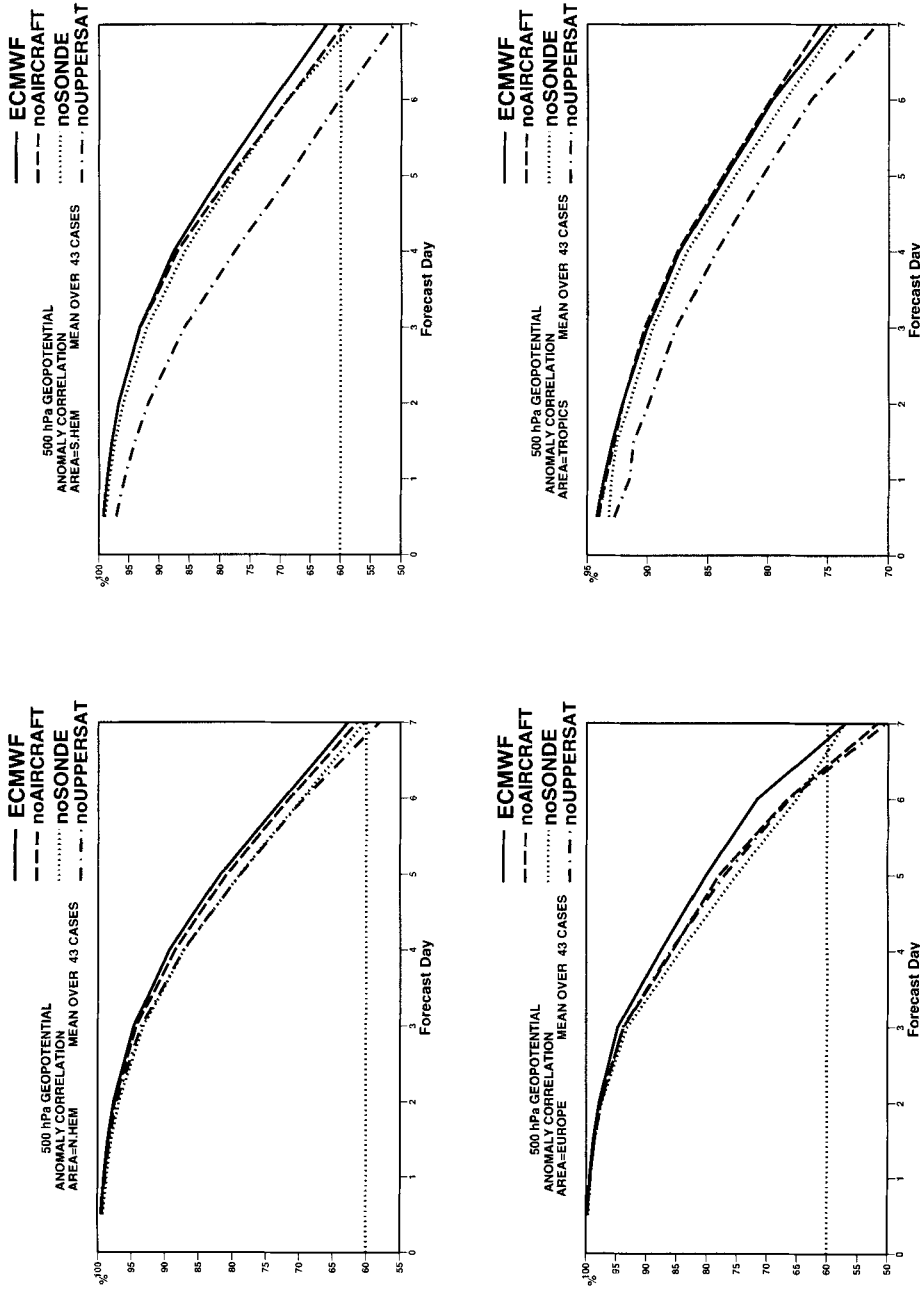


Figure 3. Average impact on the forecast of the 500 hPa geopotential-height anomaly correlation, over four areas, of denying radiosonde, aircraft and upper-level satellite data in the ECMWF four-dimensional variational assimilation system (verification against the ECMWF operational analysis).

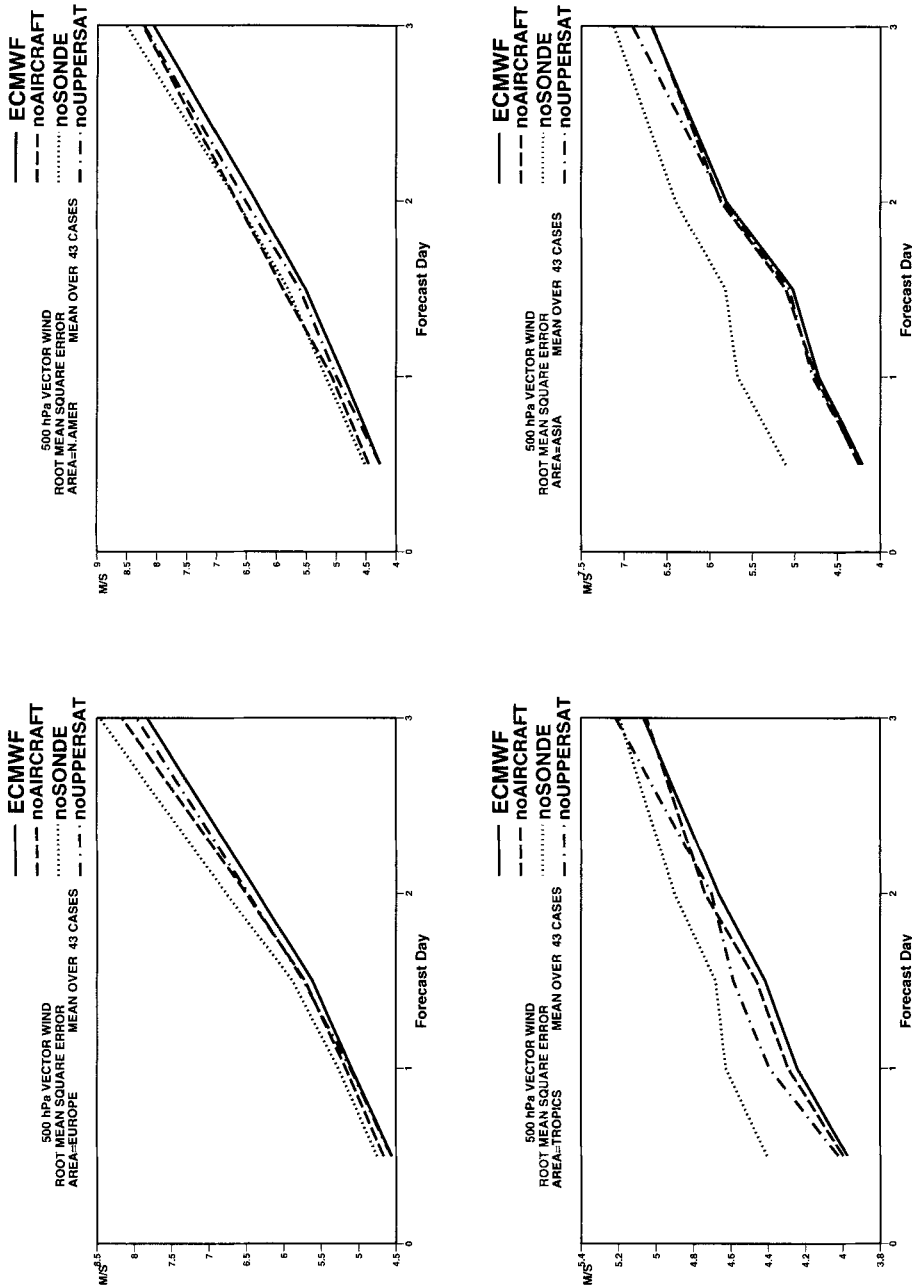


Figure 4. Average impact on the root mean square forecast error of the 500 hPa wind, over four areas, of denying radiosonde, aircraft and upper-level satellite data in the ECMWF four-dimensional variational assimilation system (verification against radiosonde observations).

more informative and less sensitive to deep bias structures). The use of aircraft data has improved, with more and more data being made available with increasing quality. The main results shown in Figs. 3 and 4 are:

- In the northern hemisphere, the most important medium-range forecast impact is obtained equally from satellite data and from sondes; aircraft have a smaller impact. This is at variance with previous experiments which showed a dominating impact from the sondes in earlier years. For instance, in Fig. 7 of Undén *et al.* (1997), radiosonde data are found to provide 24 h of forecast skill in the 5-day range.
- In the southern hemisphere, the satellite data clearly dominate, with both sondes and aircraft impacts amounting to less than one third of the benefit of satellite data, and actually less than TOVS taken on their own.
- Over Europe in the medium range, the impact can only be appreciated up to the 5-day range; the sondes contribute more to the medium-range skill than satellite data. They provide about 16 hours of forecast skill at the 5-day range, which is less than in previous years.
- In the tropics, the aircraft data have very little impact (few are available in this area; see Fig. 4 rather than Fig. 3 which is affected by the choice of verification; the sign of such a small impact cannot be reliably estimated in these experiments). The sondes do have a significant beneficial impact, but less than satellite data.
- In the northern hemisphere in the short range, the impacts of aircraft and satellites are comparable, and have about half of the sondes' impact. There are wide variations from one sub-area to the other (Fig. 4): in Europe, the aircraft have more short-range impact than satellite data, probably because of the excellent aircraft coverage over North America and the North Atlantic. Over North America, the situation is different, with the impact from satellite data similar to aircraft and radiosonde data in the short (and medium) range. A possible explanation is that satellites are the major contributors to the analyses over the tropical and northern Pacific. Over Asia, the impact of sondes is extremely large, whereas aircraft and satellite data have little effect. The large relative impact of radiosondes seems to stem from the high density of radiosonde networks over Europe and western Russia. The small impact of satellite data probably stems from the fact that few satellite data are used over land at ECMWF. Note that over all areas (including Australia/New Zealand) the impact of radiosondes dominates in the very short range (less than one day).

The impact of observations over the northern hemisphere depends highly on the range and area considered, because the observing systems are very irregular in space. The correspondence between the forecast impact in a given area and the location of the observations that caused it is not clear. Only conjectures can be made, since these are global OSEs: the way perturbations propagate from observations to features of the forecasted fields is rarely intuitive. Errors can develop during the assimilation process in very complex ways. In order to obtain detailed information, one must resort to more expensive OSEs as undertaken by institutions such as NAOS (North American Observing System) or EUCOS, or to using more specific methodologies such as adjoint-based techniques (Baker and Daley 2000).

(c) Comparison between buoy and PAOB observing systems

The impact of buoys and PAOB data can be seen by comparison between ECMWF, noDRIBU, noPAOB and noDRIBUnoPAOB experiments shown in Fig. 5. This was only done in the winter period, i.e. the summer in the southern hemisphere, which may not provide a complete picture. Buoys and PAOBs are expected to have an impact mainly in

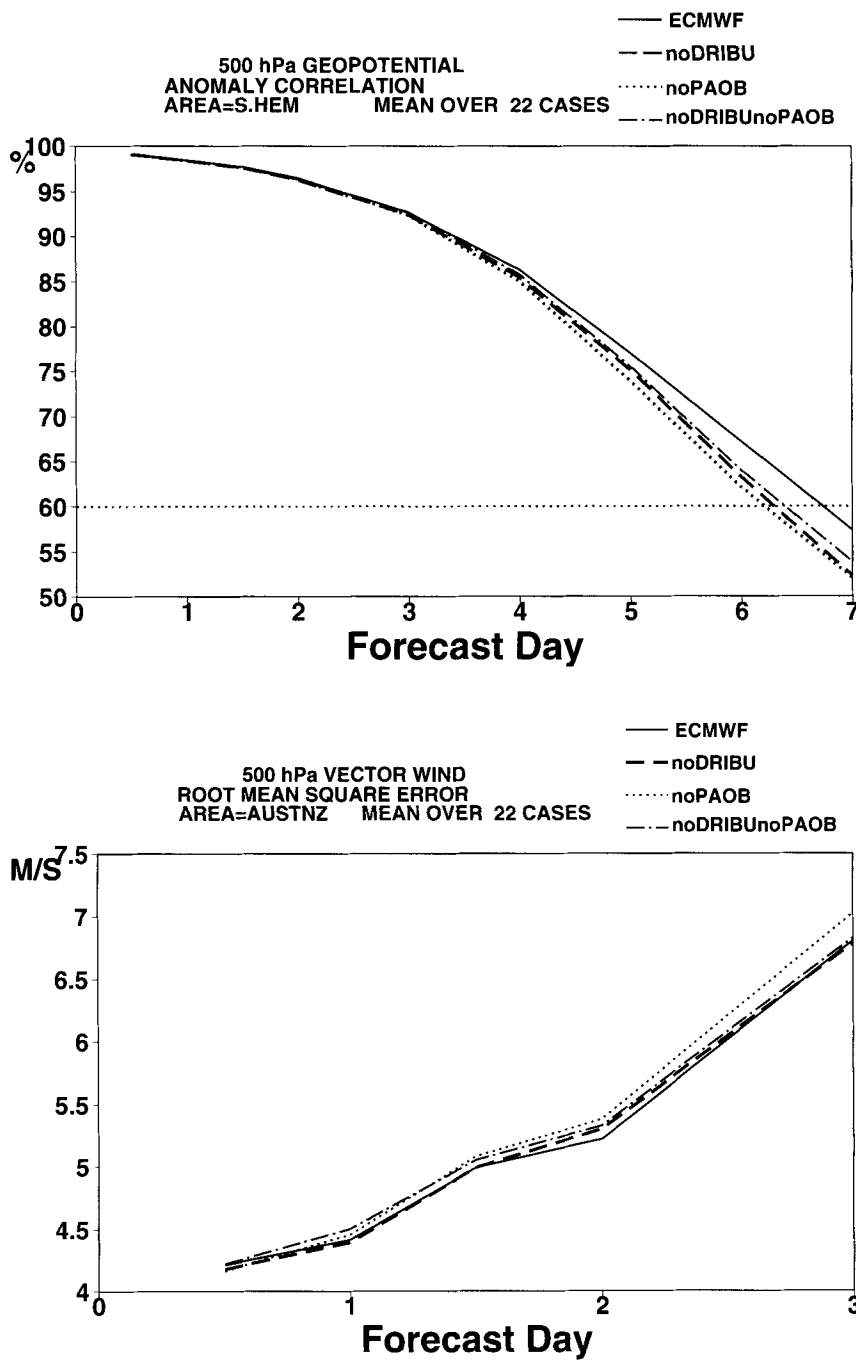


Figure 5. Average impact of denying DRIBU, PAOB and both observing systems (see text) in the ECMWF four-dimensional variational assimilation system. Top panel: medium-range impact on the 500 hPa geopotential anomaly correlation over the southern hemisphere, verified against the ECMWF operational analysis. Bottom panel: short-range impact on the root mean square error of the 500 hPa wind over Australia/New Zealand, verified against radiosonde observations.

the southern hemisphere, where they are the main source of surface pressure data over the vast oceans. Buoy winds and pressures are used, but low-level winds only have a very small weight in the 4D-Var system. The weight is small because the assumed wind observation error is set to a large value. The assumed observation error is large because of uncertainties in the surface roughness and possible incompatibilities with speed bias corrections in SCAT and SSM/I wind retrievals. The weight is small for another reason, too: 4D-Var assimilation will by construction set the equivalent background-error variance to a low value. The background-error covariance model was calibrated using model forecast differences that are damped near the ground (Derber and Bouttier 1999), so the modelled background error is small. In 4D-Var assimilation the effective background-error variance may be further reduced because the adjoint model in the 4D-Var method is diffusive in the planetary boundary layer and not forced at the bottom by a suitable model for roughness uncertainties (Mahfouf and Rabier 2000). This is acknowledged as a weakness in the current 4D-Var system; it implies that the so-called DRIBU impact is, in effect, a measure of the DRIBU surface pressure data. The main results shown in Fig. 5 are:

- In the northern hemisphere and tropics, the impact of DRIBU and PAOBs is very small and below the measurement accuracy of the OSE technique (plots not shown).
- In the southern hemisphere in the medium range, both PAOBs and DRIBUs are very beneficial, and PAOBs have the largest impact. The impacts are far from additive, which suggests that there may be some incompatibilities between both observing systems.
- In the southern hemisphere and in the short range, the forecasts can only be reliably verified against observations and in a data-rich area, in this case Australia/New Zealand. There, the DRIBUs and PAOBs are both beneficial, except in the very short range which seems to show an imbalance problem in the data assimilation system (perhaps a wind-speed bias between the DRIBU and TEMP observation operators). Interestingly, the combined use of DRIBUs and PAOBs is beneficial at all ranges.

These impacts are very small, sensitive to the verification technique, and probably to the choice of period as well. A likely cause for the small size of the impacts is the fact that all experiments used scatterometer wind data.

6. STATISTICAL SIGNIFICANCE TESTS

For guidance, an objective statistical significance test was applied to the score plots that are presented in this paper. The test is the Student *t*-test applied to the forecast score differences between each impact experiment and the ECMWF control. The range is at forecast day 5 for the medium-range plots verified against the ECMWF operational analysis, and at day 2 for the short-range plots verified against the radiosonde observations; the other characteristics of the scores are exactly as on the corresponding plots. In the list below, the percentage written between parentheses is the best significance level that was found: the smaller the percentage, the more significant the impact. The maximum significance tested was 0.1%; a difference that was not even significant at the 10% level is regarded as non significant. The '(y%)' notation means that the results are significant at the *y*% level. The main conclusions can be summarized as follows:

noTOVS at day 5 degrades the 500 hPa geopotential height in the northern hemisphere (0.2%), in the southern hemisphere (0.1%), over Europe (10%), and over the tropics (5%).

noTOVS at day 2 degrades the 850 hPa wind in the northern hemisphere (0.2%); no significant impact over Europe.

noTOVS at day 2 over the tropics has no significant wind impact at 850 hPa or 200 hPa.

noSATOB at day 5 has no significant impact on the 500 hPa geopotential height in the northern hemisphere, the southern hemisphere, or over Europe or the tropics.

noSATOB at day 2 has no significant impact on the 850 hPa wind in the northern hemisphere or over Europe.

noSATOB at day 2 over the tropics *improves* the wind at 850 hPa (10%), but degrades it at 200 hPa (5%).

noUPPERSAT at day 5 degrades the 500 hPa geopotential height in the northern hemisphere (0.1%), the southern hemisphere (0.1%), over Europe (5%), and the tropics (0.1%).

noUPPERSAT at day 2 degrades the 850 hPa wind in the northern hemisphere (0.5%) and over Europe (10%).

noUPPERSAT at day 2 in the tropics degrades the wind at 200 hPa (1%).

noUPPERSAT at day 2 degrades the 500 hPa wind over North America (10%), but has no significant impact over Europe, the tropics or Asia.

noSONDE at day 5 degrades the 500 hPa geopotential height in the northern hemisphere (0.1%), the southern hemisphere (0.5%), over Europe (1%), and the tropics (5%).

noSONDE at day 2 degrades the 500 hPa wind over Europe, North America, the tropics, and Asia (all at 0.1%).

noAIRCRAFT at day 5 degrades the 500 hPa geopotential height in the southern hemisphere (0.5%); no significant impact in the northern hemisphere, over Europe, or the tropics.

noAIRCRAFT at day 2 degrades the 500 hPa wind over Europe (10%), North America (0.1%), the tropics (10%), and Asia (10%).

In the southern hemisphere at day 5, the 500 hPa geopotential height is degraded by noDRIBU (5%), noPAOB (0.5%), and noDRIBUnoPAOB (10%).

In Australia/New Zealand at day 2, the 500 hPa wind is degraded by noDRIBU noPAOB (5%), the impacts of noDRIBU and noPAOB are not significant.

One should not exaggerate the value of these tests, because they are based on two assumptions: that the errors are uncorrelated between the forecasts, and that they are a representative sample of the distribution of possible forecast errors. These assumptions are not strictly true because the experiments only span a fraction of the variety of the possible atmospheric situations. Some specific comments made in the previous sections may seem to contradict the above list, because the author's opinion is based on many more forecast results than these *t*-tests, which are only shown to help in the interpretation of the plots, and to highlight the most significant impacts. For instance,

the degradation in noSATOB over the northern hemisphere and Europe is visible on most score plots, and it is confirmed by a study of the 4D-Var cost function as suggested in section 8. Unfortunately, it is too small to be deemed significant by the *t*-test on these areas.

7. GEOGRAPHICAL ASPECTS

The objective forecast scores suggest that some of the impact of denying observations is sensitive to the choice of verification area. There are several reasons why the impact should have spatial variations. One is that the observing systems are not uniform in space; for instance, most of the satellite data are used over the sea. Another reason is that the error growth in the data assimilation and forecasting system is not uniform in space. It is sensitive to the local weather and in particular to the presence of dynamical instabilities such as baroclinically unstable jets or active convective areas. Of course, some of the error growth is due to flaws in the design of the model and data assimilation system itself. Such flaws may introduce extra errors in specific areas, in a way that can be a function of the weather conditions.

These considerations make it worthwhile to look at the maps of forecast-error differences. Maps give an indication of the spatial variability of the errors inside each verification area, which is a way of assessing the statistical significance of score differences: the same variation in average r.m.s. forecast error could be obtained either by a uniform, small improvement over the whole verification area, or by a mixture of large small-scale improvements and degradations. Small-scale features are likely to be caused by a few exceptional cases, which would not stand out as much in averages over a longer period.

Maps of average forecast-error differences were examined for each impact experiment, for the 500 hPa geopotential at day 5. The maps are presented in terms of the relative change in r.m.s. error averaged in time, where 'relative change' is defined as follows: if ε_{exp} is the average r.m.s. error of an impact experiment named 'exp' and $\varepsilon_{\text{ECMWF}}$ is the average r.m.s. error of the reference 'ECMWF' experiment, the relative change is

$$\frac{\varepsilon_{\text{exp}} - \varepsilon_{\text{ECMWF}}}{\max(\varepsilon_{\text{exp}}, \varepsilon_{\text{ECMWF}})}.$$

This definition ensures that the relative change is between plus and minus 100%. The result is a set of maps that show where each observing system has the largest impact on the geopotential forecast; it does not tell what the relative importance of each observing system in each area is.

There is no room in this publication to display maps for all impact experiments; an example is displayed in Fig. 6. The results (for the 500 hPa geopotential only, at a range of 5 days) can be summarized as follows:

- Maps of relative change of r.m.s. forecast error, for all impact experiments, show rather noisy structures, with many small-scale features. This suggests that the experimentation is too short for a detailed depiction of the impact of each observing system. The following tentative conclusions are likely to be specific to the weather conditions encountered in the experiments.
- All experiments show a mixture of large positive and negative impact along the southern extratropical jet stream; apparently the structures are entirely caused by the local weather conditions, meaning that the impact in the southern hemisphere can only be appreciated using averaged scores.

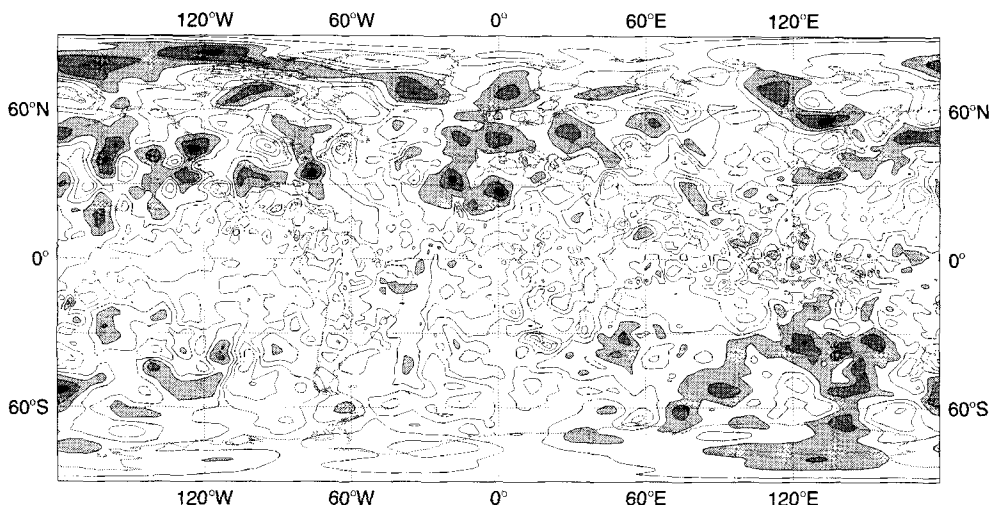


Figure 6. Impact of sounding data on the forecast skill of the 500 hPa geopotential height at the 5-day range. This is the relative change for the root mean square of forecast errors of the noSONDE experiment with respect to the ECMWF experiment (see text). The isoline interval is 10%, with an isoline at 5%. Positive values (larger than 5%) are shaded, which indicates where sounding data most reduce the forecast errors.

- No experiment shows a large impact in the tropical region (between 20°N and 20°S), except the noSATOB and noUPPERSAT experiments which show that these data have a large beneficial impact. The interpretation may not be obvious because the 500 hPa geopotential in the tropics is sensitive to diurnal and tidal oscillations.
- In the northern hemisphere, the use of TOVS data provides a well defined improvement around the north pole and over Siberia. Over Europe the impact is small. Over the other areas (notably North America) there is a mixture of improvement and degradation, with no obvious pattern.
- In the northern hemisphere, the impact of the noSATOB and noUPPERSAT experiments has a complex structure, with no obvious geographical pattern.
- The benefits of using radiosonde data are most pronounced over Europe and the north-eastern Atlantic, as well as over the Pacific area including Japan and the American west coast. In the southern hemisphere most of the benefit is found in the southern Indian Ocean and over Australia.
- Using aircraft data in the northern hemisphere provides the greatest benefit downstream of areas with many ascent and descent data (Europe and the USA), i.e. over the Atlantic, and over Asia.
- Using drifting-buoy data and/or PAOB data is beneficial poleward of the southern extratropical jet stream, suggesting that the data are mainly helpful in correcting the location of low-pressure systems.

8. IMPACT ON THE VARIATIONAL ANALYSIS

The previous sections have highlighted the value of several observing systems for improving the forecast performance. For numerical-weather-prediction centres, using data has a cost. Some of the cost is purely computational, because data processing requires computational power and may slow down the analysis algorithm. Another aspect of the cost is the effect of data on the statistical optimality of the analysis. Here we examine the impact of each experiment on the computational cost of the incremental

4D-Var analysis only (excluding data preparation, but including quality-control checks). This impact needs to be considered in relation to possible changes in the way 4D-Var assimilation uses the observational data in the OSEs.

The impact on Central Processor Unit (CPU) time (measured on a Fujitsu VPP5000 machine) is a sensitive issue since most of the CPU cost of performing the ECMWF data assimilation is in the 4D-Var process. The impact of radiosondes, drifting buoys and PAOBs is negligible (below 1%). TOVS, SATOB and aircraft data are responsible, respectively, for 5%, 1.5% and 2% of the CPU cost. The main conclusion is that the benefit of radiance data is obtained at a non-negligible numerical cost, which suggests that special computer resources will need to be allocated for the use of future high-volume radiances from systems such as the Atmospheric InfraRed Sounder (AIRS), the Infrared Atmospheric Sounding Interferometer (IASI) or geostationary satellites.

The impact on the speed of convergence of 4D-Var assimilation can be measured by the rate of decrease of the cost-function gradient norm in the minimization procedure (Rabier *et al.* 2000). Currently the bulk of the cost of 4D-Var assimilation is proportional to the number of iterations performed in the minimization, which is set to 50 and 20 for each of the two minimization steps (Mahfouf and Rabier 2000). Experience shows that performing more iterations does not improve the forecasts, but doing many less would degrade them. Thus, it is important to know if any observing system is responsible for a loss of conditioning of 4D-Var assimilation, which would be tantamount to an increase in CPU cost. Since 4D-Var assimilation is preconditioned by the background term, one might expect that, everything else being equal, using more observations would degrade the convergence.

In fact, the speed of convergence is generally improved when more data are used. This is probably because, in the data assimilation, using more data improves the background fields, which in turn means that the observation departures are smaller at the start of the minimization. The speed of minimization appears to be more sensitive to the meteorological quality of the background fields than to the number of observations being processed. Given the speed of convergence of 4D-Var assimilation there is no reason to be restrictive about the number of data allowed in the assimilation. The only exception is SSM/I, which noticeably degrades the speed of convergence of 4D-Var assimilation when linearized physics are used (the final gradient norm increases by 30% when SSM/I data are used). A likely explanation is the poor conditioning of the humidity analysis in the ECMWF 4D-Var method, which assimilates total precipitable-water information in terms of the model's specific-humidity variable. Convergence problems related to humidity observations have been documented by Andersson *et al.* (2000).

Another important issue is how each observing system impacts on the use of the other observations. The first issue to check is how the quality-control system behaves in the impact experiments. When withdrawing one observing system from the data assimilation, it is not obvious whether the remaining observations are still used in the same way, because some quality-control decisions are sensitive to changes in the background fields. Indeed it is found that the number of used observations changes by less than 0.1% for each observing system and in each impact experiment, except of course for the observing systems that were intentionally withdrawn.

The final diagnosis is how well the observations are fitted by the analysis. This can be measured by the average value of the observation cost function J_o at the end of the 4D-Var analyses. The function J_o is, to a large extent, a sum of the squared distances between model fields and observations, for each observed variable, normalized by the expected observation-error variances. A rigorous interpretation of the J_o values is given in Talagrand (1999). The average value of J_o (weighted by the numbers of observations

used) provides a non-dimensional measure of the quadratic distance between model and observations for each data assimilation experiment. In most OSEs, this quantity is found to increase by several tens of percent, meaning that in the full system each observing system is supported by the others to produce consistent analysis fields. The exception is aircraft data, perhaps because of incompatibilities with radiosonde or SATOB observations; it would be interesting to investigate this problem further.

9. CONCLUSIONS

The OSEs have confirmed that there is a clear and beneficial impact from using all the considered observing systems in the ECMWF global data assimilation system. This shows that, even if all the useful information may not be extracted from the observations, the 4D-Var system is certainly able to blend them in a sensible way. OSEs in previous years suggested that radiosondes were the main component of the observing system in the northern hemisphere (Undén *et al.* 1997). The key property demonstrated here is the outstanding role played by satellite data and, notably, the TOVS radiances. Over data-poor areas, satellite data seem to be the main contributor to the forecast performance. Over data-rich areas, satellite data contribute with the same order of magnitude as conventional observing systems such as radiosondes and aircraft. This means that the impact of satellite data has increased, because the products themselves have improved through better instruments and pre-processing systems, and because the ECMWF data assimilation system makes better use of these observations thanks to better quality-control procedures, observation operators, forecast model and the 4D-Var algorithm.

Some of the decrease in the relative impact of radiosondes is obviously caused by the degradation in the observing network; at ECMWF the number of radiosonde reports received daily has decreased by about 15% over the past 8 years (F. Lalaurette, personal communication). It would be interesting to conduct such OSEs on older periods in order to demonstrate this effect. This will be facilitated by the re-analysis databases that are being prepared in several institutions.

Retrieved observations, such as SATOBs, often have quality problems in that they do not always clearly improve the short-range forecasts. Apparently, they create imbalances in the data assimilation system. A similar argument could be made for PAOBs and SSM/I retrievals in some areas. However, they do improve the medium-range forecasts, because they are useful in observing large-scale features.

Conversely, sparse observing systems such as drifting buoys clearly improve the forecasts, even in the short range, over data-poor areas such as the southern hemisphere. In this region one could have assumed that conventional in-situ measurements such as buoys and radiosondes are unimportant compared with satellite data. In reality, a good use of satellite data relies on some careful tuning; this tuning can only be set up and maintained if a decent network of in-situ observations is continuously available. This is crucial for the use of scatterometer and passive radiance sounding data.

Generally, the findings of this work are in agreement with similar studies carried out in other modelling centres such as the National Centers for Environmental Prediction and the Met Office (see contributions in Pailleux *et al.* 1997), notably, the general impression about the usefulness of radiosondes and SATOBs.

There are relationships between the quantity of observations being assessed in an OSE and the sample length required to measure the impact on forecast quality. Here we have seen that two three-week periods seem sufficient to assess the large-scale forecast impact up to the 5-day range or so, for major components of the global observing system. A contrario, the impact of a smaller number of observations can barely be estimated in

a two-month period such as, for instance, in the EUCOS study in Cardinali (2000). This suggests that OSEs cannot be used to assess the value of a regional observing system in the medium range, unless extremely long and expensive impact experiments are funded. Still, regional observing systems can probably be assessed in terms of the impact on short-range, regional forecasts, and on exceptional situations such as destructive storms, if enough independent cases can be selected for objective testing.

ACKNOWLEDGEMENTS

Thanks are due to A. Hollingsworth and A. Simmons for valuable comments on the manuscript, and to J. Haseler and N. Wedi who provided the facility to run assimilation and forecast experiments. Two anonymous reviewers and A. Lorenc provided detailed editorial comments that notably improved the quality of the paper.

REFERENCES

- | | | |
|--|------|--|
| Andersson, E. and Järvinen, H. | 1999 | Variational quality control. <i>Q. J. R. Meteorol. Soc.</i> , 125 , 697–722 |
| Andersson, E., Hollingsworth, H., Kelly, G., Lönnberg, P., Pailleux, J. and Zang, Z. | 1991 | Global observing systems experiments on operational statistical retrievals of satellite sounding data. <i>Mon. Weather Rev.</i> , 119 , 1851–1864 |
| Andersson, E., Fisher, M., Munro, R. and McNally, A. | 2000 | Diagnosis of background errors for observed quantities in a variational data assimilation scheme, and the explanation of a case of poor convergence. <i>Q. J. R. Meteorol. Soc.</i> , 126 , 1455–1472 |
| Baker, N. and Daley, R. | 2000 | Observation and background adjoint sensitivity in the adaptive observation targeting problem. <i>Q. J. R. Meteorol. Soc.</i> , 126 , 1431–1454 |
| Cardinali, C. | 2000 | ‘Observing system experiments on the European conventional observing system’. In Proceedings of the second CGC/WMO workshop on the impact of observing systems on NWP, 6–8 March 2000, Toulouse, France. Available from WMO, Geneva, Switzerland |
| Courtier, P., Thépaut, J.-N. and Hollingsworth, A. | 1994 | A strategy for operational implementation of 4D-VAR, using an incremental approach. <i>Q. J. R. Meteorol. Soc.</i> , 120 , 1367–1388 |
| Derber, J. and Bouttier, F. | 1999 | A reformulation of the background error covariance in the ECMWF global data assimilation system. <i>Tellus</i> , 51A , 195–222 |
| Gérard, É. and Saunders, R. | 1999 | 4D-Var assimilation of SSM/I total column water vapour in the ECMWF model. <i>Q. J. R. Meteorol. Soc.</i> , 125 , 3077–3102 |
| Järvinen, H. and Undén, P. | 1997 | ‘Observation screening and background quality control in the ECMWF 3D-Var data assimilation system’. ECMWF Research Department Technical Memorandum no. 236. Available from ECMWF, Shinfield Park, Reading RG2 9AX, UK |
| Kelly, G., Pailleux, J., Rabier, F. and Thépaut, J.-N. | 1993 | ‘Observing system experiments made with the ECMWF system’. World Weather Watch Technical Report no. 16, WMO/TD no. 594. Available from WMO, Geneva, Switzerland |
| Klinker, E., Rabier, F., Kelly, G. and Mahfouf, J.-F. | 2000 | The ECMWF operational implementation of four-dimensional variational assimilation. Part III: Experimental results and diagnostics with operational configuration. <i>Q. J. R. Meteorol. Soc.</i> , 126 , 1191–1216 |
| Mahfouf, J.-F. and Rabier, F. | 2000 | The ECMWF operational implementation of four-dimensional variational assimilation. Part II: Experimental results with improved physics. <i>Q. J. R. Meteorol. Soc.</i> , 126 , 1171–1190 |
| Pailleux, J. | 1997 | ‘Impact of various observing systems on numerical weather prediction’. WMO/TD No. 868, Proceedings of CGC/WMO workshop. Available from WMO, Geneva, Switzerland |
| Rabier, F., Järvinen, H., Klinker, E., Mahfouf, J.-F. and Simmons, A. | 2000 | The ECMWF operational implementation of four-dimensional variational assimilation. Part I: experimental results with simplified physics. <i>Q. J. R. Meteorol. Soc.</i> , 126 , 1143–1170 |

- Talagrand, O.
- Tomassini, M., Kelly, G. and Saunders, R.
- Undén, P., Kelly, P., Le Meur, D. and Isaksen, L.
- Uppala, S., Hollingsworth, A., Tibaldi, S. and Källberg, P.
- 1999 'A posteriori evaluation and verification of analysis and assimilation algorithms'. Pp. 17–28 in ECMWF workshop proceedings on diagnosis of data assimilation systems. Available from ECMWF, Shinfield Park, Reading RG2 9AX, UK
- 1999 Use and impact of satellite atmospheric motion winds on ECMWF analyses and forecasts. *Mon. Weather Rev.*, **127**, 971–986
- 1997 'Observing system experiments with the 3D-Var assimilation system'. ECMWF Research Department Technical Memorandum no. 244. Available from ECMWF, Shinfield Park, Reading RG2 9AX, UK
- 1985 'Results from two recent observing system experiments'. Pp. 165–202 in ECMWF seminar/workshop on data assimilation systems and observing system experiments, with particular emphasis on FGGE, Reading. Available from ECMWF, Shinfield Park, Reading RG2 9AX, UK

Article

3D-VAR Data Assimilation of SEVIRI Radiances for the Prediction of Solar Irradiance in Italy Using WRF Solar Mesoscale Model—Preliminary Results

Sabrina Gentile ^{1,2,*}, Francesco Di Paola ¹, Domenico Cimini ^{1,2}, Donatello Gallucci ¹, Edoardo Geraldi ¹, Salvatore Larosa ¹, Saverio T. Nilo ¹, Elisabetta Ricciardelli ¹, Ermann Ripepi ¹, Mariassunta Viggiano ¹ and Filomena Romano ¹

¹ Institute of Methodologies for Environmental Analysis, National Research Council (IMAA/CNR), 85100 Potenza, Italy; francesco.dipaola@imaa.cnr.it (F.D.P.); domenico.cimini@imaa.cnr.it (D.C.); donatello.gallucci@imaa.cnr.it (D.G.); edoardo.geraldi@imaa.cnr.it (E.G.); salvatore.larosa@imaa.cnr.it (S.L.); saverio.nilo@imaa.cnr.it (S.T.N.); elisabetta.ricciardelli@imaa.cnr.it (E.R.); ermann.ripepi@imaa.cnr.it (E.R.); mariassunta.viggiano@imaa.cnr.it (M.V.); filomena.romano@imaa.cnr.it (F.R.)

² Center of Excellence Telesensing of Environment and Model Prediction of Severe Events (CETEMPS), University of L'Aquila, 67100 L'Aquila, Italy

* Correspondence: sabrina.gentile@imaa.cnr.it; Tel.: +39-0971-427266

Received: 27 January 2020; Accepted: 10 March 2020; Published: 12 March 2020



Abstract: Solar power generation is highly fluctuating due to its dependence on atmospheric conditions. The integration of this variable resource into the energy supply system requires reliable predictions of the expected power production as a basis for management and operation strategies. This is one of the goals of the Solar Cloud project, funded by the Italian Ministry of Economic Development (MISE)—to provide detailed forecasts of solar irradiance variables to operators and organizations operating in the solar energy industry. The Institute of Methodologies for Environmental Analysis of the National Research Council (IMAA-CNR), participating to the project, implemented an operational chain that provides forecasts of all the solar irradiance variables at high temporal and horizontal resolution using the numerical weather prediction Advanced Research Weather Research and Forecasting (WRF-ARW) Solar version 3.8.1 released by the National Center for Atmospheric Research (NCAR) in August 2016. With the aim of improving the forecast of solar irradiance, the three-dimensional (3D-Var) data assimilation was tested to assimilate radiances from the Spinning Enhanced Visible and Infrared Imager (SEVIRI) aboard the Meteosat Second Generation (MSG) geostationary satellite into WRF Solar. To quantify the impact, the model output is compared against observational data. Hourly Global Horizontal Irradiance (GHI) is compared with ground-based observations from Regional Agency for the Protection of the Environment (ARPA) and with MSG Shortwave Solar Irradiance estimations, while WRF Solar cloud coverage is compared with Cloud Mask by MSG. A preliminary test has been performed in clear sky conditions to assess the capability of the model to reproduce the diurnal cycle of the solar irradiance. The statistical scores for clear sky conditions show a positive performance of the model with values comparable to the instrument uncertainty and a correlation of 0.995. For cloudy sky, the solar irradiance and the cloud cover are better simulated when the SEVIRI radiances are assimilated, especially in the short range of the simulation. For the cloud cover, the Mean Bias Error one hour after the assimilation time is reduced from 41.62 to 20.29 W/m² when the assimilation is activated. Although only two case studies are considered here, the results indicate that the assimilation of SEVIRI radiance improves the performance of WRF Solar especially in the first 3 hour forecast.

Keywords: solar irradiance; WRF; assimilation; SEVIRI; radiance; 3DVAR; numerical weather prediction

1. Introduction

The rise of renewable energy in global energy production requires the development of procedure to better manage these highly variable sources. In recent years, the contribution of solar power to electricity has incremented rapidly; in Italy solar power has grown from 3.6 GW in 2010 to more than 20 GW in 2018, which represents about 7% of the gross national electricity and the 20% of the total energy from renewable sources [1]. Solar energy usage is expected to continue growing for the foreseeable future. Thus, the prediction of solar radiation is becoming crucial to estimate in advance how much energy will be available and what share can be covered with renewable sources. Contrary to the conventional energy sources (fossil and nuclear), solar energy is considered a variable source because the energy production is dependent on the intensity of solar irradiance that is mainly attenuated by atmospheric aerosols and clouds passing between the sun and the solar-powered plants. Given this variability in the generation of solar power, nowadays it becomes imperative to focus on a realistic modelling and accurate prediction of this variable, which is essential for management, strategies operations and regulation of power supplies.

Solar power prediction is pursued through different techniques for various time scales. Indeed, the forecast temporal interval helpful for the operators range from few minutes to days, so different methods are necessary. The strategies used for the prediction of the Global Horizontal Irradiance (GHI) can be divided mainly into two groups. The first group includes numerical weather prediction (NWP) models, which solves the equations of atmospheric dynamics and thermodynamics to infer cloud and radiative information up to several days ahead [2,3]. The second group relies on the analysis of satellite or ground based remote sensing to infer cloud motion and short-term forecasting from minutes to few hours [4–8]. Most of the works [9–11] shows that the second group outperforms the first one for forecasts within 4–5 h, with the time window depending on the localization. For a longer forecast horizon, numerical models are more appropriate [12]. Some recent studies suggest that NWP forecasts are becoming competitive with respect to satellite-based methods even on short-time scale [10,12].

Several studies assess the performances of mesoscale models. The Weather Research and Forecasting (WRF) model has been tested in the forecasts of GHI in Spain [13] and in several European and North American sites [14], reporting relative Root Mean Square Error (RMSE) of about 40% for 24 h forecast horizon. Similar results have been found in Europe [15]. In Southern Italy, a comparison of two atmospheric regional models (the Regional Atmospheric Modeling System (RAMS) and the WRF model) has been reported for clear and cloudy sky conditions finding RMSE values for both models in overcast conditions about 80 W/m² larger than in clear sky conditions [16]. A seasonal characterization using the RAMS model over the western Mediterranean Coast has been performed to evaluate the solar radiation using ground-based weather stations measurements for the winter 2010–2011 and the summer 2011. The statistically daily evaluations show absolute bias values varying from –50 to 160 W/m² and a RMSE from 60 to 240 W/m² [17]. A similar evaluation has been performed for the WRF/RAMS models over a region in Eastern Spain under distinct atmospheric conditions using in-situ observations and remote sensing data derived from the Spinning Enhanced Visible and Infrared Imager (SEVIRI) aboard the Meteosat Second Generation (MSG) and the uncoupled Land Surface Model (LSM) Global Land Data Assimilation System (GLDAS) during a 7-day period in summer 2011. Both the models show difficulties to forecast clouds with values of Mean Bias Error (MBE) and RMSE in overcast conditions ranging, respectively, from –70 to –80 W/m² and from 140 to 190 W/m² for WRF and from –80 to –110 W/m² and from 200 to 400 W/m² for RAMS [18].

An important milestone in solar radiation applications has been the development of WRF-Solar within the project Sun4Cast [19]. This study asserts that the use of WRF-Solar significantly improves the solar irradiance forecast and the combination of the NWP with satellite-based method produces accurate forecast also in the short range 1–6 h time scale [20]. This paper focuses on the following forecasting challenge: improve the short-term forecast of solar irradiance using satellite data assimilation. The forecast skill is indeed strongly influenced by the accuracy of the cloud and thermodynamics analyses in the initial representations, which can improve significantly using satellite data assimilation [21].

Satellite are the primary source of cloud information and therefore can play an important role also for solar power forecasting [21–23]. One of the methods used to improve the forecast of the clouds and consequently of the solar irradiance is the assimilation of the satellite radiances from geostationary meteorological satellites. The main advantage of the radiance assimilation is that the observed radiances can be directly ingested into the NWP without the need of retrieval methods. Retrievals provide an estimate of the simulated variable from the observed quantity based on inversion of a physical or empirical model; these techniques usually produce large uncertainties [21].

The main focus in recent years has been on radiance assimilation from polar orbiting satellites to improve the NWP forecast. Two studies analyzed the impact of the assimilation of radiance data from the Advanced Microwave Sounding Unit-A (AMSU-A) [24] and from the Advanced Microwave Scanning Radiometer 2 (AMSR2) [25] for the hurricane Sandy forecasts and the results proved that the radiance assimilation improved the short and medium range forecast [24] and the hurricane structure and cloud distributions [25]. Similar results can be found in References [26,27], where radiances from AMSU-A and AMSU-B [26] and from the Microwave Humidity Sounder (MHS) [27] have been assimilated in the WRF model to simulate an event of heavy rainfall in Beijing [26] and to forecast a binary system typhoons [27].

Besides polar-orbiting satellites, geostationary instruments were also found to be useful source of information and have been introduced to data assimilation more recently. Despite recent progress in data assimilation, the potentiality of geostationary sensors is far from being fully exploited [28]. One advantage of geostationary instruments is the nearly continuous picture of the weather event evolution due to their high temporal resolution. The impact of geostationary radiances from three infrared channels of SEVIRI using a four-dimensional data assimilation has been investigated using the High-Resolution Limited Area Model (HIRLAM) under clear sky and low-level cloud conditions [29–31]. The tests have been performed in a domain with a horizontal resolution of 22 km converting the measured radiances by SEVIRI to brightness temperatures and cloud products. Results show a positive impact for almost all upper-air variables; the main improvements are obtained for geopotential height and humidity [29–31]. The impact of assimilating Geostationary Operational Environmental Satellite (GOES) imager radiances on the analysis and forecast of a convective process over Mexico was assessed for the first time using a rapid refresh assimilation system with a convection permitting model setting [32]. Improved humidity and temperature analysis and significant standard deviation reductions were produced when the assimilation is activated [32].

In this study we present the preliminary results of the first attempt to assimilate the SEVIRI radiance in the WRF-Solar model in convection-permitting configuration to improve the solar irradiance forecast especially in the short-medium range. The paper is organized as follows: Section 2 describes the WRF-Solar with its configuration, the data assimilation system, the observation data sets, the two simulated periods and the statistical methodology. Section 3 provides the results and the statistical analysis both in clear sky and cloudy conditions and Section 4 draws conclusions and future developments.

2. Materials and Methods

In this study, the tool used to forecast the solar irradiance is the NWP model WRF, Solar version. The model has been tested both in the control configuration (CNTRL) without any type of assimilation and in assimilated mode (ASSIM) using the three-dimensional (3D-Var) data assimilation technique. The radiances measured by the imager radiometer SEVIRI onboard MSG geostationary satellite have been ingested in the NWP. The model performances are evaluated using two types of data: the ground-based observations from the weather stations of Regional Agency for the Protection of the Environment (ARPA) Lombardy and two European Organization for the Exploitation of Meteorological Satellites (EUMETSAT) products derived by SEVIRI.

2.1. Numerical Weather Prediction Model and the WRF-IMAA-Solar Setup

The WRF model is a next-generation mesoscale NWP system designed for flexible purposes from atmospheric investigations to operational forecasting requests. The Advanced Research WRF (ARW) dynamical core system has been developed by the collaborations of several research institutes directed by the National Center for Atmospheric Research (NCAR, <http://www.wrf-model.org>). The WRF-ARW core is based on an Eulerian solver for the fully compressible nonhydrostatic equations, using a mass vertical coordinate varying with height and it used for time-integration scheme a third-order Runge-Kutta. WRF-ARW supports horizontal nesting (one- or two-way) to allow a spatial resolution enhancement through the introduction of additional domains. The full physics schemes (microphysics, cumulus convection, atmospheric and surface radiation, planetary boundary layer and land-surface) provided by WRF vary from simple and efficient to the most sophisticated and computationally expensive [33].

The Solar version of WRF has been specifically conceived to improve the solar irradiance prediction. WRF-Solar is the first NWP model expressly planned to join the rising request for dedicated forecast variables for solar energy purposes [34]. The direct normal irradiance (DNI) and diffuse (DIF) components of solar irradiance in addition to the GHI component are calculated in the radiative budgets within the NWP system [34]. This calculation is performed by the radiative parameterization Rapid Radiative Transfer Model for Global (RRTMG) that explicitly solves the radiative transport equation for all the components. In addition, WRF-Solar introduces the direct effect in aerosol-radiation feedback to obtain a better representation of the components of diffuse and direct radiation and the indirect effect in the aerosol-cloud feedback that considers the interaction between the hydrometeors and the aerosols [35]. This link between the microphysical and the radiative scheme, leading to a physically more consistent representation of the distribution of the hydrometeors, is a novelty since usually in NWP models the distribution functions are imposed with an effective radius of the constant cloud particle.

The WRF-IMAA-Solar version 3.8.1 is operative at the Institute of Methodologies for Environmental Analysis of the National Research Council (IMAA-CNR) since 2016 and it has been developed during the SolarCloud project financed by the Italian Ministry of Economic Development (MISE), with the aim of providing high temporal and spatial resolution forecasts of solar irradiance variables to solar energy industry purposes.

Two-way nested domains have been selected for the implemented configuration: the larger domain is centered over the Mediterranean basin with 9 km grid spacing while the inner domain includes Italy with 3 km horizontal resolution (Figure 1). The domains are represented with a Lambertian projection using staggered Arakawa-C horizontal grid and the land-use and the Digital Elevation Model (DEM) are obtained by the Moderate Resolution Imaging Spectroradiometer (MODIS) database at 30 s of arc (about 900 m) updated in 2008. The vertical grid is common to all the domains with 36 vertical levels, ranging from the surface to the model top set to 50 hPa.

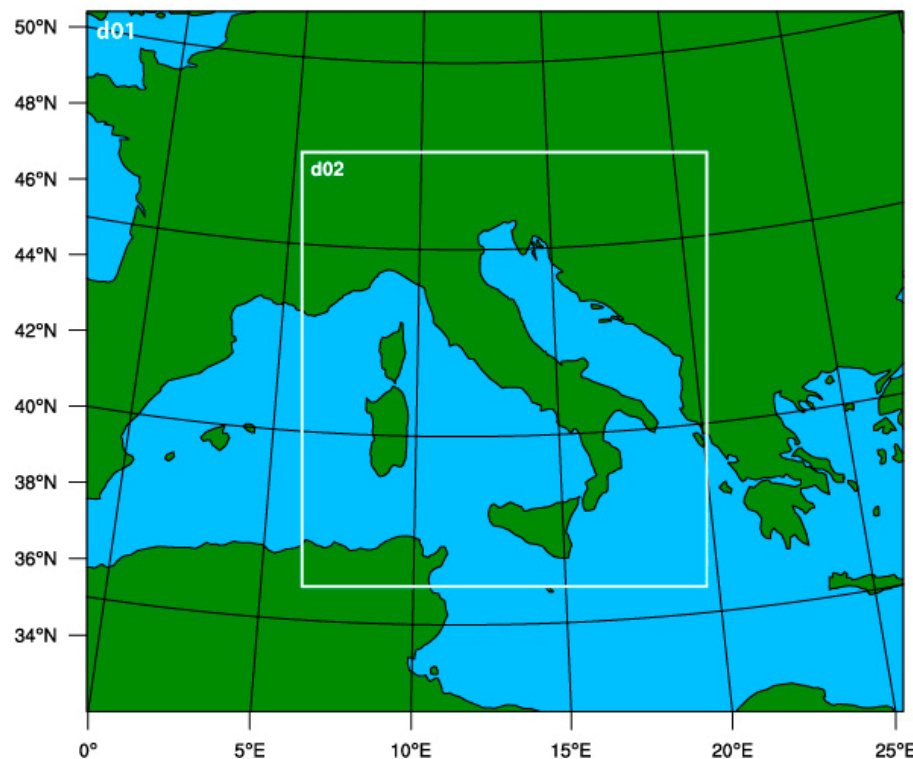


Figure 1. Model domains for Weather Research and Forecasting (WRF) simulations: d01 the mother domain with a grid spacing of 9 km, d02 the inner domain with 3 km horizontal resolution.

The simulations are initialized using the weather forecast of the Global Forecast System (GFS) produced by the National Centers for Environmental Prediction (NCEP) at 0.25 degree and 35 vertical levels, upgraded every 6 h. A preliminary sensitivity analysis was carried out before making the model operational within the SolarCloud project to derive the optimum configurations. The Planetary Boundary Layer (PBL) has been simulated using the non-local-K Yonsei parameterization [36], the microphysics has been computed through the Thompson parameterization [35] and for the shortwave and the longwave the RRTMG radiation scheme [37]. The convective scheme has been activated only for the outer domain using the Kain-Fritsch [38]; the inner domain explicitly resolves the convective motion. The cumulus and the PBL scheme are called every time step, whereas the irradiances (GHI, DNI and DIF) are computed every 3 min, each time the radiation scheme is called and the instantaneous values are stored in output every hour.

2.2. D-VAR Data Assimilation of SEVIRI Radiance

The idea to assimilate satellite radiance data arises from the need to have the most accurate initial state of the atmosphere to better predict its future state and hence that of the solar irradiance reaching the surface [21,26,39]. Outgoing radiance is related to the geophysical atmospheric state, providing very useful thermodynamic information both over land and over sea. It can be simply measured by a satellite and directly ingested into the NWP using a variational method and a Radiative Transfer Model (RTM).

The radiance measured by SEVIRI is considered for data assimilation in this article. SEVIRI is an imager radiometer onboard MSG geostationary platform providing accurate weather monitoring data through twelve spectral channels. Eight channels are in the thermal infrared, providing data about the temperature of clouds, atmosphere, land and sea surfaces. The remaining four channels are in the visible and near-infrared range. The imaging sampling distance at nadir is 3 km for standard channels and approximately 1 km for the High Resolution Visible (HRV) channel [40]. The radiance data are available through National Centers for Environmental Prediction (NCEP) public interface in near real

time (with 6 h delay) in Binary Universal Form for the Representation of meteorological data (BUFR) format (<ftp://nomads.ncdc.noaa.gov/GDAS/>).

The data assimilation used in this work is the 3D-Var version 3.8 developed by NCAR and included into the WRF Data Assimilation (WRFDA) system. The data assimilation is a technique by which observations are combined with the NWP product (the first guess or background) and their respective error statistics to provide an improved estimate (the analysis) of the atmospheric state [41,42]. Variational data assimilation achieves this through the iterative minimization of a prescribed cost function $J(x)$:

$$J(x) = (x - xb)^T B^{-1} (x - xb) + [y - H(x)]^T R^{-1} [y - H(x)], \quad (1)$$

where x is the state vector defined by the atmospheric and surface parameters, xb is the background vector, y is the observation, B is the background error covariance matrix, H is the operator that converts the model state to the observation space and R is the observation error covariance matrix. The aim is to minimize the cost function (1) that measures the distance of a field x from the observations y and from the background xb . A correct evaluation of the error covariance matrices, both B and R , is crucial to a good-quality final analysis. For the direct radiance assimilation, the observation operator $H(x)$ include the RTM that calculates the radiances from the model variables of a state vector x . The RTM evaluates the physical processes modulating the Earth's radiant energy balance. The modulations depend on the cloud microphysical details (particle size, shape, orientation, presence of aerosols), the cloud macrophysical properties (cloud top temperature, morphology, optical thickness) and environment context (water vapor, surface albedo, vertical profile of temperature). Actually, the RTM codes supported by the WRFDA are the Community Radiative Transfer Model (CRTM) and the Radiative Transfer for TOVS (RTTOV). The first has been developed by the Joint Center for Satellite Data Assimilation (JCSDA) and the second one by the European Centre for Medium-range Weather Forecasts (ECMWF) and the United Kingdom Meteorology Office (MetOffice). Both RTM codes can calculate radiances for several current and past instruments in orbit. WRFDA allows to select the desired RTM via the namelist parameter. In this study, the CRTM is chosen because this package is distributed with WRFDA without licensing restrictions and is compiled automatically [41,42]. The CRTM provides fast, accurate satellite radiance simulations under all weather and surface conditions, including both a forward model, which simulates the upwelling radiances for a given sensor and its Jacobian, which calculates the radiance derivatives with respect to the input atmospheric state variables. The CRTM is capable of accounting for the absorption of atmospheric gases as well as the multiple scattering of water clouds, of ice clouds and of a variety of aerosols [43].

The instruments to be assimilated are controlled by four integer namelist parameters: RTMINIT_NSENSOR (the total number of sensors to be assimilated), RTMINIT_PLATFORM (the platforms IDs array to be assimilated), RTMINIT_SATID (satellite IDs array) and RTMINIT_SENSOR (sensor IDs array) [41,42]. For the assimilation of the SEVIRI radiance these parameters are set to 1, 12, 3 and 21, respectively.

As highlighted above, the background error covariance matrix plays a crucial role to provide proper weight to the background term in defining the analysis cost function J . Two different types of B are available for use in the WRF 3D-Var technique: one is the generic background error statistics that can be used for any case and the second one is a domain specific B matrix that considers the climatological aspects of the area. It is strongly recommended to use a domain-specific background error to consider the scale of the motions especially in the area with a complex orography [44]. In this study, a specific background B matrix is computed with a 1-month dataset using the National Meteorological Centre (NMC) technique [45]. This method evaluates the initial state error using differences of pairs of forecasts valid at the same time but with one of them having a delayed start time.

Before assimilating the satellite radiances in the system, a quality control is performed to discard faulty observations and the bias correction is carried out using the Variational Bias Correction (VarBC) scheme to remove possible biases from the measurements. A further procedure applied over the raw radiance data is the 120 km thinning mesh. Thinning methods are necessary to downsize the large

satellite data sets and to reduce spatial error correlations between the observations in order to obtain the fundamental information of the data for a proper use in data assimilation technique. It should also be mentioned that WRFDA reads directly the BUFR radiance files distributed by EUMETSAT with no need for separate pre-processing. The whole processing, such as quality control, thinning, bias correction and so forth, is carried out within WRFDA. This is different from conventional observation assimilation, which requires a pre-processing package (OBSPROC) to generate WRFDA readable ASCII files. The WRFDA system requires three input files to run: the WRF first guess file (initial condition file for the WRF model), the observations (BUFR file) and the background error statistics file. The outputs of the WRFDA system becomes the inputs for the ASSIM simulations.

Currently, the WRF 3D-Var is able to assimilate the eight thermal infrared channels of SEVIRI (4–11).

2.3. Observational Data Sets

GHI data (W/m^2) are obtained from the ground-based pyranometers of the Regional Network of Meteorological Survey of the ARPA of Lombardy region (Figure 2). These data are freely available from the ARPA website (<http://www.arpalombardia.it/>) in Comma Separated Values (CSV) format. The 23 weather stations are reported in Table 1 and have a sample frequency of 10 minutes. Table 1 reports also the above sea level (asl) elevations of the stations and the corresponding ones extracted from the DEM of the WRF. ARPA agency is responsible for the observation acquirement and the quality control. The pyranometers (mainly CM6B, HE20/K and DPA) used by the ARPA network are heterogeneous and produced by various companies, all belonging to the International Organization for Standardization (ISO) “First Class” classification and the World Meteorological Organization (WMO) “Good quality” classification; the uncertainties on the daily data declared by the manufacturers are $\pm 5\%$. [46–50].

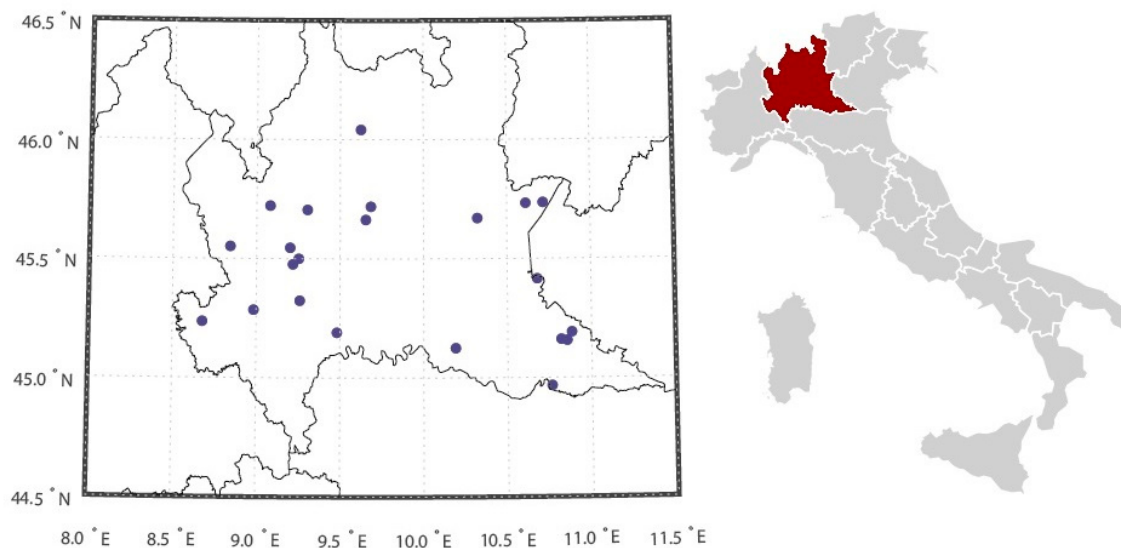


Figure 2. (left) Location of the Regional Agency for the Protection of the Environment (ARPA) radiometric stations; (right) position of Lombardy region within Italy.

Table 1. Name, position and real/simulated elevation of the ARPA weather stations.

Station	Longitude	Latitude	Elevation (m)	WRF Elevation (m)
Arconate	8.847	45.548	120	183
Bergamo	9.659	45.660	211	206
Bergamo – v. Goisis	9.689	45.716	290	283
Bigarello	10.887	45.188	15	23
Bione	10.327	45.667	911	663
Casatenovo	9.309	45.702	360	312
Castello d'Agogna	8.683	45.233	106	105
Cinisello Balsamo	9.205	45.543	142	142
Cornale	8.914	45.040	74	70
Gargnano	10.617	45.730	984	929
Gonzaga	10.767	44.964	22	17
Landriano Cascina Marianna	9.264	45.321	88	86
Mantova	10.824	45.158	25	22
Mantova Tridolino	10.859	45.153	22	22
Mezzoldo Passo S.Marco	9.629	46.038	1824	1685
Milano	9.222	45.473	122	124
Milano Lambrate	9.257	45.497	120	128
Motta Visconti	8.988	45.282	100	83
Ponti sul Mincio	10.683	45.413	113	91
Pieve San Giacomo	10.195	45.122	39	34
San Colombano al Lambro	9.486	45.187	80	68
Tignale Oldesio	10.721	45.733	374	229
Vertemate con Minoprio	9.085	45.719	310	303

The products from the MSG mission have been used to further evaluate the performance of the WRF-IMAA-Solar. Satellite observations were directly downloaded from the Data Centre of the EUMETSAT Earth Observation Portal where it is possible to order online long-term archived data and generated products from EUMETSAT.

The EUMETSAT products used here are:

- The MSG Meteorological Product Extraction Facility (MPEF) Cloud Mask (CLM) product describes the scene type (either 'clear' or 'cloudy') on a pixel level. The MPEF-CLM algorithm uses a set of threshold tests on reflectance, brightness temperature and brightness temperature differences of channel properly chosen in order to classify each pixel as clear sky over water, clear sky over land, cloud, or not processed (off Earth disc). Data are available in network Common Data Form (netCDF) format and have a frequency of 15 min [51–53].
- The Ocean and Sea Ice Satellite Application Facility (OSI SAF) hourly shortwave Surface Solar Irradiance (SSI) (W/m^2) gives an estimate of the solar irradiance reaching the Earth's surface. It is derived from the $0.6 \mu\text{m}$ visible channel of SEVIRI from MSG platform and it is produced by remapping over a 0.05° regular grid. The data are available in GRIdded Binary 2 (GRIB2) format with an hourly frequency [54,55].

2.4. The Two Simulated Periods

To evaluate WRF-IMAA-Solar two periods have been selected, one characterized by sunny days used to test CNTRL configuration and one by overcast conditions for ASSIM.

For the clear sky sensitivity test, two days of stable conditions have been selected: the 20–21 January 2017. During these days a robust ridge of high pressure of approximately 1040 hPa at the surface centered in the northern Europe (Figure 3a) guarantees clear sky conditions over the northern part of Italy (Figure 3b). The vertical alignment of the ridge between the surface and the 500 hPa level ensures the persistence of the stability conditions (Figure 3a).

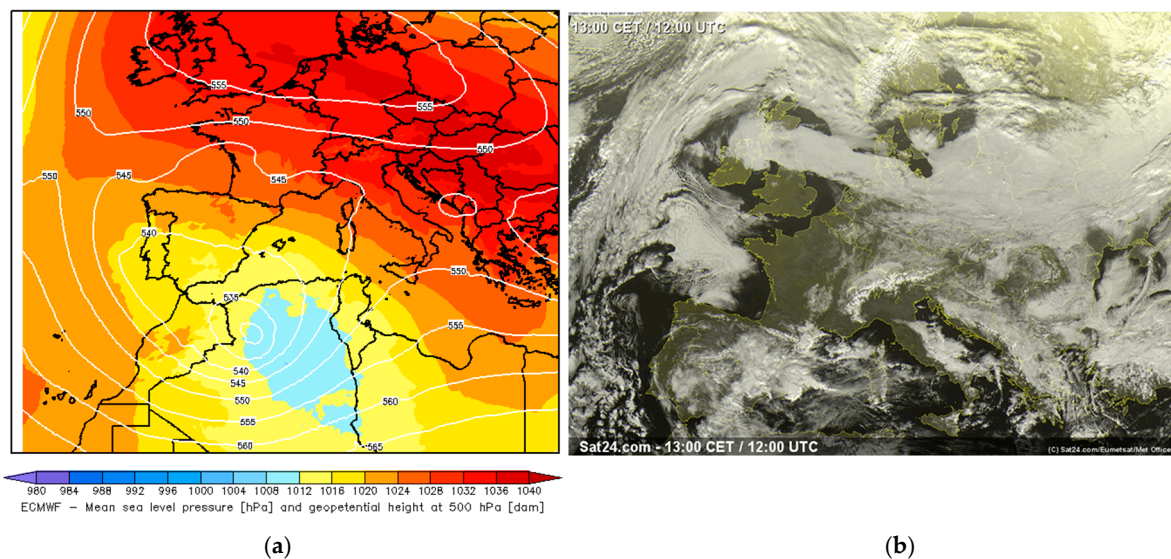


Figure 3. Synoptic analysis at 12:00 UTC (Coordinated Universal Time), 20 January 2017: (a) European Centre for Medium-Range Weather Forecasts (ECMWF) 500 hPa geopotential height (white lines) and ECMWF mean sea level pressure; (b) the cloud cover observed by Meteosat Second Generation (MSG).

For cloudy conditions, 01–02 April 2017 is selected, as during these days the southward regression of the high pressure centered over Italy allows the descent of a deep trough in the north-central Europe (Figure 4a). This synoptic structure encourages the rising from south-west of warm and wet air (Figure 4a) fostering the development of scattered clouds in Northern Italy (Figure 4b).

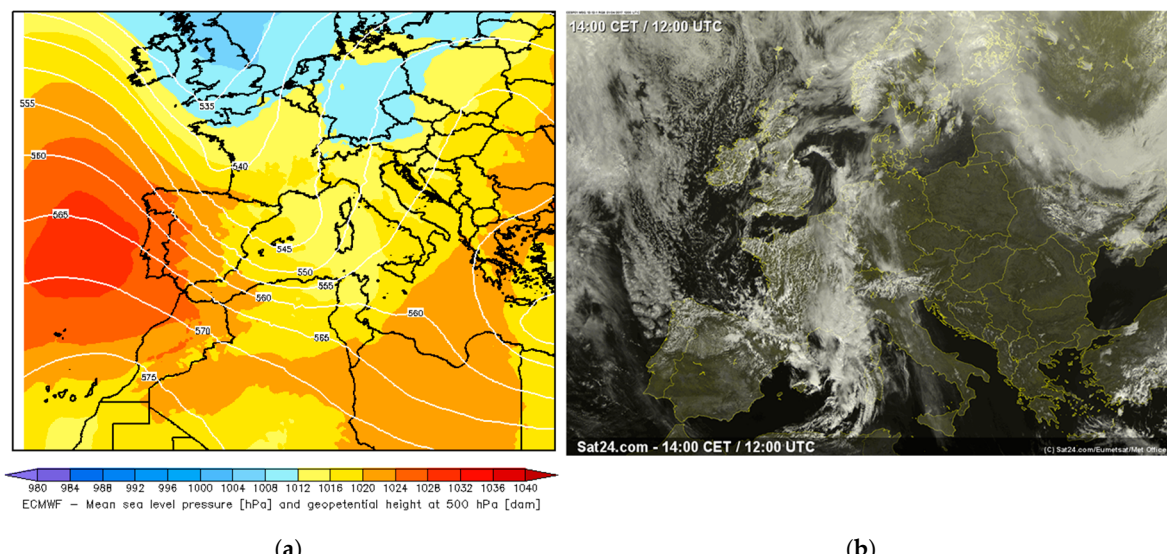


Figure 4. Synoptic analysis at 12:00 UTC, 01 April 2017: (a) ECMWF 500 hPa geopotential height (white lines) and ECMWF mean sea level pressure; (b) the cloud cover observed by MSG.

2.5. The Statistical Methodology

The validation of this preliminary test in the two selected periods against the ground-based and satellite products is performed through the evaluation of statistical skills.

Four commonly-used statistical indexes are considered for the analysis of the GHI observed by the ARPA stations and for the MSG SSI [56]: the Mean Absolute Error (MAE), the Mean Bias Error (MBE), the Root Mean Square Error (RMSE) and the correlation (CORR), defined as follows:

$$\text{MAE} = \frac{1}{N} \sum_{i=1}^N |m_i - o_i| \quad (2)$$

$$\text{MBE} = \frac{1}{N} \sum_{i=1}^N (m_i - o_i), \quad (3)$$

$$\text{RMSE} = \left[\frac{1}{N} \sum_{i=1}^N (m_i - o_i)^2 \right]^{1/2} \quad (4)$$

$$\text{CORR} = \frac{\text{cov}(m, o)}{\sigma_m \sigma_o}, \quad (5)$$

where m and o represent model data and observations, respectively, cov is the covariance, N indicates the length of data, σ_m and σ_o are respectively the standard deviation of simulated and observed data.

For completeness the normalized scores have also been evaluated, so to reduce the dependence of the statistical indexes on the values of the GHI:

$$\text{NMBE} = \frac{\text{MBE}}{\bar{o}}; \quad (6)$$

$$\text{NRMSE} = \frac{\text{RMSE}}{\bar{o}} \quad (7)$$

$$\text{NMAE} = \frac{\text{MAE}}{\bar{o}}; \quad (8)$$

where \bar{o} is the average of the observations and MBE, RMSE and MAE are calculated respectively using the Equations (2)–(4).

For the evaluation of the cloud mask additional statistical indexes are introduced. These scores are based on the contingency table (Table 2), which summarizes the relationship between two categorical variables.

Table 2. Two by two contingency table.

Cloud Mask	Observation – yes	Observation – no
Simulation – yes	A	B
Simulation – no	C	D

These statistical scores are defined using the frequency distributions in Table 2:

- Proportion Correct (PC) = $(A + D)/(A + B + C + D)$;
- False Alarm Rate (FAR) = $B/(A + B)$;
- Miss Rate (MR) = $C/(A + C)$;
- BIAS = $(A + B)/(A + C)$;

where A indicates event both observed and simulated, B simulated but not observed, C observed but not simulated and D not observed and not simulated.

3. Results and Discussion

This section presents the comparison of the WRF-IMAA-Solar in the two configurations CNTRL and ASSIM against the observations described in Section 2.3. The statistical analysis is carried out through the indexes reported in Section 2.5. An initial sensitivity test has been performed with

the ground-based observations in clear and overcast conditions. The clear sky evaluation has been presented only for the model in CNTRL configuration since in absence of cloud the impact of radiance assimilation is of little relevance. For the clear sky sensitivity test the 20–21 January 2017 period has been used (Figure 3a,b). The comparison is done extracting from the numerical model the GHI over the four nearest grid points to the station coordinates and then performing a distance weighted mean. Figure 5a reports the diurnal cycles of the solar irradiance for the 20–21 January 2017 simulated by WRF-IMAA-Solar (red line) and observed by ARPA radiometers (black line). For clear sky conditions, the model correctly reproduces the observed evolution even though a slight overestimation ($\sim 5 \text{ W/m}^2$) can be observed in the maximum of the mean solar irradiance (Figure 5a). The mean scatter plot of the GHI, reported in Figure 5b, shows a distribution with grouped points, due to the hourly samples; in clear sky conditions the GHIs increase before noon and decrease after the maximum with a similar trend among the stations. The standard deviation reported in Figure 5a,b for both observations and simulations is calculated between the stations to take into account the variability between them. The widths of the standard deviations for the observations (about $20\text{--}30 \text{ W/m}^2$) are approximately comparable for all the GHI values (Figure 5b). These gaps are easily visible from Figure 5a at midday when the derivative of the curve approaches zero and they seem negligible in the rapid phase of growth and decrease of the GHI. In addition, note from Figure 5b that the standard deviations calculated among the stations are larger for the observations than for the simulated ones, meaning that the observed GHI of the 23 stations show larger variability than the simulations. That indicates that the model may miss some of the differences between sites that are fairly close. To highlight the differences among the stations, statistical scores have been evaluated separately for each station and reported in Table 3. From Table 1 we note that the model tends to underestimate the elevation of the stations and to smooth the height of the stations, especially the ones with higher elevations, leading to underestimation and less variable GHI among the observation sites. This is evident at stations like Bione, Mezzoldo Passo S. Marco and Tignale Oldesio where the GHI is underestimated, especially in the maximum of the solar irradiance of approximately $20\text{--}30 \text{ W/m}^2$, as demonstrated by the negative values of the MBE (Table 3, clear sky). For some stations, particularly the ones located in urban areas (e.g. Milano, Milano Lambrate and Cinisello Balsamo), the model shows positive $\text{MBE} > 5 \text{ W/m}^2$, indicating an overestimation of the GHI probably due to an underestimation of GHI extinction caused by pollution aerosols or to excessively high albedo associated to improper land use category (Table 3, clear sky). Furthermore, larger RMSE, ranging from 20 to 30 W/m^2 , are associated to stations showing the greatest differences between real and model elevation, that is, Bione, Mezzoldo Passo S.Marco and Tignale Oldesio (Table 3, clear sky). In clear sky conditions, significant differences among real and model elevations could explain the model deviations from observations, indeed the vertical profile of global irradiance is determined by the change of the optical path length.

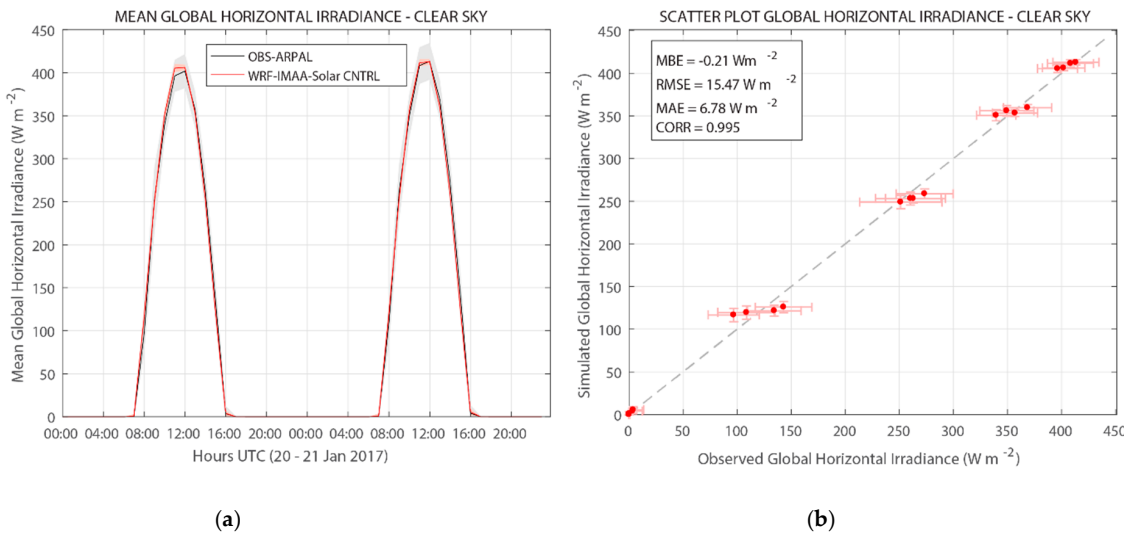


Figure 5. The solar irradiance in clear sky conditions. (a) The simulated and observed diurnal cycles of the solar irradiance for the 20–21 January 2017, the values are averaged over all the 23 ARPA stations and the shaded areas represent the standard deviations among the stations. (b) The mean scatter plot with the standard deviations of the global horizontal irradiance (GHI) among the stations, the box on the top left reports the averaged statistical indexes.

Table 3. The Mean Absolute Error (MAE), the Mean Bias Error (MBE), the Root Mean Square Error (RMSE) and the correlation (CORR) for each single ARPAL station in clear and cloudy sky conditions for three model runs: the control (CNTRL), the control started at 12 UTC (CNTRL 12 UTC) and the run with assimilation of SEVIRI radiance at 12 UTC (ASSIM 12 UTC).

Station	TEST	MBE W/m ²	RMSE W/m ²	MAE W/m ²	CORR
Arconate	Clear Sky: CNTRL	-2.72	5.73	3.06	0.999
	Cloudy sky: CNTRL12 UTC	90.03	171.83	90.03	0.928
	Cloudy sky: ASSIM 12 UTC	56.53	120.94	56.53	0.932
Bergamo	Clear Sky: CNTRL	1.59	4.97	2.71	0.999
	Cloudy sky: CNTRL12 UTC	-18.24	38.48	19.45	0.992
	Cloudy sky: ASSIM 12 UTC	5.58	39.53	20.4	0.99
Bergamo – v. Goisis	Clear Sky: CNTRL	3.12	16.74	4.52	0.995
	Cloudy sky: CNTRL12 UTC	20.65	135.59	57.56	0.86
	Cloudy sky: ASSIM 12 UTC	42.68	154.97	58.73	0.852
Bigarello	Clear Sky: CNTRL	-3.79	16.74	8.3	0.993
	Cloudy sky: CNTRL12 UTC	34.45	155.78	47.17	0.846
	Cloudy sky: ASSIM 12 UTC	51.23	135.72	65.17	0.901
Bione	Clear Sky: CNTRL	-10.68	19.63	7.2	0.995
	Cloudy sky: CNTRL12 UTC	6.35	12.01	6.35	0.968
	Cloudy sky: ASSIM 12 UTC	4.41	10.22	4.61	0.979
Casatenovo	Clear Sky: CNTRL	2.16	10.16	5.52	0.998
	Cloudy sky: CNTRL12 UTC	26.15	98.8	53.98	0.932
	Cloudy sky: ASSIM 12 UTC	5.28	84.58	41.92	0.947
Castello d'Agogna	Clear Sky: CNTRL	4.11	16.73	4.12	0.994
	Cloudy sky: CNTRL12 UTC	25.67	113.98	29.98	0.885
	Cloudy sky: ASSIM 12 UTC	38.47	136.96	39.27	0.87

Table 3. Cont.

Station	TEST	MBE W/m ²	RMSE W/m ²	MAE W/m ²	CORR
Cinisello Balsamo	Clear Sky: CNTRL	4.41	19.86	7.54	0.992
	Cloudy sky: CNTRL12 UTC	32.45	108.65	36.85	0.844
	Cloudy sky: ASSIM 12 UTC	32.78	126.82	39.59	0.847
Cornale	Clear Sky: CNTRL	-4.54	17.82	6.8	0.994
	Cloudy sky: CNTRL12 UTC	27.8	126.12	25.78	0.852
	Cloudy sky: ASSIM 12 UTC	31.3	128.52	55.49	0.853
Gargnano	Clear Sky: CNTRL	-2.21	9.22	4.4	0.999
	Cloudy sky: CNTRL12 UTC	47.6	102.01	47.6	0.978
	Cloudy sky: ASSIM 12 UTC	44.44	96.67	44.44	0.977
Gonzaga	Clear Sky: CNTRL	4.76	18.35	7.32	0.993
	Cloudy sky: CNTRL12 UTC	26.87	121.5	45.87	0.858
	Cloudy sky: ASSIM 12 UTC	42.58	136.96	49.04	0.853
Landriano Cascina Marianna	Clear Sky: CNTRL	1.58	18.22	8	0.995
	Cloudy sky: CNTRL12 UTC	39.36	120.05	57.12	0.88
	Cloudy sky: ASSIM 12 UTC	61.6	133.91	72.84	0.867
Mantova	Clear Sky: CNTRL	-2.77	5.61	2.91	0.99
	Cloudy sky: CNTRL12 UTC	1.54	47.21	20.81	0.971
	Cloudy sky: ASSIM 12 UTC	-1.76	45.62	20.13	0.972
Mantova Tridolino	Clear Sky: CNTRL	3.15	15.67	8.37	0.995
	Cloudy sky: CNTRL12 UTC	3.62	61.02	29.4	0.96
	Cloudy sky: ASSIM 12 UTC	-0.04	60.06	28.56	0.971
Mezzoldo Passo S.Marco	Clear Sky: CNTRL	-11.18	21.54	9.45	0.992
	Cloudy sky: CNTRL12 UTC	15.42	154.16	29.78	0.831
	Cloudy sky: ASSIM 12 UTC	38.27	149.38	49.64	0.862
Milano	Clear Sky: CNTRL	7.29	18.89	6.16	0.993
	Cloudy sky: CNTRL12 UTC	-6.67	108.63	23.65	0.845
	Cloudy sky: ASSIM 12 UTC	48.48	119.95	56.7	0.842
Milano Lambrate	Clear Sky: CNTRL	6.56	19.88	10.68	0.999
	Cloudy sky: CNTRL12 UTC	56.49	119.37	56.49	0.911
	Cloudy sky: ASSIM 12 UTC	31.49	77.6	37.2	0.96
Motta Visconti	Clear Sky: CNTRL	2.06	20.72	11.18	0.998
	Cloudy sky: CNTRL12 UTC	89.41	190.75	95.85	0.937
	Cloudy sky: ASSIM 12 UTC	76.17	149.96	76.17	0.984
Ponti sul Mincio	Clear Sky: CNTRL	2.19	9.39	16.61	0.98
	Cloudy sky: CNTRL12 UTC	-16.79	28.75	16.79	0.966
	Cloudy sky: ASSIM 12 UTC	-14.07	25.33	14.07	0.987
Pieve San Giacomo	Clear Sky: CNTRL	-5.13	15.36	5.75	0.996
	Cloudy sky: CNTRL12 UTC	3.51	48.79	29.59	0.955
	Cloudy sky: ASSIM 12 UTC	-4.42	38.64	20.5	0.962
San Colombano al Lambro	Clear Sky: CNTRL	1.83	6.61	3.56	0.999
	Cloudy sky: CNTRL12 UTC	95.89	169.23	95.89	0.924
	Cloudy sky: ASSIM 12 UTC	94.06	166.41	94.06	0.916
Tignale Oldesio	Clear Sky: CNTRL	-10.23	31.47	4.55	0.999
	Cloudy sky: CNTRL12 UTC	-2.40	14.62	7.43	0.978
	Cloudy sky: ASSIM 12 UTC	0.6	15.35	8.3	0.979
Vertemate con Minoprio	Clear Sky: CNTRL	3.59	16.49	7.16	0.995
	Cloudy sky: CNTRL12 UTC1	84.92	152.53	88.69	0.954
	Cloudy sky: ASSIM 12 UTC	72.99	144.3	76.34	0.965

The statistical scores averaged over all the stations are reported in the first line of Table 4. The values for the clear sky conditions confirm the positive performance of the WRF-IMAA-Solar with a MBE of -0.21 W/m^2 , a RMSE of 15.47 W/m^2 , a MAE of 6.78 W/m^2 (comparable to the instrument uncertainty) and a CORR of 0.995.

Table 4. Statistical scores for the preliminary tests in clear and cloudy sky for the control simulation and the assimilated of Spinning Enhanced Visible and Infrared Imager (SEVIRI) radiance at 00/12 UTC ones.

Test	MBEW/m ²	RMSEW/m ²	MAEW/m ²	CORR
Clear sky				
WRF-IMAA-Solar – CNTRL	-0.21	15.47	6.78	0.995
Cloudy sky- Assim Time: 00 UTC				
WRF-IMAA-Solar – CNTRL	41.31	142	73.27	0.866
WRF-IMAA-Solar – ASSIM1	43.04	142.73	72.78	0.869
WRF-IMAA-Solar – ASSIM2	54.33	141.48	72.49	0.886
Cloudy sky- Assim Time: 12 UTC				
WRF-IMAA-Solar – CNTRL	29.95	104.34	44	0.915
WRF-IMAA-Solar – ASSIM	32.98	100.05	44.77	0.92

To conclude the comparison with the ARPAL stations, the model performances in overcast conditions have been evaluated. For this purpose, the period 01–02 April 2017 is selected (Figure 4a,b). For this case study the evaluation is performed for both the CNTRL and ASSIM configurations. For the ASSIM configuration, two different settings have been tested to choose the best performing one:

- ASSIM1: WRFDA uses the default B matrix.
- ASSIM2: WRFDA uses a domain specific B matrix that considers the climatological aspects of the area.

For both ASSIM1 and 2, the model assimilates radiances from the eight thermal infrared channels of SEVIRI (4–11) at the start time (00 UTC). The comparison is done in the same manner of clear sky conditions, with the ARPA observations and using the distance weighted mean. The first 24 h of simulation of the two runs have been selected for the comparison. The statistical scores obtained for the cloudy sky and averaged all over the stations are reported in Table 4. The performances of the model in overcast sky get worse than the ones in clear sky, confirming the difficulty for the model to correctly reproduce clouds in both space and in time. The introduction of the assimilation tends to improve the irradiance forecast. In fact, the RMSE, MAE and CORR are better for the ASSIM configurations than the CNTRL one. Only the MBE gets worse for ASSIM tests than the CNTRL one, which is probably due to the underestimation of the cloud cover. The assimilation test with the domain specific B matrix has better scores than the one with the default one.

Even though the ASSIM2 configuration shows slightly higher performances than CNTRL ones, except for the MBE, another test has been performed to further investigate the impact of the assimilation of the SEVIRI radiance at 12 UTC. To better evaluate, indeed, the impact of the assimilation on the forecast of the solar irradiance, it is preferable to choose diurnal hours for the assimilation time, when GHI is relatively high. In addition, at 00 UTC the cloudiness over Lombardy region is quite limited, hinting a little impact of the assimilation on the performance of the model.

For the ASSIM at 12 UTC, the model is set using the configuration with best scores in the preliminary tests (ASSIM2); hence from now on the acronym ASSIM will refer to the configuration mentioned above as ASSIM2.

Figure 6a shows the time series of simulated and observed solar irradiance with the respective standard deviations of the stations. Close to the assimilation time (12 UTC), ASSIM shows values closer to observations than CNTRL. Figure 6b confirms the tendency for both the configurations to overestimate the GHI, in fact the points lay above the 1:1 line. The underestimation of the cloud cover and the associated overestimation of radiation is a common problem in NWP modeling due to the incomplete representation of the complex and often nonlinear cloud processes into the parameterizations [12,57–60]. Even for this test, the standard deviation reported in Figure 6a,b for observations and simulations is calculated between the stations to take into account the variability between them. As seen for the clear sky in Figure 5b, the standard deviations of the stations are larger

for the observed GHI than the simulated ones. To the possible reasons listed above, we can also add the difficulty for the model to simulate the right location and timing of clouds.

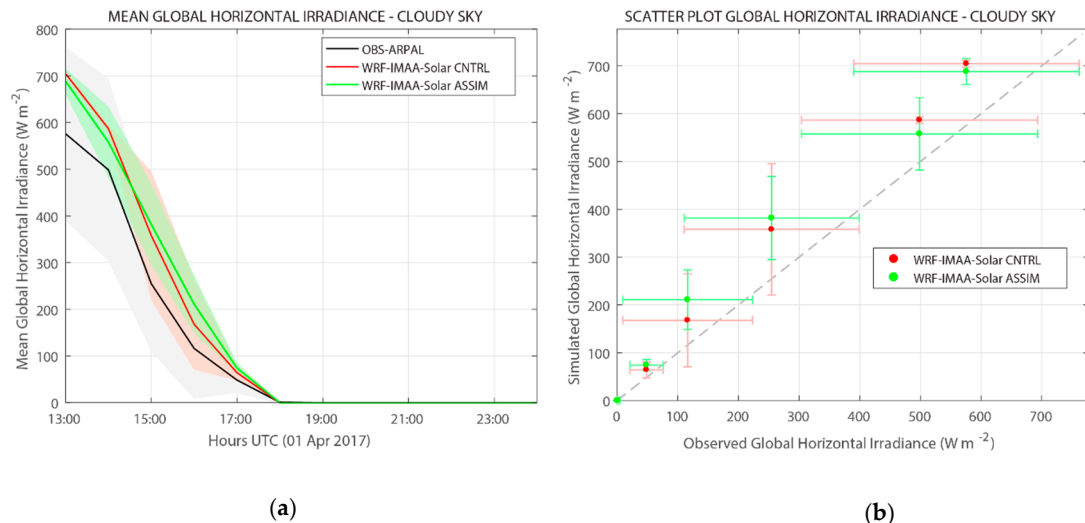


Figure 6. The solar irradiance in cloudy sky conditions. (a) The simulated and observed solar irradiance for 1 April 2017, the values are averaged all over the 23 ARPA stations and the shaded areas represent the standard deviations of the stations. (b) Scatter plot of the GHI with the respective standard deviations among the stations.

The statistical scores reported in Table 4 reveal better values for the two simulations initialized at 12 UTC than for the three initialized at 00 UTC. These improvements are due both to the assimilation during diurnal time, when GHI is relatively high and to the interval time considered for the statistical scores closer to the start and assimilation times.

For this test, the statistical indexes have also been evaluated separately for each station (Table 3, cloudy sky). For the MBE and MAE indexes, the number of stations where ASSIM or CNTRL prevail is very similar (respectively 8 for the MBE and 6 for the MAE). For the RMSE and CORR scores, instead, the number of stations where the ASSIM values are better than the CNTRL ones, prevails. The stations that perform best for ASSIM are located on the east and west side of the Lombardy region, leaving a central area (the Milan and Bergamo area) where the CNTRL configuration prevails. This can be explained by looking at Figure 5a where we can distinguish two bands of clouds over northern Italy which leave an area of clear sky in the central part of Lombardy. Therefore, in the areas where the cloud cover is observed, the impact of assimilation of radiance from SEVIRI is positive and improves the model's performance.

The statistical indexes averaged over all the stations for CNTRL and ASSIM are similar, though ASSIM shows better RMSE, decreasing from 104.34 W/m² to 100.05 W/m² and CORR, increasing from 0.915 to 0.920 (Table 4).

To increase the size of validation points, we extended the comparison to the satellite observations described above. The first evaluation is against the CLM from MSG. The cloud cover computed by WRF-IMAA-Solar-ASSIM is compared with the cloud cover observed by MSG satellite at 13 UTC (1 hour later the assimilation). Figure 7 clearly shows the impact of the assimilation—the ASSIM produce more cloudiness (Figure 7b) with respect to CNTRL (Figure 7c) which is confirmed by MSG observations (Figure 7a). The CNTRL simulation misses most of clouds over Italy, reproducing only the convective clouds related to the incoming front in North-West Italy. The analysis is further divided by cloud height (low, medium and high) as shown in Figure 8. It is clear that the SEVIRI assimilation allows the model to recover both the cirrus (Figure 8c) and the convective activity producing medium and low clouds (Figure 8a,b) towards the western boundary.

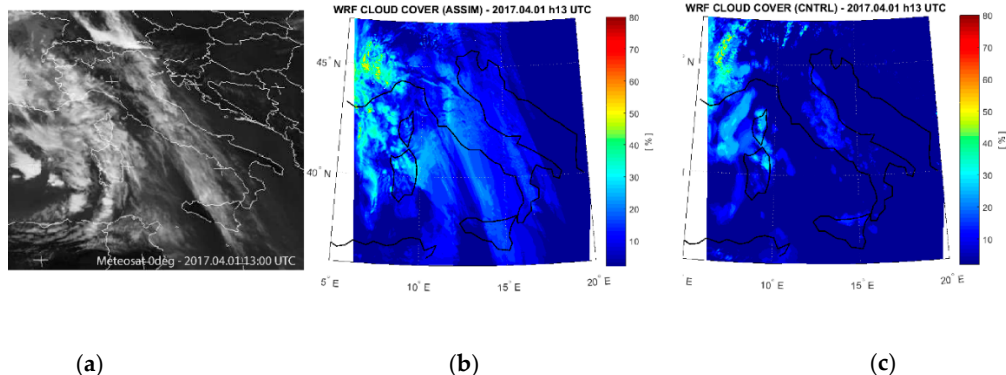


Figure 7. The cloud cover at 13 UTC of 1 April 2017 observed by MSG (a), simulated by WRF-IMAA-Solar in assimilated mode (ASSIM) (b) and simulated by WRF-IMAA-Solar in control configuration (CNTRL) (c).

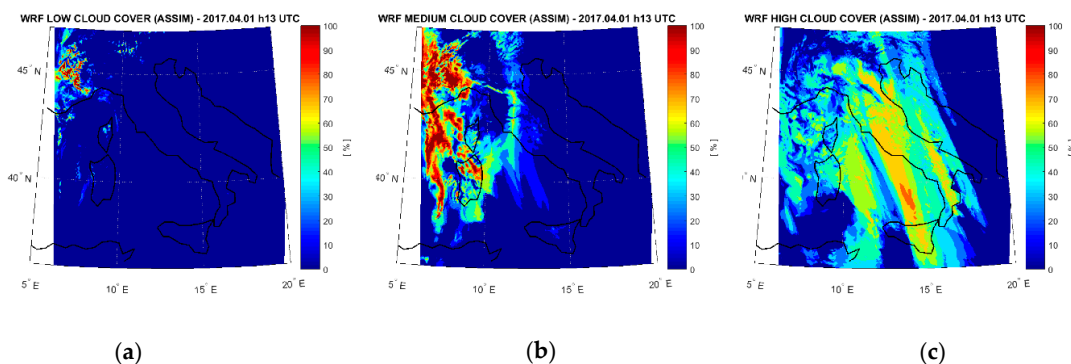


Figure 8. The cloud cover at 13 UTC of 1 April 2017 simulated by WRF-IMAA-Solar-ASSIM divided by height: low (a), medium (b) and high clouds (c).

The comparison between the CLM from MSG and the simulations (CNTRL and ASSIM) is done interpolating the observations on the grid of the model and producing the CLM from the WRF cloud cover. For this comparison the simple persistence method has been introduced as benchmark to evaluate the convenience of using the assimilation technique. The persistence is a very simple method, for which the current status is projected as is to the future assuming that conditions remain unchanged in subsequent time intervals [5].

The impact of the assimilating process is most relevant at 13 UTC of 1 April, that is, one hour after the assimilation. Indeed, the first line of Figure 9 shows that WRF ASSIM gives a cloud mask very similar to the observed one, even though an overestimation of the cloud can be observed. This is confirmed by Figure 10, where PC, FAR, MR and BIAS are reported for the first 6 h after the assimilation. It is evident that the CNTRL configuration misses the 59% of cloud grid points against only the 11% for ASSIM; also the PC confirms that ASSIM well simulates the 81% of pixels cloud/no cloud versus the 63% for CNTRL and the BIAS for ASSIM is very close to the best value (1.09 for ASSIM and 0.43 for CNTRL). On the other hand, FAR increases for ASSIM (18%) with respect to CNTRL (5%). One hour later, at 14 UTC, the CNTRL simulation starts to recover the gap and indeed more clouds appear in central-southern Italy (Figure 9, second row). The statistical scores (Figure 10) confirm this recovery, especially for PC (82% for ASSIM and 80% for CNTRL), though remaining below the ASSIM performances (MR: 9% for ASSIM and 26% for CNTRL; BIAS: 1.10 for ASSIM and 0.80 for CNTRL). Three hours later the start time (15 UTC, third row Figure 9) the two WRF simulations are very similar even though the CNTRL maintains the tendency to underestimate the presence of clouds, for example around Sardinia, as shown by the MR reported in Figure 10 (MR: 7% for ASSIM and 16% for CNTRL) and the ASSIM to overestimate the cloud cover, as indicated by the FAR reported in Figure 10 (FAR:

16% for ASSIM and 9% for CNTRL). In the following hours (Figure 9: 16 UTC fourth row and 17 UTC fifth row) the CNTRL and ASSIM cloud masks are close to each other and no particular feature can be detected as confirmed by the PC ranging from 84% of CNTRL to 86% of ASSIM (Figure 10) and by the BIAS oscillating between 1.03 and 1.06 for both the configurations. For the statistical scores FAR and MR the differences decrease reaching respectively 13% and 8%. The comparison highlights that the persistence outperforms ASSIM only in the first half hour of simulation for the PC and FAR indexes; later in time the enhancement for ASSIM with respect to the persistence is remarkable (Figure 10). The improvement of ASSIM relative to the persistence model is negligible at the first hour of simulation for the MR and BIAS scores and increases with time (Figure 10). In addition, persistence tends to worsen with time according to all statistical indices, as opposed to the ASSIM and CNTRL configurations for which the performances improve over time (Figure 10). Therefore, WRF-IMAA-Solar outperforms the persistence model, especially when the assimilation is used. Indeed, all the mean statistical scores are always worse for the persistence than ASSIM (Table 5). The CNTRL configuration is outperformed by the persistence only for the MR index (Table 5).

Table 5. Proportion Correct (PC), False Alarm rate (FAR), Miss Rate (MR) and BIAS for the evaluation of the CLM simulated by WRF-IMAA-Solar – CNTRL, ASSIM and by the persistence method. The values are averaged between 13 UTC and 18 UTC.

Test	PC	FAR	MR	Bias
WRF-IMAA-Solar – CNTRL	0.8	0.1	0.22	0.87
WRF-IMAA-Solar – ASSIM	0.84	0.15	0.08	1.08
Persistence	0.78	0.23.	0.14	1.21

Summarizing the impact of the radiance assimilation on the cloud mask, it is evident that the benefits are very clear especially within 3 h after the assimilation time; after this interval the performances of the CNTR and ASSIM are very similar. The statistical scores reported in Table 5 assert best results for ASSIM than CNTRL for the PC, MR and BIAS; only the FAR is worst for ASSIM with respect to CNTRL.

The second evaluation with MSG products focuses on the Hourly Shortwave Solar Irradiance. As for the cloud mask, the observations have been interpolated over the WRF model grid.

The GHI at 13 UTC of 1 April 2017 (first row of Figure 11) clearly reproduces what already seen above for the cloud mask (Figure 9): the overestimation produced by the CNTRL simulation is due to the lack of high clouds over central Italy and also the cloudy system north-west of Corsica is underestimated compared to the observed one. The ASSIM simulation better reproduces the GHI pattern over Italy but overestimates the GHI in the west side of the domain due to a lower extinction by the simulated cloud system, which appears more scattered than the observed one. We note a different behavior of the GHI by MSG over land and water; indeed, clear gaps appear over Sicily and central Italy where the lower values of GHI suddenly interrupt passing from sea to land. These observational gaps can be due to a different retrieval technique over land and over water and could have effects on the evaluation.

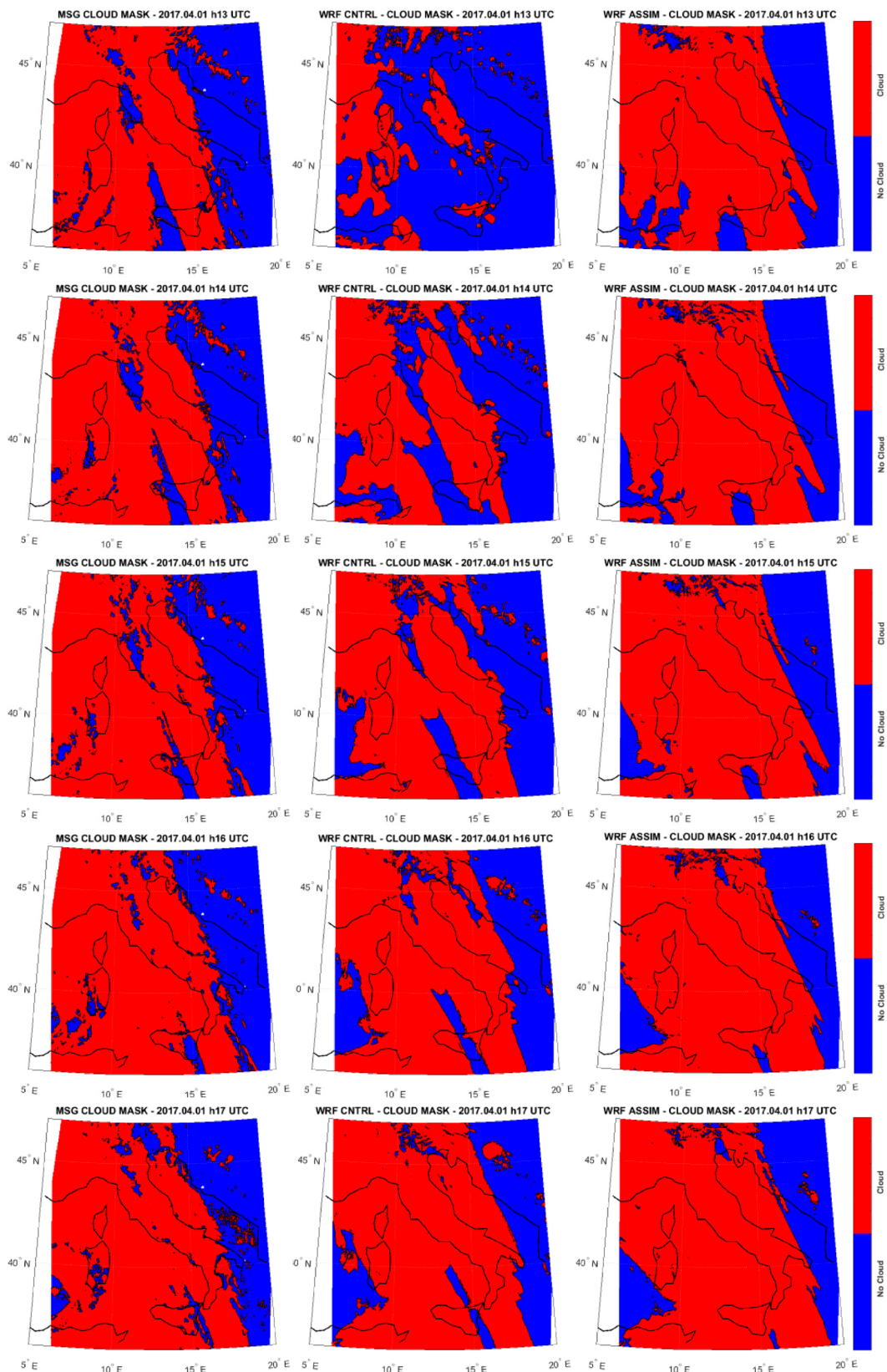


Figure 9. The cloud cover of 1 April 2017 from 13 UTC (first line) to 17 UTC (fifth line) observed by MSG (first column), simulated by WRF-IMAA-Solar-CNTRL (second column) and simulated by WRF-IMAA-Solar-ASSIM (third column).

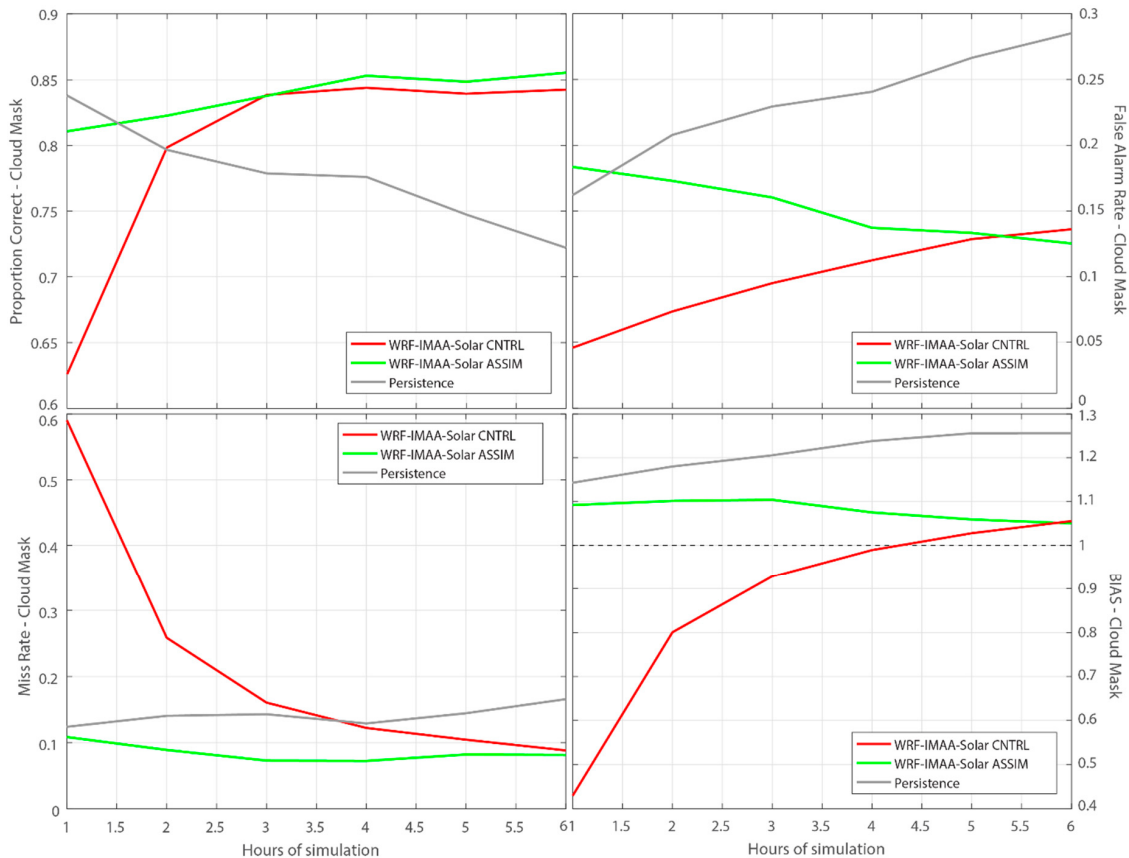


Figure 10. The statistical scores for the Cloud Mask (CLM) vs hour of simulation from the start time (12 UTC). The red line refers to the CNTRL, the green one to ASSIM configuration, the gray one to the persistence and the black dotted one to the best value of the BIAS. Top panels show Proportion Correct (PC) (left) and False Alarm rate (FAR) (right); bottom panels show Miss Rate (MR) (left) and BIAS (right).

For this reason, the statistical indexes have also been calculated by selecting only the grid points over the sea, which seem more reasonable and more consistent with respect to the observed clouds.

Both the MBE and the NMSE indexes confirm the GHI overestimation more pronounced for the CNTRL configuration than the ASSIM one (Figure 12). In fact, the values of the MBE range from a maximum 68 W/m^2 to a minimum 54 W/m^2 for CNTRL and from a maximum 62 W/m^2 to a minimum 49 W/m^2 for ASSIM. The NMSE shows an increase of the overestimation with time (Figure 12, first row), with at least 2% above for ASSIM with respect to CNTRL. The mean values of the NMSE are 19% for ASSIM and 21% for CNTRL as reported in the Table 6. Let us highlight the improvement of both the MBE and the NMSE when only the water grid points are selected. This is more pronounced for ASSIM; in fact, the mean value of the MBE passes from 54.43 W/m^2 to 38.85 W/m^2 for ASSIM and from 60.57 W/m^2 to 58.40 W/m^2 for CNTRL (Table 6).

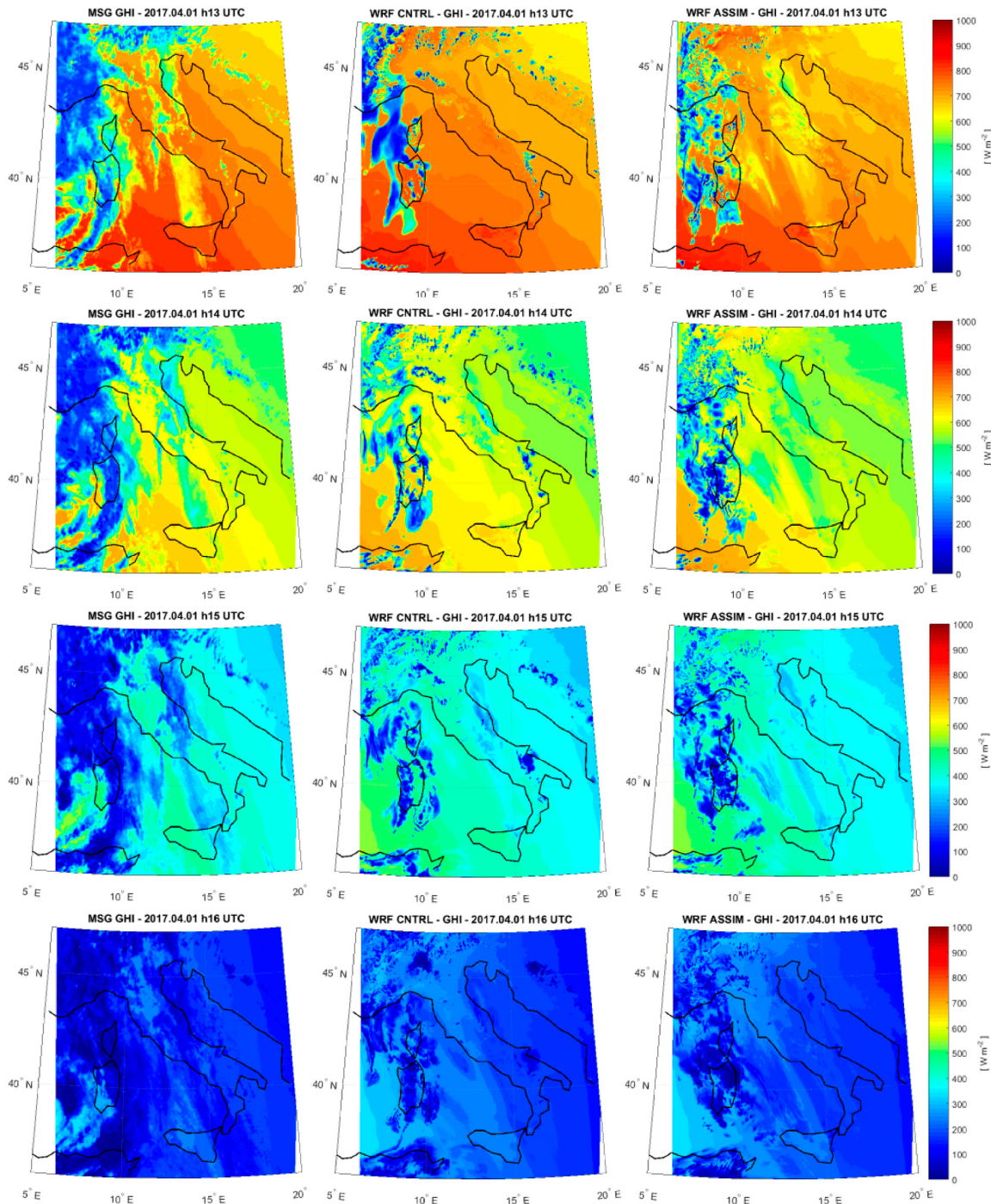


Figure 11. The GHI of 1 April 2017 from 13 UTC (top row) to 16 UTC (bottom row) observed by MSG (first column), simulated by WRF-IMAA-Solar-CNTRL (second column) and simulated by WRF-IMAA-Solar-ASSIM (third column).

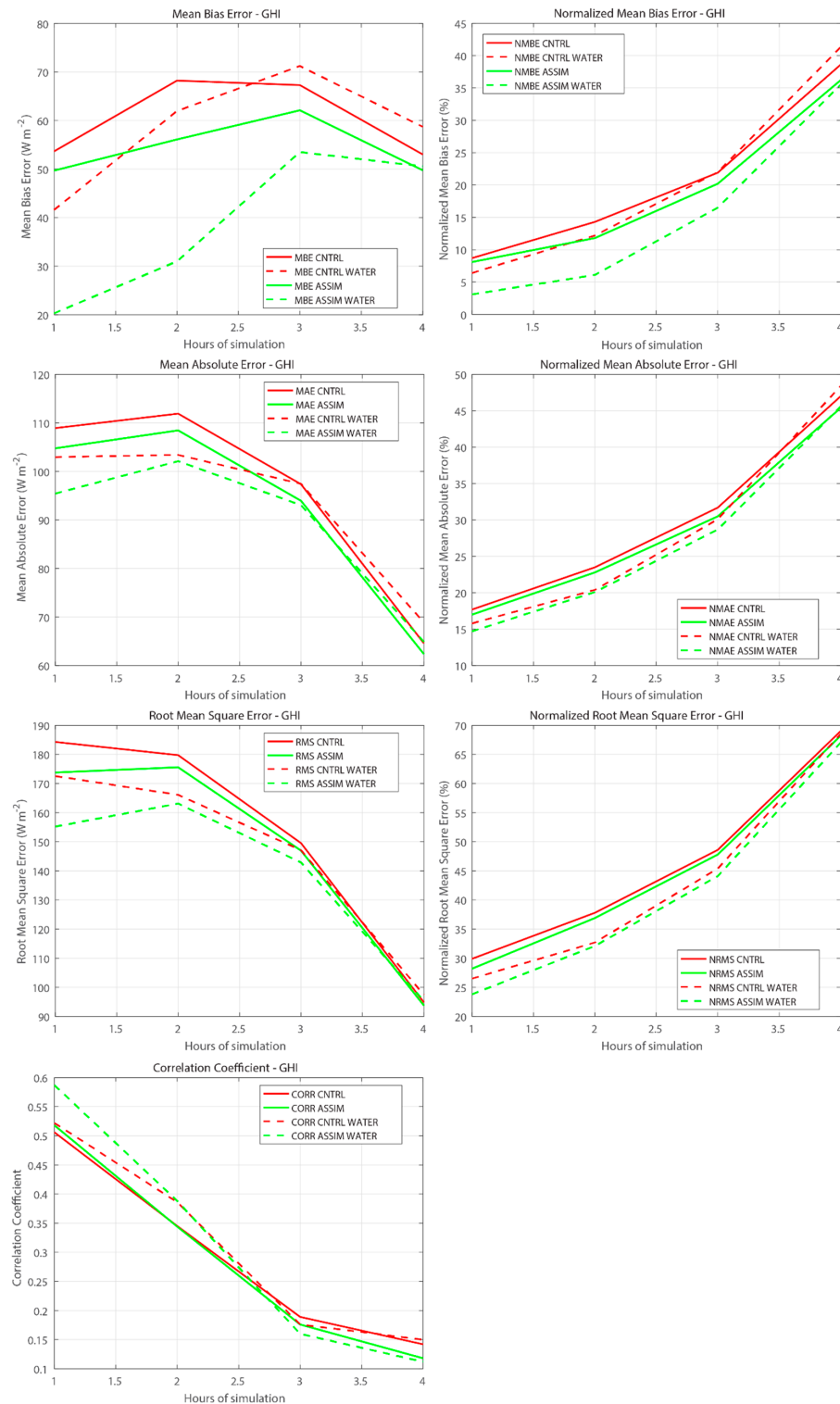


Figure 12. The statistical scores for the GHI vs hour of simulation starting from the start time (12 UTC). The red lines refer to the CNTRL and the green ones to the ASSIM configuration. The dotted lines refer to the indexes evaluated only over the water grid points. In the first row are reported on the left the Mean Bias Error (MBE) and on the right the Normalized Mean Bias Error (NMBE); in the second row the Mean Absolute Error (MAE) on the left and the Normalized Mean Absolute Error (NMAE) on the right; in the third row the Root Mean Square Error (RMSE) and the Normalized Root Mean Square Error (NRMS), respectively on the left and on the right and in the fourth row the Correlation (CORR).

Table 6. The Normalized Mean Bias Error (NMBE), the Normalized Root Mean Square Error (NRMSE), the Normalized Mean Absolute Error (NMAE), the Mean Bias Error (MBE), the Root Mean Square Error (RMSE), the Mean Absolute Error (MAE) and the correlation (CORR) for the evaluation of the GHI simulated by WRF-IMAA-Solar – CNTRL and ASSIM, by the persistence and observed by MSG. The indexes have been calculated also only on the water grid point. The values are averaged between 13 UTC and 18 UTC.

Test	NMBE %	NRMSE %	NMAE %	MBE W/m ²	RMSE W/m ²	MAE W/m ²	CORR
WRF-IMAA-Solar – CNTRL	21	46	30	60.57	152.10	95.71	0.29
WRF-IMAA-Solar – ASSIM	19	45	29	54.43	147.52	92.40	0.29
Persistence	45	58	47	321.15	361.66	332.39	0.22
WRF-IMAA-Solar – CNTRL WATER	20	43	29	58.40	145.81	93.18	0.31
WRF-IMAA-Solar – ASSIM WATER	15	42	27	38.85	139.13	88.88	0.31

Later in time (Figure 11) the GHI decreases because of sun setting and the overestimation in the left side of the domain remains more evident in the CNTRL than ASSIM simulation. The RMSE and MAE apparently seem to improve with time but this is due to the decreasing of the values of the GHI and not to an improvement of the forecast performances (second and third rows of Figure 12). For this reason, it is more appropriate to analyze the normalized indices, which indicate a slight superiority for ASSIM with respect to CNTRL and clearly show the worsening of the forecast skills with the time of simulation. The values of NMAE move from 17% of the first hour of simulation to 45% of the fourth one for ASSIM and from 18% to 47% for CNTRL. The same trend can be found for the NRMSE showing values ranging from 28% to 68% for ASSIM and from 30% to 69% for CNTRL. Slight better performances are given over water, with a maximum improvement for the NRMSE of 5% for ASSIM and 4% for CNTRL; the maximum improvement for NMAE is 3% for both ASSIM and CNTRL.

The correlation shows very similar results for both the configurations with a maximum of 59% for ASSIM WATER one hour after the assimilation (Figure 12, fourth row); values worsen with time, reaching approximately 12–14% after four hours. The persistence method has been used as benchmark also for the evaluation of the GHI. The mean values of the scores confirm that WRF-IMAA-Solar, both CNTRL and ASSIM, outperforms the persistence method. This result is expected, as this simple method can be used in clear sky conditions and is not suitable when the atmospheric dynamics involves rapid cloud cover variations.

Summarizing these preliminary results, it can be asserted that the WRF model overestimated the GHI and the assimilation process tends to reduce the error up to 4 h after the start time, when the SEVIRI radiance has been assimilated. The average scores confirm better performances for ASSIM, especially considering grid points only over water (Table 6).

4. Conclusions

The solar irradiance is particularly variable both in space and in time because of the complexity of the dynamic evolution of clouds. Geostationary satellite data can be taken into account to produce a more realistic representation of the atmospheric state using a data assimilation tool in a convective permitting model. Therefore, with the aim to improve the prediction of solar irradiance, preliminary tests have been performed to assess the impact of the 3D-VAR data assimilation of SEVIRI radiance in Italy using WRF Solar mesoscale model. The performances of the model have been analyzed both in clear conditions and cloudy sky. In clear sky the model has been tested without assimilation (CNTRL configuration) using the ARPAL radiometric stations. The statistical scores for the clear sky conditions confirm the positive performance of the WRF-IMAA-Solar with a MBE of -0.21 W/m^2 , a RMSE of 15.47 W/m^2 , a MAE of 6.78 W/m^2 comparable to the instrument uncertainty and a CORR of 0.995.

For cloudy sky, simulations with data assimilation (ASSIM configuration) have been performed. A preliminary test allows us to select the best settings for the use of the 3D-VAR data assimilation: the eight thermal infrared channels of SEVIRI have been assimilated at 12 UTC using a domain specific B matrix to consider the climatological aspects of the area, the VarBC scheme correction to remove the

biases from the measurements and the 120 km thinning mesh to avoid correlations between adjacent observations. The solar irradiance is better simulated by ASSIM than CNTRL configuration, especially in the 2–3 h nearest to the assimilation time, even though both the configurations overestimate the GHI. The statistical indexes calculated using the ARPAL stations improve for the ASSIM configuration, especially for the RMSE. The improvements introduced by the 3D-VAR data assimilation of SEVIRI radiances are confirmed also by the comparison with the EUMETSAT products: the Cloud Mask and the Hourly Shortwave Solar Irradiance. The use of the radiance assimilation on the simulation of cloud mask clearly produces better results especially in the 3 h later the assimilation time; after this interval the performances of the CNTRL and ASSIM are very similar. In particular one hour after the assimilation time the CNTRL configuration misses the 59% of cloud grid points against only the 11% for ASSIM; the PC statistical score passes from the 63% of CNTRL to the 81% of ASSIM and the BIAS for ASSIM is very close to the best value (1.09 for ASSIM and 0.43 for CNTRL). After the first hour of simulation, the better performance for the ASSIM configuration persists even though the difference is less significant.

The improvement related to the SEVIRI radiance assimilation is confirmed also by the comparison of the WRF-IMAA-Solar with the MSG products of the Hourly Shortwave Solar Irradiance. The statistical indexes confirm the GHI overestimation of the model is more pronounced for CNTRL than ASSIM. In the first hour of simulation the RMSE is reduced from 185 to 173 W/m² and the MBE from 54 to 49 W/m² when the assimilation is activated. The normalized statistical indexes are better by ~2% using the ASSIM configuration. A discontinuity is noted for MSG GHI over water and over land, probably due to a different retrieval technique. Calculating the statistical scores for only the over-water grid points, which seem to have a more consistent pattern with the observed clouds, the values improve further. Indeed, the value of the MBE one hour after the assimilation time passes from 49 W/m² to 20 W/m² for ASSIM and from 54 W/m² to 42 W/m² for CNTRL, using only the water grid points and the behavior is similar for the remaining indexes. The statistical scores obtained are comparable or slightly better than the values obtained from similar works, where a NWP is used to estimate the GHI [13–18]. The results from these preliminary tests show that the assimilation of geostationary satellite data increase the performances of the WRF-Solar model especially in the short-term range of the forecasts. This confirms the findings of other works [61–63], that is the effect of satellite data assimilation has high impact in the first 3–4 h of simulation and the improvement due to the assimilation decreases going forward with the simulation.

Note that this technique has been tested on two case studies only (one in clear sky and one in cloudy conditions) as preliminary tests for checking whether it is worth the effort to implement this change on our operational chain. Encouraged by the positive results, we are planning to increase the dataset and also to focus on the diffuse and direct components of the GHI.

Further improvements could be made considering other SEVIRI channels, for example, in the visible range. In the future, we plan to test assimilation with RTTOV model, since its most recent version allows for the assimilation of visible channels in addition to the infrared channels ones. The visible channels and specially the HRV channel with 1 km spatial resolution, carry more information and detail on the cloud pattern and properties, possibly foreshadowing an improved solar irradiance forecast. In addition, other advanced assimilation methods such as 4D-Var could be tested to take advantage of the frequent interval of scanning (15 min for SEVIRI).

Author Contributions: Conceptualization, S.G.; Methodology, S.G.; Software, E.R. (Ermann Ripepi); Validation, F.D.P.; Formal Analysis, M.V.; Investigation, S.G.; Resources, S.G.; Data Curation, D.G. and E.G.; Writing—Original Draft Preparation, S.G.; Writing—Review & Editing, D.C., S.L., S.T.N. and E.R. (Elisabetta Ricciardelli); Visualization, S.L.; Supervision, F.R.; Project Administration, E.G.; Funding Acquisition, D.C. All authors have read and agreed to the published version of the manuscript.

Funding: This work has been funded by the Italian Ministry of Economic Development (MISE) in the framework of the SolarCloud project, contract No. B01/0771/04/X24.

Conflicts of Interest: The authors declare no conflict of interest. The funders had no role in the design of the study; in the collection, analyses, or interpretation of data; in the writing of the manuscript, or in the decision to publish the results.

References

1. GSE (Gestore dei Servizi Energetici) Statistical Report (Italian Only). Available online: https://www.gse.it/documenti_site/Documenti%20GSE/Rapporti%20statistici/Solare%20Fotovoltaico%20-%20Rapporto%20Statistico%202018.pdf (accessed on 27 January 2020).
2. Perez, R.; Lorenz, E.; Pelland, S.; Beauharnois, M.; Knowe, G.V.; Hemker, K.; Heinemann, D., Jr.; Remund, J.; Müller, S.C.; Traunmüller, W.; et al. Comparison of numerical weather prediction solar irradiance forecasts in the US, Canada and Europe. *Sol. Energy* **2013**, *94*, 305–326. [[CrossRef](#)]
3. Remund, J.; Perez, R.; Lorenz, E. Comparison of solar radiation forecasts for the USA. In Proceedings of the 23rd European Photovoltaic Solar Energy Conference, Valencia, Spain, 1–5 September 2008.
4. Chow, C.W.; Urquhart, B.; Kleissl, J.; Lave, M.; Dominguez, A.; Shields, J.; Washom, B. Intra-hour forecasting with a total sky imager at the UC San Diego solar energy testbed. *Sol. Energy* **2011**. [[CrossRef](#)]
5. Pedro, H.T.; Coimbra, C.F. Assessment of forecasting techniques for solar power production with no exogenous inputs. *Sol. Energy* **2012**, *86*, 2017–2028. [[CrossRef](#)]
6. Lorenz, E.; Hammer, A.; Heinemann, D. Short term forecasting of solar radiation based on satellite data. In Proceedings of the EUROSUN2004 (ISES Europe Solar Congress), Freiburg, Germany, 20–23 June 2004.
7. Gallucci, D.; Romano, F.; Cersosimo, A.; Cimini, D.; Di Paola, F.; Gentile, S.; Geraldi, E.; Larosa, S.; Nilo, S.T.; Ricciardelli, E.; et al. Nowcasting Surface Solar Irradiance with AMESIS via Motion Vector Fields of MSG-SEVIRI Data. *Remote Sens.* **2018**, *10*, 845. [[CrossRef](#)]
8. Romano, F.; Cimini, D.; Cersosimo, A.; Di Paola, F.; Gallucci, D.; Gentile, S.; Geraldi, E.; Larosa, S.; Nilo, S.T.; Ricciardelli, E.; et al. Improvement in Surface Solar Irradiance Estimation Using HRV/MSG Data. *Remote Sens.* **2018**, *10*, 1288. [[CrossRef](#)]
9. Perez, R.; Kivalov, S.; Schlemmer, J.; Hemker, K.; Renné, D.; Hoff, T.E. Validation of Short and Medium Term Operational Solar Radiation Forecasts in the US. *Sol. Energy* **2010**, *84*, 2161–2172. [[CrossRef](#)]
10. Diagne, M.; David, M.; Lauret, L.; Boland, J.; Schmutz, N. Review of solar irradiance forecasting methods and a proposition for small-scale insular grids. *Renew. Sustain. Energy Rev.* **2013**, *27*, 65–76. [[CrossRef](#)]
11. Nonnenmacher, L.; Coimbra, C.F. Streamline-based method for intra-day solar forecasting through remote sensing. *Sol. Energy* **2014**, *108*, 447–459. [[CrossRef](#)]
12. Inman, R.H.; Pedro, H.T.C.; Coimbra, C.F.M. Solar forecasting methods for renewable energy integration. *Prog. Energy Combust. Sci.* **2013**, *39*, 535–576. [[CrossRef](#)]
13. Lara-Fanego, V.; Ruiz-Arias, J.A.; Pozo-Vázquez, D.; Santos-Alamillos, F.J.; Tovar-Pescador, J. Evaluation of the WRF model solar irradiance forecasts in Andalusia (southern Spain). *Sol. Energy* **2012**, *86*, 2200–2217. [[CrossRef](#)]
14. Perez, R.; Hoff, T. *Solar Anywhere Forecasting*, in: *Solar Energy Forecasting and Resource Assessment*; Kleissl, J., Ed.; Elsevier: Amsterdam, The Netherlands, 2013. [[CrossRef](#)]
15. Lorenz, E.; Remund, J.; Müller, S.C.; Traunmüller, W.; Steinmauer, G.; Pozo, D.; Ruiz-Arias, J.A.; Lara Fanego, V.; Ramirez, L.; Romeo, M.G.; et al. Benchmarking of Different Approaches to Forecast Solar Irradiance. In Proceedings of the 24th European Photovoltaic Solar Energy Conference, Hamburg, Germany, 21–25 September 2009; pp. 4199–4208. [[CrossRef](#)]
16. Lo Feudo, T.; Avolio, E.; Gulli, D.; Federico, S.; Calidonna, C.R.; Sempreviva, A.M. Comparison of hourly solar radiation from a ground-based station remote sensing and weather forecast models at a coastal site of South Italy (Lamezia Terme). *Energy Procedia* **2015**, *76*, 148–155. [[CrossRef](#)]
17. Gómez, I.; Caselles, V.; Estrela, M.J. Seasonal Characterization of Solar Radiation Estimates Obtained from a MSG-SEVIRI-Derived Dataset and a RAMS-Based Operational Forecasting System over the Western Mediterranean Coast. *Remote Sens.* **2016**, *8*, 46. [[CrossRef](#)]
18. Gómez, I.; Caselles, V.; Estrela, M.J.; Miró, J.J. Comparative assessment of RAMS and WRF short-term forecasts over Eastern Iberian Peninsula using various in-situ observations, remote sensing products and uncoupled land surface model datasets. *Atmos. Res.* **2018**, *213*, 476–491. [[CrossRef](#)]

19. Haupt, S.E.; Kosovic, B.; Jensen, T.L.; Lee, J.; Jimenez Munoz, P.; Lazo, J.K.; Hinkleman, L. The Sun4Cast Solar Power Forecasting System: The Result of the Public-Private-Academic Partnership to Advance Solar Power Forecasting (No. NCAR/TN-526+STR). *Natl. Center Atmos. Res. (NCAR) Boulder (CO) Res. Appl. Lab. Weather Syst. Assess. Program (US)* **2016**. [[CrossRef](#)]
20. Haupt, S.E.; Kosović, B.; Jensen, T.; Lazo, J.K.; Lee, J.A.; Jiménez, P.A.; Cowie, J.; Wiener, G.; McCandless, T.C.; Rogers, M.; et al. Building the Sun4Cast system: Improvements in solar power forecasting. *Bull. Am. Meteorol. Soc.* **2017**, *99*, 121–136. [[CrossRef](#)]
21. Kurzrock, F.; Cros, S.; Ming, F.C.; Otkin, J.A.; Hutt, A.; Linguet, L.; Lajoie, G.; Potthast, R. A Review of the Use of Geostationary Satellite Observations in Regional-scale Models for Short-term Cloud Forecasting. *Meteorol. Z.* **2018**, *27*, 277–298. [[CrossRef](#)]
22. Cros, S.; Sébastien, N.; Liandrat, O.; Schmutz, N. Cloud pattern prediction from geostationary meteorological satellite images for solar energy forecasting. In Proceedings of the SPIE. Remote Sensing of Clouds and the Atmosphere XIX; and Optics in Atmospheric Propagation and Adaptive Systems XVII, Amsterdam, The Netherlands, 22 and 24–25 September 2014; p. 924202. [[CrossRef](#)]
23. Lorenz, E.; Kühnert, J.; Heinemann, D. Overview of irradiance and Photovoltaic Power Prediction. In *Weather Matters for Energy*; Troccoli, A., Dubus, L., Haupt, S.E., Eds.; Springer: New York, NY, USA, 2014; pp. 429–454.
24. Tanvir, I.; Srivastava, P.K.; Kumar, D.; Petropoulos, G.P.; Dai, Q.; Zhuo, L. Satellite radiance assimilation using a 3DVAR assimilation system for hurricane Sandy forecasts. *Nat. Hazards* **2016**, *82*, 845–855. [[CrossRef](#)]
25. Yang, C.; Liu, Z.; Bresch, J.; Rizvi, S.R.H.; Huang, X.-Y.; Min, J. AMSR2 all-sky radiance assimilation and its impact on the analysis and forecast of Hurricane Sandy with a limited-area data assimilation system. *Tellus* **2016**, *68A*, 30917. [[CrossRef](#)]
26. Xie, Y.; Xing, J.; Shi, J.; Dou, Y.; Lei, Y. Impacts of radiance data assimilation on the Beijing 7.21 heavy rainfall. *Atmos. Res.* **2016**, *169*, 318–330. [[CrossRef](#)]
27. Xu, D.; Min, J.; Shen, F.; Ban, J.; Chen, P. Assimilation of MWHS radiance data from the FY-3B satellite with the WRF Hybrid-3DVAR system for the forecasting of binary typhoons. *J. Adv. Model. Earth Syst.* **2016**, *8*, 1014–1028. [[CrossRef](#)]
28. Gustafsson, N.; Janjić, T.; Schraff, C.; Leuenberger, D.; Weissmann, M.; Reich, H.; Brousseau, P.; Montmerle, T.; Wattrelot, E.; Bućánek, A.; et al. Survey of data assimilation methods for convective-scale numerical weather prediction at operational centres. *Quart. J. R. Meteorol.* **2018**. [[CrossRef](#)]
29. Stengel, M.; Undén, P.; Lindskog, M.; Dahlgren, P.; Gustafsson, N.; Bennartz, R. Assimilation of SEVIRI infrared radiances with HIRLAM 4DVar. *Q. J. R. Meteorol. Soc.* **2009**, *135 Pt B*, 2100–2109. [[CrossRef](#)]
30. Stengel, M.; Lindskog, M.; Undén, P.; Gustafsson, N.; Bennartz, R. An extended observation operator in HIRLAM 4D-VAR for the assimilation of cloud-affected satellite radiances. *Q. J. R. Meteorol. Soc.* **2010**, *136*, 1064–1074. [[CrossRef](#)]
31. Stengel, M.; Lindskog, M.; Undén, P.; Gustafsson, N. The impact of cloud-affected IR radiances on forecast accuracy of a limited-area NWP model. *Q. J. R. Meteorol. Soc.* **2013**, *139*, 2081–2096. [[CrossRef](#)]
32. Yang, C.; Liuz, Z.; Gao, F.; Child, P.P.; Min, J. Impact of assimilation goes imager clear-sky radiance with a rapid refresh assimilation system for convection-permitting forecast over Mexico. *J. Geophys. Res. Atmos.* **2017**, *122*, 5472–5490. [[CrossRef](#)]
33. Skamarock, W.C.; Klemp, J.B.; Dudhia, J.; Gill, D.O.; Barker, D.M.; Wang, W.; Powers, J.G. A description of the Advanced Research WRF Version 3; NCAR Technical Note, NCAR/TN-475+STR. 2008. Available online: <http://opensky.ucar.edu/islandora/object/technotes:500> (accessed on 25 May 2018).
34. Jimenez, P.A.; Hacker, J.P.; Dudhia, J.; Haupt, S.E.; Jose, R.A.; Gueymard, C.A.; Thompson, G.; Eidhammer, T.; Deng, A. WRF-Solar: Description and Clear-Sky Assessment of an Augmented NWP Model for Solar Power Prediction. *Bull. Am. Met. Soc.* **2016**, *97*, 1249–1264. [[CrossRef](#)]
35. Thompson, G.; Eidhammer, T. A Study of Aerosol Impacts on Clouds and Precipitation Development in a Large Winter Cyclone. *J. Atmos. Sci.* **2014**, *71*, 3636–3658. [[CrossRef](#)]
36. Hong, S.Y.; Noh, Y.; Dudhia, J. A New Vertical Diffusion Package with an Explicit Treatment of Entrainment Processes. *Mon. Weather Rev.* **2006**, *134*, 2318–2341. [[CrossRef](#)]
37. Iacono, M.J.; Delamere, J.S.; Mlawer, E.J.; Shephard, M.W.; Clough, S.A.; Collins, W.D. Radiative forcing by long-lived greenhouse gases: Calculations with the AER radiative transfer models. *J. Geophys. Res. Atmos.* **2008**, *113*. [[CrossRef](#)]

38. Kain, J.S. The Kain–Fritsch Convective Parameterization: An Update. *J. Appl. Meteorol.* **2004**, *43*, 170–181. [[CrossRef](#)]
39. Singh, R.; Ojha, S.P.; Kishtawal, C.M.; Pal, P.K.; Kumar, A.S.K. Impact of the assimilation of INSAT-3D radiances on short-range weather forecasts. *Quart. J. R. Meteor. Soc.* **2016**, *142*, 120–131. [[CrossRef](#)]
40. Schmid, J. The SEVIRI Instrument. In Proceedings of the 2000 EUMETSAT Meteorological Satellite. Data User’s Conference, Bologna, Italy, 29 May–2 June 2000; Darmstadt, Germany, EUMETSAT ed (2000). pp. 13–32.
41. Barker, D.M.; Huang, W.; Guo, Y.-R.; Bourgeois, A.; Xiao, Q. A Three-Dimensional Variational (3DVAR) Data Assimilation System For Use With MM5: Implementation and Initial Results. *Mon. Weather Rev.* **2004**, *132*, 897–914. [[CrossRef](#)]
42. Barker, D.; Huang, X.-Y.; Liu, Z.; Auligné, T.; Zhang, X.; Rugg, S.; Ajjaji, R.; Bourgeois, A.; Bray, J.; Chen, Y.; et al. The Weather Research and Forecasting Model’s Community Variational/Ensemble Data Assimilation System: WRFDA. *Bull. Am. Meteorol. Soc.* **2012**, *93*, 831–843. [[CrossRef](#)]
43. Han, Y.; van Delst, P.; Liu, Q.; Weng, F.; Yan, B.; Treadon, R.; Derber, J. *Community Radiative Transfer Model (CRTM): Version 1*; NOAA Technical Report; NOAA: Washington, DC, USA, 2006; 122p.
44. Maiello, I.; Gentile, S.; Ferretti, R.; Baldini, L.; Nicoletta, R.; Picciotti, E.; Alberoni, P.P.; Marzano, F.S. Impact of multiple radar reflectivity data assimilation on the numerical simulation of a flash flood event during the HyMeX campaign. *Hydrol. Earth Syst. Sci.* **2017**, *21*, 5459–5476. [[CrossRef](#)]
45. Parrish, D.F.; Derber, J.C. The national meteorological center’s spectral statistical-interpolation analysis system. *Mon. Weather Rev.* **1992**, *120*, 1747–1763. [[CrossRef](#)]
46. Steinacker, R.; Haberli, C.; Pottschacher, W. A transparent method for the analysis quality evaluation of irregularly distributed noisy observational data. *J. Appl. Meteorol.* **2000**, *12*, 2303–2316. [[CrossRef](#)]
47. Lussana, C.; Ubaldi, F.; Salvati, M.R. A spatial consistency test for surface observations from mesoscale meteorological networks. *Q. J. R. Meteorol. Soc.* **2010**, *136*, 1075–1088. [[CrossRef](#)]
48. *Guide to Meteorological Instruments and Methods of Observation*; WMO-No. 8; WMO: Geneva, Switzerland, 2018.
49. Reda, I. *Method to Calculate Uncertainties in Measuring Shortwave Solar Irradiance Using Thermopile and Semiconductor Solar Radiometers*; NREL/TP-3B10-52194; National Renewable Energy Lab.(NREL): Golden, CO, USA, 2011.
50. Wilcox, S.M.; Myers, D.R. *Evaluation of Radiometers in Full-Time Use at the National Renewable Energy Laboratory Solar Radiation Research Laboratory*; NREL/TP-550-44627; National Renewable Energy Lab.(NREL): Golden, CO, USA, 2008.
51. MTG-FCI: ATBD for Cloud Mask and Cloud Analysis Product. Doc.No. EUM/MTG/DOC/10/0542, Issue: v3, Date: 17 January 2013 WBS: MTG-834200. Available online: <http://www.eumetsat.int> (accessed on 27 January 2020).
52. MSG Meteorological Products Extraction Facility Algorithm Specification Document. Doc.No., EUM/MSG/SPE/022, Issue: v7B e-signed, Date: 23 October 2015. Available online: <http://www.eumetsat.int> (accessed on 27 January 2020).
53. Lutz, H.J. Cloud processing for Meteosat Second Generation. *EUMETSAT Tech. Department Tech. Memo.* **1999**, *4*, 26. Available online: https://www.eumetsat.int/website/wcm/idc/idcplg?IdcService=GET_FILE&dDocName=PDF_TM04_MSG-CLOUD-PROCESSING&RevisionSelectionMethod=LatestReleased&Rendition=Web (accessed on 27 January 2020).
54. EUMETSAT, 2018 (I): SAF/OSI/CDOP3/MF/TEC/MA/182, GEO DLI & SSI PUM, 26 February 2018, “Geostationary Radiative Fluxes Product User Manual”. Available online: http://www.osi-saf.org/lml/doc/osisaf_cdop2_ss1_pum_geo_fly.pdf (accessed on 27 January 2020).
55. EUMETSAT, 2018 (II): SAF/OSI/CDOP3/MF/SCI/RP/328, Anne Marsouin, Météo-France/CMS, 6 November 2018, “Radiative fluxes validation report for GOES-16 OSI-305-a OSI-306-a Meteosat-11 OSI-303-a OSI-304-a Meteosat-8 OSI-IO-DLI OSI-IO-SSI”. Available online: http://www.osi-saf.org/lml/doc/osisaf_cdop2_ss1_geo_fly_val_rep.pdf (accessed on 27 January 2020).
56. Gallucci, D.; Romano, F.; Cimini, D.; Di Paola, F.; Gentile, S.; Larosa, S.; Nilo, S.T.; Ricciardelli, E.; Ripepi, E.; Viggiano, M.; et al. Improvement of Hourly Surface Solar Irradiance Estimation Using MSG Rapid Scanning Service. *Remote Sens.* **2019**, *11*, 66. [[CrossRef](#)]
57. Haiden, T.; Trentmann, J. Verification of cloudiness and radiation forecasts in the greater Alpine region. *Meteorol. Z.* **2015**, *25*, 3–15. [[CrossRef](#)]

58. Yang, H.; Kleissl, J. Preprocessing WRF initial conditions for coastal stratocumulus forecasting. *Sol. Energy* **2016**, *133*, 180–193. [[CrossRef](#)]
59. Yucel, I.; Shuttleworth, W.J.; Pinker, R.T.; Lu, L.; Sorooshian, S. Impact of Ingesting Satellite-Derived Cloud Cover into the Regional Atmospheric Modeling System. *Mon. Weather Rev.* **2002**, *130*, 610–628. [[CrossRef](#)]
60. Cintineo, R.; Otkin, J.A.; Xue, M.; Kong, F. Evaluating the Performance of Planetary Boundary Layer and Cloud Microphysical Parameterization Schemes in Convection-Permitting Ensemble Forecasts Using Synthetic GOES-13 Satellite Observations. *Mon. Weather Rev.* **2014**, *142*, 163–182. [[CrossRef](#)]
61. Bauer, P.; Auligné, T.; Bell, W.; Geer, A.; Guidard, V.; Heilliette, S.; Kazumori, M.; Kim, M.-J.; Liu, E.H.-C.; McNally, A.P.; et al. Satellite cloud and precipitation assimilation at operational NWP centres. *Quart. J. R. Meteor. Soc.* **2011**, *137*, 1934–1951. [[CrossRef](#)]
62. Bauer, P.; Ohring, G.; Kummerow, C.; Auligne, T. Assimilating Satellite Observations of Clouds and Precipitation into NWP Models. *Bull. Am. Meteor. Soc.* **2011**, *92*, ES25–ES28. [[CrossRef](#)]
63. Bayler, G.M.; Aune, R.M.; Raymond, W.H. NWP Cloud Initialization Using GOES Sounder Data and Improved Modeling of Nonprecipitating Clouds. *Mon. Weather Rev.* **2000**, *128*, 3911–3920. [[CrossRef](#)]



© 2020 by the authors. Licensee MDPI, Basel, Switzerland. This article is an open access article distributed under the terms and conditions of the Creative Commons Attribution (CC BY) license (<http://creativecommons.org/licenses/by/4.0/>).

Johannes Schmetz, Paolo Pili, Alain Ratier, Sergio Rota and Stephen Tjemkes
EUMETSAT, Am Kavalleriesand 31, D-64295 Darmstadt, Germany

1. INTRODUCTION

Meteosat Second Generation (MSG) is the new generation of European geostationary meteorological satellites MSG (Meteosat Second Generation). It has capabilities greatly enhanced over the current Meteosat series. The twelve channel imager, called SEVIRI (Spinning Enhanced Visible and Infrared Imager), observes the full disk of the Earth with an unprecedented repeat cycle of 15 minutes. Pixels are sampled with a distance of 3 km and the high resolution visible (HRV) channel even has 1 km sampling distance. The spectral channels, at 3.9, 6.2, 7.3, 8.7, 9.7, 10.8, 12.0 and 13.4 μm and at 0.6, 0.8 and 1.6 μm , draw on experience from existing satellites, thus providing continuity of services and facilitating the development of novel operational applications. Thermal IR channels have an onboard calibration and for the solar channels an operational vicarious procedure is developed aiming at an accuracy of 5%. The core operational meteorological products are derived by the Meteorological Product Extraction Facility (MPEF) at EUMETSAT in Darmstadt. Other products will be derived in Satellite Application Facilities (SAF), a decentralised part of the Applications Ground Segment. As additional scientific payload MSG carries a Geostationary Earth Radiation Budget (GERB) instrument. The MSG system is established under a cooperation between ESA and EUMETSAT. The MSG Programme consists of a series of three identical satellites, which will provide observations and services over at least 12 years. The first launch of MSG is scheduled for 2002. A novelty of MSG is the full disk imaging at time intervals of 15 minutes. Studies have shown that this has great potential to improve wind products mainly used for global Numerical Weather Prediction (NWP). The repeat cycle also provides unprecedented multi-spectral observations of rapidly changing phenomena (e.g. deep convection) and provides novel insight into rapid changes in cloud microphysics. Ongoing studies reveal the potential for monitoring atmospheric instability.

Corresponding author: Johannes Schmetz,
EUMETSAT, Am Kavalleriesand 31, D-64295
Darmstadt, Germany, email: schmetz@eumetsat.de

2. THE SEVIRI INSTRUMENT

The primary mission of MSG is the continuous observation of the Earth's full disk. This is achieved with the Spinning Enhanced Visible and Infrared Imager (SEVIRI) imaging radiometer, a twelve channel imager observing the Earth-atmosphere system with a spatial sampling distance of 3 km in eleven channels. A high-resolution visible (HRV) channel covers half of the full disk with a 1 km spatial sampling. The actual field of view of the channels is about 4.8 km and 1.67 km.

A repeat cycle of 15 minutes for full-disk imaging provides unprecedented multi-spectral observations of rapidly changing phenomena (e.g. deep convection) and provides better and more numerous wind observations from the tracking of cloud features. Rapid scans of limited latitude belts are possible with shorter time intervals.

The imaging is performed by combining the satellite spin with the rotation (stepping) of the scan mirror. The images are taken from South to North and East to West. The nominal spin rate is 100 revolutions per minute. The spin axis is nominally parallel to the North-South axis of the Earth. The scan from South to North is achieved with 1250 E-W scans; this provides 3750 image lines for channels 1 through 11 (see Table 1) since 3 detectors for each channel are used for the imaging. For the HRV (channel 12) 9 detectors sweep the Earth for one line scan. The number of line scans is programmable such that shorter repeat cycles can be performed. A full disk image is obtained within about 12 minutes (see Figure 1). This is followed by the calibration of thermal IR channels (see section 2.2).

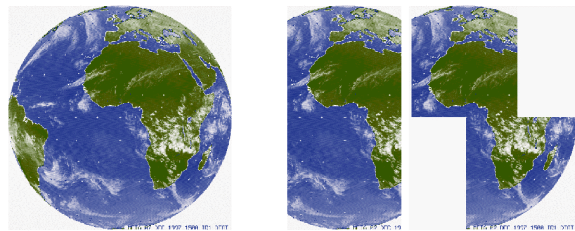


Figure 1: Coverage of MSG for the repeat cycle of 15 minutes for channels 1 through 11 (ref. Table 1). The High resolution Visible (HRV), i.e. channel 12, covers only half the Earth in E-W, however the area of imaging can be selected.

Channel No.		Channel Spectral Band in μm		
		λ_{cen}	λ_{min}	λ_{max}
12	HRV	Broadband (silicon response)		
1	VIS0.6	0.635	0.56	0.71
2	VIS0.8	0.81	0.74	0.88
3	NIR1.6	1.64	1.50	1.78
4	IR3.9	3.90	3.48	4.36
5	WV6.2	6.25	5.35	7.15
6	WV7.3	7.35	6.85	7.85
7	IR8.7	8.70	8.30	9.1
8	IR9.7	9.66	9.38	9.94
9	IR10.8	10.80	9.80	11.80
10	IR12.0	12.00	11.00	13.00
11	IR13.4	13.40	12.40	14.40

Table 1: Spectral channel characteristics of SEVIRI providing central, minimum and maximum wavelength of the channels.

Most SEVIRI spectral channels build upon the heritage from other satellites which has the great advantage that the operational user community can readily use existing know-how to utilise SEVIRI radiance observations. The heritage of channels can be summarised as follows:

VIS0.6 and VIS0.8: Known from the Advanced Very High Resolution Radiometer (AVHRR) of the polar orbiting NOAA satellites. Essential for cloud detection, cloud tracking, scene identification, aerosol and land surface and vegetation monitoring.

NIR1.6: Discriminates between snow and cloud, ice and water clouds, and provides aerosol information.

IR3.9: Known from AVHRR. Primarily for low cloud and fog detection (Eyre et.al., 1984). Also supports measurement of land and sea surface temperature at night. For MSG, the spectral band has been broadened to higher wavelengths to improve signal-to-noise ratio.

IR6.2 and IR7.3: Continues mission of Meteosat broadband water vapour channel for observing water vapour and winds. Enhanced to two channels peaking at different levels in the troposphere. Also support height allocation of semitransparent clouds.

IR8.7: Known from the High resolution Infra Red Sounder (HIRS) instrument on the polar orbiting NOAA satellites. The channel provides quantitative information on thin cirrus clouds and supports the discrimination between ice and water clouds.

IR9.7: Known from HIRS and current GOES satellites. Ozone radiances could be used as an input to Numerical Weather Prediction (NWP). As an experimental channel, it will be used for tracking of ozone patterns that should be representative for wind motion in the lower stratosphere. The evolution of the total ozone field with time can also be monitored.

IR10.8 and IR12.0: Well-known split window channels (e.g. AVHRR). Essential to measure sea- and land-surface and cloud top temperatures.

IR13.4: CO₂ absorption channel known from former GOES VAS instrument. It improves height allocation of tenuous cirrus clouds (Menzel et al., 1983). In cloud

free areas, it will provide temperature information from the lower troposphere that can be used to infer static instability.

2.1 Radiometric Performance

The radiometric requirements for SEVIRI specify: i) short term error or noise, ii) mid-term drift error, and iii) bias or long-term drift error.

The short term error or noise requirement includes all factors affecting the radiometry during one nominal repeat cycle (15 minutes duration) and applies to in-orbit conditions at End Of Life (EOL). These are essentially: random noise, stability of temperature of detectors, crosstalk and straylight, stability of gain. Table 2 provides the measured performance of SEVIRI on MSG-1 and the specified requirements. Measured performance is based on tests complemented by a prediction of in-flight performances. Except for channel NIR1.6, the predicted in-orbit radiometric performances at EOL are better than the requirements. Thus excellent radiometric image quality can be expected.

The mid-term drift requirement limits the variation of the mean radiometric error in a sequence of nominal images. The requirement for the warm channels is a maximum drift over 1 day (i.e. 96 nominal repeat cycles) of less than 0.1% of the maximum of the dynamic range. The requirement for the cold (i.e. the thermal IR with cooled detectors) channels is a maximum drift between two on-board calibrations of less than 0.05K (or 0.1K for WV6.2 and WV7.3) at the maximum temperature of the dynamic range. The ground tests have shown that the worst case applies to channel IR12.0 requiring an on- board calibration every 10 images. It should, however, be noted that the baseline design of SEVIRI enables to perform one calibration per image cycle.

Channel	Short term radiometric error performances	Short term radiometric error requirements
HRV	0.93 at 1.3 W/(m ² sr μm)	1.07 at 1.3 W/(m ² sr μm)
VIS0.6	0.37 at 5.3 W/(m ² sr μm)	0.53 at 5.3 W/(m ² sr μm)
VIS0.8	0.37 at 3.6 W/(m ² sr μm)	0.49 at 3.6 W/(m ² sr μm)
NIR1.6	0.25 at 0.75W/(m ² sr μm)	0.25 at 0.75 W/(m ² sr μm)
IR3.9	0.24K at 300K	0.35K at 300K
WV6.2	0.40K at 250K	0.75K at 250K
WV7.3	0.48K at 250K	0.75K at 250K
IR8.7	0.17K at 300K	0.28K at 300K
IR9.7	0.24K at 255K	1.5K at 255K
IR10.8	0.15K at 300K	0.25K at 300K
IR12.0	0.22K at 300K	0.37K at 300K
IR13.4	0.30K at 270K	1.80K at 270K

Table 2: Noise equivalent radiances and temperatures for the channels of the SEVIRI instrument on MSG-1 compared with the requirements. Values for the thermal IR channels refer to a focal plane temperature of 95K.

The bias and long-term drift requirement specifies the absolute radiometric error (i.e. the difference between the measured radiance and the actual radiance at the input of the instrument). Tests confirmed that the performance for all thermal IR channels is about 0.5 K for typical warm scene temperatures of 300 to 335 K (see also following section on calibration).

2.2 SEVIRI Calibration

The thermal IR channels of SEVIRI are calibrated with an on-board blackbody (Pili, 2000). The relationship between digital counts and the observed radiance is assumed to be linear:

$$C(L) = g L(\lambda, T) + C_0$$

Where $C(L)$ is the digital count output from SEVIRI, $L(\lambda, T)$ the measured radiance, λ the wavelength (in practice a spectral interval), T the effective blackbody temperature of an observed scene, g the gain (or calibration coefficient) and C_0 the offset. The assumption of a linear relationship between counts and radiance is valid since small non-linearity are corrected for on ground before applying the linear calibration procedure.

SEVIRI uses the deep space as cold source and an internal blackbody as warm source for the calibration. While the deep space view is obtained by viewing through the complete optical path of the instrument the blackbody is moved into the optical path avoiding the front optics. This design necessitates a correction to be applied to the blackbody calibration considering the optical properties of the front optics, whose characteristics have been measured before launch and whose temperature is monitored continuously. The blackbody can also be heated to allow for the determination of the correction factor. Overall a calibration performance better of about 0.5 K is expected for all thermal IR channels (Pili, 2000).

The solar channels (channels 1 –3 and 12) do not have an on-board calibration but have to rely on a vicarious method based on radiance observations over well-characterised targets (clear-sky desert, clear-sky ocean and optically thick high level clouds) and radiative transfer simulations (Govaerts et al., 2000). This new method of solar channel calibration will achieve an accuracy of the about 5% after the first year of operations as the characterisation of targets improves and quality control parameters will become better tuned.

3. MSG PRODUCTS

The derivation of level 2.0 meteorological products, is performed within the Applications Ground Segment (AGS) which consists of:

- 1) a central Meteorological Products Extraction Facility (MPEF)

2) a network of satellite Application Facilities (SAF) located at National Weather Services and other institutions of EUMETSAT member states.

3.1 Products from the Central MPEF

The Scenes Analysis (SCE) is the first step and an intermediate product of the MSG MPEF which is further used in the derivation of other products requiring either cloudy or clear pixels. The results of Scenes Analysis algorithm will provide per pixel and repeat cycle:

- i) Identification of cloudy and clear pixels and a cloud mask,
- ii) Identification of scene type for each pixel,
- iii) Radiances at the top of the atmosphere.

The Scenes Analysis algorithm is based on threshold techniques (e.g. Saunders and Kriebel, 1988). Advantage is taken of the 15 minute repeat cycle by using results of the previous image as first guess in the current image. SCE and Cloud Analysis are described in more detail by Lutz (1999).

Cloud Analysis (CLA) is based on the Scenes Analysis results and provides on a scale of 100 km x 100 km (or better) information about cloud cover, cloud top temperature, cloud top pressure/height and cloud type and phase. An important objective of the Cloud analysis product is to support the generation of the Atmospheric Motion Vectors (AMV). Therefore an intermediate product for each pixel and repeat cycle, which provides the necessary internal input to the Atmospheric Motion Vectors, is derived, but not disseminated. This intermediate (pixel scale) Cloud Analysis is also used for the Cloud Top Height product. It also provides input to the statistical information contained in the off-line Climate Data Sets product.

Cloud Top Height (CTH) is a derived product image, which provides the height of the highest cloud at a super-pixel resolution of 3x3 pixels. This product is for use in aviation meteorology. It provides the heights with a vertical resolution of 300 meter.

Clear Sky Radiance (CSR) gives mean radiances (in $\text{Wm}^{-2} \text{sr}^{-1} (\text{cm}^{-1})^{-1}$) for cloud-free pixels. Operational NWP centres will use CSR products from the MSG infrared channels in their analyses. The benefit will emerge with the advent of 4-d variational data assimilation systems that have the capability to utilise the frequent time observations from geostationary orbit (e.g. Munro et al., 1998).

Tropospheric Humidity (TH) provides estimates of layer-mean relative humidity for two tropospheric layers. One layer humidity (between about 600 and 200 hPa) is based on 6.3 μm clear sky radiances; this product is also known as UTH (upper tropospheric humidity) from the current Meteosat MPEF. The mean relative humidity of a second layer (between 850 and 350 hPa) uses clear sky 7.3 μm and is named MTH (mid-tropospheric humidity). The algorithm follows the improved UTH retrieval presented in Schmetz et al. (1995).

Atmospheric Motion Vectors (AMV) are the most important product for numerical weather prediction. The tropospheric AMVs will be derived from cloud and water vapour motion using primarily the 0.6 or 0.8 μm channel, the 10.8 μm channel and the 6.2 and 7.3 μm channels, respectively. The capabilities to extract lower stratospheric displacements vectors from ozone will also be exploited.

The product is based on conceptually validated ideas and methods (e.g. Schmetz et al., 1993 and Holmlund, 2001). An important feature, already implemented in the current Meteosat products, is the improved automatic quality control using quality indicators (Holmlund, 1998). The MSG algorithm also features novel concepts, such as i) a wind vector assignment to the exact target position, ii) improved target selection and enhancement, iii) improved quality control which benefits from the fact that wind fields from a single repeat cycle are used to derive a spatially dense final AMV product, iv) improved height assignment for semitransparent cloud tracers.

ISCCP Data Set (IDS) continues the support to the International Satellite Cloud Climatology Programme (ISCCP) providing three different data formats.

High Resolution Precipitation Index (HPI) continues the support to the Global Precipitation Climatology Project (GPCP) and provides the frequency of pixels for classes of brightness temperatures. Since it is indicative of convective (tropical) rainfall the product is confined to the latitudes between 40°S and 40°N.

Climate Data Set (CDS) provides statistical information about the scene classes in a processed segment (nominally 32x32 pixels). It is a concise summary of the radiances observed in a segment and potentially very useful for climatological studies of cloud and radiation fields.

Global Instability Index (GII) is an air mass parameter indicating the stability of the atmosphere at a scale of about 30 km. It is closely related to products from the SAF for Nowcasting and Very Short Range Forecasting, except that the GII is derived globally and disseminated. Based on successful applications and experience by NOAA/NESDIS with GOES lifted index products (Menzel et al., 1998) the idea for the GII emerged. Two algorithms are currently foreseen for the GII product i) a physical retrieval (Ma et al., 1999) and ii) an artificial neural network. Details on GII product are provided in this issue (König et al., 2001).

Total Ozone Product (TOZ) uses the 9.7 μm channel, other SEVIRI channels and correlative data and is derived with a regression algorithm (Orsolini and Karcher, 2000). The ozone observations are useful input for monitoring and forecasting UV radiation at the ground level. Preliminary studies show that ozone observations at high temporal and spatial resolution may provide useful information about the winds in the upper troposphere and lower stratosphere, although the derivation of dense vector fields seems difficult. Alternatively, the ozone observations can be assimilated into a numerical model with a suitable multivariate data assimilation system in which the

forecast includes a prognostic equation for ozone (e.g. Riishojaard, 1996).

3.2 Products from Sattellite Application Facilities (SAF)

Satellite Application Facilities (SAF) are specialised development and processing centres within the EUMETSAT Applications Ground Segment. Utilising specialised expertise in Member States, they will complement the production of meteorological products derived from satellite data at EUMETSATs Central Facilities (the MPEF) and will also distribute user software packages. There are currently seven SAFs. Links to relevant web pages are provided via the EUMETSAT web page www.eumetsat.de/SAF/. A generic list of products, relevant of the use of MSG, from the Ocean and Sea Ice SAF, the SAF for Land Surface Analysis and the Climate SAF reads as follows:

- Examples of products from the Ocean and Sea Ice SAF include i) Atlantic Sea Surface Temperature, ii) Surface radiative fluxes over the Atlantic, iii) Sea Ice (Polar Atlantic): ice edge/cover, thickness/age.
- Examples of products from the Climate SAF are i) Sea Surface Temperature and sea ice cover, ii) Cloud parameters, iii) Surface radiation budget components, iv) Radiation budget components at TOA, v) humidity products.
- Examples of targeted products from the Land Analysis SAF are i) Vegetation parameters and biophysical indicators, ii) Snow cover, iii) Land Surface Temperature, emissivity and moisture, iv) Short wave and long wave radiation parameters.

Some SAF products are composites and based on multi-mission data including MSG data as one source. It is also noted that the SAF on Nowcasting and Very Short Range Forecasting develops software for a suite of products that can be derived from MSG. The software will be made available for local implementation.

3.3 Development Toward New Applications

The improvement of products will be a continuous task. Several improvements are already planned. For instance, Tjemkes and Watts (2000) report on a research study which investigates new ways to perform a scenes analysis. The new method uses 'optimum estimation' Rodgers (1976) as novel way to infer simultaneously a set of cloud parameters and possibly surface features. This Enhanced Cloud Product (ECP) derives the following cloud microphysical properties from SEVIRI observations: Optical Thickness, Mean Particle Radius, Cloud Top Temperature, Cloud Top Pressure, and Cloud Phase.

An area for improvement are the Atmospheric Motion Vectors (Holmlund, 2001) where two products will complement the current Day-1 baseline products:

i) Ozone Motion Vectors describe the displacement of total ozone features and include a height assignment of the derived vectors. In the baseline of the MSG-MPEF the use of total ozone product derived from observations in the IR 9.6 channel for the derivation of displacement vectors in the stratosphere was not foreseen. ii) Low Level Winds over Land and Ocean will be an enhancement of the current low-level wind products. It gives the displacement of low level clouds derived from HRVIS, 0.6, 0.8 and 3.9 μm observations. In order to improve the quality of the low level wind field over land a new target selection, image enhancement, and cloud height and tracking procedures are developed that utilise the full capabilities of the SEVIRI instrument. Initial study results are encouraging (Szantai et al., 2000).

MSG will also provide new potential for observing components of the hydrological cycle which undergo rapid changes. Convective cloud processes related to thunderstorms or frontal systems require an appropriate monitoring with a high temporal repeat cycle. Cloud glaciation and precipitation formation occur rapidly and imagery from current geostationary satellites at the 30 minute time scale seem to be inadequate for capturing the transient processes that influence precipitation formation. The change in time of cloud microphysical state as observable from multispectral imagery may provide useful information on the formation of precipitation. Recent work by Rosenfeld and Lensky (2000) shows that microphysical processes, relevant to precipitation, can be observed with multispectral satellite imagery.

MSG also provides novel perspectives for applications over land (see EUMETSAT-SAI Report, 1999) because of its multispectral imagery in the visible, near-infrared and thermal infrared bands. The quantitative application of the visible and near-infrared bands will be facilitated through the development of an accurate operational vicarious calibration (Govaerts, 2000a). An interesting application is the monitoring of the land surface reflectance. The utility of such a product has been demonstrated by Pinty et al. (2000a and b) who derive a Meteosat surface albedo (i.e. confined to the spectral band of the VIS channel of the current generation of Meteosat satellite) with an algorithm accounting for water vapour and ozone absorption, aerosol scattering and surface anisotropy.

4. GERB

The Geostationary Earth Radiation Budget Experiment (GERB) is a visible-infrared radiometer for Earth radiation budget studies (Harries, 2000). It makes accurate measurements of the shortwave (SW) and longwave (LW) components of the radiation budget at the top of the atmosphere. It is the first ERB experiment from geostationary orbit. It measures the solar waveband from 0.32 – 4 μm and the total from 0.32 – 30 μm . The LW from 4 – 30 μm is obtained

through subtraction. With a nominal pixel size of about 45 by 40 km (NS x EW) at nadir view it obtains an absolute accuracy better than $2.4 \text{ Wm}^{-2}\text{ster}^{-1}$ (< 1%) in the SW and better $0.4 \text{ Wm}^{-2}\text{ster}^{-1}$ for the SW. The channel co-registration with respect to SEVIRI is 3 km at the subsatellite point. The cycle time for full disk is 5 minutes for both channels (15 minutes for full radiometric performance). The derivation of products from GERB is described by Dewitte et al. (2000).

5. CONCLUDING REMARKS

The Meteosat Second Generation (MSG) system will significantly enhance the observation capabilities for rapidly changing phenomena such as cloud and water vapour structures. These will help nowcasting, short range forecasting and numerical weather prediction through improved and more frequent products. The capabilities of MSG are also expected to be of great value to research in various disciplines. Notably investigations of convective phenomena will benefit from the operational 15 minute repeat cycle. It will be a major challenge to enhance the utilisation of the multispectral image data in weather forecasting (e.g. NWP and Nowcasting). Images do contain a wealth of information on cloud and humidity structures which can be used to improve the corresponding analyses of humidity and cloud; however this has only an impact on the very short range forecast unless the wind and mass fields get also adjusted in consistent way. Sequences of images do contain information on dynamical development, which currently is hardly used in a quantitative manner. Future developments of models resolution, the ability of models to represent humidity and cloud features together with the development of 4-d assimilation systems may provide the basis for improved utilisation of the satellites image data (Eyre, 2001).

The current network of Satellite Application Facilities provides the basis for a wide use of the capabilities of MSG in various disciplines in meteorology. More information on MSG is available on the EUMETSAT webpage under www.eumetsat.de (go to Meteosat Second Generation) and www.eumetsat.de/saf/.

6. REFERENCES

- Eyre, J., Brownscombe, J. L., Allam, R. J., 1984: Detection of fog at night using Advanced Very High Resolution Radiometer (AVHRR) imagery. Meteorological Magazine, 113, 1984.
- Eyre, J., 2001: Planet Earth seen from space: Basic concepts. In seminar proceedings on 'Exploitation of the new generation of satellite instruments for numerical weather prediction. ECMWF Seminra, 4 – 8 September 2000, p. 5 – 19.
- Dewitte, S., N. Clerbaux, L. Gonzalez, A. Hermans, A. Ipe, A. Joukoff and G. Sadowski, 2000: Generation of GERB unfiltered radiances and fluxes. Proceedings of the 2000 EUMETSAT Meteorological Satellite Data Users' Conference, Bologna, EUM-P29, p. 72 – 78.

- EUMETSAT and SAI, 1999: Meteosat Second Generation Opportunities for Land Surface Applications. Report compiled by J. Cihlar, A. Belward and Y. Govaerts, EUM SP 01, pp. 67.
- Govaerts, Y. A. Arriaga and J. Schmetz, 2000a: Operational vicarious calibration of the MSG/SEVIRI solar channels. To appear in *Advances in Space Research*.
- Harries, J.E., 2000: The Geostationary Earth radiation Budget experiment: Status and Science. Proceedings of the 2000 EUMETSAT Meteorological Satellite Data Users' Conference, Bologna, EUM-P29, p. 62 – 71.
- Holmlund, K., 1998: The utilisation of statistical properties of satellite-derived atmospheric motion vectors to derive quality indicators. *Wea. Forecasting*, 13, 1093 – 1104.
- Holmlund, K., 2001: Atmospheric Motion Vectors with Meteosat Second Generation, This issue.
- König, M., S. Tjemkes and J. Kerkmann, 2001: Atmospheric instability parameters derived from MSG SEVIRI observations. This issue.
- Lutz, H J, 1999: Cloud processing for Meteosat Second Generation. EUMETSAT Technical Department, Technical Memorandum No. 4, pp. 26.
- Ma, X.L., T. Schmit and W.L. Smith, 1999: A non-linear retrieval algorithm – its application to the GOES-8/9 sounder. *J. Appl. Meteorol.*, 38, 501 – 513.
- Menzel, W.P., W.L. Smith and T.R. Stewart, 1983: Improved cloud motion wind vector and altitude assignment using VAS. *Journal of Climate and Applied Meteorology*, 22, 377-384.
- Menzel, W.P., F.C. Holt, T.J. Schmit, R.M. Aune, A.J. Schreiner, G.S. Wade and D.G. Gray, 1998: Application of GOES-8/9 soundings to weather forecasting and nowcasting. *Bull. Am. Meteor. Soc.*, 79, 2059 - 2077.
- Munro, R., G. Kelly, M. Rohn and R. Saunders, 1998: Assimilation of Meteosat radiance data within the 4dvar system at ECMWF. Proceedings of the 4th International Winds Workshop, Saanenmöser, Switzerland, 20 – 23 October 1998, EUM Publication P 24, 299 – 306.
- Orsolini, Y.J. and F. Karcher, 2000: Total-ozone imaging over North America with GOES-8 infrared measurements. *Q. J. R. Meteorol. Soc.*, 126, 1557 – 1561.
- Pili, P., 2000: Calibration of SEVIRI. Proceedings of 'The 2000 EUMETSAT Meteorological Satellite Data Users' Conference', Bologna, Italy, 29 May – 2 June 2000, EUM P-29, p. 33 – 39.
- Pinty, B., Roveda, F., Verstraete, M.M., Gobron, N., Govaerts, Y., Martonchik, J.V., Diner, D.J., and Kahn, R.A. (2000a) Surface albedo retrieval from Meteosat: Part 1: Theory, *Journal of Geophysical Research*, Vol. 105, 18099-18112.
- Pinty, B., Roveda, F., Verstraete, M.M., Gobron, N., Govaerts, Y., Martonchik, J.V., Diner, D.J., and Kahn, R.A. (2000b) Surface albedo retrieval from Meteosat: Part 2: Applications, *JGR, Journal of Geophysical Research*, Vol.105, 18113-18134.
- Riishojaard, L. P. On four-dimensional variational assimilation of ozone data in weather prediction models. *Q. J. R. Meteorol. Soc.*, 122, 1545-1571, 1996.
- Rodgers, C., 1976: Retrieval of atmospheric temperature and composition from remote measurements of thermal radiation. *Rev. Geophys. And Space Physics*.
- Rosenfeld, D., and I.W. Lensky, 2000: Satellite-based insights into precipitation formation processes in continental and maritime clouds. *Bull. American Meteorol. Soc.*, 79, 2457 – 2476.
- Saunders R.W. and K.T. Kriebel, 1988: An improved method for detecting clear sky and cloudy radiances from AVHRR data. *Int. J. Remote Sensing*, 9, 123- 150.
- Schmetz J., K. Holmlund, J. Hoffman, B. Strauss, B. Mason, V. Gaertner, A. Koch and L. van de Berg, 1993: Operational cloud motion winds from Meteosat infrared images, *J. Appl. Met.*, 32, 1206- 1225.
- Schmetz, J., C. Geijo, W.P. Menzel, K. Strabala, L. van de Berg, K. Holmlund and S. Tjemkes, 1995: Satellite observations of upper tropospheric relative humidity, clouds and wind field divergence. *Beitr. Phys. Atmosph.*, 68, 345 - 357.
- Szantai, A., F. Desalmand, M. Desbois and P. Lecomte, 2000: Tracking low-level clouds over Central Africa on Meteosat images. Proceedings of 'The 2000 EUMETSAT Meteorological Satellite Data Users' Conference', Bologna, Italy, 29 May – 2 June 2000, EUM P-29, p. 813 – 820.
- Tjemkes, S.A. and J. Schmetz, 1997: Synthetic Satellite Radiances using the Radiance Sampling Method, *J. Geophys. Res.*, Vol. 102(D2), 1807- 1818.
- Tjemkes, S. and P. Watts, 2000: Cloud properties from Meteosat. Proceedings of the 2000 EUMETSAT Meteorological Satellite Data Users' Conference, Bologna, EUM-P29, p. 314 – 317.
- Velden, C. S., D. Stettner and J. Daniels, 2000: Wind vector fields derived from GOES rapid-scan imagery. Proceedings of the 10th Conference on Satellite Meteorology and Oceanography. 9 – 14 January 2000, Long Beach California, American Meteorological Society, p. 20 - 23.

Assimilation of Meteosat radiance data within the 4D-Var system at ECMWF: Data quality monitoring, bias correction and single-cycle experiments

By ROSEMARY MUNRO, CHRISTINA KÖPKEN*, GRAEME KELLY,
JEAN-NOËL THÉPAUT and ROGER SAUNDERS
European Centre for Medium-Range Weather Forecasts, Reading, UK

(Received 23 December 2002; revised 15 October 2003)

SUMMARY

This paper describes the direct assimilation of water vapour (WV) clear-sky radiance (CSR) data from geostationary satellites within the context of the ECMWF four-dimensional variational assimilation (4D-Var) system. The assimilation of Meteosat-7 WV CSR data became operational on 9 April 2002. As 4D-Var includes a time dimension, the high temporal resolution of the geostationary radiance data can be exploited to provide information not only on the upper-tropospheric humidity but also on the upper-tropospheric wind field. The data assimilated have a spatial resolution of approximately 80 km and a time resolution of 1 hour. Extensive pre-operational monitoring of the CSR data has been carried out, showing a systematic warm bias of approximately 2–3 K in the Meteosat WV CSR data compared to radiances simulated from model first-guess fields. The systematic biases between the brightness temperatures derived from the model and the observations are investigated and compared to other satellite radiance data. For assimilation purposes this is accounted for by using a bias correction based on a statistical regression. The monitoring also shows contamination of certain time slots caused by intruding solar stray light and a certain degree of residual cloud contamination present in the CSR. Data quality control is introduced to exclude affected data. Initial single-cycle 3D-Var with first guess at appropriate time and 4D-Var experiments demonstrate both the direct and indirect effects of the Meteosat WV CSR data on the model fields, particularly of humidity and wind. The operational implementation of the assimilation of the Meteosat WV CSR data, including results from pre-operational experiments and forecast impacts, is discussed in a companion paper.

KEYWORDS: Geostationary satellites Numerical weather prediction Water vapour radiances

1. INTRODUCTION

In the context of numerical weather prediction (NWP), the primary use of radiance data from geostationary satellites has been for the generation of atmospheric motion vectors (AMVs). These products, which are produced by tracking cloud features in successive images, have been successfully assimilated for some time (Holmlund 1993; Velden *et al.* 1992; Rohn *et al.* 2001). From the Meteosat satellites, the data currently assimilated operationally at the European Centre for Medium-Range Weather Forecasts (ECMWF) are wind vectors derived from tracking cloud features in the visible, infrared (IR) and water vapour (WV) channels.

Clear-sky WV winds can also be produced from the WV radiances, in this case by tracking clear-sky moisture features, but height assignment is particularly problematic as the radiation in the WV channel under clear-sky conditions is emitted from a deep upper-tropospheric layer (Velden *et al.* 1997). An alternative approach is the direct assimilation of WV radiances within a variational data assimilation system. With the move, on 24 November 1997, to four-dimensional variational assimilation (4D-Var) as the operational system at ECMWF, a new opportunity to exploit WV clear-sky radiance (CSR) data from geostationary satellites became available. Within 4D-Var, it is possible to take advantage of the high temporal resolution of geostationary radiance data by assimilating observations at times other than 00, 06, 12 and 18 UTC, thereby providing information about the time evolution of the upper-troposphere humidity (UTH) field and indirectly the model dynamics and wind field in this region (Kelly *et al.* 1996;

* Corresponding author, present affiliation: Deutscher Wetterdienst (DWD), Postfach 10 04 65, 63004 Offenbach/Main, Germany. e-mail: christina.koepken@dwd.de

© Royal Meteorological Society, 2004.

Munro *et al.* 1999). The IR CSR data are currently used primarily for model validation, in particular for the diagnosis of the diurnal cycle in skin temperature (Köpken *et al.* 2002; Trigo and Viterbo 2003). Furthermore, future geostationary instruments will have enhanced atmospheric sounding capabilities and preparation for the use of these data in NWP is needed.

This paper describes the use of WV CSR data from Meteosat within the 4D-Var system at ECMWF and is split into two parts. This first part examines data quality and bias-related issues and also studies increment structures. After giving an overview of the basic principles of 4D-Var assimilation in section 2, the Meteosat WV CSR data are introduced in section 3. Prior to their assimilation, extensive monitoring has been carried out to examine the data quality, with emphasis on biases between the model first guess and the observations. These biases are of particular importance, as the 4D-Var assimilation system assumes unbiased observations. Also, as geostationary imagers were originally intended only to provide images for direct use in forecasting, little emphasis has been placed in the past on accurate calibration of the radiance data. Recently this calibration has improved, with a change from vicarious calibration to a more stable black-body calibration. Nonetheless, biases are still seen between the Meteosat WV CSR data and radiances simulated from model fields. These results are summarized in section 3 and different possible sources are examined in turn, including the calibration method, the radiative transfer model (RTM) used for the generation of simulated radiances, and biases in the model first-guess fields themselves. In addition, a cross-comparison with other satellite data provides an independent verification of the source of the bias. Data from the High-Resolution Infrared Sounder (HIRS) channel 12 and the Advanced Microwave Sounding Unit (AMSU)-B channel 3 on the National Oceanic and Atmospheric Administration NOAA-16 satellite (subsequently referred to as NOAA-16 HIRS-12 and AMSUB-3) are considered, in addition to WV CSR data from the WV channel on the Geostationary Operational Environmental Satellites GOES-08 and GOES-10. The NOAA-16 HIRS-12 and GOES-08 and GOES-10 WV channels have similar characteristics to the Meteosat WV channels and the NOAA-16 AMSUB-3 lies in the microwave part of the spectrum. Biases believed to originate from the Meteosat WV CSR data must be corrected before the data are used in the assimilation system. The characteristics of the bias correction scheme used are described in section 4. Subsequently, both the direct and indirect effect of the Meteosat WV CSR data on the model fields are illustrated in section 5, using results from a single-cycle 3D-Var experiment with first guess at appropriate time (FGAT) and a single-cycle 4D-Var experiment. Finally the main conclusions of the work are summarized in section 6. The companion paper (Köpken *et al.* 2004) describes the operational implementation of the assimilation of the Meteosat WV CSR data and discusses results from pre-operational experiments and forecast impacts.

2. OVERVIEW OF 4D-VAR AND ANALYSIS OF HUMIDITY

(a) *The 4D-Var formulation*

The variational method of data assimilation relies on the minimization of an objective cost function, $J(\mathbf{x})$, with respect to an atmospheric state, \mathbf{x} , which has the form, assuming Gaussian errors:

$$J(\mathbf{x}) = J^o + J^b, \quad (1)$$

where

$$J^o = \frac{1}{2} \cdot \{\mathbf{y} - \mathbf{H}(\mathbf{x})\}^T \cdot (\mathbf{O} + \mathbf{F})^{-1} \cdot \{\mathbf{y} - \mathbf{H}(\mathbf{x})\} \quad (2)$$

and

$$J^b = \frac{1}{2} \cdot (\mathbf{x} - \mathbf{x}^b)^T \cdot \mathbf{B}^{-1} \cdot (\mathbf{x} - \mathbf{x}^b). \quad (3)$$

Here \mathbf{x}^b is the background state, commonly referred to as the first guess, with estimated error covariance \mathbf{B} , and \mathbf{y} represents the observations with error covariance \mathbf{O} . Furthermore, \mathbf{H} is a suitable linearized version of the observation operator with forward model error covariance \mathbf{F} . In the case of the Meteosat radiance data, \mathbf{H} includes the RTM for the TIROS operational vertical sounder (RTTOV, Saunders *et al.* 1999). For this study, the version used was RTTOV-6M with improved predictors (Matricardi *et al.* 2001), which is equivalent to version RTTOV-7.

For a 3D-Var assimilation, the observation vector, \mathbf{y} , includes all observations within the six-hour 3D-Var assimilation window. Here the minimization is carried out using one first-guess field, irrespective of the time of the observations within the assimilation window. Alternatively, in a 3D-Var FGAT assimilation, the first-guess fields are computed for the exact time of the observations within a six-hour assimilation window using a short-range forecast derived from the last analysis. In this case, the model trajectory is not updated in the course of the minimization. Therefore, although the mean assimilation result should be improved in a 3D-Var FGAT assimilation, the dynamic information contained within the observations is not used.

In the case of the incremental formulation of 4D-Var currently in use at ECMWF (Rabier *et al.* 1998), the objective cost function is expressed as a function of the initial increment at low resolution at the time of the background, $\delta\mathbf{x}_0$, that will be added to the background to provide the analysis when the objective cost function reaches a minimum, such that

$$J(\delta\mathbf{x}_0) = J^o + J^b, \quad (4)$$

where

$$J^o = \frac{1}{2} \cdot \sum_{i=0}^N [\mathbf{d}_i - \mathbf{H}_i(\delta\mathbf{x}_i)^T \cdot (\mathbf{O}_i + \mathbf{F}_i)^{-1} \cdot \{\mathbf{d}_i - \mathbf{H}_i(\delta\mathbf{x}_i)\}] \quad (5)$$

and

$$J^b = \frac{1}{2} \cdot (\delta\mathbf{x}_0)^T \cdot \mathbf{B}^{-1} \cdot (\delta\mathbf{x}_0). \quad (6)$$

Here N is the total number of one-hour time slots within the assimilation window, \mathbf{H}_i is the tangent linear of the observation operator appropriate to time slot i , and

$$\delta\mathbf{x}_i = \mathbf{M}(t_i, t_0)(\delta\mathbf{x}_0) \quad (7)$$

is the initial increment evolved according to the tangent linear of the forecast model, \mathbf{M} . Furthermore, for timeslot i ,

$$\mathbf{d}_i = \mathbf{y}_i - H(\mathbf{x}_i), \quad (8)$$

where H is the full non-linear observation operator and \mathbf{x}_i is the background propagated in time using the full non-linear forecast model.

Consequently, in 4D-Var the input to the observation operator H includes a full non-linear model integration from the time of the background to the time of the observation, as depicted schematically in Fig. 1. The model trajectory is updated using the full non-linear model at high resolution, referred to as the outer loop, a limited number of times during the course of the minimization (currently twice in the operational ECMWF implementation), to partially account for nonlinearities in the system. Therefore, there is an implicit coupling in J^o between changes in specific humidity and the model wind and temperature fields. However in the current formulation of \mathbf{B} (Derber and Bouttier 1999), humidity and other model variables excluding temperature are assumed uncorrelated,

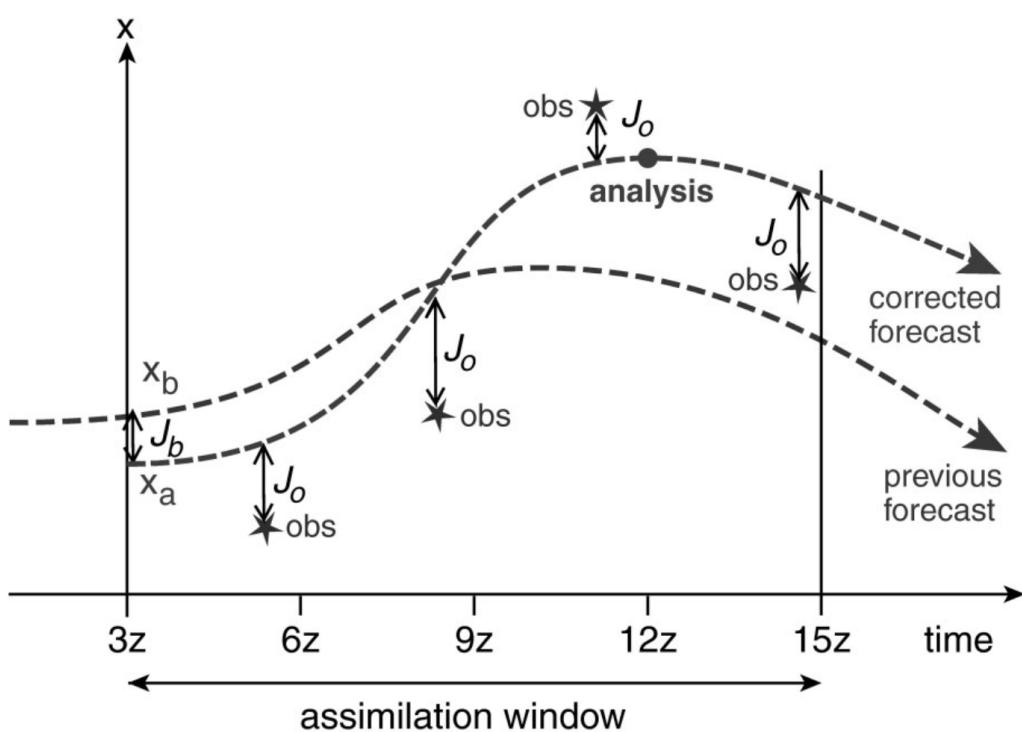


Figure 1. Schematic of the four-dimensional variational assimilation system.

and humidity and temperature are only weakly coupled through the specification of the background variances in J^b . The analysis increments are calculated during the inner loops of the minimization at lower resolution. Note that an additional cost term, J^c , is added in Eq. (4) to further constrain the fast modes of the estimated state (Gauthier and Thépaut 2001). It is omitted here for the sake of simplicity.

(b) Specific humidity analysis

Early investigation into the assimilation of Meteosat WV channel radiance data highlighted certain problems with the ECMWF humidity analysis that needed to be resolved before these data could be assimilated effectively. In particular, when the radiance data were included in the assimilation, problems with the speed of convergence of the minimization were noticed. Further investigation of the eigenvectors of the analysis system showed that undue emphasis was being given to specific datum points. These points corresponded to extremely dry model profiles associated with an unrealistic specification of the background error in specific humidity, corresponding in some cases to an error in radiance space of up to 32 K. This should be compared to a specified measurement error of 2 K. As the weight that a measurement is given in the analysis system is related to the ratio of the background to the observation error, such an unrealistic specification of background error is difficult for the assimilation to accommodate. Furthermore, there was no indication of particularly large first-guess departures for these datum points and therefore the specified background error was clearly not representative in these cases. In order to prevent these high background errors, the background error in specific humidity has been limited to a maximum of 125% of the background value. This change was implemented in operations from 13 July 1999. For further details see Andersson *et al.* (2000). Future plans at ECMWF include a complete revision of the analysis of humidity within the assimilation system. In particular, current work concentrates on a change of the humidity analysis variable



from specific humidity to normalized relative humidity (Holm *et al.* 2002). This formulation leads to a reduction of the extremely large forecast errors in radiance space in very dry areas, so that the current artificial limitation will no longer be necessary (see Fig. 20 of Köpken *et al.* 2003).

3. WV CLEAR-SKY RADIANCES AND DATA QUALITY MONITORING

(a) *The clear-sky radiance product*

The WV observations from geostationary platforms have a spatial resolution of approximately 5 km at the sub-satellite point (SSP), which is very high compared to the resolution of the current 4D-Var analysis increments (T159, approximately 125 km). Furthermore, uncertainties in the model cloud parameters and their interaction with radiation transfer, and limitations in the accuracy of the tangent linear and adjoint models of 4D-Var, currently present difficulties for the assimilation of cloudy observations. Further research in these areas is under way, but at present the measured 6.3 μm WV radiances are pre-processed by the European Meteorological Satellite (EUMETSAT) system to produce the CSR product. This product represents averages of those pixels of a 16×16 pixel quadrant that have been diagnosed as cloud-free in a histogram analysis using the IR, the WV, and, when available, the visible-wavelength channels. For further details on the EUMETSAT segment processing and cloud detection, see EUMETSAT (1996). The resulting resolution of the CSR product corresponds to approximately $80 \times 80 \text{ km}^2$ at the SSP, increasing to approximately $125 \times 125 \text{ km}^2$ at 50° from the SSP. Also included in the CSR product are the percentages of the quadrant that are cloudy and cloud-free, and the standard deviation of the brightness temperatures (TBs) from the cloud-free pixels. Additionally, quality indicators are appended for each channel. These are currently functions of the percentage of cloud-free pixels and the standard deviation of the TB within the quadrant. The CSR data are received hourly in Binary Universal Form (BUFR).

The spectral filter response functions of the Meteosat-7 and Meteosat-5 WV channels are shown for reference in Fig. 2, compared with the well-known NOAA HIRS-12 WV channel data which are routinely assimilated at ECMWF. In this case, the filter response shape for the HIRS-12 WV channel on NOAA-14 is shown. Note that the Meteosat filter functions are significantly broader than that of the NOAA-14 HIRS-12 WV channel. Figure 3 shows the Jacobians, equivalent to the vertical-weighting functions defined as $\delta(\text{TB})/\delta q$, of both the Meteosat and HIRS-12 WV channels for a moist tropical atmospheric profile. These indicate the layer of the atmosphere that emits the radiation detected by the WV channel. The Meteosat Jacobian, although having a peak at a similar pressure to the HIRS weighting function, extends over a deeper layer of the atmosphere. This is a reflection of the broader spectral-filter response function.

(b) *Calibration of the Meteosat WV radiances*

The Meteosat satellites include an on-board black body for radiometric calibration purposes. However, due to mechanical problems, the on-board black body on Meteosat-5 cannot be used. Instead, a vicarious calibration, based on collocated radiosonde data and RTM calculations, was implemented (van de Berg *et al.* 1995; EUMETSAT 1996). The vicarious calibration was used operationally until recently for Meteosat-5, Meteosat-6 and Meteosat-7 data. Monitoring of the observed radiances versus values calculated from short-range forecast first-guess fields showed that this calibration was not stable enough for data assimilation purposes. Changes of 1–2 K (occasionally even larger) occurred sometimes within one day (see e.g. Munro *et al.* 1999; Köpken 2001).



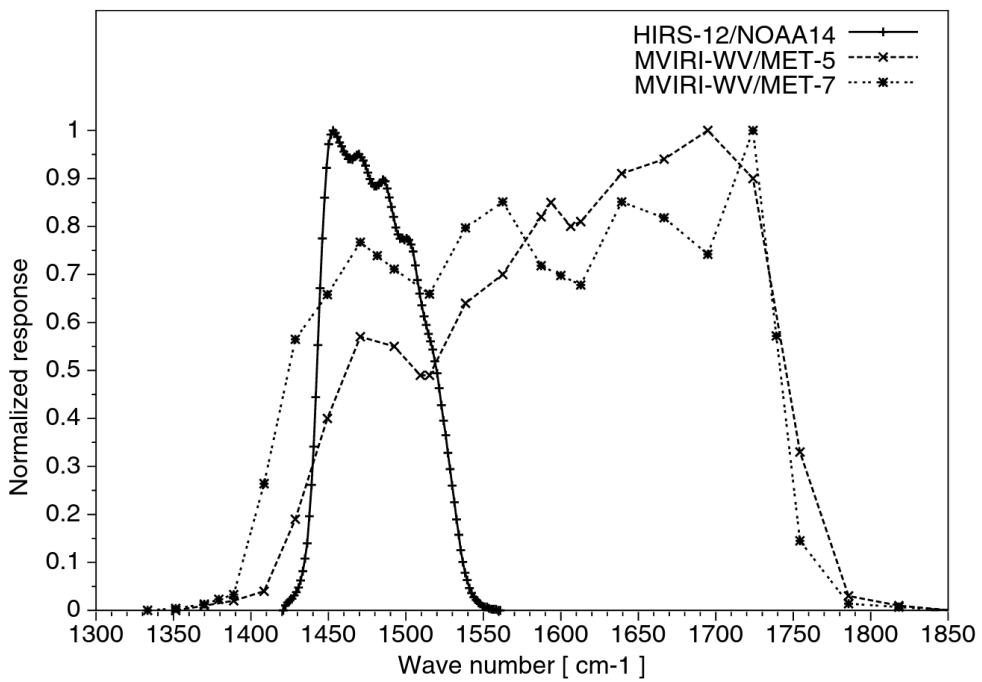


Figure 2. Filter response function versus wave number of the Meteosat-5, Meteosat-7 and NOAA-14 HIRS-12 water vapour channels.

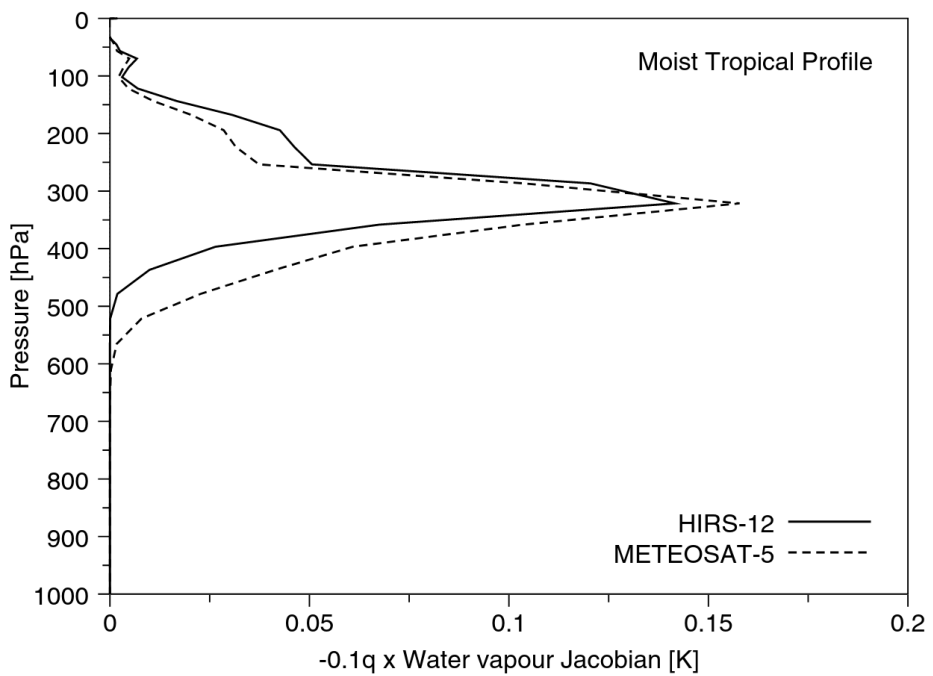


Figure 3. Vertical weighting function or Jacobian ($\delta\text{TB}/\delta q$) of the Meteosat-5 and NOAA-14 HIRS-12 water vapour channels. The Jacobian is multiplied by $-0.1q$, so it refers to the brightness temperature change (K) due to a 10% change in specific humidity.



Consequently, for Meteosat-7, a calibration based on its on-board black body has been developed, and introduced at 1230 UTC on 29 May 2000 (van de Berg, personal communication). This has resulted in much-improved stability in the radiance data (Köpken 2001). Subsequently, a cross-calibration was developed for Meteosat-5 (positioned at 63°E), using measurements from the overlap area between Meteosat-5 and Meteosat-7. Collocations are restricted to the band with a maximum viewing angle difference of 5°. Since 31 May 2001, Meteosat-5 has been operationally cross-calibrated with respect to Meteosat-7 using this method.

(c) Passive monitoring within the ECMWF model

The Meteosat CSRs have been routinely monitored within the ECMWF operational assimilation suite since 13 July 1999 (Munro *et al.* 1999). For this purpose, the expected TBs are calculated from the temperature, humidity and ozone profiles and sea surface temperatures of the model short-range forecast first-guess fields using RTTOV-6M. The expected TBs are then compared to the observed TBs. The data are not actively used in the assimilation. The evaluation of the time series of both the mean bias (mean of the observation minus model values) and the standard deviation of the biases in the Meteosat area have been enhanced to allow monitoring at the full hourly resolution of the WV CSR, in order to check for possible diurnal effects (Köpken 2001). This has proved very useful for detecting contamination effects in the WV CSR (caused by solar stray light) that were not visible in the six-hourly monitoring used previously.

Figure 4 shows an example of monitoring time series for Meteosat-7 and Meteosat-5 from mid-January to mid-March 2002. When looking at all CSR data, Meteosat-7 observations are on average about 3.8 K warmer than the TBs calculated from the model profiles. The bias for Meteosat-5 is systematically lower at 3 K, despite the fact that Meteosat-5 is cross-calibrated with respect to Meteosat-7. This difference in the monitoring occurs also when the comparison is restricted to the small strip actually used for the cross-calibration (not shown) and is thus not caused by a systematic difference in model first-guess accuracy in the different satellite areas. Further investigation is needed of the reason for this difference. Another striking feature in the hourly Meteosat monitoring time series are regular spikes. These are caused by solar stray light intruding into the radiometer close to local midnight, causing bowed bands of increased radiances and very bright spots on the WV image. Effects become stronger towards the eclipse seasons, when cold anomalies in large parts of the image are also observed, in this case after midnight. During the period when effects are strongest, some slots are excluded from processing and dissemination by EUMETSAT. However, some effects are present throughout the year. For a more detailed description of these anomalies, see Köpken (2004).

Since the introduction of the black-body calibration at the end of April 2000 for Meteosat-7, and the cross-calibration for Meteosat-5 since June 2001, the mean biases are generally stable. Previously, changes of 1–2 K or more within a few days occurred frequently. However, during the eclipses of 2000 and 2001, a slow drop and rise of the biases by about 0.5 K could be observed (see Köpken 2001). This is believed to be related to the strong temperature changes of the whole spacecraft during the eclipse season (van de Berg, personal communication). In the spring eclipse of 2002 this small change did not occur, but a sudden jump of about 0.5 K was observed after 26 February (see Fig. 4). Since then, the biases are about 3.2 K for Meteosat-7 and 2.5 K for Meteosat-5. The geographical distribution of biases indicates that the bias is fairly homogeneous, apart from local effects probably linked to clouds and convection. In particular, no dependence of the bias on scan angle is noted.

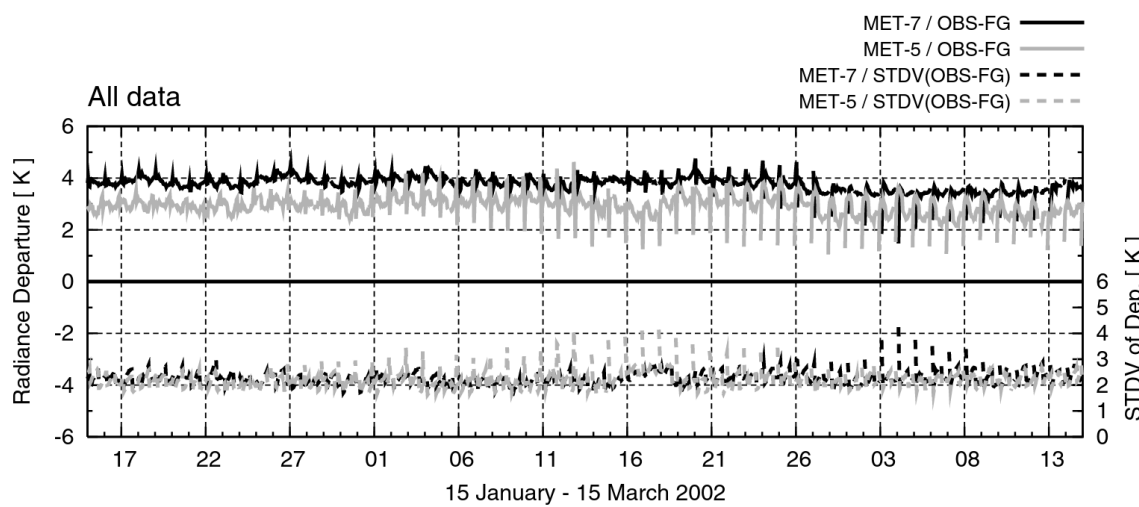


Figure 4. Time series of mean differences between water vapour clear-sky radiance observations and model first-guess brightness temperature (left axis) and standard deviation of the differences (right axis) for Meteosat-7 (black) and Meteosat-5 (grey) from 15 January to 15 March 2002.

For both satellites, a diurnal variation in biases is visible with an amplitude of a few tenths of a degree for Meteosat-7 and about 0.5 K for Meteosat-5. This variation occurs mostly over land and convective areas, and is visible from maps of mean biases on a geographical grid for 00 and 12 UTC (not shown). While some cloud contamination is present in the CSR, a main cause of these local changes in bias is believed to be linked to deficiencies in the representation of convective processes in the model. During the eclipse season, the diurnal variation in biases of Meteosat-5 increases considerably and seems more stepwise (see Fig. 4; compare end of February with mid-January). Further investigation of this behaviour is needed. The standard deviations of the difference (observation minus values calculated from first-guess fields) are similar for Meteosat-5 and Meteosat-7 at about 2.5 K. The higher values from 15 to 18 February are due to a degradation in first-guess fields caused by a gap in the operationally assimilated HIRS-12 data. The standard deviations show a regular growth pattern of about 0.5 K amplitude over each 12-hourly assimilation and monitoring period. This is caused by a growth of the model error with increasing forecast times.

In order to assimilate the WV CSR, an accurate calibration (or, as a substitute, bias correction) is essential, since the 4D-Var assumes unbiased observations. Before removing a bias, it is important to understand whether it is caused by the observations or the model. Sources for the deviations of radiances from the model may lie in the calibration of the satellite or the derivation of the CSR product, but also in inaccuracies in the RTM used, or the first-guess model profiles of temperature and humidity. Possible sources of bias are investigated further in the following sections.

(d) Radiative transfer model calculations

The accuracy of the RTM used is investigated in Fig. 5, showing a comparison of RTTOV-6M (Matricardi *et al.* 2001) to the Synthetic Satellite Radiances (SYNSATRAD, Tjemkes and Schmetz 1997) RTM, based on profiles from a set of 13 000 representative model profiles (Chevallier 1999). SYNSATRAD was shown to reproduce line-by-line calculations with very good accuracy in intercomparison studies for HIRS data (Soden *et al.* 2000; Garand *et al.* 2001) and is therefore taken as a reference. Note that line-by-line calculations will also contain errors resulting from

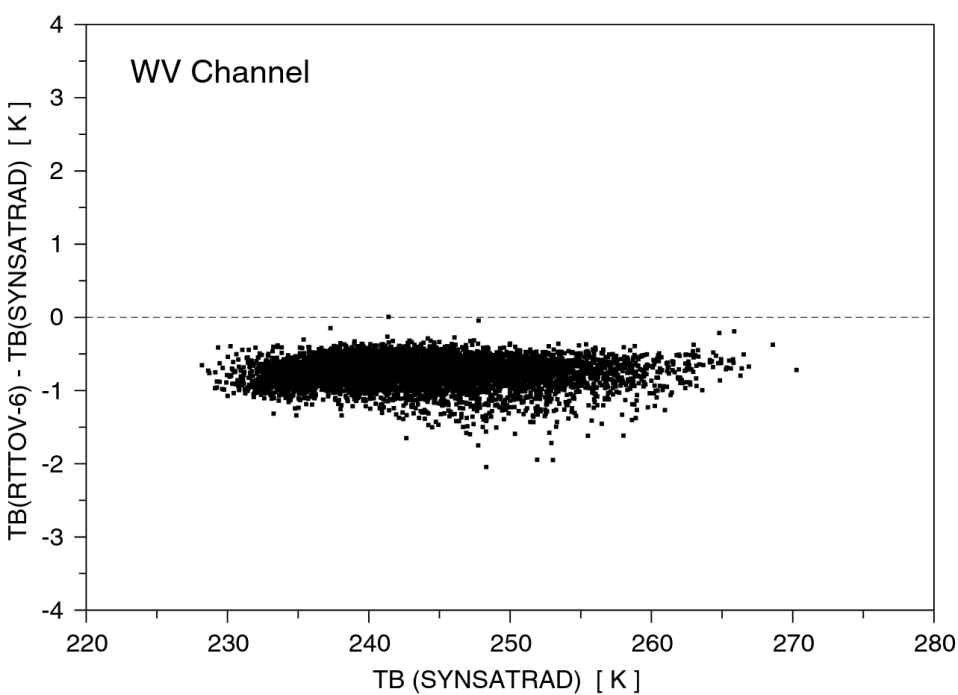


Figure 5. Differences in brightness temperature (TB) calculated with RTTOV-6M and SYNSATRAD as a function of TB from SYNSATRAD for 8987 atmospheric profiles.

inaccuracies in the input spectroscopic data, however they can be expected to provide a higher level of accuracy than faster RTMs which are necessarily simplified. In the context of this comparison, line-by-line calculations are therefore assumed to provide the closest representation of the truth. The root-mean-square error for the WV radiances is 0.7 K. This represents a considerable reduction of the large scatter in biases seen in the earlier RTTOV-5 version (see Köpken *et al.* 2002). This reduction is due to the new set of predictors used for the WV transmittances. In particular, no dependence of the bias on latitude or air mass (represented here by the modelled TB) can be seen for RTTOV-6M, whereas a dependence was present for RTTOV-5. The mean bias of -0.7 K contributes to the positive bias found for the Meteosat WV radiances when compared to the modelled radiances. This mean offset is probably caused by the fact that the regressions do not model the very wide filter function of Meteosat appropriately (see Fig. 2). However, for assimilation this bias is implicitly corrected for within the applied bias correction.

(e) Cross-calibration of satellite data

A comparison of Meteosat radiances with other satellites that sense the humidity of approximately the same atmospheric layer can help to decide whether diagnosed biases are to be attributed to the model or to the observations. This is done here by comparing the deviations of HIRS, AMSUB, GOES, and Meteosat with respect to the model first guess. The model first guess thus acts as a common reference and the differences between the spectral response functions are taken into account through the forward radiative transfer calculations. Figure 6(a) shows statistics for the WV channel of HIRS-12 and AMSUB-3 of NOAA-16 for mid-January to mid-March 2002 of observed minus model TB, averaged over a square covering the area of the Meteosat-7 disk. In order to eliminate cloud contamination for HIRS, or rain contamination for AMSUB, checks based on their window channels have been applied.



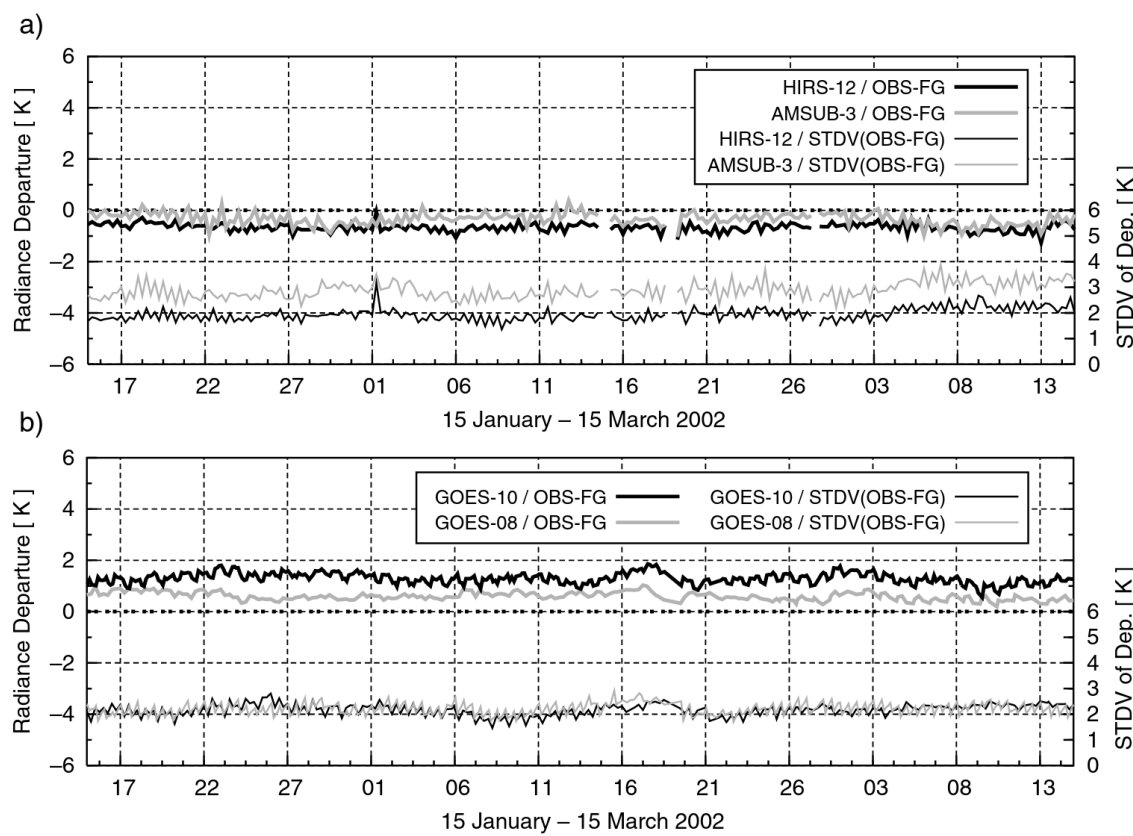


Figure 6. Time series of mean difference between observation and model first guess (OBS-FG), and its standard deviation (STDV), for water vapour clear-sky radiances of (a) NOAA-16 HIRS-12 and AMSUB-3, and (b) GOES-08 and GOES-10, from 15 January to 15 March 2002. In the case of the NOAA-16 data, averages are for a square covering the Meteosat-7 disk area.

Additionally, statistics for GOES-08 and GOES-10 imager CSR data are shown (Fig. 6(b)). In this case, data are averaged over the respective GOES disks. While the bias of Meteosat-7 is about 3.8 K (RTTOV contributes approximately 0.7 K, see above), HIRS-12 and AMSUB-3 have mean biases of about -0.7 K and -0.3 K, respectively. Results for NOAA-15 are nearly identical. Furthermore, with biases of 1.5 K and 0.8 K for GOES-10 and GOES-08 respectively, the GOES CSRs are in much closer agreement with the model than Meteosat-5 and Meteosat-7 (see Fig. 4 compared with Fig. 6(b)). For all the geostationary satellites with hourly data, a diurnal cycle can be found in the biases with smaller biases during daytime. While they are believed to be partly due to model deficiencies in convection and thus upper-level moisture, some cloud contamination is also present in the observations, although the availability of the visible channel should improve cloud detection during daytime. Note that the standard deviations of observations minus values calculated from first-guess fields are similar (about 2 K) for Meteosat, GOES, and HIRS-12, so that the Meteosat data differ only in terms of bias.

Based on these intercomparisons, the biases of Meteosat-5 and Meteosat-7 radiances compared to the model are believed to be mostly attributed to the calibration of the Meteosat satellites. The biases are currently estimated to be about 2.2 K and 3 K for Meteosat-5 and Meteosat-7, respectively. A different intercomparison study using the 183 ± 1 GHz channel of the Special Sensor Microwave Water Vapour Profiler SSM/T-2 finds a warm bias of 3 K for Meteosat-7 (Sohn *et al.* 2000), which supports the current results.



4. BIAS CORRECTION OF THE METEOSAT WV CHANNEL DATA

Since the theory of variational assimilation assumes unbiased observations and first-guess fields, a bias correction of the Meteosat observations prior to assimilation is necessary. A remaining bias or change of bias in the Meteosat calibration is readily transmitted to the model fields when CSRs are assimilated, since the only other direct control of the upper-tropospheric humidity field is through HIRS-12 data and radiosonde humidity, with the latter being used only up to 300 hPa. Additionally, biases of observations from different satellites relative to each other (e.g. Meteosat WV channel and HIRS-12) have to be eliminated to avoid presenting contradictory information to the assimilation system. The bias correction used here satisfies both purposes and follows the statistical regression method applied operationally for other radiance data (Harris and Kelly 2001). For data from the NOAA satellites, the bias correction is composed of a first correction depending on the scan angle and a second correction using the skin temperature, thicknesses of deep troposphere and stratosphere layers (300–1000 hPa and 50–100 hPa) and the vertically integrated WV. The geographical distribution of the bias of Meteosat is relatively homogeneous and does not display any characteristic variation with increasing scan angle. Therefore, no scan correction is applied to the Meteosat data. Also, the skin temperature is removed from the set of predictors, because the WV channel sounds the upper troposphere, and it is found that this predictor has no influence. The presence of the vertically integrated WV as a predictor can imply a correction of the data to fit the first-guess total column WV field. However, investigations have shown that the modulation of the bias correction through this predictor is generally not large and a removal of this predictor did not improve assimilation results. Therefore, it has been retained for consistency with the HIRS WV channel bias correction. The day–night difference in biases visible over convective land areas is believed to be a model feature and therefore no separate bias correction is attempted for day and night, or land and sea areas. To estimate observation biases of the different data, the model analyses in the vicinity of radiosonde stations are taken as the best approximation for the true atmospheric profiles. Regression coefficients are calculated using statistics of the predictors and observed minus analysis deviations from about two weeks to a month. In this way, the bias correction also implicitly includes a correction for systematic errors in the RTM used within the observation operator. For the purpose of calculation of bias statistics, the data for which the bias correction is to be calculated are excluded from the active assimilation system. To derive a bias correction value that is consistent with the biases of the data used in the assimilation, the same data quality criteria, aimed at possible solar stray light and cloud contamination, are used for accumulating the statistics. Figure 7 shows that the resulting bias correction is essentially flat (i.e. principally removing a mean bias) which is consistent with the fact that neither the CSR nor RTTOV-6M exhibit an air-mass-dependent bias. The modulation of the mean bias is of the order of a few tenths of a degree only, however the regression scheme has been retained for consistency with the usage of HIRS WV channel data. Furthermore, small deviations from a mean bias originating in errors in line-by-line calculations will be implicitly accounted for in the regression.

5. SINGLE-CYCLE ASSIMILATION EXPERIMENTS AND RESULTS

Two single-cycle experiments have been set up as part of the investigation into the impact of Meteosat WV channel radiance data on the 4D-Var assimilation system. The experiments are based on the assimilation of Meteosat-7 WV CSR in the ECMWF pre-operational testing environment as configured on 9 April 2002. The first of the two



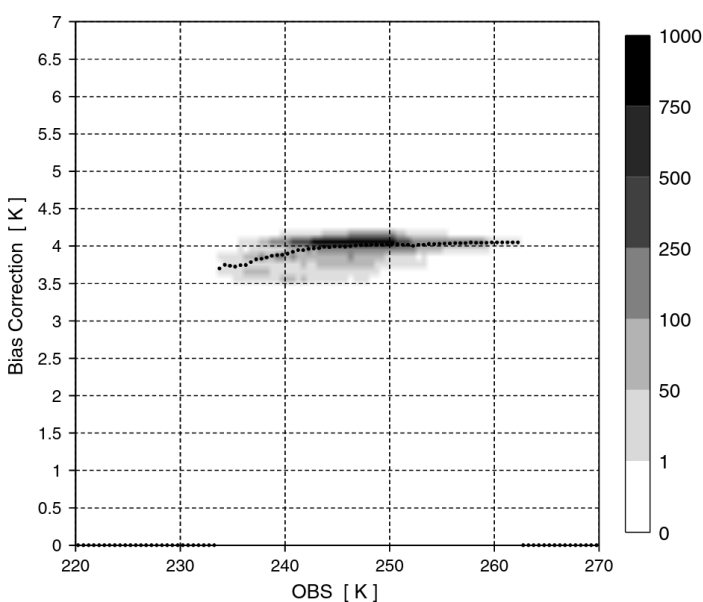


Figure 7. Scatter plot of calculated bias correction versus observed brightness temperature using data from the 12-hour 4D-Var cycle at 00 UTC on 3 March 2002. The grey scale gives the number of observations and the black dotted line shows the mean bias correction value within each temperature bin.

experiments is a 3D-Var FGAT for a single cycle in which only Meteosat-7 WV CSR data are assimilated. No other data are included. The second is a 4D-Var experiment for a single cycle including all operationally assimilated observations plus Meteosat-7 data. The 3D-Var FGAT and 4D-Var experiments are not carried out for the same assimilation cycle. This is not considered to be a problem since significantly more observations are used in a 4D-Var assimilation due to the longer time window and therefore even experiments carried out for the same cycle could not be directly compared.

(a) 3D-Var FGAT

The single cycle 3D-Var FGAT analysis is done for 00 UTC on 7 April and is initialized from the pre-operational testing environment. In this experiment only the Meteosat-7 WV CSR data are assimilated using the bias correction as described in section 4. For assimilating the CSRs, several quality control steps are applied. First, data from time slots that may be affected by solar stray light are excluded (resulting for this experiment in exclusion of data from 23, 00, 01 and 02 UTC). This is based on observation time and date. To minimize remaining cloud influence in the CSR, data with a low percentage of clear pixels in the CSR are excluded; for more details see Köpken *et al.* (2004). Also, data with a higher percentage of clear pixels are given preference within the data thinning step where data are thinned geographically to 1.25° resolution. Furthermore, data over high orography and at large scanning angles ($>60^\circ$) are excluded, as the cloud analysis is potentially less reliable for high view angles and RTTOV is valid only up to angles of 65° . Finally a first-guess check and an additional variational quality control are applied (Andersson and Järvinen 1999). Additional details on these quality checks can be found in Köpken *et al.* (2004).

The information contained in the WV CSRs is primarily a description of the upper-troposphere humidity field with secondary information about upper-troposphere temperature. Any information about the wind field is implicit and depends on the time evolution of the CSR product rather than its instantaneous state. The 3D-Var does not include the time dimension via a model integration (and its adjoint) for deriving the



analysis increments (analysis minus first-guess fields). Therefore the 3D-Var increments do not reflect the temporal evolution of the atmospheric state or the CSR over the assimilation window, but only reflect the direct influence of the Meteosat-7 WV CSR data on the atmospheric state in terms of humidity and temperature.

The main features of these analysis increments are as follows. First the increments in relative humidity (RH) (Fig. 8) are largely confined to the Meteosat-7 disk area. Any increments outside this area are limited and may be explained in terms of the horizontal correlations in the background error specification (Derber and Bouttier 1999). The increments in RH typically lie in the range $\pm 15\%$ and are very structured in the horizontal. Within the Meteosat-7 disk area, the dense Meteosat-7 WV CSR observations dominate the background error in the determination of the structure of the increments, so that these do not reflect the broader scale of the background error correlations.

An example of the vertical structure of the increments is given in Fig. 9, showing a vertical cross-section through the RH increments at 40°E . The increments typically occur between 100 and 700 hPa, peaking at 300 to 400 hPa. The peak and vertical extent of the increments clearly reflect the Meteosat WV channel sensitivity as shown in Fig. 3, but are modulated by the first-guess errors and vertical correlation functions. This increases the vertical extent and shifts the peak of the increments slightly downwards compared to the primary radiance sensitivity. It can also be clearly seen that the vertical extent of the increments is limited by tropopause height with its typical variation with latitude.

It should be noted that, in some instances (e.g. at 40°N), the increments may reach the surface despite the fact that the WV channel is not sensitive to the low levels of the atmosphere. To further illustrate this physically undesirable behaviour, the vertical structure of the increments is shown for two specific profiles (Fig. 10), one at 12°N with positive increments and one at 39°N with negative increments. The profiles are displayed both in terms of specific humidity, q , (the analysis variable) and as RH. In both cases, the increments in q (Figs. 10(a) and (b)) at the surface are of equal or even larger magnitude than the increments at the peak of the WV weighting function, although the WV CSR does not provide information about the surface. Such increments at low levels can arise from high vertical correlation in the background error specification, derived from statistics of forecast errors (Derber and Bouttier 1999). If the vertical correlation is sufficiently broad for a given location, an increment placed at 400 hPa (for example) to fit Meteosat-7 WV CSR measurements may result in a correlated increment at lower levels in order to satisfy the background error constraints. Furthermore, as the analysis variable, q , increases strongly towards the surface, so do the background errors for q , resulting in less constraint on the minimization at low levels. In this way the minimization may generate increments at the surface, even though they may not be directly indicated or constrained by the Meteosat WV CSR data. In terms of RH (Figs. 10(c) and (d)), the important variable for the physical processes, the main increments do reflect the peak of the WV channel weighting function with maximum increments at about 300 and 400 hPa, respectively, for these example profiles. However, small increments of about 2% in RH occur also at lower levels (below 700 hPa). It is likely that physical parametrizations within the model (e.g. the convection scheme) are sensitive to such increments. These effects are considered to be unsatisfactory but are expected to be eliminated with the revision of the analysis of humidity within the assimilation and the move from specific humidity to normalized relative humidity as the analysis variable (Holm *et al.* 2002). Experiments have been conducted using the new background error covariances derived in the context of the ongoing revision of



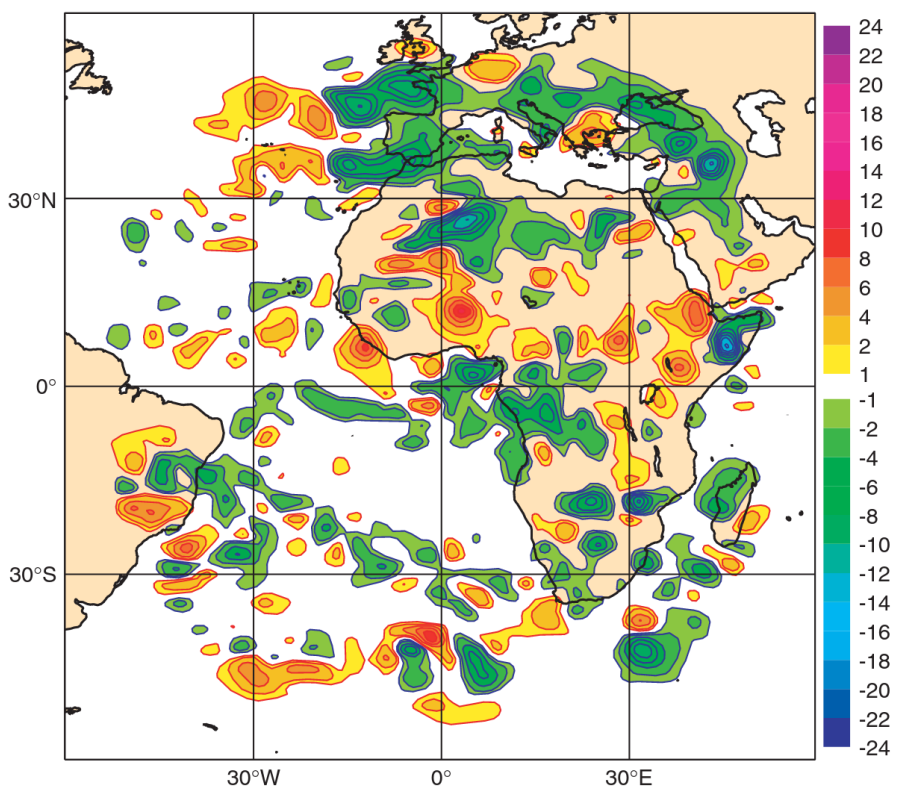


Figure 8. Relative humidity increments (analysis minus first guess) at 400 hPa for the 3D-Var First Guess at Appropriate Time experiment for 00 UTC on 7 April 2002. The colour scale gives the relative humidity increments as a percentage difference.

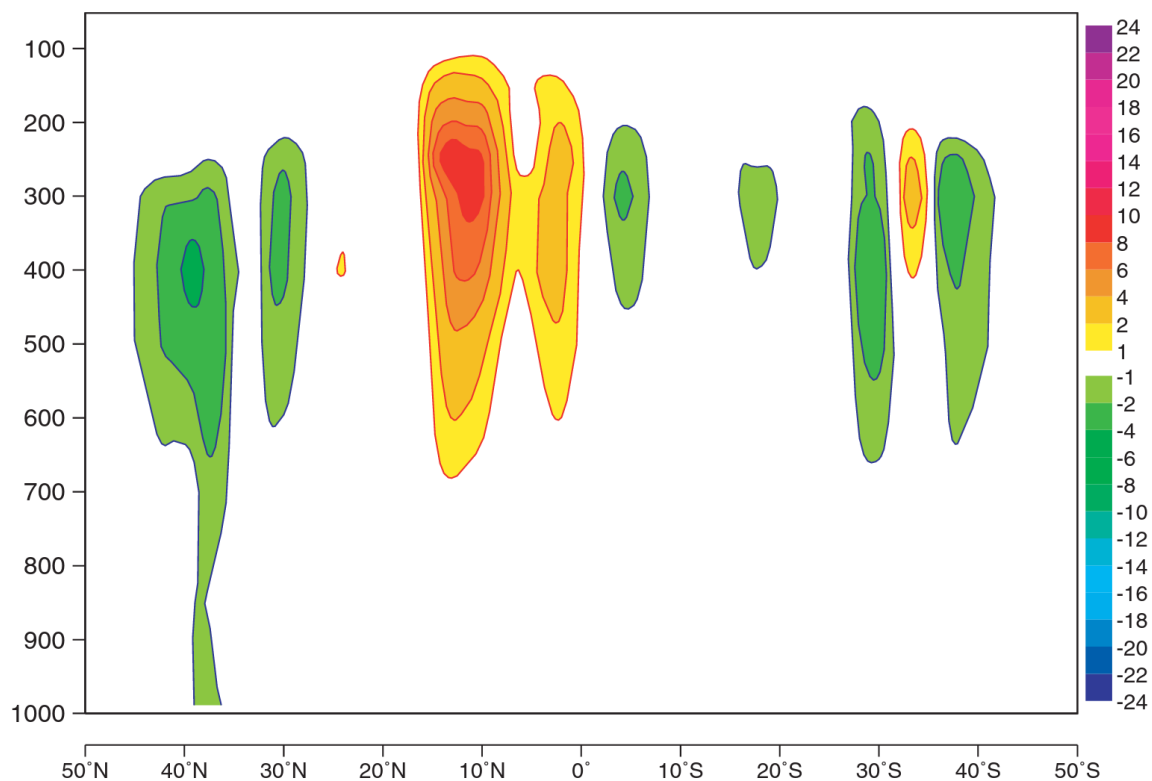


Figure 9. Pressure versus latitude cross-section of the relative humidity increments (analysis minus first guess) at 40°E for the same experiment and time as Fig. 8. Colour scale is as Fig. 8.



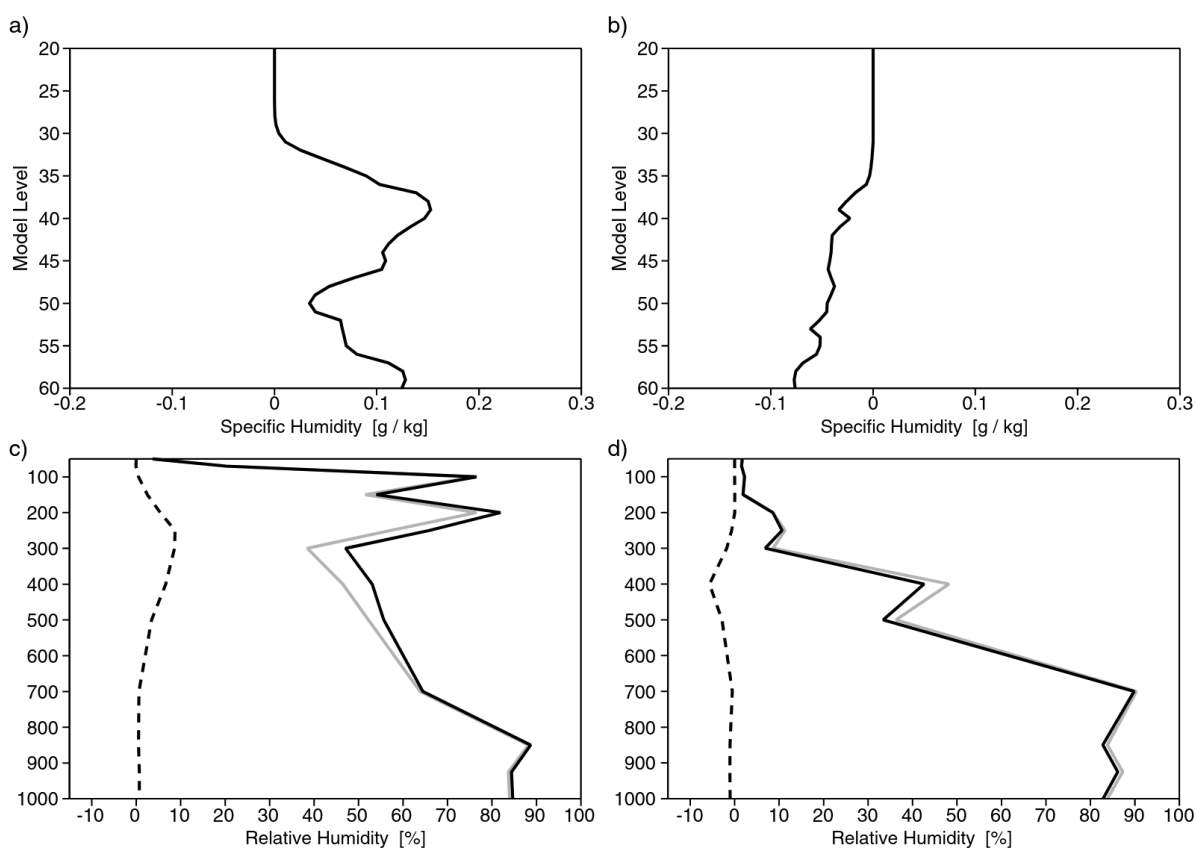


Figure 10. Profile of humidity increments at 40°E for the same experiment and time as Fig. 8: specific humidity at (a) 12°N and (b) 39°N, with altitude shown as model levels with 25 ≈ 100 hPa, 30 ≈ 200 hPa, 33 ≈ 300 hPa, 39 ≈ 500 hPa and 44 ≈ 700 hPa; (c) and (d) as (a) and (b), but for relative humidity (dashed) versus pressure (hPa), and also showing the first-guess (grey solid) and the analysis (black solid) profiles.

the humidity analysis variable. Here the occurrence of near-surface increments due to assimilation of Meteosat WV radiance data appears significantly reduced (see Fig. 22 of Köpken *et al.* 2003). It can therefore be expected that, following revision of the humidity analysis variable, more optimal use will be made of the Meteosat WV CSR and other similar data.

(b) 4D-Var

The 4D-Var experiment is a single-cycle experiment corresponding to the pre-operational testing environment at 12 UTC on 1 April 2002. In addition to the conventional *in situ* measurements, both Meteosat-5 and Meteosat-7 AMVs are included in the assimilation. AMSU-A radiance data, HIRS-12 WV data, scatterometer winds and Special Sensor Microwave/Imager integrated total column WV data are also assimilated. Additionally the Meteosat-7 WV CSR data are assimilated as described above. The current assimilation window for 4D-Var is 12 hours. In the control experiment the Meteosat-7 WV CSR data are excluded from the assimilation.

Since the 4D-Var assimilation includes a model integration over the 12-hour 4D-Var assimilation window, implicit information about the evolution of the wind field is provided by information on the time evolution of the WV field contained in the high-temporal-resolution WV CSR data. To examine the impact of the assimilation of the Meteosat WV radiance data on the ECMWF 4D-Var assimilation system, it is therefore relevant to examine the changes to the vector wind fields in addition to the upper-troposphere humidity and temperature fields.

Figure 11 shows the observed increments (analysis minus first guess) in RH at 300 hPa. Increments shown are for the start of the assimilation window, i.e. here 03 UTC (cf. Fig. 1). In general, increments lie in the range $\pm 25\%$ and are extremely local in nature, as discussed for the 3D-Var experiment. The increments are vertically coherent (other levels not shown) and on average there appears to be more moistening than drying in this case. A full discussion of the mean influence of the Meteosat WV CSR data on the assimilation model fields is given in Köpken *et al.* (2004).

Figure 12 shows the observed increments in temperature at 300 hPa. These are generally in the range ± 0.6 K and arise both from the sensitivity of the Meteosat WV channel to temperature, as described by the RTTOV-6M, and via the coupling implicit in the 4D-Var minimization (see section 2). Note that the broader horizontal scale seen in the temperature increments (compared with the humidity increments) is a reflection of the difference in horizontal correlations imposed by the background error structure functions.

Examining the vector wind increments clearly shows the potential of the Meteosat WV radiance data to correct the model dynamics in the upper troposphere. Figure 13 shows the vector wind difference field and Fig. 14 the first-guess wind field for the control. Both fields are for the start of the assimilation window, i.e. here 03 UTC at 300 hPa. The contours give the associated speed of the wind difference vectors. The increments clearly occur primarily within the Meteosat area. However, especially in the jet-stream areas outside the western edge of the disk observed by Meteosat-7, increments extend further upstream. This is linked to 4D-Var using data from the following 12 hours to correct the initial state at the beginning of this window. In this analysis case the influence of the CSR data is marked in the region of the trough around 25°N, 20°W, and also in the region 15°S, 25°W. It is also possible to see adjustments to the subtropical and midlatitude jets, demonstrating the ability of the WV radiance data to correct the model wind field, both in tropical and extratropical regions. Furthermore, the difference fields show coherence over a relatively deep vertical layer which is appropriate to the response function of the instrument. Early investigations indicating a broadly similar response in terms of horizontal increment structures may be obtained from the assimilation of the associated clear-sky WV wind product (Munro *et al.* 1998), however differences in data coverage and problems associated with the assignment of a single height to the wind vector will result in differences in impact. It would clearly be desirable to develop a more sophisticated method for describing the vertical distribution of information in the clear-sky WV wind product (Kelly *et al.* 1998) that more realistically represents the thickness of the atmospheric layer from which the wind information is derived. Work is ongoing at ECMWF in this area (personal communication, N. Bormann, ECMWF).

6. CONCLUSIONS

The processing and direct assimilation of clear-sky WV radiances from geostationary imagers has been implemented within the 4D-Var system at ECMWF. The current study concentrates on the use of WV CSR from the Meteosat satellites and extensive data monitoring and pre-operational tests have been carried out. The monitoring of the Meteosat WV CSR radiance data shows that the Meteosat-7 WV radiances have a positive bias of approximately 3 K with respect to radiances calculated from model first-guess fields. By comparison, the WV channel radiance data from NOAA-16 HIRS, AMSUB-3, and from GOES-08 and GOES-10 fit radiances calculated from model first-guess fields to within approximately 1 K in terms of bias. Despite cross-calibration of



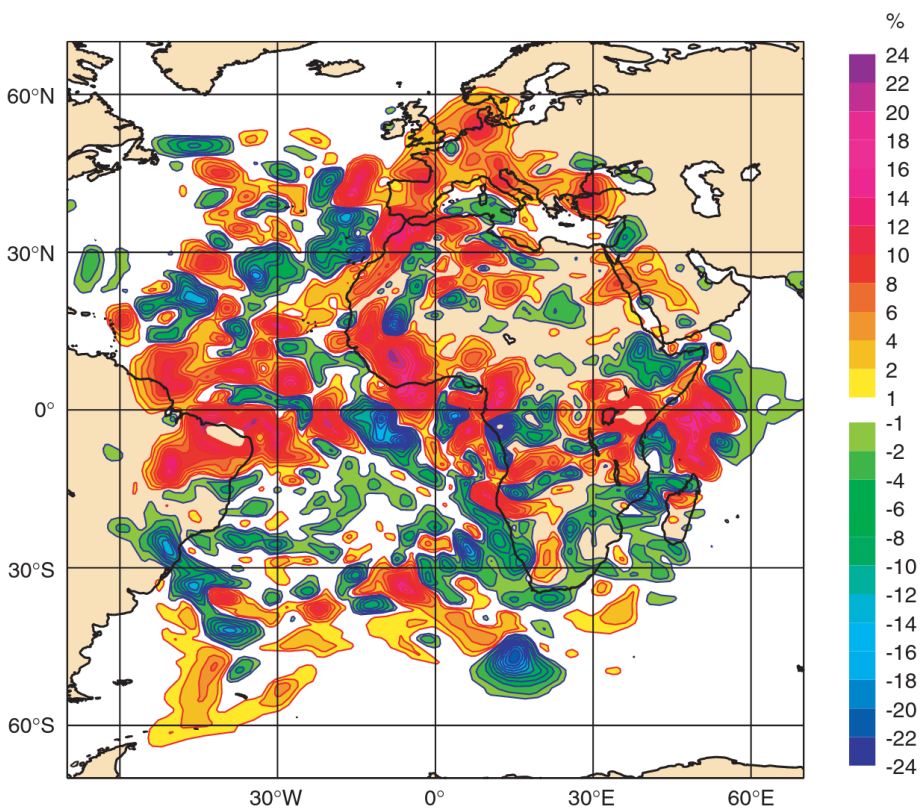


Figure 11. Relative humidity increments (analysis minus first guess) at 300 hPa for the single-cycle 4D-Var experiment. The differences are calculated from the analysis fields (valid at 03 UTC) from the analysis cycle of 12 UTC on 1 April 2002. Colour scale as Fig. 8.

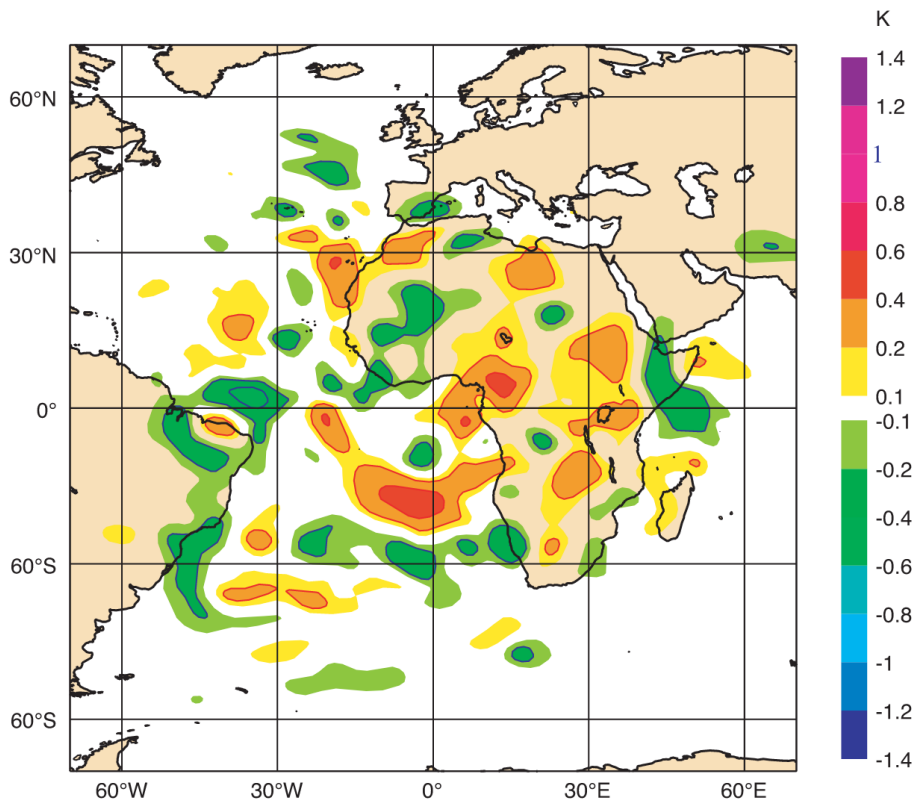


Figure 12. As for Fig. 11, but showing temperature increments (K).



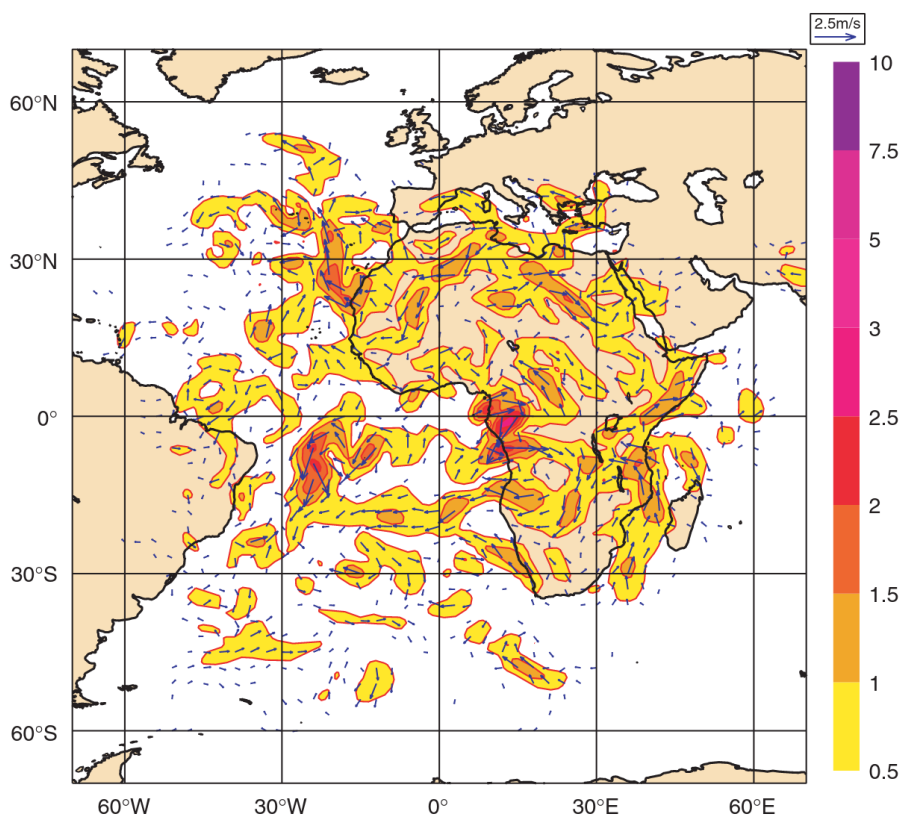


Figure 13. As for Fig. 11, but showing vector wind increments. Arrow lengths and colour scale give the wind speed in m s^{-1} .

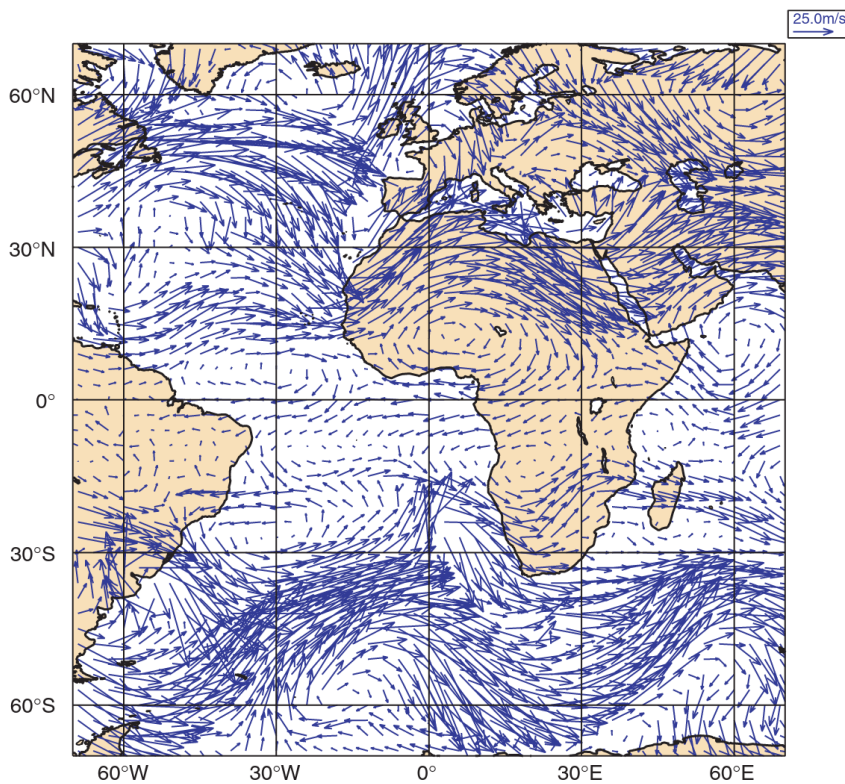


Figure 14. Vector wind first-guess field at 300 hPa for the same experiment and time as Fig. 11.



Meteosat-5 data with respect to Meteosat-7 data, Meteosat-5 WV CSR data are systematically colder than those of Meteosat-7 by approximately 0.7 K. Prior to assimilation, the bias in the WV channel data is removed using a statistical bias correction based on model predictors. Data affected by solar stray light and residual cloud contamination are also excluded. Data are then assimilated using a thinning to 1.25° and hourly time resolution.

A 3D-Var FGAT single-cycle experiment with assimilation of only the Meteosat-7 WV CSR has demonstrated the direct impact of the Meteosat WV radiance data on the humidity fields of the model. The increments are coherent over a vertical range consistent with the Meteosat WV channel weighting functions. However, increment structures are modulated by the first-guess error covariances. This leads on some occasions to small increments in RH close to the surface where the WV observations exhibit no sensitivity. This problem is expected to be resolved with the planned revision of the analysis of humidity within the assimilation (Holm *et al.* 2002). Furthermore a 4D-Var single-cycle experiment has clearly shown that the direct assimilation of high-temporal-resolution geostationary WV channel radiance data, within a 4D-Var system, may be used indirectly to correct the model dynamics in the upper troposphere. The impact of the assimilation of the Meteosat WV CSR data on operational forecasts is described in Köpken *et al.* (2004).

ACKNOWLEDGEMENTS

This work was carried out through the EUMETSAT Fellowship programme hosted in this case by ECMWF. The contributions and assistance provided by Erik Andersson, Mike Fisher, Jan Haseler, Marco Matricardi, Rob Hine and others at ECMWF, and Stephen Tjemkes, Leo van de Berg, Johannes Schmetz and Kenneth Holmlund of EUMETSAT have been greatly appreciated. The authors also wish to thank the reviewers for their helpful comments.

REFERENCES

- | | | |
|--------------------------------|------|---|
| Andersson, E. and Järvinen, H. | 1999 | Variational quality control. <i>Q. J. R. Meteorol. Soc.</i> , 125 , 697–722 |
| Andersson, E., Fisher, M., | 2000 | Diagnosis of background errors for observed quantities in a variational data assimilation scheme, and the explanation of a case of poor convergence. <i>Q. J. R. Meteorol. Soc.</i> , 126 , 1455–1472 |
| Munro, R. and McNally, A. | | |
| Chevallier, F. | 1999 | ‘A TIGR-like sampled database of atmospheric profiles from the ECMWF 50-level forecast model.’ NWP SAF Report No. 1, available from ECMWF, Shinfield Park, Reading RG2 9AX, UK |
| Derber, J. and Bouttier, F. | 1999 | A reformulation of the background error covariance in the ECMWF global data assimilation system, <i>Tellus</i> , 51A , 195–222 |
| EUMETSAT | 1996 | ‘MTP MPEF Algorithm Specification Document.’ EUM-MTP-SPE-030 and Appendix A, available from http://www.eumetsat.de/ , follow links to Data, Products and services, Meteorological product extraction, Documentation |



- Garand, L., Turner D. S., Larocque, M., Bates, J., Boukabara, S., Brunel, P., Chevallier, F., Deblonde, G., Engelen, R., Hollingshead, M., Jackson, D., Jedlovec, G., Joiner, J., Kleespies, T., McKague, D. S., McMillin, L., Moncet, J.-L., Pardo, J. R., Rayer, P. J., Salathe, E., Saunders, R., Scott, N. A., Van Delst, P. and Woolf, H., Gauthier, P. and Thépaut J.-N. 2001 Radiance and Jacobian intercomparison of radiative transfer models applied to HIRS and AMSU channels. *J. Geophys. Res.*, **106**, 42017–42031
- Harris, B. A. and Kelly, G. 2001 Impact of the digital filter as a weak constraint in the preoperational 4DVAR assimilation system of Météo-France. *Mon. Weather Rev.*, **129**, 2089–2102
- Holm, E., Andersson, E., Beljaars, A., Lopez, P., Mahfouf, J.-F., Simmons, A. and Thépaut, J.-N. Holmlund, K. 2002 A satellite radiance bias correction scheme for radiance assimilation. *Q. J. R. Meteorol. Soc.*, **127**, 1453–1468
- Kelly, G., Tomassini, M. and Matricardi, M. 1993 ‘Assimilation and Modelling of the Hydrological Cycle: ECMWF’s Status and Plans.’ Tech. Memorandum No. 383, available from ECMWF, Shinfield Park, Reading RG2 9AX, UK
- Kelly, G., Munro, R., Rohn, M. and Holmlund, K. 1996 ‘Operational water vapour wind vectors from Meteosat imagery data.’ Pp. 77–84 of Proceedings of the Second International Winds Workshop, Tokyo, Japan, 13–15 December 1993, EUMETSAT publ. 14.
- Köpken, C. 1998 ‘Meteosat cloud-cleared radiances for use in three/four dimensional variational data assimilation.’ Pp. 105–116 of Proceedings of the Third International Winds Workshop, Ascona, Switzerland, 10–12 June 1996, EUMETSAT publ. 18.
- Köpken, C., Kelly, G. and Thépaut, J.-N. 1998 ‘Impact of atmospheric motion vectors (AMVs) on the ECMWF system and the development of a water vapour AMV observation operator.’ Pp. 125–137 of Proceedings of the Fourth International Winds Workshop, Saanenmöser, Switzerland, 20–23 October 1998, EUMETSAT publ. 24.
- Köpken, C., Kelly, G. and Thépaut, J.-N. 2001 ‘Monitoring of Meteosat WV radiances and solar stray light effects.’ EUMETSAT/ECMWF Fellowship Report No. 10.
- Matricardi, M., Chevallier, F. and Tjemkes, S. 2001 ‘Solar stray light effects in Meteosat radiances observed and quantified using operational data monitoring at ECMWF. *J. Appl. Meteorol.*, **43**, 28–37.
- Munro, R., Kelly, G., Rohn, M. and Saunders, R. 2001 ‘Monitoring and assimilation of Meteosat radiances within the 4DVAR system at ECMWF.’ EUMETSAT/ECMWF Fellowship Report No. 9.
- Munro, R., Kelly, G., Rohn, M. and Saunders, R. 2003 ‘Assimilation of geostationary WV radiances from GOES and Meteosat at ECMWF.’ EUMETSAT/ECMWF Fellowship Report No. 14.
- Rabier, F., Thépaut, J.-N. and Courtier, P. 2003 Assimilation of Meteosat radiance data within the 4D-Var system at ECMWF: Assimilation experiments and forecast impact. *Q. J. R. Meteorol. Soc.*, **130**, 2277–2292
- Rohn, M., Kelly, G. and Saunders R. 2001 ‘An improved fast radiative transfer model for the assimilation of radiance observations.’ Tech. Memorandum No. 345, available from ECMWF, Shinfield Park, Reading RG2 9AX, UK
- Rohn, M., Kelly, G. and Saunders R. 1998 ‘Assimilation of Meteosat radiance data within the 4DVAR system at ECMWF.’ Proceedings of the Fourth International Winds Workshop, Saanenmöser, Switzerland, 20–23 October 1998, 299–306
- Rohn, M., Kelly, G. and Saunders R. 1999 ‘Assimilation of Meteosat radiance data within the 4DVAR system at ECMWF.’ EUMETSAT/ECMWF Fellowship Report No. 8.
- Rohn, M., Kelly, G. and Saunders R. 2001 Extended assimilation forecast experiments with a four-dimensional variational assimilation system. *Q. J. R. Meteorol. Soc.*, **124**, 1861–1887
- Rohn, M., Kelly, G. and Saunders R. 2001 Impact of a new cloud motion wind product from Meteosat on NWP analyses and forecasts. *Mon. Weather Rev.*, **129**, 2392–2403

- Saunders, R., Matricardi, M. and Brunel, P. 1999 An improved fast radiative transfer model for assimilation of satellite radiance observations. *Q. J. R. Meteorol. Soc.*, **125**, 1407–1425
- Soden, B., Tjemkes, S., Schmetz, J., Saunders, R., Bates, J., Ellingson, B., Engelen, R., Garand, L., Jedlovec, G., Kleespies, T., Knig, M., Randel, D., Rayer, P., Salathe, E., Schwarzkopf, D., Scott, N., Sohn, B., de Souza-Machado, S., Strow, L., Tobin, D., Van Delst, P. and Wehr, T. 2000 An intercomparison of radiation codes for retrieving upper tropospheric humidity in the 6.5-micron band: A report from the 1st GVAP Workshop. *Bull. Am. Meteorol. Soc.*, **81**, 797–808
- Sohn, B. J., Schmetz, J., Tjemkes, S., Knig, M., Lutz, H., Arriaga, A and Chung, E. S. 2000 Intercalibration of the Meteosat-7 water vapour channel with SSM/T-2. *J. Geophys. Res.*, **105**, 15673–15680
- Tjemkes, S. and Schmetz, J. 1997 Synthetic satellite radiances using the radiance sampling method. *J. Geophys. Res.*, **102(D)**, 1807–1818
- Velden, C. S., Hayden, C. M., Menzel, W. P., Franklin, J. L. and Lynch, J. S. 2003 Clear-sky window channel radiances: a comparison between observations and the ECMWF model. *J. Appl. Meteorol.*, **42**, 1463–1479
- Velden, C. S., Niemann, S. J., Menzel, W. P. and Wanzong, S. T. 1995 On the calibration of the Meteosat Water Vapour channel. *J. Geophys. Res.*, **100**, 21069–21076
- Velden, C. S., Niemann, S. J., Menzel, W. P. and Wanzong, S. T. 1992 The impact of satellite-derived winds on numerical hurricane track forecasting. *Weather and Forecasting*, **7**, 107–118
- Velden, C. S., Niemann, S. J., Menzel, W. P. and Wanzong, S. T. 1997 Upper tropospheric winds derived from geostationary satellite water vapour observations. *Bull. Am. Meteorol. Soc.*, **78**, 173–195



Assimilation of SEVIRI infrared radiances with HIRLAM 4D-Var

M. Stengel,^{a*} P. Undén,^a M. Lindskog,^a P. Dahlgren,^a N. Gustafsson^a and R. Bennartz^b

^aSwedish Meteorological and Hydrological Institute, Norrköping, Sweden

^bAtmospheric and Oceanic Sciences Department, University of Wisconsin, Madison, Wisconsin, USA

ABSTRACT: Four-dimensional variational data assimilation (4D-Var) systems are ideally suited to obtain the best possible initial model state by utilizing information about the dynamical evolution of the atmospheric state from observations, such as satellite measurements, distributed over a certain period of time. In recent years, 4D-Var systems have been developed for several global and limited-area models. At the same time, spatially and temporally highly resolved satellite observations, as for example performed by the Spinning Enhanced Visible and InfraRed Imager (SEVIRI) on board the Meteosat Second Generation satellites, have become available.

Here we demonstrate the benefit of a regional NWP model's analyses and forecasts gained by the assimilation of those radiances. The 4D-Var system of the High Resolution Limited Area Model (HIRLAM) has been adjusted to utilize three of SEVIRI's infrared channels (located around 6.2 μm , 7.3 μm , and 13.4 μm , respectively) under clear-sky and low-level cloud conditions. Extended assimilation and forecast experiments show that the main direct impact of assimilated SEVIRI radiances on the atmospheric analysis were additional tropospheric humidity and wind increments. Forecast verification reveals a positive impact for almost all upper-air variables throughout the troposphere. Largest improvements are found for humidity and geopotential height in the middle troposphere. The observations in regions of low-level clouds provide especially beneficial information to the NWP system, which highlights the importance of satellite observations in cloudy areas for further improvements in the accuracy of weather forecasts. Copyright © 2009 Royal Meteorological Society

KEY WORDS limited-area NWP model; IR satellite observations; clear-sky conditions; low-level clouds

Received 28 April 2009; Revised 2 July 2009; Accepted 21 July 2009

1. Introduction

Since the first usage of satellite observations in Numerical Weather Prediction (NWP) systems, which focused on the TIROS Operational Vertical Sounder (TOVS), this type of observation has become increasingly important for atmospheric analyses and weather forecasting (Kelly and Thépaut, 2007). The introduction of variational data assimilation and the development of fast radiative transfer models and their adjoints have enabled the direct assimilation of satellite radiances into NWP systems (e.g. Andersson *et al.*, 1994). This approach provides a more efficient and less time-consuming use of satellite observations by avoiding preceding retrievals of atmospheric parameters, which can be subject to additional errors.

For global NWP models, satellite data nowadays contribute an amount of information to the atmospheric analysis which is comparable to radiosondes (Kelly and Thépaut, 2007). The main focus in recent years has been on polar-orbiting satellites carrying sounding instruments such as the Advanced Microwave Sounding Unit (AMSU), the Atmospheric Infrared Sounder (AIRS), or the Infrared Atmospheric Sounding Interferometer (IASI). Their spatial coverage is high compared to

ground-based measurements. In remote and data-sparse regions, like the Tropics or the Southern Hemisphere, satellite data have become the single most important source of observational data and the biggest analysis increments are usually found there. These regions also show the largest increase in forecast accuracy due to the satellite data. In the Northern Hemisphere, which is characterised by denser ground-based measurements, positive impacts of these observations are mostly found in the medium- and long-range forecasts, after an integration time of a few days.

Besides polar-orbiting satellites, geostationary instruments, such as the Meteosat Visible and InfraRed Imager (MVIRI) and the Spinning Enhanced Visible and InfraRed Imager (SEVIRI), on board the Meteosat satellites were also found to be a valuable source of information and were introduced to data assimilation successfully in recent years. On the one hand, those instruments have for the time being lower spectral resolution, and therefore less capability in terms of vertical sounding of the atmosphere than polar-orbiting instruments. On the other hand, geostationary instruments provide a comprehensive and almost continuous picture of the evolution of weather phenomena due to their high spatial and temporal resolution. Studies highlighting the impact of the geostationary radiances on the European Centre for Medium-Range

*Correspondence to: M. Stengel, FoUp, Swedish Meteorological and Hydrological Institute, Folkborgsvagen 1, 601 76 Norrköping, Sweden.
E-mail: martin.stengel@smhi.se

Weather Forecasts (ECMWF) model are for example documented in Köpken *et al.* (2004) for MVIRI on board Meteosat-7 and Szyndel *et al.* (2005) for SEVIRI on board Meteosat-8.

Evaluating the benefit of satellite observations for regional NWP models is somewhat harder than for global models, since model domains are usually much smaller and the integration time is typically not longer than two or three days. The impact of assimilated satellite data on regional NWP models might further strongly depend on the region where the model is run. Operational limited-area models in Europe and North America usually also benefit strongly from the dense upper-air observation network of radiosondes and aircraft measurements and are constrained by the host model's accuracy at the boundaries.

Nonetheless, studies in recent years have shown that satellite data can also be valuable on a regional scale. For example, Montmerle *et al.* (2007) investigated the impact of polar-orbiting and geostationary satellite radiances in the Aladin/France model, using a 3D-Var system. One result was that SEVIRI radiances have a positive impact on the very short-range forecast, resulting in decreased background departures of moisture sensitive channels of HIRS and AMSU-B. Furthermore, they found an increased accuracy of short-range precipitation forecasts.

In this paper we investigate the benefit of assimilating SEVIRI radiances using the 4D-Var system of the High Resolution Limited Area Model (HIRLAM; Undén *et al.*, 2002). The assimilation of SEVIRI observations in a 4D-Var system of a limited-area model is fairly new and to our knowledge has not yet been evaluated in the peer-reviewed literature. In our study, SEVIRI data with an hourly resolution, equally distributed over a 6 h assimilation window, were assimilated. In 4D-Var, this results in flow-dependent assimilation increments in, for example, moisture and temperature fields inferred by additional adjustments of the dynamical control variables, which is complementary to the balances in the background-error structure functions. Furthermore, we introduced a sophisticated procedure to identify useful SEVIRI observations in the presence of low-level clouds. Evaluating their impact on forecast accuracy compared to the observations in clear-sky conditions is another central point of our study.

In the following section we describe the experimental framework of our studies, giving an overview of the HIRLAM model and its assimilation system, SEVIRI observations and their processing for our studies, and describing the experiment series we performed. The impact of SEVIRI on the analysis is discussed in section 3. Furthermore, we present forecast-error verifications for the conducted experiments in section 4.

2. Experimental framework

2.1. The HIRLAM model and its 4D-Var system

The HIRLAM model is a limited-area NWP model, which is used operationally at SMHI as well as in other countries

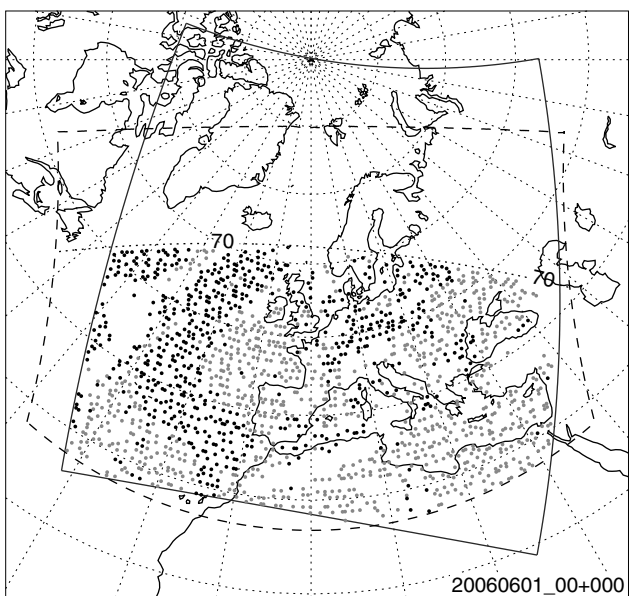


Figure 1. Locations of screened clear-sky (CLS, black dots) and low-level cloud (LLC, grey dots) observations after data selection for 0000 UTC on 1 June 2006. The black line and grey dashed line border the HIRLAM/SMHI-C22 domain and the MSG sub-area as currently processed at SMHI. The black dotted line marks the SEVIRI 70° zenith angle.

participating in the HIRLAM project. The hydrostatic model is in our studies specified with a horizontal resolution of around 22 km and with 60 vertical levels. The model domain is shown in Figure 1. The HIRLAM model contains a variational data assimilation system (HIRVDA). A description of the 3D-Var specifications and initial tests can be found in Gustafsson *et al.* (2001) and Lindskog *et al.* (2001), respectively. Its current 4D-Var system is largely along the lines of Huang *et al.* (2002) and Gustafsson (2006). In our studies, two sequenced cost function minimizations were performed with a model resolution of 66 km during the first and 44 km during the second minimization process. The cost function J is formulated as in Equation (1) as the sum of the background part (J^b), the initialisation part (J^c), and the observational part (J^o):

$$J = J^b + J^c + J^o. \quad (1)$$

The background part is described in Equation (2), where \mathbf{B} denotes the background-error covariance matrix and $\delta\mathbf{x}_0$ the increment in model space with respect to background \mathbf{x}_0^b at the beginning of the assimilation window:

$$J^b = \frac{1}{2}(\delta\mathbf{x}_0)^T \mathbf{B}^{-1} \delta\mathbf{x}_0. \quad (2)$$

The initialization part of the cost function is formulated as a weak digital filter constraint following Gustafsson (1992) and Gauthier and Thépaut (2001). The observational part of the cost function is shown in Equation (3), which is formulated as the sum over all K observation

window contributions:

$$J^o = \frac{1}{2} \sum_{i=0}^K \{\mathbf{d}_i + \mathbf{H}(\delta\mathbf{x}_i)\}^T \mathbf{R}^{-1} \{\mathbf{d}_i + \mathbf{H}(\delta\mathbf{x}_i)\}. \quad (3)$$

\mathbf{R} represents the observation-error covariance matrix, which accounts for errors in the observations as well as in the forward modelling. $\delta\mathbf{x}_i$ is the increment in model space propagated forward in time from the beginning of the assimilation window to each observation window i using the tangent-linear forecast model. The difference vector \mathbf{d}_i is formulated as

$$\mathbf{d}_i = H(\mathbf{x}_i^b) - \mathbf{y}_i^o, \quad (4)$$

and stands for the innovations between the observations \mathbf{y}_i and the modelled radiances $H(\mathbf{x}_i^b)$.

\mathbf{H} represents the tangent-linear of the observation operator H , which is, in case of satellite radiances, the widely-used fast Radiative Transfer Model for TOVS (RTTOV) (Eyre, 1991; Saunders *et al.*, 1999). Version 8.7 of RTTOV was used in our studies.

The RTTOV model computes radiances for passive infrared and microwave satellite instruments. It is very time-efficient by using the polychromatic approximation of the radiative transfer equation. In this approximation, the radiative transfer calculation is performed using transmittances and Planck functions convolved with respect to the spectral response function of each channel. This is in contrast to the convolution of radiances inferred from line-by-line calculations. An important feature of RTTOV is that it also computes the gradient of the radiances with respect to the state vector variables, which is crucial for the direct assimilation of satellite radiances in NWP systems.

The state vector variables in HIRVDA are surface pressure and upper-air values of the wind components in the x - and y -directions, temperature and moisture. Specific humidity has recently been replaced by a pseudo-relative humidity (Hólm *et al.*, 2002) as moisture variable. This induces a flow-dependency of the background-error humidity correlations. In addition, large areas of strong supersaturation are avoided due to the near-Gaussian error characteristics. In general, Gaussian error characteristics of the background fields as well as of the observations are assumed in the present formulation of the cost function and are needed to obtain the optimal analysis results.

The background-error statistics for the state vector variables were derived, as proposed in Parrish and Derber (1992), from differences between 36 h and 12 h forecasts valid at the same time, utilizing a statistical balance operator (Berre, 1997; Derber and Bouttier, 1999).

The 4D-Var assimilation window was specified as 6 h covering the time period of -3.5 to $+2.5$ h relative to the analysis time.

In our studies the HIRLAM forecast model is characterized by a semi-Lagrangian advection scheme, physical parametrisations for radiation (Savijärvi, 1990) and for convection and large-scale condensation processes (Rasch

and Kristjánsson, 1998; Kain, 2004), a moist conserved turbulence scheme (Cuxart *et al.*, 2000), and the ISBA (Interaction Soil Biosphere Atmosphere) land surface scheme (Noilhan and Mahfouf, 1996). ECMWF forecasts (6 to 12 h old) were provided as lateral boundaries with a 3 h interval.

2.2. SEVIRI radiances and used cloud products

The SEVIRI instrument (Schmetz *et al.*, 2002) is the main payload of the Meteosat Second Generation (MSG) satellite series. The first of this series, Meteosat-8 (MSG-1), became operational in January 2004. Since April 2007 Meteosat-9 (MSG-2), the second satellite of this series, has been the prime satellite. SEVIRI provides continuous observations for the full Earth's disc with an imaging cycle of 15 min. Eight of its 12 channels are located in the infrared, one in the near-infrared and three in the visible part of the electromagnetic spectrum. The central wavelengths of the infrared channels are $3.90\text{ }\mu\text{m}$, $6.25\text{ }\mu\text{m}$, $7.35\text{ }\mu\text{m}$, $8.70\text{ }\mu\text{m}$, $9.66\text{ }\mu\text{m}$, $10.80\text{ }\mu\text{m}$, $12.00\text{ }\mu\text{m}$ and $13.40\text{ }\mu\text{m}$. The spatial resolution of the IR channels is about 3 km at the sub-satellite point and $\approx 4\text{--}5$ km over Central Europe. For practical reasons, the SEVIRI data processing in our studies was limited to a sub-area of the entire disk, which covers approximately 2/3 of the chosen model domain (Figure 1). However, after rejecting measurements with scan angles exceeding 70° , the covered part of the model domain is reduced to approximately the southern half. To identify cloud-contaminated pixels, a cloud mask (Derrien and Le Gléau, 2005) is utilized, which is part of a software package (Le Gléau and Derrien, 2002) developed by the EUMETSAT Satellite Application Facility on Nowcasting and Very Short Range Forecasting (SAFNWC). This package provides a pixel-based distinction into three classes: completely cloud-filled, partly cloud-filled, or clear-sky. Using this information, all clear-sky observations are identified in a first step. In a second step, radiances in completely cloud-filled pixels undergo a local test to identify channel radiances which are not or only slightly affected by the cloud. Here, a cloud top pressure (CTP) estimation, documented as PGE03 in (Le Gléau and Derrien, 2002), is used. A detailed description of this procedure is given in the following section. For simplicity all partly cloud-covered pixels were generally rejected in our studies.

2.2.1. Observation selection

For the time being, we have focused on the assimilation of the two water vapour channels (WV062 and WV073 hereafter), located at $6.2\text{ }\mu\text{m}$ and $7.3\text{ }\mu\text{m}$, and the CO₂ channel (IR134 hereafter), which is placed around $13.4\text{ }\mu\text{m}$ within a wing of a strong CO₂ absorption band. The modelled sensitivity of these radiances with respect to temperature and moisture (Jacobians) in the absence of radiance-affecting clouds are displayed in Figure 2. The shown profiles were generated using RTTOV and averaged over approximately 150 summer cases over Europe. Due to their spectral location, the

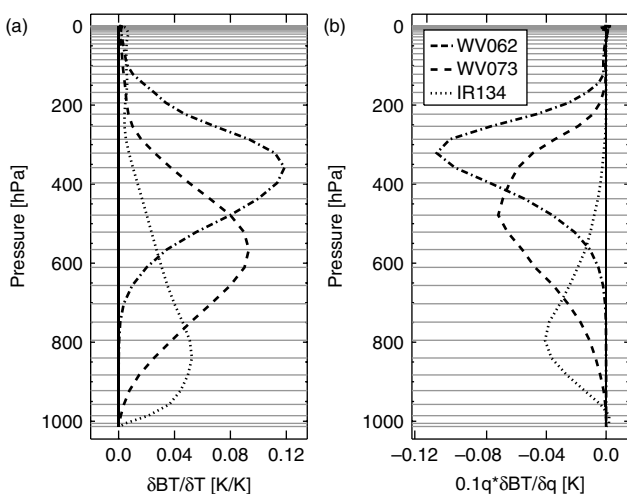


Figure 2. Mean Jacobians with respect to (a) temperature and (b) specific humidity. The humidity Jacobians were scaled at each level by 10% of the corresponding background specific humidity value before averaging.

water vapour radiances comprise mainly information about moisture and temperature in the middle and upper troposphere. Their temperature Jacobians peak on average around 600 hPa (WV073) and around 350 hPa (WV062), respectively. The profile for IR134 shows a moderate temperature sensitivity throughout the troposphere with a maximum amplitude around 850 hPa. Its radiance is also affected by the water vapour continuum absorption in the lower troposphere. Furthermore, this radiance is usually affected by surface emissions. Due to this the IR134 channel is only used over ocean. There, background sea-surface temperatures and sea-surface emissivities, calculated internally in RTTOV, are of proper quality in the forward modelling.

Due to an insufficient treatment of clouds in our current observation operator, we blacklisted all radiances that were significantly affected by clouds. In the following we describe two classes of retained observations which were used within the assimilation. The first class is composed by selecting all observations in cloud-free pixels according to the cloud mask. In the following the abbreviation ‘CLS’ for clear-sky will be used for this class of observations.

Furthermore, we define a second class of observations, which contains observations under mainly low-level cloud conditions, hereafter referred to as ‘LLC’. These observations must fulfil two criteria. All pixels within this class had to be identified as cloud-filled by the cloud mask and the CTP estimate for these pixels had to be below a certain height to limit the impact of clouds on the observed radiances. This critical height was determined by the local clear-sky temperature Jacobian (e.g. Figure 2) co-located at each observation point. In detail, each Jacobian was integrated from bottom upwards and the critical height was determined to be where the integrated value reached 5% of the total integrated Jacobian. Subsequently, all observations were included in LLC for which the CTP estimate did not exceed this critical height.

This procedure was done for each channel separately. Generally, and when considering an average atmospheric profile as in Figure 2, this critical height might lie around 550 hPa for channel WV062 and around 850 Pa for the WV073 channel.

In order to provide a spatially optimal and non-redundant set of observations, various preparatory data selection steps were performed. As an initial step, SEVIRI pixels located outside the model domain and pixels with zenith angles greater than 70° were rejected. The zenith angle threshold was chosen as a compromise between the spatial SEVIRI coverage of the model domain and the growing representativeness error of the background profiles for large satellite zenith angles. Additionally, pixels covering mountain regions with altitudes higher than 1 km were rejected. Errors in land surface emissivities and temperatures would increase simulation errors in cases of high-altitude land regions. Furthermore, a data thinning was performed and only one pixel out of each 10×10 pixel-box was kept for further usage, which led at this stage to an average spatial sampling of about 50 km over central Europe. Subsequently, a background check was done, filtering all observations with innovations exceeding the limit of 4 K. These observations were assumed to be affected by gross errors. The final spatial thinning, removing possible spatial error correlations in the observations, had a thinning length of approximately 90 km. This value was chosen with respect to the length-scale of the background-error structure functions. One example of retained SEVIRI pixels after all preparation steps is shown in Figure 1 for 0000 UTC on 01 June 2006.

2.2.2. Bias investigation and correction

Initially, the background equivalents in radiance observation space ($H(\mathbf{x}^b)$), which were simulated every 6 h using HIRLAM 6 h forecast fields, were monitored against co-located observations (\mathbf{y}^o) for a 2-month period in summer 2005 (not shown). The calculated error statistics of the innovations ($H(\mathbf{x}^b) - \mathbf{y}^o$) showed a permanent bias in the WV062 channel remaining during the investigated time period. The background appeared to be much warmer for this channel than the observations. The mean bias was calculated to be 2.6 K. This value is a bit larger than the 1.7 K which were found by Szyndel *et al.* (2005). This bias might originate from systematic deviations in the upper troposphere in the NWP fields, which could be too dry and/or too warm. One might also speculate that this is partly caused by slight deviations in the brightness temperature definitions in RTTOV and the SAFNWC software that had been used. Furthermore, a diurnal cycle of the bias was found for all three channels, which was also discovered in Szyndel *et al.* (2005) for the two water vapour channels. The innovations increased during the night and decreased during the day (Figure 3). The reasons for this diurnal oscillation is not fully understood so far, but it may indicate a possible diurnal dependency of the NWP model performance or differences in the cloud mask between daytime and night-time scenes. A possibly

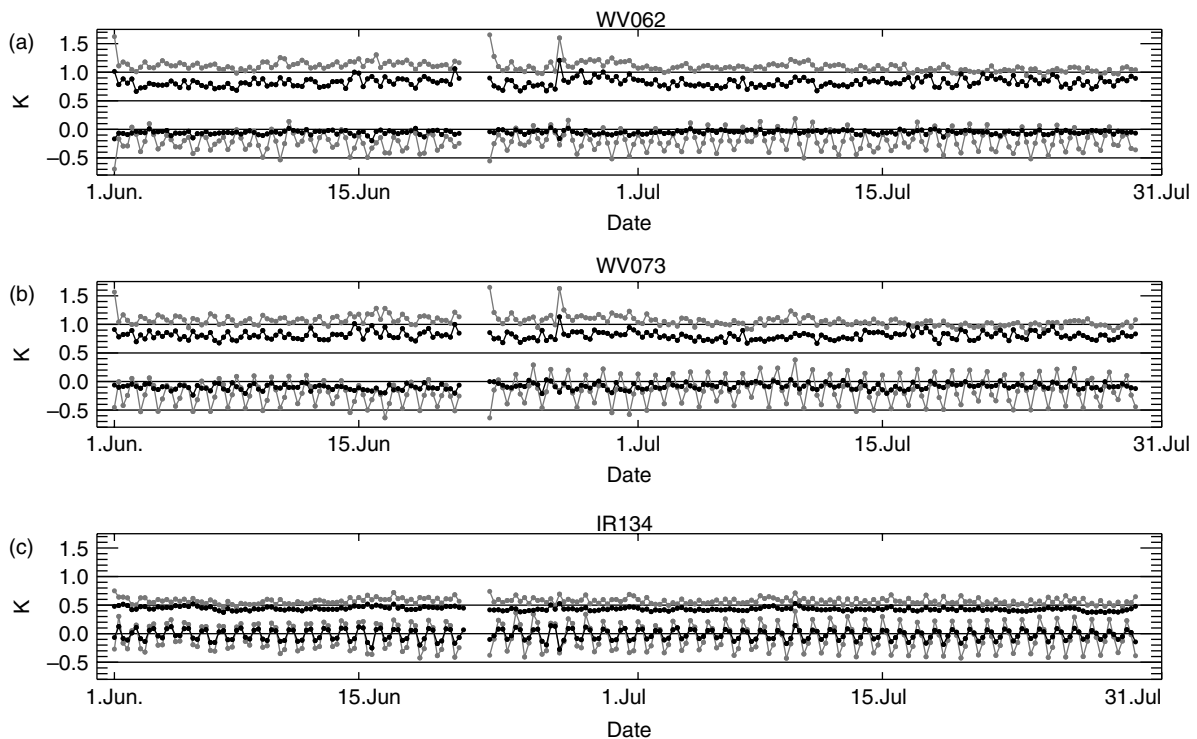


Figure 3. Monitoring of biases and RMS errors of CLS observation departures for background (grey dots) and analysis (black dots) for the SEVCLS experiment and channels (a) WV062, (b) WV073, and (c) IR134. The displayed data were time-averaged within each assimilation cycle resulting in a resolution of 6 h. Gaps in the graphs indicate cycles with no SEVIRI data available.

increased number of undetected clouds in the observations during night-time would shift the innovation bias towards higher values, which is in line with the observed feature. The amplitude of the diurnal bias variation often reaches 1 K. This behaviour would have to be taken into account when applying advanced bias correction schemes such as proposed by Harris and Kelly (2001). For the time being, a flat bias correction was applied to the WV062 channel by means of adding a fixed offset of 2.6 K to the observations. A possible scan-angle dependence was not considered here because of the fairly small variation of scan-angle within the model domain. The channels WV073 and IR134 were not bias-corrected due to a relatively small bias in the investigated period.

2.3. Experiment specifications

Three different data assimilation and forecast experiments were conducted (CNTRL, SEVCLS and SEVLLC hereafter). The specifications of the assimilation system as well as of the forecast model were identical. Differences were only in the assimilated observation types, which were specified as follows:

- CNTRL: Conventional observations only
- SEVCLS: Conventional and CLS observations
- SEVLLC: Conventional, CLS and LLC observations

The conventional observations comprise surface station (SYNOP), radiosonde, and pilot-balloon reports, as well as measurements from ships, aircraft and buoys. These

data, which were retrieved from the Meteorological Archival and Retrieval System (MARS) at ECMWF, were the same in each experiment. The term SEVIRI experiments will in the following stand for both SEVCLS and SEVLLC.

In both SEVIRI experiments, observations from six SEVIRI time slots, which were equally distributed over the 6 h assimilation window, were used, resulting in an effective temporal resolution of 1 h. This temporal thinning is based on assimilation characteristics of the HIRLAM model, which assumes the provided observations to be in the centre of each 1 h observation window. Higher temporal resolutions could therefore introduce persistence errors in the current model version due to misrepresentation of the time of the observations. The data preparation as mentioned above was done separately for each SEVIRI time slot. The observation errors were specified higher than SEVIRI's radiometric noise to account for forward modelling errors, and to avoid SEVIRI observations to be too dominant during the assimilation process. The chosen value for both water vapour channels was 2 K in both SEVIRI experiments. The IR134 observations were assigned to have an error of 1.5 K. The period of the assimilation experiments covers almost two full months from 1 June 2006 until 28 July 2006. An assimilation cycle was performed every 6 h, utilizing new observations, and subsequently the forecast model was run until 48 h integration time.

Bias and RMS error statistics of the observation departures for background and analysis fields for the SEVCLS experiment are monitored in Figure 3, including

all CLS observations used in the minimization. The corresponding values for SEVLLC are very similar and are not shown.

3. Analysis increments

Generally speaking, the largest impacts on the analyses, when assimilating SEVIRI, were found in the moisture and wind fields. The moisture was mainly changed in the mid- and upper troposphere, whereas noticeable wind increments were also found in the lower troposphere. The other upper-air fields as well as surface pressure were also affected but to a smaller extent.

In the following the analysis impact of one particular assimilation cycle (1 June 2006 at 0000 UTC) is discussed, in which all three experiments used the same background state conditions. Figure 4 shows the differences in the analysed relative humidity at 500 hPa. The increments of SEVCLS and SEVLLC, each compared to CNTRL, correspond to the location of the selected observations as displayed in Figure 1. For relative humidity, many small-scale features are found within the range of $\pm 20\%$. In a few locations, even higher values are found. The deflection, if drying or moistening, at this pressure level is in general in line with the innovations for channel WV073. A similar relation is found between moisture at higher levels and the WV062 channel. A comparison between the humidity analyses of the SEVIRI experiments (Figure 4) reveals some small-scale features in the difference patterns but also the amplification and attenuation of moisture increments. Those differences in SEVLLC compared to SEVCLS are again more or less directly co-located to the additional LLC observations in SEVLLC (Figure 1).

The wind fields at 500 hPa in Figure 5 show small increments over Central Europe and larger increments over the Atlantic Ocean, in the eastern Mediterranean Sea, and parts of Northern Africa. The small impact over land might be due to the conventional observations being dominant for wind in those regions and/or the agreement of those with the satellite observations. Similar to relative humidity, we find also for wind relatively large differences between SEVCLS–CNTRL and SEVLLC–CNTRL, which are also co-located with the region of additional LLC observations in SEVLLC.

Comparative 3D-Var experiments for this case were conducted to study the difference between 3D-Var and 4D-Var. In 3D-Var, SEVIRI data from only one time slot were assimilated. In general, the 3D-Var experiments exhibit much smaller changes in the moisture increments (not shown). Changes in wind increments in 3D-Var were also significantly smaller than in 4D-Var and almost not noticeable.

An additional statistical investigation of the 4D-Var wind analysis increments over the full domain and for the entire experiment period show clearly the impact of SEVIRI observation on the wind fields, especially in the upper troposphere (not shown). The differences are more pronounced for SEVLLC than for SEVCLS. The standard

deviations of the increments in the SEVIRI experiments are in general increased over ocean and decreased over land compare to the control run.

Generally, our results suggest that additional dynamical information were incorporated by assimilating SEVIRI with 4D-Var.

Furthermore, we calculated observation fit statistics of the 4D-Var analyses against radiosondes for the entire period of the experiments. These statistics highlight a slightly increased deviation in both SEVIRI experiments compared to the control run. This behaviour is found for all upper-air parameters in the upper troposphere except geopotential height. The maximum of this deviation is found for relative humidity at 300 hPa. It is also visible in Figure 7 at 500 hPa (0 h forecast length), but to a smaller extent.

4. Impact on short-range forecast

Radiosoundings and SYNOP reports, which were selected according to the station list established by the European Working Group on Limited-Area Modelling, were used to verify the short-range forecasts. Co-located profiles were extracted from the forecast fields for all three experiments. Based on this dataset, we calculated the root mean square (RMS) and mean errors for various parameters for all three experiment series at 12, 24, 36 and 48 h forecasts.

4.1. Impact on upper-air variables

Figure 6 displays the time-averaged scores for the upper-air parameters temperature, relative humidity, geopotential height and wind speed. Here, the RMS and mean errors are averaged over all forecast lengths.

Generally, the RMS error values of the temperature forecast are very similar in all three experiments. At 500 hPa the values are slightly reduced for SEVCLS and SEVLLC. We found furthermore a slight degradation of forecast accuracy for temperature at 300 hPa for the 24 and 36 h forecasts (not shown). The mean errors for temperature for SEVCLS and SEVLLC seem to be increased a bit in the lower troposphere. In Figure 7(a) the temperature forecast errors at 500 hPa are shown as a function of forecast length.

A larger positive impact is visible for relative humidity with the biggest change at 300 and 500 hPa. At 500 hPa the forecast error is reduced by $\approx 1\%$ relative humidity for both SEVIRI experiments, which is a relative error reduction of 4–5%. The largest impact is found for the 12 h forecast and then decreasing with forecast time afterwards (Figure 7(b)). A general slight drying throughout the troposphere is found when assimilating SEVIRI.

The change in the geopotential height scores is also characterized by an RMS error reduction. Here, the positive impact is visible throughout the entire troposphere. The RMS errors of SEVLLC are estimated to be 0.5 to

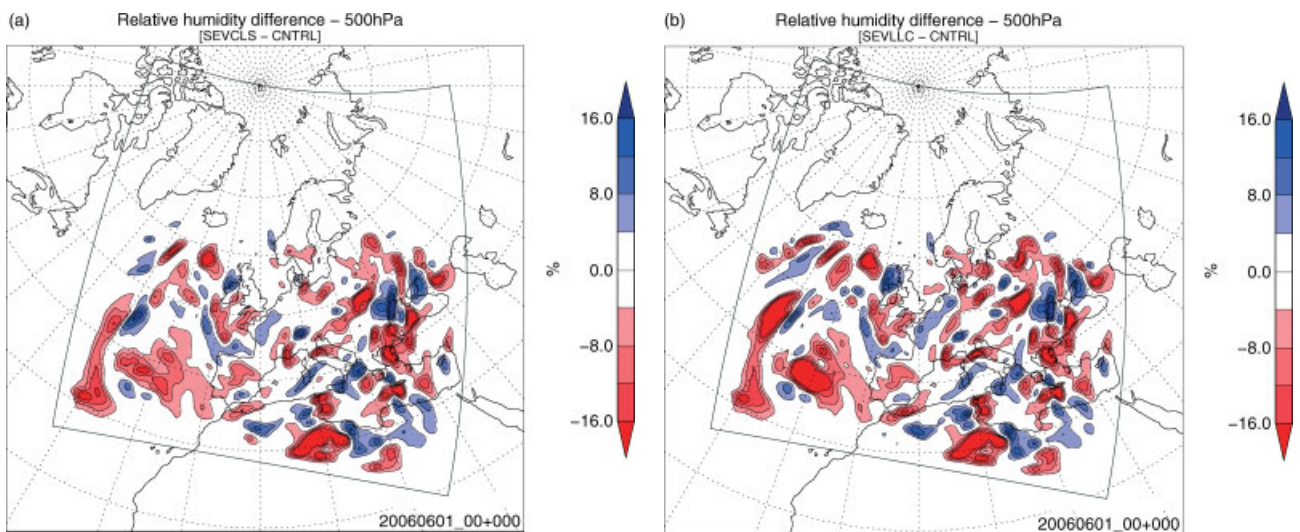


Figure 4. Difference in analysed relative humidity at 500 hPa for (a) SEVCLS minus CNTRL and for (b) SEVLLC minus CNTRL. A horizontal smoothing was applied to the data.

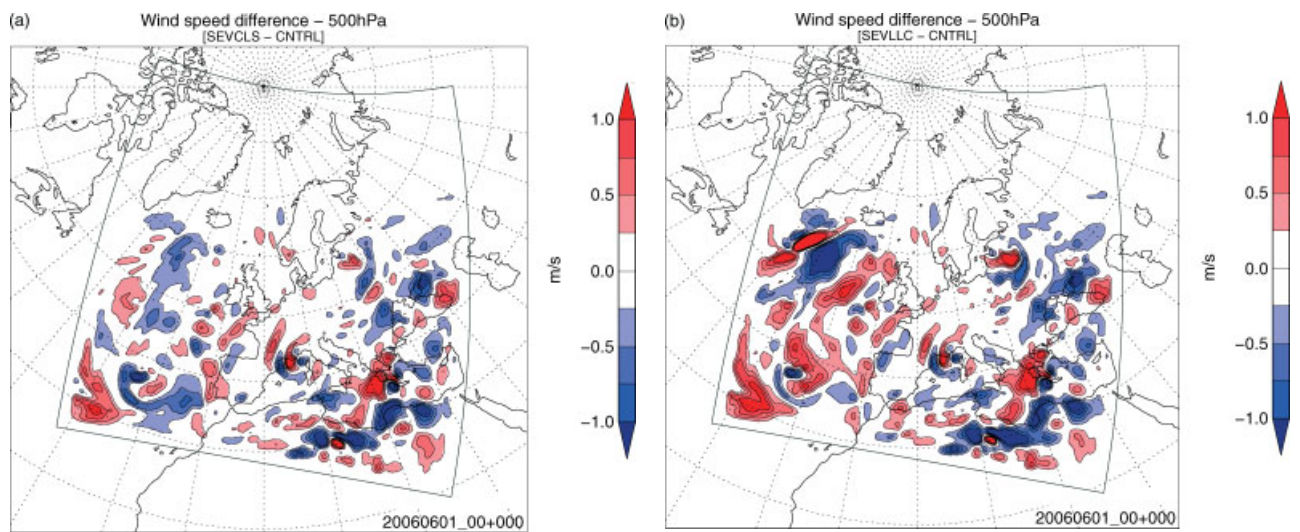


Figure 5. As Figure 4, but for wind speed.

1 m ($\approx 3\text{--}5\%$) smaller at 500 and 300 hPa than the corresponding values of CNTRL. The impact in SEVCLS is smaller for this parameter, but still slightly positive at most levels. In general, the positive effect appears to be increasing towards forecast lengths of 36 and 48 h for both SEVIRI experiments (Figure 7(c)).

The error values for wind speed are quite similar to those for geopotential height. Here, we also found decreased forecast errors with the largest extent at 300 and 500 hPa. Furthermore SEVLLC performs better than SEVCLS. The same can be observed in Figure 7(d), where SEVLLC shows the lowest RMS errors for wind at 500 hPa at all considered forecast lengths. The mean error values for this variable show only minimal changes.

4.2. Impact on surface variables

For many investigated surface variables, the forecast errors in the SEVIRI experiments are nearly identical to the control experiment. However, small positive effects

are found for surface pressure, where the error is reduced for forecast lengths from 36 to 48 h (Figure 8(a)). Furthermore we found a slight positive impact on precipitation scores for both SEVIRI experiments and all considered forecast lengths (not shown). Here, RMS errors are reduced by up to 5% in SEVCLS and slightly less in SEVLLC compared to CNTRL. A similar picture shows the frequency distribution of the clustered rain amounts (Figure 8(b)). For five of the six shown precipitation bins, the values for SEVLLC are closer to the observation values than the CNTRL. For SEVCLS this applies for four of the six bins.

5. Summary and discussion

This paper presents a study investigating the impact of assimilated geostationary IR radiances on analyses and forecasts of the limited-area model HIRLAM using a four-dimensional data assimilation framework. For this

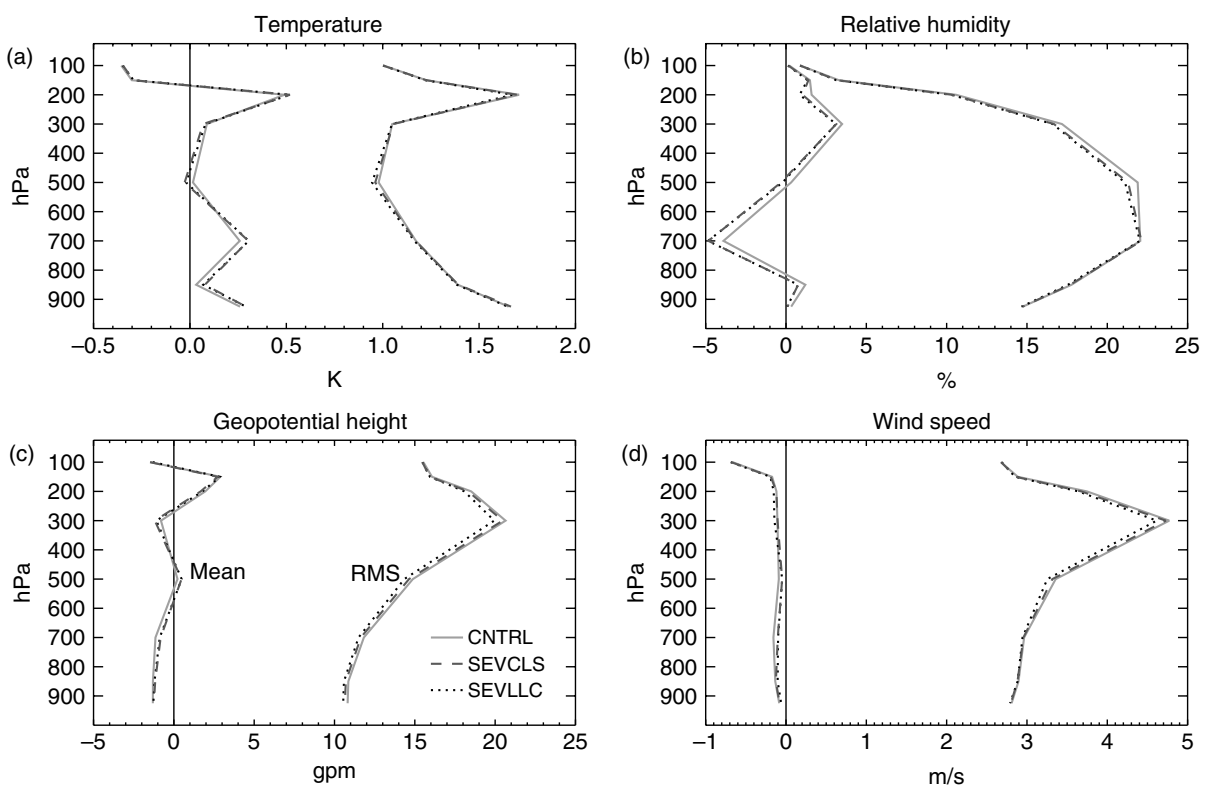


Figure 6. Profiles of RMS and mean forecast errors based on 0000 UTC and 1200 UTC analyses, time-averaged over forecast lengths 12, 24, 36, and 48 h.

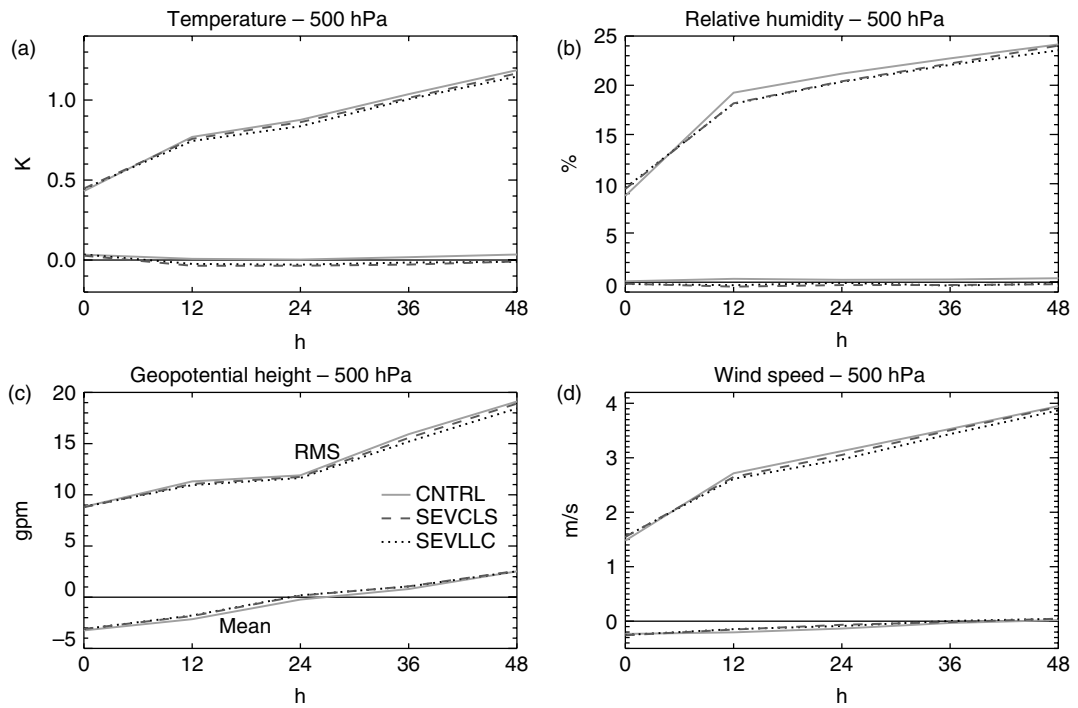


Figure 7. RMS and mean forecast errors based on 0000 UTC and 1200 UTC analyses, as a function of forecast lengths 00, 12, 24, 36, and 48 h.

purpose radiances measured by SEVIRI were converted to brightness temperatures and corresponding cloud products (a cloud mask and a CTP retrieval) were processed. The channels considered in our study were the two water vapour channels ($6.2\text{ }\mu\text{m}$ and $7.3\text{ }\mu\text{m}$) and the $13.4\text{ }\mu\text{m}$ channel. Due to its surface sensitivity, the

$13.4\text{ }\mu\text{m}$ channel was not used for land surfaces. Several data preparation steps were defined and, together with the actual data handling, implemented into the variational data assimilation system of the HIRLAM model. Three independent experiments were carried out over a time period of almost two months. These experiments

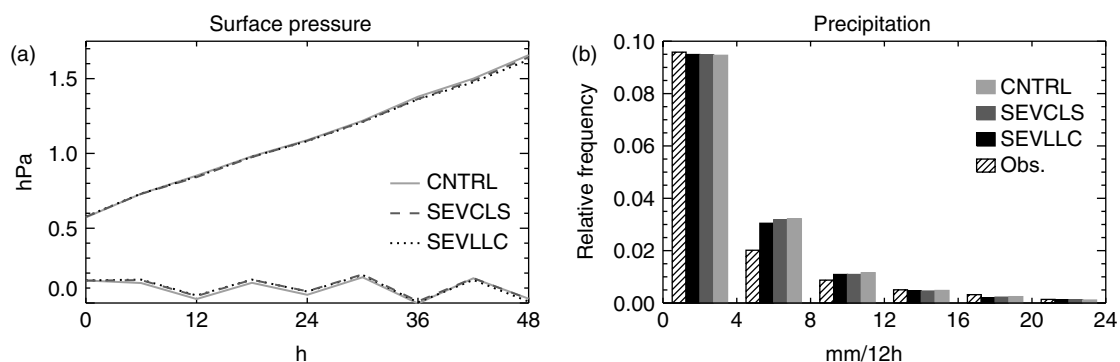


Figure 8. (a) RMS and mean forecast errors of surface pressure. (b) Relative frequency distribution for precipitation. The bin sizes are shown on the x -axis. The values of the lowest bin are scaled by 0.1.

only differ in the types of satellite observations that were assimilated. Besides a control run using conventional observations only, one SEVIRI experiment made use of SEVIRI radiances in clear-sky conditions on top of the conventional observations. A second SEVIRI experiment additionally used the two water vapour channels in low-level cloud conditions, where the radiances were not affected by the cloud.

The major differences in the analysis increments of the SEVIRI experiments compared to CNTRL were found for humidity and the wind components in the mid- and upper troposphere. The differences for wind were smaller in regions with denser radiosonde coverage, due to the constraints of these observations. In a comparison experiment using a 3D-Var technique, these wind increments could not be found.

Generally, these results suggest that additional dynamical information was extracted from the assimilated temporally highly resolved SEVIRI radiances, and that the characteristic trait of 4D-Var systems to gain increments in mass and/or wind fields by ‘tracking’ certain features in the satellites images might also be beneficial at regional scales.

The evaluation of the HIRLAM forecast accuracy against radiosondes revealed very encouraging results for the investigated period. The RMS errors of the forecasts for almost all upper-air variables decreased when SEVIRI data were assimilated. The largest positive impacts were found for moisture and geopotential height in the middle and upper troposphere. A slight degradation of the forecast scores was found for temperatures around 300 hPa and forecast lengths of 24 and 36 h. The evaluation of the forecast accuracy for surface variables showed small improvements for surface pressure and precipitation. Both the cloud-free and the low-level cloud SEVIRI experiments were found to perform better than the control run. The best results were achieved for the SEVLLC experiment including observations under low-level cloud conditions.

The results of our study highlight the potential benefit of assimilating SEVIRI observations in a limited-area model using a four-dimensional variational data assimilation system. The results suggest further that the

assimilation of observations under low-level cloud conditions provide additionally useful information to the NWP system and highlight the importance of cloudy satellite observations for further improvements in numerical weather forecasts.

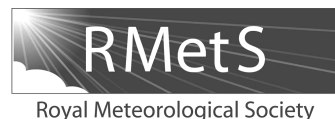
Acknowledgements

This work was supported by the European Organisation for the Exploitation of Meteorological Satellites (EUMETSAT) in the framework of the Research Fellowship Program and by the Swedish National Space Board (Contract Dnr 105/08:1). The contribution of one of the co-authors (Bennartz) was funded by the US Joint Center for Satellite Data Assimilation (JCSDA). The valuable comments of two anonymous referees are appreciated.

References

- Andersson E, Paillex J, Thépaut J-N, Eyre JR, McNally AP, Kelly GA, Courtier P. 1994. Use of cloud-cleared radiances in three/four-dimensional variational data assimilation. *Q. J. R. Meteorol. Soc.* **120**: 627–653.
- Berre L. 1997. ‘Non-separable structure functions for the HIRLAM 3D-Var’. HIRLAM Technical Report 30.
- Courtier P, Thépaut J-N, Hollingsworth A. 1994. A strategy for operational implementation of 4D-Var, using an incremental approach. *Q. J. R. Meteorol. Soc.* **120**: 1367–1387.
- Cuxart J, Bougeault P, Redelsperger JL. 2000. A turbulence scheme allowing for mesoscale and large-eddy simulations. *Q. J. R. Meteorol. Soc.* **126**: 1–30.
- Derber J, Bouttier F. 1999. A reformulation of the background error covariance in the ECMWF global data assimilation system. *Tellus* **51A**: 195–221.
- Derrien M, Le Gleau H. 2005. MSG/SEVIRI cloud mask and type from SAFNWC. *Int. J. Remote Sensing* **26**: 4707–4732.
- Eyre JR. 1991. ‘A fast radiative transfer model for satellite sounding systems’. Technical Memo. 176, ECMWF: Reading, UK.
- Gauthier P, Thépaut J-N. 2001. Impact of the digital filter as a weak constraint in the pre-operational 4D-Var assimilation system of Météo-France. *Mon. Weather Rev.* **129**: 2089–2102.
- Gustafsson N. 1992. ‘Use of a digital filter as weak constraint in variational data assimilation’. In *Proceedings of workshop on variational assimilation, with special emphasis on three-dimensional aspects*. ECMWF: Reading, UK. pp 327–338.
- Gustafsson N. 2006. ‘Status and performance of HIRLAM 4D-Var’. *HIRLAM Newsletter* **51**.
- Gustafsson N, Berre L, Hornquist S, Huang XY, Lindskog M. 2001. Three-dimensional variational data assimilation for a limited area model. Part I: General formulation and the background error constraint. *Tellus* **53A**: 425–446.

- Harris BA, Kelly G. 2001. A satellite radiance-bias correction scheme for data assimilation. *Q. J. R. Meteorol. Soc.* **127**: 1453–1468.
- Hólm E, Andersson E, Beljaars A, Lopez P, Mahfouf J-F, Simmons A, Thépaut J-N. 2002. ‘Assimilation and modelling of the hydrological cycle: ECMWF’s status and plans’. Technical Memo. 383, ECMWF: Reading, UK.
- Huang XY, Yang X, Gustafsson N, Mogensen KS, Lindskog M. 2002. ‘Four-dimensional variational data assimilation for a limited area model’. HIRLAM Technical Report **57**.
- Janisková M, Thépaut J-N, Geleyn J-F. 1999. Simplified and regular physical parameterizations for incremental four-dimensional variational assimilation. *Mon. Weather Rev.* **127**: 26–45.
- Kain JS. 2004. The Kain–Fritsch convective parameterization: An update. *J. Appl. Meteorol.* **43**: 170–181.
- Kelly G, Thépaut J-N. 2007. ‘Evaluation of the impact of the space component of the Global Observing System through Observing System Experiments’. In *Proceedings of Seminar on recent developments in the use of satellite observations in numerical weather prediction*. ECMWF: Reading, UK. pp 327–348.
- Köpken C, Kelly G, Thépaut J-N. 2004. Assimilation of Meteosat radiances data within the 4D-Var system at ECMWF: Assimilation experiments and forecast impact. *Q. J. R. Meteorol. Soc.* **130**: 2277–2292.
- Le Gléau H, Derrien M. 2002. ‘User manual for the PGE01-02-03 of the SAFNWC/MSG: Scientific part’. EUMETSAT documentation SAF, NWC/IOP/MFL/SCI/SUM/01. Available from: Centre de Météorologie Spatiale, Météo-France, Toulouse, France.
- Lindskog M, Gustafsson N, Navascués B, Mogensen KS, Huang XY. 2001. Three-dimensional variational data assimilation for a limited-area model. Part II: Observation handling and assimilation experiments. *Tellus* **53A**: 447–468.
- Montmerle T, Rabier F, Fischer C. 2007. Relative impact of polar-orbiting and geostationary satellite radiances in the Aladin/France numerical weather prediction system. *Q. J. R. Meteorol. Soc.* **133**: 655–671.
- Munro R, Köpken C, Kelly G, Thépaut J-N, Saunders R. 2004. Assimilation of Meteosat radiances data within the 4D-Var system at ECMWF: Data quality monitoring, bias correction and single-cycle experiments. *Q. J. R. Meteorol. Soc.* **130**: 2293–2313.
- Noilhan J, Mahfouf J-F. 1996. The ISBA land surface parameterisation scheme. *Global and Planetary Change* **13**: 145–159.
- Parrish DF, Derber JC. 1992. The National Meteorological Center’s spectral statistical-interpolation analysis system. *Mon. Weather Rev.* **120**: 1747–1763.
- Rasch PJ, Kristjánsson JE. 1998. A comparison of the CCM3 model climate using diagnosed and predicted condensate parameterizations. *J. Climate* **11**: 1587–1614.
- Saunders R, Matricardi M, Brunel P. 1999. An improved fast radiative transfer model for assimilation of satellite radiance observations. *Q. J. R. Meteorol. Soc.* **125**: 1407–1425.
- Savijärvi H. 1990. Fast radiation parameterization schemes for mesoscale and short-range forecast models. *J. Appl. Meteorol.* **29**: 437–447.
- Schmetz J, Pili P, Tjemkes S, Just D, Kerkmann J, Rota S, Ratier A. 2002. An introduction to Meteosat Second Generation (MSG). *Bull. Am. Meteorol. Soc.* **83**: 977–992.
- Szyndel MDE, Kelly G, Thépaut J-N. 2005. Evaluation of potential benefit of assimilation of SEVIRI water vapour radiance data from Meteosat-8 into global numerical weather prediction analyses. *Atmos. Sci. Lett.* **6**: 105–111.
- Tompkins AM, Janisková M. 2004. A cloud scheme for data assimilation: Description and initial tests. *Q. J. R. Meteorol. Soc.* **130**: 2495–2518.
- Undén P, Rontu L, Järvinen H, Lynch P, Calvo J, Cats G, Cuxart J, Eerola K, Fortelius C, García-Moya JA, Jones C, Lenderlink G, McDonald A, McGrath R, Navascués B, Woetman Nielsen N, Odegaard V, Rodriguez E, Rummukainen M, Room R, Sattler K, Hansen Sass B, Savijärvi H, Wickers Schreur B, Sigg R, The H, Tijm A. 2002. ‘HIRLAM-5 Scientific Documentation, HIRLAM-5 Project’. Available from: SMHI, S-601 767 Norrköping, Sweden.
- Veersé F, Thépaut J-N. 1998. Multiple-truncation incremental approach for four-dimensional variational data assimilation. *Q. J. R. Meteorol. Soc.* **124**: 1889–1908.



The growing impact of satellite observations sensitive to humidity, cloud and precipitation

A. J. Geer,^{a*} F. Baordo,^{a,b} N. Bormann,^a P. Chambon,^c S. J. English,^a M. Kazumori,^d H. Lawrence,^a P. Lean,^a K. Lonitz^a and C. Lupu^a

^aEuropean Centre for Medium-Range Weather Forecasts, Reading, UK

^bForecast Systems, Weatherzone, Sydney, New South Wales, Australia

^cCNRM UMR 3589, Météo-France/CNRS, Toulouse, France

^dJapan Meteorological Agency, Tokyo, Japan

*Correspondence to: A. J. Geer, ECMWF, Shinfield Park, Reading RG2 9AX, UK. E-mail: alan.geer@ecmwf.int

Ten years ago, humidity observations were thought to give little benefit to global weather forecasts. Nowadays, at the European Centre for Medium-range Weather Forecasts, satellite microwave radiances sensitive to humidity, cloud and precipitation provide 20% of short-range forecast impact, as measured by adjoint-based forecast sensitivity diagnostics. This makes them one of the most important sources of data and equivalent in impact to microwave temperature sounding observations. Forecasts of dynamical quantities, and precipitation, are improved out to at least day 6. This article reviews the impact of and the science behind these data. It is not straightforward to assimilate cloud and precipitation-affected observations when the intrinsic predictability of cloud and precipitation features is limited. Assimilation systems must be able to operate in the presence of all-pervasive cloud and precipitation ‘mislocation’ errors. However, by assimilating these observations using the ‘all-sky’ approach, and supported by advances in data assimilation and forecast modelling, modern data assimilation systems can infer the dynamical state of the atmosphere, not just from traditional temperature-related observations, but from observations of humidity, cloud and precipitation.

Key Words: satellite; microwave; cloud and precipitation; NWP; all-sky

Received 3 May 2017; Revised 29 August 2017; Accepted 28 September 2017; Published online in Wiley Online Library

1. Introduction

It is broadly appreciated that weather forecasts can be improved by assimilating measurements sensitive to the dynamical state, such as pressure, temperature and wind. Less appreciated is the benefit of measurements sensitive to the moist atmosphere. Historically, humidity observations showed little impact on forecasts (Bengtsson and Hodges, 2005) but modern assimilation systems, whether based on variational or ensemble techniques, are able to infer the dynamical state from such observations, and now it is also possible to use their sensitivity to cloud and precipitation (e.g. Andersson *et al.*, 1994; Peubey and McNally, 2009; Geer *et al.*, 2014; Lien *et al.*, 2016). Satellite microwave data sensitive to moist atmospheric variables are now one of the most important parts of the global observing system.

Figure 1 shows the sensitivity of 24 h forecast errors to assimilated observations (Forecast Sensitivity to Observation Impact, FSOI; Langland and Baker, 2004; Cardinali, 2009) in the European Centre for Medium-range Weather Forecasts (ECMWF) operational analyses. Between 2012 and 2016, the impact of microwave humidity, cloud and precipitation-sensitive observations ('MW WV') has increased from 8% to 21% of the total observational impact. As the sensitivity is given in relative

terms, it does not necessarily mean that other observation types have decreased in usefulness, just that the impact of microwave observations has improved faster. The impact of 8% in 2012 demonstrates the benefit of the all-sky assimilation of microwave imagers that had recently been introduced (Bauer *et al.*, 2010; Geer *et al.*, 2010; Geer and Bauer, 2011). Since then increases have come by applying all-sky assimilation to microwave humidity sounding channels, for the SSMS instrument (Geer, 2013; Baordo and Geer, 2016) and later MHS (Geer *et al.*, 2014), along with the activation of ATMS (Bormann *et al.*, 2013, in clear skies only to date; the Appendix gives satellite and sensor acronyms). Further benefits have come from the all-sky assimilation of new microwave imagers AMSR2 and GMI (Kazumori *et al.*, 2016; Lean *et al.*, 2017) and the novel sounder MWHS-2 (Lawrence *et al.*, 2015). As of 2016, a total of nine instruments are being assimilated through the all-sky route. A more detailed examination of these results is in section 3.

The first purpose of this article is to review the developments that have helped make all-sky microwave humidity observations an important part of the global observing system. The focus is on the work at ECMWF, but where possible it is presented in the context of wider developments. The other aims are to examine the forecast impact results in more detail and, finally,

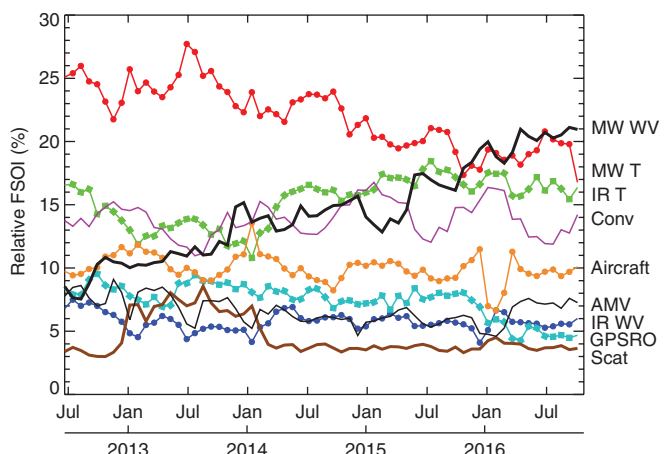


Figure 1. Forecast Sensitivity to Observation Impact (FSOI) in the ECMWF operational system from June 2012 to October 2016, averaged in 25 day bins, normalized so total impact is 100%; section 3 gives details. Acronyms are given in the Appendix. [Colour figure can be viewed at wileyonlinelibrary.com].

to show how it is even possible to assimilate something with such limited predictability, and such large model errors, as cloud and precipitation. Microwave temperature-sensitive radiances are assimilated with observation errors of around 0.25 K into a model state with equivalent background errors of around 0.1 K. In contrast, all-sky moisture-sensitive observations might be assigned an observation error of 50 K and assimilated into a system that cannot predict the exact time and location of cloud and precipitation. There are problems of predictability, representativeness, linearity and systematic errors in model and observation operators (e.g. Errico *et al.*, 2007). Yet, as this article will show, modern assimilation systems are capable of deriving great benefit from humidity, cloud and precipitation observations.

2. Development of all-sky assimilation

2.1. Assimilating humidity

Before the introduction of variational assimilation into operational weather forecasting, it was possible to assimilate observations only directly related to the analysis control variables (i.e. the basic dynamical state) and with the assumption that the observations were valid at the analysis time. Satellite radiances could not be used directly but required a prior retrieval to derive a temperature and moisture profile (e.g. Eyre *et al.*, 1993) which could then be assimilated into the Optimal Interpolation (OI) analysis systems used at the time. As was recognised, this is a sub-optimal approach (e.g. Joiner and Da Silva, 1998). Despite the assimilation of humidity-related observations, even the climatological representation of humidity was inaccurate. Monthly-mean errors were observed in total column water vapour (up to 60%, Vesperini, 1998) and upper-tropospheric humidity (Schmetz and van de Berg, 1994) which were linked to inadequate representation of the Hadley circulation.

Variational data assimilation transformed the quality of the humidity analysis as much as the dynamical analysis. Three-dimensional variational assimilation (3D-Var; e.g. Courtier *et al.*, 1998; Derber and Wu, 1998) made it possible to assimilate observations of any quantity, such as a satellite radiance, that can be simulated from the assimilation control variables using an observation operator. However, the observation operator must include a tangent-linear (TL) and adjoint capability. With the direct assimilation of temperature- and humidity-sensitive radiances (Andersson *et al.*, 1994) the worst climatological errors were eliminated (e.g. Geer and Harries, 1998). However, satellite moisture-sensitive observations still moistened the zonal or regional mean lower-tropospheric humidity analysis by 2–4% relative to a control (e.g. Gérard and Saunders, 1999; Andersson *et al.*, 2007). In the forecast, the model returned quickly to

its preferred drier climate, losing water through precipitation and leading to a poor hydrological balance. This became a well-known problem of the ERA-40 re-analysis, which used a 3D-Var configuration similar to the ECMWF operational system in 1997 (Uppala *et al.*, 2005). In a similar system, Bengtsson and Hodges (2005) showed that the removal of humidity-related observations had no effect on the quality of day 5 forecasts of 500 hPa geopotential height. Some other centres did get reasonable forecast impact with humidity-related observations in 3D-Var (e.g. Chouinard and Hallé, 2003) though it is possible that the main effect was correcting humidity biases and thus reducing errors in latent heating or radiation during the forecast.

Four-dimensional variational assimilation (4D-Var; Courtier *et al.*, 1994; Rabier *et al.*, 2000) brought the ability to assimilate observations related to any physical quantity prognosed by the forecast model, not just the control variables, and at any time during the assimilation window. This requires not just the observation operator but also the forecast model to include a TL and adjoint capability. In 4D-Var, water vapour- and ozone-sensitive observations can provide information on the dynamical state of the atmosphere (e.g. Andersson *et al.*, 1994; Daley, 1995; Riishøjgaard, 1996; Peuch *et al.*, 2000; Allen *et al.*, 2013, 2014). In the absence of moist processes or chemistry, these are atmospheric tracers, and in the presence of a tracer gradient, winds can be inferred using the adjoint of the continuity equation.

Andersson *et al.* (2007) performed humidity observing system experiments, but using a version of the ECMWF operational system from October 2004. Compared to the ERA-40 configuration, this included 4D-Var assimilation along with additional humidity-related observations, more careful bias correction, a new humidity control variable (Hölm *et al.*, 2002) and an improved moist physical parametrization in the forecast model. Activating all humidity-sensitive observations (i.e. infrared and microwave satellite data, plus conventional data) reduced day 5 midlatitude temperature and wind forecast errors by around 1–3%. Peubey and McNally (2009) demonstrated practically that, unlike 3D-Var, a 4D-Var system could extract dynamical information from humidity-sensitive radiances, and that this was achieved using the tracer-advection mechanism. Hence, although many developments will have contributed to the beneficial assimilation of humidity data demonstrated by Andersson *et al.* (2007), a main explanation was the ability to infer dynamical information through the humidity-tracing mechanism in 4D-Var.

2.2. Assimilating cloud and precipitation

Attempts to use cloud and precipitation observations to improve weather forecasts go back to the 1980s, with empirical techniques like inferring heating rates from satellite observations of precipitation and incorporating these in forecast models through normal-mode initialization (e.g. Krishnamurti *et al.*, 1984; Heckley *et al.*, 1990). The advent of 4D-Var provided the first theoretically consistent framework for the exploitation of cloud and precipitation data. 4D-Var can in principle infer winds, temperature and humidity, not just from the continuity equation of a tracer, but from the more complex equations that describe the formation of cloud and precipitation. Many studies (e.g. Zou *et al.*, 1993; Źupanski and Mesinger, 1995; Tsuyuki, 1997; Zou, 1997) explored these possibilities but practical and theoretical difficulties prevented the immediate application of these ideas in operational forecasting (e.g. Fillion and Errico, 1997; Errico *et al.*, 2000). Some of these difficulties were outlined by Errico *et al.* (2007) and we examine them over the following paragraphs.

With regard to observations, it might appear convenient to assimilate cloud or precipitation retrievals. However, these suffer from the same problems of non-optimality found with temperature and moisture retrievals in the days before direct radiance assimilation. In addition, cloud and precipitation observations cannot be assimilated when cloud or precipitation

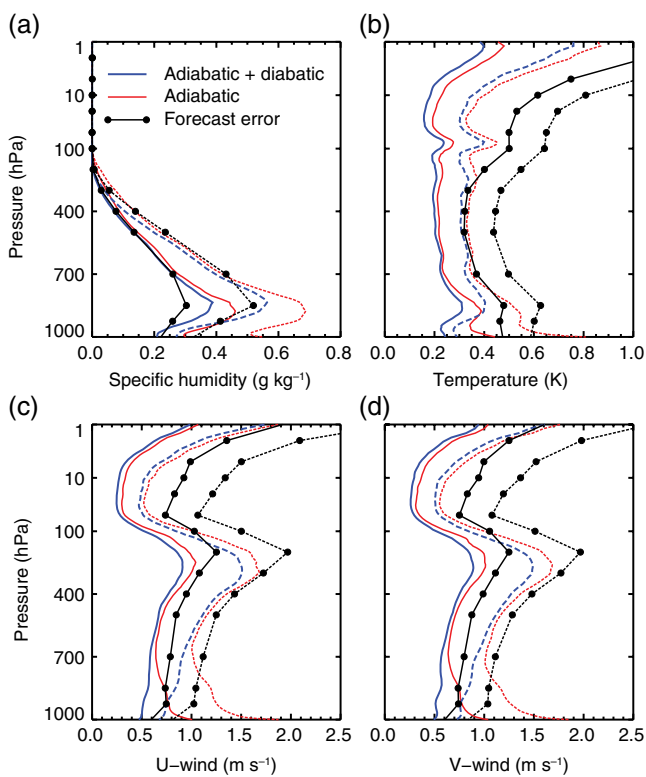


Figure 2. Global mean absolute error in the tangent linear (TL) approximation, after 12 h (solid) and 24 h (dashed) with a purely adiabatic TL and with adiabatic and diabatic process including moist physics, compared to the typical standard deviation of global forecast errors (based on own-analysis). Initial perturbations are for 0000 UTC 5 January 2014 and are typical 4D-Var increments; the same spectral resolution of T399 has been used in the nonlinear and linear models. The error in the TL approximation is $M(x + \delta x) - M(x) - M(\delta x)$ where M is the nonlinear model, M the tangent linear model, x the model state and δx the increment. [Colour figure can be viewed at wileyonlinelibrary.com].

is missing in the first guess (FG), due to the zero-gradient problem. Also the error statistics of these observations can be far from Gaussian. Assimilating radiances is a more optimal way of using the data, and a side benefit is that radiances often have a more continuous sensitivity to humidity, cloud and precipitation. Assimilation schemes can adjust atmospheric humidity to better fit radiances, and thus to create cloud or precipitation indirectly, even if there is no sensitivity to cloud or precipitation (Moreau *et al.*, 2004). A final advantage of radiances is that error statistics can be more Gaussian (e.g. Bauer *et al.*, 2006a).

With regard to modelling, it is hard to realistically simulate cloud and precipitation in the forecast model, and hard to create an accurate observation operator to simulate the scattering and absorption of radiation by cloud and precipitation particles. As a result, there may be biases (between inadequate forward models and the observations) which are much larger than any useful information that the observations can provide. In variational assimilation, the TL and adjoint models of the moist physical processes link a change in the 4D-Var control variables with a change in cloud and precipitation fields (Janisková and Lopez, 2013). These moist processes have discontinuities and strong gradients that can cause the variational assimilation to fail. The recent availability of ensemble assimilation techniques (e.g. Hunt *et al.*, 2007) that can be used for cloud and precipitation assimilation without the need to develop TL and adjoint models (e.g. Snyder and Zhang, 2003; Otkin, 2010; Zhang *et al.*, 2013; Lien *et al.*, 2016) does not circumvent the difficulty of dealing with nonlinear and discontinuous cloud and precipitation processes.

Errico *et al.* (2007) also mentioned the need to better understand the predictability of cloud and precipitation, and this is also a key issue. All the issues they raised have needed to be considered during the development of operational cloud and precipitation assimilation, as will be seen in the following

pages, but the success of that development shows they are not fundamental blocks to progress.

The move to 4D-Var encouraged ECMWF to further develop its humidity assimilation and to work towards including cloud and precipitation assimilation (Hólm *et al.*, 2002; Andersson *et al.*, 2005). It was noted that meteorologically sensitive areas are often obscured by cloud, limiting the ability of clear-sky radiance assimilation to improve the analysis in these areas (McNally, 2002). For microwave radiance assimilation, one key development was the computationally efficient, scattering-capable radiative transfer code (Bauer, 2001; Chevallier and Kelly, 2002; Smith *et al.*, 2002; Bauer *et al.*, 2006c) that is now available as the RTTOV-SCATT package. However, the most critical developments were the TL and adjoint moist physics models (Janisková *et al.*, 1999; Tompkins and Janisková, 2004; Lopez and Moreau, 2005). These moist physics developments were intended to improve the quality of the TL approximation to the full nonlinear atmospheric model beyond what was achievable with a purely adiabatic approach (Mahfouf, 1999). However, the potential for cloud and precipitation assimilation was clear.

The derivation of a TL physics package starts with making a simplified, regularized version of the full nonlinear model, removing or smoothing over the worst of the nonlinearities (e.g. Janisková and Lopez, 2013). The TL equivalent is then created, by hand, differentiating each line of nonlinear code. Careful testing is needed and further regularization may be necessary if the initial models show excessively strong instabilities. These models may be simplified but they can represent the nonlinear evolution of forecast perturbations, including cloud and precipitation, with reasonable skill out to at least 24 h. For example, Figure 2 compares the errors in the TL approximation with the size of typical forecast errors at the same time range. Using diabatic and adiabatic processes in the TL reduces the error compared to an adiabatic version, particularly near the surface. The errors shown here are a worst-case scenario because they are based on the full data assimilation increments from one assimilation cycle. In the incremental formulation of 4D-Var used at ECMWF, the size of the increments needing to be evolved by the TL model become progressively smaller as the state gets closer to the analysis. This substantially reduces the size of the TL errors. Bauer *et al.* (2010) demonstrated the accuracy of the cloud and precipitation TL approximation, which is not perfect for the initial large increments but becomes increasingly good as the minimization converges. Along with the regularization applied in the linearized physics model, the incremental formulation helps avoid the issues raised by Errico *et al.* (2007) and others.

With a 4D-Var system capable of assimilating information from cloud and precipitation, ECMWF explored a great variety of strategies. Different observation types were tried including cloud- and precipitation-affected passive microwave radiances (Chevallier and Kelly, 2002; Moreau *et al.*, 2003) and infrared radiances (Chevallier and Kelly, 2002; Chevallier *et al.*, 2004), precipitation retrievals (Marécal and Mahfouf, 2000, 2002; Marécal and Bauer, 2002; Lopez and Bauer, 2007), radar reflectivities (Benedetti *et al.*, 2005; Lopez *et al.*, 2006) and cloud optical depth retrievals (Benedetti and Janisková, 2007). Rather than assimilate these observations directly in 4D-Var, it was generally preferred to follow the path of clear-sky assimilation developments (e.g. Eyre *et al.*, 1993) and to first apply a 1D-Var retrieval to derive profiles of temperature and moisture (or just column-integrated water vapour) which could then be assimilated as pseudo-observations in the 4D-Var system (Marécal and Mahfouf 2003; Moreau *et al.*, 2004). The 1D-Var retrieval uses TL and adjoint versions of both the observation operator and the model physics to translate from changes in radiance to changes in cloud and precipitation, and from changes in cloud and precipitation into changes in the vertical profile of temperature and moisture. An initial benefit of 1D-Var was the ability to screen out any difficult observations, such as those for which convergence was not even possible in 1D-Var, before assimilation in 4D-Var.

The argument against direct assimilation was also based on poor initial results and the apparently detrimental effects of cloud and precipitation nonlinearity during the 4D-Var minimization. An operational centre must avoid the risk of failures during the analysis.

As with the great variety of experimentation into cloud and precipitation assimilation which was happening elsewhere (e.g. Alexander *et al.*, 1999; Bayler *et al.*, 2000; Xiao *et al.*, 2000; Hou *et al.*, 2004; Vukicevic *et al.*, 2004; Deblonde *et al.*, 2007) only a few approaches were developed to the level where they could be adopted for operational weather forecasting. At ECMWF, operational assimilation of cloud- and precipitation-affected microwave radiances started in 2005 using the 1D+4D-Var approach (Bauer *et al.*, 2006a, 2006b). For infrared radiances, limited use of cloud-affected data was introduced, focusing on the clear-air signal above the ‘surface’ provided by an unbroken cloud top (McNally, 2009; Lupo and McNally, 2012). Across the main operational centres, some operational use of cloud and precipitation observations began to prove viable (Bauer *et al.*, 2011). In the infrared, this followed the general approach of using clear-air information above a retrieved cloud top (Pavelin *et al.*, 2008; Guidard *et al.*, 2011). There was also assimilation of precipitation rates and cloud fractions (e.g. Tauchi *et al.*, 2004; Koizumi *et al.*, 2005; Taylor *et al.*, 2008; Renshaw and Francis, 2011) and of Bayesian humidity retrievals from radar reflectivities (Wattrelot *et al.*, 2014).

2.3. All-sky assimilation

As soon as the 1D+4D-Var technique was operational for microwave imagers, ECMWF started working towards direct assimilation of cloud- and precipitation-affected radiances into 4D-Var. A main motivation was to avoid the theoretical sub-optimality of 1D+4D-Var (Lopez and Bauer, 2007; Geer *et al.*, 2007, 2008). Without methods to remove the 1D-Var *a priori* (e.g. Migliorini *et al.*, 2008) it incorporates this *a priori* as ‘new’ information in the pseudo-observation that is given to the 4D-Var analysis. Also, the 1D+4D-Var technique suffered from biases whose consequences were most obvious in reanalyses. In a parallel with the problems of assimilating humidity radiances in ERA-40, the new ERA-Interim underestimated global rainfall for the years when the 1D+4D-Var cloud- and precipitation-affected microwave imager data were assimilated (Dee *et al.*, 2011). The main bias affecting cloudy 1D+4D-Var came from an error (since corrected) in the simplified moist physics, which produced too much modelled rain so that the observations were generally trying to remove rain from the analysis. This had been hiding a more fundamentally important bias in the sampling: the asymmetric selection of observations into the ‘clear-sky radiance’ and ‘cloudy 1D+4D-Var’ paths (Geer *et al.*, 2008).

To examine these issues of sampling, Table 1 shows brightness temperature biases in three possible configurations (based on the current system including the corrected moist physics.) First is clear-sky; observations affected by cloud are discarded and the observation operator does not take account of model cloud. However, cloud detection is not perfect so there is residual cloud in the ‘clear’ observations. Since cloud raises the brightness temperatures at low microwave frequencies, there is a small positive bias in both the obs clear/model clear and obs clear/model cloudy categories (+0.71 and +1.1 K). This can be interpreted by the assimilation system as a lack of moisture in the model, and the analysis can be moistened incorrectly. Second is the result of adding the cloudy observations in a new stream, similar to what was done with 1D+4D-Var at ECMWF. In our example the new stream uses a radiative transfer model that accounts for cloud and precipitation, whereas the clear-sky stream is unchanged and still uses clear-sky radiative transfer. Although the observations going through the cloudy stream are guaranteed to be cloudy (by design), around 40% of corresponding model points are clear, leading to a +3.3 K bias in the obs cloudy/model clear category.

Table 1. Percentage of observations and mean first-guess (FG) departure bias (observation minus simulation) in the SSMIS 37v channel, by contingency table category, for different assimilation configurations.

	Model clear	Model cloudy
Clear-sky		
Obs cloudy	N/A	N/A
Obs clear	Clear stream 41.7%	Clear stream 11.9% +1.1 K
Clear and cloudy separated		
Obs cloudy	Cloudy stream 19.2% +3.3 K	Cloudy stream 27.2% +0.95 K
Obs clear	Clear stream 41.7% +0.71 K	Clear stream 11.9% +1.1 K
All-sky		
Obs cloudy	19.2% +3.3 K	27.2% +0.95 K
Obs clear	41.7% −0.28 K	11.9% −4.33 K

Cloud is detected by a 0.05 threshold in the C_{37} cloud predictor of Geer and Bauer (2011). Based on a sample of observations from SSMIS F-17 from 2 to 5 May 2016 screened by removing land and areas possibly affected by sea-ice or cold-sector bias. Bias corrected using the operational (all-sky) correction.

This bias can be interpreted by the assimilation system as a lack of cloud or moisture, but either way the analysis will be moistened still further. The only way to resolve these issues is to assimilate all observations using a cloud- and precipitation-capable observation operator throughout: an ‘all-sky’ approach. Now, the positive sampling bias in the obs cloudy/model clear category is counterbalanced by a negative sampling bias in the obs clear/model cloudy category. Further, in the obs clear/model clear category, ‘undetected’ cloud now equally affects the observed and the simulated all-sky brightness temperatures, reducing the bias in this category too. However, a benefit of the all-sky system is there is no need to separate the observations into categories like this. All-sky assimilation recognises that 4D-Var (or alternatively nowadays, ensemble) systems are capable of handling cloud and precipitation as just another part of the atmospheric state, despite all the possible theoretical problems.

Single observation test cases showed the ability of incremental 4D-Var to fit observed cloud and precipitation by modifying the moist and dynamical initial conditions (Bauer *et al.*, 2010; Geer *et al.*, 2014). For example, in Figure 3 an MHS observation has indicated that the model FG is over-predicting snow on the leading edge of a developing front. To fit this observation, the pressure of the developing low-pressure system has been increased by around 0.2 hPa at the beginning of the assimilation window, leading to a less intense snowfall along the front that develops 8 h later. Importantly, no increments are made to the moisture at the beginning of the assimilation window; instead it is the dynamical initial conditions that are adjusted. At midlatitudes, these kind of results have been repeated in many case-studies. In the Tropics, in deep convection, the single-observation case-studies occasionally fail to fit the observations. This may be due to the difficulty of assimilating convection in the Tropics, where it is the product of seasonal and diurnal variations alongside tropical phenomena such as Kelvin and easterly waves. Despite this, many single-observation case-studies do achieve a better fit to observations in the Tropics by successfully moving, increasing or reducing convective precipitation. All these case-studies support the basic ability of a 4D-Var system to assimilate cloud and precipitation, and illustrate the mechanism of ‘4D-Var tracing’.

The assimilation of microwave imagers was moved to an all-sky approach in 2009, replacing the previous combination of direct assimilation for clear-sky radiances and 1D+4D-Var assimilation for cloud-affected radiances. However, it was implemented with

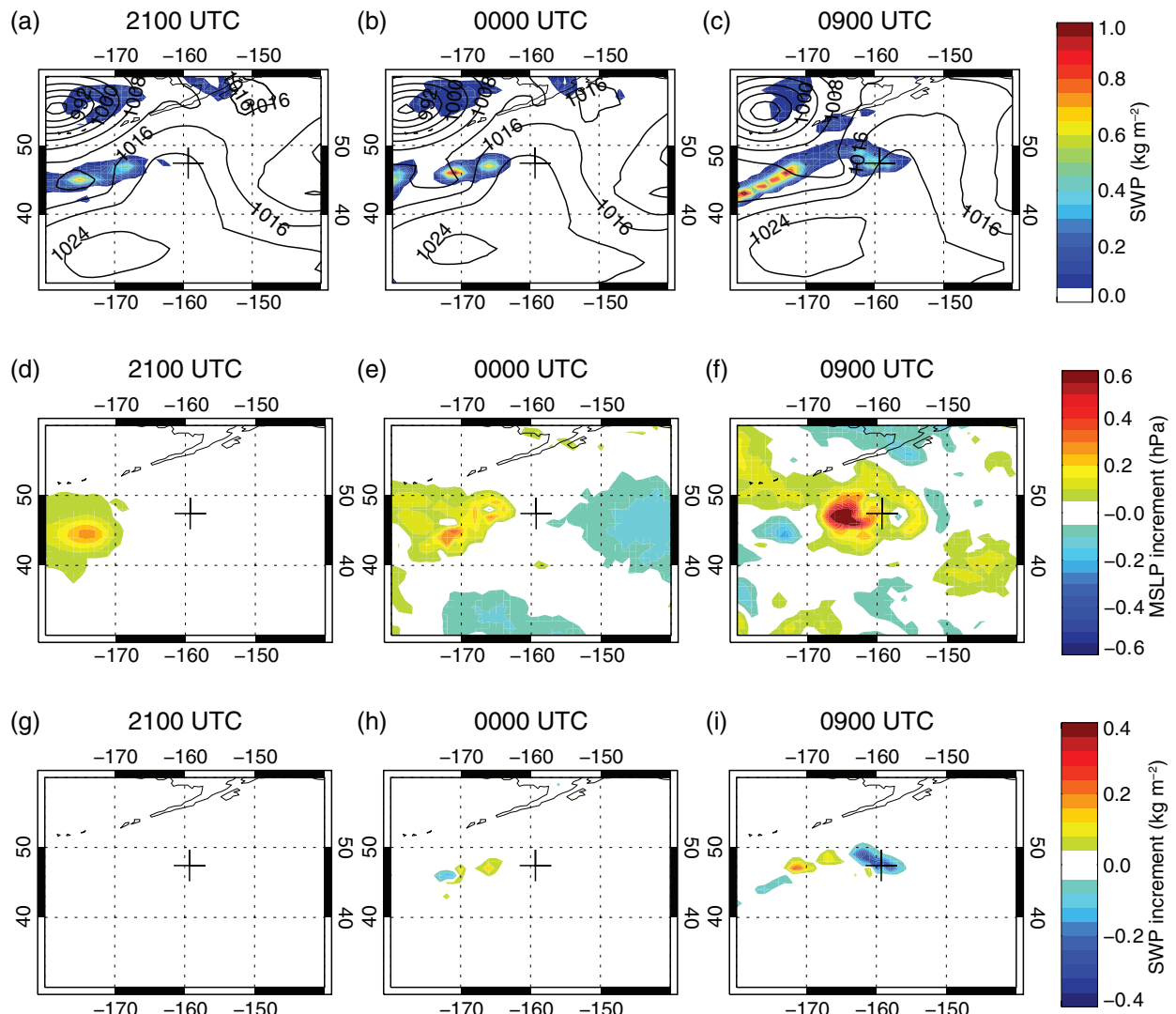


Figure 3. Model fields through the assimilation window (2100–0900 UTC) in single observation of Geer *et al.*, 2014 (their case J). (a–c) First-guess mean sea-level pressure (MSLP, hPa, line contours) and snow water path (SWP, shaded contours), (d–f) increments in MSLP, and (g–i) increments in SWP. The cross shows the location of the Metop-B MHS observation, which was made at 0800 UTC.

an observation-error model that inflated observation errors as a function of distance from grid-point centre, trying to account for representivity error (Bauer *et al.*, 2010; Geer *et al.*, 2010). This was later seen to be a poor predictor for observation error, and also the settings of this particular model meant that it gave little weight to the observations.

To improve the observation-error model, the key insight was that, although cloud and precipitation features are generally well represented by the forecast model, often their intensity or location is slightly wrong when compared to observations; all these errors are referred to as ‘mislocation’ though, as discussed later, the terminology is imprecise. The distance between an observation and a model grid-point had little effect on the size of the FG departures for distances less than 100 km, because cloud and precipitation features are not fully predictable over 12 h on that scale. Wherever cloud and precipitation is present, mislocation errors dominate and produce large FG departure variances. There is usually a clear relationship (often linear or quadratic) between the inferred ‘cloud amount’ and the size of these variances. Geer and Bauer (2010, 2011) introduced an error model exploiting this effect, termed ‘symmetric’ because the observation error is inflated whether the cloud is present in the model or in the observations. Generally for imager channels the ‘cloud amount’ is a quantity sensitive to liquid cloud and precipitation derived from the 37 GHz polarization difference; for sounding channels it is usually a scattering index, indicating the presence of frozen precipitation particles. A main benefit of the new error model was to produce nearly Gaussian FG departures, addressing another

of the issues raised by Errico *et al.* (2007). The new error model was implemented in 2010, and gave an immediate increase in the forecast impact of microwave imager observations as measured by FSOI (Cardinali and Prates, 2011).

The symmetric observation-error model has been explored in many contexts (e.g. Okamoto *et al.*, 2014; Chambon *et al.*, 2014; Harnisch *et al.*, 2016; Yang *et al.*, 2016). Hence just a brief example is given here. Figure 4 illustrates the link between the mislocation error and the assigned observation error. In Figure 4(a), heavy precipitation in a mesoscale convective system (MCS) just south of the island of Sumatra has caused high observed 19 GHz brightness temperatures between 8 and 13°S, over a distance of roughly 500 km. The forecast model’s FG represents the same MCS, but it is incorrectly restricted between 11°S and 13°S. As shown in Figure 4(b), this gives a typical ‘dipole’ pattern of FG departures, even if the error itself is more complicated than a simple displacement. These dipoles, of different shapes and scales, are a major feature of any map of all-sky FG departures. The analysis, based on all observations including the all-sky data, is able to extend the area of precipitation to match observations, though in this case it fails to reduce precipitation between 11°S and 13°S where it is too intense in the model. The observation-error model inflates observation errors (also shown on Figure 4(b)) across the region where precipitation is present in either the observations or the FG.

It is complicated to assess the forecast impact of these initial developments in all-sky assimilation. The forecast scores presented in support of 1D+4D-Var (Bauer *et al.*, 2006b; Kelly

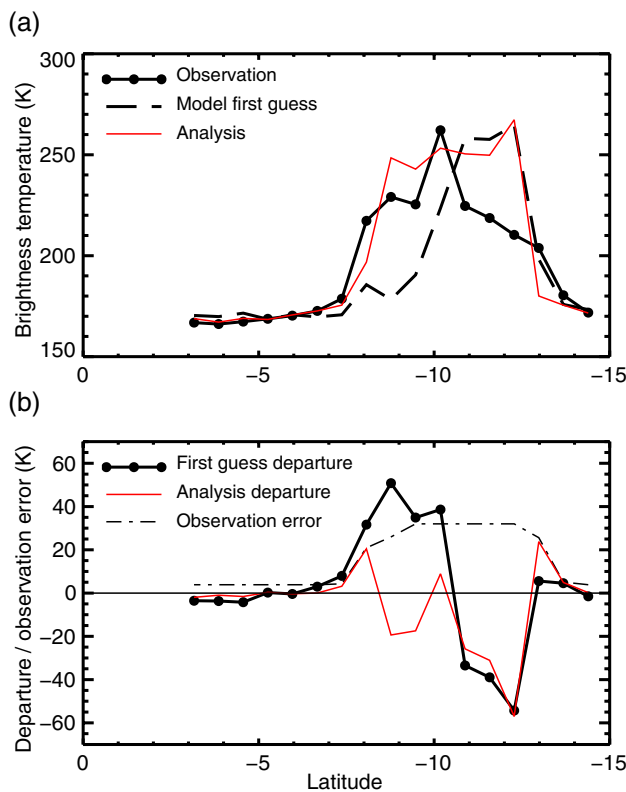


Figure 4. Assimilating SSMIS F17 channel 19 h observations in the presence of precipitation displacement and intensity errors. (a) Observed, modelled and analysed brightness temperatures; (b) first-guess departure, analysis departures, and observation error. A north–south transect has been taken at 100°E through observations valid at 0000 UTC on 3 May 2016. Multiple raw observations are superrobed in a circular area of approximately 60 km radius. [Colour figure can be viewed at wileyonlinelibrary.com].

et al., 2008) are affected by the ‘recycling’ of the *a priori* as new data in 1D+4D-Var, which has the side-effect of making analysis-based forecast scores falsely favourable to 1D+4D-Var in observing system experiments (OSEs; Geer et al., 2010). More generally, short-range humidity scores in the Tropics are hard to interpret. Some of the most reliable measures presented by Geer et al. (2010) and Geer and Bauer (2010) are the FG fits to humidity radiosondes and the day 5 Southern Hemisphere (SH) wind scores. These show that short-range moisture forecasts worsened after moving to direct all-sky assimilation with the initial error model and then recovered to the level of quality of 1D+4D-Var with the implementation of the symmetric observation error model (which agrees with the FSOI results of Cardinali and Prates, 2011). However, the medium-range dynamical impact remained similar across all three configurations, at around 0% in the NH and 2% in the SH. At the time it was rarely possible to generate long-enough periods of experimentation to provide a level of statistical confidence that would allow us to examine this in more detail (Geer, 2016). Even if some scores were only maintained, rather than improved, it was desirable to implement the new technique operationally, so as to be able to prove it, and to develop it further.

Once all-sky assimilation was working for microwave imagers, it was tried on AMSU-A temperature-sounding channels, some of which have weighting functions low enough to be strongly sensitive to liquid water cloud. This was not successful, partly due to the poor quality of radiative transfer modelling for the AMSU-A channels in conditions of strong scattering from frozen hydrometeors at that time (Geer et al., 2012). Figure 5 shows the impact of developments in radiative transfer modelling on the zonal mean bias between observations and the model. In response to radiative transfer modelling biases uncovered by Geer et al. (2008), the cloud overlap representation had been improved (Geer et al., 2009). However in some cases this uncovered even larger biases, which were finally traced to an inadequate representation

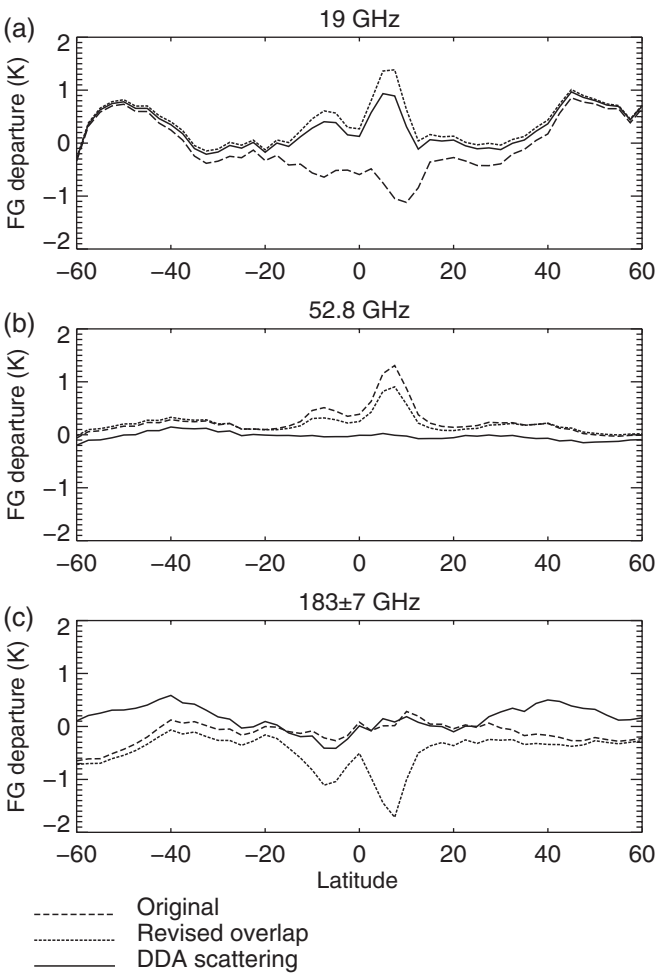


Figure 5. Zonal mean of SSMIS F-17 FG departures after bias correction for (a) 19 GHz, (b) 52.8 GHz and (c) 183 GHz, averaged over 1 May to 25 June 2016, with three versions of the RTTOV-SCATT radiative transfer code.

of scattering from frozen particles (Geer and Baordo, 2014). Using a discrete-dipole-based representation of scattering properties of snow particles (Liu, 2008), cloud and precipitation observations could be simulated with more realism at AMSU-A frequencies like 52.8 GHz but also up to 183 GHz, making the humidity-sounding channels viable candidates for all-sky assimilation.

It was quickly seen that all-sky assimilation of the moisture-sounding channels at 183 GHz on SSMIS, MHS and MWHS-2 provided significant benefits to medium-range forecasts (Geer, 2013; Geer et al., 2014; Lawrence et al., 2015). It is the full exploitation of these observations that has led to all-sky assimilation becoming such a major part of the operational observing system. This is not just about all-sky developments, but also the increase in data utilization over sea-ice, snow and land surfaces (e.g. Krzeminski et al., 2009; Di Tomaso et al., 2013; Baordo and Geer, 2016). Developments in all-sky assimilation have also been supported by broader improvements of the assimilation system such as increasingly accurate background errors (e.g. Bonavita et al., 2015).

To use all-sky observations successfully it has also been necessary to take care of situations where model errors cause large systematic biases between model and observations. If assimilated, these biases can cause degradations to the forecasts, so it is usually best to screen these data out completely. It is sometimes hoped that bias-correction schemes can be used to correct cloud- and precipitation-related biases, but in practice such biases are difficult to characterize in a way that can be implemented in such a scheme, and there are potential pitfalls if the cloud-bias predictor implies an asymmetric sampling with respect to model or observations (Geer and Bauer, 2010; Chambon et al., 2014). Two examples of these situation-dependent biases, are, first, a lack of supercooled liquid water in the forecast model in cold-air

outbreaks that has been addressed with careful quality control (e.g. Lonitz and Geer, 2015). Second, there appears to be an underprediction of cloud liquid water in maritime stratocumulus areas (Kazumori *et al.*, 2016) although in this case it is more beneficial to assimilate the affected observations, rather than to discard them (Lonitz and Geer, 2017). Beyond identifying and screening out the problem areas, all-sky assimilation is starting to give guidance for improving the forecast model. The supercooled liquid water deficit in cold-air outbreaks, first identified in the all-sky observations, is being addressed by changes to the ice–liquid partitioning of detrainment from shallow convection in the forecast model (Forbes *et al.*, 2016).

Aside from the all-sky radiances, ECMWF has introduced direct assimilation of rain rates from radar and rain-gauges (Lopez, 2011). At other weather centres, all-sky assimilation is now being introduced operationally (e.g. Zhu *et al.*, 2016) and preparations are being made to assimilate all-sky microwave radiances in regional models (Guerbet *et al.*, 2016; Yang *et al.*, 2016). Geer *et al.* (2017) will give a broader survey of developments at other operational centres.

3. Current status and observation impact

Table 2 shows the utilization of microwave humidity, cloud and precipitation radiances in the ECMWF operational system in August 2016. Two instruments are awaiting a transition to the all-sky approach, but nine others are assimilated in all-sky conditions. To have so many satellites is unprecedented and it has coincided with our developing ability to use the data, both in cloud and precipitation but also over land surfaces, snow and sea-ice. Three different types of channel are used:

1. Microwave humidity sounding channels around the strong 183 GHz water vapour line, which normally have limited sensitivity to the surface and sense humidity in the mid and upper-troposphere (e.g. Buehler and John, 2005). In cloudy conditions they also see ice cloud and deep convection because these scatter the upwelling radiation, decreasing the brightness temperatures (e.g. Hong *et al.*, 2005; Doherty *et al.*, 2007). These channels can be assimilated over most surfaces, such as ocean, sea-ice, and land including snow-covered land.
2. Microwave imaging channels between 19 and 92 GHz with strong sensitivity to the surface, and used only over oceans between 60°S and 60°N (and note the horizontally polarized 37 GHz and 89/92 GHz channels are not yet used). The ocean surface presents a radiometrically cold and strongly polarized background against which water vapour, cloud and precipitation stand out as warm,

Table 2. Microwave humidity assimilation using an all-sky approach or a clear-sky approach in the ECMWF operational system, August 2016.

Satellite	Instrument	Sounder				Imager (ocean)	118 GHz (ocean)
		O	L	S	I		
All-sky							
DMSP-F17	SSMIS	x	x	x	x	x	
DMSP-F18	SSMIS	x					
NOAA-18	MHS	x	x	x	x		
NOAA-19	MHS	x	x	x	x		
Metop-A	MHS	x	x	x	x		
Metop-B	MHS	x	x	x	x		
FY-3C	MWHS-2	x	x	x	x	x	
GCOM-W	AMSR2					x	
GPM	GMI					x	
Clear-sky							
Suomi-NPP	ATMS	x	x				
FY-3B	MWHS-1	x					

O = ocean, L = land, S = snow, I = sea-ice.

non-polarized emitters (though scattering effects are also present in higher-frequency channels, and lead to decreasing brightness temperatures). There is no use of these channels over land, snow or sea-ice where the surface has high emissivity and is difficult to model accurately, making it far harder to extract any useful atmospheric information.

3. The novel 118 GHz channels on MWHS-2. These channels are centred on an oxygen line and technically are temperature-sounding channels, but they have high instrument noise relative to the size of FG temperature errors, so much of their benefit comes through sensitivity to water vapour, cloud and precipitation (Lawrence *et al.*, 2015).

A more detailed description of data usage for the instruments used in all-sky conditions can be found in Geer *et al.* (2014), Kazumori *et al.* (2016), Lawrence *et al.* (2015) and Lean *et al.* (2017); note that SSMIS has temperature-sounding channels but these are not used. For the moment we keep all-sky imager-channel usage to three instruments because the benefits from additional imaging data can be outweighed by the effect of the additional biases (e.g. Kazumori *et al.*, 2016). All additional microwave humidity sounding data have so far proved entirely beneficial, so we currently use humidity sounding channels from nine instruments. Some of these sensors are not yet utilized over all surfaces, in part because of technical issues: for example DMSP-F18 has lost a 150 GHz channel that is not assimilated, but is still needed for surface emissivity retrievals. ATMS and MWHS-1 are still only assimilated in clear skies (Bormann *et al.*, 2013; Chen *et al.*, 2015); for ATMS this is partly because its temperature channels are also assimilated, and the all-sky framework cannot yet support this.

Microwave humidity imaging and sounding observations have become a leading contributor to short-range forecast skill alongside microwave temperature-sounding observations and infrared observations. Figure 1 shows the percentage of FSOI contributed by the main observation types. FSOI measures the reduction in 24 h forecast errors generated by the observations assimilated in one data assimilation cycle (here using a dry norm of 36 h minus 24 h errors; Langland and Baker, 2004; Cardinali, 2009; also section 4.1 gives caveats). In 2006, microwave humidity observations gave just 6% of the total FSOI, compared to 35% from microwave temperature sounding and 24% from infrared instruments (Cardinali, 2009). At this time, the microwave imager SSM/I was used with direct assimilation of clear-sky radiances plus a 1D+4D-Var for the cloud-affected data. Microwave humidity sounding observations from MHS and AMSU-B were also included, but only in clear skies and over oceans. The introduction of all-sky assimilation with the revised observation-error model boosted the FSOI of the microwave imagers (Cardinali and Prates, 2011) so that by the start of the available timeseries in Figure 1, the FSOI of all microwave water vapour data was around 8%.

In the unsmoothed version of this timeseries (not shown) the clearest and most well-attributed step increases are:

September 2012, with the introduction of ATMS humidity sounding channels in clear skies (Bormann *et al.*, 2013). Its temperature sounding channels contribute to the ‘MW T’ category on Figure 1;

November 2013, with the introduction of all-sky SSMIS humidity sounding channels over ocean (Geer, 2013);

May 2015, with the transfer of four MHS instruments from clear-sky to all-sky (Geer *et al.*, 2014);

March 2016, with the introduction of F18 SSMIS humidity sounding channels and the inclusion of snow-covered land surfaces.

Some improvements in the microwave humidity observations do not seem to have boosted the FSOI so clearly, and sometimes the FSOI goes down again, likely due to natural variability or the addition of competing instruments. Natural variability occurs

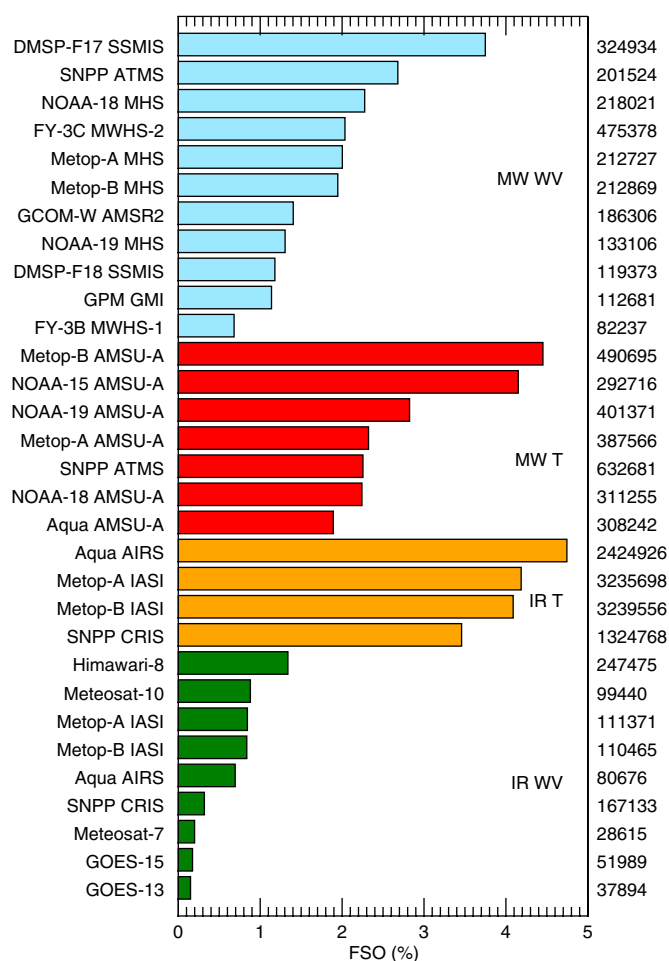


Figure 6. Forecast sensitivity to satellite radiance observations (FSOI) in the ECMWF operational system, given as a percentage of the total FSOI, over 20 July to 20 August 2016. Observations are grouped by type (infrared, IR, or microwave, MW) and sensitivity (water vapour, cloud and precipitation, WV, or temperature, T). The right-hand column gives the number of observations assimilated per day. [Colour figure can be viewed at wileyonlinelibrary.com].

on different time-scales, clearest in the aircraft data and other conventional observations ('Conv') which have a predominantly NH coverage, and hence their FSOI usually peaks around January when NH winter errors dominate the global error norm. Despite this, the overall trend in FSOI for microwave humidity instruments is clear.

Figure 6 breaks down satellite radiance FSOI by sensor and by sensitivity to water vapour or temperature, based on a time period in July and August 2016. The leading all-sky microwave sensor is the SSMIS on F-17, which combines microwave imaging and humidity-sounding channels, and has near-global utilisation (Table 2). This SSMIS has similar impact to the most important temperature sensors like AMSU-A and IASI. Other microwave water-vapour sensors have less impact individually, but gain strength in numbers. Temperature information still dominates the impact of infrared sensors; infrared humidity-sounding channels have relatively little impact, although Himawari-8, which is assimilated hourly and has more water vapour sounding channels than other geostationary satellites, gives some indication of the remaining potential in infrared humidity channels. Further, it is hoped eventually to move the IR humidity sounding channels to all-sky assimilation.

Some aspects of Figure 6 can only be understood with detailed knowledge of observation usage at ECMWF. For example the loss of important mid- and upper-tropospheric channels from the AMSU-As on Aqua, NOAA-18 and Metop-A means they have around half the impact of the best AMSU-As. This deterioration explains part of the reduction in FSOI from the microwave temperature sensors between 2012 and 2016 shown in Figure 1. The impact of ATMS is particularly intriguing.

Its humidity-sounding channels have more impact than its temperature-sounding channels. The temperature channels have an assigned observation error of typically 0.35 K partly because of correlated instrument errors (Bormann *et al.*, 2013). Compared to the 0.2 K error used for AMSU-A, this gives the ATMS channels less weight in the assimilation system. In contrast, its humidity-sounding channels are assimilated only in clear-sky conditions (Table 2) but they have more impact than any all-sky MHS sensor. Several factors contribute: ATMS has five available humidity channels, it is in an orbit that does not overlap with many of the other humidity sensors, and it observes sensitive areas over Canada, Siberia and South America at the right time for maximum impact on the ECMWF forecasts, towards the end of the assimilation window.

Figure 7(a) shows the FSOI from all observations in the ECMWF system, for the same July–August 2016 period as before. The SH has generally the largest values, consistent with faster error growth in the winter storm tracks. Outside of the Southern Extratropics, areas of high sensitivity stand out in North America, Africa, Siberia, and the Northwest Pacific. The 11 microwave humidity instruments (Figure 7(b)) provide at least 25%, and peaking at 45%, of all FSOI over the world's oceans. Over some areas of North America, Europe, East Asia and Australia, where many conventional and aircraft observations are available, impact is limited. In many other land areas, such as Canada, Siberia, South America and Africa, the microwave humidity sounders provide around 25% of FSOI. This occurs despite the microwave imaging channels not being used over land surfaces, and despite restrictions on the use of humidity sounding data, particularly

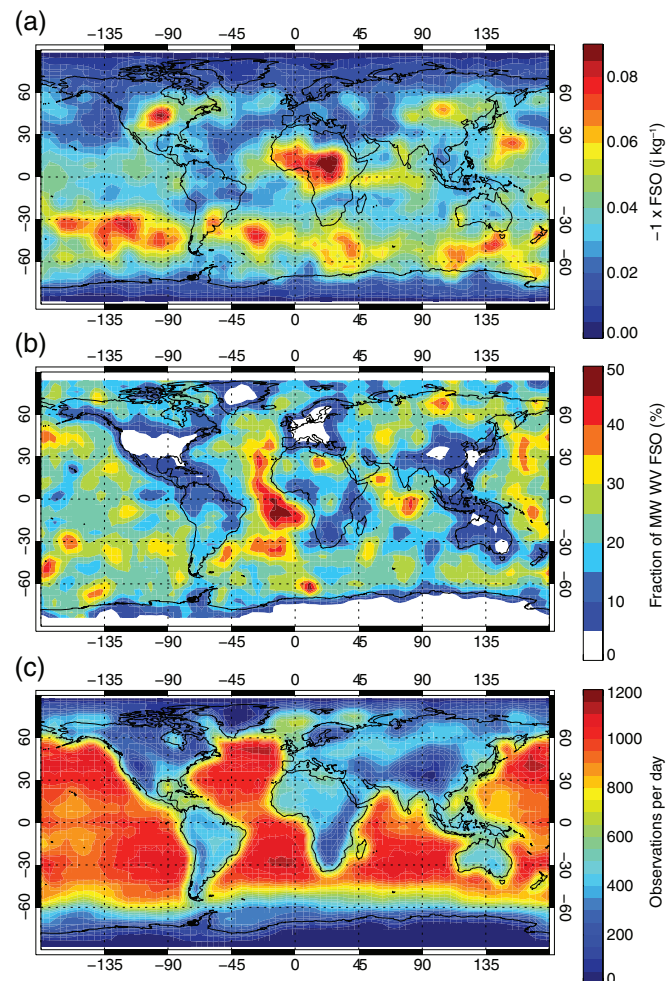


Figure 7. Forecast sensitivity to (a) all observations in the ECMWF operational system, (b) the fraction of that FSOI coming from the 11 microwave humidity sensors, (c) the number of observations available from those sensors. Statistics are accumulated over 20 July to 20 August 2016 in $4^\circ \times 4^\circ$ bins, but with $12^\circ \times 12^\circ$ boxcar smoothing applied.

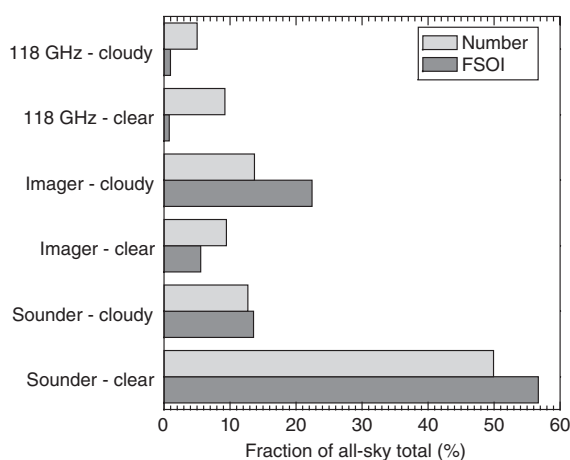


Figure 8. FSOI (dark grey bar) and number of observations (light grey bar) for the nine all-sky instruments, broken down by type of channel (118 GHz temperature/cloud, sounder or imager) and by whether or not the observation (or the model equivalent) is affected by cloud or precipitation. Statistics have been accumulated over 20 July to 20 August 2016 and are given as percentages relative to the total across the nine all-sky instruments.

over high-altitude areas (Figure 7(c)). Over Greenland and Antarctica, the difficult combination of snowy surfaces and high orography means the microwave humidity sounders are barely used and provide little benefit. The humidity radiances gain their large impact by being available almost globally, a reminder that the development of satellite assimilation is not just about cloud and precipitation, but also about using as many surface types as possible.

For the nine instruments assimilated in all-sky conditions, we can break down the FSOI statistics according to whether the data is in clear skies, or whether it is affected by cloud or precipitation in the model or observations, using the cloud predictor that drives the observation-error model (section 2.3). The threshold indicating significant cloud or precipitation is not exact; it has been chosen so that around 40% of imager channels are considered clear. A different threshold is used for humidity-sounding channels, giving about 80% clear, since these channels are less sensitive to low-level and/or thinner cloud. However, these ‘clear’ scenes would not necessarily be safe to assimilate in a clear-sky approach. Figure 8 shows the results, broken down by channel type. The novel 118 GHz channels do not yet provide much impact, but there is scope for future improvement (Lawrence *et al.*, 2015). For the imager channels, as demonstrated by Cardinali and Prates (2011), FSOI is dominated by cloudy scenes. Cloud affects around 60% of imager data and these scenes produce around 80% of the impact. For the sounding channels, impact is mainly from the ‘clear’ scenes, given these scenes dominate numerically. However, cloudy scenes have impact in rough proportion to their numbers.

Figure 9 bins the results as a function of the symmetric cloud and rain predictor. The 10% of most cloud-affected scenes generate over 40% of imager channel FSOI on Figure 9(a): this reinforces the importance of all-sky assimilation to getting good impact from microwave imaging channels. The most influential cloudy scenes are in the Tropics (not shown) although the outperformance of these scenes is clear in both Tropics and midlatitudes. In contrast, the impact of sounder channels is fairly constant on a per-observation basis across clear and cloudy scenes (Figure 9(b)). The first bin, representing true clear-sky conditions, provides around 38% of observation numbers and 45% of forecast impact. To get another 45% of forecast impact requires adding data from bins at 0.05 and 0.1, where some cloud and precipitation is present (either in the model or in the observations) and an all-sky technique is the most appropriate way to use the data. A clear-sky approach hoping to use these scenes would risk (a) aliasing undetected cloud or precipitation

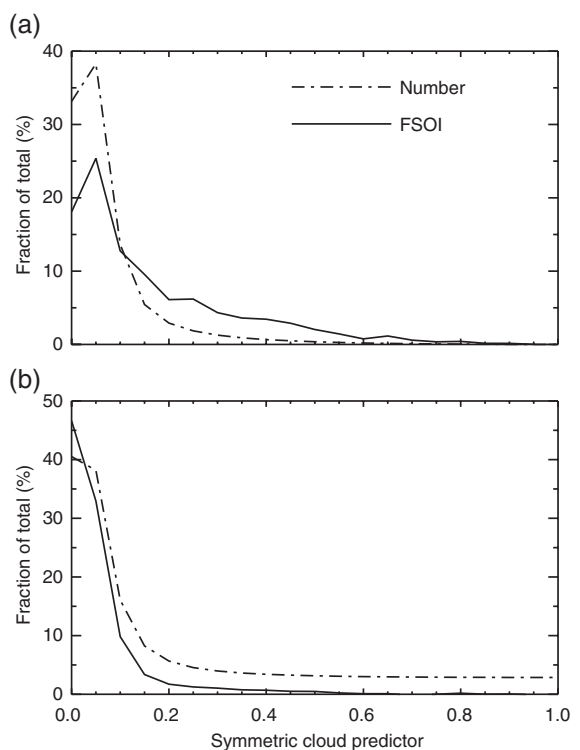


Figure 9. FSOI and number of observations for F-17 SSMIS channels over ocean for (a) imager channels and (b) sounder channels. The number of observations, and the total FSOI, are presented as a percentage of the total in each channel category. Bin size is 0.05.

into the humidity analysis and (b) incorrectly drying the analysis through asymmetric sampling.

4. OSE impact

4.1. OSE description

It is still necessary to conduct OSEs to properly understand forecast impact in the medium range. FSOI gives a convenient way to summarize data utilization and to compare short-range forecast impact between sensors, but it could still be questioned whether it can predict impact in the medium-range (other perspectives can be found in Gelaro and Zhu, 2009). For example, early revisions to the all-sky observation-error model that gave more weight to microwave imager observations brought strong benefits to short-range forecasts and to FSOI, but did not much increase the medium-range impact (compare Geer and Bauer, 2010; Cardinali and Prates, 2011).

The OSE examined here shows the impact of activating data assimilation from microwave humidity, cloud and precipitation sensors in the full ECMWF operational configuration. One experiment contains all available observations including the microwave instruments that are assimilated in all-sky conditions. The other (the ‘denial’) removes those all-sky sensors. These experiments represent the ECMWF operational configuration as of September 2015, being based on cycle 41r1 with a horizontal resolution of TL1279 (16 km). Experiments cover the period from 26 February to 13 September 2015. Except for a few minor differences, data usage is as illustrated in Figure 1 (showing the broad groupings being assimilated) and Figure 6 (showing satellite radiance usage) and Table 2 (for the detailed usage of all-sky data). The differences are that in September 2015, the instruments MWHS-2 and F-18 SSMIS were not yet assimilated, and snow-covered land surfaces had not yet been introduced in the all-sky system; with regard to clear-sky radiance assimilation, Himawari-8 had not yet replaced Himawari-7, and HIRS was still being used. These experiments measure the impact of activating seven all-sky sensors: F-17 SSMIS, four MHS, GMI and AMSR2.

26–Feb–2015 to 13–Sep–2015 from 380 to 399 samples. Verified against own-analysis.

Confidence range 95% with AR(2) inflation and Sidak correction for 4 independent tests

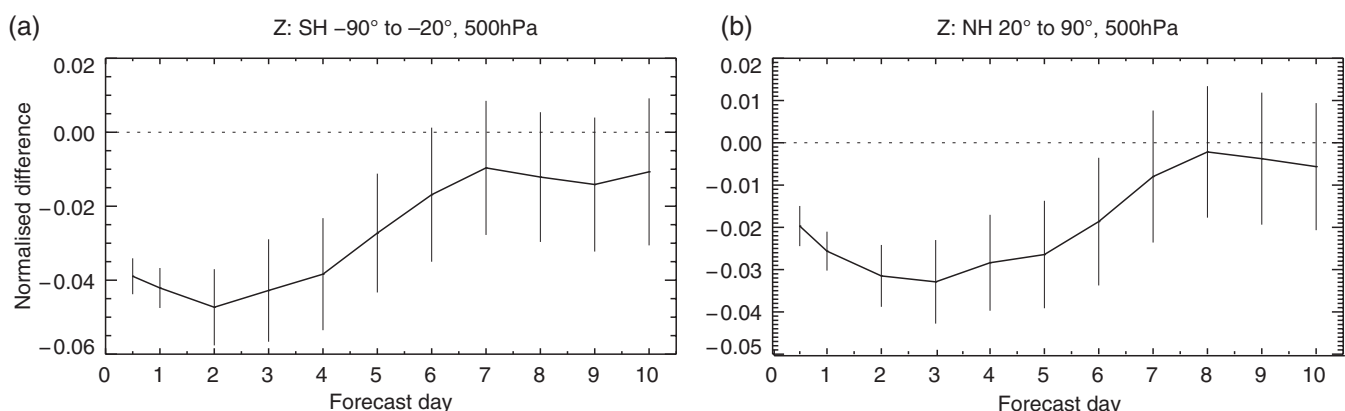


Figure 10. Normalized change in RMS error in 500 hPa geopotential in (a) the SH and (b) the NH coming from the addition of seven microwave humidity instruments in all-sky conditions in an ECMWF system representative of the operational configuration in September 2015 (between 380 and 399 samples from 26 February to 13 September 2015). Confidence range 95%, computed following Geer (2016) with corrections for time autocorrelation and multiple comparisons.

Note that, because the rest of the global observing system is assimilated in both experiments, the clear-sky humidity channels of MWHS and ATMS remain active, as do all other humidity observations (from conventional, aircraft and infrared sensors). In both experiments, background errors are taken from the same operational ensemble of data assimilations (EDA; Bonavita *et al.*, 2015) and the standard assumption is made that the change in quality of the short-range forecast is small enough that the same background errors are applicable in each experiment. Overall the experiments capture a large part of the impact of the microwave humidity observing system, that is the seven all-sky instruments that were active in September 2015. Here we investigate the combined impact of imaging and humidity sounding channels; for the separate impacts see respectively Kazumori *et al.* (2016) and Geer *et al.* (2014).

4.2. Dynamical and moisture

Figure 10 shows the reduction in synoptic forecast error that comes from adding all-sky microwave humidity instruments in the ECMWF operational system. The figures show the change in RMS error in geopotential height at 500 hPa and this is well correlated with other synoptic medium-range scores and represents the quality of the synoptic midlatitude forecasts (Geer, 2016, gives the statistical background to these scores). Medium-range forecasts are improved across the SH and NH with statistically significant impact out to day 5 or day 6. The biggest error reduction is around day 2–3, reaching 4.5% in the SH and 3% in the NH. This level of impact may not seem large in comparison to an FSOI of around 20%, but this reflects the different properties of the two statistics. Likely much of the FSOI from the all-sky sensors was replaced by the large number of other humidity observations remaining in the system. (We did not compute FSOI results from the denial experiment to confirm this.) In any case, a day 5 impact from the seven all-sky instruments of about 2.5% is a significant improvement in an already very good forecasting system. For example, it is comparable with the improvement seen with the introduction of 3D-Var assimilation at ECMWF (Andersson *et al.*, 1998, 1% and 5% in NH and SH). It is also larger than the impact of all humidity observations (conventional, aircraft, infrared and microwave) in the OSEs of Andersson *et al.* (2007), which was no more than 2% in either hemisphere. These results confirm the growing importance of the all-sky observations in synoptic forecasting.

Maps of the reduction in RMS error (Figure 11) show that in the early-range (e.g. T + 12) impact is concentrated over the oceans. This is where the data are most numerous and supply 25–40% of FSOI (Figure 7). As already illustrated, the

analysis and short-range forecast is already well constrained by conventional observations over many land areas. However, during the first few days of the forecast, the mainly oceanic impact of the all-sky observations propagates over land areas with the atmospheric flow, for example giving 5–10% reductions in forecast error over much of Europe and the SH landmasses in the 48–72 h time range. The benefit to North America is less, perhaps due to the flow regime during the verification period. The downstream propagation of observation impact from the oceans to the land is well known (e.g. Kelly *et al.*, 2007) but it has not been demonstrated with such clarity from humidity-related observations before. Beyond day 3, the impacts become more diffuse. From Figure 10 we know the hemispheric impact at day 4 (96 h) and beyond is still significant, but there is less significance to the spatial pattern of this impact.

To summarize forecast impacts more broadly, Figures 12 and 13 show the zonal distribution of the reduction in error standard deviation. At day 5 in the Extratropics this is broadly consistent across all the dynamical variables (temperature, geopotential and wind vector). This is expected, given the strong correlations between such scores (Geer, 2016). The improvements in dynamical forecasts propagate into the stratosphere, particularly in the SH. However the picture in the Tropics and in the short-range is more mixed. Microwave humidity sounders provide less forecast impact near the Equator, where 4D-Var tracing appears to be less effective (Geer *et al.*, 2014). The apparent increase in forecast errors at 850 hPa in temperature and relative humidity is mainly due to microwave imager assimilation and has been investigated by Geer and Bauer (2010) and Kazumori *et al.* (2016). Observation-based verification of the FG forecast (as shown later) clearly demonstrates that all-sky observations improve the quality of short-range forecasts globally and across all levels of the troposphere, including in humidity and temperature in the tropical lower troposphere. However, own-analysis verification in the short-range is sensitive not just to real changes in forecast error, but also to changes in the size of the forecast corrections being made by the analysis system. The apparent degradation is due mainly to an increase in the size of small-scale temperature and humidity increments coming from the addition of new data*. The apparent increase in errors at day 5 in the Tropics is also spurious and is also related to increased structure in the analysis coming from the assimilation of microwave imager data (Geer and

*It may be surprising that the geopotential scores do not show the same effect, given geopotential is dependent on the vertical integral of virtual temperature, but humidity and temperature increments are anti-correlated and they partly conserve virtual temperature. Also, the large reduction in size of virtual temperature increments in the mid-upper troposphere outweighs any increases lower down.

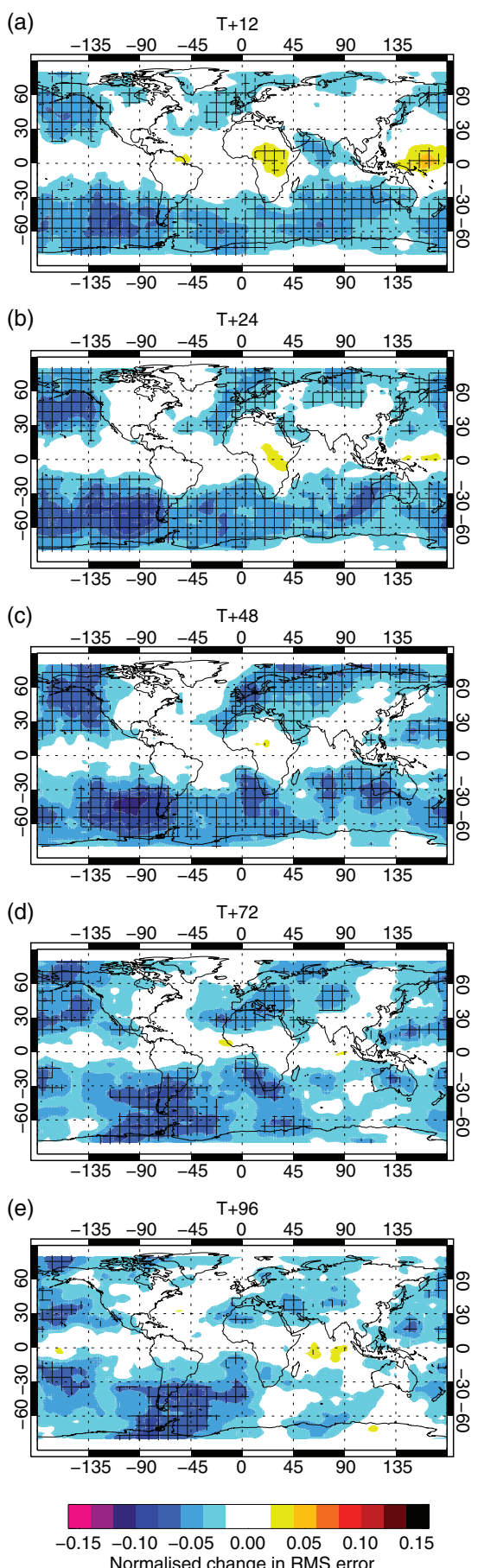


Figure 11. Normalized change in RMS error in 500 hPa geopotential, coming from the addition of seven all-sky instruments, computed in a moving box of 22.5° longitude and latitude, for forecasts valid at (a) T+12 h, (b) T+24 h, (c) T+48 h, (d) T+72 h, and (e) T+96 h. Blue colours indicate reductions in error when all-sky assimilation is activated. Cross-hatching indicates results with at least 95% confidence, without correction for time autocorrelation; the moving box method addresses spatial multiple comparisons but not other possible multiple comparisons.

Bauer, 2010). One demonstration of this (not shown) is that the ‘error increases’ at day 5 can be seen in own-analysis verification, but they disappear when both experiment and control forecasts are verified against the same analysis. These misleading effects in own-analysis forecast scores are worth highlighting because they have slowed the acceptance of all-sky assimilation at ECMWF; they also indicate a need for better verification approaches in the Tropics and at short range, including more use of verification against observations.

There is one degradation of the own-analysis forecast scores in Figures 12 and 13 which is linked to a real problem. This is the increased day 1 errors in humidity and temperature beyond 70°N and 70°S . Here, the dynamical emissivity retrieval method does not work well enough over sea-ice in the winter, leading to a bias between modelled and observed brightness temperatures (Baordo and Geer, 2015). The problem is likely the assumption of specular reflection in the radiative transfer modelling, which is often not valid over snow surfaces. This aliasing of the resulting bias into the analyses causes a moistening of more than 2% in relative humidity over the sea-ice zones, and changes in temperature of up to 0.1 K. However, the benefit of data over sea-ice seems to outweigh any problems (Geer *et al.*, 2014), so we prefer to use these observations rather than screen them.

Figure 14 summarizes the improvement in the FG forecast as indicated by the reduction in standard deviation of FG departures to other assimilated observations. These broad improvements show how misleading the own-analysis verification for moisture and temperature can be (cf. Figure 13). The radiosonde and aircraft temperatures, and AMSU-A radiances (Figure 14(a)–(c)) confirm temperature improvements through the troposphere and extending into the stratosphere. AMSU-A channel 5 senses a broad layer temperature from the surface up to around 300 hPa, so the improvement in this channel is consistent with the roughly 1% improvement in fit to the *in situ* temperatures across a similar pressure range. Higher channels see increasing parts of the stratosphere, where the temperature improvement is smaller. GPSRO (Figure 14(d)) also sees the temperature improvements in the stratosphere, but in the lower troposphere its information content is mostly humidity. Hence the lower-level GPSRO fits, along with radiosonde humidities and HIRS infrared radiances (Figure 14(d)–(f)) demonstrate improved tropospheric humidity fields. Winds are also improved, as shown by conventional and satellite wind observations (Figure 14(g) and (h)). There is no space to explore the finer levels of detail in these results, but they deserve further study[†]. Most importantly, adding the all-sky instruments provides clear, significant improvements in short-range forecast fits to almost all observations and at most levels in the atmosphere (also in all regions, including the Tropics, not shown).

4.3. Precipitation

Cloud and precipitation verification is difficult because of representativity issues coming from the often small time- and space-scales involved, and from measurement and retrieval errors that affect both *in situ* and remote-sensing precipitation estimates. Verification in brightness temperature space can mitigate some of these issues, particularly retrieval error. In an assimilation system where additional, non-assimilated microwave sensors are being monitored, this is a valuable tool for independent verification. Figure 15 shows the standard deviations of FG and analysis departures from SSMIS on F-16, which is passively monitored.

[†]For example, the magnitude of any change in observation fit is influenced by the size of observation errors relative to the forecast errors. Also, the coverage is different: satellites represent broadly global improvements; conventional data fits are dominated by the landmasses. Finally, sensitivities can be different, such as comparing the broad layer-integrated temperature seen by a satellite like AMSU-A versus the local temperature observed by an *in situ* sensor. For example, the different impacts on conventional winds and AMVs are likely explained by a combination of these factors.

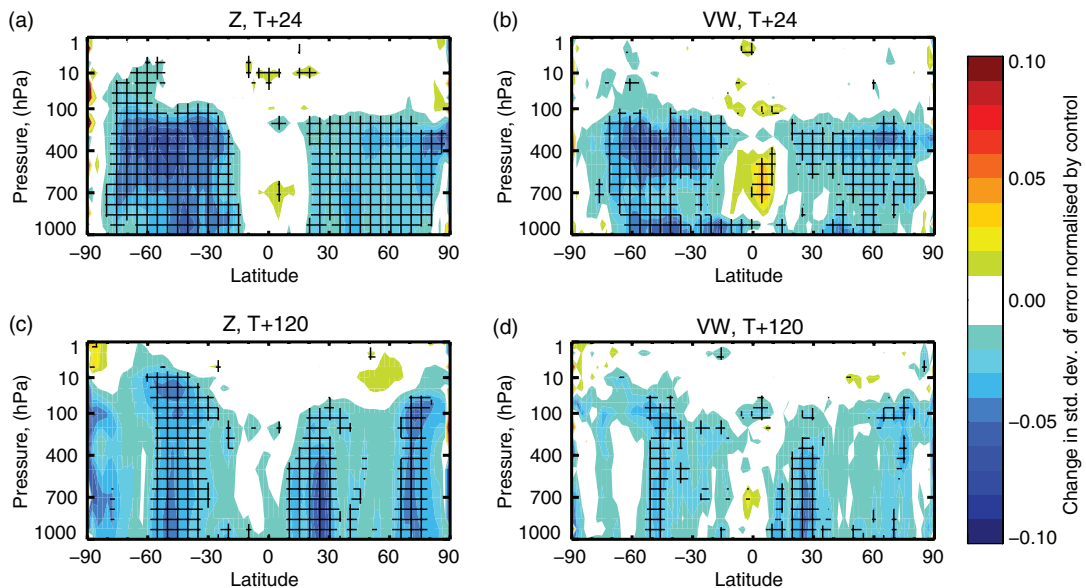


Figure 12. Normalized change in standard deviation of error in (a, c) geopotential, Z , and (b, d) wind vector, VW , coming from the addition of seven all-sky instruments at (a, b) $T+24$ h and (c, d) $T+120$ h. Cross-hatching indicates the 95% confidence level, in which zonal multiple comparisons are addressed with a Šidák correction assuming 20 independent zonal pieces of information; time autocorrelation and other multiple comparison possibilities are not addressed.

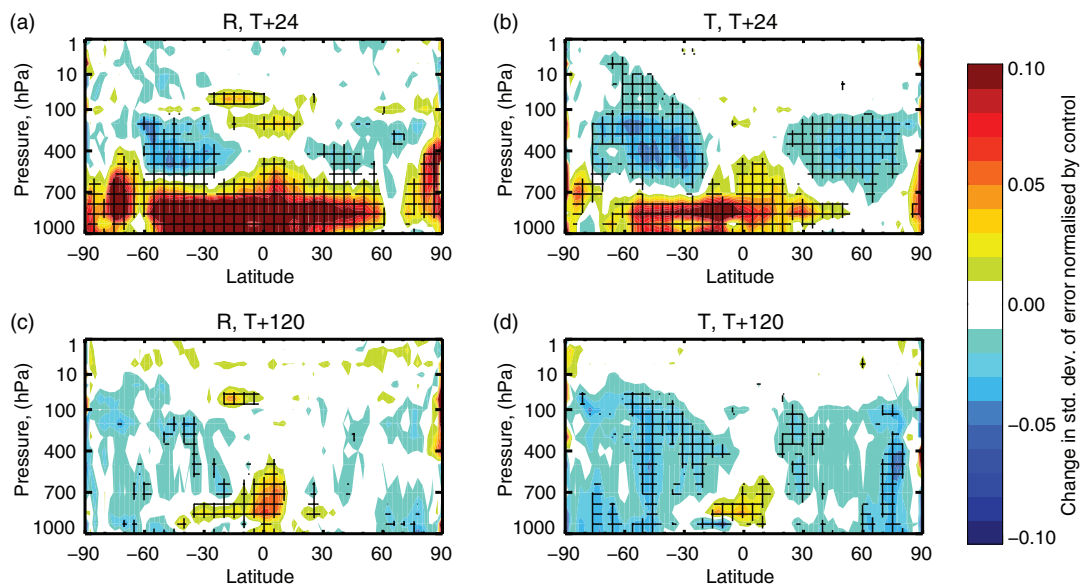


Figure 13. As Figure 12 but for (a, c) relative humidity, R , and (b, d) temperature, T .

Results are based on the 19 GHz h-polarised channel, which has particular sensitivity to rain (as well as cloud and water vapour); however, results are similar from higher-frequency channels (such as 37 GHz) which have stronger cloud sensitivity. Observations and model equivalents have been averaged in circles of varying radius. The 50 km scale here has no additional averaging beyond the superobbing that is applied to microwave imagers in the ECMWF system. (This averages all raw observations in roughly a 60 km radius; Geer and Bauer, 2010.) The 100 km scale averages 4–5 superobs, and the 500 km averages around 75. At smaller scales, these departures measure the ‘mislocation’ errors (e.g. displacement and intensity errors of humidity, cloud and precipitation features) in the forecast brightness temperatures, which often look like dipoles. Averaging over progressively larger spatial scales, the dipoles start to average out, and are mixed with clear-sky scenes, and the standard deviation of FG departures declines.

Without the all-sky observations, Figure 15 shows that the analysis is little better than the FG. When the all-sky observations are assimilated, the FG forecasts are better even than the analyses in the all-sky denial. This shows that all-sky assimilation brings real improvements in the quality of the precipitation analyses

and forecasts. At the 50 km scale, the scale of a single superob, the analysis standard deviation is around 17% smaller than that of the FG. At 100 km the analysis is 27% better. This likely illustrates the filtering properties of the data assimilation system: increments are smoothed by the horizontal correlations in the background errors, and by the inflation of observation errors in precipitating areas (Figure 4). To some extent, the assimilation seems to be filtering out the finer and less predictable scales of precipitation (for example 50 km and below) and concentrating on slightly larger scales.

To support the observation-space verification, we verify surface precipitation accumulations against the near-global TRMM 3B42 daily precipitation accumulations. The regular spatial coverage of the TRMM dataset allows the use of the Fractions Skill Score (FSS; Roberts and Lean, 2008). Figure 16 shows the results for neighbourhood scales of 100 km and for both light (3 mm) and heavy (20 mm) precipitation thresholds. Figure 16(a) shows the skill for the heavy precipitation is lower, which is consistent with the increased difficulty of predicting convective, rather than stratiform, precipitation (e.g. Ebert *et al.*, 2007). Figure 16(b) shows that adding the seven all-sky instruments improves precipitation with statistical significance out to day 5 or day 6, and

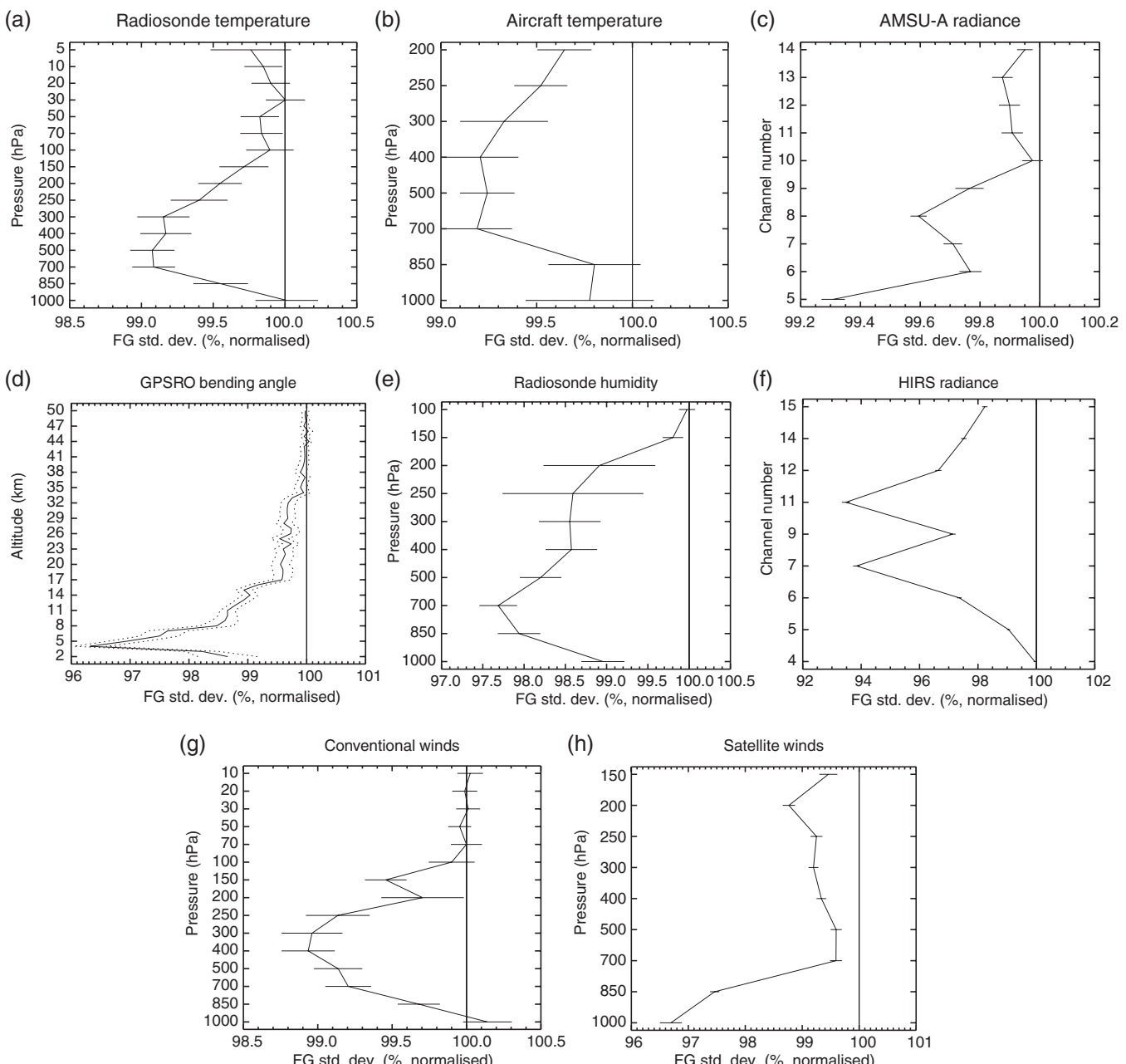


Figure 14. Change in global standard deviation of FG departures caused by activating seven all-sky instruments, normalized so that the control (removing seven all-sky instruments) is 100%, for (a) radiosonde temperature, (b) aircraft temperature, (c) AMSU-A radiance, (d) GPSRO bending angle, (e) radiosonde humidity, (f) HIRS radiance, (g) conventional winds and (h) satellite winds. The observational sample is based on assimilated observations, so it varies between the two experiments. In two cases (HIRS and AMSU-A) the number of observations increases by 2–3% due to a better humidity first guess allowing more observations through cloud screening; otherwise observation numbers are approximately constant. Horizontal bars show the 95% confidence range, computed without correction for autocorrelation or multiple comparison.

that it is the heavy precipitation that benefits most. Similar relative improvements are seen with a 50 km neighbourhood (not shown). More generally, the impact of all-sky assimilation on precipitation appears consistent with its impact on dynamical and humidity variables shown in the previous section; this is not unexpected, given the relatively strong correlations between different forecast scores (Geer, 2016). Broadly, better precipitation forecasts are dependent on better synoptic forecasts.

5. Open issues and future developments

5.1. More observations

The success of the current all-sky assimilation motivates efforts to develop the technique more widely. As regards microwave sounders, the impact of adding additional observations at 183 GHz has not yet saturated (e.g. Lawrence *et al.*, 2015). In 2017 we will begin operational assimilation of the 183 GHz

humidity sounding channels of GMI and of SAPHIR. We will also try to develop all-sky assimilation for the temperature-sounding channels of AMSU-A and ATMS despite earlier unsuccessful attempts (Geer *et al.*, 2012). The National Centre for Environmental Prediction (NCEP) has already made all-sky AMSU-A assimilation operational for non-precipitating cloudy scenes (Zhu *et al.*, 2016). Applying all-sky techniques to temperature-sounding channels is challenging. They cannot directly take advantage of clear-sky water vapour sensitivity to get around the problem of zero gradients to cloud or precipitation. Nevertheless, most temperature sounders include some co-located imaging channels. These channels, originally intended for cloud screening, could continue to play a role in all-sky assimilation by helping to avoid the zero-gradient problem. Another issue is to avoid signals relating to forecast errors in temperature, which are of order 0.1 K, from being contaminated by forecast errors in cloud, which can be up to 100 K in observation space. Fundamentally, this is a challenge of modelling

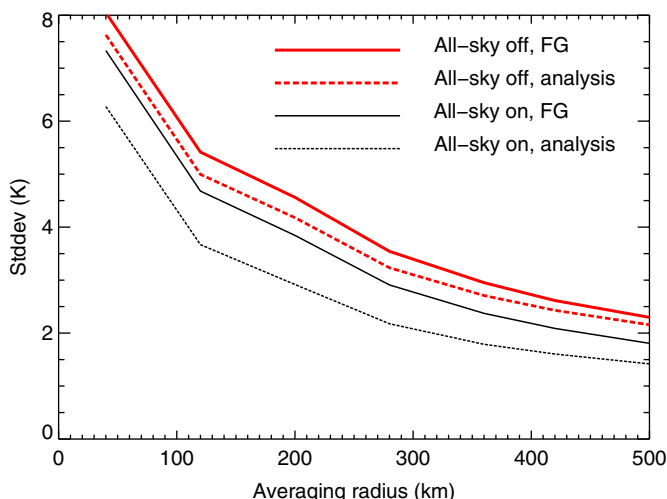


Figure 15. Standard deviation of global SSMIS F-16 channel 19 h departures using different averaging scales, for March, April and May 2015. F-16 is passively monitored and in a different orbit to the assimilated all-sky instruments. Hence, it provides an independent measure of the improvement in WV, cloud and precipitation in the analysis and forecast. Statistical significance testing has been performed on the difference between each of these lines, which is statistically significant, but the 95% confidence range is too small to see (it is around ± 0.03 K). [Colour figure can be viewed at wileyonlinelibrary.com].

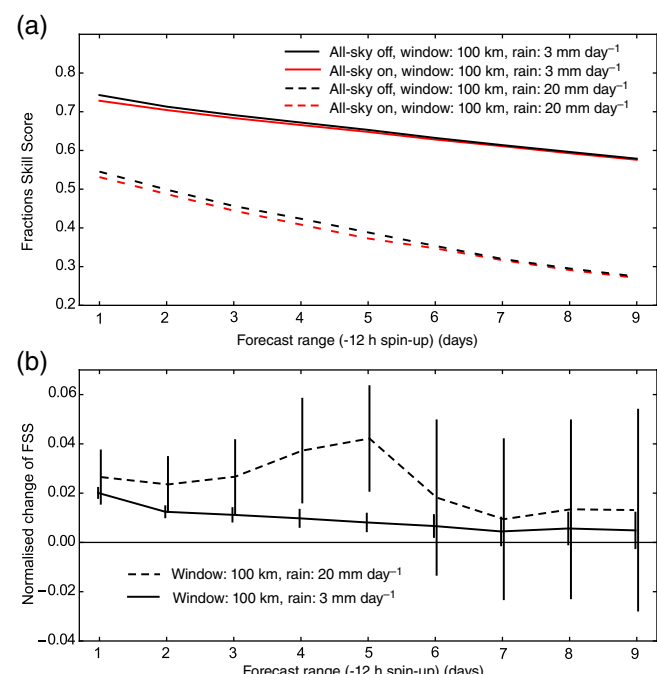


Figure 16. (a) Fraction skill score (FSS) and (b) change in FSS, with 99% confidence range (with no additional corrections) using the TRMM 3B42 v7 global precipitation product as a reference, over the period 1 May to 31 August 2015. This combines rain-gauges, microwave and infrared precipitation retrievals, here using the 0.25° by 0.25° (roughly 28 km) resolution daily accumulations. [Colour figure can be viewed at wileyonlinelibrary.com].

both background error and observation error accurately enough.

We limit microwave imager usage to three satellites (currently GMI, AMSR2 and F-17 SSMIS) because it is hard to show additional positive impact on the forecast scores. Instead we see even more of the large temperature and moisture increments shown in Figure 13 which, although not harmful, may still indicate a deficiency in the assimilation system, if it cannot retain this information over 12 h. Also, there is greater vulnerability to difficult-to-correct biases, as illustrated by Kazumori *et al.* (2016). If these issues can be understood, there is a wealth of additional humidity and cloud information available from microwave window channels on imagers such as WindSat and

the SSMIS on F-16 and F-18, as well as the window channels of AMSU-A and ATMS. The current aim is to extend usage of AMSR2 and GMI down to 10 GHz. These frequencies are not used because of the difficulty of modelling sea surface emissivity and temperature, the relatively large fields of view at low frequencies, and larger biases, possibly associated with rainfall (Geer and Baordo, 2014). This will be challenging but, as well as bringing more information on heavy rain over oceans, it should drive improvements in modelling, both in forecasting tropical convection, and in simulating the radiative transfer.

ECMWF is developing the capability for all-sky infrared assimilation (e.g. Chevallier and Kelly, 2002; Chevallier *et al.*, 2004; Matricardi, 2005; Okamoto *et al.*, 2014) but this is still some way from being operational despite promising impacts on forecast scores (unpublished). Elsewhere, much progress is being made (e.g. Vukicevic *et al.*, 2006; Otkin, 2012; Martinet *et al.*, 2013; Stengel *et al.*, 2013; Harnisch *et al.*, 2016) but nothing is yet operational. One example of the difficulties is that the all-sky observation-error model will have to simultaneously model inter-channel error correlations, which have proved important in clear-sky infrared assimilation (e.g. Weston *et al.*, 2014; Bormann *et al.*, 2016), and also inflate errors in cloudy conditions. This would require new sophistication in observation-error modelling.

To better constrain ice cloud microphysics, there is also great interest in extending all-sky microwave techniques to support the Ice Cloud Imager (ICI), a future EUMETSAT mission at sub-mm wavelengths (183–664 GHz). Further in the future, the assimilation of visible satellite data could help to better constrain cloud microphysics, since radiative transfer at these frequencies is so sensitive to effective radius of cloud droplets. The necessary forward operators are only just starting to be developed (e.g. Kostka *et al.*, 2014; Scheck *et al.*, 2016). A possible side-benefit of both the visible and the sub-mm assimilation may be to improve the radiation budget in the forecast model, which is less accurate at visible wavelengths. This article has concentrated on passive satellite observations, but work is ongoing to assimilate space-borne cloud and precipitation radar (e.g. Di Michele *et al.*, 2012) and other novel precipitation-related observations, such as lightning imagers (Lopez, 2016).

5.2. Data assimilation aspects

During the development of all-sky assimilation at ECMWF, various data assimilation issues have been identified and left aside for future development. So far, none have proved fundamental blocks to progress, but they may become so as we try to extract even more information from cloud- and precipitation-affected radiances. These issues are:

1. As also mentioned in the previous section, the current all-sky observation-error model does not deal with inter-channel error correlation, despite the fact that observation errors in some microwave imager channels can become almost entirely correlated in cloudy conditions (Bormann *et al.*, 2011).
2. The dominating source of error in the comparison between model and all-sky observations comes from what we broadly referred to as ‘mislocation errors’ here (Geer and Bauer, 2011; also Figure 4). These could be described as errors of predictability, given that convective error growth-scales can saturate well within the 12 h assimilation window of 4D-Var (e.g. Zhang *et al.*, 2007). Alternatively they could be described as representivity errors, but of a different kind to those that arise when observations resolve smaller space- or time-scales than the model (e.g. Waller *et al.*, 2014). These errors are currently included in the observation-error model, as ‘representivity’ error, but might be better represented as model error. However that might require weak-constraint 4D-Var, rather than the current strong-constraint approach which ignores it. A deeper understanding of representivity, predictability and

- model error is needed (e.g. Hodges and Nichols, 2015). This is a broader problem than just the ECMWF system; for example Harnisch *et al.* (2016) and Zhang *et al.* (2016) have demonstrated a similar need to inflate observation errors for all-sky observations in ensemble Kalman filters.
3. Since the days of 1D+4D-Var the assimilation system has been better at acting on drying increments than on moistening increments (Geer *et al.*, 2008). Even in the current system, the assimilation of microwave imagers causes a slight drying over oceans at 850 hPa and it is more difficult to create cloud and precipitation than to destroy it. The origins of this asymmetry are still not fully clear.
 4. We still do not have a control variable for cloud or precipitation in the data assimilation. As illustrated by Figure 3, this is not usually a problem, since in the Extratropics the best way to fit observed cloud and precipitation is to adjust the dynamical or humidity initial conditions (Geer *et al.*, 2014). However, for observations close enough to the beginning of the assimilation window to be within the time-scales of cloud and precipitation formation, it might be better to fit the observations by incrementing cloud or precipitation directly in a control variable, rather than by trying to adjust the dynamics. Also, there may be benefit in representing background-error correlations between dynamical variables, humidity and cloud. We plan to examine these questions in more detail in the near future.

5.3. Modelling

As this article has illustrated, our ability to use cloud- and precipitation-affected observations is being slowly unlocked as we develop our capability to model the atmosphere and to simulate the radiative transfer. Part of this is learning where the models are reliable and where they are not. It is necessary to screen areas where the discrepancies between model and observations are too great (such as in cold-air outbreaks) and to extend data usage to new areas when it becomes scientifically possible (such as over snow-covered land surfaces). Success in an operational context has also depended on attention to technical performance, i.e. speed and memory usage, identification and correction of bugs that affect scientific performance, and maintaining the accuracy of the TL and adjoint models. To further improve the impact of all-sky assimilation will likely require just as much detailed hard work.

To identify just a few areas, in the future we would hope to benefit from better modelling of 3D-radiative transfer effects in clouds, better surface emissivity modelling over ocean, land and sea-ice, and improved representations of marine stratocumulus in forecast models. One big area to address, but also an area of currently rapid progress, is the consistent representation of the microphysics of cloud and precipitation in forecast models, for example describing particle habits, sizes and riming, and in modelling the scattering properties of such particles in the radiative transfer.

6. Conclusion

This article has given an overview of 20 years of development towards the assimilation of satellite observations sensitive to water vapour, cloud and precipitation, and particularly the last four years, during which the all-sky technique has been applied to microwave humidity sounding channels, in addition to the microwave imagers where the technique started. Eleven humidity-sensitive satellite microwave sensors are now assimilated in the ECMWF operational system, most of them using the all-sky approach. In terms of FSOI, the impact of these observations has risen from just 6% of FSOI in 2006 to around 20% now, making them one of the most important observation types in the system, alongside clear-sky radiances and conventional data. These

developments have depended on the availability of fundamental scientific building blocks such as a high-quality forecast model and data assimilation system, a TL and adjoint moist physics model, cloud and precipitation-permitting observation operators, and a way to model the variation in observation errors across clear and cloudy skies.

All-sky assimilation improves the quality of forecasts through the medium range to at least day 6. This is done by inferring the dynamical initial conditions required to support these observations of humidity, cloud and precipitation. It also provides two other long-hoped-for benefits. First, the observations directly improve the humidity, cloud and precipitation fields; second, by highlighting areas of disagreement between forecast and observations, they motivate the development of better cloud and precipitation modelling, whether in the forecast model or the radiative transfer modelling. It is hoped that this will inspire further development of humidity, cloud and precipitation assimilation for operational forecasting, and moreover, that it may show the way for a broader earth-system treatment of these observations. They also have strong sensitivities to sea-ice, surface snow, soil moisture, and sea-surface temperature. Currently this information is included in model forecasts indirectly, using retrieval schemes external to the data assimilation, and subject to the many sub-optimalities that have affected the assimilation humidity, cloud and precipitation retrievals in the past. For earth-system variables, the way forward is also likely to be a direct assimilation of the radiances into an integrated ocean–ice–land–atmosphere assimilation system.

Acknowledgements

P. Lopez is thanked for providing the tangent linear errors in Figure 2. KL is currently, and AJG, FB and HL were earlier during this work, funded through the EUMETSAT Research Fellowship Programme. CL was funded through the EUMETSAT NWP-SAF programme.

Appendix

Table A1. Acronyms.

AMV	Atmospheric motion vectors
AMSR2	Advanced Microwave Scanning Radiometer 2
AMSU-A	Advanced Microwave Sounding Unit-A
ATMS	Advanced Technology Microwave Sounder
Conv	Conventional data (here excluding aircraft)
DMSP	Defense Meteorological Satellite Program
GCOM-W	Global Change Observation Mission – Water
GMI	GPM Microwave Imager
GPM	Global Precipitation Measurement
GPSRO	GPS radio occultation
HIRS	High-resolution InfraRed Sounder
IASI	Infrared Atmosp. Sounding Interferometer
IR T	Infrared radiances sensitive to temperature
IR WV	Infrared radiances sensitive to water vapour
MHS	Microwave Humidity Sounder
MWHS	MicroWave Humidity Sounder
MWHS-2	MicroWave Humidity Sounder-2
MW T	Microwave radiances sensitive to temperature
MW WV	Microwave radiances sensitive to water vapour, cloud and precipitation
NOAA	National Oceanic and Atmospheric Administration
SAPHIR	Sondeur Atmosphérique du Profil d'Humidité Intertropicale par Radiométrie
Scat	Scatterometer
SSM/I	Special Sensor Microwave Imager
SSMIS	Special Sensor Microwave Imager/Sounder
Suomi-NPP	Suomi National Polar-orbiting Partnership

References

- Alexander GD, Weinman JA, Karyampudi VM, Olson WS, Lee A. 1999. The effect of assimilating rain rates derived from satellites and lightning on forecasts of the 1993 superstorm. *Mon. Weather Rev.* **127**: 1433–1457.
- Allen DR, Hoppel KW, Nedoluha GE, Kuhl DD, Baker NL, Xu L, Rosmond TE. 2013. Limitations of wind extraction from 4D-Var assimilation of ozone. *Atmos. Chem. Phys.* **13**: 3501–3515, <https://doi.org/10.5194/acp-13-3501-2013>.
- Allen DR, Hoppel KW, Kuhl DD. 2014. Wind extraction potential from 4D-Var assimilation of stratospheric O₃, N₂O, and H₂O using a global shallow-water model. *Atmos. Chem. Phys.* **14**: 3347–3360.
- Andersson E, Pailleux J, Thépaut J-N, Eyre JR, McNally AP, Kelly GA, Courtier P. 1994. Use of cloud-cleared radiances in three/four-dimensional variational data assimilation. *Q. J. R. Meteorol. Soc.* **120**: 627–653.
- Andersson E, Haseler J, Undén P, Courtier P, Kelly G, Vasiljević D, Brankovic C, Cardinali C, Gaffard C, Hollingsworth A, Jakob C, Janssen P, Klinker E, Lanzinger A, Miller M, Rabier F, Simmons A, Strauss B, Thépaut J-N, Viterbo P. 1998. The ECMWF implementation of three-dimensional variational assimilation (3D-Var). III: Experimental results. *Q. J. R. Meteorol. Soc.* **124**: 1831–1860.
- Andersson E, Bauer P, Beljaars A, Chevallier F, Hólm E, Janisková M, Källberg P, Kelly G, Lopez P, McNally AP, Moreau E, Simmons AJ, Thépaut J-N, Tompkins AM. 2005. Assimilation and modeling of the atmospheric hydrological cycle in the ECMWF forecasting system. *Bull. Am. Meteorol. Soc.* **86**: 387–402.
- Andersson E, Hólm E, Bauer P, Beljaars A, Kelly GA, McNally AP, Simmons AJ, Thépaut J-N, Tompkins A. 2007. Analysis and forecast impact of the main humidity observing systems. *Q. J. R. Meteorol. Soc.* **133**: 1473–1485.
- Baordo F, Geer AJ. 2015. ‘Microwave surface emissivity over sea-ice’. EUMETSAT NWP-SAF Visiting Scientist Report NWPSAF-EC.VS.026. https://nwpsaf.eu/publications/vs_reports/nwpsaf-ec-vs-026.pdf (accessed 13 October 2017).
- Baordo F, Geer AJ. 2016. Assimilation of SSMIS humidity-sounding channels in all-sky conditions over land using a dynamic emissivity retrieval. *Q. J. R. Meteorol. Soc.* **142**: 2854–2866, <https://doi.org/10.1002/qj.2873>.
- Bauer P. 2001. Including a melting layer in microwave radiative transfer simulation for cloud. *Atmos. Res.* **57**: 9–30.
- Bauer P, Lopez P, Benedetti A, Salmond D, Moreau E. 2006a. Implementation of 1D+4D-Var assimilation of precipitation-affected microwave radiances at ECMWF. I: 1D-Var. *Q. J. R. Meteorol. Soc.* **132**: 2277–2306.
- Bauer P, Lopez P, Salmond D, Benedetti A, Saarinen S, Moreau E. 2006b. Implementation of 1D+4D-Var assimilation of precipitation-affected microwave radiances at ECMWF. II: 4D-Var. *Q. J. R. Meteorol. Soc.* **132**: 2307–2332.
- Bauer P, Moreau E, Chevallier F, O’Keeffe U. 2006c. Multiple-scattering microwave radiative transfer for data assimilation applications. *Q. J. R. Meteorol. Soc.* **132**: 1259–1281.
- Bauer P, Geer AJ, Lopez P, Salmond D. 2010. Direct 4D-Var assimilation of all-sky radiances: Part I. Implementation. *Q. J. R. Meteorol. Soc.* **136**: 1868–1885.
- Bauer P, Auligné T, Bell W, Geer AJ, Guidard V, Heillette S, Kazumori M, Kim MJ, Liu EHC, McNally AP, Macpherson B, Okamoto K, Renshaw R, Riishojaard LP. 2011. Satellite cloud and precipitation assimilation at operational NWP centres. *Q. J. R. Meteorol. Soc.* **137**: 1934–1951.
- Baylor GM, Aune R, Raymond W. 2000. NWP cloud initialization using GOES sounder data and improved modeling of nonprecipitating clouds. *Mon. Weather Rev.* **128**: 3911–3920.
- Benedetti A, Janisková M. 2007. ‘Assimilation of MODIS cloud optical depths in the ECMWF model’. Technical Memorandum 515. ECMWF: Reading, UK.
- Benedetti A, Lopez P, Bauer P, Moreau E. 2005. Experimental use of TRMM precipitation radar observations in 1D+4D-Var assimilation. *Q. J. R. Meteorol. Soc.* **131**: 2473–2495.
- Bengtsson L, Hodges K. 2005. On the impact of humidity observations in numerical weather prediction. *Tellus* **57A**: 701–708.
- Bonavita M, Isaksen L, Hólm E, Fisher M. 2015. The evolution of the ECMWF hybrid data assimilation system. *Q. J. R. Meteorol. Soc.* **142**: 287–303, <https://doi.org/10.1002/qj.2652>.
- Bormann N, Geer AJ, Bauer P. 2011. Estimates of observation-error characteristics in clear and cloudy regions for microwave imager radiances from NWP. *Q. J. R. Meteorol. Soc.* **137**: 2014–2023.
- Bormann N, Fouilloux A, Bell W. 2013. Evaluation and assimilation of ATMS data in the ECMWF system. *J. Geophys. Res. Atmos.* **118**: 12970–12980, <https://doi.org/10.1002/2013JD020325>.
- Bormann N, Bonavita M, Dragani R, Eresmaa R, Matricardi M, McNally A. 2016. Enhancing the impact of IASI observations through an updated observation-error covariance matrix. *Q. J. R. Meteorol. Soc.* **142**: 1767–1780.
- Buehler SA, John VO. 2005. A simple method to relate microwave radiances to upper tropospheric humidity. *J. Geophys. Res. Atmos.* **110**: D02110, <https://doi.org/10.1029/2004JD005111>.
- Cardinali C. 2009. Monitoring the observation impact on the short-range forecast. *Q. J. R. Meteorol. Soc.* **135**: 239–250.
- Cardinali C, Prates F. 2011. Performance measurement with advanced diagnostic tools of all-sky microwave imager radiances in 4D-Var. *Q. J. R. Meteorol. Soc.* **137**: 2038–2046.
- Chambon P, Zhang SQ, Hou AY, Županski M, Cheung S. 2014. Assessing the impact of pre-GPM microwave precipitation observations in the Goddard WRF ensemble data assimilation system. *Q. J. R. Meteorol. Soc.* **140**: 1219–1235.
- Chen K, English SJ, Bormann N, Zhu J. 2015. Assessment of FY-3A and FY-3B MWHS observations. *Weather and Forecasting* **30**: 1280–1290, <http://doi.org/10.1175/WAF-D-15-0025.1>.
- Chevallier F, Kelly G. 2002. Model clouds as seen from space: Comparison with geostationary imagery in the 11 m window channel. *Mon. Weather Rev.* **130**: 712–722.
- Chevallier F, Lopez P, Tompkins MA, Janisková M, Moreau E. 2004. The capability of 4D-Var systems to assimilate cloud-affected satellite infrared radiances. *Q. J. R. Meteorol. Soc.* **130**: 917–932.
- Chouinard C, Hallé J. 2003. ‘The assimilation of AMSU-B radiances in the CMC global data assimilation system: Difficulties and impact relative to AMSU-A radiances’. In *13th International TOVS Study Conference, 29 October 2003–4 November 2003 (proceedings)*. Sainte Adèle, Canada. University of Wisconsin-Madison, Space Science and Engineering Center, CIMSS, Madison, WI. <http://cimss.ssec.wisc.edu/itwg/itsc13/proceedings/> (accessed 13 October 2017).
- Courtier P, Thépaut J-N, Hollingsworth A. 1994. A strategy for operational implementation of 4D-Var, using an incremental approach. *Q. J. R. Meteorol. Soc.* **120**: 1367–1387.
- Courtier P, Andersson E, Heckley W, Vasiljevic D, Hamrud M, Hollingsworth A, Rabier F, Fisher M, Pailleux J. 1998. The ECMWF implementation of three-dimensional variational assimilation (3D-Var). I: Formulation. *Q. J. R. Meteorol. Soc.* **124**: 1783–1807.
- Daley R. 1995. Estimating the wind field from chemical constituent observations: Experiments with a one-dimensional extended Kalman filter. *Mon. Weather Rev.* **123**: 181–198.
- Deblonde G, Mahfouf J-F, Bilodeau B, Anselmo D. 2007. One-dimensional variational data assimilation of SSM/I observations in rainy atmospheres at MSC. *Mon. Weather Rev.* **135**: 152–172.
- Dee DP, Uppala SM, Simmons AJ, Berrisford P, Poli P, Kobayashi S, Andrae U, Balmaseda MA, Balsamo G, Bauer P, Bechtold P, Beljaars ACM, van de Berg L, Bidlot J, Bormann N, Delso C, Dragani R, Fuentes M, Geer AJ, Haimberger L, Healy S, Hersbach H, Hólm EV, Isaksen L, Källberg P, Köhler M, Matricardi M, McNally AP, Monge-Sanz BM, Morcrette JJ, Peubey C, de Rosnay P, Tavolato C, Thépaut J-N, Vitart F. 2011. The ERA-Interim reanalysis: Configuration and performance of the data assimilation system. *Q. J. R. Meteorol. Soc.* **137**: 553–597.
- Derber JC, Wu WS. 1998. The use of TOVS cloud-cleared radiances in the NCEP SS1 analysis system. *Mon. Weather Rev.* **126**: 2287–2299.
- Di Michele S, Ahlgrimm M, Forbes R, Kulie M, Bennartz R, Janisková M, Bauer P. 2012. Interpreting an evaluation of the ECMWF global model with CloudSat observations: Ambiguities due to radar reflectivity forward operator uncertainties. *Q. J. R. Meteorol. Soc.* **138**: 2047–2065, <https://doi.org/10.1002/qj.1936>.
- Di Tomaso E, Bormann N, English S. 2013. ‘Assimilation of ATOVS radiances at ECMWF: Third year EUMETSAT fellowship report’. EUMETSAT/ECMWF Fellowship Programme Research Report No. 29. <http://www.ecmwf.int/en/library> (accessed 13 October 2017).
- Doherty AM, Sreerekha TR, O’Keeffe UM, English SJ. 2007. Ice hydrometeor microphysical assumptions in radiative transfer models at AMSU-B frequencies. *Q. J. R. Meteorol. Soc.* **133**: 1205–1212.
- Ebert EE, Janowiak JE, Kidd C. 2007. Comparison of near-real-time precipitation estimates from satellite observations and numerical models. *Bull. Am. Meteorol. Soc.* **88**: 47–64.
- Errico RM, Fillion L, Nychka D, Lu ZQ. 2000. Some statistical considerations associated with the data assimilation of precipitation observations. *Q. J. R. Meteorol. Soc.* **126**: 339–359.
- Errico RM, Bauer P, Mahfouf J-F. 2007. Issues regarding the assimilation of cloud and precipitation data. *J. Atmos. Sci.* **64**: 3785–3798.
- Eyre JR, Kelly GA, McNally AP, Andersson E, Persson A. 1993. Assimilation of TOVS radiance information through one-dimensional variational analysis. *Q. J. R. Meteorol. Soc.* **119**: 1427–1463.
- Fillion L, Errico R. 1997. Variational assimilation of precipitation data using moist convective parameterization schemes: A 1D-Var study. *Mon. Weather Rev.* **125**: 2917–2942.
- Forbes R, Geer AJ, Lonitz K, Ahlgrimm M. 2016. ‘Reducing systematic errors in cold-air outbreaks’. *ECMWF Newslett.* **146**: 17–22.
- Geer AJ. 2013. ‘All-sky assimilation: Better snow-scattering radiative transfer and addition of SSMIS humidity sounding channels’. Technical Memorandum 706. ECMWF: Reading, UK.
- Geer AJ. 2016. Significance of changes in medium-range forecast scores. *Tellus A* **68**: 30229, <http://dx.doi.org/10.3402/tellusa.v68.30229>.
- Geer AJ, Baordo F. 2014. Improved scattering radiative transfer for frozen hydrometeors at microwave frequencies. *Atmos. Meas. Tech.* **7**: 1839–1860, <https://doi.org/10.5194/amt-7-1839-2014>.
- Geer AJ, Bauer P. 2010. ‘Enhanced use of all-sky microwave observations sensitive to water vapour, cloud and precipitation’. Technical Memoranda 620, ECMWF: Reading, UK (also ECMWF/EUMETSAT Fellowship Reports 20).

- Geer AJ, Bauer P. 2011. Observation errors in all-sky data assimilation. *Q. J. R. Meteorol. Soc.* **137**: 2024–2037.
- Geer AJ, Harries JE. 1998. Comparison of upper-tropospheric humidity radiances from ECMWF operational analyses and the Meteosat water vapour channel. In: *Ninth Conference on Satellite Meteorology and Oceanography*, May 1998. UNESCO, Paris (Proceedings). 393–396. American Meteorological Society: Boston, MA.
- Geer AJ, Bauer P, Lopez P. 2007. 'Lessons learnt from the 1D+4D-Var assimilation of rain and cloud affected SSM/I observations at ECMWF'. Technical Memorandum 535, ECMWF: Reading, UK (also ECMWF/EUMETSAT Fellowship Reports 17).
- Geer AJ, Bauer P, Lopez P. 2008. Lessons learnt from the operational 1D+4D-Var assimilation of rain- and cloud-affected SSM/I observations at ECMWF. *Q. J. R. Meteorol. Soc.* **134**: 1513–1525.
- Geer AJ, Bauer P, O'Dell CW. 2009. A revised cloud overlap scheme for fast microwave radiative transfer. *J. Appl. Meteorol. Clim.* **48**: 2257–2270.
- Geer AJ, Bauer P, Lopez P. 2010. Direct 4D-Var assimilation of all-sky radiances: Part II. Assessment. *Q. J. R. Meteorol. Soc.* **136**: 1886–1905.
- Geer AJ, Bauer P, English SJ. 2012. 'Assimilating AMSU-A temperature sounding channels in the presence of cloud and precipitation'. Technical Memorandum 670, ECMWF: Reading, UK (also ECMWF/EUMETSAT Fellowship Reports 24).
- Geer AJ, Baordo F, Bormann N, English S. 2014. 'All-sky assimilation of microwave humidity sounders'. Technical Memorandum 741, ECMWF: Reading, UK.
- Geer AJ, Lonitz K, Weston P, Kazumori M, Okamoto K, Zhu Y, Liu EH, Collard A, Bell W, Migliorini S, Chambon P, Fourrié N, Kim MJ, Köpken-Watts C, Schraff C. 2017. All-sky satellite data assimilation at operational weather forecasting centres. *Q. J. R. Meteorol. Soc.*, <https://doi.org/10.1002/qj.3202>.
- Gelaro R, Zhu Y. 2009. Examination of observation impacts derived from observing system experiments (OSEs) and adjoint models. *Tellus A* **61**: 179–193.
- Gérard E, Saunders R. 1999. Four-dimensional variational assimilation of Special Sensor Microwave/Imager total column water vapour in the ECMWF model. *Q. J. R. Meteorol. Soc.* **125**: 3077–3102.
- Guerbet J, Mahfouf J-F, Plu M. 2016. Towards the assimilation of all-sky microwave radiances from the SAPHIR humidity sounder in a limited-area NWP model over tropical regions. *Tellus A* **68**(*1*): <http://dx.doi.org/10.3402/tellusa.v68.28620>.
- Guidard V, Fourrié N, Brousseau P, Rabier F. 2011. Impact of IASI assimilation at global and convective scales and challenges for the assimilation of cloudy scenes. *Q. J. R. Meteorol. Soc.* **137**: 1975–1987.
- Harnisch F, Weissmann M, Periáñez Á. 2016. Error model for the assimilation of cloud-affected infrared satellite observations in an ensemble data assimilation system. *Q. J. R. Meteorol. Soc.* **142**: 1797–1808.
- Heckley WA, Kelly G, Tiedtke M. 1990. On the use of satellite-derived heating rates for data assimilation within the tropics. *Mon. Weather Rev.* **118**: 1743–1757.
- Hodyss D, Nichols N. 2015. The error of representation: Basic understanding. *Tellus A* **67**: 24822, <http://dx.doi.org/10.3402/tellusa.v67.24822>.
- Hölm E, Andersson E, Beljaars A, Lopez P, Mahfouf J-F, Simmons A, Thépaut J-N. 2002. 'Assimilation and modelling of the hydrological cycle: ECMWF's status and plans'. Technical Memorandum 383, ECMWF: Reading, UK.
- Hong G, Heygster G, Miao J, Kunzi K. 2005. Detection of tropical deep convective clouds from AMSU-B water vapor channels measurements. *J. Geophys. Res.* **110**: D05205, <https://doi.org/10.1029/2004JD004949>.
- Hou AY, Zhang SQ, Reale O. 2004. Variational continuous assimilation of TMI and SSM/I rain rates: Impact on GEOS-3 hurricane analyses and forecasts. *Mon. Weather Rev.* **132**: 2094–2109.
- Hunt BR, Kostelich EJ, Szunyogh I. 2007. Efficient data assimilation for spatio-temporal chaos: A local ensemble transform kalman filter. *Physica D* **230**: 112–126.
- Janisková M, Lopez P. 2013. Linearized physics for data assimilation for Atmospheric, Oceanic and Hydrologic Applications, Vol. II: 251 assimilation at ECMWF. In *Data Assimilation for Atmospheric, Oceanic and Hydrologic Applications*, Vol. II: 251–286. Park SK, Xu L (eds). Springer: Berlin.
- Janisková M, Thépaut J-N, Geleyn J-F. 1999. Simplified and regular physical parameterizations for incremental four-dimensional variational assimilation. *Mon. Weather Rev.* **127**: 26–45.
- Joiner J, Da Silva A. 1998. Efficient methods to assimilate remotely sensed data based on information content. *Q. J. R. Meteorol. Soc.* **124**: 1669–1694.
- Kazumori M, Geer AJ, English SJ. 2016. Effects of all-sky assimilation of GCOM-W/AMSR2 radiances in the ECMWF numerical weather prediction system. *Q. J. R. Meteorol. Soc.* **142**: 721–737, <https://doi.org/10.1002/qj.2669>.
- Kelly G, Thépaut J-N, Buizza R, Cardinali C. 2007. The value of observations. I: Data denial experiments for the Atlantic and the Pacific. *Q. J. R. Meteorol. Soc.* **133**: 1803–1815.
- Kelly GA, Bauer P, Geer AJ, Lopez P, Thépaut J-N. 2008. Impact of SSM/I observations related to moisture, clouds and precipitation on global NWP forecast skill. *Mon. Weather Rev.* **136**: 2713–2726.
- Koizumi K, Ishikawa Y, Tsuyuki T. 2005. Assimilation of precipitation data to the JMA mesoscale model with a four-dimensional variational method and its impact on precipitation forecasts. *SOLA* **1**: 45–48.
- Kostka PM, Weissmann M, Buras R, Mayer B, Stiller O. 2014. Observation operator for visible and near-infrared satellite reflectances. *J. Atmos. Oceanic Technol.* **31**: 1216–1233.
- Krishnamurti T, Ingles K, Cocke S, Pasch R, Kitade T. 1984. Details of low-latitude medium-range numerical weather prediction using a global spectral model, II: Effect of orography and physical initialization. *J. Meteorol. Soc. Jpn.* **62**: 613–649.
- Krzeminski B, Bormann N, Karbou F, Bauer P. 2009. 'Improved use of surface-sensitive microwave radiances at ECMWF'. In *Proceedings of EUMETSAT Meteorological Satellite Conference, Bath, UK*. EUMETSAT: Darmstadt, Germany, pp. 21–25.
- Langland RH, Baker NL. 2004. Estimation of observation impact using the NRL atmospheric variational data assimilation adjoint system. *Tellus A* **56**: 189–201.
- Lawrence H, Bormann N, Lu Q, Geer A, English S. 2015. An evaluation of FY-3C MWHS-2 at ECMWF. EUMETSAT/ECMWF Fellowship Programme Research Report No. 37.
- Lean P, Geer AJ, Lonitz K. 2017. 'Assimilation of global precipitation mission (GPM) microwave imager (GMI) in all-sky conditions'. Technical Memorandum 799, ECMWF: Reading, UK.
- Lien GY, Miyoshi T, Kalnay E. 2016. Assimilation of TRMM multisatellite precipitation analysis with a low-resolution NCEP global forecast system. *Mon. Weather Rev.* **144**: 643–661.
- Liu G. 2008. A database of microwave single-scattering properties for nonspherical ice particles. *Bull. Am. Meteorol. Soc.* **111**: 1563–1570.
- Lonitz K, Geer AJ. 2015. 'New screening of cold-air outbreak regions used in 4D-Var all-sky assimilation'. EUMETSAT/ECMWF Fellowship Programme Research Report 35, ECMWF: Reading, UK.
- Lonitz K, Geer A. 2017. 'Effect of assimilating microwave imager observations in the presence of a model bias in marine stratocumulus'. EUMETSAT/ECMWF Fellowship Programme Research Report 44, ECMWF: Reading, UK.
- Lopez P. 2011. Direct 4D-Var assimilation of NCEP stage IV radar and gauge precipitation data at ECMWF. *Mon. Weather Rev.* **139**: 2098–2116.
- Lopez P. 2016. A lightning parameterization for the ECMWF Integrated Forecasting System. *Mon. Weather Rev.* **144**: 3057–3075.
- Lopez P, Bauer P. 2007. '1D+4D-Var' assimilation of NCEP stage IV radar and gauge hourly precipitation data at ECMWF. *Mon. Weather Rev.* **135**: 2506–2524.
- Lopez P, Moreau E. 2005. A convection scheme for data assimilation: Description and initial tests. *Q. J. R. Meteorol. Soc.* **131**: 409–436.
- Lopez P, Benedetti A, Bauer P, Janisková M, Köhler M. 2006. Experimental 2D-Var assimilation of ARM cloud and precipitation observations. *Q. J. R. Meteorol. Soc.* **132**: 1325–1347.
- Lupu C, McNally AP. 2012. 'Assimilation of cloud-affected radiances from Meteosat-9 at ECMWF'. EUMETSAT/ECMWF Fellowship Programme Research Report No. 25, ECMWF: Reading, UK.
- McNally AP. 2002. A note on the occurrence of cloud in meteorologically sensitive areas and the implications for advanced infrared sounders. *Q. J. R. Meteorol. Soc.* **128**: 2551–2556.
- McNally AP. 2009. The direct assimilation of cloud-affected satellite infrared radiances in the ECMWF 4D-Var. *Q. J. R. Meteorol. Soc.* **135**: 1214–1229.
- Mahfouf J-F. 1999. Influence of physical processes on the tangent-linear approximation. *Tellus A* **51**: 147–166.
- Marécal V, Mahfouf J-F, Bauer P. 2002. Comparison of TMI rainfall estimates and their impact on 4D-Var assimilation. *Q. J. R. Meteorol. Soc.* **128**: 2737–2758.
- Marécal V, Mahfouf J-F. 2000. Variational retrieval of temperature and humidity profiles from TRMM precipitation data. *Mon. Weather Rev.* **128**: 3853–3866.
- Marécal V, Mahfouf J-F. 2002. Four-dimensional variational assimilation of total column water vapour in rainy areas. *Mon. Weather Rev.* **130**: 43–58.
- Marécal V, Mahfouf J-F. 2003. Experiments on 4D-Var assimilation of rainfall data using an incremental formulation. *Q. J. R. Meteorol. Soc.* **129**: 3137–3160.
- Martinet P, Fourrié N, Guidard V, Rabier F, Montmerle T, Brunel P. 2013. Towards the use of microphysical variables for the assimilation of cloud-affected radiances. *Q. J. R. Meteorol. Soc.* **139**: 1402–1416.
- Matricardi M. 2005. 'The inclusion of aerosols and clouds in RTIASI, the ECMWF fast radiative transfer model for the infrared atmospheric sounding interferometer'. Technical Memorandum 474, ECMWF: Reading, UK.
- Migliorini S, Piccolo C, Rodgers CD. 2008. Use of the information content in satellite measurements for an efficient interface to data assimilation. *Mon. Weather Rev.* **136**: 2633–2650.
- Moreau E, Bauer P, Chevallier F. 2003. Variational retrieval of rain profiles from spaceborne passive microwave radiance observations. *J. Geophys. Res.* **108**: 4521, <https://doi.org/10.1029/2002JD003315>.
- Moreau E, Lopez P, Bauer P, Tompkins AM, Janisková M, Chevallier F. 2004. Variational retrieval of temperature and humidity profiles using rain rates versus microwave brightness temperatures. *Q. J. R. Meteorol. Soc.* **130**: 827–852.

- Okamoto K, McNally AP, Bell W. 2014. Progress towards the assimilation of all-sky infrared radiances: An evaluation of cloud effects. *Q. J. R. Meteorol. Soc.* **140**: 1603–1614.
- Otkin JA. 2010. Clear and cloudy sky infrared brightness temperature assimilation using an ensemble Kalman filter. *J. Geophys. Res. Atmos.* **115**: D19207, <https://doi.org/10.1029/2009JD013759>.
- Otkin JA. 2012. Assimilation of water vapor sensitive infrared brightness temperature observations during a high-impact weather event. *J. Geophys. Res. Atmos.* **117**, D19203, <https://doi.org/10.1029/2012JD017568>.
- Pavelin EG, English SJ, Eyre JR. 2008. The assimilation of cloud-affected infrared satellite radiances for numerical weather prediction. *Q. J. R. Meteorol. Soc.* **134**: 737–749.
- Peubey C, McNally AP. 2009. Characterization of the impact of geostationary clear-sky radiances on wind analyses in a 4D-Var context. *Q. J. R. Meteorol. Soc.* **135**: 1863–1876.
- Peuch A, Thepaut J-N, Pailleux J. 2000. Dynamical impact of total-ozone observations in a four-dimensional variational assimilation. *Q. J. R. Meteorol. Soc.* **126**: 1641–1659.
- Rabier F, Järvinen H, Klinker E, Mahfouf J-F, Simmons A. 2000. The ECMWF operational implementation of four-dimensional variational assimilation. I: Experimental results with simplified physics. *Q. J. R. Meteorol. Soc.* **126**: 1148–1170.
- Renshaw R, Francis PN. 2011. Variational assimilation of cloud fraction in the operational Met Office Unified Model. *Q. J. R. Meteorol. Soc.* **137**: 1963–1974.
- Riishojgaard LP. 1996. On four-dimensional variational assimilation of ozone data in weather-prediction models. *Q. J. R. Meteorol. Soc.* **122**: 1545–1571.
- Roberts NM, Lean HW. 2008. Scale-selective verification of rainfall accumulations from high-resolution forecasts of convective events. *Mon. Weather Rev.* **136**: 78–96.
- Scheck L, Frèrebeau P, Buras-Schnell R, Mayer B. 2016. A fast radiative transfer method for the simulation of visible satellite imagery. *J. Quant. Spectrosc. Radiat. Transfer* **175**: 54–67.
- Schmetz J, van de Berg L. 1994. Upper tropospheric humidity observations from Meteosat compared with short-term forecast fields. *Geophys. Res. Lett.* **21**: 573–576, <http://dx.doi.org/10.1029/94GL00376>.
- Smith EA, Bauer P, Marzano FS, Kummerow CD, McKague D, Mugnai A, Panegrossi G. 2002. Intercomparison of microwave radiative transfer models for precipitating clouds. *IEEE Trans. Geosci. Remote Sensing* **40**: 541–549.
- Snyder C, Zhang F. 2003. Assimilation of simulated Doppler radar observations with an ensemble Kalman filter. *Mon. Weather Rev.* **131**: 1663–1677.
- Stengel M, Lindskog M, Undén P, Gustafsson N. 2013. The impact of cloud-affected IR radiances on forecast accuracy of a limited-area NWP model. *Q. J. R. Meteorol. Soc.* **139**: 2081–2096.
- Tauchi T, Takeuchi Y, Sato Y. 2004. ‘Assimilation of the Aqua/AMSR-E data to numerical weather predictions’. In *2004 IEEE International Geoscience and Remote Sensing Symposium 2004 IGARSS’04. Proceedings*, Vol. 5. IEEE: Piscataway, NJ, pp. 3199–3202.
- Taylor RBE, Renshaw RJ, Saunders RW, Francis PN. 2008. ‘Assimilation of SEVIRI cloud-top parameters in the Met Office regional forecast model’ In *2008 EUMETSAT Meteorological Satellite Conference. Darmstadt, Germany*.
- Tompkins AM, Janisková M. 2004. A cloud scheme for data assimilation: Description and initial tests. *Q. J. R. Meteorol. Soc.* **130**: 2495–2517.
- Tsuyuki T. 1997. Variational data assimilation in the tropics using precipitation data. Part III: Assimilation of SSM/I precipitation rates. *Mon. Weather Rev.* **125**: 1447–1464.
- Uppala SM, Källberg PW, Simmons AJ, Andrae U, da Costa Bechtold V, Fiorino M, Gibson JK, Haseler J, Hernandez A, Kelly GA, Li X, Onogi K, Saarinen S, Sokka N, Allan RP, Andersson E, Arpe K, Balmaseda MA, Beljaars ACM, Van de Berg L, Bidlot J, Bormann N, Caires S, Chevallier F, Dethof A, Dragosavac M, Fisher M, Fuentes M, Hagemann S, Hólm E, Hoskins BJ, Isaksen L, Janssen PAEM, Jenne R, McNally AP, Mahfouf J-F, Morcrette J-J, Rayner NA, Saunders RW, Simon P, Sterl A, Trenberth KE, Untch A, Vasiljević D, Viterbo P, Woollen J. 2005. The ERA-40 re-analysis. *Q. J. R. Meteorol. Soc.* **131**: 2961–3012.
- Vesperini M. 1998. Humidity in the ECMWF model: Monitoring of operational analyses and forecasts using SSM/I observations. *Q. J. R. Meteorol. Soc.* **124**: 1313–1327.
- Vukicevic T, Greenwald T, Županski M, vZupanski D, Vonder Haar T, Jones A. 2004. Mesoscale cloud state estimation from visible and infrared satellite radiances. *Mon. Weather Rev.* **132**: 3066–3077.
- Vukicevic T, Sengupta M, Jones A, Vonder Haar T. 2006. Cloud-resolving satellite data assimilation: Information content of IR window observations and uncertainties in estimation. *J. Atmos. Sci.* **63**: 901–919.
- Waller JA, Dance SL, Lawless AS, Nichols NK, Eyre JR. 2014. Representativity error for temperature and humidity using the Met Office high-resolution model. *Q. J. R. Meteorol. Soc.* **140**: 1189–1197.
- Wattrelot E, Caumont O, Mahfouf JF. 2014. Operational implementation of the 1D+3D-Var assimilation method of radar reflectivity data in the AROME model. *Mon. Weather Rev.* **142**: 1852–1873.
- Weston P, Bell W, Eyre JR. 2014. Accounting for correlated error in the assimilation of high-resolution sounder data. *Q. J. R. Meteorol. Soc.* **140**: 2420–2429.
- Xiao Q, Zou X, Kuo YH. 2000. Incorporating the SSM/I-derived precipitable water and rainfall rate into a numerical model: A case study for the ERICA IOP-4 cyclone. *Mon. Weather Rev.* **128**: 87–108.
- Yang C, Liu Z, Bresch J, Rizvi SR, Huang XY, Min J. 2016. AMSR2 all-sky radiance assimilation and its impact on the analysis and forecast of hurricane Sandy with a limited-area data assimilation system. *Tellus A* **68**: 30917, <http://dx.doi.org/10.3402/tellusa.v68.30917>.
- Zhang F, Bei N, Rotunno R, Snyder C, Epifanio CC. 2007. Mesoscale predictability of moist baroclinic waves: Convective-permitting experiments and multistage error growth dynamics. *J. Atmos. Sci.* **64**: 3579–3594.
- Zhang SQ, VZupanski M, Hou AY, Lin X, Cheung SH. 2013. Assimilation of precipitation-affected radiances in a cloud-resolving WRF ensemble data assimilation system. *Mon. Weather Rev.* **141**: 754–772.
- Zhang F, Minamide M, Clothiaux EE. 2016. Potential impacts of assimilating all-sky infrared satellite radiances from GOES-R on convection-permitting analysis and prediction of tropical cyclones. *Geophys. Res. Lett.* **43**: 2954–2963, <http://dx.doi.org/10.1002/2016GL068468>.
- Zhu Y, Liu EH, Mahajan R, Thomas C, Groff D, van Delst P, Collard A, Kleist D, Treadon R, Derber J. 2016. All-sky microwave radiance assimilation in the NCEP’s GSI analysis system. *Mon. Weather Rev.* **144**: 4709–4735, <http://dx.doi.org/10.1175/MWR-D-15-0445.1>.
- Zou X. 1997. Tangent linear and adjoint of ‘on-off’ processes and their feasibility for use in four-dimensional variational data assimilation. *Tellus A* **49**: 3–31.
- Zou X, Navon I, Sela J. 1993. Variational data assimilation with moist threshold processes using the NMC spectral model. *Tellus A* **45**: 370–387.
- Županski D, Mesinger F. 1995. Four-dimensional variational assimilation of precipitation data. *Mon. Weather Rev.* **123**: 1112–1127.

Relative impact of polar-orbiting and geostationary satellite radiances in the Aladin/France numerical weather prediction system

Thibaut Montmerle*, Florence Rabier and Claude Fischer
Météo-France/CNRM, Toulouse, France

ABSTRACT: For its short-range forecasts over Western Europe, Météo-France runs the limited-area model ALADIN operationally with four daily analyses obtained with a 3D-Var data assimilation system. This system includes, among other observation types, radiances from AMSU-A, AMSU-B, HIRS and SEVIRI radiometers. SEVIRI is on board the geostationary platform Meteosat-8 and provides continuous observations in space and in time over the region of interest at several wavelengths, while the others, which are on board polar-orbiting satellites, have poorer temporal and horizontal resolutions but a better spectral resolution than SEVIRI. Observing System Experiments (OSEs) have been performed with the operational 3D-Var to assess the impact of such satellite data on analyses and on forecasts. DFS (Degrees of Freedom for Signal) have been computed and have shown the complementarity between WV channels from the different radiometers. In the operational version of the 3D-Var, DFS values show that analyses are strongly controlled by SEVIRI data in the mid to high troposphere. This is consistent with the large number of assimilated SEVIRI radiances. HIRS and AMSU-B WV data would provide more information if SEVIRI data were not assimilated and if ATOVS data were used with a higher density. However, using ATOVS data with a higher horizontal resolution makes the analyses more dependent on these data, and it does not appear to be beneficial in this particular context, probably because of a non-optimal bias correction. In that case however, the individual impact of each pixel decreases because of the horizontal correlation lengths of the structure functions. Forecast scores and predicted precipitation patterns display the positive impact of SEVIRI data. Copyright © 2007 Royal Meteorological Society

KEY WORDS 3D-Var; SEVIRI; ATOVS; radiance assimilation

Received 22 February 2006; Revised 23 November 2006; Accepted 28 November 2006

1. Introduction

Infrared and microwave radiance data such as those from the Advanced TIROS Operational Vertical Sounder (ATOVS) have been shown to be beneficial to NWP global model forecasts because they provide valuable information on atmospheric temperature and humidity (English *et al.*, 2000; Bouttier and Kelly, 2001). For global models, these data affect large scales and are dominant over the tropical and southern oceans, since satellite observations are often the only available data in these areas. At present, these data are far more useful over the oceans than over land, since information about emissivity and surface temperature over land is not very accurate and induces the removal of low-peaking channels in the assimilation process. Improvements in both assimilation techniques and instruments will push the benefit of radiances further. In particular, sounders such as the Advanced Infrared Sounder (AIRS) and the Infrared Atmospheric Sounding Instrument (IASI) show more potential than ATOVS observations through

their much finer spectral and vertical resolution (Prunet *et al.*, 1998). Limited-area models (LAMs) can also benefit from polar-orbiting satellite data for short-term forecasting at the mesoscale, provided they are at an adequate horizontal and temporal resolution. Radiometers such as ATOVS have a horizontal resolution which seems well suited for regional studies (between 15 and 45 km, depending on instruments). However, their potential impact strongly depends on their availability within the domain of interest.

Despite their lower spectral resolution, radiometers on board geostationary satellites are particularly well adapted to weather predictions at the mesoscale to the convective scale, since they allow almost continuous access to information about the evolution of temperature and humidity fields at a high horizontal resolution. For instance, the Spinning Enhanced Visible and Infrared Imager (SEVIRI) on board Meteosat-8 has a horizontal resolution between 4 and 6 km over Western Europe. Assimilation of geostationary data in NWP global models is quite recent, e.g. GOES imager data at the US National Centers for Environmental Prediction (NCEP, Derber, 2003), at the Canadian Meteorological Centre (CMC, Garand and Wagner, 2002) and at the European

*Correspondence to: Thibaut Montmerle, Météo-France/CNRM, 42 av. G. Coriolis, 31057 Toulouse, France.
E-mail: montmerle@cnrm.meteo.fr

Centre for Medium-range Weather Forecasts (ECMWF, Köpken *et al.*, 2003); Meteosat-7 and -8 at ECMWF (Köpken *et al.*, 2003; Szyndel *et al.*, 2004, respectively). In these studies at global scale, the main impact of geostationary radiances is generally a small improvement in the analysis and in the forecasts of mid- to high-tropospheric humidity. The scope of our study is to investigate the relative impact of geostationary versus polar-orbiting satellites and their possible complementarity in a context of weather forecasting at regional scale. For that purpose, radiances from SEVIRI and from ATOVS on board AQUA and the NOAA satellites are considered.

To evaluate the impact of a specific observation type on the forecast, Observing System Experiments (OSEs), which consist of comparing forecast scores from experiments that use different observation scenarios, are performed. The drawback of such a method is the large amount of computational resource which is required. Other methods have been implemented to diagnose the impact of observations on analyses, i.e. to infer the statistical variance reduction induced by the assimilation of one particular type of observations. These methods are mainly based on measurements of the so-called DFS (Degrees of Freedom for Signal) that allow the amount of information brought by subsets of observations in assimilation systems to be quantified. The DFS computation has been implemented in the four-dimensional variational (4D-Var) assimilation scheme of operational global models such as the ECMWF model (Cardinali *et al.*, 2004) and the French ARPEGE model (Action de Recherche Petite Echelle Grande Echelle, Chapnik *et al.*, 2006) using an extension of a randomization procedure initially described by Desroziers and Ivanov (2001). These methods seem particularly well suited to this study, since they give an objective way to diagnose the relative impact of assimilated radiances coming from different platforms, and they have been adopted here to the LAM context.

The LAM ALADIN/France (Aire Limitée Adaption Dynamique et développement International), which has been running operationally at Météo-France since July 2005, is used with four daily analyses obtained with a 3D-Var data assimilation system. The operational suite provides short-range forecasts over Western Europe, with a 10 km horizontal resolution. An overview and an evaluation of this complete assimilation/forecast system is given by Fischer *et al.* (2005, F2005 below). Different OSEs, based on this configuration, have been performed to study the relative impacts of the assimilated radiances.

The main characteristics of the ALADIN/France operational suite are presented in section 2, with special emphasis put on the set-up of satellite radiance. The relative impact of the radiances in the analysis is then discussed in the following sections. Section 3 focuses on the sensitivity of the analysis with respect to the different types of data using DFS; section 4 presents the relative impact of polar-orbiting and geostationary satellite data in weather forecasting at regional scale, using forecast scores against conventional data and comparing

precipitation forecasts for a case-study. Finally, section 5 presents some concluding remarks.

2. Experimental framework

2.1. The ALADIN 3D-Var

The variational code of the ALADIN 3D-Var is based on the incremental formulation originally introduced in the ARPEGE/Integrated Forecast System global assimilation (Courtier *et al.*, 1994). In F2005, the specification of the background-error covariance matrix is discussed and has led to the selection of ensemble-based covariances that were sampled from an ensemble of ALADIN forecasts, with initial conditions taken from an ensemble of analyses from the coupling model ARPEGE (Ştefănescu *et al.*, 2006). This background-error covariance matrix includes finer-scale structure functions than those used for the global model. For instance, the horizontal correlation lengths for temperature and specific humidity are around 70 km in the mid-troposphere for ALADIN compared to more than 250 km for ARPEGE (Berre *et al.*, 2006). Compared to ARPEGE, the shorter length-scales in ALADIN 3D-Var lead to finer structures in the analysis increments. The operational version of ALADIN/France has been evaluated on a daily basis by computing forecast scores against observations and by analyzing simulated precipitation patterns. Montmerle (2005) and F2005 have shown encouraging results compared to the spin-up model (i.e. ALADIN used as a dynamical adaptation of ARPEGE), in particular for short-range precipitation forecasts.

2.2. Main features of the operational suite

As in the global model ARPEGE, the operational suite of ALADIN 3D-Var (*OPER* in the following) consists of two parallel cycles. The assimilation cycle uses a ±3-hour assimilation window and is coupled with the ARPEGE assimilation cycle that uses long cut-off times. This cycle produces 6-hour forecasts which are used as background fields for the next analysis in both assimilation and production cycles. The production cycle also uses a ±3-hour assimilation window but it is coupled with the ARPEGE production cycle that has a short cut-off time (1 h 50 min for the 00 UTC analysis). Short-range forecasts are run from each production cycle. Each ALADIN analysis uses surface fields that have been analyzed for ARPEGE for the same assimilation time, i.e. no surface analysis is formed specifically for ALADIN.

In ALADIN, the same observations as in ARPEGE are used, with the addition of SEVIRI radiances and of surface measurements. The latter two are presented in sections 2.3 and 2.4, respectively. Radiosondes, surface observations, buoys, ship and aircraft measurements, wind profilers, horizontal winds from atmospheric motion vectors (AMVs) and the QuikSCAT scatterometer, AMSU-A radiances from NOAA-15, NOAA-16 and

AQUA, AMSU-B radiances from NOAA-16 and NOAA-17, and High-Resolution Infrared Sounder (HIRS) radiances from NOAA-17 are common to both systems. Details about the use of ATOVS radiances (channel selection, quality control, cloud detection, etc.) in ARPEGE can be found in Gérard *et al.* (2003). Innovations (i.e. observation minus guess) in brightness temperature (T_b) have been bias-corrected following the method developed at ECMWF by Harris and Kelly (2001). Biases due to scan angle and those dependent on air mass have been removed. The air-mass-dependent biases have been computed using multiple linear regressions based on four predictors: thicknesses between 1000 and 300 hPa and between 200 and 50 hPa, surface temperature and the total column water vapour (WV). It has to be noted that, for all experiments presented herein, the regression coefficients are the same as for ARPEGE, assuming that they are valid for the limited-area domain. For AMSU-A data, Randriamampianina (2005) has shown that this hypothesis might lead to more variable daily forecast scores compared to coefficients computed especially from LAM innovations. For the sake of simplicity, the same coefficients are used in this study. The values of specified observation error variances for ATOVS radiances are between 0.5 and 0.75 K for HIRS 4, 5, 6, 7, 14 and 15; 1 and 2 K for HIRS WV 11 and 12 respectively; 3, 2.5 and 2 K for AMSU-B 3, 4 and 5 respectively; and between 0.35 and 0.8 K for AMSU-A channels.

As shown in Figure 1, there is a large difference in the number of active data (i.e. data that enter the minimization) between the ATOVS and SEVIRI radiances in the OPER configuration. This is due to the different initial data sampling and to the large thinning lengths used in ARPEGE for ATOVS data (260 km) whereas 70 km is used for SEVIRI. No HIRS radiances are present for the 06 and 18 UTC analysis and almost no AMSU-B data are used at 18 UTC. In a 3D-Var context, the time differences of ATOVS measurements relative to analysis time can reach a few hours. In fact, NOAA-16 and NOAA-17 fly over western Europe around 0435 and 1425 UTC and around 1100, 1950 and 2150 UTC, respectively. This time difference between observations and analysis can possibly lead to an analysis degradation, e.g. in cases of rapidly developing mesoscale convective systems. However, on average, extra data such as these time-shifted ATOVS data generally add valuable information in data-void regions. Furthermore, and as is demonstrated in section 3, the imbalance between numbers of active data from geostationary and polar-orbiting satellites implies that the resulting analyses are strongly controlled by SEVIRI radiances, which mitigates the potential negative effect of the time-shifted ATOVS observations.

Mean weighting functions of channels that are considered in the assimilation, computed for 20 midlatitude atmospheric profiles using the fast radiative transfer model RTTOV (Radiative Transfer for TIROS Operational Vertical sounder; Saunders *et al.*, 1999), are plotted in Figure 2 for the four radiometers. These plots show that mid- to high-tropospheric humidity-sensitive HIRS

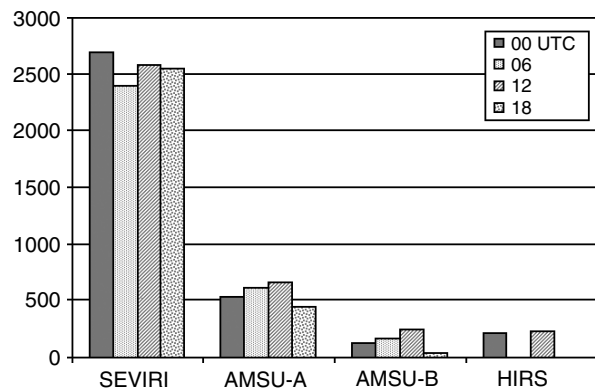


Figure 1. Number of assimilated satellite radiances for the four daily analysis steps for OPER on 5 June 2005.

channels 11 and 12, AMSU-B channels 3 and 4 and SEVIRI channels 2 and 3 are characterized by weighting functions that have similar shapes and intensities. As a consequence, the individual impact of one single observation from these different WV channels should be comparable, provided their specified errors are similar. On the contrary, SEVIRI low-peaking infrared channels seem to be more sensitive to surface conditions than those from HIRS. Finally, the AMSU-A channels are sensitive to high-tropospheric/low-stratospheric temperature variations, and thus their impacts are expected to be different from those of the other three radiometers.

2.3. SEVIRI radiances

The first Meteosat Second Generation (MSG) satellite, known as Meteosat-8, has been operational since January 2004. It carries the SEVIRI composed of twelve channels, eight of which are in the infrared spectrum with wavelengths of 3.9, 6.2, 7.3, 8.7, 9.7, 10.8, 12 and 13.4 μm . The 6.2 and 7.3 μm are designated as WV channels 2 and 3 in Figure 2. More details about this particular instrument can be found in Schmetz *et al.* (2000). A clear-sky radiance (CSR) product is operationally produced by EUMETSAT and assimilated in the ECMWF model (Sznydel *et al.*, 2004). It is generated by averaging radiances from cloud-free pixels over segments of 16×16 pixel squares. In our study, the higher spatial resolution of the analysis motivated us to use these observations directly at high resolution.

The details of the data processing are as follows. The near-IR 3.9 μm channel is blacklisted because of possible solar contamination and because of its broad spectral resolution that makes its modelling by the radiative transfer model difficult. The ozone IR 9.7 μm channel is also blacklisted because the model does not consider ozone as a prognostic variable and because of the poor vertical resolution of the model in the high troposphere/low stratosphere. Finally, the CO₂ 13.4 μm channel has also been blacklisted because of a persistent bias-correction problem, explained below. Of the remaining channels, one pixel out of five is extracted and thinning to 70 km is applied. The relevance of this choice is discussed in detail

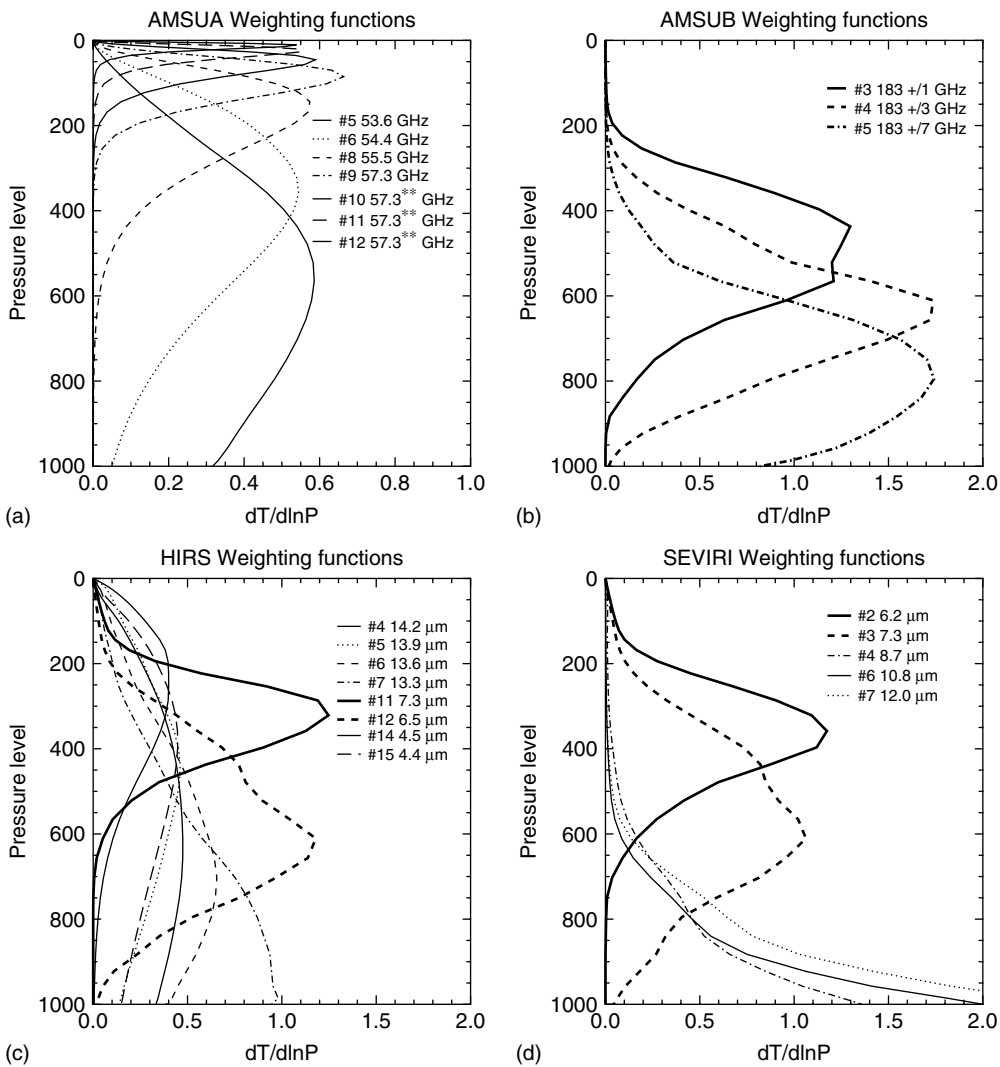


Figure 2. Mean weighting functions (or variations of the transmittance per vertical layer) for 20 midlatitude summertime profiles for channels that are used in the assimilation process for (a) AMSU-A, (b) AMSU-B, (c) HIRS and (d) SEVIRI. WV channels are in bold lines.

in section 2.5. Observation error variances of 1 and 1.7 K have been used for IR and WV channels respectively, which is comparable to what has been set for ATOVS channels, as seen in the previous section.

For SEVIRI, the bias due to the scan angle is not relevant because of small scan angle values inherent to the geostationary scanning strategy. The remaining air-mass-dependent bias is then deduced from multiple linear regressions as in Harris and Kelly (2001) on a volume of data which is sufficient to get statistically stable results over the ALADIN domain. The coefficients of the bias correction used in this study were computed from a one-month period of innovations (April–May 2005) for which comparable weather regimes for those of the experiments were observed. The predictors of that regression are the same as for ATOVS (see section 2.2). To correct biases of the two WV channels from the SEVIRI CSR product in the ECMWF global model, Szyndel *et al.* (2004) use only three predictors, the surface temperature not being taken into account since they do not take into consideration the low-peaking IR channels in the

assimilation. The corrected innovation biases present a narrow Gaussian distribution centred on zero for all the assimilated channels except the 13.4 μm. For the CO₂ 13.4 μm channel, this distribution is constantly centred on +0.4 K, perhaps because of unsuited predictors for this particular channel which is sensitive to the temperature throughout most of the troposphere. Consequently, this channel has been temporarily blacklisted. If a radical change of weather regime occurs over the limited area covered by the model, the results can be degraded, the regression coefficients being misfitted. In that particular case, new coefficients should be computed (typically every new season).

The cloud-type product developed by CMS (Centre de Météorologie Spatiale, Lannion, France) in the framework of the MSG Satellite Application Facility to Nowcasting has been used (Derrien *et al.*, 2005) to avoid contamination by clouds and to keep in the assimilation process channels whose weighting functions peak above the cloud top. The two WV channels are kept above low clouds, for which the fixed cloud-top pressure levels are

below the tail of the weighting functions, and the low-peaking channels 8.7, 10.8 and 12 μm are used over sea, only in clear-sky conditions.

2.4. 2 m measurements

The 2 m measurements of temperature and humidity, coming mainly from the French RADOME (Réseau d'Acquisition de Données et d'Observations Météorologiques Étendues) network consisting of synoptic and automatic surface measurements, are another observation type assimilated in ALADIN/*OPER* and not in the global model. In addition to the fact that these data give a better analysis of the boundary layer, a strong complementarity with SEVIRI WV channels has been found. The information brought by the latter on the mid-tropospheric humidity can artificially propagate downwards too strongly, because the background-error vertical correlations poorly represent the height of the boundary layer. The addition of these ground-based data somehow allows this anomaly to be corrected.

2.5. Observing system experiments

OSEs have been carried out and run for three weeks, from 5 to 23 June 2005, with the same cycling strategy as *OPER*. This time period was chosen because of the large sample of precipitating cases that were observed over the ALADIN domain. Three main precipitating periods occurred during that period: from the 7 to 9 and around 23 June, when unstable conditions prevailed in the south of France leading to strong convective activity, and from 13 to 18 June, when a more synoptic-scale weather regime brought successive westward-propagating rain bands over Western Europe. The different OSEs considered in this study are as follows:

- *noSEV* denotes *OPER* without SEVIRI data.
- *moreATOVS* denotes *OPER* with additional ATOVS data used with a finer thinning (see next section for details). For the 00 UTC assimilation cycle, this configuration inserts in the assimilation process approximately eight times more HIRS, AMSU-A and AMSU-B data than in *OPER*.
- *moreATOVSnosev* denotes *moreATOVS* without SEVIRI data. This experiment has been carried out to study the impact of additional ATOVS data independently of SEVIRI.
- *OPER-SEVnoIR* denotes *OPER* without SEVIRI IR radiances (e.g. only considering WV channels).

These experiments have been run to infer the relative impact of SEVIRI and of denser ATOVS radiances in an operational configuration. Discussion will be carried out mainly using the *noSEV* and *moreATOVS* OSEs, the two other OSEs helping to draw conclusions reported in section 3.3.

2.6. Thinning of satellite observations

Using denser data in the variational process does not necessarily mean an improvement of the analyses. In fact, and as pointed out by Liu and Rabier (2003), if the error correlation between two adjacent pixels becomes greater than a threshold value (around 0.2 in their study) and if the observation-error covariance matrix \mathbf{R} is diagonal (which is the case here), then the system becomes sub-optimal which degrades the analyses and the resulting forecasts. On the contrary, if observations are uncorrelated, adding new data generally improves the results. The thinning lengths for SEVIRI and ATOVS radiances have thus been chosen in order to find a good compromise between the spatial resolution of the data and a sufficiently small correlation value between selected observations to ensure the optimality hypothesis made in the variational process.

For that purpose, the tuning coefficients s^o for observation-error variances described by Desroziers and Ivanov (2001) and Chapnik *et al.* (2004) have been used indirectly. This method aims at producing tuned variances consistent with the innovations (i.e. observation minus guess), assuming that the correlation patterns of the specified matrices are correct. As a consequence, if the observational error is spatially correlated while the corresponding specified observation-error matrix \mathbf{R} is diagonal, after some iterations the tuning coefficients will drop to zero. This behaviour has been used as a tool to tune the thinning. For instance, Chapnik *et al.* (2006) have used this particular property to point out the high spatial correlations of geostationary wind vectors. The theory and the method that has been used to compute this tuning coefficient are detailed in Appendix A.

In practice, the tuning coefficients computed for each SEVIRI channel in *OPER* and for each ATOVS channel in *moreATOVS* have been re-injected in new analyses. With 70 and 80 km thinning lengths for SEVIRI and ATOVS data respectively (while *OPER* uses 260 km for ATOVS), the values of s^o that have been diagnosed after that second iteration were larger than their initial value and were converging towards unity, which is specific to uncorrelated data. This test confirmed the relevance of the different thinning intervals selected in this study. As displayed in Figure 3, *moreATOVS* uses a coverage for ATOVS data more comparable to that of SEVIRI which seems better suited for regional-scale studies within the ALADIN domain.

3. Sensitivity of the analysis to observations

3.1. Verification versus ATOVS and SEVIRI observations

For *noSEV* and *moreATOVS*, the fit of the model first guess and the analysis to conventional observations remains mostly unchanged compared with *OPER*. However, discrepancies appear for statistics involving AMSU-B and HIRS channels. Figure 4 shows such statistics

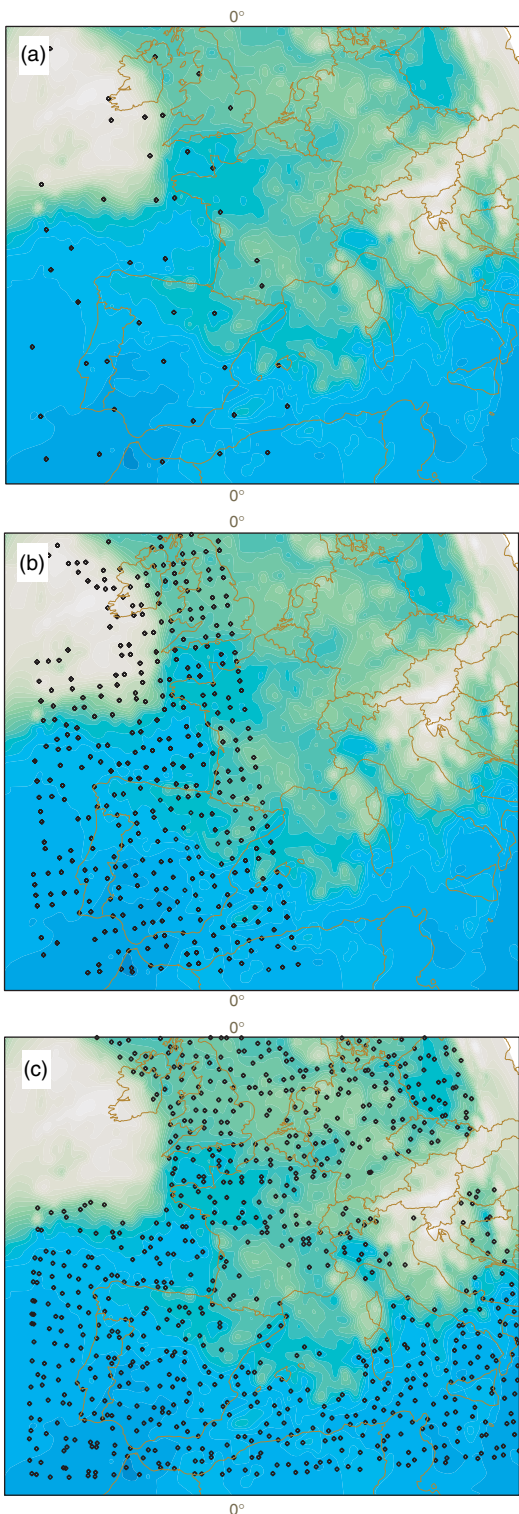


Figure 3. Example of the localization of active data that enter the minimization at 00 UTC with a long cut-off time for (a) AMSU-B in *OPER*, (b) AMSU-B in *moreATOVS* (c) SEVIRI WV $6.4\mu\text{m}$ in both experiments, all plotted over brightness temperature observed by the SEVIRI $10.8\mu\text{m}$ channel. This figure is available in colour online at www.interscience.wiley.com/qj

for *noSEV* compared with *OPER*. For HIRS channels 11 and 12 and AMSU-B, smaller background departure r.m.s. errors are displayed for *OPER*, which indicates that 6-hour forecasts are closer to these observations when

SEVIRI radiances are considered. On the contrary, the corresponding analysis departure r.m.s. errors are larger for *OPER* than for *noSEV* because of the high number of assimilated SEVIRI data which highly constrains the cost function. One can see that AMSU-B 3 and 4 are poorly bias corrected. The monitoring of this bias (not shown), as well as for HIRS channels, displays highly variable features (typically between $\pm 1\text{ K}$) because of the low number of data that are taken into account in the statistics, and also probably because the regression coefficients were not computed specifically over the ALADIN domain explained in section 2.2. Concerning this last point, the relevance of those coefficients is difficult to evaluate precisely, because the low number of assimilated ATOVS data is making the statistics unstable. However, biased ATOVS observations are less problematic for *OPER* than for *noSEV*, because of the small influence of ATOVS data in the *OPER* analyses, as shown in the next section. Figure 4 shows that adding a high number of correctly bias-corrected SEVIRI data seems to improve the guess since r.m.s. errors and biases have lower values for AMSU-B 3 and 4. In *noSEV*, the larger innovation biases thus seem to be mainly due to poorer short-term forecasts of mid- to high-level humidity.

The same statistics are plotted in Figure 5 for *moreATOVS* compared to *OPER*. Concerning background and analysis departure r.m.s. errors, the same characteristics as for *noSEV* are observed, but in a much less pronounced manner; adding extra ATOVS data to an experiment that assimilates high-resolution SEVIRI data has far less impact than adding SEVIRI data to an experiment that uses only sparse ATOVS data. It seems that (observation minus guess) biases are generally degraded for HIRS when more ATOVS data are used, although smaller values for AMSU-B 3 and 4 are shown. This indicates that the background becomes poorer and poorer throughout the cycling when using biased and/or weakly correlated data, as pointed out in the previous section. In fact, statistics computed for the initial analysis time show smaller biases and background departures for *moreATOVS* than for *OPER*, whereas the contrary is obtained for the last analysis time (not shown). This drawback could be partly solved by using greater observation-error variances σ_o^2 for ATOVS data in order to decrease their weight in the minimization. For that purpose (and also to check the relevance of the thinning lengths, as mentioned in section 2.6), tuning factors have been computed as in Chapnik *et al.* (2006) in order to get prescribed covariance matrices that fulfil an optimality criterion, and have been applied to an extra experiment (see Appendix A for more details). Unfortunately, no significant impact either on the analysis or on forecasts has been obtained for this experiment, although the resulting observation-error variances per channel seem to be realistic too. This result shows that covariance matrices are globally finely tuned in *moreATOVS*. As a consequence, only results from *moreATOVS* will be discussed below. Another issue when using denser ATOVS data would be to compute the regression coefficients used for the bias correction

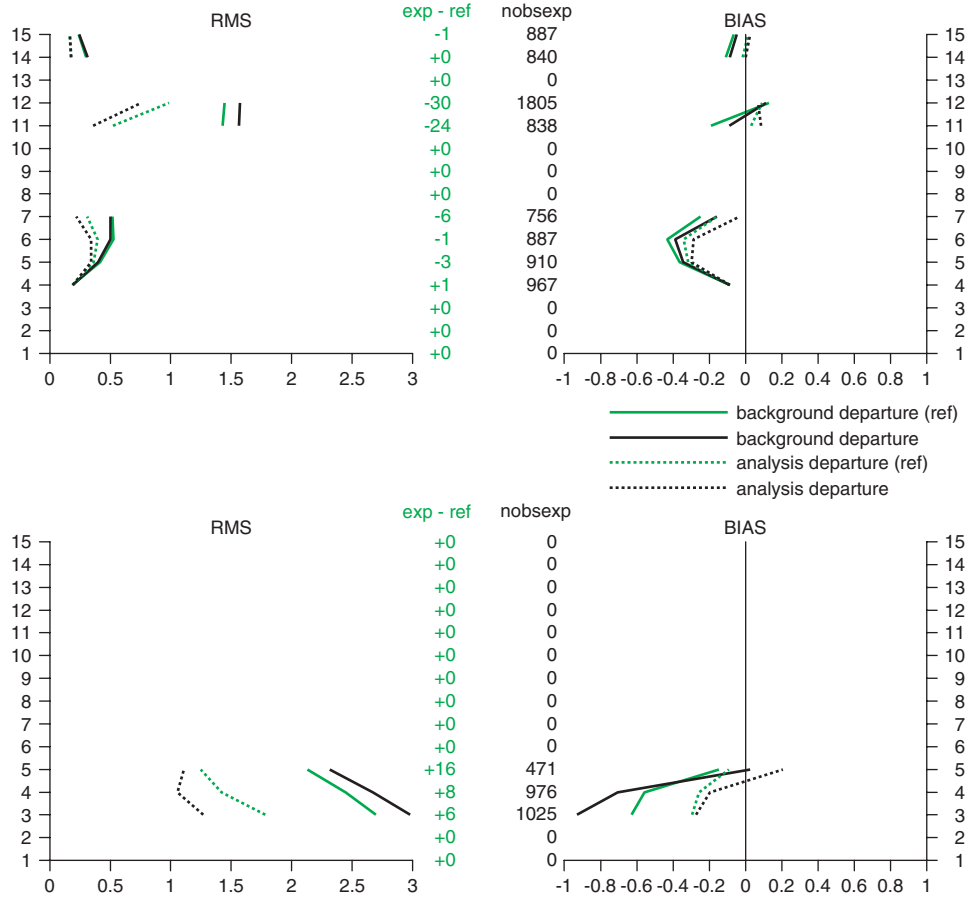


Figure 4. Brightness temperature (a) r.m.s. error and (b) bias (K) of observation minus guess (solid line) and observation minus analysis (dashed line) for noSEV (black) and OPER (grey) between 6 and 22 June 2005, for HIRS on board NOAA-17. (c) and (d) are as (a) and (b), but for AMSU-B on board NOAA-16. The vertical axis represents the channel number and numbers in the middle the amount of assimilated data. This figure is available in colour online at www.interscience.wiley.com/jq

specifically over the ALADIN/France domain, in order to ensure a better fit to predictors, instead of using coefficients computed over the global ARPEGE domain, as is the case for the three OSEs.

3.2. Use of the DFS

3.2.1. Theory

The relative influence of each type of observation can be quantified by computing Degrees of Freedom for Signal (DFS), which is equal to the trace of the derivative of the analysis written in the observation space with respect to the observations:

$$\text{DFS} = \text{Tr} \left\{ \frac{\delta(\mathbf{H}\mathbf{x}_a)}{\delta \mathbf{y}} \right\}, \quad (1)$$

where \mathbf{x}_a represents the analysis, and \mathbf{y} the observations. \mathbf{H} is the tangent linear operator of H , which is the observation operator that writes model variables in observation space (spatial interpolations and radiative transfer model RTTOV-8; Saunders *et al.* 1999). More information on the theory and on the properties of the DFS can be found in Rodgers (1996). This diagnostic has been recently used by Rabier *et al.* (2002) to perform channel selection

on simulated IASI observations and by Cardinali *et al.* (2004) to study the respective influence of different types of observations in the ECMWF data assimilation system. More recently, Fourrié *et al.* (2006) have also used this quantity to diagnose the contribution of targeted observations on analyses in the context of the international programme THORPEX (The Observing system Research and Predictability Experiment).

For an optimal case, the analysis increment $\delta\mathbf{x}$ can be written as

$$\begin{aligned} \delta\mathbf{x} &= \mathbf{x}_a - \mathbf{x}_b \\ &= (\mathbf{B}^{-1} + \mathbf{H}^T \mathbf{R}^{-1} \mathbf{H})^{-1} \mathbf{H}^T \mathbf{R}^{-1} (\mathbf{y} - H[\mathbf{x}_b]) \\ &= \mathbf{K}(\mathbf{y} - H[\mathbf{x}_b]), \end{aligned} \quad (2)$$

where \mathbf{x}_b represents the background, \mathbf{B} is the background-error covariance matrix and \mathbf{R} is the observation-error covariance matrix composed of instrumental errors and errors in the observation operator H , already presented in section 2.4. \mathbf{K} is the Kalman gain matrix.

In a linear case, we can deduce from (1) and (2):

$$\text{DFS} = \text{Tr}(\mathbf{HK}). \quad (3)$$

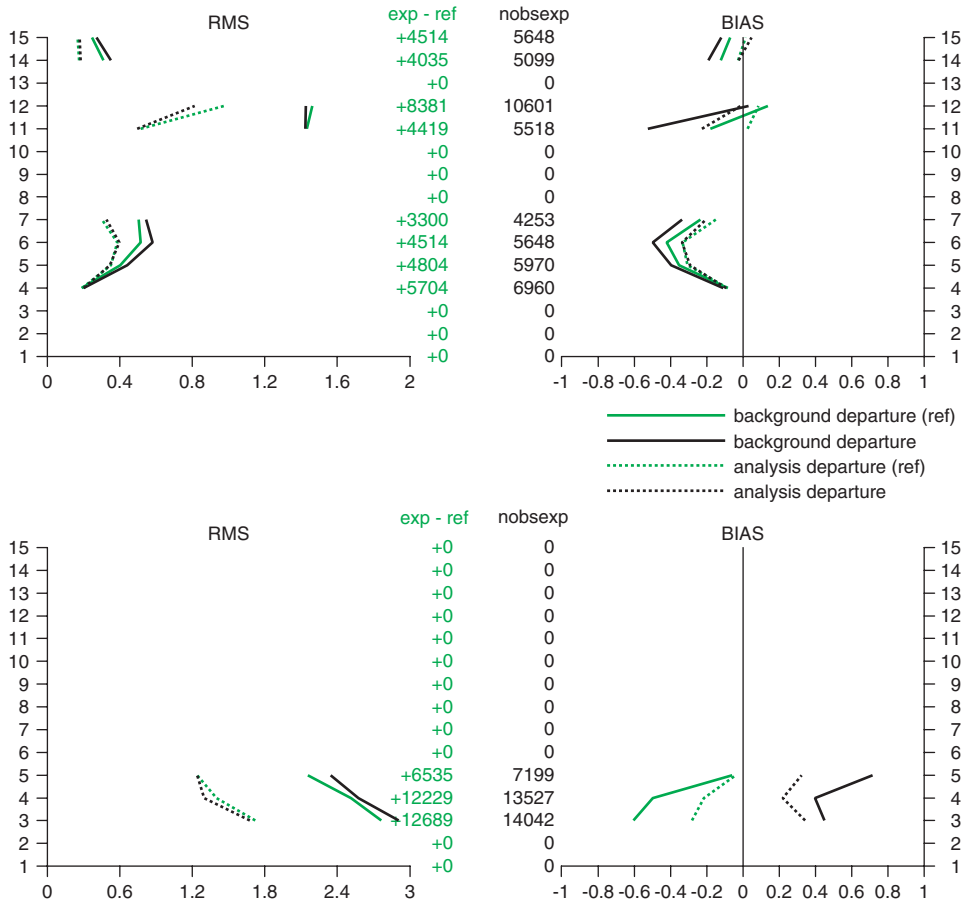


Figure 5. As Figure 4, but for *moreATOVS* (black) and *OPER* (grey). This figure is available in colour online at www.interscience.wiley.com/qj

This diagnostic can be computed for a subset of observations y_i , as long as they are uncorrelated, by using a projection operator Π_i^o :

$$\text{DFS}_i = \text{Tr}(\Pi_i^o \mathbf{H} \mathbf{K} \Pi_i^{oT}). \quad (4)$$

It is difficult to estimate the DFS using (3), because of the size of the matrices that are involved and because the Kalman gain matrix is unavailable in a variational scheme. As in Chapnik *et al.* (2006), a Monte Carlo method to approximate the trace of the operator is therefore used (Girard, 1987). This method requires a random perturbation of the observation vector \mathbf{y} . Let $\delta\mathbf{y}^*$ be this random vector of the same size as \mathbf{y} that follows a normalized Gaussian probability density function $\delta\mathbf{y}^* \in \mathcal{N}(0, I)$. If the size of this vector is sufficiently large, the following relationships hold:

$$\delta\mathbf{y}^{*T} \mathbf{H} \mathbf{K} \delta\mathbf{y}^* = \text{Tr}(\mathbf{H} \mathbf{K} \delta\mathbf{y}^* \delta\mathbf{y}^{*T}) \simeq \text{Tr}(\mathbf{H} \mathbf{K}). \quad (5)$$

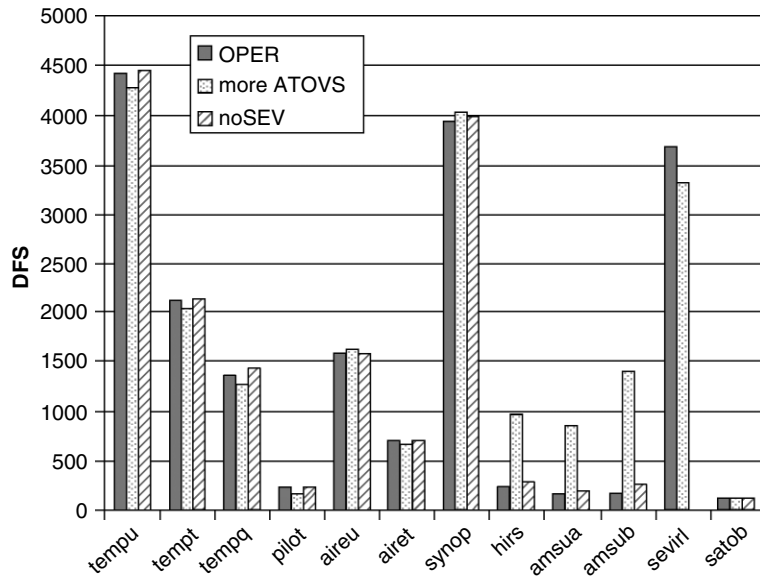
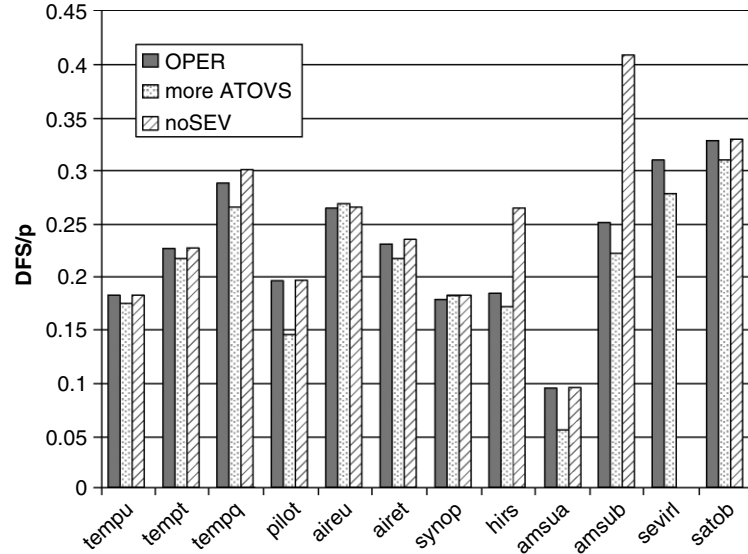
This method needs two parallel analyses: the original \mathbf{x}_a retrieved from the available observations \mathbf{y} and the background state \mathbf{x}_b , and a second one \mathbf{x}_a^* from the very same set of observations but randomly perturbed $\mathbf{y}^* = \mathbf{y} + \mathbf{R}\delta\mathbf{y}^*$ and the same guess \mathbf{x}_b . After applying (2) for the two cases, and considering (4):

$$\text{DFS} = \text{Tr}(\mathbf{H} \mathbf{K}) = (\mathbf{y}^* - \mathbf{y})^T \mathbf{R}^{-1} \mathbf{H} (\mathbf{x}_a^* - \mathbf{x}_a).$$

3.2.2. Results

As pointed out by Sadiki and Fischer (2005), a sufficient number of samples is needed to compute a reliable estimate of the $\text{Tr}(\mathbf{H} \mathbf{K})$ with this kind of Monte Carlo method. While applying the projection operator Π_i^o to a particular set of data (humidity from radiosondes for instance), the sample size can drop and corrupt the result. To solve this potential problem, the Monte Carlo estimate has been generalized for a series of trace operators valid for four different analysis dates (5, 10, 15 and 20 June at 00 UTC) by simply adding all the individual random estimates. Analyses taken five days apart have been chosen following the recommendation given by Sadiki and Fischer (2005) to ensure the ergodicity of the signal that requires the data of each analysis step to be uncorrelated with other analysis times. This decorrelation time probably results from the meteorological variability over Western Europe and from the propagation time of a synoptic system inside the computational domain.

Figure 6 shows DFS values per observation type for the three experiments. For *OPER* and for the 00 UTC assimilation time, SEVIRI radiances are as informative as either ground-based data (SYNOP) or the sum of temperature and humidity from radiosonde data (TEMP). Other satellite observations (HIRS, AMSU-A and AMSU-B) have much less impact on the analyses, with values of 209, 181 and 163 respectively, compared to 3685 for

Figure 6. DFS values per observation type for *OPER*, *moreATOVS* and *noSEV*.Figure 7. DFS values per observation type normalized by the number of observations for *OPER*, *moreATOVS* and *noSEV*.

SEVIRI. As stated in section 2 for ATOVS data, the same thinning lengths as for ARPEGE have been kept (260 km) which reduces drastically the number of radiances entering the minimization. Furthermore, the fact that these radiometers are on board polar-orbiting satellites makes the number of available data over Western Europe strongly dependent on time of day. For instance, as has been pointed out in section 2.1, no HIRS and almost no AMSU-B data are present for the 6 and 18 UTC assimilation times. The high temporal resolution and the fast reception of SEVIRI radiances are thus an obvious advantage for regional-scale data assimilation compared to polar-orbiting satellites.

For conventional data, the *moreATOVS* experiment displays comparable DFS values to *OPER*. However, as expected, ATOVS data and especially AMSU-B data

have more impact on the analyses, with values reaching 1392. On the contrary, SEVIRI data show smaller DFS values of 3315 in that case. This result is due to the fact that the new observations, radiances from HIRS and AMSU-B, are sensitive to the mid- to high-tropospheric humidity. As a consequence, the influence of SEVIRI WV channels is impaired. For the same reason, adding more ATOVS data reduces the impact of one single radiance, as plotted in Figure 7 which shows the DFS normalized by the number of associated observations: for HIRS, AMSU-A and AMSU-B, this normalized DFS drops from 0.18 to 0.17, from 0.1 to 0.05 and from 0.25 to 0.22, respectively. Such a decrease of DFS coupled with an increase of the number of data has also been shown for targeted observations by Fourrié *et al.* (2006). This behaviour is due to a redundancy of data

and to the structure functions in the background-error covariance matrix which have a ‘dissolving’ effect on the information brought by one single pixel. For AMSU-A, this reduction is accentuated because this radiometer is mostly sensitive to temperature variations from the high troposphere to the low stratosphere (Figure 2), altitudes at which these structure functions are broader, with horizontal correlation lengths around 80 km for temperature and humidity compared to 70 km in the mid-troposphere, as stated in subsection 2.1. (Ştefanescu *et al.*, 2006, give more details.)

Without any SEVIRI radiances (*noSEV* experiment), the DFS associated with HIRS and AMSU-B increase, with respective values of 315 and 262 (Figure 6). In parallel, the DFS per single observation notably increases with values reaching 0.26 and 0.4 respectively (Figure 7), especially for AMSU-B. The impact of humidity from radiosondes (TEMPQ) also increases slightly from 0.28 to 0.3. This shows the complementarity between datasets that are sensitive to the same atmospheric components. When all radiances are available, the information brought by each pixel become somehow redundant and their relative impact decreases.

DFS are also useful to study the sensitivity of the analysis to different channels of a particular radiometer (Figure 8). For each AMSU-A channel, the normalized DFS decrease when the number of pixels that enter the minimization increases, but they do not change depending on the use of SEVIRI observations since this radiometer is not sensing the same atmospheric levels (Figure 8(a)). As shown in Figure 8(c), WV channels 11 and 12 have the largest DFS for HIRS, especially channel 11. This

result confirms the findings of Cardinali *et al.* (2004) for the ECMWF data assimilation system. For *noSEV*, the DFS associated with the latter HIRS channels have larger values, which denotes a higher impact of these particular channels whose spectral responses are close to the 7.3 and 6.4 μm SEVIRI channels respectively. The large number of additional AMSU-B data in *moreATOVS* (ten times more than in *OPER*) implies a loss of the potential individual information for every channel compared to the operational configuration (Figure 8(b)). The AMSU-B pixels that are more comparable to SEVIRI WV channels (channels 3 and 4) become more informative in *noSEV*. As one could expect, the two WV channels are the most informative for SEVIRI, especially the 6.2 μm (Figure 8(d)) that has a DFS of 0.36, while the three remaining IR channels have almost the same DFS values of around 0.23. For *moreATOVS*, these values decrease slightly by about 10%.

3.3. Impact on specific humidity increments

Mean increments for specific humidity have been computed over the 3-week period of interest. *OPER* has been compared to *noSEV* to infer the relative mean impact of SEVIRI data on the analyses. However it is difficult to draw conclusions about the individual impact of denser ATOVS data, considering only the three OSEs presented above. The *moreATOVS* experiment indeed uses both SEVIRI and ATOVS data. For that purpose and for the particular point discussed in this section, an extra experiment, denoted *moreATOVSnoSEV*, has been

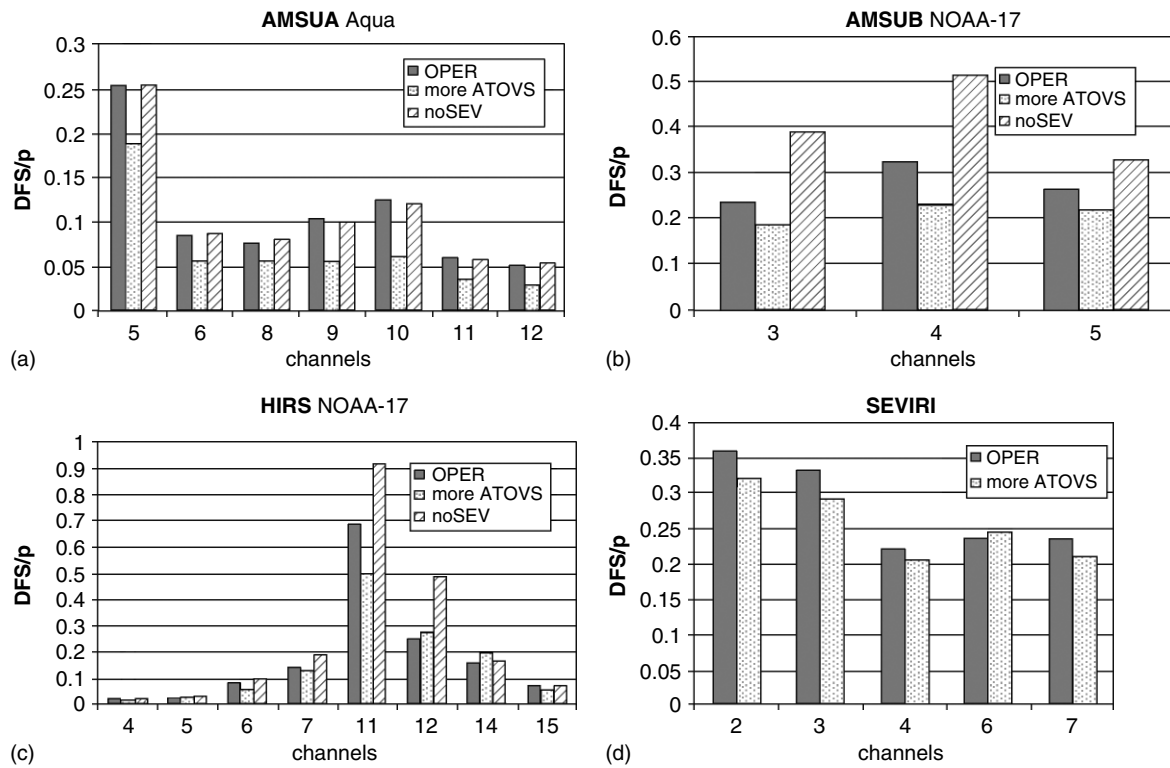


Figure 8. As Figure 7, but for each channel of (a) AMSU-A, (b) AMSU-B, (c) HIRS and (d) SEVIRI.

run considering only denser ATOVS data in the assimilation process. Differences of the mean specific increments between *OPER* and *noSEV*, and between *moreATOVSnoSEV* and *noSEV* are plotted in Figure 9. At 550 hPa, the shape and localization of the resulting fields are comparable; the assimilation of SEVIRI and denser ATOVS data allows moistening of an area covering northern Spain, southern France, and around Gibraltar and Sicily, and drying over the sea (Figures 9(a) and (c)). Some discrepancies appear over Northern Europe and over the inflow region located west of Ireland where the denser ATOVS data seem to accentuate the moistening and the drying over these regions respectively. In general, however, the impacts of these radiometers are consistent at 550 hPa, which shows that the information brought by their WV channels in the analyses is comparable.

In the analyses at lower levels, strong discrepancies appear: at 750 hPa, while SEVIRI data produce a global drying mostly over the Mediterranean Sea and the Bay of Biscay (Figure 9(b)), denser ATOVS data have the opposite effect (Figure 9(d)). The corresponding zonal average

displayed in Figure 10 confirms that this affects the analysis from 750 hPa to sea level, mainly south of 48°N. This strong difference of behaviour is obviously linked to the assimilation of low-peaking channels whose weighting functions have different shapes and intensities, as is shown in Figure 3. The individual impacts of SEVIRI IR channels is displayed in Figure 11, where we show a comparable zonal average of mean specific humidity increments between *OPER* and a second extra experiment that corresponds to *OPER* without IR channels (*OPER-SEVnoIR* in the plot). This picture shows that SEVIRI IR channels are responsible for the relatively strong drying over the Mediterranean Sea and that the background-error vertical correlations spread out this low-level information up to 600 hPa in that area. The very different features found with the *moreATOVSnoSEV* experiment can be due to the different shapes of the HIRS and SEVIRI weighting functions for the low-peaking channels (Figures 3(c) and (d)). An alternative explanation would be a poor simulation of those channels in the assimilation because of a bad representation of surface emissivity and of surface

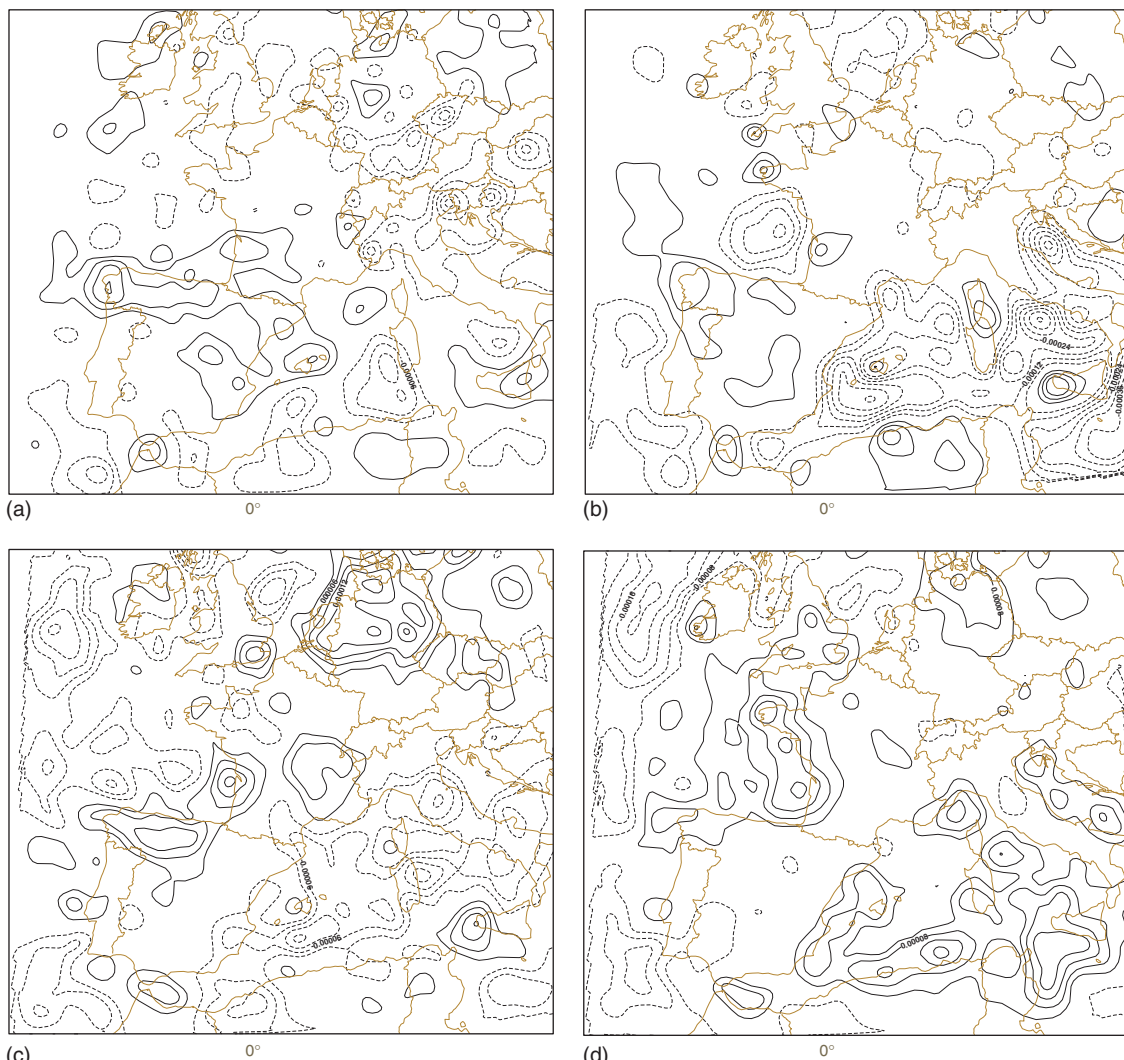


Figure 9. Difference of mean specific humidity increment (*OPER* minus *noSEV*) at (a) 550 hPa and (b) 750 hPa, over the period 5–23 June 2005. (c) and (d) are as (a) and (b), but for (*moreATOVSnoSEV* minus *noSEV*). The contour interval is $2 \times 10^{-5} \text{ kg kg}^{-1}$, with the zero contour omitted. This figure is available in colour online at www.interscience.wiley.com/qj

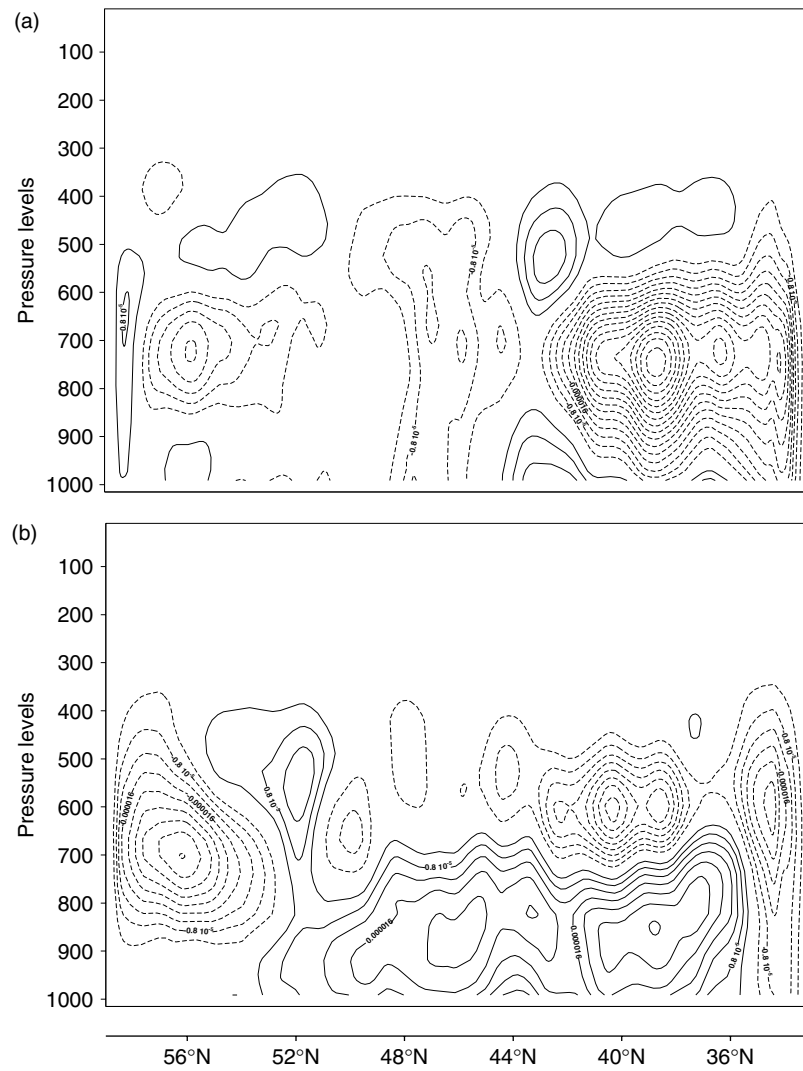


Figure 10. Zonal average of the difference of the mean specific humidity increment for (a) *OPER* minus *noSEV* and (b) *moreATOVSnoSEV* minus *noSEV*, for 5–23 June 2005. The contour interval is $0.4 \times 10^{-5} \text{ kg kg}^{-1}$, with the zero contour omitted.

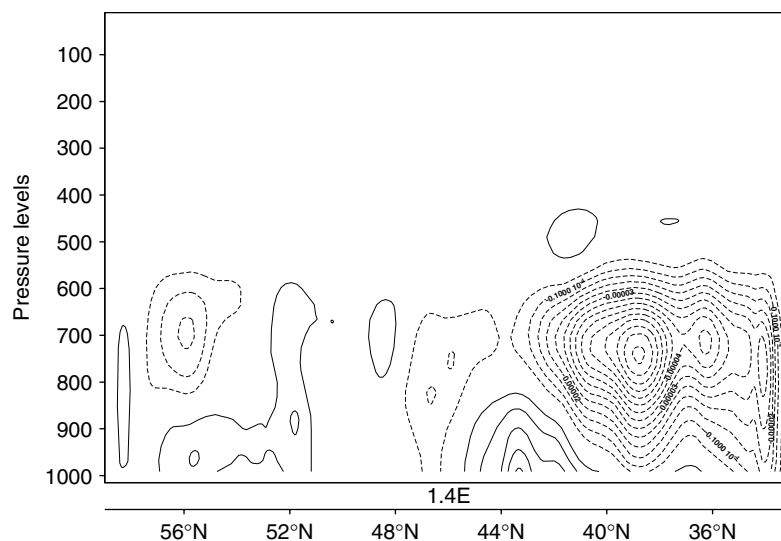


Figure 11. As Figure 10 but for (*OPER* minus *OPER-SEVnoIR*), with contour interval $0.5 \times 10^{-5} \text{ kg kg}^{-1}$ and the zero contour omitted.

temperature in the model, this non-realistic information in the low-troposphere being spread by the background-error vertical correlations. The assimilation of IR channels indeed requires a realistic evaluation of these two surface parameters, which explains why no IR channels are considered over land where their modelled values are known to be often far from the truth. The fact that SEVIRI IR channels are strongly constrained by surface conditions (cf. Figure 3(d)) raises the question of the relevance of their use in the 3D-Var, even over sea. For instance, Szyndel *et al.* (2004) use only WV channels in the ECMWF global model. This particular point has been addressed during the set-up of satellite observations in the pre-operational version of ALADIN. The conclusions of these tests were that adding SEVIRI IR channels in the variational process generally improved forecast scores, which seems to indicate that surface emissivity values diagnosed by the model (using wavelength-dependent precomputed tables) are reasonable. These latter channels have thus been kept in the assimilation process.

4. Impact on forecasts

Forecast scores against conventional data for each OSE are discussed in the first part of this section. Precipitation forecasts are then compared for a particular case-study.

4.1. Forecast scores

As discussed in Montmerle (2005), using the 3D-Var with the *OPER* configuration presented in section 2 generally improves the forecast scores compared with the spin-up model, i.e. ALADIN without data assimilation. For instance, this allows the initial (i.e. up to 18-hour forecasts) r.m.s. error and biases of 2 m humidity and of 3-hour accumulated precipitation to be reduced. Reduction of r.m.s. error for forecasts up to 12 hours in the tropospheric temperature, humidity and wind have also been obtained compared with radiosonde measurements. On the other hand, some deterioration has been noticed on high-tropospheric/low-stratospheric biases of temperature and humidity and of low-tropospheric bias of temperature at all forecast ranges. During the set-up of the configuration of the 3D-Var, F2005 have shown that this high-level temperature bias is produced by the model integration and is maintained through the cycling.

Concerning the three OSEs presented here, comparisons between radiosonde data and forecasts interpolated at the observation's location show very comparable behaviour. Adding SEVIRI data or denser ATOVS observations has no particular impact on this kind of score. A small degradation of the relative humidity bias ($\simeq 3\%$) around 300 hPa for forecasts up to 12 hours is however visible with SEVIRI data, which indicates that SEVIRI data are constraining the analyses towards a new solution which is, on average, slightly different from what the radiosonde observations indicate (not shown).

Table 1 shows the only significant discrepancies between the three experiments for forecast scores against

ground-based data over the whole test period. SEVIRI data indeed lead to better short-range forecasts of 3-hour accumulated precipitation over the ALADIN domain, especially at the 6-hour forecast range where the corresponding r.m.s. error is significantly smaller for *OPER* than for *noSEV*. The likely non-optimality of *moreATOVS*, already pointed out in section 3.1, seems to be the cause of worse scores than *OPER*; using a better ATOVS coverage does not improve the short-range precipitation forecast, as the larger r.m.s. errors at 6 hours for *moreATOVS* indicate. A slight deterioration of the mean-sea-level pressure bias for forecasts up to 12 hours has also been noticed for *moreATOVS* (not shown). Biases displayed in Table 1 are almost unchanged. Scores for 2 m temperature, for 2 m humidity and for 10 m wind show similar values for the three OSEs, which indicates that the additional mid- to high-tropospheric information brought by new satellite data has no significant impact on the model's lowest vertical levels. After 18 hours, *OPER* shows slightly degraded r.m.s. scores against the two other experiments (not shown), mainly because of two particular precipitating cases that occurred during the test period. However, it has to be noted that, at those ranges, forecasts are more sensitive to the growing influence of lateral boundary conditions.

4.2. Precipitation forecast

For the precipitating cases within the period, the three OSEs produce their own solution. However, some conclusions on the general behaviour can be drawn from the examination of the simulated precipitating patterns. For example, Figure 12 shows accumulated rainfall forecast between 12 and 18 hours of simulation for 23 June 2005 by the three experiments, compared with rain-gauge observations (Figure 12(e)). This case was characterized by easterly and south-easterly winds in the south-east of France, bringing unstable moist air from the Mediterranean Sea. During the day, these unstable conditions triggered convective activity, mainly over the mountains of the Massif Central, the Pyrenees and the Alps.

For that particular case, the spin-up model generally underestimates the precipitation, especially over the Massif Central. The strong convective activity that has developed along a north-south convergence line that links the Pyrenees to the Massif Central is well represented in intensity, but is located too far east. These drawbacks are typical for the spin-up model which often captures the large-scale precipitation pattern but is less accurate for smaller scales. For all the precipitating cases of the 3-week experiment, *OPER* and *moreATOVS* show very similar patterns for the simulated precipitation. For example, Figures 12(b) and (d) display comparable forecasts. These two experiments represent quite well the main bow-shaped precipitation line with a realistic amount, which is also reflected by better quantitative precipitation forecast scores than the spin-up model and *noSEV* over

Table I. Mean biases and r.m.s. errors of *OPER*, *noSEV* and *moreATOVS* against ground-based observations of 3-hour accumulated precipitation.

Forecast range (hours)	<i>OPER</i>		<i>noSEV</i>		<i>moreATOVS</i>	
	6	12	6	12	6	12
r.m.s. bias	1.02 −0.02	0.95 0.15	1.20 0.00	0.97 0.15	1.20 0.02	0.97 0.15

Values were computed over France using hourly observations from 1475 rain gauges.

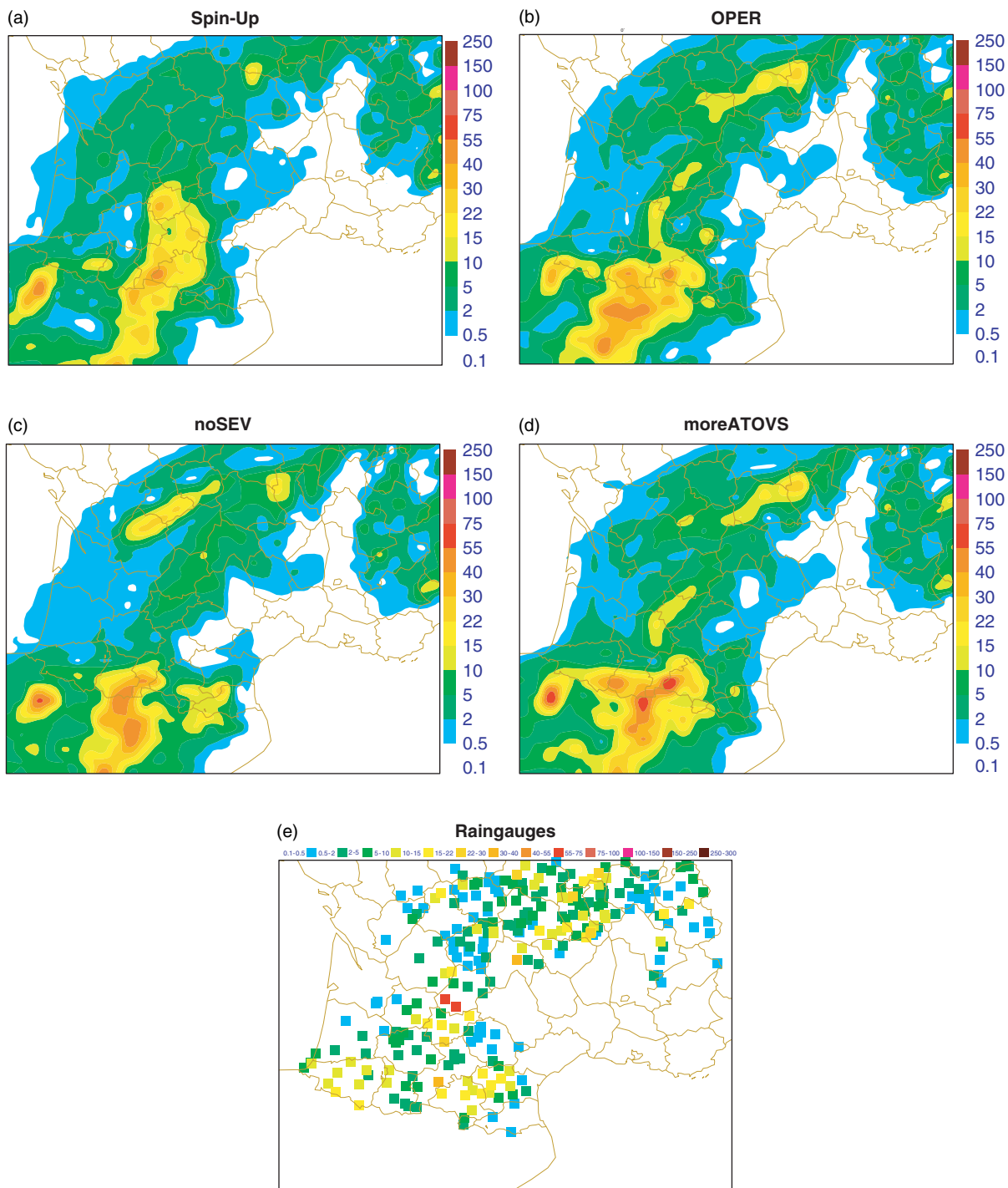


Figure 12. Accumulated rainfall (mm) between 12 and 18 hours of the forecast over France on 13 June 2005 from (a) the spin-up model, (b) *OPER*, (c) *noSEV*, (d) *moreATOVS*, and (e) rain-gauge observations. This figure is available in colour online at www.interscience.wiley.com/qj

France (not shown). As noticed in the previous section, adding extra ATOVS data reduces the individual impact of each ATOVS and SEVIRI pixel, because of the structure functions, of information redundancy and probably because of weak observation correlations between adjacent pixels. In the case where SEVIRI data are present at high resolution in the assimilation process as in *OPER*, using denser ATOVS data does not seem to be beneficial. Finally, *noSEV* seems to be less accurate for that particular case than the two other OSEs; an unrealistic cell of more than 40 mm in 6 hours developed in the south-western part of the Massif Central, and precipitation over the Toulouse region is underestimated. The absence of SEVIRI data and thus the low number of observation types that are sensitive to mid- to high-tropospheric humidity in *noSEV* is truly prejudicial not only for that case, but also for the other precipitating events of the studied period.

5. Concluding remarks

The use and impact of satellite data in the regional 3D-Var assimilation system based on ALADIN-France has been evaluated. The ALADIN 3D-Var is different from ARPEGE mainly because of its ensemble-based background-error covariance matrix that provides structure functions better suited for analyses at regional scale (F2005), and by the use of specific observation types, namely the 2 m temperature and humidity and the SEVIRI data at high resolution. These data are taken into account using a cloud-type classification in order to keep only data uncontaminated by clouds in the variational process. A specific air-mass-dependent bias-correction scheme and a quality control are then applied on the remaining pixels. Forecast scores against surface and radiosonde measurements show a better behaviour for the 3D-Var suite than the spin-up model (i.e ALADIN without data assimilation), especially for precipitation.

OSEs have been performed, in order to infer the potential impact of SEVIRI and of denser ATOVS data. A strong complementarity has been found between satellite observations that are sensitive to the same atmospheric component, namely AMSU-B, HIRS and SEVIRI WV channels. As a consequence, the high temporal resolution of SEVIRI allows information to be obtained about the mid- to high-tropospheric humidity even when no AMSU-B and HIRS data are present, which is especially the case for the 06 and 18 UTC analysis times. However, ATOVS observations could bring precious information if transmission problems occur for SEVIRI data at 00 or 12 UTC analyses times. In that particular case, having more ATOVS data (1 pixel within a thinning box of 70 km instead of 260 km, for example) would surely be beneficial. On the contrary, if SEVIRI data are already present at high resolution, the redundancy of information, the shape of the structure functions and the possible horizontal correlation between adjacent pixels reduce the individual potential impact of denser ATOVS

data on the analyses. As a matter of fact, forecast scores show neutral results with a small degradation for precipitation and comparable simulated precipitation patterns for the *moreATOVS* OSE. Another consequence of the complementarity between satellite data, in the case of the operational suite, is that the high number of geostationary data (if their corresponding innovation biases are well corrected) decreases the potential harmful effect of poorly bias-corrected ATOVS data. Météo-France is planning to test an adaptative variational bias correction based on linear predictor models for the air-mass-dependent component of the bias, comparable to those implemented at NCEP (Derber and Wu, 1998) and at ECMWF (Dee, 2004), to correct those flow-dependent biases. Furthermore, tuning of observation-error variances should be performed for every new observation type that is taken into account in the system to ensure the best possible optimality in the assimilation process. Similar studies are planned to be carried out for other weather regimes (typically for a winter period), in order to verify if our conclusions for a summer period are still valid in those cases.

A specific version of the ALADIN assimilation suite has been set up to support the NWP needs of the African Monsoon Multidisciplinary Analyses experiment during summer 2006. This version shares the same code and configuration as the one presented in this paper, except that the background-error statistics have been computed to reflect the uncertainty of forecasting the main meteorological features of the Western African Monsoon. Montmerle *et al.* (2006) have shown that the statistics and balance properties of the background-error covariances exhibit very different features than those obtained over Western Europe and favour the assimilation of tropical convective systems such as squall lines. Over this area, and as discussed by Nuret *et al.* (2006), the lack of conventional observations such as radiosondes or surface measurements makes the analyses strongly dependant on satellite observations, especially WV channels of AMSU-B, HIRS and SEVIRI, since the computational domain covers mainly the African mainland. Unrealistic downward spreading of mid-tropospheric humidity information brought by these channels, due to vertical background-error correlations, could occur without a compensation from low-level measurements, contrary to what has been shown over Europe (see section 2.3). The use of satellite data over an area with very few operational conventional data presents an interesting challenge and the conclusions drawn for Europe in this paper should be different for Africa. As a first stage, careful tuning and appropriate bias correction of ATOVS and SEVIRI radiances are currently under progress at Météo-France.

As pointed out in F2005, further studies are planned to improve the ALADIN assimilation: 3D-Var using FGAT (First Guess at Appropriate Time) that will enable consideration of innovations with better timing, 4D-Var based on a semi-Lagrangian formulation of the advection scheme for the adjoint model, use of a new variational

term in the cost function in order to relax the limited-area analyses towards the coupling system analyses, the formulation of the humidity analysis following the work performed at ECMWF, assimilation of cloudy radiances, and better estimation of surface emissivity and surface temperature to assimilate IR channels over land. Concerning observations, SSMI microwave radiances and ground-based GPS measurements have recently been inserted in the operational ALADIN. ALADIN will also inherit the future developments made for ARPEGE at global scale for the infrared radiometers AIRS and IASI. However, at regional scale the impact of these instruments should be less important than at global scale because of their low temporal resolution due to the fact that they are on board only one polar-orbiting platform for the moment.

Acknowledgements

The authors are very grateful to EUMETSAT for supporting a great part of this work (contract EUM/PER/LET/03/2149) and Jean Maziejewski for his welcome help in improving the English of the original manuscript.

Appendix

A1 Computation of the tuning coefficient s^o

The principle of the incremental formulation used by the ALADIN 3D-Var (Courtier *et al.*, 1994) is to seek the increment $\delta\mathbf{x}$ to be added to the background \mathbf{x}_b , so that the analysis given by $\mathbf{x}_a = \mathbf{x}_b + \delta\mathbf{x}$ minimizes the cost function

$$\begin{aligned} J(\delta\mathbf{x}) &= J^b(\delta\mathbf{x}) + J^o(\delta\mathbf{x}) \\ &= \frac{1}{2}\delta\mathbf{x}^T\mathbf{B}^{-1}\delta\mathbf{x} \\ &\quad + \frac{1}{2}\{(\mathbf{y} - H[\mathbf{x}_b]) - \mathbf{H}\delta\mathbf{x}\}^T\mathbf{R}^{-1} \\ &\quad \times \{(\mathbf{y} - H[\mathbf{x}_b]) - \mathbf{H}\delta\mathbf{x}\}. \end{aligned} \quad (\text{A1})$$

The background term J^b measures the distance between the analysis \mathbf{x}_a and the background \mathbf{x}_b , with \mathbf{B} the background-error covariance matrix. The observation term J^o represents the distance between the innovation vector $(\mathbf{y} - H[\mathbf{x}_b])$ and the increment written in the observation space through the linearized observation operator \mathbf{H} (see subsection 3.2.1 for more details). The tuning operation consists of the multiplication of the covariance matrices in order to get closer to optimality. On-line tuning coefficients based on an optimality criteria have been discussed by Desroziers and Ivanov (2001) (DI01 hereafter) and an example of their use in the ARPEGE framework is given by Chapnik *et al.* (2004). The ‘true’ background and observation error covariance matrices $\mathbf{B}_t = E(\epsilon^b\epsilon^{bT})$ and $\mathbf{R}_t = E(\epsilon^o\epsilon^{oT})$ (where ϵ^b and ϵ^o denote the unbiased background and observation errors respectively, E is the expectation operator, and T the transpose) can be deduced from the operationally

specified \mathbf{B} and \mathbf{R} using a tuning parameter vector $\mathbf{s} = (s^o, s^b)$:

$$\left. \begin{array}{l} \mathbf{B}_t = s^b\mathbf{B}, \\ \mathbf{R}_t = s^o\mathbf{R}. \end{array} \right\} \quad (\text{A2})$$

In parallel, DI01 have shown that the expectations of each term of the cost function J described by Equation (A1) at the minimum are

$$\left. \begin{array}{l} E(J^o) = \frac{1}{2}\text{Tr}(\mathbf{I}_p - \mathbf{HK}), \\ E(J^b) = \frac{1}{2}\text{Tr}(\mathbf{KH}), \end{array} \right\} \quad (\text{A3})$$

where \mathbf{I}_p stands for the identity matrix with order the number of observations p and \mathbf{K} the Kalman gain matrix as defined in Equation (2). While tuning the covariance matrices, one tries to minimize an optimal cost function that can be written from Equations (A1) and (A2):

$$J^{\text{opt}} = \frac{J^o}{s^o} + \frac{J^b}{s^b}.$$

Each term of this optimal cost function should then be close to its expected value given by Equation (A3), which leads to a definition the components of \mathbf{s} :

$$\begin{aligned} s^b &= \frac{2J^b\{\mathbf{x}_a(\mathbf{s})\}}{\text{Tr}\{\mathbf{K}(\mathbf{s})\mathbf{H}\}}, \\ s^o &= \frac{2J^o\{\mathbf{x}_a(\mathbf{s})\}}{\text{Tr}\{\mathbf{I}_p - \mathbf{HK}(\mathbf{s})\}}, \end{aligned}$$

where $\mathbf{x}_a(\mathbf{s})$ is the minimizer of J^{opt} tuned with the \mathbf{s} vector and $\mathbf{K}(\mathbf{s})$ the Kalman gain matrix constructed from the tuned error covariance matrices. In the same way as Equation (4) for the DFS, these expressions can be written for subsets of observations y^l and of background \mathbf{x}_b^k , using respectively the projection operators $\mathbf{\Pi}_l^o$ and $\mathbf{\Pi}_k^b$:

$$\begin{aligned} s_k^b &= \frac{2J^b\{\mathbf{x}_a(\mathbf{s})\}}{\text{Tr}\{\mathbf{\Pi}_k^b\mathbf{K}(\mathbf{s})\mathbf{H}\mathbf{\Pi}_k^{bT}\}}, \\ s_l^o &= \frac{2J^o\{\mathbf{x}_a(\mathbf{s})\}}{\text{Tr}[\mathbf{\Pi}_l^o(\mathbf{I}_p - \mathbf{HK}(\mathbf{s}))\mathbf{\Pi}_l^{oT}]}. \end{aligned}$$

DI01 proposed a fixed-point algorithm to compute iteratively these expressions. If \mathbf{s}_i is the parameter vector at step i of the algorithm, \mathbf{s}_{i+1} is deduced from

$$\begin{aligned} s_{k,i+1}^b &= \frac{2J^b\{\mathbf{x}_a(\mathbf{s}_i)\}}{\text{Tr}\{\mathbf{\Pi}_k^b\mathbf{K}(\mathbf{s}_i)\mathbf{H}\mathbf{\Pi}_k^{bT}\}}, \\ s_{l,i+1}^o &= \frac{2J^o\{\mathbf{x}_a(\mathbf{s}_i)\}}{\text{Tr}(\mathbf{\Pi}_l^o[\mathbf{I}_p - \text{Tr}\{\mathbf{HK}(\mathbf{s}_i)\}]\mathbf{\Pi}_l^{oT})}. \end{aligned}$$

Generally one or two iterations are sufficient to get stable results. The main practical problem is the computation of the trace terms. As in subsection 3.2.1 for the computation of the DFS, the same approach as Chapnik *et al.* (2006) has been used to approximate these terms using a Monte Carlo method proposed by Girard (1987). Parallel

analyses have thus been performed using perturbated observations. This has led to the following approximation for the denominator of s^o (s^b being deduced from the DFS computation since $\text{Tr}(\mathbf{KH}) = \text{Tr}(\mathbf{H}\mathbf{K})$):

$$\begin{aligned} & \text{Tr}(\mathbf{I}_p - \mathbf{HK}) \\ &= (\mathbf{y}^* - \mathbf{y})^T \mathbf{R}^{-1} \{(\mathbf{y}^* - \mathbf{Hx}_a^*) - (\mathbf{y} - \mathbf{Hx}_a)\}. \end{aligned}$$

References

- Berre L, Štefănescu SE, Belo Pereira M. 2006. The representation of the analysis effect in three error simulation techniques. *Tellus* **58A**: 196–209.
- Bouttier F, Kelly G. 2001. Observing-system experiments in the ECMWF 4D-Var data assimilation system. *Q. J. R. Meteorol. Soc.* **127**: 1469–1488.
- Cardinali C, Pezzoli S, Andersson E. 2004. Influence matrix of a data assimilation system. *Q. J. R. Meteorol. Soc.* **130**: 2767–2787.
- Chapnik B, Desroziers G, Rabier F, Talagrand O. 2004. Properties and first application of an error-statistics tuning method in variational assimilation. *Q. J. R. Meteorol. Soc.* **130**: 2253–2275.
- Chapnik B, Desroziers G, Rabier F, Talagrand O. 2006. Diagnosis and tuning of observational error in a quasi-operational data assimilation setting. *Q. J. R. Meteorol. Soc.* **132**: 543–565.
- Courtier P, Thépaut J-N, Hollingsworth A. 1994. A strategy for operational implementation of 4D-Var using an incremental approach. *Q. J. R. Meteorol. Soc.* **120**: 1367–1387.
- Dee D. 2004. ‘Variational bias correction of radiance data in the ECMWF system’. Pp 97–112 in Proceedings of workshop on assimilation of high spectral resolution sounders in NWP, 28 June–1 July 2004, ECMWF, Reading, UK.
- Derber JC, Wu W-S. 1998. The use of TOVS cloud cleared radiances in the NCEP SSI analysis system. *Mon. Weather Rev.* **126**: 2287–2299.
- Derber J. 2003. ‘Enhanced use of radiance data in NCEP data assimilation systems’. In Proceedings of the ITSC XIII, Ste. Adèle, Canada.
- Derrien M, Le Gléau H, Daloze J-F, Haeffelin M. 2005. ‘Validation of SAFNWC/MSG cloud products with one year of SEVIRI data’. In Proceedings of EUMETSAT conference on Satellite Meteorology, Dubrovnik, Croatia.
- Desroziers G, Ivanov S. 2001. Diagnosis and adaptative tuning of information error parameters in a variational assimilation. *Q. J. R. Meteorol. Soc.* **127**: 1433–1452.
- English SJ, Renshaw RJ, Dibben PC, Smith AJ, Rayer PJ, Poulsen C, Saunders FW, Eyre JR. 2000. A comparison of the impact of TOVS and ATOVS satellite sounding data on the accuracy of numerical weather forecasts. *Q. J. R. Meteorol. Soc.* **126**: 2911–2931.
- Fischer C, Montmerle T, Berre L, Auger L, Štefănescu SE. 2005. An overview of the variational assimilation in the Aladin/France numerical weather prediction system. *Q. J. R. Meteorol. Soc.* **131**: 3477–3492.
- Fourrié N, Marchal D, Rabier F, Chapnik B, Desroziers G. 2006. Impact study of the 2003 North Atlantic THORPEX Regional Campaign. *Q. J. R. Meteorol. Soc.* **132**: 275–295.
- Garand L, Wagneur 2002. ‘Assimilation of GOES imager channels at MSC’. Proceedings of the ITSC XII, Lorne, Australia.
- Gerard E, Rabier F, Lacroix D, Sahaoui Z. 2003. ‘Use of ATOVS raw radiances in the operational assimilation system at Météo-France’. Proceedings of the ITSC XIII, Ste. Adèle, Canada.
- Girard D. 1987. ‘A fast Monte-Carlo cross-validation procedure for large least-square problems with noisy data’. Tech. Report 687-M, IMAG, Grenoble, France.
- Harris BA, Kelly G. 2001. A satellite radiance bias-correction scheme for data assimilation. *Q. J. R. Meteorol. Soc.* **127**: 1463–1468.
- Köpken C, Thépaut J-N, Kelly G. 2003. ‘Assimilation of geostationary WV radiances from GOES and Meteosat at ECMWF’. Research report No. 14, EUMETSAT/ECMWF Fellowship programme, ECMWF, Reading, UK.
- Liu Z-Q, Rabier F. 2003. The potential of high-density observations for numerical weather prediction: A study with simulated observations. *Q. J. R. Meteorol. Soc.* **129**: 3013–3035.
- Montmerle T. 2005. ‘Impact of SEVIRI IR radiances in Météo-France’s operational 3D-Var assimilation system at regional scale’. In Proceedings of EUMETSAT conference on Satellite Meteorology, Dubrovnik, Croatia.
- Montmerle T, Lafore J-P, Berre L, Fischer C. 2006. Limited-area model error statistics over Western Africa: Comparisons with midlatitude results. *Q. J. R. Meteorol. Soc.* **132**: 213–230.
- Nuret M, Lafore J-P, Montmerle T, Sénési S, Autunes F. 2006. ‘Mesoscale analysis and simulation of the West African monsoon’. In Proceedings of EUMETSAT conference on Satellite Meteorology, Helsinki, Finland.
- Prunet P, Thépaut JN, Cassé V. 1998. The information content of clear-sky IASI radiances and their potential for numerical weather prediction. *Q. J. R. Meteorol. Soc.* **124**: 211–241.
- Rabier F, Fourrié N, Chafaï D, Prunet P. 2002. Channel selection method for IASI radiances. *Q. J. R. Meteorol. Soc.* **128**: 1011–1032.
- Randriamampianina R. 2005. Radiance-bias correction for a limited-area model. *Időjárás* **109**: 143–155.
- Rodgers CD. 1996. *Inverse methods for atmospheric sounding: Theory and practice*. World Scientific: Singapore.
- Sadiki W, Fischer C. 2005. A posteriori validation applied to the 3D-Var ARPEGE and ALADIN data assimilation systems *Tellus* **57A**: 21–34.
- Saunders R, Matricardi M, Brunel P. 1999. An improved fast radiative model for assimilation of satellite radiance observations. *Q. J. R. Meteorol. Soc.* **125**: 1407–1425.
- Schmetz J, Pili P, Tjemkes S. 2000. ‘Meteosat Second Generation (MSG)’. Pp 111–121 in Proceedings of seminar on exploitation of the new generation of satellite instruments for numerical weather prediction, 4–8 September 2000, ECMWF, Reading, UK.
- Štefănescu SE, Berre L, Belo Pereira M. 2006. The evolution of dispersion spectra and the evaluation of model differences in an ensemble estimation of error statistics for a limited-area analysis. *Mon. Weather Rev.* in press.
- Szyndel M, Kelly G, Thépaut J-N. 2004. ‘Evaluation and potential for assimilation of SEVIRI radiance data from Meteosat-8’. Research report No. 15, EUMETSAT/ECMWF Fellowship programme, ECMWF, Reading, UK.

Thermal Radiance Assimilation In the North (TRAIN)

1 Aim and objectives

1.1 Significance of the research project in relation to current knowledge, and research-based starting points

Regional Numerical Weather Prediction (NWP) requires continuous flow of accurate, reliable, and timely observational data to help maintain a realistic description of atmospheric state. Networks of meteorological satellites constitute an observing system well suited to respond to the need (Eyre et al., 2020; Saunders, 2021). Established and sophisticated data assimilation methods are routinely used to retrieve meteorological information from data provided by geostationary and polar-orbiting satellites. Radiance observations, made at specific infrared and microwave frequencies, are of particular importance in the numerical analysis of atmospheric temperature, humidity, and wind. Owing to extensive methodological development in the past 30-40 years, several operational and research-oriented NWP implementations nowadays apply the framework of variational data assimilation to measurement data from diverse satellite instruments (e.g., Bauer et al., 2011; Kazumori, 2014; Qi Wang and Randriamampianina, 2021).

Several factors contribute towards making the satellite data assimilation a success story. Long and continuing history of steady progress in a wide front of numerical, physical, and statistical aspects has greatly improved the NWP skill (Bauer et al., 2015). The difficulties in resolving ambiguities of geophysical inversion are eased by the modern accuracy of short-range NWP forecast. Specifically in the handling of radiance data, computation of atmospheric emission, absorption, and scattering (i.e. radiative transfer models; RTM) has gained from new science on molecular absorption spectra and surface emissivity (Saunders et al., 2018). Treatment of random, systematic, and gross errors, all inherent to all types of observations, is another crucially important area that is continuously being developed for ever increasing realism (Geer and Bauer, 2011; Bormann et al., 2016; Lupu et al., 2016).

Being specifically reliant on frequent reception of new observations, regional NWP at high latitudes needs to deal with physical and practical limitations in current satellite data. While high latitudes may enjoy several daily overpasses of polar orbiters in Low-Earth Orbit (LEO), a single LEO satellite provides new information only up to five or six times a day. Constellations of small and inexpensive LEO satellites may provide pseudo-continuous data flow in time frame of 5-10 years from now. In shorter time frame, one may hope to build on coordinated use of European, American, Chinese, and Russian LEO satellites to maximize data coverage from three or four distinct orbital planes. In contrast to

the 100-minute revisit time from LEO satellite overpasses, Geostationary Earth Orbit (GEO) satellites are able to provide frequent updates, but their usability at latitudes higher than approximately 65 degrees has been somewhat questionable until now. Against this background, the space program of Roscosmos (i.e., the space agency of Russian Federation) brings a wealth of potential for application in Arctic NWP. In particular, the recent launch of Arctica-M N1 satellite into a Highly Elliptical Orbit (HEO; see Fig. 1 for an illustration of data coverage) enables monitoring of Northern polar regions with continuous coverage of up to 6-8 hours twice a day. The additional launches of similar kind, currently in preparation by Roscosmos, may guarantee a truly continuous monitoring of Arctic regions in a time frame of 3 to 5 years from now. The Arctica-M satellites include a visible/infrared imager that provides information on cloud cover, surface temperature, and upper-tropospheric humidity in much the same way as GEO satellites do today.

We are targeting extensive use of frequently-updating thermal radiance data in circumstances typical to regional NWP in Northern Europe. The approach builds on existing methodological framework of variational data assimilation (Rabier et al., 2000; Gustafsson et al., 2012). Putting emphasis on aggressive use of satellite data types capable of sub-hourly update intervals, we see a huge potential to significantly enhance short-range NWP at high latitudes. The satellite launches most relevant for this project are summarized in Table 1: considering satellites in GEO, we foresee methodological breakthroughs that will allow extracting meteorological information at the Arctic Circle and beyond. For the case of satellites in HEO, our proposal is pioneering since no earlier studies exist on their use in practical meteorological applications.

Table 1: Satellites and thermal sounding/imaging instruments to be used.

Satellite	Launch date	Orbit type	Thermal sounder/imager
Meteosat-11	7/2015	GEO	SEVIRI ¹
Arctica-M N1	2/2021	HEO	MSU-GS/A ²
MTG-I1	2022	GEO	FCI ³
MTG-S1	2024	GEO	IRS ⁴

¹ Spinning Enhanced Visible Infra-Red Imager

² Electro-L Imager for Arctica

³ Flexible Combined Imager

⁴ Infra-Red Sounder

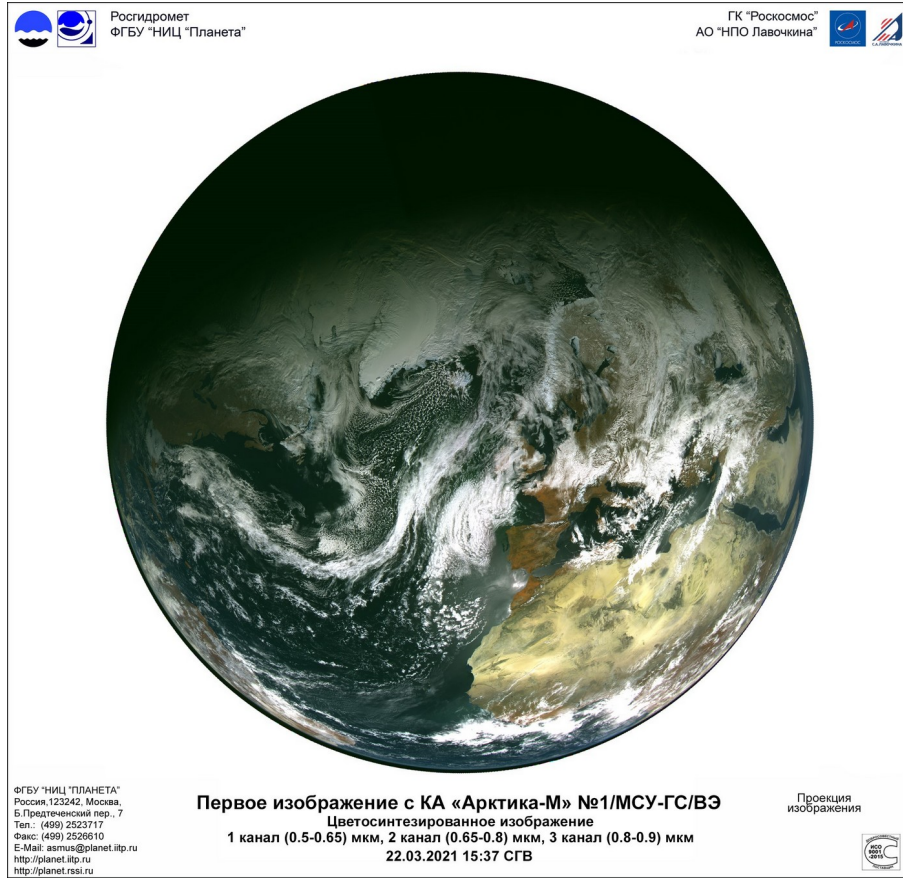


Figure 1: The first published satellite image from the Arctica-M N1 satellite, launched into HEO on 28 February 2021.

To the best of our knowledge, there are no earlier studies on the use of GEO in the vicinity of the Arctic Circle. As is the case in all data assimilation concerning satellite-measured radiances, the data use is constrained by validity limits of fast RTM coefficients. These are generated by mathematical regression, where input data comes from accurate line-by-line spectroscopic databases. In the early sets of fast RTM coefficients, there was a 75 degree cut-off for satellite zenith angle; in the latest available sets the validity limit is increased to 84 degrees. Figure 2 shows the variation in zenith angle for a GEO satellite at Greenwich meridian, as viewed at high latitudes in Europe. The new coefficients will have a game-changing impact on data coverage.

Previous studies indicate a significant benefit from the assimilation of humidity-sensitive channels from GEO (Peubey and McNally, 2009; Stengel et al., 2009). When accounting for dynamic atmospheric evolution inside the assimilation time window, the frequent measurement of water vapour allows sensing not only humidity but also wind: this is the humidity-wind tracing effect. Because of the limitations in the use of GEO, and the lack of satellites in HEO, the effect has not been made use of at high latitudes to date. Considering the dominance of upper-tropospheric wind in determining high-latitude weather, we see much potential for full exploitation of radiances from both GEO and HEO.

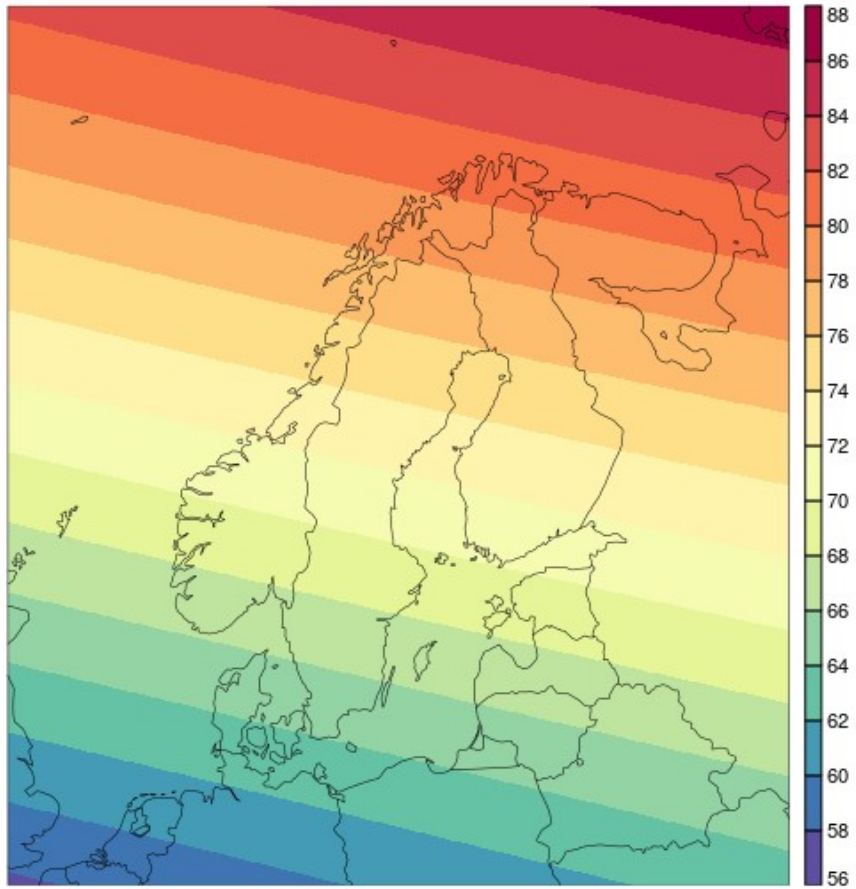


Figure 2: Zenith angle of a geostationary satellite, placed above the Greenwich meridian, as viewed from Northern Europe.

We have recently run initial assimilation experiments to facilitate the use of radiance data from the SEVIRI instrument on Meteosat Second Generation (MSG) satellites. In this work, we have followed the concept of Trojáková et al. (2019) to remove cloud-affected data on the basis of the cloud mask product of the Nowcasting Satellite Application Facility (NWC-SAF) of the European Organization for Exploitation of Meteorological Satellites (EUMETSAT). Our preliminary findings suggest that quality-controlled, cloud-screened radiance data still include a non-negligible amount of residual cloud contamination. This is a violation against the fundamental assumption of Gaussian-distributed, zero-mean observation errors. Improving the accuracy of the observation quality control specifically at high latitudes is one of our goals in this research project. Additionally, we recognize two recent advances with particular relevance: Firstly, forward modelling of radiance observation is made more accurate when accounting for the slanted observing geometry, as suggested by Bormann (2017). Secondly, the widening of the satellite observation footprint at large view angles can be taken into account using the concept presented in Mile et al. (2021). Both of these developments will directly improve the feasibility of GEO radiance assimilation in the North.

1.2 Research questions and hypotheses

Questions in the use of GEO stem from the desire to go beyond the current limits in data use. We believe that making the best possible use of data will require introducing situation dependence in handling of observation errors. This will involve all aspects of error: gross errors are dealt with in the observation quality control; systematic errors are compensated for during observation bias correction; random errors are modelled in statistical sense during the data assimilation. *The working hypothesis is that optimizations in relevant data assimilation procedures will allow pushing the limit of GEO usage far beyond the Arctic Circle.*

Unleashing the potential of a completely new observing geometry, such as HEO, will likely require answering questions that we can't even think of as yet. There may be periodical effects in data quality that will need to be accounted for in one way or another. Such effects might originate from the large variations in spacecraft altitude and associated changes in the field-of-view size (and pixel resolution) at ground level. *The associated hypothesis is that, once sufficiently well understood, effects of this kind can be compensated for by a dedicated bias correction scheme and situation-dependent characterization of observation error statistics.*

1.3 Expected research results and their anticipated scientific impact

This proposal is pioneering in two aspects. Firstly, in the field of NWP, there are no earlier attempts to use GEO radiance data in the vicinity of the Arctic Circle. Secondly, there are no earlier studies on meteorological use of satellites in HEO.

We expect a series of scientific breakthroughs specifically in the area of situation-dependent handling of observation error at extreme view angles. Such methodological advances will be directly beneficial to many NWP system developers who may deal with observational data collected from edges of GEO disk. More generally, situation-dependent specification for the representation of random error is a megatrend in NWP. Understanding the situation-dependence as it appears in GEO and HEO data will be of interest to a large audience.

A solid positive forecast impact from HEO data would be another game changer leading to a significant boost in international community's interest towards the Russian space programme. Even if benefits in practical data assimilation experiments turn out to be modest, the characterization and documentation of observation errors and quality control procedures for the new data type will be a welcome scientific addition to the scientific development of NWP.

2 Implementation

2.1 Work plan and schedule

Work Package 1: Pushing the limit of usable GEO data further North

Kickoff – 7 months: Implement the method of Bormann (2017) for slant-path radiative transfer calculation and the method of Mile et al. (2021) to account for satellite footprint size in a state-of-the-art regional NWP system (HARMONIE; see Section 2.2 for details). Refine observation quality control and bias-correction methods to match the behaviour of gross and systematic observation errors in MSG-SEVIRI data at large satellite zenith angles.

7 months – 14 months: Characterize statistical properties of random observation error in MSG-SEVIRI data as a function of satellite view angles. Implement the methodology to allow for situation-dependent formulation of observation error statistics in the HARMONIE NWP system. Adapt the methodological framework to MTG-FCI by refining the quality control, bias correction, and random error description.

14 months – 21 months: Study the sensitivity of HARMONIE NWP system performance to variations in the use of spectral channels and cut-off satellite zenith angles. Run extensive four-dimensional variational data assimilation (4D-Var) experiments and quantify the impact of GEO radiance in regional NWP at high European latitudes.

21 months – 24 months: Document the methodology and meteorological impact in an open-access scientific publication.

Work Package 2: Paving the way for routine use of HEO

24 months – 31 months: Adapt the HARMONIE NWP system to technically process radiance data from Arctica-M N1 MSU-GS/A instrument. Assess the radiance data quality in thermal channels of MSU-GS/A. Develop a dedicated observation quality control scheme.

31 months – 38 months: Comprehensively analyse statistical properties and characteristic patterns in MSU-GS/A radiance observation errors. Develop and fine-tune a dedicated bias correction scheme. Introduce situation-dependent handling for random observation errors that accounts for periodical variations in data quality.

38 months – 45 months: Run extensive 4D-Var assimilation experiments to quantify the impact of thermal HEO radiance data in the HARMONIE NWP system.

45 months – 48 months: Document the methodology and meteorological impact in an open-access scientific publication.

2.2 Research data and material, methods, and research environment

The research will be performed at the Finnish Meteorological Institute and under the umbrella of the ACCORD (A Consortium for Convection-Scale Modeling Research and Development) consortium. ACCORD is a combined effort of 26 European and African meteorological services for research and development on fine-scale regional NWP. Closely related, Nordic countries (Estonia, Finland, Norway, and Sweden) have built their operational use of NWP on collaboration taken place over the last 30 years in HIRLAM (High-resolution Limited Area Model) and HARMONIE (HIRLAM-ALADIN Research to Mesoscale Operational NWP in Europe) consortia (Bengtsson et al., 2017). The latest stable release of the HARMONIE NWP system (Cy43h2.2) includes support on 4D-Var, that we will employ to take full advantage of the high time resolution of GEO and HEO satellite data.

The HARMONIE NWP system contains an interface to the Radiative Transfer for TOVS (RTTOV), i.e., a fast RTM used inside several variational assimilation systems. The assimilation of a new type of satellite data will require a set of fast RTM coefficients that match the exact characteristics of the instrument in question. We will acquire the necessary fast RTM coefficients via the Numerical Weather Prediction Satellite Application Facility (NWP-SAF) of EUMETSAT.

The access to, and user support on, new HARMONIE NWP system releases is guaranteed through FMI's participation in the ACCORD consortium. The data assimilation experiments will be run on supercomputers under maintenance of the European Centre for Medium-range Weather Forecasts (ECMWF), an international organization that Finland is a member of. The radiance measurement data to be used will be acquired via the Eumetcast satellite data broadcast service maintained by EUMETSAT. As a member of EUMETSAT, FMI will have near-real-time access to all these data.

2.3 Risk assessment and alternative implementation strategies

The implementation of the proposed work is potentially at risk in scenarios involving either instrument malfunctions or delays in satellite launches and/or access to third-party data. Given the internationally established reputation of EUMETSAT and their transparency throughout the planning of all their work, we don't expect considerable delays in the launch of MTG-I1 satellite. Despite that Arctica-M N1 satellite was launched already in 2021, uncertainty remains regarding the date on which measurement data becomes available to us. In our proposed time schedule, we allow 42 months between the launch and data

access for Arctica-M N1. In case that real data remains inaccessible for longer than this, we will shift our focus on the hyperspectral Infra-Red Sounder (IRS) that will be launched into GEO in 2024 as part of the Meteosat Third Generation (MTG) programme of EUMETSAT. On MTG-IRS, we will seek to make extensive use of the wealth of humidity information contained in the hundreds of fine spectral channels across the thermal water vapour absorption band.

3 Research team and collaborators

3.1 Project personnel and their project-relevant key merits

Reima Eresmaa (Ph.D., Project Leader) is a group leader for NWP activities in the Meteorological Research unit of FMI. He has experience from data assimilation in limited-area NWP at FMI (2001–2009 and 2020–present) and in global NWP at ECMWF (2009–2020), and enjoys internationally-recognized expertise in the field of satellite data assimilation, in particular the use of thermal radiance data. He maintains working contacts with numerous staff at global NWP centres, international organizations, and space agencies. He has authored or co-authored a number of scientific articles on the assimilation of thermal radiance data from LEO satellites.

David Schönach (M.Sc., Principal Investigator) is a scientist in the NWP research group at FMI. He has experience from data assimilation in limited-area NWP at FMI (2018–present). His particular expertise is in the use of GEO satellite data to optimize data assimilation methods suitable to very short-range applications of NWP (i.e., nowcasting). He also contributes regularly to the development of satellite data assimilation within the Nordic co-operation for regional NWP.

3.2 Collaborators and their project-relevant key merits

Magnus Lindskog (Ph.D.) is a senior scientist at the Swedish Meteorological and Hydrological Institute (SMHI). With more than 20 years of working experience, he has gained broad knowledge of various aspects of data assimilation, including algorithms, observation handling, and quality control. He has been involved in national and international projects focusing on the use of remote-sensing observations in regional NWP, and he has contributed to introducing several types of satellite-based radiances into operational NWP systems. He is currently a Project Leader on Data Assimilation and Use of Observations in the international HIRLAM-C programme. In this research project, Magnus's role is to provide support and assistance on matters specific to the use of satellite observations in the HARMONIE NWP system.

4 Responsible science

4.1 Research ethics

While we cannot recognize any ethical questions with relevance for the research project, we will make sure to follow the ethical recommendations of the Finnish Advisory Board on Research Integrity throughout the continuation of the work.

4.2 Equality and nondiscrimination

FMI is an equal opportunity employer. As the research project employs only one scientist, no gender equality in the strictest sense can be achieved. The project will secure funding for the Ph.D. student David Schönach, a citizen of Austria with demonstrated willingness to work in the international research group at FMI.

4.3 Open science

We foresee publication of a total of four scientific articles (two from each of the Work Packages listed in Section 2) to describe and document the new scientific results that will be produced in the project. In accordance with the FMI publication policy, all of the articles will be made openly accessible.

Externally-provided thermal radiance measurement data and internally-produced NWP model data will be stored on long-term archival platforms at FMI and ECMWF for the duration of the project. After the end of the project, all of the data will be made publicly available on a platform maintained by FMI.

4.4 Sustainable development objectives

The proposal seeks to enhance the role of Russian space administration in international activities relating to satellite meteorology. Particularly in the use in NWP, history is mostly written from Western societies' perspective, building on extensive exploitation of data production of European and American space agencies (i.e., EUMETSAT, European Space Agency, the National Aeronautics and Space Administration, the National Oceanographic and Atmospheric Administration). Shifting the focus of the international community towards greater co-operation with Russia is a desired outcome as such. Referring to the United Nations 2030 Agenda for Sustainable Development, we will support the implementation of "Goal 17: Strengthen the means of implementation and revitalize the global partnership for sustainable development".

5 Societal impact

5.1 Effects and impact beyond academia

The project will put emphasis on applied research to broaden the use of satellite measurements as part of routine weather forecasting processes. The broadened data use will mean added reliability and robustness in the performance of operationally-run NWP systems, which in turn will result in increased confidence in publicly-accessible weather forecasts. Overall the project will contribute to continuous and gradual improvement in weather forecasts. This will benefit a wide range of societal applications such as agriculture, travel and transport including road, rail, sea, and air, and the production of renewable energy.

6 References

Bauer, P., Auligné, T., Bell, W., Geer, A., Guidard, V., Heilliette, S., Kazumori, M., Kim, M.-J., Liu, E., McNally, A., Macpherson, B., Okamoto, K., Renshaw, R., Riishojgaard, L.-P.: Satellite cloud and precipitation assimilation at operational NWP centres, Q.J.R.Meteorol.Soc., 137, 1934-1951, <https://doi.org/10.1002/qj.905>, 2011.

Bauer, P., Thorpe, A., and Brunet, G.: The quiet revolution of numerical weather prediction, Nature, 525, 47-55, <https://doi.org/10.1038/nature14956>, 2015.

Bengtsson, L., Andrae, U., Aspelien, T., Batrak, Y., Calvo, J., de Rooy, W., Gleeson, E., Hansen-Sass, B., Homleid, M., Hortal, M., Ivarsson, K.-I., Lenderink, G., Niemelä, S., Pagh Nielsen, K., Onvlee, J., Rontu, L., Samuelsson, P., Santoz Munoz, D., Subias, A., Tijm, S., Toll, V., Yang, X., and Koltzow, M.: The HARMONIE-AROME Model Configuration in the ALADIN-HIRLAM NWP System, Mon. Wea. Rev., 145, 1919-1935, <https://doi.org/10.1175/MWR-D-16-0417.1>, 2017.

Bormann, N.: Slant path radiative transfer for the assimilation of sounder radiances, Tellus A, 69, 1272779, <https://doi.org/10.1080/16000870.2016.1272779>, 2017.

Bormann, N., Bonavita, M., Dragani, R., Eresmaa, R., Matricardi, M., and McNally, A.: Enhancing the impact of IASI observations through an updated observation-error covariance matrix, Q.J.R.Meteorol.Soc., 142, 1767-1780, <https://doi.org/10.1002/qj.2774>, 2016.

Eyre, J., English, S., and Forsythe, M.: Assimilation of satellite data in numerical weather prediction. Part I: The early years, Q.J.R.Meteorol.Soc., 146, 49-68, <https://doi.org/10.1002/qj.3654>, 2020.

Geer, A., and Bauer, P.: Observation errors in all-sky data assimilation, Q.J.R.Meteorol.Soc., 137, 2024-2037, <https://doi.org/10.1002/qj.830>, 2011.

Gustafsson, N., Huang, X.-Y., Yang, X., Mogensen, K., Linskog, M., Vignes, O., Wilhelmsson, T., and Thorsteinsson, S.: Four-dimensional variational data assimilation for a limited area model, Tellus A, 64, 14985, <https://doi.org/10.3402/tellusa.v64i0.14985>, 2012.

Kazumori, M.: Satellite Radiance Assimilation in the JMA Operational Mesoscale 4DVAR System, Mon. Wea. Rev., 142, 1361-1381, <https://doi.org/10.1175/MWR-D-13-00135.1>, 2014.

Lupu, C., Geer, A., Bormann, N., and English, S.: An evaluation of radiative transfer modelling errors in AMSU-A data, ECMWF Tech. Memo., 36 pp, 2016.

Mile, M., Randriamampianina, R., Marseille, G.-J., and Stoffelen, A.: Supermodding – A special footprint operator for mesoscale data assimilation using scatterometer winds, Q.J.R.Meteorol.Soc., 147, 1382-1402, <https://doi.org/10.1002/qj.3979>, 2021.

Peubey, C., and McNally, A.: Characterization of the impact of geostationary clear-sky radiances on wind analyses in a 4D-Var context, Q.J.R.Meteorol.Soc., 135, 1863-1876, <https://doi.org/10.1002/qj.500>, 2009.

Qi Wang, Z., and Randriamampianina, R.: The Impact of Assimilating Satellite Radiance Observations in the Copernicus European Regional Reanalysis (CERRA), Rem. Sens., 13, <https://doi.org/10.3390/rs13030426>, 2021.

Rabier, F., Järvinen, H., Klinker, E., Mahfouf, J.-F., and Simmons, A.: The ECMWF operational implementation of four-dimensional variational assimilation. I: Experimental results with simplified physics, Q.J.R.Meteorol.Soc., 126, 1143-1170, <https://doi.org/10.1002/qj.49712656415>, 2000.

Saunders, R.: The use of satellite data in numerical weather prediction, Weather, 76, 95-97, <https://doi.org/10.1002/wea.3913>, 2021.

Saunders, R., Hocking, J., Turner, E., Rayer, P., Rundle, D., Brunel, P., Vidot, J., Roquet, P., Matricardi, M., Geer, A., Bormann, N., and Lupu, C.: An update on the RTTOV fast radiative transfer model (currently at version 12), Geosci. Model. Dev., 11, 2717-2737, <https://doi.org/10.5194/gmd-11-2717-2018>, 2018.

Stengel, M., Undén, P., Lindskog, M., Dahlgren, P., Gustafsson, N., and Bennartz, R.: Assimilation of SEVIRI infrared radiances wth HIRLAM 4D-Var, Q.J.R.Meteorol.Soc., 135, 2100-2109, <https://doi.org/10.1002/qj.501>, 2009.

Trojáková, A., Mile, M., and Tudor, M.: Observation Preprocessing System for RC LACE (OPLACE), Adv. Sci. Res., 16, 223-228, <https://doi.org/10.5194/asr-16-223-2019>, 2019.

See discussions, stats, and author profiles for this publication at: <https://www.researchgate.net/publication/276227213>

USING THE METEOSAT-9 IMAGES TO THE DETECTION OF DEEP CONVECTIVE SYSTEMS IN BRAZIL

Article in *Journal of Hyperspectral Remote Sensing* · January 2012

DOI: 10.5935/2237-2202.20120007

CITATIONS

4

READS

354

3 authors, including:



Humberto Alves Barbosa
Universidade Federal de Alagoas

48 PUBLICATIONS 1,097 CITATIONS

[SEE PROFILE](#)



Leandro Rodrigo Macedo da Silva
Universidade Federal de Campina Grande (UFCG)

7 PUBLICATIONS 58 CITATIONS

[SEE PROFILE](#)

Some of the authors of this publication are also working on these related projects:



G-WADI-LAC Research Group on Remote Sensing for Precipitation Estimation [View project](#)



ANÁLISE E PREVISÃO DOS FENÓMENOS HIDROMETEOROLÓGICOS INTENSOS DO LESTE DO NORDESTE BRASILEIRO [View project](#)

USING THE METEOSAT-9 IMAGES TO THE DETECTION OF DEEP CONVECTIVE SYSTEMS IN BRAZIL

HUMBERTO ALVES BARBOSA¹ AYDIN GÜROL ERTÜK² LEANDRO RODRIGO MACEDO DA SILVA³

¹ Professor Adjunto do Departamento de Meteorologia – UFAL. Endereço: Av. Lourival Melo Mota, s/n, Tabuleiro do Martins. Instituto de Ciências Atmosféricas, 1º andar sala 5 - Maceió - AL - CEP: 57072-970. E-mail: barbosa33@gmail.com

² Turkish State Meteorological Service – Edereço: Kalaba/ANKARA – Turkey. E-mail: agerturk@meteoroj.gov.tr

³ Graduando em Meteorologia da UFAL. Endereço: Av. Lourival Melo Mota, s/n, Tabuleiro do Martins. Instituto de Ciências Atmosféricas, 1º andar sala 5 - Maceió - AL - CEP: 57072-970. E-mail: macedo.leandr0@gmail.com

Received 05 October 2011; revised 11 November 2012; accepted 20 December 2012

Abstract

The purpose of this article is to present a simple method of identification of deep convective clouds using water vapor (WV) and thermal infrared (IR) brightness temperature differences from the multispectral images of Spinning Enhanced Visible and Infra-Red Imager (SEVIRI) sensor. The use of this method is part of an international effort to calibrate the radiances of SEVIRI sensor for microphysical properties of deep convective systems. This approach was applied to the image from 08 September 2009 for the demonstration of its efficacy analysis. The results show that the difference values larger than -2° C for BT Differences (WV6.2 μ m – WV7.3 μ m) and $+50^{\circ}$ C (IR3.9 μ m – IR10.8 μ m) were associated with areas of intense precipitation. The method can be easily implemented and effectively utilized in operational basis to monitor deep convective cloud clusters over Brazil.

Keywords: EUMETCast, MSG, Clouds

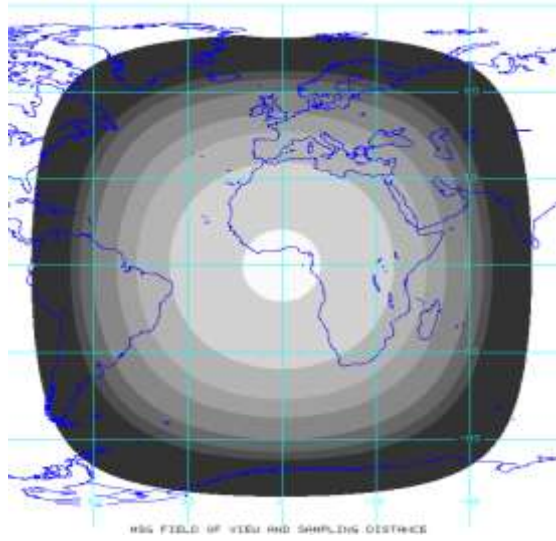
1. Introduction

EUMETSAT Meteosat Second Generation (MSG) is a geostationary satellite with a Spinning Enhanced Visible and InfraRed Imager (SEVIRI) on board. The MSG satellite was launched on the 29th of August 2002 and data has been available free to the academic and scientific communities since January 2004. The MSG SEVIRI is positioned at 0° longitude and 0° latitude, approximately 36 thousand km above the Gulf

of Guinea. This sensor operates with 11 spectral channels that provide measurements with a resolution of $3 \times 3 \text{ km}^2$ at the sub-satellite point every 15 minutes and a High Resolution Visible (HRV) channel whose measurements have a resolution of $1 \times 1 \text{ km}^2$ (EUMETSAT, 2008). The primary mission of the second-generation Meteosat satellites is the continuous observation of the Earth's full disk with a multi-spectral imager. The repeat cycle of 15 minutes for full-disk imaging provides

multi-spectral observations of rapidly changing phenomena such as deep convection. The imaging is performed by utilizing the combination of satellite spin and scan mirror rotation, a process known as stepping. The images are taken from south to north and east to west. Figure 1 provides an example the view of the sample distance on ground scanned by SEVIRI. Data is then processed and wavelet compressed, then uplinked via the EUMETCast service – a new C-band satellite reception facility to collect data from SEVIRI – to the commercial telecommunication geostationary satellites from which it can be disseminated to meteorological communities.

Figure 1. SEVIRI sampling distance on ground (MSG field of view). Source: EUMETSAT



Satellite studies of deep convective clouds detected by MSG/SEVIRI observations have used the radiative properties measured by visible and infrared radiances that are sensitive only to the top parts of clouds. The key advantage of the MSG SEVIRI sensor is the ability to capture observations for every 15 minutes over 12 bands over a 70° field

of view centered at the Greenwich Meridian and the equator. Combined with the RGB (Red-Green-Blue) colors can be used for qualitative analysis of cloud microphysics. Although the RGB combinations do not directly provide information on vertical motions (i.e., updraft strength), their contribution in detecting deep convective clouds are relevant (Lensky and Rosenfeld, 2008). Because geostationary satellite data at high temporal resolution may provide the possibility to identify potential instability, especially in places where conventional data are either sparse or unavailable. This study relies on MSG-emitted brightness temperature (BT) as a proxy for potential instability, but without any direct measurement of updrafts (EUMETSAT, 2007). Taking full advantage of the high temporal sampling of MSG and its wide gamma of spectral channels, particularly the three channels 6.2, 7.3, 10.8 μm may be viewed as a measure of convective activity. Severity of convection is largely based on infrared methods that define storm severity as a cloud top temperature than a given threshold. Different thresholds of 208–233 K have been suggested (e.g., Liu et al., 1999; Machado and Laurent, 2004). It is also well documented that cloud top BT is directly related to the cloud top level environment temperature (Schmetz et al., 2002; Barbosa and Ertürk, 2009) – valid only for opaque clouds (i.e., cumulonimbus clouds) and state of thermal equilibrium between the cloud and its environment. However, the BT thresholds alone are not able

to distinguish deep convective clouds and cirrus clouds with high precision, in part because the same cold cloud top may be generated from different convective intensities in different convective environments. An alternative approach is the use of BT differences between the WV and IR window bands for detecting convective overshooting clouds – deep convective clouds that play a key role in transport and mixing in the tropical tropopause layer at typically 14km-16km height (Gettelman et al., 2002).

Figure 2 illustrates example of the so-called weighting functions of the thermal channels – the weighting functions describe the contribution of each atmospheric layer to the radiance by the satellite. Weighting functions depend on the actual atmospheric state and the satellite viewing angle. A visual comparison between WV6.2 and WV7.3 shows how the peak of weighting functions raise in altitude with increasing satellite zenith angle at 60°. Water Vapor has an absorption band around 6 microns and therefore it absorbs radiation from below but emits radiation according to the 2nd Kirchoff law. Therefore the water vapor (WV) channels are indicative of the water vapor content in the upper part of the troposphere. The maximum signal from WV6.2 is at 350 hPa, and for WV7.3 at 500 hPa. It is also assumed that normal pressure at sea level approximate elevation is at 8980 m and 5965 m respectively. The IR channel records the emitted energy from the Earth

surface itself. Based on a classification using MSG channel IR10.8 and WV6.2, applying a threshold on the temperature difference of less than 11 Kelvin an approximation of the clouds that have a high likelihood of precipitation can be obtained. This is an empirically determined threshold reported by Kidder et al. (2005).

Several MSG SEVIRI bands provide a powerful tool in detecting convective activities (see Table 1). The main bands used are the visible VIS0.6 channel (centred at 0.6 μm), the near-infrared NIR1.6 channel (centred at 1.6 μm), the water vapor WV6.2 and WV7.3 channels (centred at 6.2 μm and at 7.3 μm , respectively), the infrared IR10.8 window channel (centred at 10.8 μm) and the difference between the WV6.2 and IR10.8 bands (defined hereafter as BTD). The BTD (WV6.2-IR10.8) is positive (WV warmer than the IR window) above most of the cloud top storms. The calibration accuracy of the solar SEVIRI channels is 5% (Govaerts and Clerici, 2004), while uncertainties in calibration of the SEVIRI 10.8 μm channel are below 0.25 K at 300 K (Schmetz et al., 2002). Differencing the 3.9 μm channel with the 10.8 μm channel allow the determination of liquid water clouds and high cirrus clouds. This is due to the 10.8 μm detecting all clouds close to blackbody temperature. Because of emissivity values of clouds in the 10.8 channel are greater than 0.9. And it detects a warmer cloud top temperature whereas 3.9 μm channel detects much less than a blackbody for water clouds.

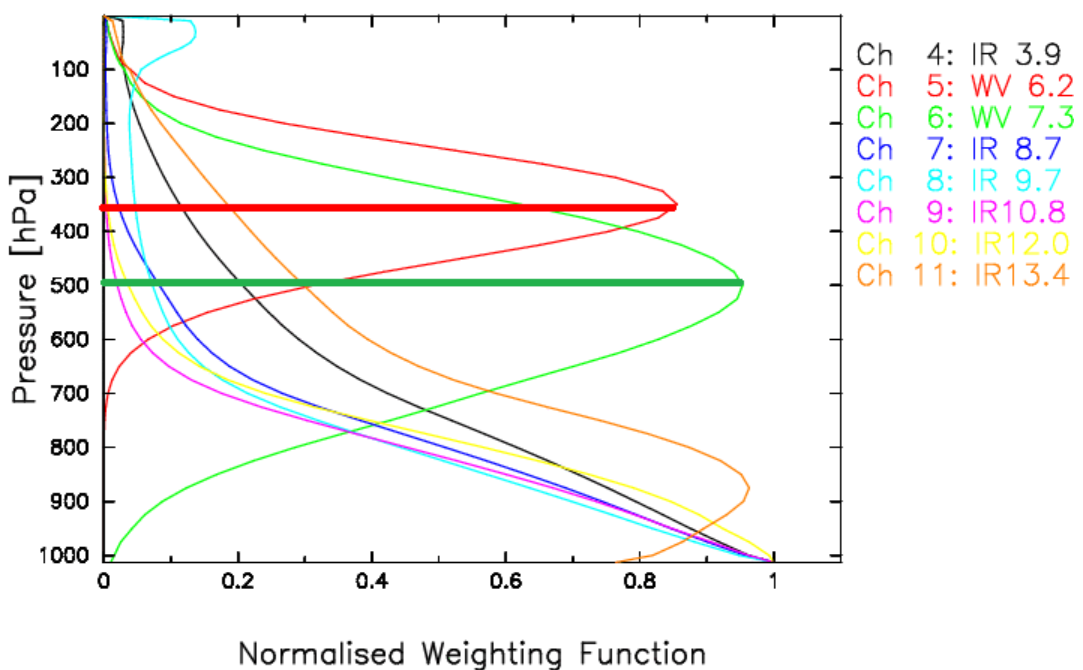


Figure 2. SEVIRI channel normalized weighting functions at 60°. Source EUMETSAT.

Positive difference between WV6.2–IR10.8 is associated with convective overshooting and moisture injection in the stratosphere. Fritz and Laszlo (1993) have clearly shown that the WV – IR brightness temperature difference is capable of identifying overshooting tops. Because the emitted minimum BT at the coldest overshooting tops is directly proportional to the largest positive values of BTD, it can be viewed as a measure of convective activity. However, this type of analysis with BTD method is not able to compute too high overshooting tops with high precision, in part because their height reduces the total amount of moisture above them (Setvák et al., 2008). An alternative approach is the use of 6.2 μm BT – 7.3 μm BT method to obtain more precise information concerning the

overshooting tops in comparison to the WV – IR method when the overshooting tops do not exhibit any BT minimum. The physical mechanisms associated with the overshooting tops are well documented. These were studied on the pioneering work of Fritz and Laszlo, (1993) and from a few other authors since then (e.g., Schmetz et al., 2002; Setvák et al., 2008). The BTD (WV6.2-WV7.3) approach described above can be applied for detection of the overshooting tops.

The LAPIS (Laboratório de Análise e Processamento de Imagens de Satélites in Portuguese – <http://www.lapismet.com>) laboratory is operationally recording convective storms over the Brazil since 2006. The severity criteria of the U.S. National Weather Service for a convective storm can be classified as severe if it presents on the

following characteristics: a) tornado, b) wind gusts \geq 50 knots ($\sim 25 \text{ m s}^{-1}$) and c) hailstones with diameter $\geq \frac{3}{4}$ inch ($\sim 2 \text{ cm}$) (<http://www.weather.gov/glossary/index.php?letter=t>). It is also well documented (Schmetz et al., 2002; Barbosa and Ertürk 2009; Ertürk and Barbosa 2009) that cloud top brightness temperature (BT) directly related to the cloud top level environment temperature – valid only for opaque clouds (i.e., cumulonimbus clouds) and state of thermal equilibrium between the cloud and its environment. In particular, critical to the success of any attempt to spot the satellite-based storm cell is the BT isotherm of $\sim 240 - 230 \text{ K}$. The atmosphere must already be conditionally unstable and the large-scale dynamics must be supportive of vertical cloud development.

Understanding the characteristics of convective storms that impact the weather conditions in Brazil is of importance to help forecasters to improve their capability as regards to the forecast of strong convective events. Since 2006 there were many cases when deep convective storms developed in Brazil, the 08 September 2009 storm was a strong convective event. Although this study is a preliminary one, and the number of cases is limited to only one event, the next step will be the acquisition of more events and the implementation of a database of the aforementioned information as support to the comprehension of such events and to the forecasting activity. The paper is organized as follows. Section 2 describes the MSG satellite

data acquisition, decoding, and analysis. Section 3 details a case study of a deep convective storm over the south-eastern Brazil. Section 4 concludes the paper.

2. Material and methods

2.1 Receiving and processing SEVIRI radiances

In this article, the cloud-top SEVIRI data from 08 September 2008 with a temporal resolution of 15 minutes were retrieved from the EUMETCast service through the reception station at the Federal University of Alagoas (UFAL). EUMETCast is a content delivery network used by EUMETSAT for transporting SEVIRI data (MSG-2 satellite) received at Darmstadt (Germany) to the end users. Raw count data received by this service are referred to as level 1.5 data (EUMETSAT, 2008), that is, image data ready to use with calibration and geo-location information appended. The level 1.5 data have a 10 bit digitization and provide the basis for all further processing and for the derivation of meteorological products. They are processed and uplinked to NSS-806 in wavelet compressed the high rate information transmission (HRIT) format. From there the images can be received with a standard dish receiving system in the EUMETCast C-band. At UFAL they are archived in compressed form on external drives linked to the UFAL network, and accessible through ordinary PCs. The PC system has a built in DVB-S card that is connected to the dish and besides the

EUMETCast Key Unit (EKU), which hold the key for encrypting the received data. Each file is compressed by means of a wavelet algorithm. Furthermore the PC system is connected to the UFAL LAN to have the ability to serve the end user with the MSG full disk that is composed by 8 segment files, each one consisting of 464 lines (i.e., HRIT format). This data consists of geographical arrays of 3712×3712 pixels. Each pixel contains 10 bit data that represents the radiance value, expressed in $10^{-3} \text{ Wm}^{-2}\text{sr}^{-1}[\text{cm}^{-1}]^{-1}$, codified in digital count (DC) form. MSG SEVIRI data have been received at UFAL since 2007 (Fig. 3). This processing level corresponds to image data corrected for radiometric and geometric effects, geolocated using a standard projection, finally calibrated.

To compute the radiance for each channel scaling parameters (cal_slope and cal_offset) have to be identified. The scaling parameters are contained into the header file

named “prologue” of Level 1.5 SEVIRI images (HRIT format). Radiance values can be calculated by means of the following formula (EUMETSAT, 2008):

$$L_{(i,ch)} = DC_{(i,ch)} * \text{cal_slope}_{(ch)} + \text{cal_offset}_{(ch)} \quad (1)$$

where $DC_{(i,ch)}$ and $L_{(i,ch)}$ are the digital count and radiance of pixel i and channel ch , respectively. For SEVIRI thermal channels (4-11), brightness temperature, expressed in $10^{-3} \text{ Wm}^{-2}\text{sr}^{-1}[\text{cm}^{-1}]^{-1}$, can be calculated by simply inverting the Planck function at the channel wavelength, that is:

$$\nu = \frac{10^4}{\lambda_0}, \quad BT = \frac{c_2 \nu}{\ln \left[1 + \nu^3 \frac{c_1}{L} \right]} \quad (2)$$

where λ_0 is the central wavelength of the channel expressed in μm and c_1 and c_2 channel varying constants listed in the EUMETSAT documents (EUMETSAT, 2007a).

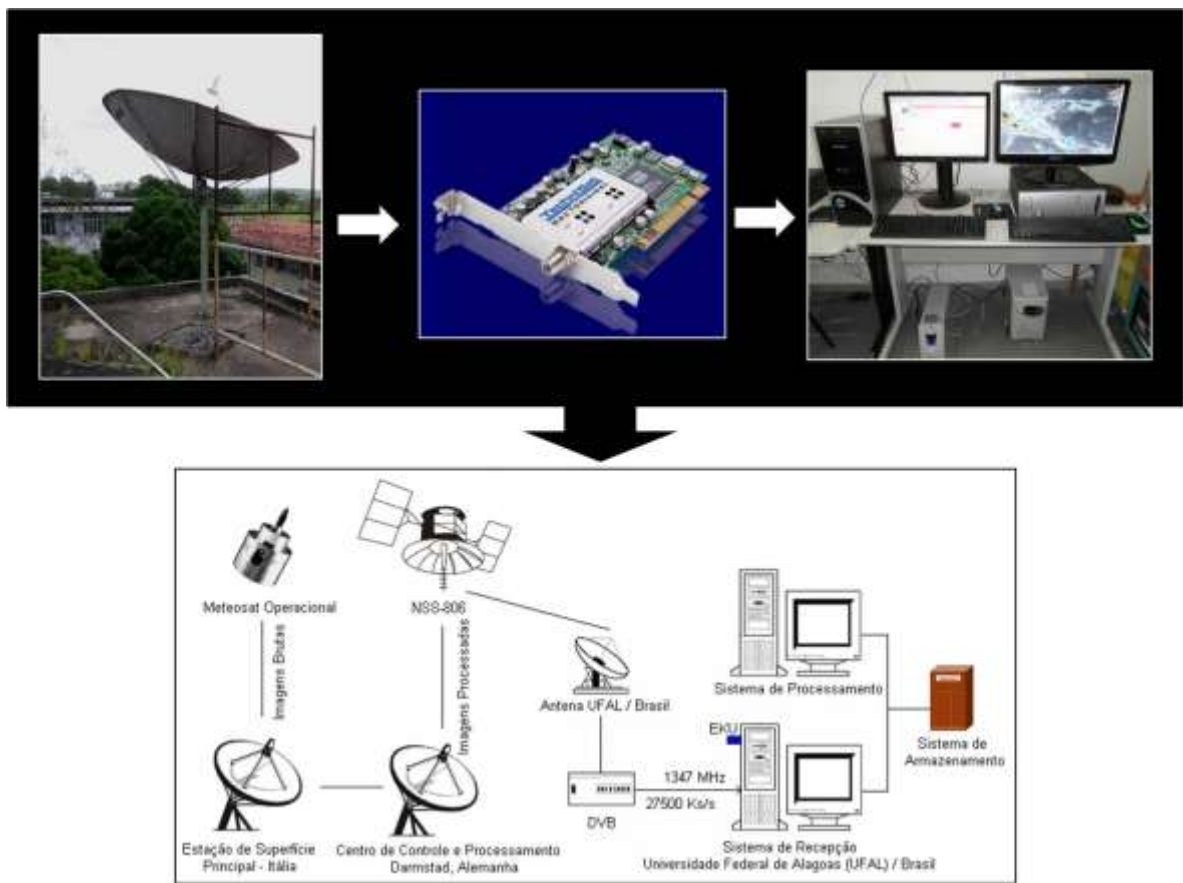


Figure 3. Overview of the broadcasting ground reception and processing system at the University of Alagoas (UFAL) in Brazil.

Meaningful RGB combinations can be used for qualitative analysis of cloud microphysics (Lensky and Rosenfeld, 2008). In order to assess RGB composites, ASCII files regarding the 12 spectral bands were extracted using open-source software tools (e.g., EUMETSAT WaveLet Transform Software used to decompress SEVIRI HRIT data files (EUMETSAT, 2009c); Geospatial Data Abstraction Library (Silva Junior et al 2009) used to read and write many geographic data formats), to allow data to be analyzed. These are spectral radiance displayed: reflectance (%) in the solar channels and brightness temperature (K) in the thermal channels. This processing level corresponds to

image data corrected for radiometric and geometric effects, geo-located using a standard projection (Silva Junior et al 2009), finally calibrated (Fig. 4). These processing steps were computed by LAPIS, at UFAL, in collaboration with Turkish State Meteorological Service (TSMS).

Analyses of the cloud-top SEVIRI data were done using different bands of RGB color compositions (convective storms). This RGB composition is widely used methods (Kerkemann et al. 2004). The “convective storm” RGB (Fig. 4), based upon the RGB combination of channels (WV 6.2 μm – WV7.2 μm ; IR3.9 μm – IR10.8 μm ; NIR1.6 μm – VIS0.6 μm), the red color appears in

clouds with larger ice particles, while darker orange for smaller ice particles. The spectral images from SEVIRI VIS0.6 (channel 1); NIR1.6 (channel 3); WV6.2 (channel 5); and IR10.8 (channel 9) were processed and displayed into reflectivity (channels 1 and 3) and BT (channels 5, and 9) by exploiting the codes developed by LAPIS. Both the reflectivity and BT time series were georectified and extracted over a grid cell limited between 25°N – 35°S and 5° – 73°W (Fig.5), with pixel spacing of about 5X6 kilometers.

The extracted pixel values over the study grid cell for each channel were then arranged as an input matrix to determine the spatial variations in cloud top. In our analyses, scatter plots through the spatial distribution in

both the reflectivity and BTs were analyzed. At the study grid cell, for each pixel the difference (WV6.2 μm – IR10.8 μm) was used as a proxy for deep convection. In the case, BTs larger at WV6.2 μm than at IR10.8 μm were explained by stratospheric water vapor, i.e. small (positive) difference. The determination of cloud-top radiances obtained from these channels of the radiometer SEVIRI relied on the following two assumptions; that clouds were cumulonimbus so they can consider optically thick and that they were considered blackbodies. These scatter plots were analyzed separately to characterize the spatial heterogeneity of cloud top at these spectra outlined.

Table 1. Spectral bands of the SEVIRI instrument, commonly used for monitoring of convective storms.

Spectral band	SEVIRI (MSG)
Visible (VIS) and shortwave end of NIR (approx. 0.4 - 1.2 μm)	band 01 VIS 0.6 (0.56-0.71 μm) band 02 VIS 0.8 (0.74-0.88 μm) band 12 HRV (0.5-0.9 μm)
Microphysical bands (NIR) (approx. 1.6 and 3.5 - 4 μm)	band 03 IR 1.6 (1.5-1.78 μm) band 04 IR 3.9 (3.48-4.36 μm)
Water vapor absorption/emission bands (WV)	band 05 WV 6.2 (5.35-7.15 μm) band 06 WV 7.3 (6.85-7.85 μm)
Thermal IR window bands (IRW)	band 07 IR 8.7 (8.30-9.10 μm) band 09 IR 10.8 (9.80-11.80 μm) band 10 IR 12.0 (11.00-13.00 μm)

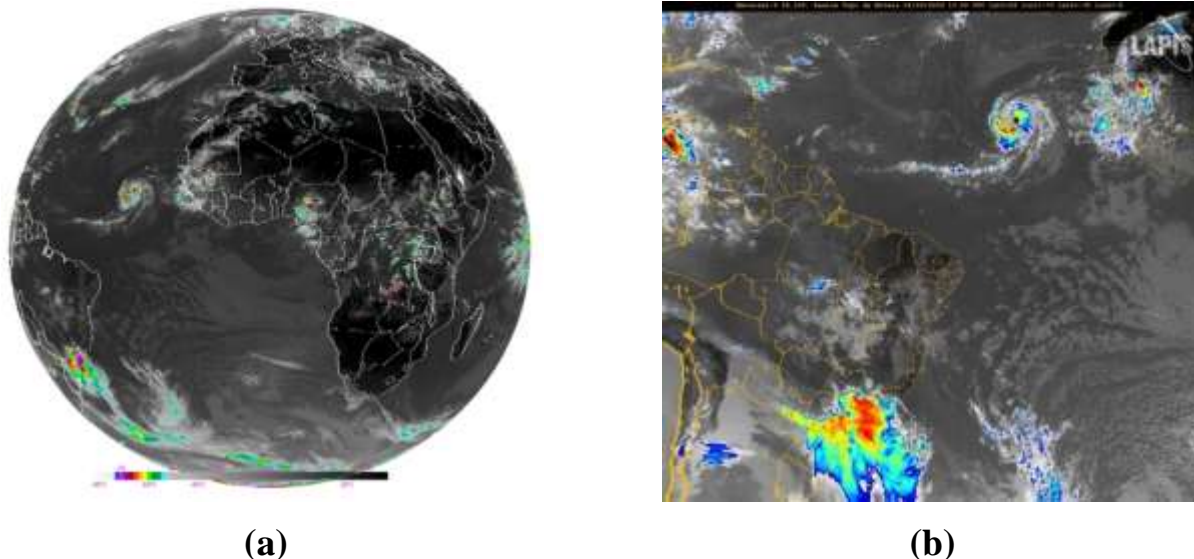


Figure 4. METEOSAT 9 SEVIRI color-enhanced IR 10.8 image dated on 08 September 2008 at 13:00 UTC. (a) For the MSG full disk. (b) For the geographic domain used in the paper.

3. Results

3.1 The 08 September 2009 storm

The case study for which results are presented here is a frontal system over south-eastern region of Brazil on 08 September 2009 at 13:00 UTC. At this time the cloud storm was already in the mature stage. This anomalous event was characterized by very unstable weather, in particular over the eastern State of São Paulo. The general situation,

shown in the synoptic chart (Fig. 5), suggests that a strong pressure gradient produced high winds bringing the cold air from South to South-eastern Brazil, producing upper-level cyclonic vortices. According to reports from meteorological stations, the average velocity of winds in parts of São Paulo city on 08 September was 70km/h. The geographic area under consideration is approximately centred over Brazil (Fig. 5). It covers from 25N to 35°S and from 5 to 73°W.

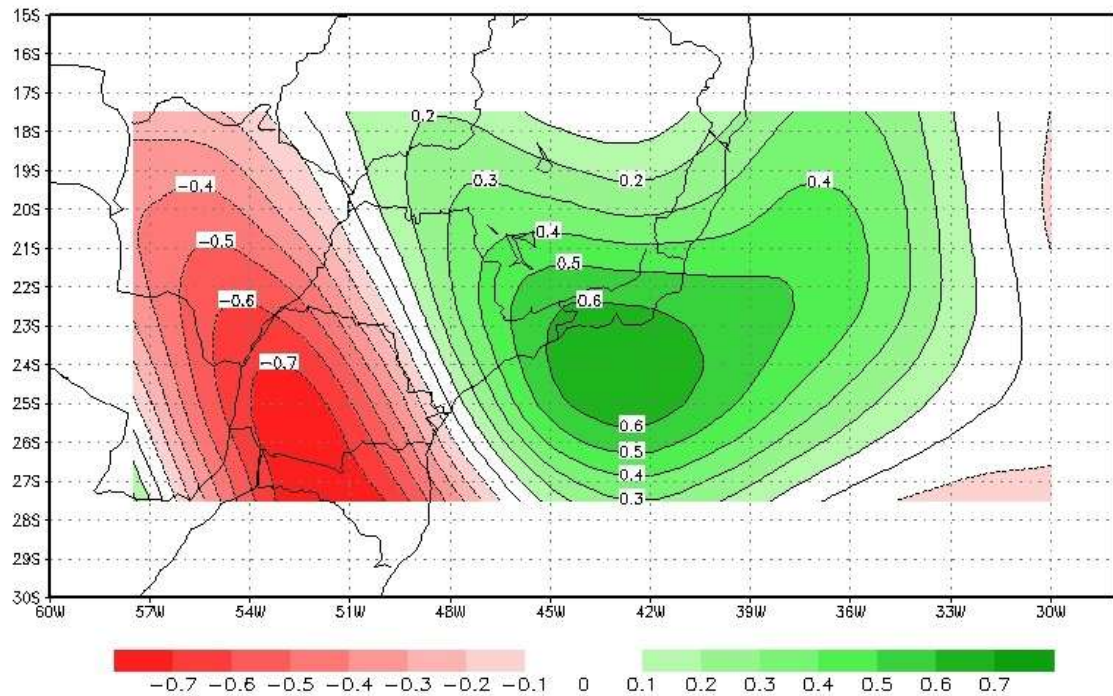


Figure 5. Relative Vorticity field ($2.5^\circ \times 2.5^\circ$ resolution) for 200 hPa derived from the NCEP reanalysis data base over South-eastern Brazil on 08 September 2009.

The “convective storms” (Fig. 6) RGB composite help us to locate the strong convective clouds take place. The figure 6 exhibits that the active convection cells (yellowish) associated with strong updrafts within Cb clouds became more organized and centered over mostly the eastern edge of Brazil south, to form stronger precipitation at this location. The visual inspection of this composite can indentify the strong cold frontal over South-eastern Brazil. Associated with this, it is relatively evident (shown in the

synoptic chart (Fig. 5)) that no upward vertical motions arose as a result of frontogenesis, it just goes to show that this was the closest variable which may have impacted and aided the severe weather, on a synoptic level. More importantly about this RGB composition, however, was the fact could be seen coming up from the moisture sources of the Atlantic Ocean and the Andes Mountains towards southeastern Brazil where the cumulus clouds are located. The warmer temperatures lead to lower stabilities also.

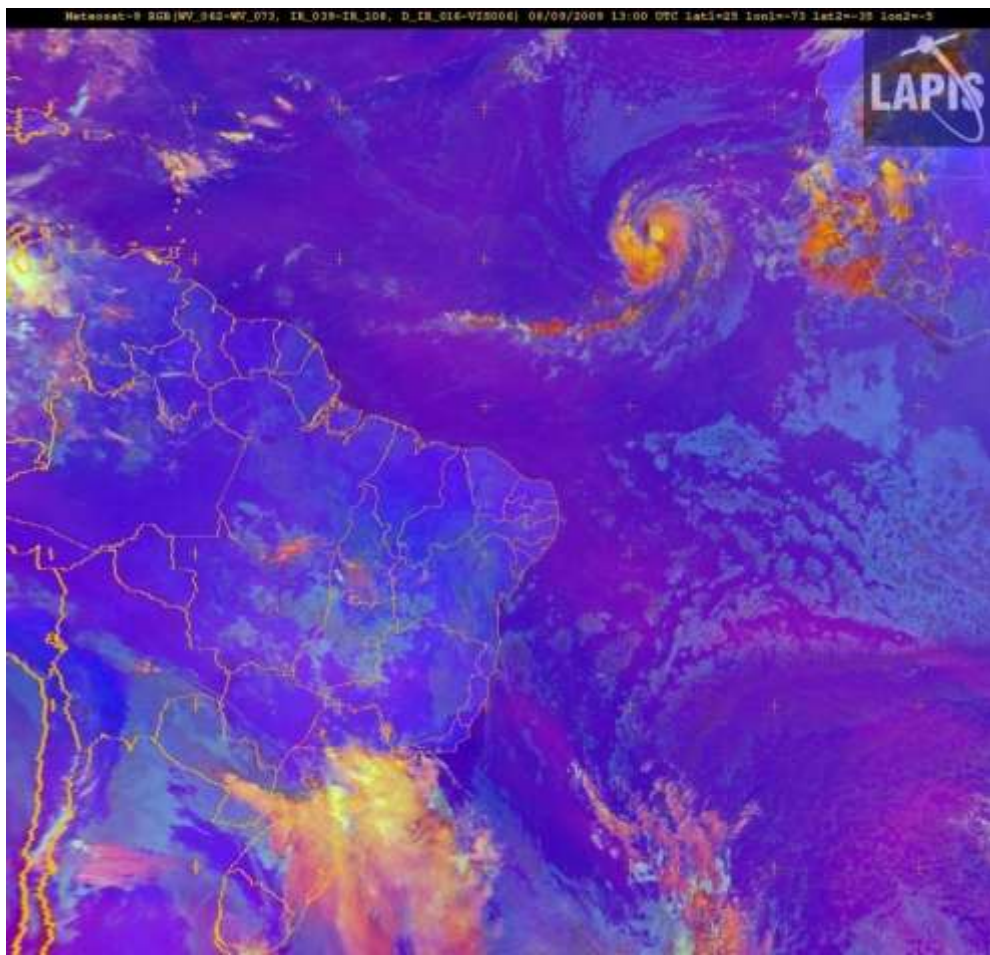


Figure 6. “Convective storms” RGB composite image dated on 08 September 2009 at 13:00 UTC.

Scatter plot diagram of BTD(WV6.2 μm – WV7.3 μm) as a function of BTD(IR3.9 μm – IR10.8 μm) and their BTD image (zoomed-in south-easternern Brazil) at 13:00 UTC are show in Fig. 7a and 7b, respectively. Difference values larger than -2°C (for 6.2–7.3 μm) and $+50^\circ \text{C}$ (for 3.9 μm –10.8 μm) are found to correspond well with intense convective clouds (red/orange), and subsequently, storms. The diagram makes it easy to note that positive BTD (WV) is likely to correspond with convective cloud tops that are at or above the tropopause (i.e. overshooting tops). Associated with this, a large number of dots clusters are shown in high yellow colors. In fact, the BTs derived

from 10.8 μm shown in Fig. 7 are fundamental for the definition of overshooting Cb clouds that have near zero or slightly positive BTD (6.2-7.3) (high yellow). With these dots clusters merging at the BTs (for 10.8 μm), the concentration areas are characterized by cloud-top temperatures (CTT) above -62°C , which may produce storms throughout much of the eastern portions of Brazil south. Therefore, the combination of 1) larger than -2°C (for 6.2–7.3 μm) that is modulated by mid-level moisture, 2) larger $+50^\circ \text{C}$ (for 3.9 μm –10.8 μm) that is stronger for cold clouds, and 3) minimum CTT of -62°C , led the severe storm at this location at this time.

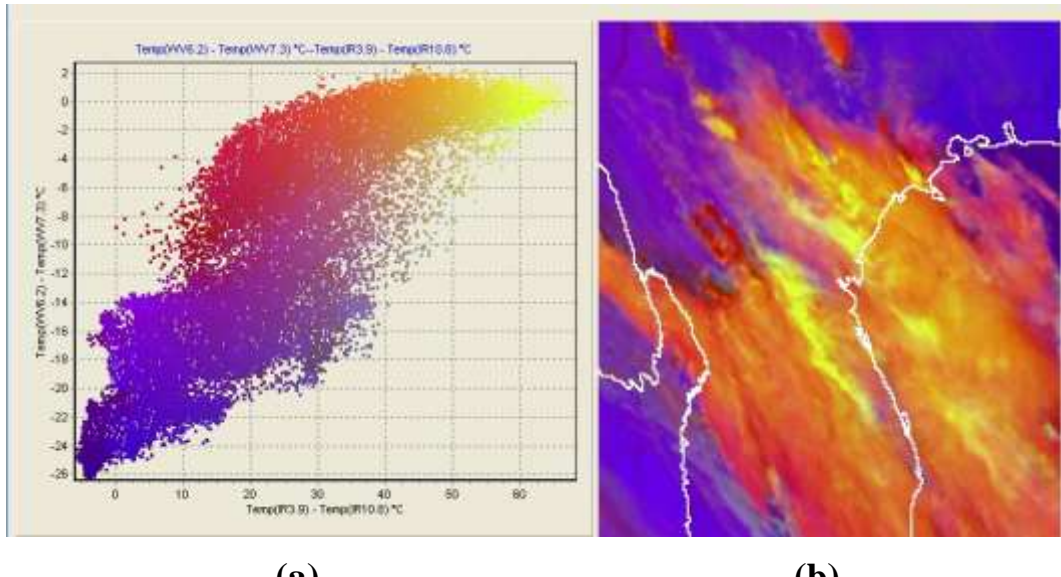


Figure 7. Scatter plot diagram of BTD(WV6.2 μm – WV7.3 μm) as a function of BTD(IR3.9 μm –IR10.8 μm) (a) and their BTD image (zoomed-in south-eastern Brazil) dated on September 2009 at 13:00 UTC (b).

4. Summary and conclusion

In this paper, we described our experiences with acquiring, processing and classifying the 1.5 Meteosat-9 SEVIRI radiances (MSG-2) received through the EUMETCast service using RGB composite for characterizing cloudy (and potentially precipitating) pixel areas relative to a severe convective event, take on 8 September 2009, over the South-eastern Brazil. In this respect, the software tools developed at LAPIS, based on open source codes for geolocation and geographical information systems, written for the transformation of the 1.5 SEVIRI radiances into the geo-physical values (i.e., the solar reflectance in the solar bands and brightness temperature in the thermal bands) were employed. In conclusion, the study shows that difference values larger than -2°C

for BT Differences (WV6.2 μm – WV7.3 μm) and $+ 50^\circ \text{ C}$ (IR3.9 μm –IR10.8 μm) were found to correspond well with deep convective storms. The study opens up an avenue for successive validation of the MSG data for weather monitoring, particularly in case of complex and intense events. In this direction its use for nowcasting is to be considered in a short while.

5. Acknowledgments

This work is part of a research funded by Brazil's Council for Scientific and Technological Development (CNPq) under number Grant 503519/2010-3 (Edital MCT/CNPq 10/2010 - AT- NS).

6. References

- BARBOSA, H. A., and Ertürk, A. G. (2009). Using multispectral SEVIRI radiances at the top of deep convective storm as a powerful tool for

short prediction in Brazil. 5th European Conference on Severe Storms, Stadtsala Bernlochner – Landsat – Germany, 12-16 October,

www.essl.org/ECSS/2009/preprints/007-7-barbosa.pdf.

EUMETSAT, (2007). A planned change to the MSG Level 1.5 image product radiance definition, Rep. EUM/OPS-MSG/TEN/06/0519, EUMETSAT, Darmstadt, Germany.

EUMETSAT. (2007a). A planned change to the MSG Level 1.5 image product radiance definition, document n. 0519. Available from: [http://www.eumetsat.int/idcplg?IdcService=GET_FILE&dDocName=PDF_MSG_PLANNED_CHANNEL_LEVEL15&RevisionSelectionMethod=LatestReleased\]](http://www.eumetsat.int/idcplg?IdcService=GET_FILE&dDocName=PDF_MSG_PLANNED_CHANNEL_LEVEL15&RevisionSelectionMethod=LatestReleased].).

EUMETSAT. (2008). A simple conversion from effective radiance back to spectral radiance for MSG images, document n. 1053. [available from: [http://www.eumetsat.int/idcplg?IdcService=GET_FILE&dDocName=pdf_msg_conv_effrad2specr&RevisionSelectionMethod=LatestReleased\]](http://www.eumetsat.int/idcplg?IdcService=GET_FILE&dDocName=pdf_msg_conv_effrad2specr&RevisionSelectionMethod=LatestReleased]).

ERTÜRK, A. G. and Barbosa, H. A. (2009). Detecting V-Storms using Meteosat Second Generation SEVIRI image and its applications: A case study over western Turkey. 5th European Conference on Severe Storms, Stadtsala Bernlochner – Landsat – Germany, 12-16 Octobe.

<http://www.essl.org/ECSS/2009/preprints/P07-11-erturk.pdf>.

FRITZ, Sigmund and Laszlo, Istvan.(1993). Detection of water vapor in the stratosphere over very high clouds in the tropics. Journal of Geophysical Research, 98(D12), 22959-22967.

GETTELMAN, A., M. L. Salby, and F. Sassi. (2002). Distribution and influence of convection in the tropical tropopause region, J. Geophys. Res., 107(D10), 4080, doi:10.1029/2001JD001048.

GOVAERTS, Y. and M. Clerici. (2004). MSG-1/SEVIRI Solar Channels Calibration Commissioning Activity Report. EUMETSAT Doc. EUM/MSG/TEN/04/2004, 35 pp.

KIDDER, S., Kankiewicz, J.A., Eis, K. (2005). Meteosat Second Generation cloud algorithms for use in AFWA. In BACIMO 2005, Monterey, CA.

SETVÁK M., Lindsey D. T., Rabin R. M., Wang P. K., Demeterová A. (2008). Indication of water vapor transport into the lower stratosphere above midlatitude convective storms: Meteosat Second Generation satellite observations and radiative transfer model simulations. Atmos. Research, 89, 170-180.

SILVA JUNIOR, I. W.; Nobrega, T.; Barbosa, H. A. (2009). VIEWSATT a Decoding and Processing Software Tool for MSG Data. In: WORLDCOMP'09 - The 2009 World Congress

in Computer Science, Computer Engineering, and Applied Computing, Las Vegas – EUA.

Supplement to An Introduction to Meteosat Second Generation (MSG). B. Am. Meteorol. Soc., 83, 991.

SCHMETZ, J., Pili, S., Tjemkes, D., Just, J., Kerkmann, S., Rota, and A. Ratier. (2002). A

A SHORT INTRODUCTION TO METEOSAT SECOND GENERATION (MSG)

Johannes Schmetz, Yves Govaerts, Marianne König, Hans-Joachim Lutz, Alain Ratier and Stephen Tjemkes
EUMETSAT

For more than 40 years, meteorological satellites have been the best way to observe the changing weather on a large scale. Typically, operational meteorology utilizes two types of satellites to provide the required information.

Polar orbiting satellites fly at relatively low altitudes of around 800 kilometres above Earth, and can provide information based on a high spatial resolution. This comes at a price: when only one polar satellite is deployed, the same spot on Earth is visited only twice per day. More than one polar satellite with different equatorial crossing times is required in order to attain more frequent observations.

Geostationary satellites in the equatorial plane at an altitude of about 36,000 kilometres above Earth have the same revolution time as the Earth itself and therefore always view the same area. They can perform frequent imaging which, in animated mode, depicts the ever-changing atmospheric processes. The disadvantage of the relatively high altitude is that it limits spatial resolution.

Advances in satellite technology have led to improved observational capabilities. The first generation of European geostationary meteorological satellites dates to 1977, with the launch of Meteosat-1. Today, Meteosat-7 is the spacecraft which operates in the nominal European orbit at 0 degrees longitude. Meteosat-5 and 6 are also in operational use, the first in operational service over the Indian Ocean at 63 degrees east longitude, and the latter with special operational service over Europe. This satellite provides so-called rapid scan imagery with a repeat cycle of 10 minutes, but observing only a third of the Earth's disk. Meteosat-6 also serves as the back-up satellite for the service provided from 0 degrees longitude.

The first of the new generation of Meteosat satellites, known as Meteosat Second Generation (MSG), was launched in August 2002 from the Kourou launch site in French Guiana. [Figure 1](#) shows a picture of the satellite.

As with the current Meteosat series, MSG is spin-stabilized, and capable of greatly enhanced Earth observations. The satellite's 12-channel imager, known formally as the spinning enhanced visible and infrared imager (SEVIRI), observes the full disk of the Earth with an unprecedented repeat cycle of 15 minutes in 12 spectral wavelength regions or channels. For comparison, the first-generation Meteosat satellite covers only three spectral channels and has an imaging repeat cycle of 30 minutes.

The MSG programme covers a series of three identical satellites which are expected to provide observations and services over at least 12 years. Each satellite has an expected lifetime of seven years.

As with the original Meteosat system, MSG is planned as dual-satellite service, where one additional satellite is available in orbit.

The primary mission of the second-generation Meteosat satellites is the continuous observation of the Earth's full disk with a multi-spectral imager. The repeat cycle of 15 minutes for full-disk imaging provides multi-spectral observations of rapidly changing phenomena such as deep convection. It also provides for better retrieval of wind fields which are obtained from the tracking of clouds, water vapour and ozone features.

Channel No.	Spectral Band (μm)	Characteristics of Spectral Band (μm)			Main observational application
		λ_{cen}	λ_{min}	λ_{max}	
1	VIS0.6	0.635	0.56	0.71	Surface, clouds, wind fields
2	VIS0.8	0.81	0.74	0.88	Surface, clouds, wind fields
3	NIR1.6	1.64	1.50	1.78	Surface, cloud phase
4	IR3.9	3.90	3.48	4.36	Surface, clouds, wind fields
5	WV6.2	6.25	5.35	7.15	Water vapor, high level clouds, atmospheric instability
6	WV7.3	7.35	6.85	7.85	Water vapor, atmospheric instability
7	IR8.7	8.70	8.30	9.1	Surface, clouds, atmospheric instability
8	IR9.7	9.66	9.38	9.94	Ozone
9	IR10.8	10.80	9.80	11.80	Surface, clouds, wind fields, atmospheric instability
10	IR12.0	12.00	11.00	13.00	Surface, clouds, atmospheric instability
11	IR13.4	13.40	12.40	14.40	Cirrus cloud height, atmospheric instability
12	HRV	Broadband (about 0.4 – 1.1 μm)			Surface, clouds

Table 1: Spectral channel characteristics of SEVIRI in terms of central, minimum and maximum wavelength of the channels and the main application areas of each channel.

The imaging is performed by utilizing the combination of satellite spin and scan mirror rotation, a process known as stepping. The images are taken from south to north and east to west. The eight thermal IR and three solar channels have a sampling distance of three kilometres at nadir and scan the full disk of the Earth. The high-resolution visible channel provides images with one kilometre sampling at nadir. Data rate limitations confine the high-resolution visible images to half the Earth in an east-west direction, however, the exact coverage of the Earth is programmable. [Figure 2](#) provides an example of the view of the Earth scanned by SEVIRI. (The right panel depicts a possible choice of east-west scanning with the high-resolution visible channel.)

SEVIRI has eight spectral channels in the thermal infrared (IR), three channels in the solar spectrum, and a broadband high resolution visible channel. The accompanying table provides more details of the characteristics of these channels, and indicates how each channel is used: for observations of clouds and surface temperatures, water vapour or ozone. [Figure 3 \(a\) and \(b\)](#) show the location of the SEVIRI bands on top of a solar and typical thermal energy spectrum, respectively. [Figure 3 \(c\) and \(d\)](#) give examples of the so-called weighting functions of the thermal channels – the weighting functions describe the contribution of each atmospheric layer to the radiance by the satellite. Weighting functions depend on the actual atmospheric state and the satellite viewing angle. A comparison between [Figure 3 \(c\)](#) and [Figure 3 \(d\)](#) reveals how the peak of weighting functions raise in altitude with increasing satellite zenith angle.

The ozone channel is a novel feature on a geostationary imaging instrument and will provide information on the total ozone content of the atmosphere. It is also useful for observing the dynamics of the stratosphere and the height of the tropopause layer.

Raw data coming from the SEVIRI instrument are preprocessed at EUMETSAT headquarters in Darmstadt, Germany and transformed into so-called level 1.5 data, that is, image data ready to use with calibration and geo-location information appended. The level 1.5 data have a 10 bit digitization and provide the basis for all further processing and for the derivation of meteorological products. Some core meteorological products are also centrally computed at EUMETSAT and are available to users within 15 minutes after image reception. These essential meteorological data include wind, cloud analysis, atmospheric humidity and atmospheric instability over the entire MSG field of view.

In addition to the central processing at EUMETSAT headquarters, satellite application facilities exist. The idea behind this network of facilities is that more products from MSG (and also from the future EUMETSAT polar system) can be derived capitalizing on the scientific expertise at national meteorological services and other national entities across the member states in Europe. Each satellite

application facility is expected to provide operational services to end-users. These services will include real-time and/or off-line product services, distribution of user software packages, and data management.

As an additional scientific payload, MSG carries a geostationary Earth radiation budget (GERB) instrument that observes the broadband thermal infrared and solar radiances exiting the Earth's atmosphere. The GERB instrument makes accurate measurements of the shortwave and longwave components of the radiation budget at the top of the atmosphere. GERB data are of interest to climatological studies and are not used for short-term weather forecasts. As the first radiation budget experiment from geostationary orbit, the GERB instrument has great potential to shed new light on climatic processes related to clouds and water vapour. In particular, simultaneous observations with SEVIRI and GERB will reveal unknown physical elements of the process of deep convection (e.g. in the tropics) and its influence on the radiation budget.

The application of the second generation of Meteosat satellites ranges from short-term forecasting to numerical weather prediction and climatological studies. The most important products for numerical weather prediction are the wind fields derived from tracking the displacement of clouds and water vapour in successive satellite images, and the spectral radiances themselves. Both winds and radiances are assimilated into the numerical computer models that compute the change of the atmosphere in the future and provide the basis for weather forecasts.

The improved depiction of the atmospheric state at a given point in time helps to achieve a more accurate forecast, especially a more accurate short-term forecast.. In addition, climatological research studies can be performed using the multi-spectral information.

MSG-1 was launched in August 2002 into a geostationary transfer orbit with excellent accuracy, and therefore the satellite can operate for its expected lifetime. By mid-September, the first MSG satellite had reached its preliminary position at 10 degrees west where the check-out, or commissioning, will be performed. Meanwhile, Meteosat-7 continues its operational role at the nominal 0 degrees longitude, which will be assigned to MSG when the commissioning has been successfully completed.

Figure 4 shows one of the first images taken with MSG-1. A false-colour image has been constructed by assigning the 0.6 micrometres (μm) channel to blue, 0.8 μm channel to green and the near-infrared channel at 1.6 μm to red. The most striking feature of the image is the blue-coloured clouds. These clouds consist of ice particles which are clearly depicted because ice particles reflect less solar radiation at a wavelength of 1.6 μm than clouds consisting of water droplets.

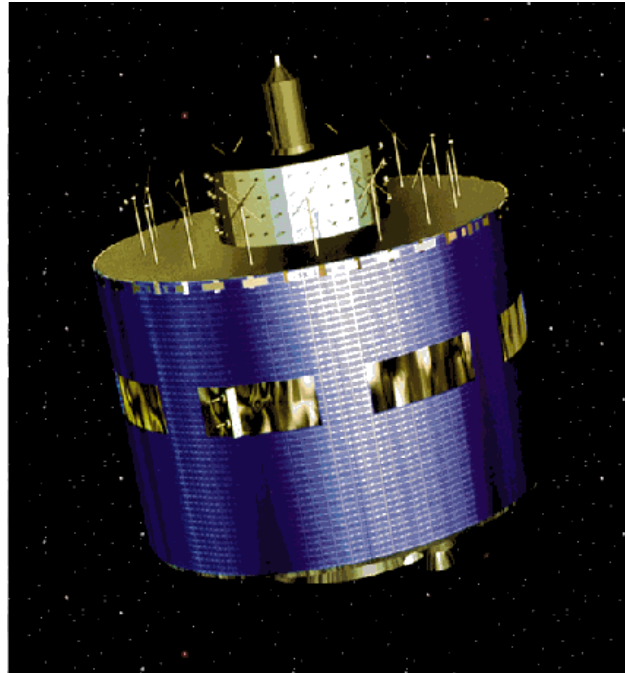
As MSG is a completely new satellite, the period for commissioning is longer than the typical six-month period, and operational service is not anticipated before autumn 2003. A limited trial of image

data involving calibration and product dissemination will begin in spring 2003 followed by a more extensive test dissemination in summer 2003. MSG-1 will be renamed Meteosat-8 after image dissemination commences. A continued parallel operation with Meteosat-7 is foreseen until the end of 2005.

In conclusion, MSG continues the successful 25-year long mission of the first-generation Meteosat satellites. The established services from the first-generation satellites will ensure a seamless operational transfer. In addition, Meteosat-8 and its successors offer a wealth of new observational capabilities which will benefit weather forecasting and will improve severe weather warning. Significant indirect benefits will come through improved weather forecasts that predict wind fields more accurately.

caption for Figure 1:

Figure 1. The first MSG satellite was launched in August 2002



caption for Figure 2:

Figure 2. Coverage area of 12-channel imager when satellite is in its nominal position at 0 degrees longitude. The full disk image has 3,712 x 3,712 pixels. The high resolution visible channel image (right panel) covers only half of the Earth in an east-west direction with 11,136 x 5,568 pixels, however the area of imaging can be selected.



caption for Figure 3:

Figure 3

Figure 3a. MSG SEVIRI spectral response functions for the solar channels plotted with the spectral reflectance of vegetation (green) and bare soil (brown) and the spectral irradiance at the top of the atmosphere (red).

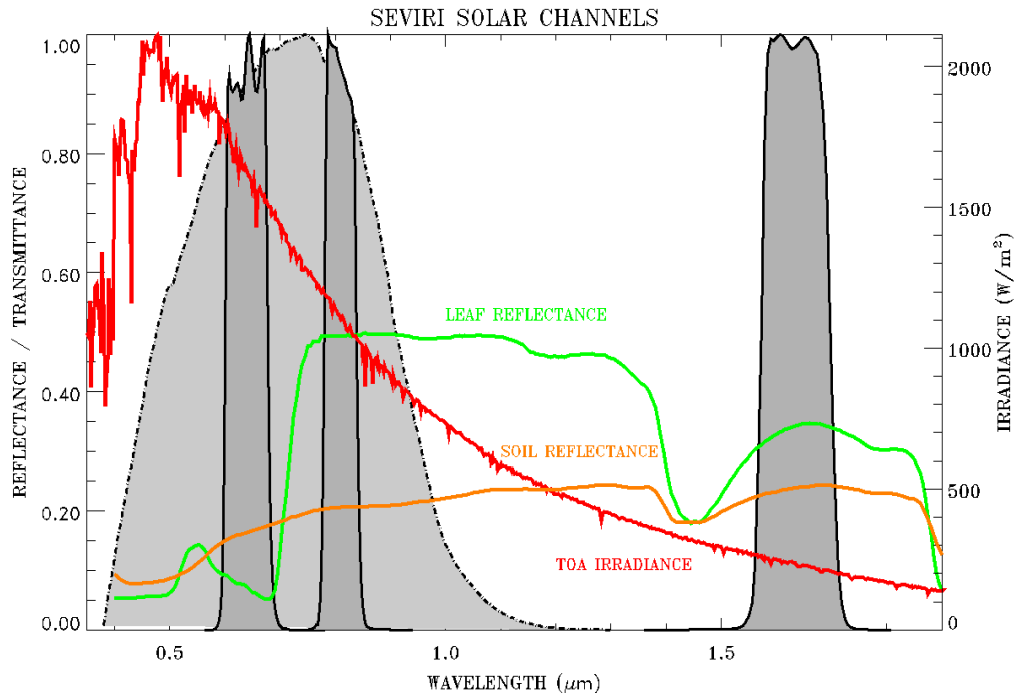


Figure 3b. Thermal terrestrial spectrum and MSG SEVIRI spectral response functions for the thermal

channels.

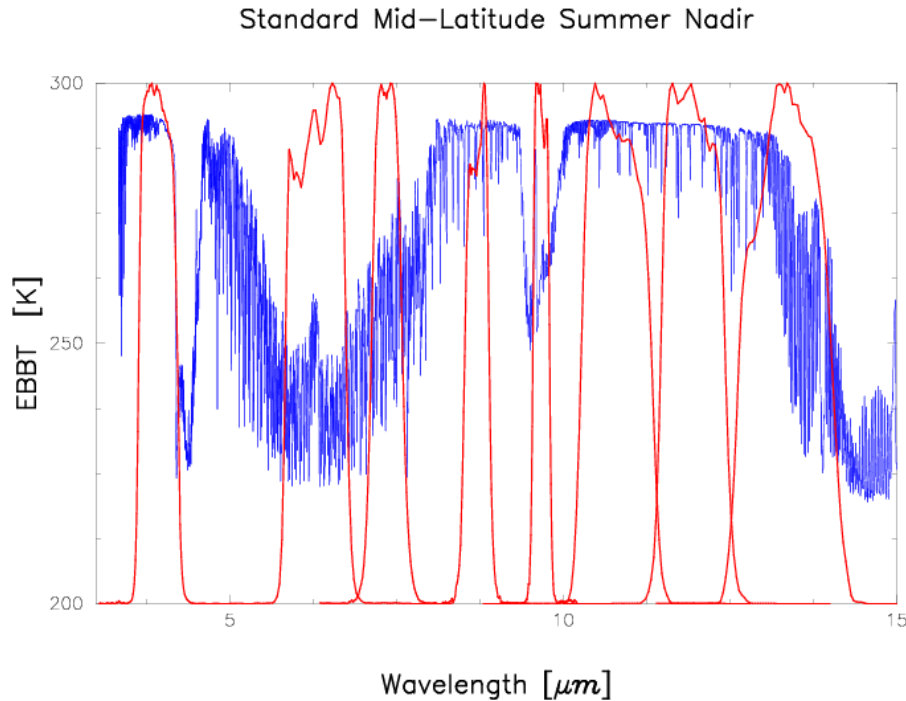


Figure 3c. Weighting functions for the MSG SEVIRI thermal channels, i.e. channels 4 to 11, for a satellite nadir view. A mid-latitude summer standard atmosphere has been assumed for the simulation with a radiative transfer model.

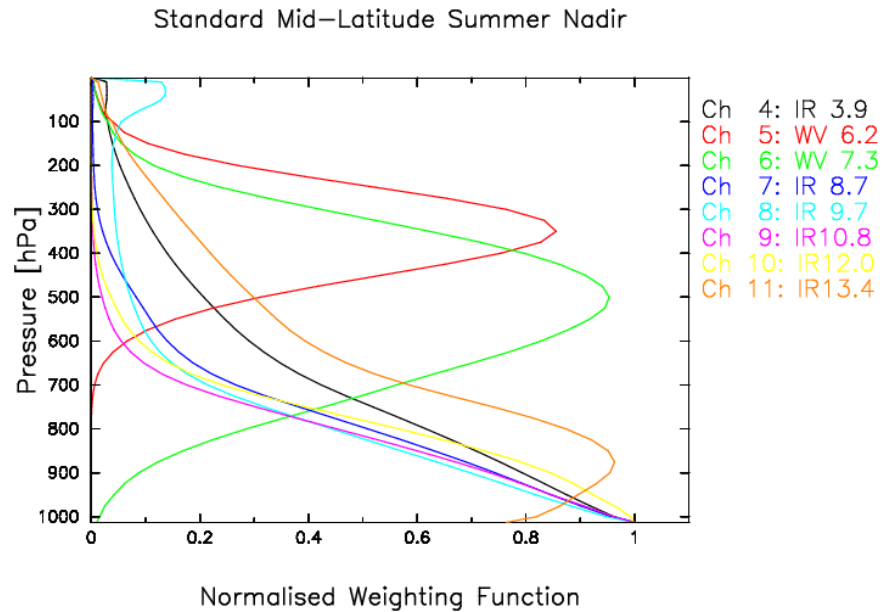
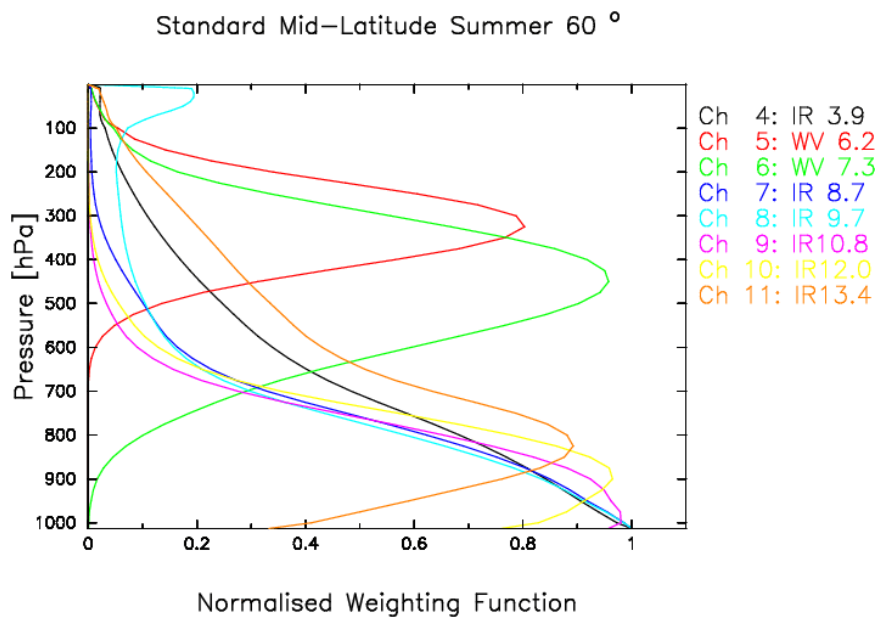


Figure 3d. As for Figure 3c except that the satellite viewing angle is 60°.



caption for Figure 4:

Figure 4. An image from the first of the MSG satellites. Three spectral channels (at 0.6, 0.8 and 1.6 μm) are assigned to blue, green and red, respectively. Ice clouds appear in blue because these clouds reflect less solar radiation at 1.6 μm than clouds made of water.

